

---

Emma J. Stone

**The Impact of Vegetation Feedbacks  
on the Evolution of the Greenland  
Ice-sheet under Future and Past  
Climates**

---

A dissertation submitted to the University of Bristol in  
accordance with the requirements of the degree of Doctor of  
Philosophy in the Faculty of Science.  
School of Geographical Sciences, July 2010

Word Count: 76,000



# Abstract

The importance of vegetation feedbacks for ice-sheet evolution has largely been neglected from previous studies but could be important in realistically modelling the past and future evolution of the Greenland ice-sheet (GrIS). Firstly, regrowth of the GrIS after complete melting under preindustrial CO<sub>2</sub> concentrations (280 ppmv) is modelled. The coupled atmosphere-ocean model, HadCM3, is used to assess the response of the climate when the GrIS is replaced with bare soil and five fixed vegetation types and a rebounded orography. Summer temperature changes relative to preindustrial are largest for trees and smallest for bare soil. Winter temperature changes are controlled by the altitude decrease and changes in atmospheric circulation while summer changes are dominated by the snow-vegetation-climate feedback. HadCM3 includes a coupled vegetation model, TRIFFID. The ice-free Greenland climate supports a mixture of shrubs and grasses in central Greenland and bare soil on the eastern mountain range. Vegetation enhances precipitation rates during the summer while orographic enhancement accounts for increases during the winter.

The Glimmer ice-sheet model is evaluated for new present-day boundary conditions and forcings where model parameters are tuned using Latin Hypercube Sampling, producing a range of experiments that accurately predict the GrIS. This parametric uncertainty is used to assess GrIS evolution. Only fixed bare soil results in significant regrowth. Interactive vegetation predicts small ice-caps in eastern Greenland indicating bistable behaviour of the GrIS under a preindustrial climate.

Finally, the models are tested by simulating the Last Interglacial (~130 to 116 thousand years ago (ka)); a time when the Arctic was significantly warmer and sea-level several metres higher than today. The importance of vegetation growth (neglected by previous studies) on the minimum extent of the GrIS is assessed. To overcome computational expense for long time integrations, Glimmer simulates (with and without vegetation feedbacks) the ice-sheet extent from 130ka to 120ka using climate linearly interpolated and weighted (no ice versus full ice) between several snapshots. Due to the uncertainty in palaeodata, however, it is not possible to conclude that vegetation feedbacks are an important missing feedback.



# Acknowledgements

Firstly, thank you to my supervisor Dan Lunt for all the encouragement and good advice he has given me over the last three and half years and devising such an enjoyable project. I have very much enjoyed our discussions at our weekly meetings. I must also thank my other supervisor Paul Valdes, for his enthusiasm and for ensuring continued progress and direction of the thesis. I am also grateful to both for allowing me to attend many International conferences and summer schools, which have been an invaluable experience. This thesis was funded by a NERC studentship.

Thanks also to my Progress Panel, Tony Payne and Andy Ridgwell, who have provided helpful discussions and advice. Thank you to Gethin Williams and Greg Tourte for answering many computing queries and solving any glitches that I have encountered on the way. Thanks also to the computer officers, Ed Thomas and Duncan Baldwin who continued to make sure my PC ran smoothly over the duration of the PhD. Further thanks to the post-docs Jenny Griggs and Rupert Gladstone for their help on Greenland data and TRIFFID simulations respectively.

Outside of Bristol, I am also grateful to Ian Rutt for never failing to answer my Glimmer questions and solving several fortran problems. I must also thank Edward Hanna for providing temperature data for Greenland so promptly and helpfully.

There are too many postgraduates to thank personally but I wish to name a few. Thanks to Sarah Shannon for helpful computing discussions and for the fun times in Vienna at EGU. Also thank you to Andy Sole and Anne LeBrocq for the fantastic three week roadtrip trip to the Karthaus ice-sheet summer school in Italy. Finally, thank you to Lauren Gregoire for her excellent knowledge of climate modelling and unix (and also for getting me to San Francisco!).

Neil, I thank you for all your help and support over the last three years, it's been great sharing the PhD experience together. As promised I also acknowledge your help with matlab figures for which I am truly grateful!

Finally, thanks go to my mum and dad for the continuous support that they have given me over the last nine years of University education; without them it would not have been possible.



# Author's Declaration

I declare that the work in this dissertation was carried out in accordance with the Regulations of the University of Bristol. The work is original, except where indicated by special reference in the text, and no part of the dissertation has been submitted for any other academic award. Any views expressed in the dissertation are those of the author.

SIGNED: ..... DATE:.....





# Contents

|  |              |
|--|--------------|
| <b>List of Figures</b>   | <b>xiii</b>  |
| <b>List of Tables</b>  | <b>xxiii</b> |
| <b>Variables, constants &amp; abbreviations</b>  | <b>xxv</b>   |
| <b>Chapter 1 : Introduction</b>  | <b>1</b>     |
| 1.1 Significance . . . . .   | 1            |
| 1.2 An introduction to Greenland . . . . .   | 2            |
| 1.3 Feedback processes in the climate - vegetation - ice-sheet system . .                      | 6            |
| 1.3.1 Ice-albedo feedback . . . . .  | 7            |
| 1.3.2 Vegetation-snow-climate feedback . . . . .   | 7            |
| 1.3.3 Ice-elevation feedback . . . . .   | 12           |
| 1.4 Future Greenland ice-sheet behaviour . . . . .   | 13           |
| 1.4.1 Future melting of the Greenland ice-sheet . . . . .                                      | 13           |
| 1.4.2 Future regrowth of the Greenland ice-sheet . . . . .                                     | 17           |
| 1.5 The state of the Greenland ice-sheet during the Last Interglacial . .                      | 20           |
| 1.5.1 Climate, sea-level and vegetation during the Last Interglacial                           | 20           |
| 1.5.2 Mechanisms for high latitude warming at the Last Interglacial                            | 24           |
| 1.5.3 The evidence for a reduced Greenland ice-sheet during the<br>Last Interglacial . . . . . | 28           |
| 1.6 Aims and objectives . . . . .  | 36           |
| 1.7 Thesis structure . . . . .   | 38           |
| <b>Chapter 2 : The ice-sheet model</b>   | <b>41</b>    |
| 2.1 Introduction . . . . .   | 41           |
| 2.2 Model description . . . . .  | 42           |
| 2.2.1 Model numerics within GLIDE . . . . .  | 45           |
| 2.2.2 Forcing Glimmer with climate . . . . .   | 50           |
| 2.3 The datasets . . . . .   | 52           |

|       |   |    |
|-------|---|----|
| 2.3.1 | EISMINT intercomparison experimental design . . . . .     | 52 |
| 2.3.2 | Recent boundary conditions/forcings . . . . .             | 53 |
| 2.4   | Sensitivity to boundary conditions and forcings . . . . . | 55 |
| 2.4.1 | Bedrock and ice thickness . . . . .                       | 56 |
| 2.4.2 | Precipitation . . . . .                                   | 58 |
| 2.4.3 | Temperature . . . . .                                     | 60 |
| 2.4.4 | Summary . . . . .   | 62 |
| 2.5   | Tuning . . . . .  | 63 |
| 2.5.1 | Tuning methodology . . . . .                              | 63 |
| 2.5.2 | Sensitivity to tuning parameters . . . . .                | 67 |
| 2.5.3 | Selecting the optimal parameter set . . . . .             | 72 |
| 2.6   | Discussion and conclusions . . . . .                      | 75 |

### **Chapter 3 : The response of the climate to a melted Greenland ice-sheet** **79**

|       |  |     |
|-------|--|-----|
| 3.1   | Introduction . . . . .   | 79  |
| 3.2   | The Hadley Centre climate model . . . . .  | 80  |
| 3.2.1 | Atmosphere . . . . .   | 80  |
| 3.2.2 | Ocean . . . . .  | 81  |
| 3.2.3 | Land surface scheme . . . . .  | 82  |
| 3.2.4 | Orographic boundary conditions . . . . .   | 90  |
| 3.3   | Climatic sensitivity to surface type and orography over Greenland .                  | 94  |
| 3.3.1 | Experimental setup . . . . .   | 94  |
| 3.3.2 | Climate model evaluation . . . . .   | 99  |
| 3.3.3 | Climatic sensitivity to surface characteristics over an ice-free Greenland . . . . . | 106 |
| 3.3.4 | Climatic sensitivity to elevation change over Greenland . . .                        | 129 |
| 3.3.5 | The impact on climate from a Greenland ice-sheet deglaciation                        | 137 |
| 3.4   | Discussion and conclusions . . . . .   | 156 |

### **Chapter 4 : The response of vegetation to a melted Greenland ice-sheet** **159**

|     |   |     |
|-----|---|-----|
| 4.1 | Introduction . . . . .                                | 159 |
| 4.2 | Vegetation model description and evaluation . . . . . | 160 |

|       |  |     |
|-------|--|-----|
| 4.2.1 | Coupling to the land surface scheme, MOSES 2 . . . . .                     | 162 |
| 4.2.2 | Vegetation dynamics . . . . .  | 163 |
| 4.2.3 | Leaf phenology . . . . .   | 165 |
| 4.2.4 | Soil carbon storage . . . . .  | 165 |
| 4.2.5 | Updating biophysical parameters . . . . .                                  | 165 |
| 4.2.6 | Spinning up TRIFFID . . . . .  | 166 |
| 4.2.7 | Model evaluation . . . . .   | 167 |
| 4.3   | The influence of interactive vegetation on the climate of a melted GrIS178 |     |
| 4.4   | Discussion and conclusions . . . . .                                       | 194 |

**Chapter 5 : The response of a dynamic ice-sheet model to the climate  
of a melted Greenland ice-sheet** **199**

|       |   |     |
|-------|---|-----|
| 5.1   | Introduction . . . . .  | 199 |
| 5.2   | Ice-sheet regrowth over a melted, rebounded Greenland . . . . . | 200 |
| 5.2.1 | Forcing methodology . . . . .                                   | 202 |
| 5.2.2 | Fixed vegetation climate simulations . . . . .                  | 204 |
| 5.2.3 | Interactive vegetation climate simulations . . . . .            | 218 |
| 5.3   | Discussions and conclusions . . . . .                           | 223 |

**Chapter 6 : Modelling the impact of vegetation feedbacks on the  
minimum extent of the GrIS during the Last Interglacial** **229**

|       |   |     |
|-------|---|-----|
| 6.1   | Introduction . . . . .                                  | 229 |
| 6.2   | Experimental methodology . . . . .                      | 230 |
| 6.2.1 | Climate model boundary conditions . . . . .             | 231 |
| 6.3   | The climate of the LIG . . . . .                        | 234 |
| 6.3.1 | Temperature changes during the LIG . . . . .            | 234 |
| 6.3.2 | Hydrological changes during the LIG . . . . .           | 238 |
| 6.3.3 | Changes in vegetation during the LIG . . . . .          | 240 |
| 6.3.4 | Sea-ice changes during the LIG . . . . .                | 244 |
| 6.4   | The minimum extent of the GrIS during the LIG . . . . . | 246 |
| 6.4.1 | Offline forcing with a 130ka climatology . . . . .      | 247 |
| 6.4.2 | Transient forcing of the GrIS during the LIG . . . . .  | 250 |
| 6.5   | Discussion and conclusions . . . . .                    | 267 |

---

|  |                |
|--|----------------|
| <b>Chapter 7 : Conclusions</b>   | <b>273</b>     |
| 7.1 Summary of results and principal findings . . . . .  | 273            |
| 7.1.1 Evaluation of the Glimmer ice-sheet model . . . . .  | 273            |
| 7.1.2 Climatic sensitivity to surface type and altitude change over<br>a melted GrIS . . . . .   | 274            |
| 7.1.3 Response of an ice-free Greenland climate to interactive vege-<br>tation . . . . .   | 275            |
| 7.1.4 Potential regrowth of the GrIS forcing Glimmer offline . . . . .   | 276            |
| 7.1.5 The response of the GrIS to climate - vegetation - ice-sheet<br>interactions during the LIG . . . . .  | 278            |
| 7.2 Future work . . . . .  | 279            |
| 7.2.1 Extending the future GrIS regrowth modelling . . . . .   | 279            |
| 7.2.2 Extending the LIG modelling . . . . .  | 281            |
| 7.2.3 Other modelling studies . . . . .  | 282            |
| <br><b>Appendix A : Synergy between altitude and surface type change in<br/>          terms of precipitation</b>   | <br><b>285</b> |
| <br><b>Appendix B : Temperature and precipitation anomalies for needle-<br/>          leaf:<sub>zo</sub><sup>nl</sup> and needleleaf:<sub>zo</sub><sup>ice</sup></b> | <br><b>287</b> |
| <br><b>Appendix C : Diagnostics for GrIS regrowth</b>  | <br><b>289</b> |
| <br><b>Appendix D : The effect of the weighting function on LIG ice-sheet<br/>          evolution</b>  | <br><b>291</b> |
| <br><b>Bibliography</b>  | <br><b>292</b> |

# List of Figures

|      |   |    |
|------|---|----|
| 1.1  | The present day state of the Greenland ice-sheet. . . . .   | 3  |
| 1.2  | Diagram of ice-albedo and vegetation-snow-climate feedback loops for a warming Arctic climate. . . . .  | 8  |
| 1.3  | Interactions between land and atmosphere for the surface energy budget. . . . .   | 9  |
| 1.4  | Diagram of the ice-elevation feedback mechanism. . . . .  | 12 |
| 1.5  | Summary of Greenland deglaciation studies. . . . .  | 17 |
| 1.6  | Time series of climate variation over the last 400,000 years from the Vostok ice core, Antarctica. . . . .  | 21 |
| 1.7  | Time-series of sea-level change over the last 800,000 years. . . . .  | 22 |
| 1.8  | Estimates of the Last Interglacial sea-level curve and GrIS contribution. . . . .   | 24 |
| 1.9  | Illustration of orbital parameters which alter the climate according to Milankovitch Theory. . . . .  | 25 |
| 1.10 | Latitudinal variation of Last Interglacial insolation anomalies. . . . .  | 27 |
| 1.11 | Locations of the deep ice core drilling sites on the GrIS. . . . .  | 29 |
| 2.1  | The interaction between two regularly staggered horizontal grids used to solve ice equations in Glimmer. . . . .  | 45 |
| 2.2  | Vertical scaling of the ice-sheet model. . . . .  | 47 |
| 2.3  | Coupling between the global climate forcing and the core of Glimmer, GLIDE, using the interface GLINT. . . . .  | 51 |
| 2.4  | Evolution of modelled ice-sheet (a) volume and (b) ice surface extent for different boundary conditions and forcings. . . . .                               | 57 |
| 2.5  | Comparison between Bamber and Letreguilly bedrock and ice thickness datasets at 20 km resolution. . . . .   | 58 |
| 2.6  | Change in precipitation over Greenland between EISMINT-3 and ERA-40 re-analysis datasets. . . . .   | 59 |
| 2.7  | Sensitivity to different temperature forcings for the GrIS: near-surface air temperature over Greenland at the beginning and end of the simulation. . . . . | 60 |

---

|      |  |     |
|------|--|-----|
| 2.8  | Sensitivity to different temperature forcings for the GrIS: net surface mass balance over Greenland at the beginning and end of the simulation.  | 61  |
| 2.9  | Distribution of 250 experiments produced by Latin-Hypercube Sampling.  | 67  |
| 2.10 | Sensitivity of three diagnostics describing the response of ice-sheet geometry to the five selected tuneable parameters.   | 69  |
| 2.11 | Ranking of LHS experiments for each diagnostic skill score.  | 71  |
| 2.12 | The distribution of each parameter for the eight experiments selected according to ranking of the different diagnostics: ice volume, ice surface extent and maximum ice thickness.   | 72  |
| 2.13 | Normalised star plots showing the relative measure of skill for each diagnostic.   | 73  |
| 2.14 | Ice-sheet configurations for (a) observed present day GrIS (from Bamber <i>et al.</i> (2001)) and (b) to (f) configurations for the five selected experiments.   | 75  |
| 3.1  | Schematic of the MOSES 2 land surface scheme.  | 86  |
| 3.2  | Evolution of the maximum Atlantic meridional overturning circulation stream function at 30°N for the preindustrial HadCM3 MOSES 2 control.   | 95  |
| 3.3  | Greenland orographic height with and without the Greenland ice-sheet.  | 96  |
| 3.4  | HadCM3 surface type mask over Greenland.   | 97  |
| 3.5  | Shaded sections over Greenland define five regions for analysis.   | 99  |
| 3.6  | Annual, winter and summer near-surface temperature error for (a) to (c) HadCM3, MOSES 2 control minus Hanna <i>et al.</i> (2005) temperature observations and (d) to (f) HadCM3, MOSES 2 preindustrial control minus AVHRR APP-x satellite observations. | 100 |
| 3.7  | Multi-model root-mean-square error for simulated surface temperature compared with observed annual mean.   | 103 |
| 3.8  | Precipitation error for HadCM3 compared with ERA-40 precipitation and other versions of the HadCM3 model.  | 104 |
| 3.9  | Near-surface temperature anomalies for noGrIS <sub>mod</sub> simulations minus preindustrial control.  | 107 |

---

|      |   |     |
|------|---|-----|
| 3.10 | Average surface albedo over Greenland during winter and summer months for the preindustrial control, and noGrIS <sub>mod</sub> simulations. . .   | 109 |
| 3.11 | Annual cycle of surface heat fluxes averaged over all of Greenland for the control and noGrIS <sub>mod</sub> simulations. . . . .   | 110 |
| 3.12 | Regional cumulative mass balance for noGrIS <sub>mod</sub> simulations. . . . .   | 113 |
| 3.13 | Average February snow cover over Greenland for the control and noGrIS <sub>mod</sub> simulations. . . . .   | 114 |
| 3.14 | Average August snow cover over Greenland for the control and noGrIS <sub>mod</sub> simulations. . . . .   | 115 |
| 3.15 | Wind speed and direction on pressure level 3 in HadCM3 (equivalent to 850 hPa over a surface at sea-level) for winter and summer months for the control and noGrIS <sub>mod</sub> simulations. Also shown by the filled contours is the surface sea-level pressure in hPa. . . . .  | 117 |
| 3.16 | Difference in wind speed and direction on pressure level 3 in HadCM3 (equivalent to 850 hPa over a surface at sea-level) for winter and summer months between noGrIS <sub>mod</sub> experiment and the preindustrial control. Also shown by the filled contours is the difference in surface sea-level pressure in hPa. . . . . | 118 |
| 3.17 | Total precipitation rate (snowfall and rainfall) for noGrIS <sub>mod</sub> simulations minus preindustrial control. . . . .   | 120 |
| 3.18 | The fractional change in sea-ice cover for the winter and summer months for noGrIS <sub>mod</sub> simulations minus preindustrial control. . . .  | 122 |
| 3.19 | Temperature and precipitation sensitivity to surface roughness length, $z_0$ , over Greenland. . . . .  | 124 |
| 3.20 | Annual cycle of surface heat fluxes (in $\text{W m}^{-2}$ ) averaged over all of Greenland for the preindustrial control, noGrIS needleleaf: $z_0^{nl}$ with rebounded orography and needleleaf: $z_0^{ice}$ also with rebounded orography. . . . .   | 126 |
| 3.21 | Near-surface temperature and precipitation anomalies over Greenland and the surrounding Arctic for lowGrIS minus preindustrial control. . . .   | 130 |
| 3.22 | Near-surface temperature and differences over Greenland and the surrounding Arctic for calculated lapse rate temperature, and lowGrIS. . . .  | 131 |

---

|      |  |     |
|------|--|-----|
| 3.23 | 850 hPa wind speed and direction anomalies over Greenland and the surrounding Arctic for the lowGrIS simulation. . . . .   | 132 |
| 3.24 | The mean winter 500 hPa geopotential height difference and the 500-1000 hPa thickness minus zonal mean in metres, control minus low-GrIS compared with Petersen <i>et al.</i> (2004). . . . .                              | 134 |
| 3.25 | Near-surface surface temperature anomalies (in °C) for noGrIS <sub>reb</sub> simulations minus preindustrial control. . . . .  | 138 |
| 3.26 | Near-surface temperature change over the Northern Hemisphere for the summer and winter months. <i>Left</i> : bare soil minus preindustrial control and <i>Right</i> : needleleaf tree minus preindustrial control. . . . . | 141 |
| 3.27 | Annual cycle of heat fluxes averaged over all of Greenland for the control and noGrIS <sub>reb</sub> simulations. . . . .  | 142 |
| 3.28 | Total precipitation rate (snowfall and rainfall) for noGrIS <sub>reb</sub> simulations minus control. . . . .  | 145 |
| 3.29 | Annual hydrological cycle for five regions over Greenland for the noGrIS <sub>reb</sub> simulations. . . . .   | 147 |
| 3.30 | Cumulative mass balance for North, South, East, West and Central Greenland for all noGrIS <sub>reb</sub> simulations. . . . .  | 149 |
| 3.31 | Average February snow cover over Greenland for the control and noGrIS <sub>reb</sub> simulations. . . . .  | 150 |
| 3.32 | Average August snow cover over Greenland for the control and noGrIS <sub>reb</sub> simulations. . . . .  | 151 |
| 3.33 | Winds at pressure level 3 in HadCM3 corresponding to 850 hPa over a surface at sea-level. . . . .  | 153 |
| 3.34 | The fractional change in sea-ice cover for the winter and summer months for noGrIS <sub>reb</sub> bare soil and needleleaf tree simulations minus preindustrial control. . . . .   | 155 |
| 4.1  | Schematic illustrating the flow of carbon for each vegetation type in the TRIFFID vegetation model. . . . .  | 162 |
| 4.2  | Schematic illustrating the coupling between TRIFFID and HadCM3. . . . .  | 163 |
| 4.3  | Comparison of modelled vegetation fractions with the IGBP-DIS land cover satellite observations (Betts <i>et al.</i> , 2004). . . . .  | 167 |



---

|      |   |     |
|------|---|-----|
| 4.4  | The average annual fractional coverage of the PFTs and bare soil in the preindustrial control simulation using HadCM3 and TRIFFID in dynamic mode. . . . .  | 168 |
| 4.5  | The average annual fractional coverage of PFTs simulated by the HadCM3LC preindustrial control simulation of Betts <i>et al.</i> (2004). . .  | 169 |
| 4.6  | The annual tolerance of the PFTs in terms of near-surface air temperature and precipitation for all gridboxes. . . . .  | 170 |
| 4.7  | The average annual fractional coverage differences of PFTs and bare soil for the preindustrial control simulation minus initial condition. . .  | 172 |
| 4.8  | Global annual, winter and summer near-surface temperature error in HadCM3 MOSES 2 TRIFF compared with CRU climatology. . . . .  | 173 |
| 4.9  | Annual, winter and summer near-surface temperature error compared with observation and other Hadley Centre model versions. . . . .  | 174 |
| 4.10 | Annual, winter and summer surface precipitation error compared with observation and other Hadley Centre model versions. . . . .   | 177 |
| 4.11 | Spin-up of surface type for bare soil, C3 and C4 grasses, shrubs, broadleaf and needleleaf trees over Greenland using TRIFFID. . . . .  | 179 |
| 4.12 | Dominant vegetation and bare soil coverage over Greenland after running TRIFFID in equilibrium mode for 2,000 years (200 equivalent years for GCM run-time) followed by 200 years of TRIFFID in dynamic mode. . . . . | 181 |
| 4.13 | Average annual near-surface air temperature vs precipitation for all gridboxes (represented by black circles) over all of Greenland. . . . .  | 182 |
| 4.14 | Vegetation cover with a melted GrIS, simulated by ORCHIDEE, forced offline by a no ice-sheet climatology ( <i>from</i> Lunt <i>et al.</i> (2004)). . . . .  | 183 |
| 4.15 | Near-surface temperature anomaly (in °C) for TRIFFID noGrIS <sub>bsi</sub> simulation minus preindustrial control. . . . .  | 185 |
| 4.16 | Average surface albedo over Greenland during winter and summer months for (a) TRIFFID preindustrial control and (b) noGrIS <sub>bsi</sub> . . .   | 186 |
| 4.17 | Average summer heat flux anomalies for the noGrIS <sub>bsi</sub> TRIFFID climate. . . . .   | 188 |
| 4.18 | Total precipitation rate (snowfall and rainfall) for TRIFFID noGrIS <sub>bsi</sub> simulation minus preindustrial TRIFFID control. . . . .  | 189 |

---

|      |  |     |
|------|--|-----|
| 4.19 | Annual hydrological cycle for the five defined regions over Greenland for the preindustrial TRIFFID control and noGrIS <sub>bsi</sub> TRIFFID simulation. . . . .  | 190 |
| 4.20 | Average August and February snow cover over Greenland for the preindustrial TRIFFID control and noGrIS <sub>bsi</sub> simulations. . . . .   | 192 |
| 4.21 | Low-level atmospheric circulation patterns for the TRIFFID control and noGrIS <sub>bsi</sub> simulations. . . . .  | 193 |
| 5.1  | Transects of rebounded Greenland bedrock topography at 20 km resolution from the Letreguilly and Bamber datasets and the Letreguilly dataset interpolated to the HadCM3 resolution for the noGrIS simulations. . . . . | 201 |
| 5.2  | Evolution of ice-sheet volume when Glimmer is forced with <i>fixed</i> surface type noGrIS <sub>reb</sub> climatologies. . . . .   | 205 |
| 5.3  | Evolution of ice surface extent when Glimmer is forced with <i>fixed</i> surface type noGrIS <sub>reb</sub> climatologies. . . . .   | 206 |
| 5.4  | Ice-sheet geometries after 50,000 years of simulation for the noGrIS <sub>reb</sub> <i>fixed</i> vegetation climatologies. . . . .   | 208 |
| 5.5  | Snapshots through time of GrIS extent when Glimmer is forced offline with a fixed bare soil noGrIS <sub>reb</sub> climatology. . . . .   | 209 |
| 5.6  | Annual accumulation over Greenland when Glimmer is forced with noGrIS <sub>reb</sub> climatologies with the different fixed surface types. . . . .   | 210 |
| 5.7  | Evolution of summer surface temperature and annual mass balance when Glimmer is forced with a bare soil noGrIS <sub>reb</sub> climatology. . . . .   | 212 |
| 5.8  | Evolution of summer surface temperature and mass balance when Glimmer is forced with noGrIS <sub>reb</sub> fixed needleleaf climatology. . . . .   | 213 |
| 5.9  | Combined figure of ice-sheet extent for all the different Glimmer model parameter sets and comparison with minimum snow cover for all fixed vegetation noGrIS <sub>reb</sub> climates. . . . .                         | 216 |
| 5.10 | Evolution of ice-sheet volume when Glimmer is forced with <i>interactive</i> noGrIS climate simulations. . . . .   | 218 |
| 5.11 | Evolution of ice surface extent when Glimmer is forced with <i>interactive</i> vegetation noGrIS climate simulations. . . . .  | 219 |

---

|      |   |     |
|------|---|-----|
| 5.12 | Ice-sheet geometries after 50,000 years of simulation for the noGrIS <i>interactive</i> vegetation climatologies with rebounded bedrock. . . . .  | 220 |
| 5.13 | Annual accumulation over Greenland when Glimmer is forced with noGrIS <sub>bsi</sub> and noGrIS <sub>nli</sub> climatologies with interactive vegetation. . . . .                       | 222 |
| 5.14 | Evolution of summer surface temperature and annual mass balance when Glimmer is forced with an interactive vegetation noGrIS <sub>bsi</sub> climatology. . . . .                        | 223 |
| 5.15 | Prediction of ice regrowth on a ice-free Greenland from previous modelling studies. . . . .   | 225 |
| 6.1  | Timeseries of insolation and CO <sub>2</sub> concentration during the LIG. . . . .  | 232 |
| 6.2  | Summer near-surface temperature change over Greenland and the surrounding region for the LIG compared with preindustrial. . . . .   | 235 |
| 6.3  | Near-surface summer temperature anomaly for the three time snapshots: 130, 125 and 120ka. . . . .   | 236 |
| 6.4  | Annual precipitation rate anomalies relative to preindustrial for the three time snapshots: 130, 125 and 120ka. . . . .   | 239 |
| 6.5  | Global dominant vegetation coverage after running TRIFFID in equilibrium mode for 1,000 years (100 equivalent years for GCM run-time) at 130, 125 and 120ka. . . . .                    | 241 |
| 6.6  | Annual average vegetation dominance fraction for the land surface between 60 to 90°N through the LIG when TRIFFID is in equilibrium mode and the GrIS is present. . . . .               | 242 |
| 6.7  | Dominant vegetation coverage over the Greenland region after running TRIFFID in equilibrium mode for 1,000 years (100 equivalent years for GCM run-time) at 130, 125 and 120ka. . . . . | 243 |
| 6.8  | Average summer sea-ice concentrations (0-1) during the LIG for the Arctic region. . . . .   | 245 |
| 6.9  | Ice volume, equivalent sea-level height and ice surface extent when Glimmer is forced offline with a 130ka fixed vegetation HadCM3 climate. . . . .                                     | 249 |
| 6.10 | Diagram illustrating the coupling methodology between climate and ice-sheet for the LIG. . . . .  | 251 |

---

|      |  |     |
|------|--|-----|
| 6.11 | Evolution of GrIS volume from 136 to 120ka using the coupling methodology when Glimmer is setup in EISMINT-3 mode. . . . .   | 254 |
| 6.12 | Ice volume and equivalent sea-level height through the LIG for the Glimmer EISMINT-3 and tuned parameter sets for initial conditions (a) modern day spun-up GrIS and (b) 136ka spun-up GrIS. . . . .   | 255 |
| 6.13 | The total icefield ablation area over Greenland for GrIS <sub>mod</sub> from 136 to 120ka (in km <sup>2</sup> ) for (a) fixed vegetation and (b) interactive vegetation. . . . .   | 258 |
| 6.14 | Minimum simulated ice thickness and extent of the GrIS during the LIG initiated from a modern spun-up and a 136ka spun-up equilibrium GrIS forced with <i>fixed</i> vegetation climatologies. . . . .  | 260 |
| 6.15 | Minimum simulated ice thickness and extent of the GrIS during the LIG initiated from a modern spun-up and a 136ka spun-up equilibrium GrIS forced with <i>interactive</i> vegetation climatologies. . . . .  | 262 |
| 6.16 | Comparison between ice volume evolution when the model is initiated with a spun-up modern GrIS with and without the weighting function included in the coupling methodology (i.e. without weighting function Glimmer is forced only with the GrIS present climatologies) for EISMINT-3 and Glimmer tuned parameter sets. . . . . | 263 |
| 6.17 | Minimum simulated ice thickness and extent of the GrIS during the LIG initiated from a modern day spun-up equilibrium GrIS forced with (a) the <i>fixed</i> vegetation climatologies and (b) the <i>interactive</i> vegetation climatologies, with the GrIS present and no weighting function included. . . . .                  | 265 |
| 7.1  | Diagram showing the asynchronous coupling between climate model and ice-sheet model where forcing corresponds to orbits and CO <sub>2</sub> concentration for the LIG. . . . .   | 282 |
| B.1  | Near-surface average annual, winter and summer temperature anomalies (in °C) for the noGrIS <sub>reb</sub> experiments (a) needleleaf: <sub>z0</sub> <sup>nl</sup> minus control and (b) needleleaf: <sub>z0</sub> <sup>ice</sup> minus control. . . . .   | 287 |
| B.2  | Near-surface average annual, winter and summer precipitation anomalies (in mm day <sup>-1</sup> ) for the noGrIS <sub>reb</sub> experiments (a) needleleaf: <sub>z0</sub> <sup>nl</sup> minus control and (b) needleleaf: <sub>z0</sub> <sup>ice</sup> minus control. . . . .  | 288 |

---

|   |     |
|---|-----|
| D.1 Comparison between ice volume evolution when the model is initiated with a spun-up 136ka GrIS with and without the weighting function included (i.e. without weighting function Glimmer is forced only with the GrIS present climatologies) for EISMINT-3 and Glimmer tuned setups. . . . . | 291 |
|---|-----|



# List of Tables

|     |  |     |
|-----|--|-----|
| 1.1 | Summary of studies investigating the extent of the GrIS during the Last Interglacial. . . . .  | 33  |
| 2.1 | List of default parameters and physical constants used in Glimmer. .   | 43  |
| 2.2 | Glimmer experiments performed to investigate the response of the GrIS to present day boundary conditions and forcings. . . . .   | 56  |
| 2.3 | Summary of the relative difference between updated boundary condition/forcing and the EISMINT-3 datasets. . . . .  | 62  |
| 2.4 | List of five parameters varied according to the ranges determined from the literature. . . . .   | 65  |
| 2.5 | Tuned parameter values for the five optimal experiments chosen according to diagnostic skill score. . . . .  | 74  |
| 3.1 | Table showing the value of Leaf Area Index of each MOSES 2 Plant Functional Type for a characteristic IGBP class ( <i>from</i> Jones (2004)).  | 83  |
| 3.2 | Albedo parameters for vegetation types ( <i>from</i> Essery <i>et al.</i> (2001)). .   | 85  |
| 3.3 | Table showing the calculated soil parameters for the three Wilson and Henderson-Sellers soil textural classes. . . . .   | 89  |
| 3.4 | Concentrations of greenhouse gases for the preindustrial control used in HadCM3 MOSES 2. . . . .   | 96  |
| 3.5 | Mean difference and mean absolute error for near-surface temperature (in °C) for HadCM3 MOSES 2 preindustrial used in this thesis, compared with observations and other model versions of the Hadley Centre model. . . . . | 101 |
| 3.6 | Near-surface average temperature anomaly over Greenland for noGrIS <sub>mod</sub> simulations minus preindustrial control. . . . .   | 106 |
| 3.7 | Average Greenland surface albedo when Greenland is replaced with bare soil and each of the PFTs and orography is modern. . . . .   | 108 |

---

|     |  |     |
|-----|--|-----|
| 3.8 | Near-surface average temperature anomaly over Greenland for noGrIS <sub>reb</sub> simulations minus preindustrial control. . . . .   | 139 |
| 3.9 | Synergy between the near-surface temperature response from change in elevation and snow-vegetation-climate feedback. . . . .   | 143 |
| 4.1 | Intraspecies competition between the PFTs in TRIFFID. . . . .  | 165 |
| 4.2 | Mean difference and mean absolute error for near-surface temperature (in °C) for HadCM3-MOSES 2 (M2) TRIFF compared with observation and alternative versions of the Hadley Centre model over Greenland. . . . . | 175 |
| 4.3 | The average annual potential NPP (in gC m <sup>-2</sup> yr <sup>-1</sup> ) which represents the difference between photosynthesis and photorespiration for each PFT over different regions of Greenland. . . . . | 184 |
| 6.1 | Orbital parameters and CO <sub>2</sub> concentration for four time snapshots between 140 and 120ka and the preindustrial. . . . .  | 234 |
| 6.2 | Table showing the average near-surface temperature anomalies for the three LIG snapshots: 130,125 and 120ka over Greenland. . . . .  | 237 |
| 6.3 | Summary of GrIS evolution when Glimmer is forced offline with a 130ka fixed vegetation climatology for 10,000 years. . . . .   | 250 |
| 6.4 | Minimum GrIS volume, maximum LIG sea-level rise and ice surface drawdown at the Summit drilling core site for all Glimmer model parameter sets. . . . .  | 257 |
| A.1 | Synergy between altitude and surface type change in terms of precipitation. . . . .  | 285 |
| C.1 | GrIS diagnostics for the ice-sheet regrowth simulations where surface type is fixed as bare soil and each of the five PFTs. . . . .  | 289 |
| C.2 | GrIS diagnostics for the ice-sheet regrowth simulations where surface type evolves initiated from bare soil and needleleaf tree when TRIFFID is equilibrium mode and dynamic mode. . . . .                       | 290 |



# Variables, constants & abbreviations

## Variables

| Symbol          | Description  | Units                            |
|-----------------|--|----------------------------------|
| $A(T^*)$        | Ice flow law parameter   | -                                |
| $A/S$           | Orographic field: silhouette area                                | -                                |
| $B$             | Basal melt rate  | $\text{m yr}^{-1}$               |
| $C_s$           | Soil carbon storage  | $\text{kgC m}^{-2}$              |
| $C_v$           | Vegetation carbon density  | $\text{kgC m}^{-2}$              |
| $C_H$           | Surface exchange coefficient for sensible and latent heat fluxes | -                                |
| $C_c$           | Canopy heat capacity   | $\text{J K}^{-1} \text{m}^{-3}$  |
| $C$             | Canopy water content   | $\text{kg m}^{-2}$               |
| $C_m$           | Canopy water capacity  | $\text{kg m}^{-2}$               |
| $C_h$           | Canopy height  | $\text{m}$                       |
| $c_{ij}$        | Intra-species competition coefficients in TRIFFID                | -                                |
| $E_c$           | Evaporation from the canopy                                      | $\text{kg m}^{-2}$               |
| $E_v$           | Evaporation via transpiration                                    | $\text{kg m}^{-2}$               |
| $E_b$           | Evaporation from bare soil                                       | $\text{kg m}^{-2}$               |
| $E_\sigma$      | Sublimation from a snow surface                                  | $\text{kg m}^{-2}$               |
| $E$             | Total evaporation  | $\text{kg m}^{-2}$               |
| $e$             | Eccentricity of the Earth's orbit                                | -                                |
| $F_{soil}$      | Fraction of land points ice-free                                 | -                                |
| $F_{ice}$       | Fraction of land points ice-covered                              | -                                |
| $f_a$           | Fraction of gridbox which has a wet canopy                       | -                                |
| $f_h$           | Measure of the stability of the air                              | -                                |
| $g_c$           | Canopy conductance   | $\text{m s}^{-1}$                |
| $G_0$           | Ground heat flux   | $\text{W m}^{-2}$                |
| $H$             | Sensible heat flux   | $\text{W m}^{-2}$                |
| $h$             | Orographic field: peak to trough height                          | $\text{m}$                       |
| $h_i$           | Vegetation height of PFT $i$ in TRIFFID                          | $\text{m}$                       |
| $K$             | Infiltration rate  | $\text{kg m}^{-2} \text{s}^{-1}$ |
| $K_s$           | Soil saturated hydraulic conductivity                            | $\text{mm s}^{-1}$               |
| $L$             | Leaf Area Index  | -                                |
| $LW_\downarrow$ | Downward longwave radiation                                      | $\text{W m}^{-2}$                |
| $LE$            | Latent heat flux   | $\text{W m}^{-2}$                |
| $L_f$           | Latent heat of fusion for water                                  | $\text{J kg}^{-1}$               |

|                         |   |                                      |
|-------------------------|---|--------------------------------------|
| $q_1$                   | Atmospheric specific humidity   | kg kg <sup>-1</sup>                  |
| $q_{sat}(T_*)$          | Saturated specific humidity at surface temperature                                | kg kg <sup>-1</sup>                  |
| $R$                     | Rainfall rate   | kg m <sup>-2</sup> s <sup>-1</sup>   |
| $R_s$                   | Microbial soil respiration  | kgC m <sup>-2</sup> yr <sup>-1</sup> |
| $r_a$                   | Aerodynamic resistance to transport of moisture                                   | m                                    |
| $S$                     | Basal melt rate   | m yr <sup>-1</sup>                   |
| $SW_{NET}$              | Net shortwave radiation   | W m <sup>-2</sup>                    |
| $S_m$                   | Rate of snowmelt  | kg m <sup>-2</sup> s <sup>-1</sup>   |
| $T_F$                   | Rainfall throughfall  | kg m <sup>-2</sup> s <sup>-1</sup>   |
| $v_1, v_0$              | Horizontal wind velocity of surface air and surface respectively                  | m s <sup>-1</sup>                    |
| $Y$                     | Surface runoff  | kg m <sup>-2</sup> s <sup>-1</sup>   |
| $z_0$                   | Roughness length  | m                                    |
| $z_1$                   | Height of atmospheric level above surface   | m                                    |
| $\alpha_0$              | Snow-free albedo  | -                                    |
| $\alpha_{c ds}$         | Cold deep-snow albedo   | -                                    |
| $\alpha_0^{\text{inf}}$ | Maximum canopy albedo   | -                                    |
| $\alpha_s^{\text{inf}}$ | Minimum snow albedo   | -                                    |
| $\alpha_s^0$            | Maximum snow albedo   | -                                    |
| $\beta$                 | Infiltration enhancement factor   | -                                    |
| $\Gamma$                | Mid-tropospheric lapse rate from HadCM3   | °C km <sup>-1</sup>                  |
| $\gamma_v$              | Disturbance parameter in TRIFFID  | yr <sup>-1</sup>                     |
| $\varepsilon$           | Obliquity of the Earth  | °                                    |
| $\epsilon$              | Fraction of gridbox covered by rainfall rate                                      | -                                    |
| $\Theta_1$              | Soil moisture concentration in top soil layer                                     | -                                    |
| $\Theta_w$              | Volumetric soil moisture concentration parameter at the wilting point             | -                                    |
| $\Theta_c$              | Volumetric soil moisture concentration parameter at the critical point            | -                                    |
| $\Theta_s$              | Volumetric soil moisture concentration parameter at saturation                    | -                                    |
| $\Lambda_l$             | Local litterfall rate in TRIFFID  | kgC m <sup>-2</sup> yr <sup>-1</sup> |
| $\Lambda_c$             | Total litterfall rate in TRIFFID  | kgC m <sup>-2</sup> yr <sup>-1</sup> |
| $\lambda$               | Thermal conductivity dependent on moisture  | W m <sup>-1</sup> K <sup>-1</sup>    |
| $\lambda$               | Partitioning coefficient in TRIFFID   | -                                    |
| $\nu$                   | Vegetated fraction of gridbox that is not wet                                     | -                                    |
| $\nu^*$                 | Fractional PFT coverage if $\nu$ greater than 0.001 else equal to 0.01 in TRIFFID | -                                    |
| $\Pi$                   | Net Primary Productivity  | kgC m <sup>-2</sup> yr <sup>-1</sup> |
| $\rho$                  | Surface air density   | kg m <sup>-3</sup>                   |
| $\phi$                  | Geographic latitude   | °                                    |
| $\varphi_s$             | Saturated soil water suction  | m                                    |

---

|   |                                   |                    |
|---|-----------------------------------|--------------------|
| $\sigma_{sn}$                           | Snow amount                       | kg m <sup>-2</sup> |
| $\sigma_h$                              | Standard deviation of orography   | m                  |
| $\sigma_{xx}, \sigma_{xy}, \sigma_{yy}$ | Sub-grid orography fields         | -                  |
| $\tau^*$                                | Effective shear stress in Glimmer | Pa                 |
| $\Omega$                                | Precession of the Earth's orbit   | -                  |

## Constants

| Symbol          | Description   | Value                   | Units                                    |
|-----------------|---|-------------------------|--|
| $a$             | Material constant for $T^* \geq 263\text{K}$  | $1.73 \times 10^{-3}$   | $\text{Pa}^3 \text{s}^{-1}$              |
| $a$             | Material constant for $T^* < 263\text{K}$   | $3.613 \times 10^{-13}$ | $\text{Pa}^3 \text{s}^{-1}$              |
| $c_p$           | Specific heat capacity of dry air   | 1005                    | $\text{J kg}^{-1} \text{K}^{-1}$         |
| $c_{ice}$       | Specific heat capacity of ice   | 2009                    | $\text{J kg}^{-1} \text{K}^{-1}$         |
| $f$             | Flow enhancement factor   | 3                       | -  |
| $G$             | Uniform geothermal heat flux  | -0.05                   | $\text{W m}^{-2}$                        |
| $g$             | Acceleration due to gravity   | 9.81                    | $\text{m s}^{-2}$                        |
| $k$             | von Karman constant   | 0.4                     | -  |
| $k_{ice}$       | Thermal conductivity of ice   | 2.1                     | $\text{W m}^{-1} \text{K}^{-1}$          |
| $k_{rock}$      | Thermal conductivity of rock  | 3.3                     | $\text{W m}^{-1} \text{K}^{-1}$          |
| $L_{blend}$     | Height between where flow is unaffected by roughness & where local flow is entirely determined by roughness | 550                     | m  |
| $L_G$           | Atmospheric temperature lapse rate in Glimmer   | -6.227                  | $^{\circ}\text{C km}^{-1}$               |
| $n$             | Flow law exponent   | 3                       | -  |
| $Q$             | Activation energy for creep for $T^* \geq 263\text{K}$  | $139 \times 10^3$       | $\text{J mol}^{-1}$                      |
| $Q$             | Activation energy for creep for $T^* < 263\text{K}$   | $60 \times 10^3$        | $\text{J mol}^{-1}$                      |
| $R$             | Universal gas constant  | 8.314                   | $\text{J mol}^{-1} \text{K}^{-1}$        |
| $\alpha_i$      | Positive degree day factor of ice   | 8                       | $\text{mm d}^{-1} ^{\circ}\text{C}^{-1}$ |
| $\alpha_s$      | Positive degree day factor of snow  | 3                       | $\text{mm d}^{-1} ^{\circ}\text{C}^{-1}$ |
| $\alpha_{soil}$ | Soil albedo :snow-free, ice, cold deep snow   | 0.17, 0.75,0.80         | -  |
| $\rho_i$        | Density of ice  | 910                     | $\text{kg m}^{-3}$                       |
| $\rho_{rock}$   | Density of rock   | 3300                    | $\text{kg m}^{-3}$                       |
| $\sigma$        | Stefan-Boltzmann constant   | $5.67 \times 10^{-8}$   | $\text{W m}^{-2} \text{K}^{-4}$          |

## Abbreviations

|          |   |
|----------|---|
| AOGCM    | Atmosphere Ocean General Circulation Model                              |
| AVHRR    | Advanced Very High Resolution Radiometer                                |
| APP-x    | AVHRR   |
| CCM3     | Community Climate Model   |
| CLIMBER  | CLIMate and BiosphERe model   |
| CMIP     | Coupled Model Intercomparison Project                                   |
| CRU      | Climate Research Unit   |
| DEM      | Digital Elevation Model   |
| DGVM     | Dynamic Global Vegetation Model   |
| DMI      | Danish Meteorological Institute   |
| ECMWF    | European Centre for Medium-Range Weather Forecasts                      |
| EISMINT  | European Ice Sheet Modeling INiTiative                                  |
| EMIC     | Earth system Model of Intermediate Complexity                           |
| ERA-40   | 40-yr ECMWF Re-Analysis Project   |
| FAMOUS   | FAst Met Office/UK Universities Simulator                               |
| GCM      | General Circulation Model   |
| GC-Net   | Greenland Climate Network   |
| GISP     | Greenland Ice Sheet Project   |
| GLIDE    | General Land Ice Dynamic Elements                                       |
| GLINT    | GLimmer INTerface   |
| GRACE    | Gravity And Recovery Climate Experiment                                 |
| GREMLINS | GRenoble Model for Land Ice in the Northern hemisphere                  |
| GRIP     | GRenland Ice core Project   |
| GrIS     | Greenland Ice-Sheet   |
| HadAM3   | Hadley Centre Atmosphere Model  |
| HadCM3   | Hadley Centre coupled Model   |
| IBIS     | Integrated BIOSphere Simulator vegetation model                         |
| IGBP-DIS | International Geosphere-Biosphere Programme Data and Information System |
| InSAR    | Interferometric Synthetic Aperture Radar                                |
| IPCC     | Intergovernmental Panel on climate Change                               |
| IPSL     | Institut Pierre Simon Laplace model                                     |
| LAI      | Leaf Area Index   |
| LHS      | Latin Hypercube Sampling  |
| LIG      | Last InterGlacial   |
| LOVECLIM | LOchVecode-Ecbilt-CLio-agIsm Model                                      |
| LPJ      | Lund-Postdam-Jena vegetation model                                      |
| MAE      | Mean Absolute Error   |
| MD       | Mean Difference   |
| MIS      | Marine Isotope Stage  |
| MOC      | Meridional Overturning Circulation                                      |

---

|           |   |
|-----------|---|
| MOSES     | Met Office Surface Exchange Scheme  |
| NAMOC     | North Atlantic Meridional Overturning Circulation                           |
| NCAR      | National Center for Atmospheric Research                                    |
| NCEP      | National Centers for Environmental Prediction                               |
| NEEM      | North Greenland Eemian Ice Drilling   |
| NGRIP     | North GRenland Ice core Project   |
| NPP       | Net Primary Productivity  |
| NRMSE     | Normalised Root Mean Square Error   |
| ORCHIDEE  | ORganizing Carbon and Hydrology in Dynamic EcosystEms                       |
| PDD       | Positive Degree Day   |
| PFT       | Plant Functional Type   |
| PMIP      | Paleoclimate Modelling Intercomparison Project                              |
| SIA       | Shallow Ice Approximation   |
| SICOPOLIS | SImulation COde for POLythermal Ice Sheets                                  |
| SST       | Sea Surface Temperature   |
| THC       | ThermoHaline Circulation  |
| TRIFFID   | Top-down Representation of Interactive Foliage and Flora including Dynamics |
| VECODE    | Vegetation COntinuous DEscription model                                     |

## Introduction

### 1.1 Significance

A major concern from current anthropogenic warming is its effect on the Earth's cryosphere now and in the future. It has been shown that future warming in Greenland will be greater than the global average since northern high latitudes will warm more readily due to the loss of snow and sea-ice creating a positive feedback as a result of a reduction in surface albedo (Holland and Bitz, 2003).

With the predicted future rise in mean global temperatures as a result of increases in greenhouse gas concentrations the threat of ice-sheet disintegration could be realised (IPCC, 2007). Complete melting of the Greenland ice-sheet (GrIS) undoubtedly would have major societal and economic implications. Projections of land zones inundated by the sea for 1 (likely) to 5 m (from unexpected rapid disintegration of the Greenland and West Antarctic ice-sheets) sea-level rise from melting of the ice-sheets in the near future have been obtained (Dasgupta *et al.*, 2009). Analysis of these projections indicate tens of millions of people in developing countries are likely to be displaced within this century accompanied also by severe economic and ecological damage. In addition to this, the North Atlantic Thermohaline Circulation (THC) could be altered as a result of the enhanced freshwater input due to mass loss from the ice-sheet (Fichefet *et al.*, 2003). This could radically change the climate of the Northern Hemisphere due to a reduction or even termination of poleward oceanic heat transport. The orography of Greenland has also been shown to have a significant impact on Northern Hemisphere atmospheric circulation patterns (Dethloff *et al.*, 2004; Petersen *et al.*, 2004; Junge *et al.*, 2005). Thus removal of the ice-sheet could result in significant changes to the storm tracks at high northern latitudes. It is therefore imperative that simulations of Arctic climate include all important feedback processes that affect the energy budget and that these are fully understood.

The GrIS has experienced a wide range of climate conditions since it was first formed approximately three million years ago (Flesche Kleiven *et al.*, 2002; Lawrence

*et al.*, 2006). Ice core measurements (Kaspar *et al.*, 2005; Anderson *et al.*, 2006) indicate during the Last Interglacial (LIG) period (130 to 116 thousand years ago (ka)) the ice-sheet was significantly smaller under the warmer conditions that prevailed compared with today. In order for future climates to be simulated the methodology developed should be applied to past climate events in order to help understand mechanisms of climate change. Attempting to model past climates offers the ability to test model accuracy particularly if the climate forcing can be specified and the response sufficiently well constrained. Furthermore, because of the long timescales involved, not all aspects of climate models can be tested against instrumental climate records (e.g. vegetation change/ice-sheet evolution) and sensitivity of the model to present day conditions (i.e. CO<sub>2</sub> concentrations) may not necessarily be the same for very altered conditions e.g. changes in continentality, insolation received at the top of the atmosphere. The LIG is a particularly interesting period of time to study and will form part of the focus of this thesis. It is thought to be the last time the Arctic experienced temperatures significantly warmer and sea-level was very likely at least 6 m higher than today (Kopp *et al.*, 2009). It therefore could provide an analogue for the future where sea-level is predicted to rise significantly under warming conditions (due to anthropogenic forcing) as a result of melting of the ice-sheets and to a lesser degree thermal expansion of the oceans. It also provides a time period where sufficient data exists to compare model output with.

The remaining part of Chapter 1 introduces present day Greenland and its history to the reader, describes the feedback processes between climate, vegetation and cryosphere and any high latitude relevant measurement and modelling case studies that explore these feedback processes. The literature is subsequently reviewed in the context of GrIS evolution for future melting, the potential for regrowth after complete melting and the behaviour of the GrIS during the LIG. Finally, aims, objectives and the thesis structure are outlined.

## 1.2 An introduction to Greenland

Greenland is the largest island in the world with an area of  $2.17 \times 10^6$  km<sup>2</sup>. Geomorphologically, the bedrock is bowl-shaped with peripheral mountainous areas surrounding a central basin that extends below sea-level by more than 200 m (Bamber



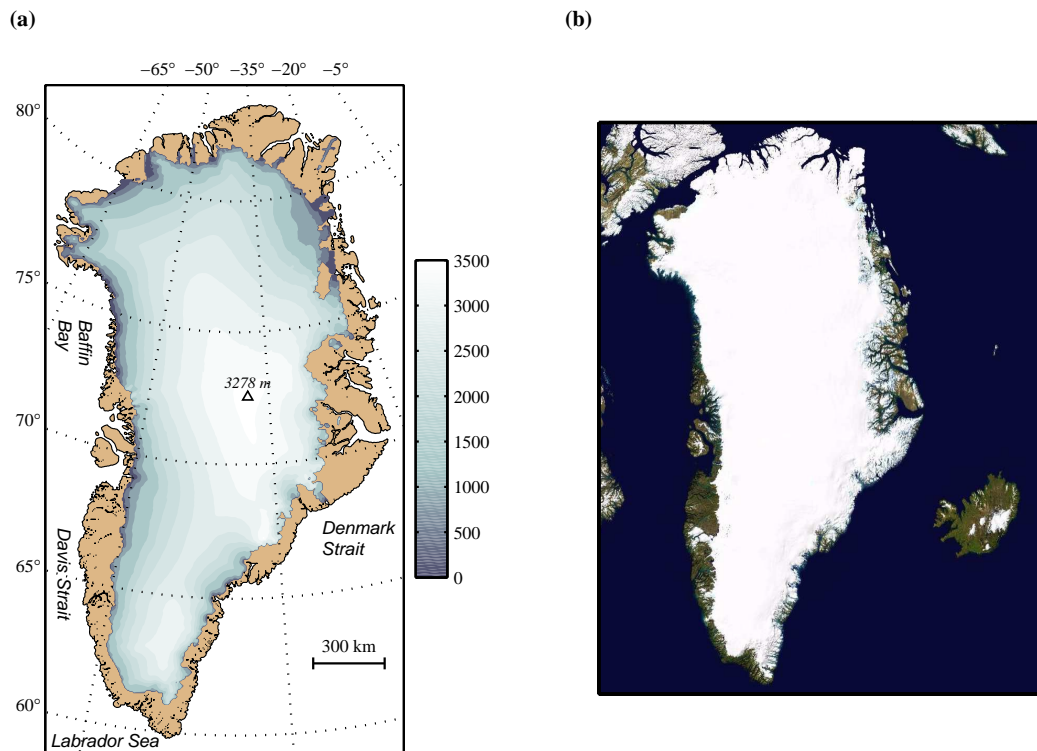


Figure 1.1: The present day state of Greenland ice-sheet with (a) surface elevation contours of the the GrIS based on Bamber *et al.* (2001) and (b) a satellite image of the GrIS and surrounding regions (*from* NASA).

*et al.*, 2001). The ice-sheet covers the central region of the island extending to the coast in places with an areal extent of  $1.7 \times 10^6$  km<sup>2</sup> (see Figure 1.1). The thickness of the ice at the ice divide is up to 3.2 km. The surface slope over most of the GrIS is not more than 1° but much greater at the margins (Serreze and Barry, 2005). Ice-free regions are mainly mountainous, cut by fjords that drain the ice-sheet and contain deposits of till and local deposits of Quaternary nonglacial sediments (Funder, 1989).

The ice-free coastal regions are home to many settlements but with the majority of inhabitants concentrated on the west coast. The population of Greenland is only 55,000 (the least populated country in the world) and predominantly Inuit. It is a nation reliant on fishing as its dominant form of trade which accounts for 95 % of exports. Although part of the Kingdom of Denmark, in recent years Greenland has moved towards relative independence based on parliamentary democracy. In the south, ruins are preserved of the Norse (viking) settlers that inhabited the island from 986 to 1408 AD (Lynnerup *et al.*, 2009).

The modern climate is characterised by very dry and cold conditions in the north

and warmer moist conditions in the south-east. The average snow accumulation rate is approximately  $30 \text{ g cm}^{-2} \text{ yr}^{-1}$  over all of Greenland. However, regional amounts differ greatly. Snow accumulation rates are up to  $100 \text{ g cm}^{-2} \text{ yr}^{-1}$  in the south-east compared with up to only  $50 \text{ g cm}^{-2} \text{ yr}^{-1}$  in the north and south-west as a result of a maritime versus polar climate (Bales *et al.*, 2009). Surface air temperatures decrease by about  $0.8^\circ\text{C}$  per degree of latitude for the eastern and western slopes of the ice-sheet with annual mean surface air temperatures decreasing with height by about  $7.1^\circ\text{C km}^{-1}$ . The ice-sheet is characterised by pronounced low-level inversion lapse rates particularly during the winter months (Serreze and Barry, 2005).

Greenland is thought to have become widely glaciated toward the end of the Pliocene epoch around 3 million years ago (Ma) when Northern Hemisphere widespread glaciation began to occur (Flesche Kleiven *et al.*, 2002). Several hypotheses have been suggested to explain this onset including closure of the Panama seaway (Haug and Tiedemann, 1998), termination of a permanent El Niño state (Wara *et al.*, 2005), uplift of the Rocky Mountains (Ruddiman, 1989) and the Himalayas and a decrease in  $\text{CO}_2$  concentration. A recent study by Lunt *et al.* (2008) using a fully coupled Atmosphere-Ocean General Circulation Model (AOGCM) in combination with an ice-sheet model indicates that glaciation of Greenland was mainly controlled by a decrease in the atmospheric  $\text{CO}_2$  concentration. Since then the ice-sheet has fluctuated in size and the LIG is thought to be the last time the GrIS was significantly smaller than today when global sea-level was higher and polar summer temperatures were 2 to  $5^\circ\text{C}$  warmer (see Section 1.5.1). During the last interglacial-glacial cycle evidence from the GRIP and GISP2 ice cores (see Figure 1.11) indicates significant variability in the climate over Greenland. Oxygen isotopes showed large, abrupt climate changes during the late stages of the last glaciation referred to as Dansgaard-Oeschger Cycles indicating the rapid reorganisation of climate in the North Atlantic on decadal timescales (Dansgaard *et al.*, 1993). These high frequency spikes observed in the record have amplitudes which imply a warming of 6 to  $7^\circ\text{C}$ , roughly half the glacial-interglacial range. It is likely these shifts in climate were involved in the redistribution of heat within the climate system associated with changes in Atlantic Ocean circulation. Another example of rapid climate change relates to the warmer conditions that prevailed at the of the deglaciation (Bolling-Allerod) being abruptly reversed for about 1,500 years (the Younger Dryas), which saw a period of ice-sheet

growth (Alley *et al.*, 1993). More recently, climatic events such as the Little Ice age (nominally 1400 to 1900 A.D.), which represented a cooler and drier period, are recorded in several northern and equatorial records. In Greenland the Norse are recorded in several northern and equatorial records. In Greenland the Norse had settled during the climatic optimum, often referred to as the Medieval Warm period, which preceded the Little Ice Age (Dansgaard *et al.*, 1975). The switch to a cooler climate and its impact on the Norse is evident from changes in diet, relying much more heavily on a marine source (shifts in C and N stable isotope measurements) with demographic modelling suggesting emigration accounted for the final abandonment of settlements (Lynnerup *et al.*, 2009). It appears that a change in Northern Hemisphere climate was the principal factor in the demise of the Norse society in Greenland.

The response of the GrIS to past climate fluctuations requires a review of the present day state of the ice-sheet. If fully melted, the ice-sheets of Greenland and Antarctica hold enough ice to raise global sea-level by approximately 64 m, of which 7.3 m would come from the GrIS (Bamber *et al.*, 2001; Lythe *et al.*, 2001). The GrIS can be thought of as a large reservoir of slow moving ice which is rapidly drained by ice-walled ice streams or rock-walled outlet glaciers. These in turn either flow into floating ice shelves, narrow ice tongues or directly into the ocean. In addition, about half of the ice lost from Greenland comes from surface melting and run-off into the sea. The dynamics of slow moving ice can currently be modelled adequately but this is not the case for the dynamics of the fast-moving ice streams and outlet glaciers. The implications of this on modelled output of the GrIS are discussed in Chapter 2.

In recent years acceleration of ice mass loss from Greenland has been reported (Rignot and Kanagaratnam, 2006; Velicogna and Wahr, 2006) as a result of surface run-off (Hanna *et al.*, 2008) and discharge from outlet glaciers in the east (Howat *et al.*, 2007; Stearns and Hamilton, 2007) and west (Luckman and Murray, 2005). The surface mass balance of the GrIS during the 1990s has been reported to be both in near balance (Zwally *et al.*, 2005) and with moderate losses of 45 to 73Gt yr<sup>-1</sup> (Krabill *et al.*, 2004). Recent mass loss estimates, however, of  $267 \pm 386$  Gt yr<sup>-1</sup> have been reported for 2007 using a combination of InSAR measurements, radio echo sounding and Positive Degree Day modelling. Moreover, results obtained from the GRACE satellite are consistent with these showing an acceleration in ice mass

loss from  $137\text{Gt yr}^{-1}$  in 2002-2003 to  $286\text{ Gt yr}^{-1}$  in 2007-2009 (Velicogna, 2009). Finally, recent work has indicated that current loss of mass from the GrIS is roughly equally partitioned between surface mass balance changes and changes in ice-sheet dynamics (Van den Broeke *et al.*, 2009).

Since interannual variability is large (mainly driven by variability in summer melting) the short time interval that is covered by the observational record makes it challenging to separate fluctuations from trends (Lemke *et al.*, 2007). Measuring the mass balance of the ice-sheet is an area of very active research and important in understanding the ice processes that are currently taking part with the intention that they can be included in future ice-sheet models.

### 1.3 Feedback processes in the climate - vegetation - ice-sheet system

A feedback mechanism acts as an internal control of a system and results from either coupling or mutual adjustment amongst two or more subsystems. A proportion of the output will return to act as an input to the system and in this way the net response of the system becomes altered. A feedback may either act to amplify the final output (a *positive* feedback) or dampen the output (a *negative* feedback) (Peixoto and Oort, 1992).

Applying this concept to the climate system is far from trivial. Under equilibrium conditions the net radiation at the top of the atmosphere is zero. Any external perturbation (e.g. changes in insolation received by the Earth, carbon dioxide concentrations, volcanic eruptions) will result in an imbalance of the net radiation at the top of the atmosphere. Variables such as surface temperature will change in order to adjust to the new equilibrium state. Examples of positive feedback loops in the climate system where a change in temperature (caused by an external factor) can result in further modification of the energy balance are snow-albedo-temperature interactions and water vapour-temperature interactions (i.e. increasing temperature increases evaporation and therefore increases water vapor in the atmosphere which is a strong absorber of longwave radiation resulting in further increases in temperature). Cloud-temperature interactions are particularly complex since they are absorbers of longwave radiation as well as reflectors of shortwave radiation and

therefore could act to increase and decrease the surface temperature accordingly (Peixoto and Oort, 1992).

Several feedbacks exist in the climate-vegetation-ice-sheet system that need to be represented accurately when modelling the evolution of ice-sheets in terms of inception and deglaciation and are the focus of discussion here. Biogeophysical feedbacks directly affect the near-surface energy balance and can be analysed in terms of the surface energy balance

$$S(1 - \alpha) + \varepsilon R - \varepsilon \sigma T^4 \pm H \pm LE = \pm G_0, \quad (1.1)$$

where  $S$  refers to insolation,  $\alpha$ , albedo,  $\varepsilon$  the emissivity,  $T$  the temperature of the surface-atmosphere interface.  $R$  is the atmospheric radiation and  $\sigma$  the Stefan-Boltzmann constant.  $H$  and  $LE$  are the turbulent fluxes of sensible heat and latent heat respectively.  $G_0$  is the ground heat flux representing the rate of transfer within the ground away from the Earth's surface with instantaneous values for land being on the order of tens of  $\text{W m}^{-2}$ . However, averaged over long time periods (months to years) the net effect of the ground heat flux on the surface energy balance of the Earth is small. This section first outlines the feedback mechanisms related to biogeophysical feedback processes followed by an evaluation of these processes in palaeoclimatic studies and finally a discussion of the ice-elevation feedback.

### 1.3.1 Ice-albedo feedback

The ice-albedo feedback mechanism (Figure 1.2) occurs where increased snow on land and increased ice over the oceans results in a higher surface albedo and, therefore, more solar radiation reflected upwards and less absorbed at the surface. In turn, this cools the surface favouring conditions for further ice-sheet growth. Likewise, a decrease in snow and ice will lower the surface albedo resulting in more solar radiation being absorbed at the surface leading to a warmer climate and conditions suitable for ice-sheet retreat (Held and Suarez, 1974).

### 1.3.2 Vegetation-snow-climate feedback

The vegetation-climate feedback (Figure 1.2) is also potentially important when modelling ice-sheet evolution although it has been largely neglected from studies

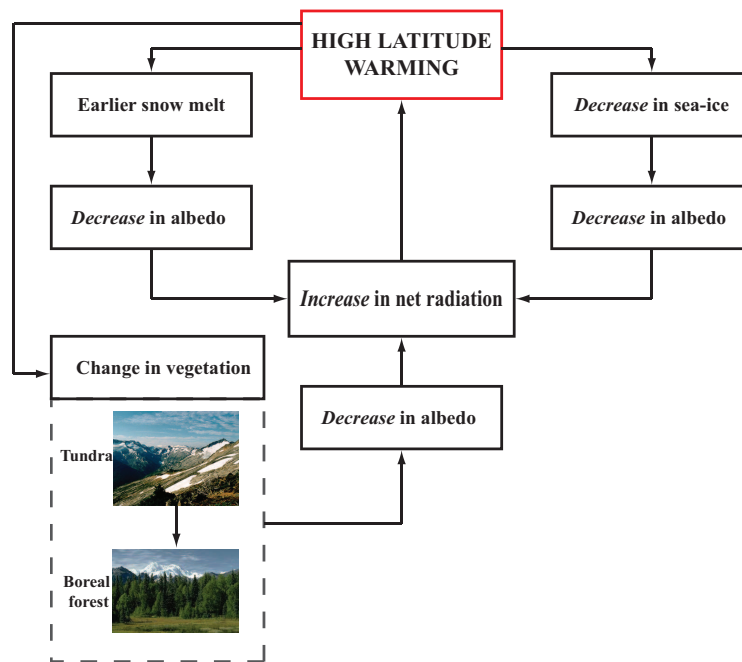


Figure 1.2: Diagram illustrating the ice-albedo and the vegetation-snow-climate feedback loops under a warming Arctic climate.

concerning the GrIS.

The amount and type of vegetative ground cover strongly affects the exchange of energy and moisture between the Earth's surface and the atmosphere (McPherson, 2007). Vegetation intercepts rainfall which may either evaporate directly back into the atmosphere or fall through to the ground. Vegetation also affects surface albedo, evapotranspiration and soil moisture and via its roughness has an effect on turbulent fluxes and near-surface winds (Kubatzki *et al.*, 2006), therefore having the potential to alter the surface energy balance given in Equation 1.1. There is also evidence that vegetation may increase clouds and rainfall (Freedman *et al.*, 2001). Figure 1.3 illustrates the interactions occurring between vegetation and atmosphere.

Thus three physical attributes of vegetation that cause interactions with the atmosphere are discussed here: (1) the response of vegetation to incoming shortwave radiation and its emission of longwave radiation, (2) the vegetation's 'physical' presence which relates to the roughness length and (3) transpiration by vegetation which affects the latent heat flux. Photosynthesis of plants which affects CO<sub>2</sub> concentrations in the atmosphere obviously is a potentially important physical attribute but is not discussed any further since focus is on the effect of vegetation on surface energy balance and moisture exchanges (McPherson, 2007).

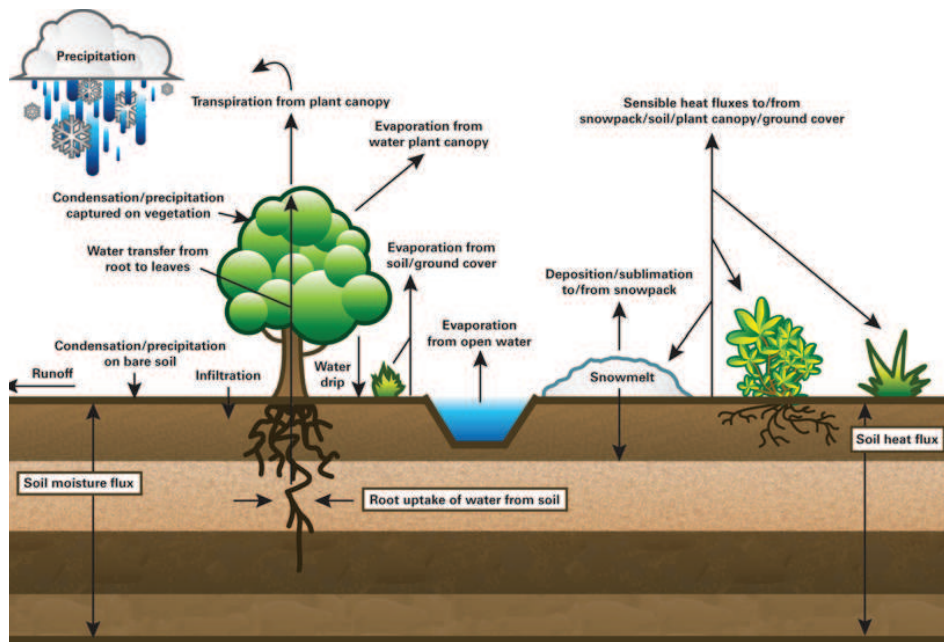


Figure 1.3: Illustration showing the interactions between shortwave and longwave radiation within the land-atmosphere system ( from McPherson (2007)).

The theory of high latitude vegetation-snow-climate feedback is based on vegetation types, notably tundra and boreal forest, interacting very differently with freshly fallen snow producing surfaces with differing albedos. When snow falls on a tundra surface little vegetation remains exposed and a high albedo surface ensues reflecting much of the downwelling shortwave radiation. However, boreal forest vegetation masks the high reflectance of snow, reducing the surface albedo such that more shortwave radiation is absorbed at the surface, leading to warmer temperatures than if they were not present (see Figure 1.2). Measurements of albedo for snow-covered grasses have been as high as 0.75 (similar to the albedo of ice) and for snow-covered forests as low as 0.2 to 0.4 (Betts and Ball, 1997). This feedback is often referred to as the taiga (boreal forest)-tundra feedback. Changes in the way the surface energy budget is partitioned into the different fluxes have been observed at the transition between Arctic tundra and forest which results in an increase in leaf area index, canopy height and decrease in albedo with the observation sites becoming drier and warmer as a result of an increase in sensible heat flux (Beringer *et al.*, 2005). If the climate cools, say due to variations in the Earth's orbit, the tundra-boreal forest ecocline shifts to maintain equilibrium with the new climate. Thus tundra gradually advances southwards replacing boreal forest and expanding the area where the

Earth has a high albedo surface. More solar radiation is reflected from this surface and the reduction leads to further cooling (Ruddiman, 2001). The significance of the snow-vegetation-albedo feedback at high latitudes using a very simple climate model where albedo is prescribed was demonstrated by Otterman *et al.* (1984). This study showed that this feedback is stronger in forest-free regions. Studies using general circulation models (GCMs), where deforestation was prescribed, show boreal forest warms both winter and summer air temperatures relative to simulations where the trees are replaced with bare ground or tundra vegetation (Bonan *et al.*, 1992; Chalita and Letreut, 1994).

Different vegetation types also have different surface roughness lengths which in turn can affect the turbulent fluxes in the boundary layer changing the radiation budget at the surface and hence altering the climate. The roughness length increases as objects extend further into the atmosphere weakening near-surface wind speeds and intensifying low-level turbulence. On the small scale this could accelerate the initiation of convection while on the synoptic scale frictional inflow into extratropical cyclones may increase, leading to possible enhanced precipitation (McPherson, 2007).

Few studies have examined the effect of surface roughness on the climate in high latitude regions. It has been widely assumed that the change in temperature as a result of a change in vegetation is predominantly an albedo effect.

### **Modelling biogeophysical feedbacks in past high latitude climates**

The role of biogeophysical feedbacks at high northern latitudes has been modelled for several time periods in the past, notably the last glacial inception and the mid-Holocene which are outlined below. The influence of biogeophysical feedbacks on the LIG are discussed in detail in Section 1.5.

It is generally accepted in the literature that vegetation feedbacks played a significant role during the last glacial inception 115,000 years ago with GCMs showing the southward migration of the boreal forest/tundra limit creating conditions favourable for ice-sheet growth by increasing the surface area with perennial snow (deNoblet *et al.*, 1996; Gallimore and Kutzbach, 1996; Crucifix and Loutre, 2002; Meissner *et al.*, 2003; Kageyama *et al.*, 2004; Wang *et al.*, 2005). However, Calov *et al.* (2005a) suggest that vegetation is less important than the snow-albedo feedback for



their simulation of the last glacial inception with oceanic processes dominating.

The evidence suggests if a change in climate forced by an external control (e.g. orbital variations, anthropogenic forcing) is great enough to evoke a change in vegetation then the positive feedback could amplify the externally driven climate change. Furthermore the response of vegetation to temperature and precipitation changes can occur on a timescale of centuries or less as demonstrated in modelling the collapse of the Laurentide ice-sheet (Shuman *et al.*, 2002). Palaeocological evidence along the boreal tree line in Canada  $\sim 5,000$  years ago provides another example, where a transition from tundra to tundra-forest took place in less than  $\sim 150$  years during a regional climatic warming event possibly caused by a shift in the summer position of the Arctic front (Macdonald *et al.*, 1993).

Palaeobotonic evidence suggests that during the early to middle Holocene (approximately 9,000 to 6,000 years ago) boreal forests extended further north than the location of the tree line today (TEMPO, 1996; Cheddadi *et al.*, 1997). The cause of this migration is assumed to be orbitally driven resulting in stronger insolation during Northern Hemisphere summers (i.e. the growing season) and weaker insolation during winter compared with present. However, it is presumed that winter and summer were warmer than today with the winter-time warming caused by the taiga-tundra feedback (Claussen *et al.*, 2004). Modelling studies for this period such as Foley *et al.* (1994) showed that the mid-Holocene climate warmed not only as a response to variations in the Earth's orbit but also due to the subsequent northward expansion of boreal forest giving rise to an extra warming of  $4^{\circ}\text{C}$  in spring and  $1^{\circ}\text{C}$  in other seasons. Other studies using different models have corroborated these results (e.g. TEMPO, 1996; Ganopolski *et al.*, 1998a; Gallimore *et al.*, 2005) and indicate the importance of vegetation-snow-albedo feedback at high northern latitudes in amplifying climate change triggered by an external forcing.

The synergism of vegetation feedbacks with other feedback processes has been evaluated (Claussen *et al.*, 2004) in context of the Holocene. When Arctic sea-temperatures and sea-ice volumes were kept constant the northward expansion of boreal forests was somewhat small. Studies have shown that by isolating different aspects of the atmosphere-ocean-biosphere system temperature changes are very different. For example, the study of Ganopolski *et al.* (1998a) found a summer warming over Northern Hemisphere continents compared with today was a result of

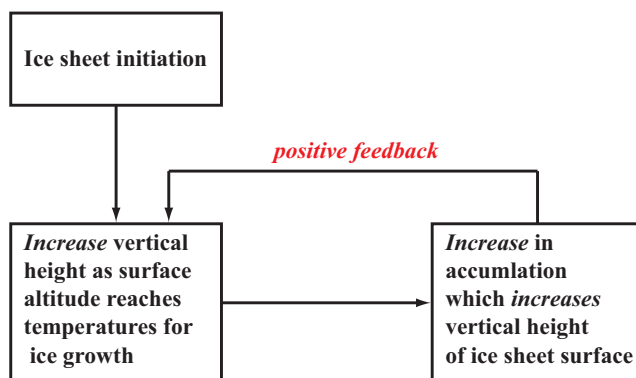


Figure 1.4: Diagram illustrating the ice-elevation feedback mechanism for ice-sheet growth. In reality the top of the ice-sheet will eventually reach elevations at which snowfall is much lower and the positive feedback will reduce.

orbital forcing on the atmosphere alone. However, when ocean-atmosphere feedbacks were included (vegetation fixed) the warming was reduced whereas the inclusion of vegetation feedbacks with no oceanic feedback enhanced summer warming. When all feedbacks were included the resultant warming was not reduced (as would be expected) but enhanced as a result of a synergism between the vegetation-snow-albedo feedback and the Arctic sea-ice albedo feedback.

### 1.3.3 Ice-elevation feedback

The ice-elevation feedback mechanism (Figure 1.4) is particularly important when considering ice-sheet inception. Accumulation of snow and ice are controlled by local climate which is particularly sensitive to topographic features. Hence, large ice-sheets begin as small mountain glaciers and ice caps at high altitudes. If the climate is sufficiently cool these will thicken and coalesce and their increased surface altitude will cool the local climate further. In turn, the ice will become thick enough to dynamically flow to lower altitudes where the ice-elevation feedback lowers the temperature adequately to ensure no melting of the ice (Marshall and Clarke, 1999). Ice-sheet models should have sufficient horizontal and vertical resolution in order to represent initial ice caps and glaciers accurately.

Comparison between GCM experiments where there is a change in altitude result in a change in temperature due to the temperature-altitude relationship discussed in terms of ice growth above. For instance, a decrease in altitude would be expected to cause a surface temperature warming of approximately  $-\Gamma\Delta z$ , where  $\Gamma$  is the lapse rate (and typically negative), and  $\Delta z$  is the change in altitude.

## 1.4 Future Greenland ice-sheet behaviour

### 1.4.1 Future melting of the Greenland ice-sheet

Several studies during the last 20 years have analysed the behaviour of the GrIS under future warming with the realisation that human induced climate change could have substantial impacts on the Earth's cryosphere. Early work such as Huybrechts *et al.* (1991) used a temperature scenario (the 'Villach II' scenario which predicted an increase in temperature of 4.2K by 2100) and precipitation perturbed from present day values, according to a change in temperature, to drive a mass balance model coupled to a 3D thermomechanical model of the ice-sheet. They found that for annual average temperatures over Greenland greater than 2.7°C the ice-sheet would begin to lose mass slowly. Letreguilly *et al.* (1991a) also used a similar approach to show annual average Greenland temperatures greater than 8°C would lead to complete disintegration of the ice-sheet in the next 5,000 years. Neither of these studies use a climate model for their precipitation and temperature forcing.

In accordance with Huybrechts *et al.* (1991) two further studies suggest for a sustained annual average Greenland temperature rise greater than 3°C, GrIS melt-down would be irreversible (Huybrechts and de Wolde, 1999; Greve, 2000). By the late 1990s the use of climate models to drive ice-sheet models had become commonplace. Huybrechts and de Wolde (1999) used a 2D energy balance climate model to force an ice-sheet model offline for a number of CO<sub>2</sub> scenarios. They also performed sensitivity experiments to highlight the role of ice dynamics and height mass balance feedback in the behaviour of the GrIS over millennial timescales. However, the model was not able to simulate dynamics on the scale of outlet glaciers and, therefore, could not replicate the ice processes currently being observed in Greenland today (e.g. Howat *et al.*, 2007). Nevertheless, their study enforced the need for ice-elevation feedback and ice dynamic processes to be included in studies of ice-sheet evolution even on a timescale of a century or less. Greve (2000) instead investigated the impact of various temperature scenarios and different snowfall and melting parameterisations on ice-sheet evolution over 1,000 model years using the 3D ice-sheet model SICOPOLIS. He found almost complete disintegration if temperatures were increased by 12°C relative to present. Furthermore, he found that varying the melt and snowfall parameterisations resulted in an uncertainty range of

up to 20 % of the present ice volume. This emphasises the need to perform several simulations with perturbed versions of the ice-sheet model parameters in future and past ice-sheet studies (see Chapter 2).

More recently, the study of Gregory *et al.* (2004) showed that almost all combinations of AOGCM perturbations and CO<sub>2</sub> stabilisation levels for the future exceeded the accepted annual average Greenland 2.7°C threshold for ice-sheet mass loss. For the modest stabilisation level of 450 ppmv the threshold was exceeded suggesting that the GrIS could very likely be eliminated by anthropogenic climate change. Alley *et al.* (2005) also investigated the evolution of the GrIS under several future warming scenarios averaged from seven IPCC climate models (CO<sub>2</sub> stabilised at 550, 750 and 1000 ppmv) by using the ice-sheet model in the Huybrechts and de Wolde (1999) study. They found that the GrIS would disappear under a sustained 1000 ppmv climate within 3,000 years. Furthermore, climates with lower CO<sub>2</sub> concentrations could eventually see the disappearance of the GrIS with melting at a slower rate (this was the case for the 550 ppmv climate).

In 2006 Gregory and Huybrechts (2006) attempted to address the need for high-resolution climate models coupled to ice-sheet models. The regions where ablation and precipitation are most important in modelling ice-sheet mass balance occur in narrow margins which are inadequately resolved in low resolution climate models such as HadCM3. Since high-resolution climate modelling is not feasible for long time integrations they combined ice-sheet averaged time-series from several AOGCMs projections for future climates with high-resolution climate model data run for short periods of time to force an ice-sheet mass balance model. They found a higher threshold than the 2.7°C at which the Greenland mass balance became negative of about 4.5°C.

The sensitivity of the GrIS to different CO<sub>2</sub> thresholds was further investigated by Lunt *et al.* (2009). Equilibrium simulations using HadCM3 and HadCM3L (a low ocean resolution version of HadCM3) were performed at 400 ppmv and 560 ppmv and 1120 ppmv respectively and used to drive Glimmer offline for 50,000 years. They found that a stabilisation of the climate at 400 ppmv would maintain 98 % of the ice-sheet volume, stabilisation at 560 ppmv would maintain 93 % of the ice-sheet volume while stabilisation at 1120ppmv would result in almost complete collapse maintaining only 12 % of the ice-sheet volume. The threshold of ice-sheet collapse

appears to be somewhere between 560 and 1120 ppmv but the nature of this should be regarded with some caution, due to the lack of interactive coupling between GCM and ice-sheet model and also missing physics in the model. This is discussed and investigated further in Chapter 2.

The studies so far described are either run with an offline ice-sheet model and so neglect important feedbacks between climate and ice-sheet or do not even use climate model forcing as input to the ice-sheet model. Few studies exist using a full 3D GCM to perform two-way coupled climate ice-sheet modelling over Greenland due to the computational demands long time integrations require. A 2D climate model of intermediate complexity asynchronously coupled to a model of the three Northern Hemisphere ice-sheets and their bedrock was used by Loutre (1995). This model, although simple compared to full GCMs, can simulate on the timescales of several millennia that are needed for ice-sheets to respond to changes in climate, with low computational costs. Doubling present CO<sub>2</sub> concentrations induced melting of the ice-sheet within 5,000 years even if concentrations were not maintained at this high level over the whole 5,000 year period.


Ridley *et al.* (2005) used a two-way coupling between the Greenland ice-sheet model (Huybrechts ice-sheet model) and the GCM, HadCM3, to include important feedbacks between the ice-sheet, climate and the ocean. Slow ice-sheet dynamics are included in the ice-sheet model with ice deformation and basal sliding being represented but deformation of subglacial sediment excluded. Preindustrial CO<sub>2</sub> concentrations were quadrupled and held constant for 3,000 years. The ice-sheet was found to have almost completely disappeared by the end of the simulation. The contribution to global average sea-level from this melting was approximately 7 m. Apart from this impact on the global sea-level, they found no other major impacts on global climate. For example, there was insufficient weakening of the THC in the North Atlantic (also referred to as the Meridional Overturning Circulation). This result contrasts with the study of Fichefet *et al.* (2003) which coupled the same GrIS to another AOGCM (Laboratoire du Météorologie Dynamique-Coupled Large-scale Ice Ocean model) and found a strong and abrupt weakening of the THC toward the end of the twenty-first century as a result of freshwater input from increased melting of the GrIS. The main difference between these results is the sensitivity of the model to the freshwater input where a freshwater flux of at least 0.1 Sv is

required to sizeably reduce the THC for Ridley's simulation. This compares with only 0.015 Sv in the case of Fichefet *et al.* (2003).


Although coupling between the components of the Earth system and more realistic ice-sheet models have been included in recent studies, none of the above included a dynamic vegetation component which could play an important role in the evolution of the ice-sheet. A few studies have used Earth System Models of Intermediate Complexity (EMIC) or low resolution full GCMs with a dynamic vegetation component included coupled to an ice-sheet model (Driesschaert *et al.*, 2007; Charbit *et al.*, 2008; Vizcaíno *et al.*, 2008). However, for the case of Driesschaert *et al.* (2007) only two functional plant types were modelled: grass and trees. Their study indicated for a radiative forcing greater than  $7.5 \text{ Wm}^{-2}$  the ice-sheet would melt within 3,000 years in agreement with Ridley *et al.* (2005). They explained the temperature change as a result of the receding ice-sheet being replaced by vegetation purely as an albedo effect, although this was not looked at in great detail. Similar to Ridley *et al.* (2005) they found no significant change in the THC. In terms of vegetation cover they predicted large parts of Greenland to be vegetatively covered as the ice-sheet melted away with grasses situated everywhere except in central Greenland and trees along southern and eastern coasts.

The study of Vizcaíno *et al.* (2008) used a low resolution Earth System Model with a range of  $\text{CO}_2$  stabilisation scenarios at  $2\times$ ,  $3\times$  and  $4\times$  preindustrial. Although the GrIS decayed in all cases after 1,000 years of model simulation they found smaller ice mass loss than previous studies (Alley *et al.*, 2005; Ridley *et al.*, 2005) with only 40 % decay of the initial volume under a  $4\times \text{CO}_2$  climate. This result was attributed to a lower climate sensitivity for their model compared with others and a weakened/collapsed North Atlantic Meridional Overturning Circulation (NAMOC) as a result of regional changes in the climate over Greenland (i.e. precipitation and evaporative changes). However, freshwater flux increases from a melting Greenland did not play an important part in weakening the NAMOC. Interestingly this study also looked at the feedback mechanism from elevation and albedo change under elevated  $\text{CO}_2$  climates. Initial modification in topographic height due to ice mass changes resulted in a negative feedback on the decay of the GrIS but acted as a positive feedback accelerating decay at a much later stage in the simulation. Other feedbacks were not important until the GrIS reached three-quarters of its original


| Study                             | Atm          | Ocn          | Ice          | Veg          | Result      |
|-----------------------------------|--------------|--------------|--------------|--------------|-------------|
| Letreguilly <i>et al.</i> (1991a) |              |              | ADVANCED     |              | Regrowth    |
| Crowley & Baum (1995)             | INTERMEDIATE | INTERMEDIATE |              |              | No Regrowth |
| Toniazzo <i>et al.</i> (2004)     | ADVANCED     | ADVANCED     |              |              | No Regrowth |
| Lunt <i>et al.</i> (2004)         | ADVANCED     | ADVANCED     | DECOUPLD     | DECOUPLD     | Regrowth    |
| Vizzaino <i>et al.</i> (2008)     | INTERMEDIATE | INTERMEDIATE | INTERMEDIATE | INTERMEDIATE | No Regrowth |
| Charbit <i>et al.</i> (2008)      | BASIC        | BASIC        | ADVANCED     | BASIC        | No Regrowth |




**ADVANCED**  
e.g. Full GCM



**INTERMEDIATE**  
e.g. Low res. GCM,  
low res. ice sheet model



**BASIC**  
e.g. EMIC



**DECOUPLD**

Figure 1.5: Compilation of studies in chronological order which have looked at subsequent regrowth of the GrIS after deglaciation using climate models of varying complexity including whether vegetation/ice-sheet components are included. The main finding of each study in terms of regrowth is given.

volume. From this point forward the albedo feedback strongly accelerated the decay of the ice-sheet.

The final recent study discussed here (Charbit *et al.*, 2008) with a vegetation component included used the EMIC, CLIMBER, to explore the response of the GrIS to various carbon emissions scenarios accounting for natural removal of anthropogenic CO<sub>2</sub> from the atmosphere. Emissions above 3,000 GtC suggested melting of the GrIS was irreversible while below 2,500 GtC there was only partial melting followed by a regrowth phase.

### 1.4.2 Future regrowth of the Greenland ice-sheet

There is less emphasis in the literature on future Greenland reglaciation if it were to completely melt as a result of future warming driven by an increase greenhouse gases in the atmosphere. This research question forms part of the focus of this thesis. Figure 1.5 shows a summary of the studies that have looked at the possibility of ice-sheet regrowth, highlighting the types of models used. The earliest study indicated that regrowth was possible. Letreguilly *et al.* (1991a) investigated the conditions under which an ice-sheet could reform using various temperature scenarios with runs starting from bare rock. Results indicated that it could reform for a climate up to 2°C warmer than present. However, accumulation is only parameterised in

terms of temperature (similar to the melting study of Huybrechts *et al.* (1991)). Changes in the distribution of accumulation due to orographic changes were also not accounted for.

Crowley and Baum (1995) looked at the regeneration of the ice-sheet in the context of inception in the mid-Pliocene. They modelled the temperature and snow cover over Greenland using a low resolution GCM with the ice sheet removed and the surface replaced with bare soil, tundra and boreal forest. Summer temperatures ranged between 6 and 14°C depending on vegetation type, orbital forcing and elevation of Greenland, with no build up of snow cover in the model. Their study suggests present day Greenland boundary conditions are sufficient to maintain an ice-free state if no pre-existing ice-sheet is left to melt. They further suggest that even with a model that could resolve high altitude mountains in eastern Greenland an ice-sheet may not develop as a result of high summer temperatures at lower altitudes enhanced by vegetation feedbacks. They attribute their difference with Letreguilly *et al.* (1991a) due to their GCM more accurately estimating regional temperature changes owing to altered boundary conditions than the parameterised scheme used by Letreguilly *et al.*.

Toniazzo *et al.* (2004) came to similar conclusions as Crowley and Baum (1995) using HadCM3. Their study was run for a substantially longer model time integration (60 years compared with 4.25 model years) when they modelled the climate over Greenland with the ice-sheet removed, orography rebounded and preindustrial greenhouse gas concentrations in place. Greater summer melting was observed compared with the current climate with partially snow-free summers and no accumulation of snow on the long-term average implying an ice-free Greenland. They also performed a sensitivity study to the surface topography used: one where the the surface topography of Greenland is given by that of the bedrock currently buried under the ice-sheet and the other where a readjustment to isostatic equilibrium of the unloaded orography is taken into account, giving higher elevations. They found no major differences in local or global climate between these two setups.

None of these studies, however, used an ice-sheet model either coupled to the climate model or driven offline. Toniazzo *et al.* (2004) do though indicate the need for high resolution ice-sheet model simulations to investigate this problem further. A more recent study using an interactive low resolution GCM which included the



ice-sheet model SICOPOLIS and the vegetation model LPJ, examined the reglaciation of Greenland starting with an initial condition of ice in the southern tip of Greenland (Vizcaíno *et al.*, 2008). After 1,000 years of simulation they found no expansion of the GrIS; rather further decay as a result of a simulated collapse of the NAMOC. The inability for regrowth was attributed to a continued decrease in albedo, the reduction in topographic height and changes in the atmospheric circulation. Although vegetation feedbacks were modelled, their relative contribution to the lack of regrowth has not been analysed.

In contrast to these results, Lunt *et al.* (2004) found that if after complete deglaciation CO<sub>2</sub> concentrations were reduced to present day values the ice-sheet is likely to regrow. Their conclusions were based on using the Institut Pierre Simon Laplace (IPSL) coupled AOGCM to investigate the climate over Greenland with the ice-sheet removed. Based on the snow diagnostic alone, Lunt *et al.* (2004) found snow accumulation in the least snowy month solely over the Ellesmere Island, northwest of Greenland. However, when climate output was used to drive an offline ice-sheet model, GREMLINS, they found recovery of the ice-sheet mainly in eastern regions. They attributed the difference in interpretation as a result of resolution. The high-resolution of the ice-sheet model means it detects areas of very high altitude in the east which are not represented in the AOGCM. It is these regions where glaciers begin to develop and then flow down toward areas of lower altitude allowing ice to grow via the ice elevation feedback mechanism. The increase in solid precipitation along the eastern coast, particularly in winter, also aids the ice-sheet development. Their result suggests using the build-up of snow cover alone in the GCM is a poor diagnostic for ice-sheet regrowth/inception.

Sensitivity of the climate-ice-sheet system to vegetation cover is largely absent from regrowth/inception studies of the Greenland ice-sheet. Even in the study of Crowley and Baum (1995) the vegetation component was neither dynamic nor coupled to the climate model. Lunt *et al.* (2004) have shown by driving an offline vegetation model (ORCHIDEE) with the climate output from their AOGCM (with the ice-sheet removed), the growth of trees in southern Greenland can be supported along with grass in central Greenland. This suggestion of trees in southern Greenland would result in a warmer Greenland climate as a result of reduced albedo and change in the energy budget at the surface. In turn, this warmer climate could potentially

inhibit ice-sheet growth. A recent study of biomolecules at the base of ice cores from Greenland reinforces this conclusion (Willerslev *et al.*, 2007a). The biomolecules indicate the presence of conifers and insects existing in the southern, high altitude regions of Greenland in the past million years. The melting study of Driesschaert *et al.* (2007) (see Section 1.4.1) also shows a warmer Greenland could support trees in southern Greenland.

## 1.5 The state of the Greenland ice-sheet during the Last Interglacial

The Last Interglacial, also known as the Eemian, and defined by the Marine Isotope Stage (MIS) 5e, lasted from  $130\pm 1$  to  $116\pm 1$  ka. It is thought to be the last time that the global climate was significantly warmer than present and therefore provides a possible analogue for future climate warming (Jansen *et al.*, 2007). Figure 1.6 shows an increase in the greenhouse gases  $\text{CO}_2$  and  $\text{CH}_4$  at the beginning of the LIG as well as a marked maximum in solar insolation (referenced at June  $65^\circ\text{N}$ ) at the beginning of the interglacial with a subsequent minimum at 116ka. It is also thought to be the last time that sea-level was higher than today (see Figure 1.7).

The following sections outline the likely state of the climate, global sea-level and vegetation from palaeorecords and modelling studies, followed by an explanation for the observed LIG warmth and finally a review of the evidence for a reduced GrIS during this time.

### 1.5.1 Climate, sea-level and vegetation during the Last Interglacial

Many studies have looked at sea-level during the LIG with considerable variability in estimates; this is shown in Figure 1.8a. This could be due to the complexity of sea-level fluctuations during this period or due to different interpretations from different sites based on various dating methods. Eustatic sea-level rise during the LIG has previously been estimated to be between +2 and +4 m from corals (Stirling *et al.*, 1998) with larger estimates between +4 to +6 m also suggested (e.g. Rostami *et al.*, 2000; Muhs *et al.*, 2002). However, it is less clear whether sea-level fluctuated significantly during this period. Some studies have suggested a lowering in sea-level at around 121ka (e.g. Stirling *et al.*, 1995, 1998) although the duration of this

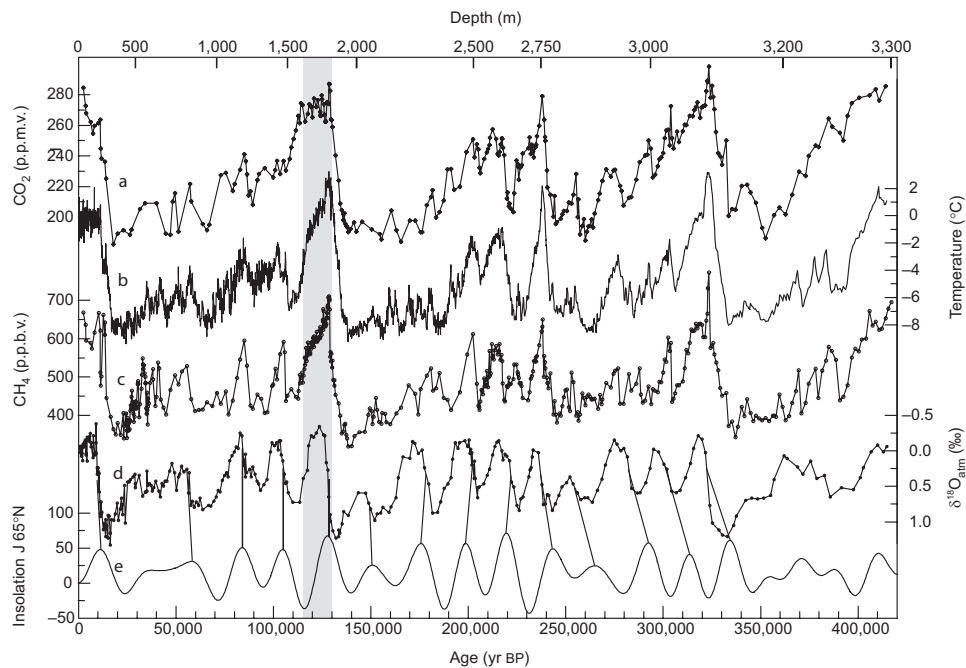


Figure 1.6: Time series over the last 400,000 years derived from the Vostok core, Antarctica, of (a)  $\text{CO}_2$ , (b) isotopic temperature of the atmosphere, (c)  $\text{CH}_4$ , (d)  $\delta^{18}\text{O}_{\text{atm}}$  and (e) mid-June insolation at  $65^\circ\text{N}$  (from Petit *et al.* (1999)). The shaded region denotes the LIG.

lowering in sea-level is unlikely to be more than 2,000 years, according to U/Th-series ages of MIS 5e corals (Szabo *et al.*, 1994). Further evidence of a lowering in sea-level at this time comes from U/Th age estimates on corals that have undergone diagenetic alteration (Thompson and Goldstein, 2005). However, controversy exists around the methods used to correct for the diagenetic alteration with continued ambiguity of the existence of sea-level within MIS 5e (Siddall *et al.*, 2007). Moreover, a recent study (see Figure 1.8b), which has compiled numerous local sea-level indicators (from regions both tectonically stable and unstable) using a statistical approach, indicates previous work underestimated the high global sea-level with their estimate of global sea-level at least 6.6 m higher and likely (67 % probability) exceeded 8.0 m compared with present day sea-level (Kopp *et al.*, 2009). This peak was reached at 124ka. Figure 1.8c shows the Northern Hemisphere ice loss during the LIG according to the Kopp *et al.* (2009) study which indicates that it was very probable that Northern Hemisphere ice volume shrunk by at least 2.5 m of equivalent sea-level. They do, however, acknowledge the use of a Gaussian distribution to represent a non-Gaussian prior in their calculations of ice volume projection.

Nevertheless, the high eustatic sea-level change observed during the LIG implies there was less glacial ice on Earth during this period indicating a reduction in size

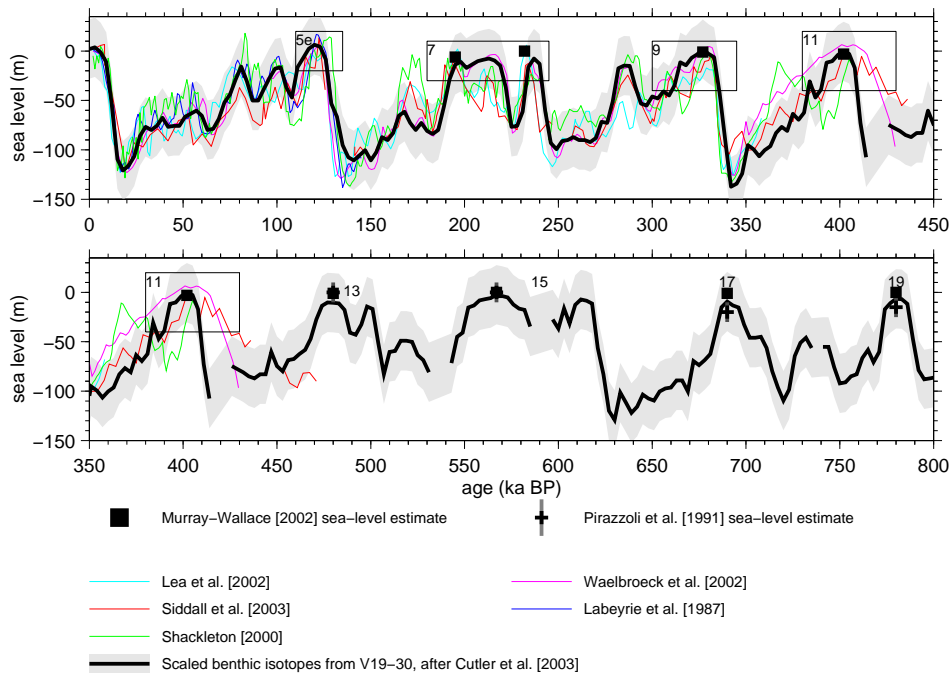


Figure 1.7: Sea-level curves for the last 800,000 years based on six different techniques for deriving sea-level from oxygen isotope ratios (*from Siddall et al. (2007)*). The section of the graph labelled stage 5e refers to the sea-level highstand of the LIG.

of the Greenland and/or the Antarctic ice-sheets. Other regions for consideration are the Arctic ice fields such as in Canada. Indeed, contributions from the GrIS to the sea-level highstand have been estimated to be between 1.5 and 5.5 m using GrIS models forced by temperature scenarios derived from data (e.g. Letreguilly *et al.*, 1991a; Cuffey and Marshall, 2000; Tarasov and Peltier, 2003; Lhomme *et al.*, 2005) and temperatures and precipitation produced by an AOGCM (Otto-Bliesner *et al.*, 2006a) (see Table 1.1).

Non-transient AOGCM simulations for the LIG, when forced with orbital forcing ranging between 130 to 125ka, produce a summer Arctic warming of up to 5°C with greatest warming over Eurasia and in the Baffin Island/Greenland region (Montoya *et al.*, 2000; Kaspar *et al.*, 2005; Otto-Bliesner *et al.*, 2006a) which could result in significant melting of the GrIS. Comparison with proxy reconstructions (e.g. Anderson *et al.*, 2006) of maximum Arctic summer warmth shows general agreement although the simulations might underestimate warmth in Siberia due to the lack of vegetation feedbacks included in the model. The simulated annual average global temperature for the LIG is similar to present day consistent with orbital forcing being the main driving mechanism.

The warmer climate during this time likely saw an extension of boreal forest and

shrubs into areas now occupied by tundra in the Arctic regions today. This transition to more temperate vegetation may have provided a feedback that not only amplified summer warmth but also contributed to winter warmth (Anderson *et al.*, 2006). Palaeo-proxies show various evidence of changes in vegetation in Siberia, Alaska and Greenland during the LIG. Palaeobotanical data suggest northward extension of certain tree species in northeast Siberia coincident with a warmer than present climate (Lozhkin and Anderson, 1995). More recent studies from northeast Siberia show the existence of shrubs interspersed with grasses in regions now occupied by Arctic tundra inferred from plant macrofossils (Kienast *et al.*, 2008) and further changes from grasses to shrub dominated vegetation at the LIG thermal optimum. This was followed by a return to grass dominance inferred from pollen records from terrestrial permafrost sections (Wetterich *et al.*, 2009). This in itself suggests a significantly warmer summer climate with an extended growing season. Pollen, macrofossil and soil records from Alaska also show extensive boreal forests over this region with probable migration of boreal forest to higher elevation now occupied by tundra (Lozhkin and Anderson, 1995; Muhs *et al.*, 2001).

Schurgers *et al.* (2007) used an Earth system model which includes interactive vegetation to assess the influence of land surface changes on the LIG climate and vice versa. The land surface parameters for feedback included those which affect the radiative fluxes (albedo) and turbulent fluxes (roughness length). A fully coupled simulation spanning the entire interglacial (128 to 113ka) was performed with temporally and regionally varying insolation. Expansion of boreal forest in high latitudes compared with the control peaked at 126ka with a gradual decrease thereafter. The decrease in forest area resulted in an increase in albedo enhancing the temperature increase at high latitudes. Comparison with experiments where the land surface was fixed showed roughly two thirds of the enhancement was due to the effect of forest presence on snow albedo and one third due to the difference in background albedo between trees and grasses and synergistic effects between these two processes. The main caveat (which they acknowledge) is that the simulations do not include interactive ice-sheets.

With regard to evidence for the presence of vegetation on Greenland itself, and therefore the inference of a reduced GrIS, a maximum abundance of the fern-spore (*Osmunda*) at approximately 121ka in an ocean core south of Greenland, indicates

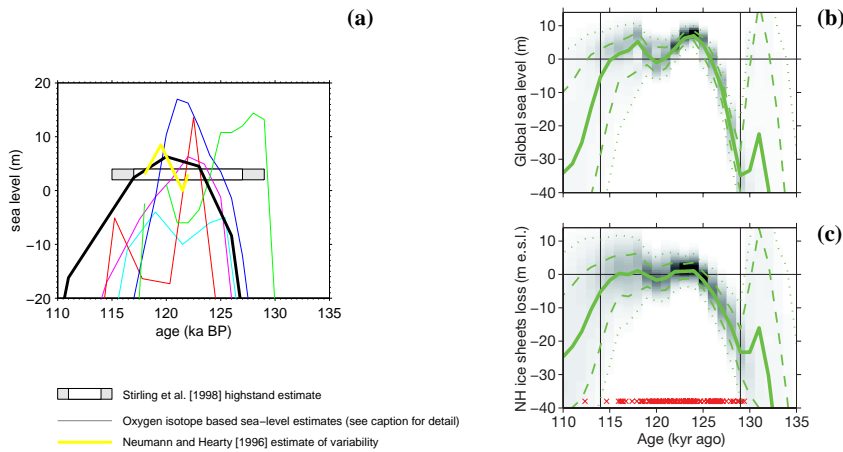


Figure 1.8: Last Interglacial sea-level curves and GrIS contribution from (a) Siddall *et al.* (2007) based on a variety of methods. Several studies converge on a highstand duration from  $128 \pm 1$  to  $116 \pm 1$  thousand years ago with sea-levels between +2 and +4 m. The yellow curve shows variation in sea-level with a mid-interglacial dip and a controversial peak at the conclusion of the LIG. Studies based on oxygen isotopes are shown by the light-blue, dark blue, red green, purple and black curves. (for more details about these studies see Siddall *et al.* (2007)). (b) Probability density plot of global sea-level from Kopp *et al.* (2009) and (c) probability density plot of Northern Hemisphere ice-sheet volume. For (b) and (c) heavy lines mark median projections, dashed lines the 16th and 84th percentiles, and dotted lines the 2.5th and 97.5th percentiles. Red crosses mark median posterior estimates of sample ages. Vertical lines mark the interval when  $> 30\%$  of samples from the distribution have standard deviations of global sea-level  $< 30\%$  of the prior standard deviation (and are included in calculations of exceedance probabilities). The horizontal line at 0 indicates modern values.

the spreading of fern-rich vegetation over southern Greenland (Hillaire-Marcel *et al.*, 2001). Macrofossil plant assemblages from marine sediments in central East Greenland from the LIG represent diverse dwarf shrub heaths with the subarctic bioclimatic zone displaced from southernmost Greenland/Iceland to Central East Greenland (Bennike and Bocher, 1994). A forested southern Greenland in the last one million years has also been inferred from ancient biomolecules found at the base of ice at the Dye-3 ice core (Willerslev *et al.*, 2007a). The authors tentatively suggest that this silty ice pre-dates the LIG (450 to 800ka) which contrasts with other studies suggesting that Dye-3 was ice-free during the LIG. Therefore, they do not discount the possibility of a LIG age for the Dye-3 ice (see Section 1.5.3 for the equivocal nature of this ice core).

### 1.5.2 Mechanisms for high latitude warming at the Last Interglacial

Links between climate and insolation forcing have been found in numerous records of past environmental changes and are explained by the astronomical theory of Milankovitch who argued that insolation during Northern Hemisphere summers is

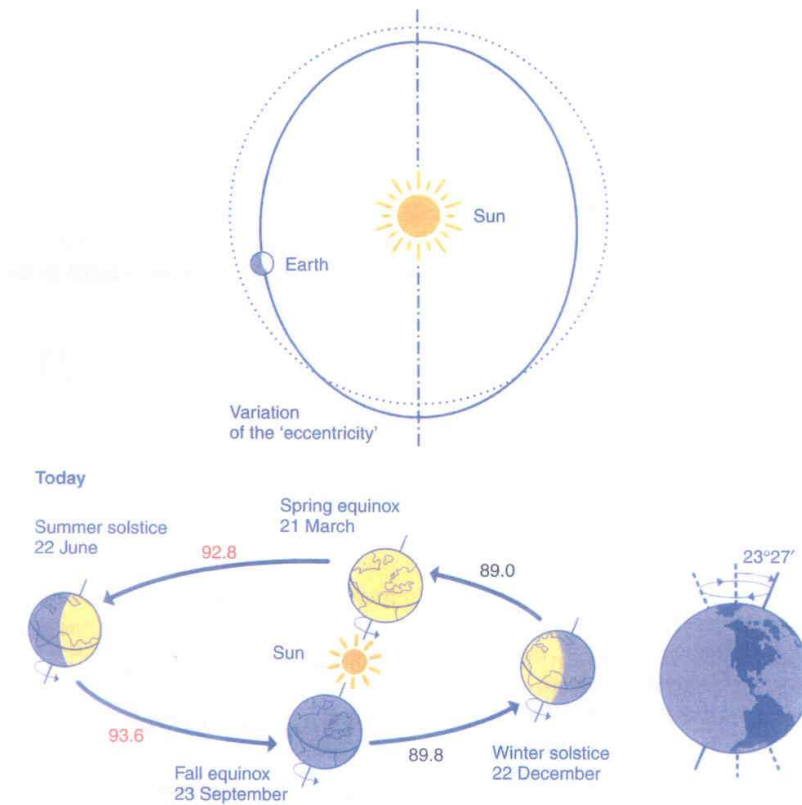


Figure 1.9: Diagram illustrating the orbital parameters which determine the amount of insolation received by Earth. The top figure shows the eccentricity, the bottom left the precession parameter and the present-day configuration of the Earth's orbit with the winter solstice occurring very close to the perihelion. Bottom right demonstrates the obliquity parameter with its present day value (from Berger *et al.* (2007).)

the critical parameter controlling glacial-interglacial cycles (Milankovitch, 1941). This theory takes changes in the orbital eccentricity, obliquity (the tilt of the Earth's rotational axis) and precession of the equinoxes into account (see Figure 1.9). These cause an alteration in the seasonal and spatial distribution of solar energy received at the top of the atmosphere and therefore are thought to alter surface temperature. Assuming a transparent atmosphere, the energy available at a given latitude,  $\Phi$ , on Earth at any time of the year is a function of the solar constant,  $S_0$ , the semi-major axis,  $a$ , of the Earth's orbit around the Sun (the elliptic), of its eccentricity,  $e$ , its obliquity,  $\varepsilon$  and the longitude of the perihelion measured from the moving equinox,  $\omega$ . The energy received per unit area of the Earth's surface and per unit time over a full year is given by

$$\overline{W_E} = \frac{S_0}{4} = \frac{S_a}{4\sqrt{1-e^2}}, \quad (1.2)$$

where  $S_a$  is the energy received by a unit of time on a unit area perpendicular to the Sun's rays at a distance  $a$ , from the Sun (Berger *et al.*, 2007). The eccentricity is the only astronomical parameter that changes the total solar energy received by the Earth in one year. Obliquity and precession only redistribute the energy among latitudes and seasons.

Changes in orbital *eccentricity* of the Earth vary in time between a highly elliptical orbit and a circular orbit with a mean periodicity of about 100,000 years superimposed on a longer period of about 400,000 years. It is only, however, responsible for very small changes in solar insolation varying by  $1 \text{ W m}^{-2}$  between the extrema of  $e$ .

The *obliquity*,  $\varepsilon$ , varies between  $21.39^\circ$  and  $24.36^\circ$  with a present value of  $23.44^\circ$  and has an impact on seasonal contrasts. It varies steadily with a periodicity of around 41,000 years. An increase in  $\varepsilon$  results in an increase in insolation at all latitudes during their summer and the reverse during their winter. The strength of this effect is small at low latitudes and maximum at high latitudes and damps the seasonal cycle in the high latitudes of both hemispheres simultaneously.

The *precession*,  $\omega$ , parameter affects the timing of the perihelion and the aphelion (position of the Earth closest and furthest away from the Sun respectively). This is caused by the rotation in the Earth's spin axis as it orbits around the Sun. The average period in long-term variations of this parameter is approximately 21,000 years resulting from four main spectral components situated around 23,000 and 19,000 years. This parameter results in opposing effects in the two hemispheres during their similar local seasons. For example, 12,000 years ago the summer solstice was at perihelion with all latitudes receiving more solar energy during the Northern Hemisphere summer. Thus Northern Hemisphere latitudes received more solar energy during the summer and less during the winter with the reverse occurring for Southern Hemisphere latitudes. The end result was a reduced seasonal gradient in the Southern Hemisphere and an increased gradient in the Northern Hemisphere (Berger *et al.*, 2007).

Therefore, in the context of a period when deglaciation is likely to have taken place (such as the LIG) an increase in solar insolation during the summer months at high latitudes is expected causing relatively warm conditions resulting in an increase in the rates of ablation at the margins of any existing ice-sheets. At the beginning



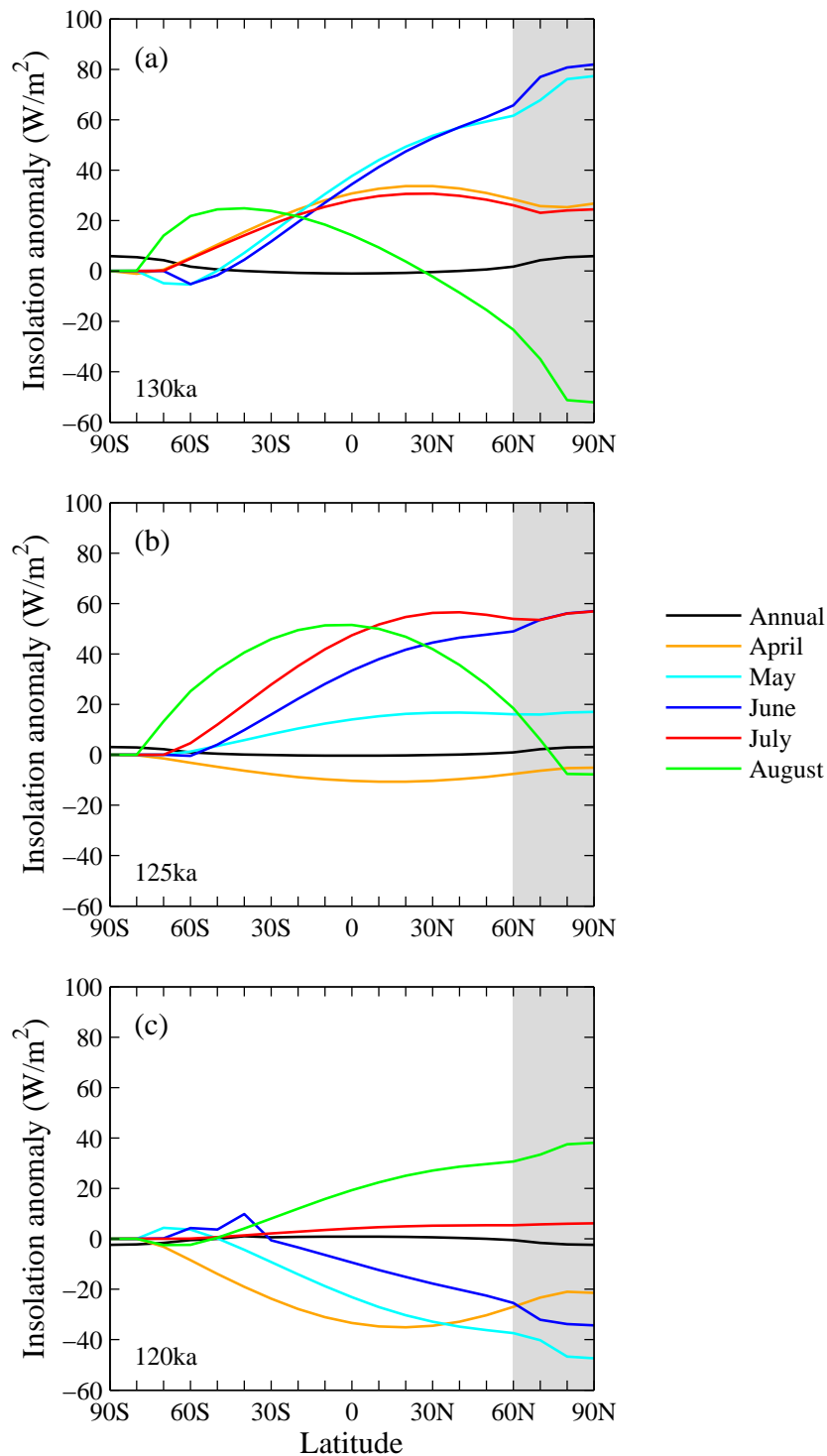


Figure 1.10: Insolation anomalies at the top of the atmosphere relative to present day as a function of latitude at (a) 130ka (thousand years ago), (b) 125ka and (c) 120ka. Large positive anomalies occur over the Arctic (shaded region) during Northern Hemisphere late spring to early summer at 130ka diminishing considerably towards 120ka. Small and positive annual high northern latitude anomalies are shown for completeness. Insolation values are calculated using the numerical solution of Laskar *et al.* (2004) (see <http://www.imcce.fr/Equipes/ASD/insola/earth/online/> accessed on [06/01/10]).

of the LIG there was an increase in eccentricity, obliquity and the perihelion (occurring around June/July) which led to greater seasonal temperature contrasts at high latitudes. In contrast, lower solar insolation values would result in colder, drier conditions during winter months and less snowfall over an ice mass. Milankovitch proposed that ice ages are triggered by minima in summer insolation near  $65^{\circ}\text{N}$  enabling winter snowfall to persist all year.

However, in the context of glaciation it has been shown that weak changes in the solar insolation driven by orbits are not always adequate to initiate ice inception and amplification of the climate response to variation in orbits is required (e.g. Desprat *et al.*, 2005). Where changes in insolation are more pronounced it appears that orbital forcing can trigger inception of ice-sheets alone while changes in vegetation, ocean and atmospheric  $\text{CO}_2$  provide additional but important feedbacks in the system (e.g. Meissner *et al.*, 2003; Calov *et al.*, 2005b; Kubatzki *et al.*, 2006; Bonelli *et al.*, 2009). This amplification or damping of the climate response occurs as a result of non-linear feedbacks previously discussed in Section 1.3 between individual climate components, including vegetation, albedo and greenhouse gases.

At the beginning of the LIG (130ka),  $\text{CO}_2$  concentrations rose from around 200 ppmv (135ka) to 260 ppmv remaining around preindustrial values (280 ppmv) for the next 10,000 years. It was, however, mainly large insolation anomalies relative to present driven by changes in the Earth's orbit, which caused the warm Northern Hemisphere climate as shown in climate simulations for the LIG (e.g. Montoya *et al.*, 2000). Figure 1.10 shows the large positive insolation anomalies relative to present at higher northern latitudes for late spring/early summer. At 130ka anomalies up to  $80 \text{ Wm}^{-2}$  are seen for May and June. By 125ka the maximum positive anomalies have decreased to  $60 \text{ Wm}^{-2}$  with the summer months of June and July dominating. By 120ka only August shows a positive anomaly of  $40 \text{ Wm}^{-2}$  with other summer months now negative. This is particularly important for the GrIS since it has shown sensitivity to summer warming when ablation is strongest (Krabill *et al.*, 2004).

### 1.5.3 The evidence for a reduced Greenland ice-sheet during the Last Interglacial

The extent of the GrIS during the warmest part of the LIG and its possible contribution to the sea-level highstand still remains uncertain based mainly on the

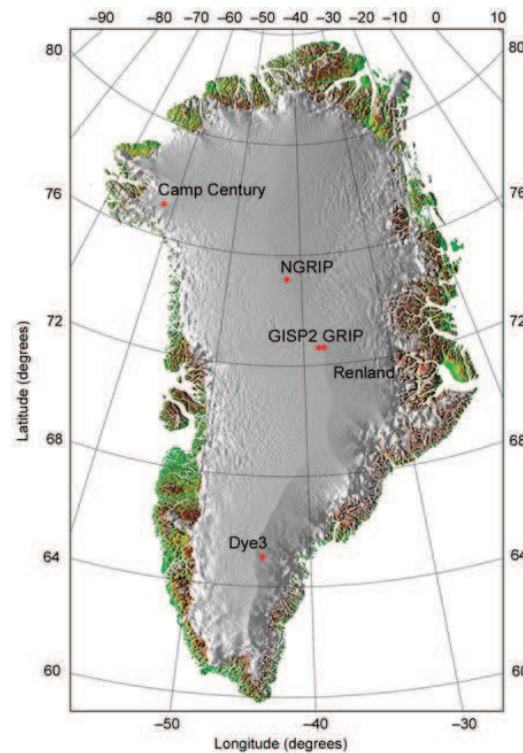


Figure 1.11: Locations of the deep ice core drilling sites on the GrIS. The sites GRIP (72.58°N, 37.38°W), GISP2 (72.58°N, 38.38°W), NGRIP (75.18°N, 42.38°W), Camp Century (77.28°N, 61.18°W), Dye3 (65.28°N, 43.88°W) and Renland (71.38°N, 26.78°W) are shown (from Andersen *et al.* (2004)).

interpretation of several ice cores in Greenland. Figure 1.11 shows the location of six ice cores: Camp Century, NGRIP, GISP2, GRIP, Renland and Dye-3 which have been used in an attempt to constrain the size of the GrIS during the LIG.

The Camp Century ice core, in northwestern Greenland, was the world's first deep ice core and reached a depth of 1390 m (Dansgaard, 2004). Tentative dating suggests that this core spans much of the LIG at least beyond 125ka (Dansgaard *et al.*, 1982, 1985). The Renland ice core on the east coast of Greenland is a short (325 m), compressed core but nevertheless reaches back to the middle of the LIG (125ka) (Johnsen *et al.*, 1992; Hansson and Holmen, 2001). The Camp Century and Renland ice core records show heavier and sustained  $\delta^{18}\text{O}$  values at the base indicative of ice from the latter part of the Eemian stage, perhaps with earlier ice melted away (Koerner and Fischer, 2002). These records though are highly compressed and do not extend throughout the LIG.

Interpretation of the Dye-3 ice core in southern Greenland is particularly controversial. Some studies indicate that the southern ice dome disappeared (Koerner

and Fischer, 2002) or was an isolated dome during the warmest phase of the LIG (Lhomme *et al.*, 2005) while others suggest that ice at the bottom of Dye-3 indicates a substantial reduction in southern Greenland ice thickness but not complete collapse (e.g. Dansgaard *et al.*, 1985; Andersen *et al.*, 2004). More recently, four dating techniques (see Willerslev *et al.* (2007b) for details and limitations of methods) were applied to the silty-rich ice layer at the base of Dye-3 by Willerslev *et al.* (2007a). They found that the four dates overlapped giving an age estimate between 450 to 800ka. From this they concluded that the ice at Dye-3 predates the LIG. However, they acknowledged that due to many uncertainties in the dating methods and the interpretation of ice age estimates, they could not rule out a possibility of a LIG age for the ice at the base of Dye-3. In addition to the evidence described here, locations with close proximity to Greenland, such as the eastern Canadian Arctic, also show an absence of pre-LIG ice for the larger ice caps. This evidence indicates widespread melting during the enhanced warmth of that time period (Koerner, 1989).

In fact, initial evidence from Camp Century, Dye-3 and the Canadian Arctic islands led to the initial conclusion that the GrIS extensively or completely melted away during the LIG (Koerner, 1989). However since then, ice cores situated within the GrIS summit region have more closely constrained the estimated minimum extent of the ice-sheet. The NGRIP core gives an undisturbed ice core record to 123ka (Andersen *et al.*, 2004) while the Greenland Ice Core Project (GRIP) and Greenland ice-sheet Project 2 (GISP2) show likely older but disturbed LIG ice (only reliable to 105ka) (Chappellaz *et al.*, 1997; Raynaud *et al.*, 1997). The results from these cores suggest the Greenland summit region remained ice-covered throughout the LIG although with an elevation perhaps about 500m lower than today (Raynaud *et al.*, 1997).

The fact that these records neither span fully the LIG (NGRIP), nor show an undisturbed LIG ice record (GRIP and GISP2) or simply that the records are too compressed to show accurate detail and are equivocal (Camp Century, Renland, Dye-3) requires the need for an ice core that penetrates the full LIG (e.g. Dahl-Jensen, 2005). Indeed, research should continue to explore this further in combination with improvements in LIG sea-level estimates and modelling techniques to predict the ice-sheet extent discussed in detail below. Currently, the North Greenland Eemian Ice Drilling project, NEEM, is being implemented which aims to retrieve such an

ice core from northwest Greenland (camp position 77.45°N 51.06°W) that reaches back through the LIG period and beyond.

Table 1.1 outlines the major studies which have predicted the size of the GrIS during the LIG using various modelling techniques as far back as the early 1990s. The first study to look at the effect of LIG warmth on the size of the GrIS was Letreguilly *et al.* (1991a). They used a 3D thermo-mechanical ice-sheet model in combination with a temperature record derived using oxygen isotopes from surface samples in central West Greenland (Pakitsoq) to evaluate the evolution of the GrIS over the last 150,000 years. Results showed a retreat of the ice-sheet margins with splitting of the ice-sheet into two main sections; one covering central and northern regions and a smaller ice cap in the south. The ice free regions were attributed to lower elevation and accumulation with the position of the margins highly sensitive to ablation processes. In terms of contribution to sea-level, simulations indicated approximately 2 m rise compared with present day. The ice-sheet margin is close to the Dye-3 ice core which lies in the ablation zone with only a small change in temperature resulting in this region possibly becoming ice-free. They found the ice-sheet did not completely collapse owing to subsequent isostatic uplift after melting and retreat of the ice margin. This brought regions to higher altitude which reduced ablation and the rate of retreat considerably. This result, however, is strongly dependent on the temperature history of the region where uncertainty in results arises much more due to errors in the derived climatology compared with errors associated with the ice-sheet model itself. Accumulation is also temperature dependent since it is generated from present day accumulation parameterised in terms of temperature variation, since at the time, precipitation from GCMs was not only quite unreliable but also highly computationally expensive to model. Furthermore, the climate record is based on surface data such that the older part is difficult to date as the ice has travelled from the central part of Greenland.

Ritz *et al.* (1997) also used a similar approach to Letreguilly *et al.* (1991a) but modelled a much larger ice-sheet during the LIG. They attributed this difference to the forcing used because the previous interglacial is longer in the Pakitsoq record than in the GRIP record used by Ritz *et al.* (1997).

More recently, Cuffey and Marshall (2000) also used the palaeothermometer technique based on oxygen isotopes. They simulated the evolution of the GrIS over

160,000 years with a 3D coupled-ice-sheet flow model where temperature, accumulation and ablation rate are governed by the temperature changes observed in the  $\delta^{18}\text{O}$  record. However, in the previous studies sensitivity of isotopic content,  $\Delta\delta^{18}\text{O}$ , to temperature,  $\Delta T$ , was assumed to be the modern value of proportionality,  $\alpha_o$ , where

$$\Delta\delta^{18}\text{O} = \alpha_o\Delta T. \quad (1.3)$$

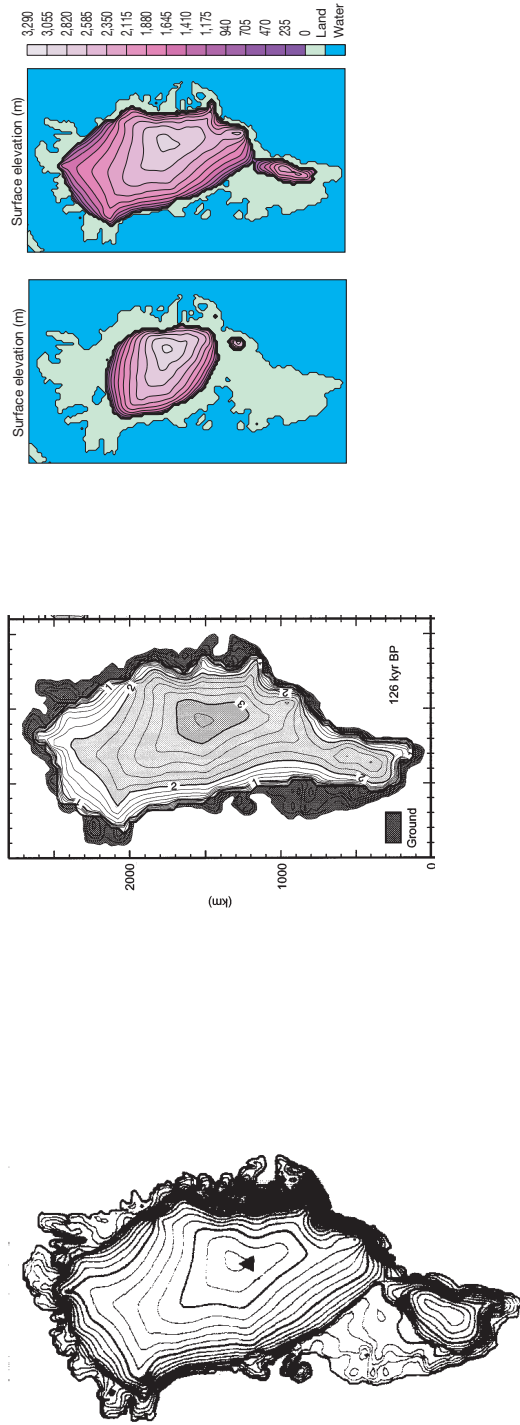
In this newer study they employed lower values of sensitivity than before based on previous work indicating temporal variability in isotopic sensitivity. The lower values of sensitivity according to Equation 1.3 would result in a warmer climate than previously thought. Simulating the evolution of the GrIS for a range of sensitivities and for a ‘fabricated’ isotopic chronology older than 98,000 years ago, the authors concluded that the contribution to the sea-level highstand could very likely be 4 to 5.5 m with a smaller and steeper GrIS than previously predicted. However, the lack of information regarding spatial distribution of accumulation and the lack of reliable palaeoclimate history for the LIG make their findings somewhat uncertain.

Tarasov and Peltier (2003) provided another independent examination of contribution to sea-level from the GrIS during the LIG using a similar but more sophisticated technique in an attempt to constrain the model more closely than Cuffey and Marshall (2000). Additional constraints to the model included adjustment of precipitation sensitivity to the climate forcing and geothermal heat flux in order to match more closely with the borehole temperature and age profile at the GRIP core and also basal temperatures at Dye-3 and Camp Century. Furthermore, the model was constrained to produce an accumulation history bounded by inferences from the GRIP and GISP2 cores. They further tuned regional precipitation and calving parameters in order to match relative sea-level observations obtained from 16 sites distributed around the entire coastline of Greenland. A very high-resolution semi-Lagrangian tracer technique to trace ice source elevation and ice age was also used. Their conservative estimate for contribution to the sea-level highstand is 2 to 5.2 m with a more likely range of 2.7 to 4.5 m. They acknowledge, however, the use of a single climate proxy in the vicinity of the summit region, when the ice-sheet extent in fact is largely governed by the climate at the ice margin and near coastal regions. This is likely the major uncertainty in constraining the volume and extent

Table 1.1: Table summarising previous studies of GrIS extent during the Last Interglacial. The first five studies use palaeothermometry from ice cores to force an ice-sheet model offline. The final, most recent study (Otto-Bliessner *et al.*, 2006a) uses a climate model in combination with an ice-sheet model to simulate the LIG climate. The sea-level contributions are from Greenland alone.

| Study         | Letreguilly <i>et al.</i> (1991a)  | Ritz <i>et al.</i> (1997)  | Cuffey and Marshall (2000)   |
|---------------|--|--|--|
| Method        | $\delta^{18}\text{O}$ temperature record and parameterised accumulation used to force ice-sheet model offline. | $\delta^{18}\text{O}$ temperature record and parameterised accumulation used to force ice-sheet model offline. | 3D coupled ice and heat flow model forced with various temperature $\delta^{18}\text{O}$ reconstructions based on different sensitivity of $\delta^{18}\text{O}$ to temperature. |
| sea-level (m) | + $\sim 1.5$ at 130ka  | Not given  | + 4 to 5.5   |

**GrIS extent**



continued on next page ...

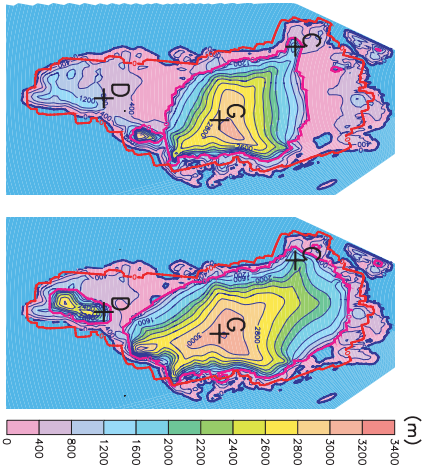
... continued from previous page

**Study** Tarasov and Peltier (2003)

**Method** 3D dynamical ice-sheet model forced with temperature record derived using semi-Lagrangian tracer methods to trace  $\delta^{18}O$ .

**sea-level (m)** +2 to 5.2 with likely range 2.7 to 4.5 at 127ka

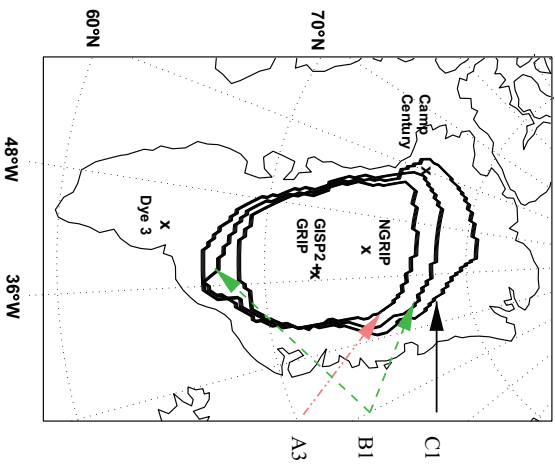
**GIS extent**



Lhomme *et al.* (2005)

Coupled model of depositional provenance and transport of glacier ice to determine palaeothermometry used to force ice-sheet model.

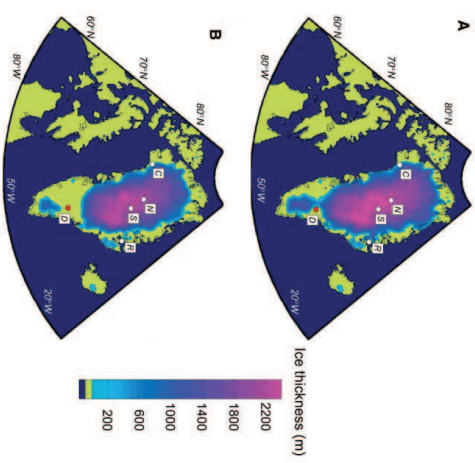
+3.5 to 4.5



Otto-Bliesner *et al.* (2006a)

One-way coupling of NCAR climate model to ice-sheet model for a constant 130ka climate (no vegetation feedbacks included.)

+1.9 to 3.04 (128 to 127ka)





of the GrIS during the LIG.

Lhomme *et al.* (2005) again employ a similar method to the previous studies using climatology derived from GRIP and Vostok records. However, they claim to improve the accuracy of the semi-Lagrangian tracer methods used to construct the age-depth relationship within the cores. Model setups which agree with present day ice geometry and the temperature and isotopic profiles at ice core sites are identified by exploring the key parameters that govern ice dynamics and the climatology (i.e. flow enhancement factor and isotopic sensitivity). According to this study, the Dye-3 and Camp Century cores are extremely sensitive to the ice dynamics and therefore greatly constrain the reconstruction of the LIG GrIS extent. As such only a select few model setups in agreement with GRIP and also Dye-3 and Camp Century data were used. The authors estimate a maximum sea-level contribution from Greenland between 2.5 to 4.5 m and a preference toward 3.5 to 4.5 m based on the sensitivity observed from Camp Century. This maxima is achieved close to 127ka. They acknowledge, however, that the use of spatially uniform climatic change and simplification of melting processes at or near the margins of the ice-sheet means the results are not completely robust. Improvements to spatially varying geothermal heat flux are also required in order to match the basal melt derived from cores. This is particularly important for palaeoclimatic studies where the age of the oldest ice is often of interest and is influenced by basal melt rate.

The most recent study to date (Otto-Bliesner *et al.*, 2006a) uses a very different technique to constrain the ice volume of the GrIS and is similar to the methodology used in this thesis. They used a coupled AOGCM (NCAR Community Climate System Model) to simulate the climate of the LIG and coupled this one-way to an ice-sheet model which spans the entire western Arctic. The climate model was forced with the large insolation anomalies predicted at 130ka. The ice-sheet model was initiated with a GrIS present at 130ka (assumed to be the same as present). Warming is observed over Greenland with temperatures greater than 3°C along the edges of the ice-sheet and up to 2.8°C in the centre of the ice-sheet, somewhat less than observation from proxy data. Results from the ice-sheet model forced with the 130ka climate show retreat of the GrIS such that the Dye-3 ice core becomes ice-free after 2,000 years. Greenland and the western Arctic ice-fields contributed 2.2 m of sea-level rise at this point in time. An additional 1,000 years were required in order

for the palaeodivide to be 570 m lower than present. In this GrIS configuration the minimum Arctic sea-level contribution was 3.4 m. Contributions purely from the GrIS therefore range from 1.9 to 3.0 m. Table 1.1 shows the resultant ice-sheet is a steeply sided ice-sheet in central and northern Greenland. The study acknowledges that the simulated GrIS is not in equilibrium and a continued warming would drive a smaller and lower ice-sheet with continued sea-level rise. However, there was no inclusion of vegetation feedbacks and the authors claim that their simulation performed a reasonable job at simulating the Arctic response to LIG warming without this feedback being included. They therefore suggest that the size of this missing feedback is likely smaller than originally thought (Montoya *et al.*, 2000; Otto-Bliesner *et al.*, 2006b). There are, however, a number of inadequacies with this study. Firstly, the climate does not evolve through the LIG but remains constant at 130ka. Secondly, the maximum sea-level contribution (and thus the minimum size of the GrIS) from the Arctic region is constrained by the interpretation of the palaeo ice core data which is not without uncertainty, particularly in the case of the southern Dye-3 ice core. Thirdly, the coupling between the climate and ice-sheet model is one-way so does not include the ice-albedo feedback between the climate and ice-sheet nor the response of the GrIS to a transient climate. The methodology in this thesis attempts to address some of these inadequacies. Firstly, the climate is simulated at various times during the LIG so does not remain constant. Secondly, the ice-sheet model is forced with this transient climate and the ice volume and GrIS geometry is compared with observations rather than constrained by them (i.e. the modelled results will be independent of observation). Thirdly, the impact of vegetation feedbacks is investigated. Fourthly, the impact of parametric uncertainty within the ice-sheet model on GrIS evolution during the LIG is assessed.

## 1.6 Aims and objectives

This thesis aims to look specifically at the impact of vegetation feedbacks on the evolution of the GrIS under future and past climates. As discussed in Section 1.3, theory indicates that this feedback occurs because changes in vegetation type affect surface albedo and energy balance at the surface, hence altering the climate which in turn alters the vegetation type and so on. These feedbacks have largely been

neglected when modelling the behaviour of the GrIS and could play an important role in its evolution during the next 100 to 1,000 years as well as changes that have occurred in the past. It has been acknowledged by the IPCC (2007) that past northward shift of the boreal treeline under warming conditions from climate and vegetation model simulations would *likely* result in a significant positive climate feedback.

In terms of future climate, focus in this thesis will be on the possible role of vegetation in regrowth of the GrIS after complete deglaciation, if CO<sub>2</sub> concentrations are reduced to near preindustrial values of 280 ppmv. While for past climate simulations the following question will be explored: ‘are vegetation feedbacks important in determining the minimum extent of the GrIS during the Last Interglacial?’.

The specific objectives of this thesis in order to satisfy the aims are outlined below:

1. Evaluation and one-way coupling of the Glimmer ice-sheet model for present day conditions.
2. Simple, decoupled simulations using the GCM, HadCM3, with the ice-sheet replaced by different fixed vegetation types in order to understand the impact of vegetation parameters on the surface energy budget. Further idealised sensitivity experiments to surface roughness length and orographic elevation are also performed.
3. Inclusion of the interactive dynamic vegetation model, TRIFFID, within the climate model HadCM3 to simulate vegetation distribution on a melted Greenland under preindustrial conditions.
4. Forcing of Glimmer offline using climate output derived from the regrowth experiments in Objectives 2 and 3.
5. As yet, fully coupled climate-ice-sheet simulations are not feasible over long time periods using full GCMs. An objective is to develop a method where Glimmer simulates (both with and without vegetation feedbacks included) the extent of the ice-sheet from 136 to 120ka using linearly interpolated and weighted (no ice versus full ice) climate output between snapshot climate simulations.

## 1.7 Thesis structure

Chapter 2 describes the ice-sheet model, Glimmer, and includes an assessment of the sensitivity to present day boundary conditions and forcings, namely bedrock and ice thickness, precipitation and temperature. The datasets currently in use by the majority of GrIS modelling studies are over two decades old and based on data collected from the 1970s and 1980s (Ohmura, 1987; Letreguilly *et al.*, 1991b; Ohmura and Reeh, 1991). An up-to-date and more accurate dataset of ice thickness in conjunction with a Digital Elevation Model (DEM) of the Greenland bedrock is now available, as are precipitation and temperature datasets. Significant differences have been found between the old and newer datasets requiring a tuning exercise to be performed in order to reproduce the modern day GrIS as closely as possible. Five parameters are varied between their uncertainty ranges simultaneously in order to obtain several optimum solutions for the present state of the ice-sheet.

Chapter 3 addresses the importance of vegetation on the climate of Greenland when the ice-sheet is removed and CO<sub>2</sub> concentrations are at preindustrial values. The climate model, HadCM3, is described here with emphasis on the land surface scheme (MOSES 2). A methodology is developed in order to examine the sensitivity of Greenland climate to different fixed vegetation types from bare soil to needleleaf forest. A further study looks at the importance of vegetation parameters such as surface roughness length. Finally, sensitivity to orographic height changes over Greenland are also evaluated.

Chapter 4 builds on the work of Chapter 3 by including an interactive vegetation model, TRIFFID. Continuation of the most contrasting experiments in terms of precipitation and temperature in Chapter 3 is performed in order to assess the sensitivity to initial vegetation conditions over Greenland.

Chapter 5 addresses the question of whether the GrIS could regrow under preindustrial conditions if removed. The climate output from Chapters 3 and 4 are used to force the Glimmer ice-sheet model offline until equilibrium is reached. This is performed for the standard setup of the ice-sheet model and the new tuned solutions in order to assess the uncertainty of ice-sheet modelling on the regrowth results.

Chapter 6 uses and develops the methodology from Chapters 2 to 5 in order to look at the importance of vegetation feedbacks on the minimum size of the GrIS

---

during the LIG. Snapshot climate simulations with and without interactive vegetation included are run for a number of LIG timeslices and used with the ice-sheet model as described in Objective 4. Sensitivity of GrIS behaviour to initial condition is also considered.

Finally, Chapter 7 summarises the work from the previous chapters, draws conclusions and discusses possible future directions for the research.



# The ice-sheet model

## 2.1 Introduction

Much attention has focussed on the stability of the GrIS under current Arctic climate conditions. Estimates of the GrIS's contribution to sea-level change during the period 1993 to 2003 range between  $+0.14$  to  $+0.28$  mm yr<sup>-1</sup> (IPCC, 2007), although recent estimates suggest as much as  $+0.75$  mm yr<sup>-1</sup> for 2006-2009 (Van den Broeke *et al.*, 2009; Velicogna, 2009) linked with significant recent increases in GrIS melt, run-off and mass loss (Hanna *et al.*, 2008; Rignot *et al.*, 2008). Recent model projections suggest that the GrIS could be eliminated within a few millennia for a mean annual global warming between 1.9 to 4.6°C over Greenland relative to preindustrial temperatures (Gregory and Huybrechts, 2006). These projections, however, are based on a numerical model which does not include a representation of fast-flowing outlet glaciers. These glaciers have been observed to undergo dynamic changes in recent years, resulting in faster ice flow and consequent ice loss (Joughin *et al.*, 2004; Luckman *et al.*, 2006; Rignot and Kanagaratnam, 2006; Howat *et al.*, 2007; Rignot *et al.*, 2008), meaning that the model probably underestimates the rate of mass-loss from the GrIS.

In order to perform an ice-sheet simulation the following are required: (1) a bedrock dataset and if necessary an ice thickness dataset as initial conditions and (2) climate forcing data (precipitation and temperature in this case). For future climate ice-sheet modelling an anomaly coupling method for the forcing data is often used (e.g. Ridley *et al.*, 2005; Driesschaert *et al.*, 2007; Vizcaíno *et al.*, 2008). This requires a good baseline modern climate on which to superimpose the anomalies. The majority of recent modelling studies of the GrIS use the data assembled for the EISMINT (European Ice-sheet Modelling INiTiative) model intercomparison project as a present day representation of the GrIS. Because the description of the data is included in the report from the 3rd EISMINT workshop (Huybrechts, 1997), it is referred to as the EISMINT-3 data. The data consist of a DEM of ice thickness and bedrock elevation, and parameterised temperature and precipitation fields, onto

which the climate anomalies are typically superimposed for both future and past climates (e.g. Huybrechts and de Wolde, 1999; Gregory *et al.*, 2004; Ridley *et al.*, 2005; Driesschaert *et al.*, 2007; Lunt *et al.*, 2008, 2009). The high-resolution bedrock and ice thickness used in EISMINT-3 are nearly two decades old and are based on data collated during the 1970s and 1980s. More recent and accurate datasets for the boundary conditions of bedrock topography and ice thickness (Bamber *et al.*, 2001) as well as temperature and (Hanna *et al.*, 2005, 2008) precipitation (ECMWF, 2006) forcings are now available. Differences in these datasets could have considerable impacts on the modelled evolution of the GrIS and hence the resulting ice-sheet volume and geometry, for simulations of past, modern and future climates.

As a foundation to the rest of the ice-sheet modelling work, the Glimmer ice-sheet model (Rutt *et al.*, 2009) is used to investigate and compare the impact on the modelled steady-state ice-sheet of two sets of boundary conditions: those used in the EISMINT-3 exercise, and the more recent and up-to-date datasets. Furthermore, a tuning exercise has been performed with respect to the most recent datasets in order to determine the values of various ice-sheet model parameters which give the best fit between modelled and observed geometry for present day conditions. In this way the best possible representation of the GrIS can be realised using the more recent datasets. The results from the tuning exercise are used in Chapter 5 to assess the importance of parametric uncertainty on the regrowth of the GrIS if it were to completely melt under elevated CO<sub>2</sub> concentrations. They are also used in Chapter 6 to show the range in minimum extent of the GrIS during the LIG arising from parametric uncertainty in the ice-sheet model. The results in this Chapter, including additional work, have been published in Stone *et al.* (2010).

## 2.2 Model description

The version of Glimmer used in this thesis is 1.0.4. Although not the most recent version of the model, this version is used for consistency with previous work (e.g. Lunt *et al.*, 2008, 2009). Changes in the 1.0.x series are restricted to bug fixes (concerning the basal sliding parameterisation scheme which is not used here) and minor enhancements to existing features such as methods to interpolate climate forcing data from the climate grid onto the ice-sheet model grid. The core of the model



| Symbol     | Value                   | Units                                     | Description  |
|------------|-------------------------|---|--|
| $\rho_i$   | 910                     | kg m <sup>-3</sup>                        | Density of ice   |
| $k_{ice}$  | 2.1                     | W m <sup>-1</sup> K <sup>-1</sup>         | Thermal conductivity of ice                            |
| $k_{rock}$ | 3.3                     | W m <sup>-1</sup> K <sup>-1</sup>         | Thermal conductivity of rock                           |
| $c_{ice}$  | 2009                    | J kg <sup>-1</sup> K <sup>-1</sup>        | Specific heat capacity of ice                          |
| $g$        | 9.81                    | m s <sup>-2</sup>                         | Acceleration due to gravity                            |
| $a$        | $1.73 \times 10^{-3}$   | Pa <sup>3</sup> s <sup>-1</sup>           | Material constant for $T^* \geq 263\text{K}$           |
| $a$        | $3.613 \times 10^{-13}$ | Pa <sup>3</sup> s <sup>-1</sup>           | Material constant for $T^* < 263\text{K}$              |
| $Q$        | $139 \times 10^3$       | J mol <sup>-1</sup>                       | Activation energy for creep for $T^* \geq 263\text{K}$ |
| $Q$        | $60 \times 10^3$        | J mol <sup>-1</sup>                       | Activation energy for creep for $T^* < 263\text{K}$    |
| $R$        | 8.314                   | J mol <sup>-1</sup> K <sup>-1</sup>       | Universal gas constant                                 |
| $\alpha_i$ | 8                       | mm water d <sup>-1</sup> °C <sup>-1</sup> | Positive degree day factor of ice                      |
| $\alpha_s$ | 3                       | mm water d <sup>-1</sup> °C <sup>-1</sup> | Positive degree day factor of snow                     |
| $L_G$      | -6.227                  | °C km <sup>-1</sup>                       | Atmospheric temperature lapse rate                     |
| $n$        | 3                       | -   | Flow law exponent                                      |
| $f$        | 3                       | -   | Flow enhancement factor                                |
| $G$        | -0.05                   | W m <sup>-2</sup>                         | Uniform geothermal heat flux                           |

Table 2.1: List of default parameters and physical constants used in the Glimmer model. Those highlighted in bold are varied in the tuning experiments (for a complete set see Rutt *et al.* (2009)).

is based on the ice-sheet model described by Payne (1999). All physical constants and parameters discussed in this section are given in Table 2.1. The following section describes the parts of the model which pertain to the model parameters which are tuned in the subsequent sections of this chapter. A full description of the model can be found in Rutt *et al.* (2009).

The model includes a surface mass balance scheme, coupled ice flow, thermodynamics and ice thickness evolution and an isostatic readjustment component. Its design allows easy coupling to a wide variety of climate models. As such there are two main components to the model GLIDE and GLINT. GLIDE (General Land Ice Dynamic Elements) forms the core part of Glimmer where ice velocities, internal ice temperature distribution, isostatic readjustment and meltwater production are calculated. It takes boundary conditions from the climate driver which provides upper surface temperature and mass balance fields, from the isostasy model which provides the lower surface elevation, and finally a geothermal model which provides a geothermal heat flux through the lower surface of the ice. GLINT is an interface which allows any standard latitude longitude climate model to be coupled to GLIDE relatively easily.

Certain aspects concerning modelling the GrIS have not been included in the ice-sheet model simulations in this thesis and are briefly described here. Firstly, the version of Glimmer used does not contain an ice shelf component. Since Glimmer uses the ‘Shallow Ice Approximation’ for modelling large-scale ice-sheets (see Section

2.2.1 for more detail) and, therefore, neglects all longitudinal stresses, modelling ice shelves is not possible since they are dominated by longitudinal and lateral stress gradients. The inclusion of a separate ice shelf model has been attempted by others (e.g. Huybrechts, 2002) but the difficulty, particularly the coupling of the two models across the grounding line, has proven far from trivial (Alley *et al.*, 2005). Although the presence of ice shelves for Antarctica is important, since they cover an area equivalent to 11 % of the entire ice-sheet and nearly all ice streams and outlet glaciers flow into these ice shelves, it is not essential to model the ice shelves around Greenland. These cover only a few thousand square kilometers and many only represent glacier floating tongues (Lemke *et al.*, 2007).

Secondly, the process of calving is parameterised at the marine margin (no attempt at modelling the process of calving has been made). For the purpose of this thesis all ice is lost once the bedrock reaches sea-level around the margins of the ice-sheet.

Thirdly, although basal sliding and basal hydrology are included as options in Glimmer they are simplistic in their attempt to model these components of the ice-sheet system (Rutt *et al.*, 2009). Since modelling the GrIS in this thesis is centered around the criteria used in the EISMINT-3 benchmark exercise (described in Section 2.3.1) basal sliding has not been included. An increase in the ice velocity, by incorporating the sliding velocity, would result in more ice transferred from the accumulation zone to the ablation zone and, therefore, reduce the volume of the ice-sheet. It is likely that if basal sliding was switched on the sliding coefficient would increase the ice velocity but initially act only in the zones where the ice base is at the melting point which corresponds to the outer parts of the ice-sheet. It has been shown in previous sensitivity experiments (Ritz *et al.*, 1997) that the surface area covered by ice would increase slightly with sliding because ice is transported faster to the edge and ablation does not remove it completely. It is also important to realise the absence of this process could have implications for tuning of the ice-sheet model. For example, in order to reproduce a realistic modern day GrIS, the parameters that control ablation may need to compensate more for the removal of ice at the margins due to the lack of dynamical changes from basal sliding, which would increase the transfer of ice from the accumulation zone to the ablation zone.

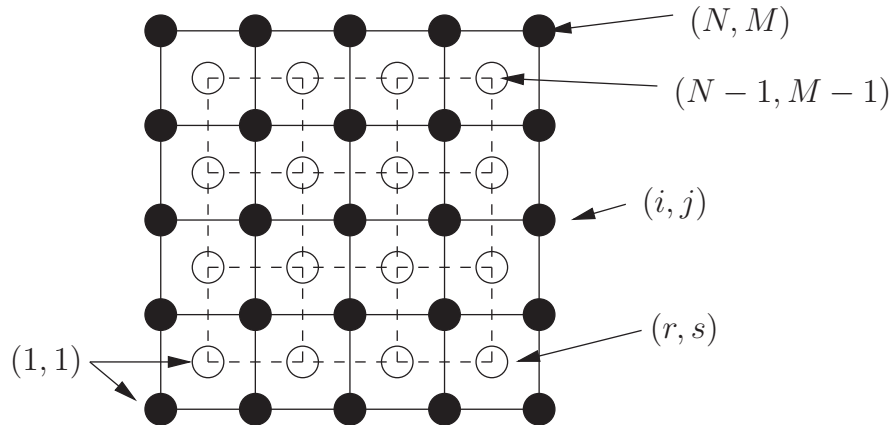


Figure 2.1: The regular horizontal grid setup used to solve the continuous ice equations which describe the ice physics of the model. The grid consists of two staggered grids -  $(i, j)$ -grid and the  $(r, s)$ -grid - which are off-set by half a grid space (*from Hagdorn et al. (2007)*).

### 2.2.1 Model numerics within GLIDE

#### The numerical grid

The Glimmer model is formulated on a Cartesian x-y grid of various resolutions. All simulations in this thesis are run at a 20 km resolution. In order to computationally solve the continuous equations which describe the ice physics outlined below they must be discretised using finite-difference methodology. Two horizontal grids with equal spacing of  $\Delta x$  and  $\Delta y$  are used in order to improve stability but are offset by half a grid-width (Figure 2.1). Ice thickness, temperatures and vertical velocities are calculated on the  $(i, j)$ -grid while horizontal velocities and associated quantities such as the diffusivity are calculated on  $(r, s)$ -grid. The vertical coordinate,  $z$ , is scaled by the ice thickness. As a result a new vertical coordinate,  $\sigma$ , is implemented such that the ice surface is at  $\sigma = 0$  and the base of the ice is at  $\sigma = 1$  (Figure 2.2). Discretisation of the vertical coordinate uses an irregular grid-spacing because ice flow is more variable at the bottom of the ice column.

#### Ice-sheet mechanics

The ice thickness ( $H$ ) evolution is driven by the mass conservation equation

$$\frac{\partial H}{\partial t} = -\nabla \cdot (\bar{\mathbf{u}}H) + B - S, \quad (2.1)$$

where  $\mathbf{u}$  is the horizontal velocity and  $\bar{\mathbf{u}}$  is the horizontal velocity averaged over the ice thickness,  $B$  is the surface mass balance rate and  $S$  is the basal melt rate.

Equation 2.1 is solved using a linearised semi-implicit method by re-writing it as a diffusion equation, with non-linear diffusion coefficient  $D$

$$\begin{aligned}\frac{\partial H}{\partial t} &= -\nabla \cdot \mathbf{q} + B - S, \\ &= -\nabla \cdot (D\nabla s) + B - S,\end{aligned}\tag{2.2}$$

where  $\mathbf{q}$  is the ice flux and  $s$  is the surface elevation. The diffusion coefficient,  $D$ , is calculated on the  $(r, s)$ -grid, staggered both in the  $x$  and  $y$  direction (Figure 2.1). The vertically averaged horizontal ice velocity,  $\mathbf{u}$ , is calculated by the sum of the internal deformation ice velocity and basal sliding velocity if basal sliding is switched on.

Generally, the Shallow Ice Approximation (SIA) is used for large ice-sheet models which assumes that bedrock and ice surface slopes are sufficiently small that the normal components of stress can be ignored (Hutter, 1983). Although using this approximation prohibits any representation of higher-order stresses in the ice, it has been shown to perform well compared with full-stress models in many glaciological situations (e.g. Leysinger Vieli and Gudmundsson, 2004). Most importantly, it allows simulations to be conducted over long time-scales due to its computational efficiency which is required for the simulations performed in this thesis. As a result the horizontal shear stress can be approximated by

$$\begin{aligned}\tau_{xz}(z) &= -\rho_i g (s - z) \frac{\partial s}{\partial x}, \\ \tau_{yz}(z) &= -\rho_i g (s - z) \frac{\partial s}{\partial y},\end{aligned}\tag{2.3}$$

where  $\rho_i$  is the ice density and  $g$  is the acceleration due to gravity. The shear strain rate,  $\dot{\epsilon}_{iz}$ , and shear stress,  $\tau_{iz}$ , are related via the non-linear viscous flow law (Glen's Flow law)

$$\dot{\epsilon}_{iz} = A(T^*) \tau_*^{n-1} \tau_{iz},\tag{2.4}$$

where  $i = x, y$ . The three parameters are the flow law exponent,  $n$ , the effective shear stress,  $\tau_*$ , and the ice flow law parameter  $A(T^*)$ , where  $T^*$  is the absolute temperature corrected for the dependence of the melting point on pressure. The effective shear stress,  $\tau^*$ , is given by the second invariant of the stress tensor; for the SIA this is

$$\tau_* = (\tau_{xz}^2 + \tau_{yz}^2).\tag{2.5}$$

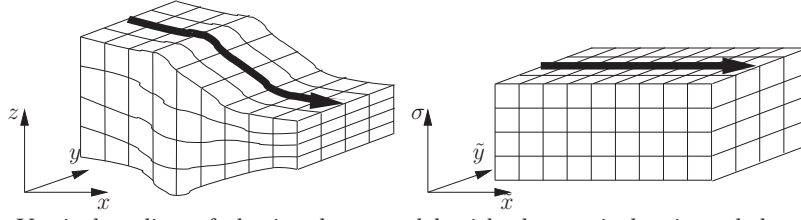


Figure 2.2: Vertical scaling of the ice-sheet model with the vertical axis scaled to unity. The horizontal coordinates are not changed (from Hagdorn *et al.* (2007)).

The values of  $A(T^*)$  and  $n$  are empirically derived from experiments where  $n$  is usually taken to be 3 and  $A(T^*)$  follows the Arrhenius relationship

$$A(T^*) = fae^{\frac{-Q}{RT^*}}, \quad (2.6)$$

where  $a$  is a temperature-independent material constant,  $Q$  is the activation energy for creep and  $R$  is the universal gas constant. In Equation 2.6,  $f$  is the flow enhancement factor, a tuneable factor which can be used to change the flow law parameter, and, hence, change the ice flow velocity. The flow enhancement factor accounts for ice impurities and development of anisotropic ice fabrics, effects not represented by separate parameters in the model.

By combining Equations 2.3, 2.4 and 2.5 an expression for the vertical gradient of  $\mathbf{u}$  can be derived

$$\frac{\partial \mathbf{u}}{\partial z} = -2A(T^*) (\rho_i g (s - z))^n |\nabla s|^{n-1} \nabla s. \quad (2.7)$$

Subsequently integrating Equation 2.7 results in the horizontal ice velocity,  $\mathbf{u}(z)$

$$\mathbf{u}(z) = -2(\rho_i g)^n |\nabla s|^{n-1} \nabla s \int_h^z A(s - z)^n dz + \mathbf{u}(h), \quad (2.8)$$

where  $\mathbf{u}(h)$  is the sliding velocity and set to zero in this thesis. Integrating again with respect to  $z$  will give an expression for the vertically averaged ice velocity,  $\bar{\mathbf{u}}H$ , shown in Equation 2.1.

Since Glen's flow law equation depends on the temperature of ice it is necessary to evaluate how the distribution of ice temperature changes with the changing geometry of the ice-sheet with time. Thus, the thermal evolution of the ice-sheet is described by

$$\frac{\partial T}{\partial t} = \frac{k_{ice}}{\rho_{ice} c_{ice}} \nabla^2 T - \mathbf{u} \cdot \nabla T + \frac{\Phi}{\rho_{ice} c_{ice}} - w \frac{\partial T}{\partial z}, \quad (2.9)$$

where  $T$  is the absolute temperature,  $k_{ice}$  is the thermal conductivity of ice,  $c_{ice}$  is the specific heat capacity of ice,  $\Phi$  is the heat generated due to internal friction and  $w$  is the vertical velocity. The four terms in Equation 2.9 represent vertical diffusion, horizontal advection, internal heat generation due to friction and vertical advection respectively. Horizontal advection is determined using an upwinding scheme while for vertical diffusion and vertical advection central difference formulae are derived to solve these terms.

### The geothermal heat flux model

Boundary conditions are required to solve the thermal evolution of the ice-sheet. At the top of the ice-sheet ice temperatures are set to the value of the surface air temperature. At the base the ice is heated by the geothermal heat flux and sliding friction. If the pressure melting point of ice is reached, ice temperatures are held constant and the excess heat generated is used to calculate a melt rate.

Geothermal heat flux ( $G$ ) can be supplied to the model as a constant or a spatially varying field (both of which are explored in Section 2.5.2). A thermal bedrock model, similar to the model developed by Ritz (1987), takes the thermal evolution of the uppermost bedrock layer into account. Initial conditions for the temperature field are found by applying the geothermal heat flux to an initial surface temperature

$$T(x, y, z) = T_0 + \frac{G}{k_{rock}}z, \quad (2.10)$$

where  $k_{rock}$  is the thermal conductivity and  $T_0$  is the initial surface temperature. This ensures that the geothermal heat flux experienced by the ice-sheet is initially equal to the regional heat flux and the temperature at the base of the bedrock layer is kept constant.

### The Isostasy Model

Glimmer also includes a representation of the isostatic response of the lithosphere to changing ice volume. The lithospheric response is assumed to behave elastically, based on the model of Lambeck and Nakiboglu (1980). The timescale for this response is 3,000 years. In all model runs described below and in subsequent chapters, the isostasy model is initialised on the assumption that the present day bedrock

depression is in equilibrium with the ice-sheet load. Although this assumption may not be entirely valid, any rates of change will not have a significant influence for present day geometry (Huybrechts and de Wolde, 1999).

### Mass balance scheme

Glimmer takes as input the surface mass-balance and mean near-surface air temperature at each time step. In this thesis, the ice dynamics time step is one year. To simulate the surface mass-balance, the Positive Degree Day (PDD) scheme described by Reeh (1991) is used. The basis of the PDD method is the assumption that the melt,  $m$ , that takes place at the surface of the ice-sheet is proportional to the time-integrated temperature above freezing point, known as the positive degree day:

$$\begin{aligned} m &= \alpha \int_{t_0}^{t_1} \max(T_a, 0) dt, \\ &= \alpha D_p dt, \end{aligned} \quad (2.11)$$

where  $T_a(t)$  is the near-surface air temperature,  $D_p$  is the number of PDDs in a year and  $\alpha$  is the PDD factor. Two PDD factors which describe the rate of melting are used, one each for snow ( $\alpha_s$ ) and ice ( $\alpha_i$ ), to take account of the different albedo and density of these materials. The integral in Equation 2.11 is calculated on the assumption of a sinusoidal annual variation in temperature,  $T_a$  (see Equation 2.12), and takes as input the mean annual temperature,  $\bar{T}_a$ , and half-range,  $\Delta T_a$ . Diurnal and other variability ( $\mathbf{R}(0, \sigma_T)$ ) is taken into account using a stochastic approach. This variability is assumed to have a normal distribution with a mean  $0^\circ\text{C}$  and standard deviation,  $\sigma_T$ , of  $5^\circ\text{C}$

$$T_a(t) = \bar{T}_a - \Delta T_a \cos\left(\frac{2\pi}{A}t\right) + \mathbf{R}(0, \sigma_T), \quad (2.12)$$

where  $A$  is the period of a year. The number of PDDs in a year,  $D_p$ , for the temperature series given by Equation 2.11 is solved as

$$D_p = \frac{1}{\sigma_T \sqrt{2\pi}} \int_A^0 \int_0^\infty \bar{T}_a \exp\left(-\frac{(\bar{T}_a - T_a)^2}{2\sigma_T^2}\right) dT dt. \quad (2.13)$$

Note that the inner integral,  $(dT)$ , in Equation 2.13 is evaluated between zero and  $T_a + 2.5\sigma_T$ . In order to solve Equation 2.13 Romberg integration is used for a range of values of  $\bar{T}_a$  and  $\Delta T_a$  when the model is initialised and the values stored in a look-up table. The use of PDD mass-balance models is well-established in coupled atmosphere-ice-sheet modelling studies of both palaeoclimate (e.g. DeConto and Pollard, 2003; Lunt *et al.*, 2008) and future climate (e.g. Ridley *et al.*, 2005; Mikolajewicz *et al.*, 2007). More recently, the Energy Balance/Snowpack mass balance scheme has been established and used to investigate the behaviour of the GrIS under future climate scenarios (e.g. Bougamont *et al.*, 2007). This is discussed in more detail in the discussion and conclusions section of this chapter.

All precipitation is assumed to be potentially available for accumulation within the Glimmer annual PDD scheme. The following possibilities are taken into account when considering the total annual ablation. Melting snow is allowed to refreeze to become superimposed ice up to a fraction,  $w$ , of the original snow depth. When the ability of the snow to hold meltwater is exceeded but the potential snow ablation is less than the total amount of precipitation (amount of snow available), run-off can occur. If the potential snow ablation is greater than precipitation, snow will melt first, and then ice, such that the total ablation is equivalent to the sum of snow melt (total precipitation minus the amount of meltwater held in refreezing) and the sum of ice melt (calculated by deducting from the total number of degree days from the number of degree days needed to melt all snow fall and converted to ice melt). Therefore, the net annual mass balance is the difference between the total annual precipitation and the total annual ablation.

### 2.2.2 Forcing Glimmer with climate

In order to include the evolution of ice-sheets in modelling the Earth system it is necessary to couple a climate model to an ice-sheet model. This can be somewhat complex since the fields required as inputs from the climate model are on different temporal and spatial scales to what is ideally required by an ice-sheet model. Indeed, the temporal and spatial scales in terms of atmospheric evolution are in the order of hours and hundreds of kilometers respectively compared with decades and tens of kilometers for ice-sheet models. This is also the case for reanalysis products such as ERA-40. In order to overcome this problem the Glimmer interface (GLINT) was



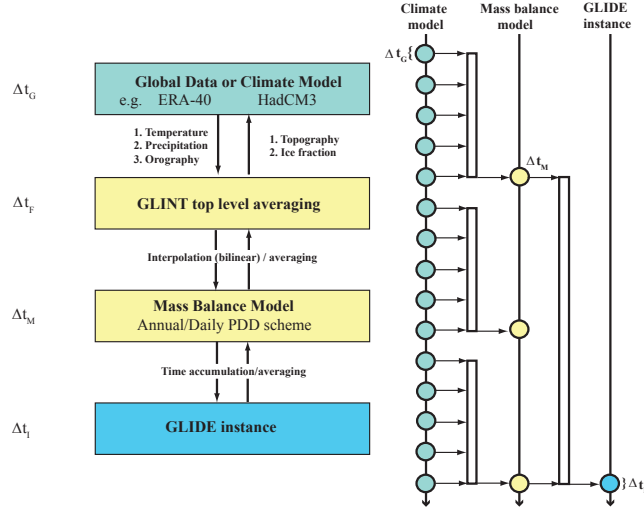


Figure 2.3: Coupling between the global climate forcing and the core of Glimmer, GLIDE, using the interface GLINT. On the right the relationship between the timesteps in GLINT are shown. The filled circles represent timesteps, the rectangles represent averaging/accumulation, and the arrows, flow of coupling fields (*modified from Hagdorn et al. (2007)*).

developed as part of Glimmer. Figure 2.3 shows the general structure of GLINT and how it connects the global climate forcing with the core of the ice-sheet model, GLIDE. Instantaneous temperature and precipitation are available at intervals of  $\Delta t_G$ , which is either the forcing timestep or the data interval depending on whether GLINT is coupled interactively or driven offline. These fields are then passed to the top level of GLINT at a forcing timestep of  $\Delta t_F$  which is either greater than or equal to  $\Delta t_G$ . The main part of the Glimmer code then accumulates these fields over the length of the mass balance timestep,  $\Delta t_M$ . The data is subsequently interpolated onto the local grid of the ice-sheet model. Finally, the mass balance calculations are accumulated over the length of the GLIDE timestep (in this case one year),  $\Delta t_I$ , before being passed to the ice-sheet model core.

The forcing data (temperature and precipitation) are transformed onto the ice model grid using bilinear interpolation. In the case of the near-surface air temperature field ( $T_a$ ), a vertical lapse-rate correction is used to take account of the difference between the high-resolution surface topography seen within Glimmer ( $s_G$ ), and that represented by the forcing data (HadCM3 in this case) ( $s$ ), such that

$$T'_a = T_a + L_G (s_G - s). \quad (2.14)$$

Here,  $T'_a$ , is the lapse corrected surface temperature as seen by the high-resolution

ice-sheet model and  $L_G$  is the vertical atmospheric lapse rate. The use of a lapse-rate correction to better represent the local temperature is established in previous work (e.g. Pollard and Thompson, 1997; Glover, 1999; Hanna *et al.*, 2005, 2008).

## 2.3 The datasets

### 2.3.1 EISMINT intercomparison experimental design

In order to evaluate the consistency in predictions between different ice-sheet models, the EISMINT validation exercise was set up (Huybrechts and Payne, 1996). EISMINT-3 (Huybrechts, 1997) was the final part of this exercise which involved modelling changes in ice mass given a climate scenario for a number of different ice-sheet models with prescribed parameters and climate forcings (Van der Veen and Payne, 2004). This included the evolution of GrIS mass changes under (1) steady-state present climate conditions, (2) a transient climate such as the last climatic cycle based on GRIP ice core data and (3) future greenhouse warming. By modelling present day steady-state conditions, it is possible to test the validity of the reconstructions that the models produce, by comparing the model predictions with observations of the present day ice-sheet. In the EISMINT-3 standard, the initial condition of bedrock and surface elevation was compiled by Letreguilly *et al.* (1991b) on a 20 km Cartesian grid. The precipitation forcing was from Ohmura and Reeh (1991) and the temperature forcing is given by the following parameterisations (Ritz *et al.*, 1997; Huybrechts and de Wolde, 1999) which were themselves based on observed surface temperature data (Ohmura, 1987)

$$T_{ann} = 49.13 - L_a H_{surf} - 0.7576\phi, \quad (2.15)$$

$$T_s = 30.78 - L_s H_{surf} - 0.3262\phi, \quad (2.16)$$

where  $H_{surf}$  is the surface elevation (m),  $\phi$  is the geographical latitude (in degrees and positive),  $T_{ann}$  is the mean annual temperature,  $T_s$  is the summer temperature (both in °C), and  $L_a = -7.992$ ,  $L_s = -6.277$  are annual and summer atmospheric lapse rates respectively (in °C km<sup>-1</sup>).

### 2.3.2 Recent boundary conditions/forcings

New and more accurate bedrock and surface elevation datasets are now available with significant differences in ice volume ( $\sim 4$  % increase) and ice thickness (factor of 10) around the margins compared with the Letreguilly dataset (Bamber *et al.*, 2001). This new dataset allows improvements in the boundary conditions of surface elevation. Ice thicknesses were derived from combining data collected in the 1970s with new data obtained from an ice penetrating radar system from 1993 to 1999. The bedrock topography was subsequently derived from a DEM of the ice-sheet and surrounding rocky outcrops. The DEM is produced from a combination of satellite remote sensing and cartographic datasets. In contrast, the Letreguilly dataset is based on cartographic maps for ice-free regions and radio echoing sounding for determination of ice thickness. No satellite-derived products were used. The Bamber dataset has the advantage of significantly more sources of accurate data and better coverage. The original Bamber dataset is on a 5 km resolution grid; for the purposes of the present work, it was interpolated onto a 20 km resolution grid, generated by pointwise averaging on the same projection. Henceforth, the EISMINT-3 bedrock and ice thickness dataset is referred to as the ‘Letreguilly’ dataset and the more recent dataset as the ‘Bamber’ dataset.

The precipitation data used in EISMINT-3 (Ohmura and Reeh, 1991) is based purely on precipitation measurements from meteorological stations (35) and pits and cores in the interior of the ice-sheet. Not only is this based on a small number of data locations but the accuracy of measurements is also a matter of contention. Catch efficiency, particularly for solid precipitation, by gauges is somewhat reduced by turbulent winds along with the potential for snow to be blown out of gauges (Yang, 1999). Measurement error may reach 100 % during the winter months, when accumulation is most important for mass balance (Serreze *et al.*, 2005). Precipitation data is derived from ERA-40 reanalysis from 1979-2001 (ECMWF, 2006) on a regular latitude-longitude  $1^\circ$  by  $1^\circ$  resolution grid. ERA-40 reanalysis is produced using a data assimilation technique which consists of a number of analysis steps (Upala *et al.*, 2005). Background information is produced from a short-range forecast and combined with observations for this same period of the forecast to produce an ‘analysis’. Statistically-based estimates of errors are used for the synthesis of back-

ground forecast and observation. Each forecast is initialised from the most recent previous analysis step. Observations do not consist of all meteorological variables but the analysis is complete in terms of the variables chosen. As such, variables can be produced from analysis (e.g. temperature) while others are purely based on forecast and, therefore, not constrained by observations (Uppala *et al.*, 2005). In ERA-40, precipitation is one such variable produced by the forecast rather than by the analysis in the ECMWF model. However, it has been shown to be reasonable for Greenland. Validation against Danish Meteorological Institute (DMI) coastal stations results in a 36 % mean excess for ERA-40 (Hanna and Valdes, 2001), although the inaccuracies in gauge measurements mean that this should be treated with some caution. In terms of other reanalysis products available, comparison studies have shown ERA-40 to be superior to NCEP-NCAR datasets in terms of smaller biases, ability to capture large scale patterns of precipitation and its depiction of interannual variability, deeming ERA-40 a more suitable choice (Bromwich *et al.*, 1998; Serreze and Hurst, 2000; Serreze *et al.*, 2005; Hanna *et al.*, 2006).

The near-surface air temperature forcing used in the EISMINT-3 exercise is based on a parameterisation of surface temperature compiled by Ohmura (1987), which has a latitudinal and altitude dependency (see Equation 2.15 and Equation 2.16). Two lapse rate values are used: the mean annual lapse rate and a summer lapse rate. Currently, lapse rate in Glimmer is not temporally or regionally varying so the summer lapse rate is used since this is when the ablation process is strongest. The parameterisations were constructed to fit data from 49 meteorological stations. A new parameterisation based on more up-to-date automatic weather station data is now available with a similar form to Equation 2.15 and Equation 2.16 (Fausto *et al.*, 2009). However, a novel approach has been chosen in this thesis to use the original temperature observations rather than a highly tuned parameterisation.

Several datasets exist in terms of satellite and re-analysis products. For satellite datasets, temperature data are available from the Advanced Very High Resolution Radiometer (AVHRR) Polar Pathfinder (APP) from 1982 - 2004 which is collated twice a day at the local solar times of 1400 and 0400. Although the data is initially on a 5 km resolution, it is sub-sampled at 25 km pixels. The APP-x product includes all-sky surface temperature with the cloudy-sky surface temperatures calculated using an empirical relationship between clear-sky surface temperature, wind speed,

and solar zenith angle (daytime). However, this only applies to surface temperatures over sea-ice and not land. Therefore, temperatures over Greenland are based only on data from clear-sky retrieval with temperatures in cloudy regions interpolated from clear-sky areas. Although useful for comparing with present day surface temperatures from climate models, this dataset is not suitable to directly force an ice-sheet model over Greenland itself. Firstly, the largest uncertainties are likely to be over Greenland (J.Key, pers. comm.). This could, in part, be due to the satellite recording ice surface temperatures rather than air temperature. Furthermore, clear-sky retrievals errors are predominantly due to uncertainties in cloud detection (Key *et al.*, 1997) particularly during the night. The low temperatures, bright surface and high elevation make remote sensing over Greenland particularly difficult in terms of accurate cloud detection. Secondly, no associated orography exists which is used to downscale from the resolution of the forcing data onto the high-resolution of the ice-sheet model.

Instead, to be consistent with precipitation, surface (2 m) air temperature data derived from ERA-40 ‘corrected’ 2 m near-surface air temperatures were used (Hanna *et al.*, 2005). The temperatures were corrected based on their derived surface lapse rates and differences between the ECMWF orography and a DEM derived from the Ekholm (1996) grid (Hanna *et al.*, 2005). Reasonable agreement exists between these model-derived temperatures and observations at the DMI station locations and GC-Net stations (Hanna *et al.*, 2005). Bilinear interpolation was used to transform the high-resolution dataset from its Cartesian 5 km resolution grid onto a  $1^\circ$  by  $1^\circ$  latitude longitude grid. Since the dataset only covers the regions where there is ice, the temperature parameterisation used in EISMINT-3 temperature is used in the ice-free regions of Greenland in conjunction with the Ekholm orography. This means that the sensitivity to temperature is specifically a sensitivity to the surface temperature of the ice-sheet and not the ice-free regions.

## 2.4 Sensitivity to boundary conditions and forcings

In order to test the sensitivity of the ice-sheet model to the various forcing inputs and boundary conditions, a set of steady-state experiments have been performed, initialised from present day geometry of the ice-sheet. The model was run for 50,000

| Bedrock and ice thickness | Temperature | Precipitation |
|---------------------------|-------------|---------------|
| O                         | O           | O             |
| N                         | O           | O             |
| O                         | N           | O             |
| O                         | O           | N             |
| N                         | N           | N             |

Table 2.2: Glimmer experiments performed to investigate the response of the GrIS to present day boundary conditions and forcings. O refers to the bedrock and ice thickness, temperature and precipitation used in the EISMINT-3 standard (Section 2.3.1) whereas N refers to the newer datasets described in Section 2.3.2.

years in order to reach equilibrium. The ice-sheet model setup was kept at that of EISMINT-3 with standard parameter values as shown in Table 2.1. For each simulation in the set, one forcing/boundary condition was changed to the most recent dataset, keeping all others at that used in EISMINT-3 (see Table 2.2). An additional experiment was performed where all the forcings and boundary conditions were changed to the most recent. Figure 2.4 shows the evolution of ice surface extent and ice volume with time for EISMINT-3 and the four sensitivity experiments.

#### 2.4.1 Bedrock and ice thickness

The quality of the bedrock topography is important in ice-sheet models since it largely determines the ice thickness at regional scales. This is because topography influences where the build up of snow and ice can occur and therefore is a major control on the threshold of ice-sheet initiation. Furthermore, topography influences the convergence and divergence of ice flow such that flow into lowland basins and valleys from surrounding higher relief regions will result in faster build up of ice compared with flow from an isolated upland region into a lower basin (Payne and Sugden, 1990). As a result, the topography influences the stress, velocity and thermal regimes of the ice-sheet (Van der Veen and Payne, 2004). There are differences in ice thickness and bedrock topography between the two bedrock and ice-thickness datasets (see Figures 2.5a and 2.5b). The bedrock topography around the margins is consistently higher for the Bamber dataset compared with the Letreguilly dataset with the ice thickness difference up to a factor of 10 to 20 thicker. When simulated to steady-state, the Bamber bedrock and ice thickness datasets results in significantly (13.7 %) greater ice volume and 11.5 % larger ice surface extent compared with the Letreguilly dataset. Ice extends further to the northern and western mar-

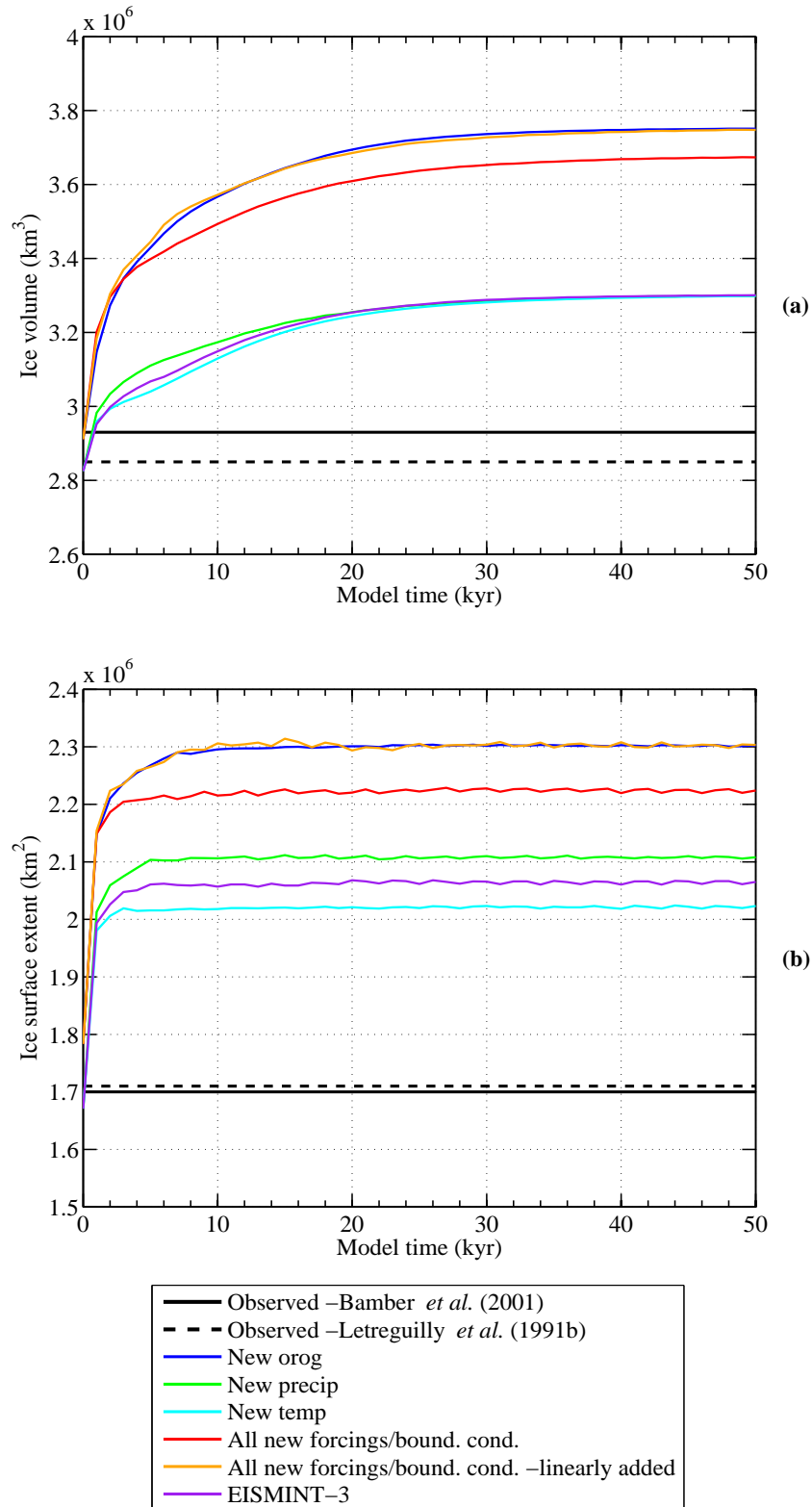


Figure 2.4: Evolution of modelled ice-sheet (a) volume and (b) ice surface extent for different boundary conditions and forcings. The EISMINT-3 experiment is also shown for comparison, and observations derived from Bamber *et al.* (2001) and Letreguilly *et al.* (1991b) datasets. Each boundary condition/forcing is changed one at a time relative to the EISMINT-3 setup. Also shown are where all forcings and boundary conditions are updated together and linearly combined.

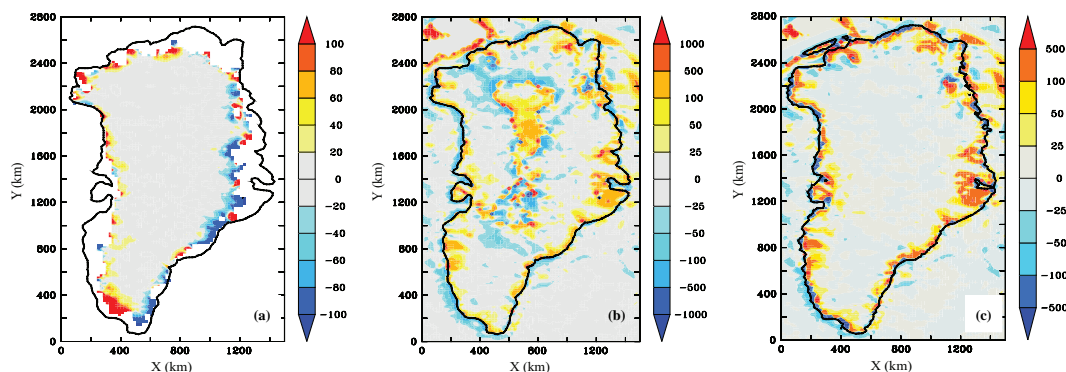


Figure 2.5: Comparison between Bamber and Letreguilly bedrock and ice thickness datasets at 20 km resolution. (a) The ratio of the difference of ice thickness of Bamber dataset and ice thickness of Letreguilly dataset ( $(z_{\text{bamber}} - z_{\text{letreguilly}}) / z_{\text{letreguilly}}$ ) expressed as a percentage. The regions of largest relative difference occur around the margins with good agreement between the datasets in the ice-sheet interior. (b) The ratio of the difference in initial bedrock topography of Bamber dataset and the topography of Letreguilly expressed as a percentage. Again the largest differences occur around the margins of Greenland and also in the central region where the bedrock is below sea-level. (c) The ratio of the difference in relaxed bedrock topography after the removal of ice and isostatic equilibrium has been reached expressed as a percentage. The resultant orography shows the relative difference around the margins of up to 500 %, with Bamber orography significantly higher.

gins of Greenland with a higher central dome. The initial higher elevation of the ice-free bedrock of the Bamber dataset provides favourable conditions for ice growth where temperatures are cold enough for mass balance to become positive. In these regions ice velocities are low compared with other marginal regions, allowing the ice-sheet to build-up with minimal ice loss. The basal temperatures are also colder than when the Letreguilly dataset is used, resulting in marginally lower velocities for ice flow. This arises because the ice in the Bamber dataset is thicker at the beginning of the simulation. The increase in ice volume and surface extent, however, can be attributed predominately to a stronger ice-elevation feedback mechanism for the Bamber dataset.

### 2.4.2 Precipitation

Changing the precipitation forcing from that of Ohmura and Reeh (as in EISMINT-3) to ERA-40, results in an increase in equilibrium ice-sheet surface extent of 2.1 %. However, there is almost no effect on the ice-sheet volume. This can be explained by the fact all precipitation that falls is assumed to be available for accumulation in the annual PDD scheme. Since the temperature forcing has no effect on the amount of snow, it is the quantity and distribution of precipitation that results in the difference in ice surface extent. Figure 2.6 shows that the annual precipitation



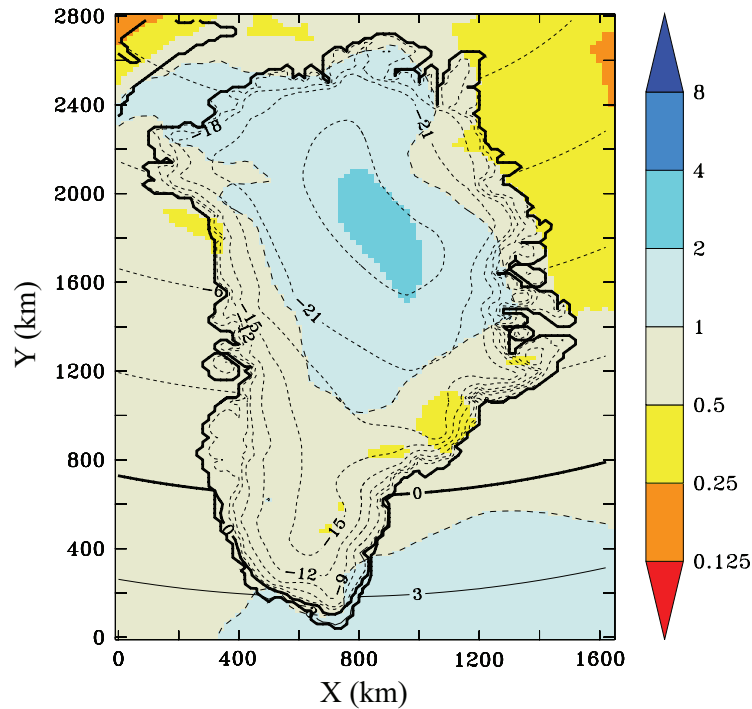


Figure 2.6: Change in precipitation over Greenland between EISMINT-3 (Ohmura and Reeh, 1991) and ERA-40 re-analysis expressed as a ratio of EISMINT-3/ERA-40. Annual surface temperature (in  $^{\circ}\text{C}$ ) contours also shown.

is up to two times greater on the eastern and western margins of Greenland for ERA-40 compared with Ohmura and Reeh (1991). The accumulation rate is greatest in south-east Greenland for both precipitation datasets but extending further north along the eastern margin for ERA-40. The extra precipitation falling over the western and eastern margins coupled with a positive ice-elevation feedback results in growth and extension of the ice-sheet into previously ice-free regions. However, the precipitation falling over central and north Greenland is three times less for ERA-40, resulting in less accumulation in the interior and lower maximum altitude of the ice-sheet. These opposing effects result in similar ice-sheet volumes. However, Hanna *et al.* (2006) show that ERA-40 is  $\sim 50\%$  too ‘dry’ in the central northern parts of Greenland, as validated using ice core data. Furthermore, it seems increasingly likely that both the Ohmura and Reeh (1991) and ERA-40 precipitation datasets underestimate precipitation and accumulation in southeast Greenland, where recent regional climate model results suggest much higher than previously observed precipitation rates (Ettema *et al.*, 2009; Burgess *et al.*, 2010).

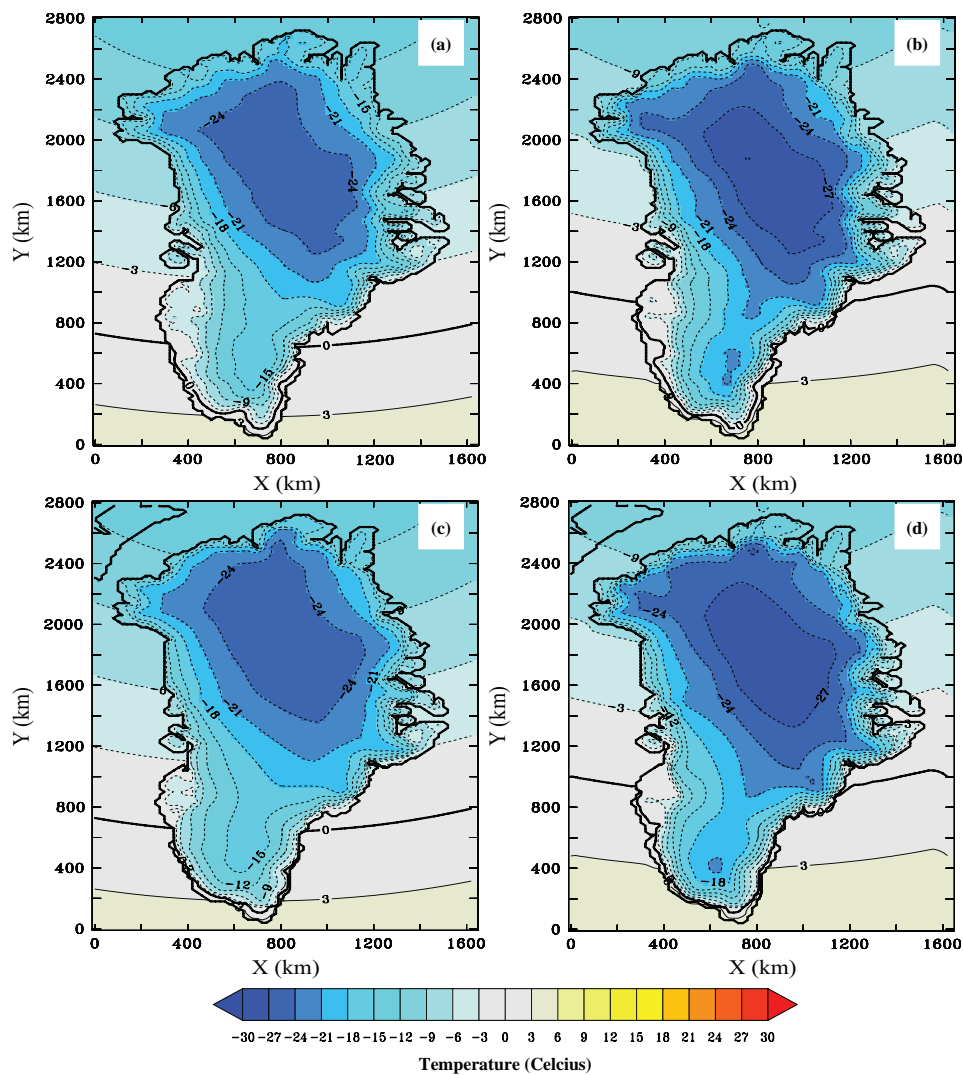


Figure 2.7: Sensitivity to different temperature forcings for the GrIS. The near-surface air temperature (in  $^{\circ}\text{C}$ ) over Greenland for (a) after 1 year of model time forced with EISMINT-3 temperatures, (b) after 1 year of model time forced with Hanna modified temperatures, (c) after years of model time forced with EISMINT-3 temperatures and (d) after 50,000 years of model time forced with Hanna modified temperatures.

### 2.4.3 Temperature

Changing the temperature forcing to the modified Hanna dataset results in almost identical ice volume compared with EISMINT-3 and a reduction in the ice-sheet extent of 2.0 %. Figure 2.7 and Figure 2.8 show the temperature distribution and the surface mass balance respectively at the beginning and end of the experiments for EISMINT-3 temperature and the Hanna modified temperature datasets. As expected, at the beginning of the simulation temperatures around the margins of the GrIS are similar (same datasets) but the Hanna ERA-40 corrected temperatures over the ice-sheet are several degrees colder (Figures 2.7a, b). By the end of the

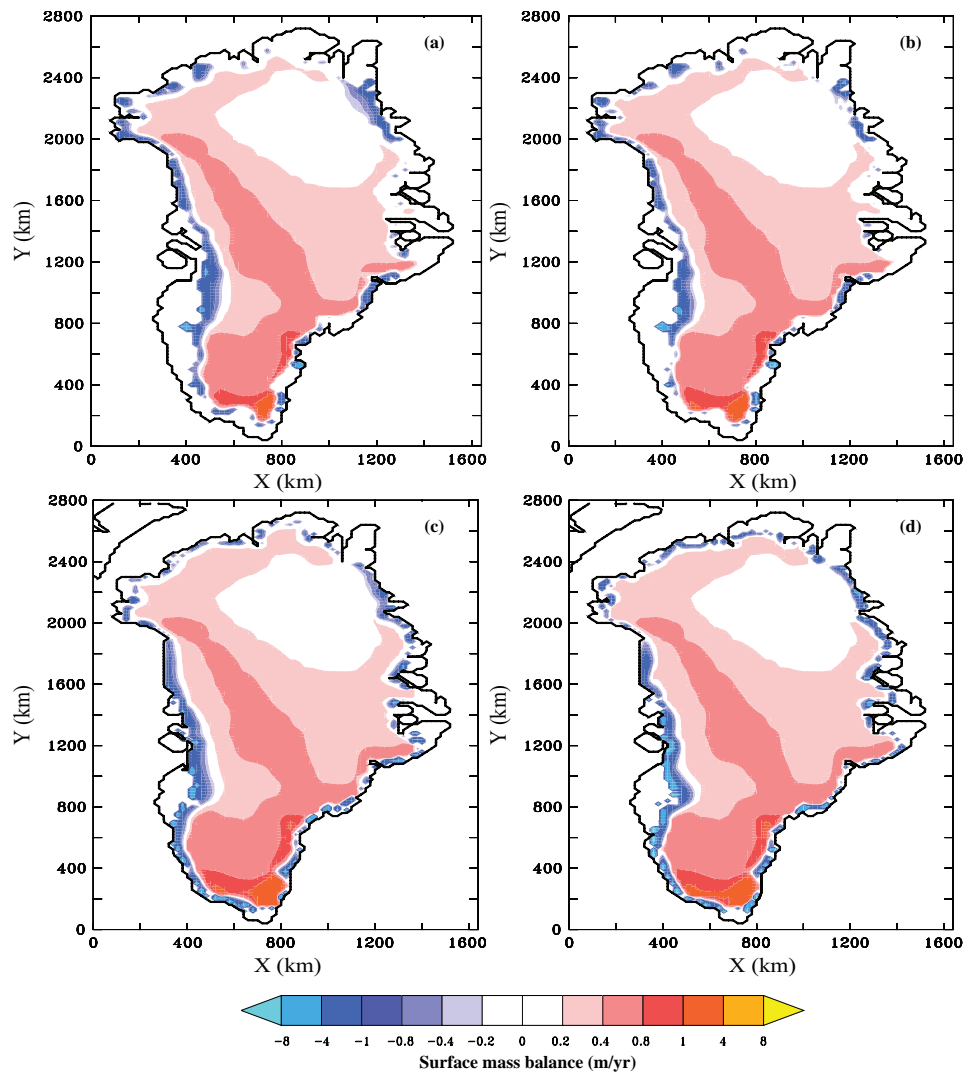


Figure 2.8: Sensitivity to different temperature forcings for the GrIS. The net surface mass balance (in m/yr) over Greenland for (a) after 1 year of model time forced with EISMINT-3 temperatures (b) after 1 year of model time forced with Hanna modified temperatures, (c) after 50,000 years of model time forced with EISMINT-3 temperatures and (d) after 50,000 years of model time forced with Hanna modified temperatures. Note the non-linearity of the scale.

simulations, temperatures over much of Greenland have become lower as a result of the positive ice-elevation feedback (Figure 2.7c, d) resulting in an increase in positive net mass balance in southern Greenland (see Figure 2.8c, d). However, the regions around the margins remain ice-free as a result of continued ablation with a net negative mass balance. The model is particularly sensitive to the temperature forcing around the margins of the ice-sheet, where temperatures are at zero or above and so close to ablation as opposed to those in the interior where the primary mass-balance change is from accumulation (Hanna *et al.*, 2005). It is, therefore, important in future modelling development that marginal temperatures close to where the net

|                               | Update<br>ppt | Update<br>temp | Update bedrock<br>& ice elev. | Update<br>all |
|-------------------------------|---------------|----------------|-------------------------------|---------------|
| <i>Ice volume (%)</i>         | -0.04         | -0.06          | +13.65                        | +11.30        |
| <i>Ice surface extent (%)</i> | +2.07         | -2.03          | +11.49                        | +7.69         |

Table 2.3: Summary of the relative difference between updated boundary condition/forcing and the EISMINT-3 datasets. Positive values correspond to an increase and negative values a decrease in ice volume/ice surface extent. Note when all boundary conditions/forcings are updated the relative change does not equal the sum of the individual changes.

mass balance becomes negative are resolved accurately in order to model the ablation process and the resulting geometry of the GrIS.

#### 2.4.4 Summary

Table 2.3 summarises the results of changing precipitation, temperature and bedrock and ice thickness independently from EISMINT-3 to the newer datasets. Bedrock and ice thickness result in the largest ice volume and ice surface extent change while changing precipitation and temperature have the least effect on the ice volume. Precipitation change acts to increase the ice surface extent by a similar amount to temperature which in contrast acts to reduce the ice surface extent.

Updating all the boundary conditions and forcings together results in a modelled GrIS ice volume 25 % larger than observed (Bamber *et al.*, 2001) and 11 % larger than EISMINT-3. The system shows some non-linearity since adding together the difference between the EISMINT-3 case and the individual response of the ice-sheet to each forcing/boundary condition results in a modelled GrIS larger than when all forcings/boundary condition are varied together. This is the case for ice volume (2 % larger than when all boundary conditions/forcings are updated together) and ice surface extent (3.6 % larger). In fact, adding the forcings together in this way results in an evolution in ice volume almost identical to the case when bedrock is varied on its own. This suggests that when the bedrock topography is varied, the ice model also becomes sensitive to how the climate forcings and bedrock are coupled together.

These results show that when using more recent boundary conditions and forcings Glimmer gives a poorer representation of the modern ice-sheet compared with observations than when using the older EISMINT-3. It is likely that some of the internal ice-sheet model parameters were tuned to work with the boundary conditions

used in EISMINT-3. In order to produce a reasonable best fit between modelled and observed geometry, a number of ice model parameters are tuned to work with the new datasets.

## 2.5 Tuning

### 2.5.1 Tuning methodology

Several parameters in large-scale ice-sheet modelling are still poorly constrained, resulting in highly variable ice-sheet volume and extent depending on the values prescribed in the model (Ritz *et al.*, 1997). This necessitates the tuning of the ice-sheet model with the recent datasets in order to determine the optimal ice-sheet for steady-state conditions (i.e. closest geometry to reality). Previous work (e.g. Ritz *et al.*, 1997) has looked at the sensitivity of ice-sheet volume and extent to a number of parameters, including flow enhancement factor ( $f$ ) in the flow law (see Equation 2.6), the sliding coefficient, the geothermal heat flux ( $G$ ) and the coefficients (PDD factors) of the ablation parameterisation for ice ( $\alpha_i$ ) and snow ( $\alpha_s$ ) (see Equation 2.11). In addition, Hebel *et al.* (2008) also looked at the effect on ice volume and extent of the Fennoscandian ice-sheet during the Last Glacial Maximum from uncertainty in model parameters (e.g. lapse rate in addition to those mentioned above) and climate forcing by performing a parametric uncertainty analysis using Glimmer. They found a variation of 65 % in equilibrium ice-sheet extent due to uncertainty in the parameters used in the ice-sheet model and up to 6.6 % due to uncertainty in topographic input.

The most common methodology in glaciological modelling sensitivity studies is to vary one parameter at a time within a prescribed range while holding all others constant (e.g. Van de Wal and Oerlemans, 1994; Fabre *et al.*, 1995; Ritz *et al.*, 1997; Huybrechts and de Wolde, 1999; Pattyn, 2003; Essery and Etchevers, 2004). However, this ignores possible non-linear interactions between parameters. This section builds on the methodology used in this previous work by using the statistical method of Latin-Hypercube Sampling (LHS) (an efficient variant of the Monte Carlo approach) which generates a distribution of plausible parameter sets within a prescribed set of ranges (McKay *et al.*, 1979). It uses a stratified-random procedure where values are sampled from the prescribed distribution of each variable. The cu-

mulative distribution of each variable is divided into  $N$  equiprobable intervals and a value selected randomly from each interval. The  $N$  values obtained for each variable are paired randomly with the other variables. The method assumes that the variables are independent of one another (which is the case here) and ensures a full coverage of the range of each variable. LHS has been used in a number of applied scientific disciplines including analysing uncertainty in vegetation dynamics (Wramneby *et al.*, 2008), rainfall models for climate assessment (Murphy *et al.*, 2006) and climate/ocean models (Edwards and Marsh, 2005; Schneider von Deimling *et al.*, 2006). However, it has yet to be used in large-scale ice-sheet modelling. The advantage of this methodology is that it is an efficient method to test the response of the ice-sheet to many different combinations of parameters by ensuring efficient coverage of the parameter space without having to test all possible model combinations (which would be extremely computationally expensive). In this way, by varying more than one parameter at a time (as for any multivariate sampling method) it also allows the influence of each parameter on the outcome of the model simulations to be assessed while taking interactions with other parameters into account.

Not only the sensitivity of the GrIS response to the following parameters is investigated, but also the combination which gives the optimal fit to the present day GrIS. The following parameters have been chosen to tune since they fundamentally affect the processes described in Section 2.2. Firstly, the flow rate of ice can be tuned with the flow enhancement factor,  $f$  (see Equation 2.6), to simulate ice flow reasonably accurately. Secondly, the surface mass balance can be tuned using the PDD factors and vertical lapse rate. The melting of ice at low altitudes is determined by ablation, which in this study is calculated according to the annual PDD scheme. Since this uses an empirical relationship, the PDD factors for ice ( $\alpha_i$ ) and snow ( $\alpha_s$ ) are varied within the ranges obtained through measurement studies (see below), and, therefore, influence the amount of melting that can occur in the ablation zones. These parameters will not, however, alter the position of these zones. This instead can be achieved by varying the vertical atmospheric lapse rate ( $L_G$ ), which can influence the regions where ablation has the potential to occur. Thirdly, ice loss by basal melt without sliding can be achieved by varying the geothermal heat flux ( $G$ ), which can raise the basal ice layer temperature to its pressure melting point. The geometry of the GrIS is controlled by the flow of ice from the ice divide in the

| Parameter  | Minimum value | Maximum value |
|--|---------------|---------------|
| Positive degree day factor for snow, $\alpha_s$ (mm d <sup>-1</sup> °C <sup>-1</sup> ) | 3             | 5             |
| Positive degree day factor for ice, $\alpha_i$ (mm d <sup>-1</sup> °C <sup>-1</sup> )  | 8             | 20            |
| Enhancement flow factor, $f$   | 1             | 5             |
| Geothermal heat flux, $G$ ( $\times 10^{-3}$ W m <sup>-2</sup> )                       | -61           | -38           |
| Near-surface lapse rate, $L_G$ (°C km <sup>-1</sup> )                                  | -4.0          | -8.2          |

Table 2.4: List of five parameters varied according to the ranges determined from the literature.  $\alpha_i$ ,  $\alpha_s$ ,  $G$  and  $f$  are similar to those used in Ritz *et al.* (1997).

interior towards the coastal regions due to internal deformation where at relatively low altitudes, typically  $< \sim 2000$  m, ice mass is lost by melting according to the PDD scheme. Ice mass can also be lost by basal melt and/or the process of basal sliding which can increase the flow of ice to regions of ablation at the edge of the ice-sheet. Since basal sliding is not included in these simulations, this process will not be considered.

LHS requires a maximum and minimum bound for each tuneable parameter to be defined. The following discusses the bounds which have selected for each value, shown in Table 2.4.

The range for the flow enhancement factor for this study is between 1 and 5. According to Dahl-Jensen and Gundestrup (1987), borehole measurements from Dye-3 give a mean enhancement factor of around 3 with a maximum value of 4.5 and a minimum value of around 1 for ice deposited during the Wisconsin. This is the range used by Ritz *et al.* (1997) and Hebel *et al.* (2008) for their sensitivity studies. Values within this range have also been used in other work (e.g. Huybrechts *et al.*, 1991; Letreguilly *et al.*, 1991b; Fabre *et al.*, 1995; Greve and Hutter, 1995).

The global average geothermal heat flux (oceans and continents) is estimated at  $87 \times 10^{-3}$  W m<sup>-2</sup> (Banks, 2008). Since it is difficult to measure geothermal heat flux beneath the ice directly, many studies (e.g. Calov and Hutter, 1996; Ritz *et al.*, 1997; Huybrechts and de Wolde, 1999) assume that the average value for Pre-Cambrian Shields (Greenland bedrock) is  $\sim 42 \times 10^{-3}$  W m<sup>-2</sup> (Lee, 1970) although a value of  $50 \times 10^{-3}$  W m<sup>-2</sup> is used in EISMINT-3, and values as high as  $65 \times 10^{-3}$  W m<sup>-2</sup> have also been used (Greve, 2000). In terms of more recent measurements inferred from ice cores, the lowest recorded heat flux over Greenland is  $38.7 \times 10^{-3}$  W m<sup>-2</sup> from Dye-3 (Dahl-Jensen and Johnsen, 1986). The average value for continents is  $61 \times 10^{-3}$  W m<sup>-2</sup> (Lee, 1970). Although values as high as  $140 \times 10^{-3}$  W m<sup>-2</sup> have

been measured at NGRIP (Andersen *et al.*, 2004; Buchardt and Dahl-Jensen, 2007) and values as low as  $20 \times 10^{-3} \text{ W m}^{-2}$  modelled by Greve (2005). The range used here is between  $38 \times 10^{-3}$  and  $61 \times 10^{-3} \text{ W m}^{-2}$  for the geothermal heat flux over the whole of Greenland. This is similar to the ranges used by previous sensitivity studies (Greve and Hutter, 1995; Ritz *et al.*, 1997). The effect of a spatially varying geothermal heat flux over Greenland (Shapiro and Ritzwoller, 2004) has also been investigated with all other parameters set at the default EISMINT-3 values. This is compared with the standard setup where the geothermal heat flux is  $50 \times 10^{-3} \text{ W m}^{-2}$  over Greenland.

Ice and snow ablation is related to air temperature by the PDD factor, which represents a simplification of processes that describe the energy balance of the glacier and overlying boundary layer. The implausibility of using one universal factor being valid for all of Greenland presents a challenge. The standard value used for ice by many modellers is  $8 \text{ mm d}^{-1} \text{ } ^\circ\text{C}^{-1}$  (e.g. Ritz *et al.*, 1997; Huybrechts and de Wolde, 1999; Lunt *et al.*, 2008, 2009). However, Braithwaite (1995) concluded that PDD factors for ice are generally larger than the standard value and could be as high as  $20 \text{ mm d}^{-1} \text{ } ^\circ\text{C}^{-1}$ . The PDD factor for snow has also been estimated to range between 3 and  $5 \text{ mm d}^{-1} \text{ } ^\circ\text{C}^{-1}$  with a standard value of 3 used by most modelling studies (Braithwaite, 1995). Modelling of PDD factors using a regional climate model in southern Greenland found ranges for the ice PDD factor between 8 and  $40 \text{ mm d}^{-1} \text{ } ^\circ\text{C}^{-1}$  and for the snow PDD factor between 3 and  $15 \text{ mm d}^{-1} \text{ } ^\circ\text{C}^{-1}$  (Lefebre *et al.*, 2002). Other Greenland ice-sheet modelling studies have used higher PDD factors than the standard (e.g. Greve, 2000; Vizcaíno *et al.*, 2008). The range for the ice PDD factor is between  $8 \text{ mm d}^{-1} \text{ } ^\circ\text{C}^{-1}$  and  $20 \text{ mm d}^{-1} \text{ } ^\circ\text{C}^{-1}$  and for the snow PDD factor between  $3 \text{ mm d}^{-1} \text{ } ^\circ\text{C}^{-1}$  and  $5 \text{ mm d}^{-1} \text{ } ^\circ\text{C}^{-1}$ .

The near-surface atmospheric lapse rate varies both spatially and temporally over Greenland. Lapse rate is known to vary significantly throughout the year due in part to changes in moisture content of the atmosphere. Observations from automatic weather stations indicate a mean annual lapse rate along the surface slope of  $-7.1 \text{ } ^\circ\text{C km}^{-1}$  with seasonally varying lapse rates varying between  $-4.0 \text{ } ^\circ\text{C km}^{-1}$  (in summer) and  $-10.0 \text{ } ^\circ\text{C km}^{-1}$  (in winter) (Steffen and Box, 2001). Relationships derived from ERA-40 reanalysis data also yield less negative summer lapse rates of  $-4.3 \text{ } ^\circ\text{C km}^{-1}$  at the margins and a more negative annual lapse rate of  $-8.2 \text{ } ^\circ\text{C km}^{-1}$ .



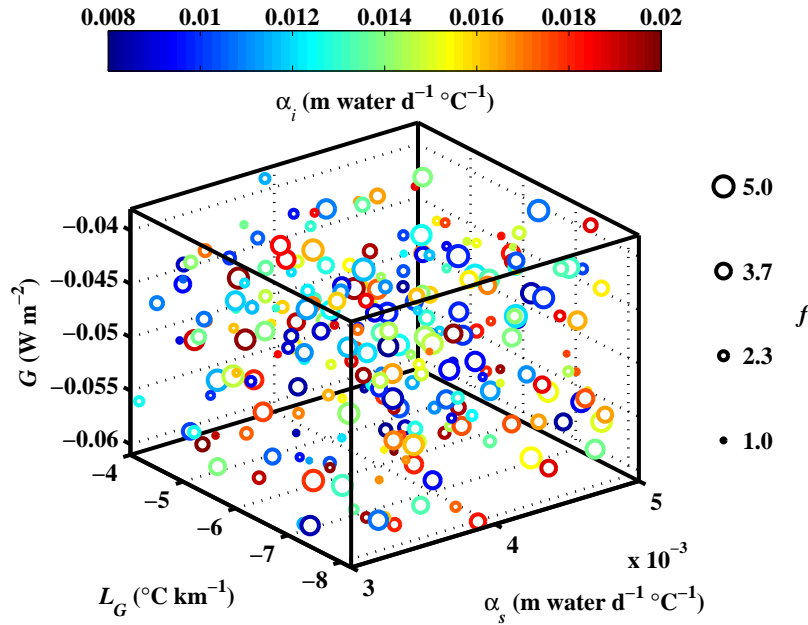


Figure 2.9: Distribution of 250 experiments produced by Latin-Hypercube Sampling. In three dimensions geothermal heat flux ( $G$ ), PDD factor for snow ( $\alpha_s$ ) and atmospheric vertical lapse rate ( $L_G$ ) are shown. In addition, for each experiment the PDD factor for ice ( $\alpha_i$ ) is shown in terms of the colour-scale and the enhancement flow factor ( $f$ ) in terms of the size of circle.

$\text{km}^{-1}$  for the bulk of the GrIS (Hanna *et al.*, 2005). Since Glimmer only uses one value for lapse rate it is varied between  $-4$  and  $-8.2^\circ\text{C km}^{-1}$  which corresponds to the seasonal variation in lapse rate. This also encompasses the range used in the EISMINT-3 standard experiment for annual and summer lapse rate given in Equation 2.15 and Equation 2.16.

### 2.5.2 Sensitivity to tuning parameters

Two hundred and fifty plausible parameter sets are generated using LHS and the ice-sheet model simulations run for 50,000 model years under a steady-state present day climate. There is no definitive way of determining the sample size based on the number of variables in the literature. However, Iman and Helton (1985) suggested sampling two to five times the number of varied model parameters although this is subjective. Since Glimmer is computationally efficient it is possible to have 50 times the number of varied parameters which easily exceeds this conservative suggestion by Iman and Helton (1985). Figure 2.9 shows the distribution of the 250 experiments with each experiment represented by a circle for three of the five tuneable parameters and the other two represented by size and colour of the circle and from this it is illustratively clear that the 5-dimensional space is covered adequately. In order to

analyse the 250 experiments' ice-sheet geometries, three diagnostics were chosen and analysed using two skill scores. These diagnostics are ice surface extent, total ice volume and maximum ice thickness. Their ability to replicate observation is described by the absolute error skill score ( $AE$ )

$$AE = |y - x| \quad (2.17)$$

where  $y$  is the experiment and  $x$  is the observation such that a value of zero is a perfect match. In addition, the Normalised Root Mean Square Error (NRMSE) is used to measure the spatial fit of ice thickness over the model domain and is given by

$$NRMSE = \sqrt{\frac{\sum_{i=1}^n (x_i - y_i)^2}{\sum_{i=1}^n (x_i - \bar{x})^2}} \quad (2.18)$$

where  $\bar{x}$  is the mean observation over Greenland and  $x_i$  and  $y_i$  are the observation and experimental ice thickness at each gridpoint respectively. Again, zero would describe a perfect match between modelled and observed ice thicknesses. The observational target against which the skill score is measured is the DEM derived by Bamber *et al.* (2001), interpolated to the 20 km resolution. Figure 2.10 summarises the sensitivity of maximum ice thickness error, ice surface extent error and ice volume error to the five tuneable parameters. Maximum ice thickness and ice volume are dependent on the flow law enhancement factor since faster flow will result in a thinner (and hence smaller) ice-sheet as a result of lowering the ice viscosity. An error of -10 % to +10 % for maximum ice thickness occurs between enhancement factors 1 and 5 respectively with an optimum maximum ice thickness occurring between enhancement factors 2.5 and 3. In contrast the optimum enhancement factor for ice volume is not reached for ice volume within the limits of the range (1 to 5) investigated. However, the enhancement flow factor has little effect on the ice surface extent due to opposing feedbacks. Faster flow will result in an increase in the flux of ice towards the ice-sheet margins. However, as the surface lowers as a result of this faster flow the ablation zone will increase at the margins leading to loss of ice. This result is similar to that found by Ritz *et al.* (1997) and Hebel *et al.* (2008), in terms of ice volume and maximum ice thickness. However, Hebel *et al.* (2008) found no increase in

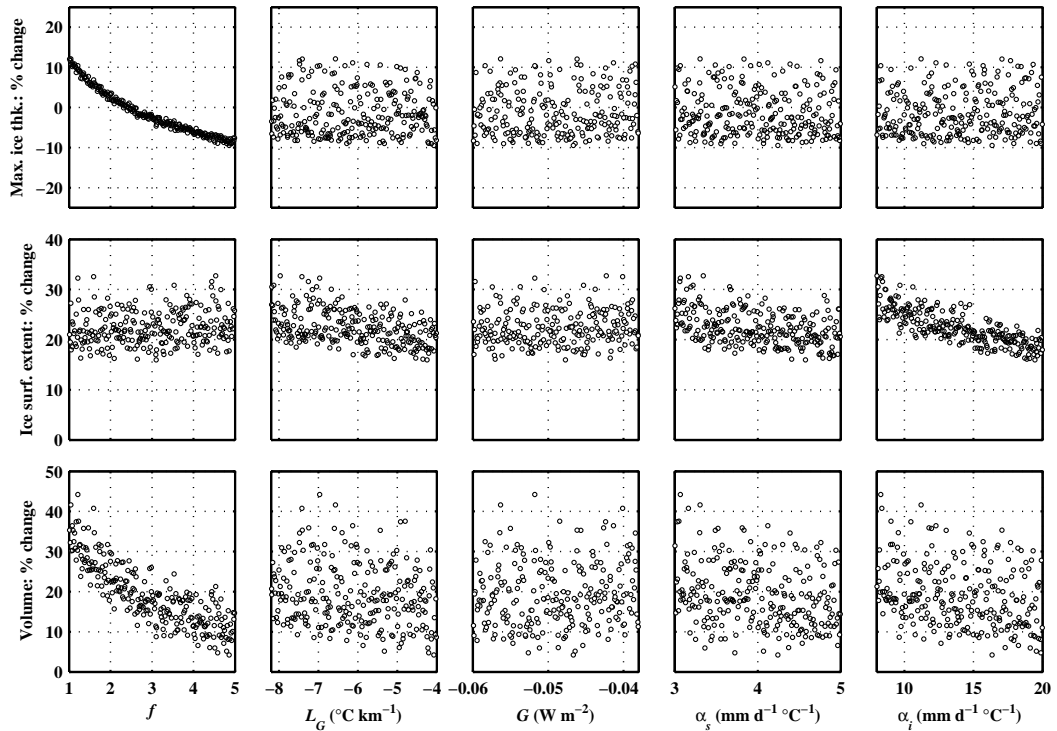


Figure 2.10: Sensitivity of three diagnostics describing the response of ice-sheet geometry (volume, ice surface extent and maximum ice thickness) to different values of the enhancement flow factor ( $f$ ), the atmospheric lapse rate ( $L_G$ ), the geothermal heat flux ( $G$ ) and the ice ( $\alpha_i$ ) and snow ( $\alpha_s$ ) PDD factors for the calculation of ablation. All values correspond to the end of the simulation at 50,000 years where equilibrium is reached.

ice surface extent of their modelled region, comparable to results shown here. In contrast, Ritz *et al.* (1997) found an initial slight increase in ice surface extent. It is possible that this arises due to the different topography and climate configurations used as hypothesised by Hebel *et al.* (2008).

There is low sensitivity of all three diagnostics to variation in the geothermal heat flux. Since this influences basal temperatures of the ice-sheet it affects the fluidity of the ice and the flow, as well as any basal melt. Ice velocity also depends on the geothermal heat flux via the basal melt rates and in turn determines the rate of sliding of the ice-sheet. This basal sliding is predicted to occur only when the basal temperature is equal to the pressure melting point of ice. However, the original EISMINT-3 experiment did not include basal sliding and in order for a clean comparison basal sliding has also been switched off in this suite of experiments. At the ice-sheet margins, the basal temperature is already at the melting point and, therefore, the geothermal heat flux is not expected to influence greatly the ice volume or ice surface extent. It is, therefore, more important in the central parts of the ice-

sheet where it could influence the flow of ice and affect the ice volume and maximum ice thickness via basal melt. Although basal temperatures in the interior are close to this threshold for all cases even those, with the highest geothermal heat flux, are not significant enough to cause basal melting in central parts of Greenland. As a result the geothermal heat flux parameter is unlikely to have become more important if basal sliding had been included in this suite of simulations. This is because the implication of sliding concerns the outer parts of the ice-sheet where the ice base is at melting point for all geothermal heat flux values investigated. A similar result was found by Hebel *et al.* (2008) for the Fennoscandian ice-sheet where the temperature forcing was so cold resulting in low ice temperatures, that the influence of geothermal heat flux on the thermal regime of the ice-sheet was minimal.

An experiment was also performed where the geothermal heat flux was spatially varying over Greenland (Shapiro and Ritzwoller, 2004) with all other parameters set at the default values. This was compared with the standard setup where the geothermal heat flux was uniform over Greenland. The differences are minimal with ice volume reduced by 0.2 %, the ice surface extent reduced by 0.3 % and the maximum ice thickness reduced by 0.1 %. Since basal sliding is switched off, the only effect this could have is on the basal melt and temperature of the ice at the base affecting the flow by changing the viscosity of ice.

Several parameters influence the near-surface air temperature in the EISMINT-3 experiment, including latitudinal dependency, seasonal variation and atmospheric lapse rate. Due to the PDD formulation of mass balance, these factors also directly affect ablation and ice-sheet evolution. Since the temperature used to force ice-sheet evolution is the near-surface air temperature at the upper surface of the ice-sheet, a vertical lapse rate correction is required to take account of the ice elevation feedback. As previously discussed, it is also required to take account of the difference between the high-resolution topography seen within Glimmer (20 km for simulations in this thesis), and that represented with the forcing input data (which are on a  $1^\circ$  by  $1^\circ$  grid or approximately 111 km resolution). Equilibrium ice surface extent increases with an increase in negative lapse rate (Figure 2.10). A similar relationship holds for ice volume but is less pronounced. This is because a less negative lapse rate results in relatively warmer near-surface air temperatures at high altitude, thereby

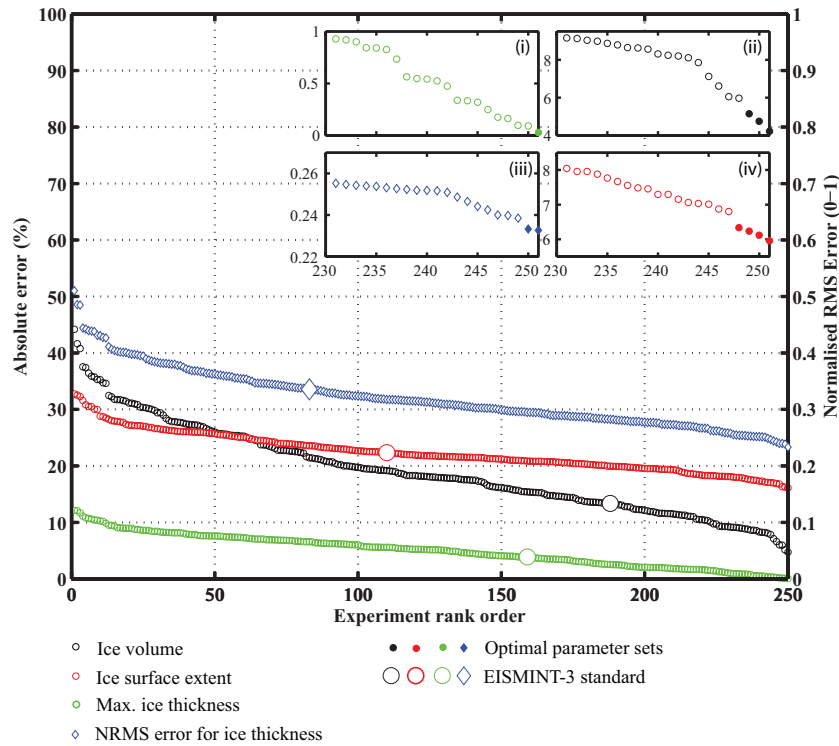


Figure 2.11: Ranking of LHS experiments for ice volume, ice surface extent and maximum ice thickness according to absolute error (left) and normalised root mean square error for ice thickness (right). The experiments rank from least agreement (1) to the closest agreement with observation (251). Observations are taken from Bamber *et al.* (2001) on the 20 km resolution grid. The larger symbols represent the rank position of the standard EISMINT-3 experiment. The inset graphs show the optimal experiments zoomed in for ranking from 230 to 251 for (i) maximum ice thickness, (ii) ice volume, (iii) normalised root mean square error for ice thickness and (iv) ice surface extent. The y-scale for each inset is independent for each diagnostic in order to see the change in gradient more clearly. Filled circles/diamonds represent the optimal parameter sets for reproducing the modern day GrIS.

expanding the area available for ablation. The least negative lapse rates result in the least error but are not typical of the annual lapse rate of  $-6.5$  to  $-8^{\circ}\text{C km}^{-1}$  used in several studies (e.g. Huybrechts and de Wolde, 1999; Ridley *et al.*, 2005; Vizcaíno *et al.*, 2008). However, those that use  $-8^{\circ}\text{C km}^{-1}$  also include a summer lapse rate. Since Glimmer only utilises one lapse rate and since the majority of melting is assumed to occur during the spring/summer months a summer lapse rate is justified as the input lapse rate correction in the model. Maximum ice thickness is completely insensitive to lapse rate. This arises because at the ice divide, where the ice thickness is highest, temperatures are already significantly below zero. Any lapse rate correction will not influence the surface mass balance greatly.

Maximum ice thickness is also insensitive to the PDD factors for ice and snow. This is because no ablation occurs in the central part of the GrIS. However, the

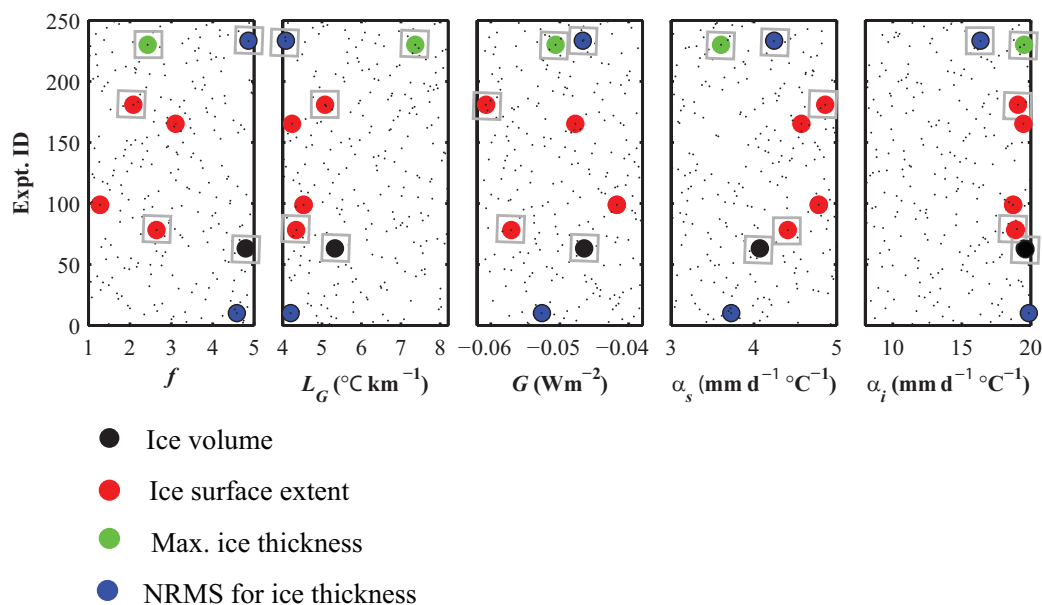


Figure 2.12: The distribution of each parameter for the eight experiments selected according to ranking of the different diagnostics: ice volume, ice surface extent and maximum ice thickness. Experiment ID number is shown on the y-axis (from 1-250) with its corresponding parameter values on the x-axis. The experiments highlighted with gray boxes are the final subset of five experiments used for ice-sheet modelling in subsequent chapter. The small black dots represent all 250 LHS experiments to show the parameter space covered.

ice surface extent is strongly affected, decreasing with increasing PDD factors. Ice volume is also sensitive to the PDD factors but less pronounced than ice surface extent. Although varying these parameters has an effect on melting rates it does not alter the position of the ablation zones. Similar results were found by both Ritz *et al.* (1997) and Hebel *et al.* (2008).

The results of these sensitivity experiments show which parameters control different aspects of the geometry of the GrIS. Ice surface extent is fundamentally dependent on those parameters which control ablation (PDD factors and lapse rate) while maximum ice thickness and ice volume are controlled by parameters affecting ice flow (flow enhancement factor). All three diagnostics are insensitive to variation in the geothermal heat flux. From this suite of experiments it is possible to select one or more parameter sets which reproduce the present day GrIS with a good fit.

### 2.5.3 Selecting the optimal parameter set

In order to select an optimal set of parameters which produce the best fit for present day ice-sheet geometry, the 250 sensitivity experiments were ranked according to each of the three diagnostics. Figure 2.11 shows ranking for the three absolute error

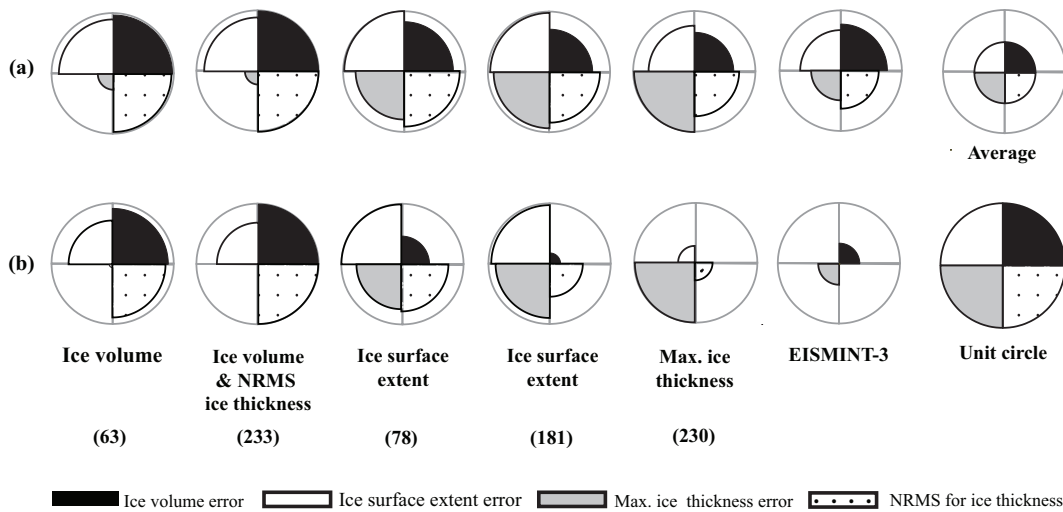


Figure 2.13: Normalised star plots showing the relative measure of skill for each diagnostic. The best skill score corresponds to a radius of 1.0 as shown by the unit circle. Relative measure of skill for (a) the five selected experiments compared with all 250 sensitivity experiments and the standard EISMINT-3 experiment and (b) the final five chosen experiments and standard EISMINT-3 compared with each other. The numbers below each experiment correspond to the experiment identification number relating to the original 250 tuning experiments and are used for identification throughout the thesis.

skill scores and the ranking for the NRMSE for ice thickness. First note that the percentage error is consistently smaller for maximum ice thickness compared with ice volume and ice surface extent.

A subset from the best-performing experiments was independently selected for each diagnostic in order to assess the effect that different parameters sets could have on GrIS modelling experiments for past and future ice-sheet evolution experiments. By having parameter sets which represent different aspects of the geometry of the ice-sheet, some idea of the uncertainty in ice-sheet evolution can be obtained: for example, future warming events. One possible way to select a subset is to choose an ensemble size, and then choose an equal number from each diagnostics' skill score. An alternative methodology was used here which selects the best performing experiments by identifying a step change in gradient in the best ranked experiments, as demonstrated in the insets of Figure 2.11. This reduces the need for an arbitrary choice in ensemble size and also excludes any experiments which are significantly worse but selected because an equal number from each diagnostic is required. This method provided eight possible parameter sets using the recent datasets, which could be used to model the GrIS more accurately in terms of different aspects of its geometry: three experiments chosen according to ice volume error, four according

| Diagnostic              | $f$    | $L_G$<br>( $^{\circ}\text{C km}^{-1}$ ) | $G$<br>( $\times 10^{-3} \text{ W m}^{-2}$ ) | $\alpha_s$<br>( $\text{mm d}^{-1} \text{ } ^{\circ}\text{C}^{-1}$ ) | $\alpha_i$<br>( $\text{mm d}^{-1} \text{ } ^{\circ}\text{C}^{-1}$ ) |
|-------------------------|--------|---|--|---|---|
| <i>Ice vol.</i>         |        |   |  |   |   |
| 63                      | 4.798  | -5.3262                                 | -46.44                                       | 4.071   | 19.553  |
| 233                     | 4.8585 | -4.0754                                 | -46.67                                       | 4.243   | 16.344  |
| <i>Ice surf. extent</i> |        |   |  |   |   |
| 78                      | 2.6494 | -4.353                                  | -57.04                                       | 4.409   | 18.862  |
| 181                     | 2.0909 | -5.079                                  | -60.72                                       | 4.863   | 19.074  |
| <i>Max. ice thk.</i>    |        |   |  |   |   |
| 230                     | 2.4275 | -7.3658                                 | -50.62                                       | 3.603   | 19.514  |

Table 2.5: Tuned parameter values for the five optimal experiments chosen according to diagnostic skill score.

to ice surface extent error and one according to maximum ice thickness error. Note the two experiments according to NRMSE selected in Figure 2.11 for ice thickness are the same as the two selected for ice volume.

A subset of five parameter sets were chosen from the eight selected simulations for ice-sheet modelling in subsequent chapters. This was because it was important to ensure that none of these eight experiments covered the same parameter space as each other, resulting in repetition. Figure 2.12 shows the eight experiments selected and the distribution of their corresponding parameter values. The subset of five are highlighted with grey boxes. Experiment ID 230 was chosen from the eight experiments because this was the best performing simulation to represent maximum ice thickness of the GrIS.

Ice surface extent has been shown to be strongly dependent on the PDD factors and lapse rate. Experiment ID's 78 and 181 were selected from the four best performing simulations in terms of ice surface extent because they had the most contrasting lapse rate and  $\alpha_s$  values (all four experiments have similar  $\alpha_i$  values).

A similar approach was applied to the three chosen ice volume experiments by discounting according to variation in lapse rate and PDD factors. Experiment ID's 63 and 233 were selected as a result of having similar flow enhancement factors but different lapse rate and  $\alpha_i$  values. Table 2.5 shows the final five experiments selected and their corresponding parameter values.

Figure 2.13 shows how well the five chosen parameter sets compare for the different diagnostic skill scores. The EISMINT-3 experiment is also included for comparison. A full unit circle would represent the experiment that out-performs all other experiments for all diagnostic skill scores. Likewise, an empty segment shows the experiment which performed worst of all for that diagnostic. By comparing this



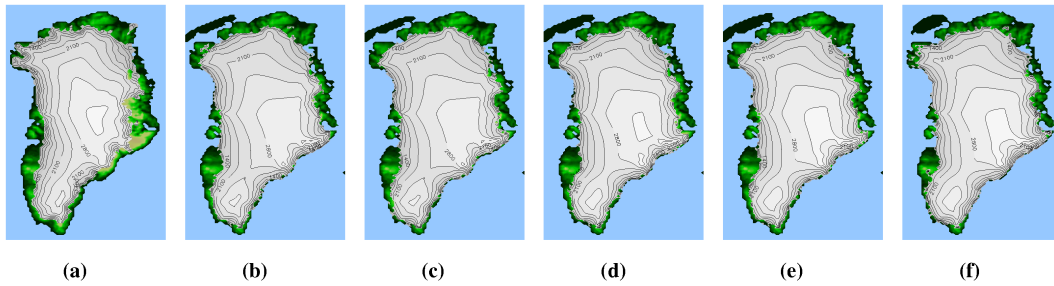


Figure 2.14: Ice-sheet configurations for (a) observed present day GrIS (from Bamber *et al.* (2001)) and (b) to (f) configurations for the five selected experiments shown in Table 4 and Figure 2.13 (experiment ID numbers 63, 233, 78, 181, 230 respectively).

measure of skill score between all 250 experiments and the EISMINT-3 experiment, three out of the five chosen parameter sets perform better than average for all diagnostics. However, two experiments perform poorly for maximum ice thickness (Figures 2.13a). The EISMINT-3 experiment (Figure 2.13a) performs on average or slightly better than average for all diagnostics. Figure 2.13b shows how well each chosen experiment compares with the other selected experiments and EISMINT-3. One will perform the worst and one the best for each diagnostic. The experiment chosen according to maximum ice thickness performs worst for all other diagnostics when compared with the other tuned experiments but is marginally better in terms of ice surface extent and NRMSE for ice thickness when compared with EISMINT-3. Those chosen according to ice volume perform poorly for maximum ice thickness. The two experiments chosen according to ice surface extent also perform well for maximum ice thickness but poorly for ice volume. EISMINT-3 performs worst for ice surface extent and NRMSE for ice thickness and below average for maximum ice thickness and ice volume.

Finally, the geometry of the GrIS is shown in Figure 2.14 for all five tuned sets and compared with the Bamber observation (Figure 2.14a). All adequately represent the limited extent of the ice-sheet in the north and west but the shape of the ice-sheet in the interior is somewhat different.

## 2.6 Discussion and conclusions

This chapter has evaluated the sensitivity to boundary conditions and climate forcings in the context of modelling the evolution of the GrIS under present day, steady-state conditions and shows the geometry and size of the ice-sheet is highly sensitive

to the initial condition of bedrock and ice thickness. An ice-sheet volume 13.7 % larger than that produced with the Letreguilly dataset results with the new and improved Bamber dataset. Overall, this study indicates that using the more recent datasets for forcings and boundary conditions with the standard set of model parameters (Table 2.5) give a poor representation of the modern ice-sheet, with an ice-sheet volume 25 % larger than observation.

Several parameters are not well-constrained in large-scale ice-sheet modelling and can influence ice-sheet volume and extent. A sensitivity/tuning study was performed in order to assess the importance of certain parameters on the geometry and size of the GrIS. The method of LHS was used in order to efficiently vary more than one parameter at a time to obtain a best fit between modelled and observed geometry. The maximum ice thickness and ice volume were shown to depend on the factors affecting ice flow. In this case increasing the flow enhancement factor makes the ice flow faster which lowers the height of the ice dome. The ice surface extent is predominantly dependent on the PDD factors and the atmospheric lapse rate. Although geothermal flux can affect ice flow since it acts to melt the ice, which is a prerequisite for basal sliding, this had little effect on the simulations presented here because basal sliding was switched off.

By selecting ‘best fit’ experiments according to different skill score diagnostics and further sub-selection according to the spread in parameter values, a range of parameter sets can be used for assessing the uncertainty in ice-sheet modelling experiments by analysing the resultant geometries. The sets of parameters that give the best fit to the present measured ice-sheet are somewhat different from the standard set most commonly used by ice-sheet modelling studies. High PDD factors (16.0 to 19.5 mm d<sup>-1</sup>°C<sup>-1</sup> for  $\alpha_i$  and 3.6 to 4.9 mm d<sup>-1</sup>°C<sup>-1</sup> for  $\alpha_s$ ) are required in all cases in order to account for both ablation and calving processes at the margin. Furthermore, less negative atmospheric lapse rates (four out of the five tuned parameter sets ranged between -4.0 and -5.3°C km<sup>-1</sup>) are generally needed to produce a good fit in terms of volume by reducing the growth of the ice-sheet. Higher flow-enhancement factors (e.g. 4.9 when  $\alpha_i$  is 0.16) are required if the ablation coefficients are reduced in order to compensate mass loss by simulating faster flow.

In contrast to many studies, the model was spun-up from present day initial conditions without taking the climate history into account. Since the GrIS is still

affected by past climatic change this assumption must be justified. The main method used to spin up the ice-sheet model over several climatic cycles has caveats of its own. It uses a temperature forcing derived from a smoothed ice core record and has been used in several studies (e.g. Huybrechts and de Wolde, 1999; Ridley *et al.*, 2005; Vizcaíno *et al.*, 2008). However, uncertainty exists in the functions used to derive a reliable temperature record and subsequent accumulation record from an oxygen isotopic record although new, more and sophisticated methods are being developed (Cuffey and Marshall, 2000; Lhomme *et al.*, 2005). The effect of ice flow processes on deeper parts of ice cores also makes them somewhat unreliable and extending beyond the last interglacial is somewhat unrealistic (Grootes *et al.*, 1993; Johnsen *et al.*, 1997). For these reasons simulations in the ice-sheet model are only initiated from the present day initial conditions, which are relatively accurate.

The process of basal sliding was not included in the experimental design, which has implications on the amount of ice mass lost dynamically. Inclusion of this missing process could result in lower PDD factors than those obtained in the tuning exercise presented here. Indeed, the study by Parizek and Alley (2004) showed an increase in GrIS sensitivity to various warming scenarios due to surface meltwater lubrication of flow. Recent modelling developments have also investigated the potential positive feedbacks from including basal sliding on the inland migration of fast-flowing glaciers increasing the drawdown of the ice-sheet interior (e.g. Price *et al.*, 2008).

Current ice-sheet models lack higher-order physics and, although able to simulate slow moving ice dynamics adequately, they are not yet able to represent the dynamics of fast-moving ice streams. Recent work has indicated that current net mass loss from the GrIS is roughly equally partitioned between surface mass balance changes and changes in dynamics (Van den Broeke *et al.*, 2009). Development of ice-sheet models in these areas is currently being researched with improvements to ice dynamics (e.g. Pattyn, 2003; Soucek and Martinec, 2008), and inclusion of accurate representation of the fast ice streams and ice shelves (Pattyn *et al.*, 2006; Schoof, 2006, 2007). Recent observations of glaciers in Greenland have documented rapid changes in marginal regions of the ice-sheet with increased flow velocities observed on Jakobshavn Glacier (Joughin *et al.*, 2004) and on other glaciers (e.g. Rignot and Kanagaratnam, 2006; Howat *et al.*, 2007). The inclusion of these fast flowing ice streams in ice-sheet models could lead to larger dynamical changes in the ice-sheet

than currently predicted by models at least on relatively short timescales of hundreds of years. However, incorporation of these fast flow features in the ice-sheet model could result in lower PDD factors obtained from tuning. It must also be noted that if these dynamical changes are marine-driven then for long-term future ice-sheet predictions, once the ice-streams are no longer marine terminating, the dynamical changes will cease. Since all the simulations in this thesis are performed over many thousands of model years, the timescales which the fast flowing ice-streams operate on mean that neglecting higher-order physics in the ice-sheet simulations is not so important.

It has also been shown that processes at the ice margin have a strong influence on the surface extent of the ice-sheet but are poorly accounted for with a coarse grid of 20 km resolution. The use of energy-balance/snow pack models (EBSM) to predict surface mass balance (e.g. Bougamont *et al.*, 2007) as opposed to the PDD approach has been shown to give contrasting results under a  $4\times$  CO<sub>2</sub> climate with the PDD scheme significantly more sensitive to a warming climate generating run-off rates almost twice as large compared with an EBSM. The ablation zone on Greenland varies from only 1 km wide along the southeast coast and up to 150 km wide along the southwest coastline and, therefore, requires a very high horizontal resolution if ablation is not to be over or underestimated in the model (Van den Broeke, 2008). Future development of the EBSM approach using a finer grid of 5 km resolution could result in a marked improvement for modelling ablation processes. It would also be highly beneficial to downscale to a  $1\times 1$  km resolution using a PDD approach (e.g. Janssens and Huybrechts, 2000) and the high-resolution Greenland DEMs now available (e.g. Bamber *et al.*, 2001).

In conclusion, the lack of higher-order physics, low resolution, absence of basal sliding and subglacial hydrology and highly parameterised surface balance inevitably means that the tuning presented here compensates for these absent processes in order to replicate as closely as possible the present day GrIS. These parameter sets are used in subsequent chapters to give a representation of spread in ice-sheet evolution results due to parametric uncertainty in the ice-sheet model.

# The response of the climate to a melted Greenland ice-sheet

## 3.1 Introduction

Several studies, outlined in Section 1.4.2 and Figure 1.5, have examined the possibility of regrowth of the GrIS under preindustrial CO<sub>2</sub> concentrations, after complete deglaciation. Such a question is of interest as it indicates to what extent anthropogenic influence on the Earth System might be irreversible. However, only one study (Crowley and Baum, 1995) looked at the sensitivity of the local climate over Greenland to surface type in order to ascertain whether ice could regrow on Greenland. Furthermore, this study did not use a realistic bedrock nor did they run their simulation for a sufficiently long time integration in order to take interannual variability into account. Sea-surface temperatures (SSTs) were fixed and the resolution of their GCM coarse (4.5° (latitude) by 7.5° (longitude)).

This chapter aims to assess the influence of vegetation cover on the climate of a deglaciated Greenland by isolating feedback processes discussed in Section 1.3, including the vegetation-snow-climate feedback and the change in orography on surface temperature via a lapse rate correction. In addition, a sensitivity to surface roughness which influences the surface energy balance is also examined. Finally, simulations are performed where surface type and orographic height are changed simultaneously in order to include all the feedback mechanisms. A wide range of variables are analysed in order to understand the changes that might arise at the surface, within the troposphere and the ocean as a result of a deglaciated Greenland. Where similar simulations have been performed by previous studies, comparisons are made. In particular, the study by Toniazzo *et al.* (2004) has many similar attributes to the experiments performed here including using a similar version of the HadCM3 climate model but with the MOSES 1 land surface scheme, a similar bedrock derived from the same dataset of Letreguilly *et al.* (1991b) and a surface type over a

deglaciated Greenland of bare soil. However, Toniazzo *et al.* (2004) did not attempt to investigate the effect of different surface types on the climate over Greenland. Nor did they attempt to isolate any of the feedback processes occurring within the Earth system.

This chapter begins by describing the climate model, HadCM3, including a detailed discussion of the land surface scheme, MOSES 2. This is followed by a comparison of modelled temperature and precipitation over Greenland in the control simulation with observations. These two variables are used for forcing the ice-sheet model in Chapter 5 and therefore it is particularly important to validate them over the Greenland region for this version of the climate model. This is followed by the results section and finally discussion and conclusions.

## 3.2 The Hadley Centre climate model

### 3.2.1 Atmosphere

The atmosphere component of HadCM3 is a global grid-point hydrostatic primitive equation model, run with a horizontal grid-spacing of  $2.5^\circ$  (latitude) by  $3.75^\circ$  (longitude) (or 73 by 96 grid points) and nineteen levels in the vertical with a time step of 30 minutes. The performance of the atmosphere component is described in Pope *et al.* (2000) where HadAM3 (the atmosphere only version of the Hadley Centre Model) is forced by observed SSTs. It has been shown to agree well with observations. The land surface scheme (MOSES 2) which includes representation of the freezing and melting of soil moisture and the formulation of evaporation includes the dependence of stomatal resistance on temperature, vapour pressure and  $\text{CO}_2$ . Within this land surface scheme ice-sheets are prescribed and are fixed. This scheme is discussed in much more detail in Section 3.2.3. Validation of HadCM3-MOSES 2, at high latitudes (i.e. over Greenland) using a preindustrial simulation is performed and discussed in Section 3.3.2. The radiation scheme used is that of Edwards and Slingo (1996) where there are six and eight spectral bands in the shortwave and longwave respectively. The convective scheme is based on Gregory and Rowntree (1990) with an additional parameterisation of the direct impact of convection on momentum (Gregory *et al.*, 1997). The cloud scheme employed is a prognostic one that diagnoses cloud amount, cloud ice and cloud water based on the total moisture

and the liquid water potential temperature. The orography of Greenland is particularly important when considering the deglaciation and possible reglaciation of the GrIS since previous work has shown it can have profound effects on atmospheric circulation patterns if the ice-sheet were removed (e.g. Petersen *et al.*, 2004; Junge *et al.*, 2005) since orographic gravity waves represent a major sink of momentum flux in the atmosphere. In order to include the effect of orographic forcing on atmospheric circulation, HadCM3 also includes a parameterisation of orographic drag (Milton and Wilson, 1996) and a gravity wave drag scheme in order to represent the mechanisms of sub-grid scale orographic forcing in stable and turbulent atmospheric flow. The scheme includes anisotropy of orography, high drag states and flow blocking as well as trapped lee waves (Gregory *et al.*, 1998). This is discussed in more detail, including the topographic datasets used, in Section 3.2.4.

### 3.2.2 Ocean

The ocean component of HadCM3 is a 20 level version of the Bryan-Cox (Bryan, 1969; Cox, 1984) model and is run with a latitude longitude grid-spacing of  $1.25^\circ$  by  $1.25^\circ$ . There are six ocean gridboxes for every atmosphere gridbox which also have the ability to have partial sea-ice cover. The vertical levels are designed such that there is enhanced resolution near to the ocean surface. Bathymetry is interpolated and smoothed from the ETOP05  $1/12^\circ$  resolution dataset.

An energy balance mixed layer model combined with a K-Theory Scheme (Pacanowski and Philander, 1981) which parameterises vertical mixing, is embedded in the ocean model where any negative surface buoyancy flux into the ocean surface is mixed down to a neutrally buoyant level by convection. This is where the density profile is statically stable and the turbulent kinetic energy available from the release of gravitational potential energy via this convection and the work done by the wind on the ocean surface is depleted. Note that only potential temperature and salinity (tracers) are mixed by these schemes (Johnsen *et al.*, 1997; Gordon *et al.*, 2000). Note also, that further vertical mixing at all depths occurs through vertical diffusion of both the tracers and momentum.

Horizontal mixing of tracers is parameterised using an adiabatic thickness diffusion scheme where tracers are diffused along isopycnal surfaces with a depth-dependent diffusivity (Gordon *et al.*, 2000). Finally, shortwave solar radiation is

selectively absorbed with depth using a double exponential decay.

### Sea-ice model

The sea-ice model parameterises ice drift and leads (narrow, linear cracks in the ice that form when ice flows diverge or shear as they move parallel to each other) (Cattle and Crossley, 1995) and uses a simple thermodynamic scheme based on the zero-layer model of Semtner (1976). Ice concentration cannot exceed 0.995 in the Arctic since completely unbroken ice cover is rarely observed in pack-ice. Ice formation occurs predominantly by freezing of water in the leads and ice removal occurs by melting at the surface during summer months and melting at the base throughout the year. The depth of sea-ice can be increased by the formation of ‘white ice’ where the weight of the ice forces the ice-snow interface below the water line (Gordon *et al.*, 2000).

Changes in ocean salinity as a result of sea-ice formation are accounted for by assuming a constant salinity of 0.6 ‰ for sea-ice. The sublimation process increases ocean salinity while white ice formation reduces it and snowfall reduces it in leads. All rainfall is assumed to reach the ocean through leads.

Surface temperatures and fluxes over the sea-ice and leads fractions of gridboxes are calculated separately in the atmosphere component of HadCM3. Surface albedo of sea-ice is 0.8 at temperatures less than  $-10^{\circ}\text{C}$  and falls linearly to 0.5 between  $-10$  and  $0^{\circ}\text{C}$ . This is to account for the aging of snow, formation of melt ponds and the relatively low albedo of bare ice.

Wind-mixing energy and oceanic heat flux into the base of the ice are accounted for as well as a simple parameterisation of sea-ice dynamics based on Bryan (1969).

### 3.2.3 Land surface scheme

The Met Office Surface Exchange Scheme (MOSES), version 2.1, is used to calculate water and energy fluxes in the version of HadCM3 used here. The previous version of MOSES (MOSES 1) is outlined in Cox *et al.* (1999). Although many of the features of MOSES 1 are retained in MOSES 2, it has the added benefits that it treats sub-grid land cover explicitly and is fully coupled to the dynamic vegetation model TRIFFID (see Chapter 4 for more detail). MOSES 2 is described in detail in Essery *et al.* (2001) and the following section summaries the main processes described



| PFT               | IGBP Class           | LAI |
|-------------------|----------------------|-----|
| <i>Broadleaf</i>  | Evergreen broadleaf  | 9.0 |
| <i>Needleleaf</i> | Evergreen needleleaf | 6.0 |
| <i>C3 Grass</i>   | Grassland            | 3.0 |
| <i>C4 Grass</i>   | Grassland            | 4.0 |
| <i>Shrub</i>      | Close Shrub          | 3.0 |

Table 3.1: Table showing the value of Leaf Area Index (LAI) of each MOSES 2 Plant Functional Type (PFT) for a characteristic IGBP class (from Jones (2004)).

in Essery *et al.* (2001) and Cox *et al.* (1999). These processes are important for understanding the sensitivity of the Greenland climate to changes in surface type.

Nine surface types are recognised by MOSES 2: broadleaf trees, needleleaf trees, C3 (temperate) grasses, C4 (tropical) grasses, shrubs (these are the five Plant Functional Types (PFTs)), urban, inland water, bare soil and permanent land ice. Excluding ice type, each land-surface gridbox can be made up of any mixture of the other eight surface types. The surface energy balance given in Equation 1.1 is explicitly solved in each gridbox. Thus, for each surface type in a gridbox surface temperatures, longwave radiative fluxes, sensible and latent heat fluxes, ground heat fluxes, canopy moisture contents, snow masses and snow melt rates are calculated. However, air temperature, humidity and windspeed on atmospheric levels above the surface are treated as homogeneous across the gridbox. Likewise, soil temperatures and moisture contents below the surface are also treated as homogeneous.

The fraction of a surface type determines how much that type contributes to the overall land gridbox surface properties. Many of the properties are weighted according to the fraction of the associated surface type such as surface albedo, infiltration rate, canopy heat capacity and soil moisture extraction by roots.

Several datasets describe the properties of the five PFTs in the land surface scheme. Firstly, the Leaf Area Index (LAI) is defined as the area of leaves per unit area of ground taking one side of the leaf into account. LAI values used are defined in Table 3.1 based on the most characteristic (International Geosphere and Biosphere Program) IGBP class. The IGBP dataset is derived from AVHRR satellite data.

The LAI values are subsequently used to calculate the canopy height (in m),  $C_h$ , according to

$$C_h = H_f L^{2/3}, \quad (3.1)$$

where  $H_f$  is a height factor for each PFT and  $L$  is the LAI.

The aerodynamic surface roughness lengths which are used by MOSES 2 to calculate surface-atmosphere fluxes of heat, water and momentum and CO<sub>2</sub>, are calculated explicitly according to the canopy height and the rate of change of roughness length with canopy height for each PFT

$$z_{0,j} = \frac{dz_0}{dC_h} \times C_{h,j}, \quad (3.2)$$

where  $z_{0,j}$  (in m) is the roughness length for momentum for surface type  $j$ . The roughness lengths for the surface-atmosphere fluxes of heat, water and CO<sub>2</sub> are equivalent to a tenth of  $z_{0,j}$ . In the case of trees  $\frac{dz_0}{dC_h}$  is set to 0.05 and 0.1 for all other vegetation types. Roughness lengths for unvegetated surface types are 1.5 m for urban,  $3 \times 10^{-4}$  m for water,  $3 \times 10^{-4}$  m for soil and  $1 \times 10^{-4}$  m for land ice. The average effective roughness length,  $z_0$ , for each land gridbox is calculated using

$$z_0 = L_{blend} \cdot \exp \left( - \sum_j \left[ \frac{\nu_j}{\ln^2(L_{blend}/z_{0,j})} \right]^{-1/2} \right), \quad (3.3)$$

where  $L_{blend}$  is a defined height presumed to be between where flow is unaffected by roughness and where local flow is entirely determined by  $z_{0,j}$  (Mason, 1988). For HadCM3, MOSES 2,  $L_{blend}$  is equal to 550 m.

Surface albedo is an important attribute of vegetation types since it determines the amount of downward shortwave heat flux that is absorbed at the surface. LAI is also used in determining the surface albedo for surfaces covered by vegetation. The surface albedo for fractional covered vegetated surface types (unweighted) is described by the snow-free (Equation 3.4) and cold deep snow (Equation 3.5) albedos

$$\alpha_0 = \alpha_{soil} + \left( 1 - \exp^{-L/2} \right) (\alpha_0^\infty - \alpha_{soil}), \quad (3.4)$$

$$\alpha_{cfs} = \alpha_s^0 + \left( 1 - \exp^{-L/2} \right) (\alpha_s^\infty - \alpha_s^0), \quad (3.5)$$

where  $\alpha_{soil}$  is the albedo for snow-free soil underlying the vegetation. The soil albedo is defined according to colour and wetness. Thus for average medium coloured soil the snow-free albedo is 0.17 and the cold deep snow albedo is 0.80. Where there is ice the soil albedo,  $\alpha_{soil}$ , is set to 0.75 and 0.80 for cold deep snow albedo. Values for the vegetation dependent parameters  $\alpha_0^\infty$ ,  $\alpha_s^\infty$  and  $\alpha_s^0$  are shown in Table 3.2.

|            | $\alpha_0^\infty$ | $\alpha_s^\infty$ | $\alpha_s^0$ |
|------------|-------------------|-------------------|--------------|
| Broadleaf  | 0.10              | 0.15              | 0.30         |
| Needleleaf | 0.10              | 0.15              | 0.30         |
| C3 Grass   | 0.20              | 0.60              | 0.80         |
| C4 Grass   | 0.20              | 0.60              | 0.80         |
| Shrub      | 0.20              | 0.40              | 0.80         |

Table 3.2: Albedo parameters for vegetation types (*from Essery et al. (2001)*).  $\alpha_0^\infty$  is the maximum prescribed canopy albedo used in calculating the snow-free albedo in Equation 3.4, while  $\alpha_s^\infty$  is the minimum snow albedo and  $\alpha_s^0$  is the maximum snow albedo used to calculate the cold deep snow albedo in Equation 3.5.

The state of the land surface is defined by the amount of lying snow mass, canopy water and temperature and moisture content of the soil layers as shown in Figure 3.1. Precipitation is partitioned into interception (via the canopy), throughfall, run-off and infiltration into the ground. Canopy water refers to the precipitation intercepted by plant leaves available for free evaporation. Thus, for a rainfall rate,  $R$  (in  $\text{kg m}^{-2}\text{s}^{-1}$ ), covering a fraction  $\epsilon$  of a gridbox (typically 1 for large scale rain or condensation and 0.3 for convective rain) the throughfall,  $T_F$  (in  $\text{kg m}^{-2} \text{s}^{-1}$ ), (i.e. water not retained in the canopy) is given by

$$T_F = R \left(1 - \frac{C}{C_m}\right) \exp\left(-\frac{\epsilon C_m}{R \Delta t}\right) + R \frac{C}{C_m}. \quad (3.6)$$

$C_m$  is the canopy water capacity (in  $\text{kg m}^{-2}$ ),  $\Delta t$  is the time interval for updating the canopy water content (30 minutes in the model) and  $C$  (in  $\text{kg m}^{-2}$ ) is the canopy water content which is updated by

$$C^{(n+1)} = C^{(n)} + (R - T_F) \Delta t. \quad (3.7)$$

The water that reaches the soil surface is either lost as surface run-off or by infiltration into the ground or both. The surface run-off,  $Y$  (in  $\text{kg m}^{-2} \text{s}^{-1}$ ), is calculated as

$$Y = \begin{cases} R \frac{C}{C_m} \exp\left(-\frac{\epsilon K C_m}{R C}\right) + R \left(1 - \frac{C}{C_m}\right) \exp\left(-\frac{\epsilon C_m}{R \Delta t}\right) & K \Delta t \leq C \\ R \exp\left[-\frac{\epsilon(K \Delta t + C_m - C)}{R \Delta t}\right] & K \Delta t > C \end{cases} \quad (3.8)$$

and is dependent on the infiltration rate,  $K$  (in  $\text{kg m}^{-2} \text{s}^{-1}$ ), which is equal to  $\beta K_s$

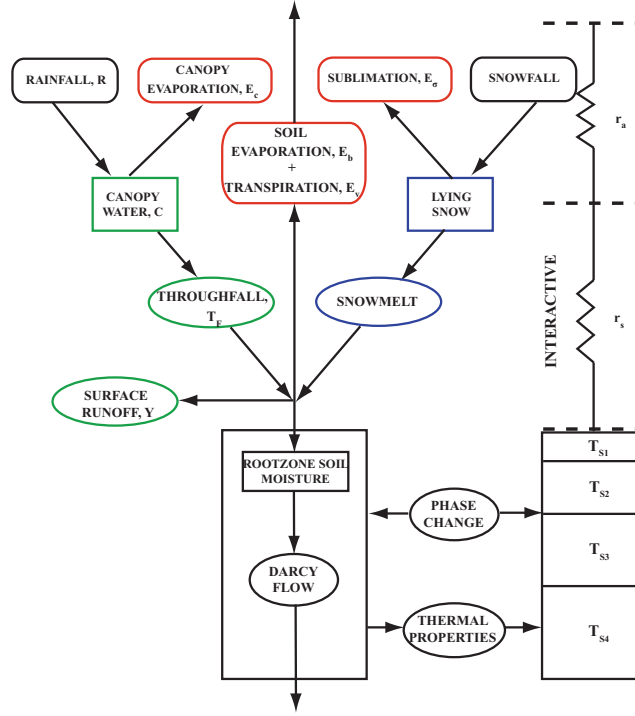


Figure 3.1: Schematic of the MOSES 2 land surface scheme (*modified from Cox et al. (1999)*). The prognostic variables are in rectangles. Those highlighted in red refer to variables related to the evaporation fluxes, those in green denote how precipitation is dealt with and those in blue relate to melt from snow.

( $\beta$  is an infiltration enhancement factor and unitless).  $K_s$  (in  $\text{mm s}^{-1}$ ) is the soil saturated hydraulic conductivity given in Table 3.3 and describes the ease at which water can move through the soil medium under saturated conditions.

As a result there are four types of evaporative fluxes that contribute to the overall moisture flux from a land gridbox.

Firstly, there is evaporation (in  $\text{kg m}^{-2}$ ) from the canopy,  $E_c$ , which only occurs from the fraction of a gridbox which has a *wet* canopy,  $f_a$

$$E_c = f_a \frac{\rho}{r_a} \{q_{\text{sat}}(T_*) - q_1\}, \quad (3.9)$$

where  $\rho$  is the surface air density (in  $\text{kg m}^{-3}$ ),  $q_1$  is the atmospheric specific humidity (in  $\text{kg}_{\text{water}} \text{kg}_{\text{air}}^{-1}$ ) and  $q_{\text{sat}}(T_*)$  is the saturated specific humidity at the surface temperature,  $T_*$  (in K). The aerodynamic roughness length,  $r_a$  (in m) represents the aerodynamic resistance to transport of moisture and heat and depends on roughness length, windspeed and atmospheric stability. It is estimated by

$$r_a = C_H (|v_1 - v_0|)^{-1}, \quad (3.10)$$

where  $v_1$  is the horizontal wind velocity of the surface air and  $v_0$  is the horizontal wind speed of the surface. Over land  $v_0$  is equal to zero but is equal to prescribed current speed over sea.  $C_H$  is the surface exchange coefficient for sensible and latent heat fluxes between the the surface and immediate atmospheric level above, at height  $z_1$ .  $C_H$  is given by

$$C_H = f_h \cdot k^2 \left[ \left( \frac{z_1 + z_0}{z_0} \right) \ln \left( \frac{z_1 + z_0}{0.1z_0} \right) \right]^{-1}, \quad (3.11)$$

where  $f_h$  is a measure of the stability of the air and  $k$  is the von Karman constant, 0.4. In Equation 3.9,  $f_a$  (the wet fraction) is determined by the ratio of canopy moisture content to canopy capacity and reaches unity at canopy capacity.

Secondly, there is evaporation via transpiration,  $E_\nu$ , from the vegetated fraction of the remainder of the gridbox,  $\nu$ . This is controlled fundamentally by the canopy conductance and aerodynamic resistance. The canopy conductance is determined by a photosynthetic model which depends on temperature, humidity deficit, incident radiation and soil moisture availability and vegetation type

$$E_\nu = (1 - f_a) \nu \frac{\rho}{r_a + \frac{1}{g_c}} \{q_{sat}(T_*) - q_1\}, \quad (3.12)$$

where  $g_c$  is the canopy conductance (in  $\text{m s}^{-1}$ ) calculated using a canopy conductance and primary productivity module.

Thirdly, evaporation occurs as bare soil evaporation from the *dry* canopy. This applies to the non-vegetated fraction of the land gridbox and depends on fixed soil surface resistance  $r_{ss}$  and a volumetric soil moisture concentration within the top soil layer,  $\Theta_1$

$$E_b = (1 - f_a) (1 - \nu) \beta(\Theta_1) \frac{\rho}{r_a + r_{ss}} \{q_{sat}(T_*) - q_1\}, \quad (3.13)$$

where

$$\beta(\Theta) = \begin{cases} 1 & \text{for } \Theta > \Theta_c \\ \frac{\Theta - \Theta_w}{\Theta_c - \Theta_w} & \text{for } \Theta_w < \Theta \leq \Theta_c. \\ 0 & \Theta \leq \Theta_w \end{cases} \quad (3.14)$$

$\Theta_w$  and  $\Theta_c$  are the soil dependent parameters for volumetric soil moisture con-

centration at the wilting and critical points assumed to correspond to soil water suctions equivalent to 1.5 MPa and 0.033 MPa respectively and are shown in Table 3.3. In turn they are dependent on the saturated soil water suction,  $\psi_s$  (in m) and volumetric soil moisture concentration at saturation parameter,  $\Theta_s$ . These parameters are calculated as geographically varying and as a function of the soil type. There are three main soil texture types, fine, medium and coarse which are described by the fraction of clay, silt and sand present which correspond to varying soil particle size. Table 3.3 shows the soil particle size fractions for the three types of soil.

Using the multiple regression relationships of Cosby *et al.* (1984) the soil dependent parameters described can be calculated depending on the soil fractions present. Table 3.3 also shows all the soil dependent parameters, their relationships and values for the three soil texture classes. These are defined as ancillary input for HadCM3 and are not calculated internally.

Fourthly there is sublimation that occurs from a snow surface,  $E_\sigma$ . If snow,  $\sigma_{sn}$ , is present on a surface the total moisture flux is solely due to this sublimation such that the overall total moisture flux can be described as

$$E = \begin{cases} E_\nu + E_b + E_c & \text{for } \sigma_{sn}=0 \\ E_\sigma & \text{for } \sigma_{sn} > 0. \end{cases} \quad (3.15)$$

MOSES 2 has four soil layers (see Figure 3.1) with thicknesses from the surface downwards set to 0.1, 0.25, 0.65 and 2 m. Moisture content of the upper soil layer (0.1 m) is increased via snow melt and throughfall and decreased according to evaporation from the soil layer, and flow of water into lower layers and draw up of water via plant roots. The extraction of water from any particular soil layer is proportional to the water lost by evapotranspiration reflecting the vertical distribution of roots. The five PFTs have different root depths such that trees are able to access moisture from soil layers at deeper depths compared with grasses and shrubs. The soil moisture content and soil water phase changes and the associated latent heat describe the thermal characteristics of soil which determine, via discretised form of the heat diffusion equation, the subsurface temperatures.

Subsurface soil temperatures are determined by the diffusive heat fluxes into and out of a soil layer and the heat flux advected from the layer by the moisture flux.

| Parameter  | Relationship   | Soil Texture          |                       |                       |
|--|--|-----------------------|-----------------------|-----------------------|
|  |  | Fine                  | Medium                | Coarse                |
| $f_{sand}$   |  | 0.21                  | 0.27                  | 0.58                  |
| $f_{silt}$   |  | 0.27                  | 0.50                  | 0.32                  |
| $f_{clay}$   |  | 0.52                  | 0.23                  | 0.10                  |
| $b$  | $= 3.10 + 15.70f_{clay} - 0.3f_{sand}$   | 11.20                 | 6.63                  | 4.50                  |
| $K_s$ (mm s <sup>-1</sup> )                          | $= e^{(-5.55-0.64f_{clay}+1.26f_{sand})}$  | $3.63 \times 10^{-3}$ | $4.72 \times 10^{-3}$ | $7.57 \times 10^{-3}$ |
| $\psi_s$ (m)   | $= 0.01e^{(2.17-0.63f_{clay}-1.58f_{sand})}$   | $3.63 \times 10^{-2}$ | $4.72 \times 10^{-2}$ | $7.57 \times 10^{-2}$ |
| $\Theta_s$   | $= 0.505 - 0.037f_{clay} - 0.142f_{sand}$  | 0.456                 | 0.458                 | 0.419                 |
| $\Theta_w$   | $= \Theta_s \left( \frac{\psi_s}{152.9} \right)^{\left(\frac{1}{b}\right)}$  | 0.221                 | 0.136                 | 0.064                 |
| $\Theta_c$   | $= \Theta_s \left( \frac{\psi_s}{3.364} \right)^{\left(\frac{1}{b}\right)}$  | 0.310                 | 0.242                 | 0.150                 |
| $C_s$ (J K <sup>-1</sup> m <sup>-3</sup> )           | $= (1 - \Theta_s) (f_{clay}c_{clay} + f_{sand}c_{sand} + f_{silt}c_{silt})$  | $1.23 \times 10^6$    | $1.19 \times 10^6$    | $1.25 \times 10^6$    |
|  | $c_{sand} = 2.133 \times 10^6 Jm^{-3}K^{-1}$   |                       |                       |                       |
|  | $c_{clay} = 2.373 \times 10^6 Jm^{-3}K^{-1}$   |                       |                       |                       |
|  | $c_{silt} = 2.133 \times 10^6 Jm^{-3}K^{-1}$   |                       |                       |                       |
| $\lambda_{dry}$ (W m <sup>-1</sup> K <sup>-1</sup> ) | $= (\lambda_{air})^{\Theta_s} (\lambda_{clay})^{((1-\Theta_s)f_{clay})} (\lambda_{sand})^{((1-\Theta_s)f_{sand})} (\lambda_{silt})^{((1-\Theta_s)f_{silt})}$ | 0.218                 | 0.227                 | 0.272                 |
|  | $\lambda_{air} = 0.25Wm^{-1}K^{-1}$  |                       |                       |                       |
|  | $\lambda_{clay} = 1.16025Wm^{-1}K^{-1}$  |                       |                       |                       |
|  | $\lambda_{sand} = 1.57025Wm^{-1}K^{-1}$  |                       |                       |                       |
|  | $\lambda_{silt} = 1.57025Wm^{-1}K^{-1}$  |                       |                       |                       |

Table 3.3: Table showing the calculated soil parameters for the three Wilson and Henderson-Sellers soil textural classes (Fine, Medium, Coarse). In descending order the parameters are fraction of sand,  $f_{sand}$ ; fraction of silt,  $f_{silt}$ ; fraction of clay,  $f_{clay}$ ; Clapp-Hornberger exponent,  $b$ ; saturated hydraulic conductivity,  $K_s$ ; saturated soil water suction,  $\psi_s$ ; volumetric soil moisture concentrations at saturation, wilting and critical points,  $\Theta_s$ ,  $\Theta_w$ ,  $\Theta_c$  respectively; dry soil volumetric heat capacity,  $C_s$ , and dry soil thermal conductivity,  $\lambda_{dry}$ . The multi-regression relationships based on Cosby *et al.* (1984) and shown in Jones (2004) are also present.

The diffusive heat fluxes from one layer to another are dependent on the local soil thermal conductivity,  $\lambda$  (in  $\text{W m}^{-1} \text{K}^{-1}$ ), which is modified in the presence of lying snow due to its insulating effects. The heat capacity of the soil takes into account the amount of frozen and unfrozen water present and also the apparent heat capacity associated with phase change.

The surface temperature is determined by the surface energy balance

$$C_c \frac{dT_*}{dt} = SW_{NET} + LW_{\downarrow} - \sigma T_*^4 - H - LE - L_f S_m - G_0. \quad (3.16)$$

$C_c$  is the canopy heat capacity (in  $\text{J K}^{-1} \text{m}^{-3}$ ) and is dependent on the amount of carbon stored in wood and leaf biomass. For non-vegetated surface this is set to zero.  $SW_{NET}$  is the net short-wave radiation ( $\text{W m}^{-2}$ ),  $LW_{\downarrow}$  is the downward long-wave radiation received at the surface and  $\sigma$  is the Stefan-Boltzmann constant ( $5.67 \times 10^{-8}$ ) where  $\sigma T_*^4$  is the upward long-wave radiation emitted from the surface.  $H$  is the sensible heat flux ( $\text{W m}^{-2}$ ) described by

$$H = \frac{\rho c_p}{r_a} \left\{ T_* - T_1 - \frac{g}{c_p} z_1 \right\}, \quad (3.17)$$

where  $c_p$  is the specific heat capacity of air (in  $\text{J kg}^{-1} \text{K}^{-1}$ ),  $g$  is the acceleration due to gravity (in  $\text{m s}^{-2}$ ) and  $T_1$  is the atmospheric temperature at a reference height  $z_1$  above the surface.  $L$  is the latent heat of evaporation (in  $\text{J kg}^{-1}$ ) and therefore  $LE$  is the energy transferred from or to the surface by moisture.  $L_f$  is the latent heat of fusion (in  $\text{J kg}^{-1}$ ) for water and  $S_m$  is the rate of snow melt (in  $\text{kg m}^{-2} \text{s}^{-1}$ ). Finally,  $G_0$  (in  $\text{W m}^{-2}$ ) describes the conductive heat flux from the surface to the centre of the top soil layer

$$G_0 = \frac{2\lambda}{\Delta z_1} \{T_* - T_{s1}\}, \quad (3.18)$$

where  $\Delta z_1$  is the top soil layer thickness and  $T_{s1}$  is the corresponding subsurface temperature and  $\lambda$  is the thermal conductivity which depends on soil moisture.

### 3.2.4 Orographic boundary conditions

A modified present day orography dataset has been constructed for use with HadCM3 using Greenland orography and ice-sheet extent derived from the Letreguilly dataset



(Letreguilly *et al.*, 1991b) described in Chapter 2. The following section describes the parameters modified for this new present day orography for the preindustrial control and a rebounded orography used in experiments where the GrIS is removed and isostatic equilibrium is achieved.

### Interpolation

Data from the Letreguilly dataset is on a regular Cartesian grid,  $(k, l)$ , of size 141 by 83 gridpoints (referred to as the local grid) with a longitude and latitude associated with each data point. Interpolation from this Cartesian grid to a regular high-resolution latitude-longitude grid,  $(i, j)$ , of  $1^\circ$  by  $1^\circ$  resolution (referred to as the global grid) has been performed. A binning program was constructed whereby the Letreguilly datapoints were ‘binned’ into their associated regular latitude-longitude gridbox on the global grid. A land sea mask was created where gridboxes with a fraction of land points greater than 50 % were classified as land and those less than or equal to 50 % classified as sea in accordance with UM documentation (Jones, 2004). The orography is therefore determined by the following

$$\begin{aligned}
 H^L(i, j) &= H_{br}^L(k, l) + H_{ice}^L(k, l) \text{ if } H^L(k, l) > 0, \\
 H(i, j) &= \frac{1}{n} \sum_{m=1}^n H^L(i, j)_m,
 \end{aligned}
 \tag{3.19}$$

where  $H^L$  is the Letreguilly orography datapoints that were binned into their associated latitude-longitude box on the global grid,  $H_{br}^L$  is the bedrock orography from the Letreguilly dataset,  $H_{ice}^L$  is the ice thickness from the Letreguilly dataset,  $n$ , is the total number of Letreguilly orography datapoints that are binned into a latitude-longitude box (global grid) and  $H$  is the average orography for each latitude-longitude gridbox (global grid). The average orography is then multiplied by the land sea mask for consistency.

### Orography and Related Fields

There are seven orographic related fields that represent the orography in HadCM3 described below and given in more detail in Webster (2003).

*Orographic Mean Height*

The average orography of Greenland derived (see Equation 3.19) on a regular latitude-longitude  $1^\circ$  by  $1^\circ$  grid is upscaled onto the regular HadCM3 latitude-longitude grid. Outside of Greenland the topography is derived from ETOPO5 which is the standard present day topography dataset for HadCM3.

The following fields described are used in the flow blocking and gravity wave drag scheme and represent sub-grid scale processes.

*Standard deviation*

The standard deviation orography field is used within the gravity wave parameterisation scheme. In order to address the low-level barrier effect of mountains an enhanced orography can be developed where some multiple of the sub-grid scale standard deviation is added to the mean orography. Ideally, the HadCM3 grid should be significantly coarser than the grid of the source data to calculate this standard deviation. This field is defined by

$$\sigma_h = \sqrt{\frac{1}{N} \sum_i^N (H_i - \bar{H})^2}, \quad (3.20)$$

where  $H_i$  is the mean orography at the  $1^\circ$  by  $1^\circ$  resolution,  $\bar{H}$  is the mean orography for the HadCM3 gridbox into which the high-resolution data point falls into and  $N$  is the number of source datapoints within the HadCM3 gridbox.

 *$\sigma_{xx}, \sigma_{xy}, \sigma_{yy}$* 

The sub-grid fields  $\sigma_{xx}$ ,  $\sigma_{xy}$ ,  $\sigma_{yy}$  are grid-box summary information of small-scale mountain ridges within a model gridbox, and similar to the standard deviation are also used within the gravity wave parameterisation scheme. They are defined as

$$\sigma_{xx} = \overline{\left(\frac{\partial h}{\partial x}\right)^2} = \overline{\left(\frac{\Delta h}{\Delta x}\right)^2}, \quad (3.21)$$

$$\sigma_{yy} = \overline{\left(\frac{\partial h}{\partial y}\right)^2} = \overline{\left(\frac{\Delta h}{\Delta y}\right)^2}, \quad (3.22)$$

$$\sigma_{xy} = \overline{\left(\frac{\partial h}{\partial x} \cdot \frac{\partial h}{\partial y}\right)} = \overline{\left(\frac{\Delta h}{\Delta x} \cdot \frac{\Delta h}{\Delta y}\right)}. \quad (3.23)$$

Using  $\sigma_{xx}$  as an example, the above are calculated in the following way.  $\Delta x$  is the source dataset x-direction grid spacing,  $\Delta h$  is the difference in the source dataset height at adjacent points and the overbar denotes the UM gridbox average. It is thus the average of the square of the local x-gradient for all source datapoints within the UM gridbox.

#### *Orographic roughness fields*

The remaining two orography fields are used in the orographic drag parameterisation scheme. The first is the silhouette area  $A/S$ , where  $A$  is the frontal area of the sub-grid orography per unit horizontal area  $S$ . In the standard version of HadCM3,  $A/S$  is calculated from  $\sigma_h$  using a simple linear relationship

$$A/S = a\sigma_h, \quad (3.24)$$

where  $a$  is a derived coefficient and equal to 0.000084454 for the climate model. The second roughness field is the peak to trough height,  $h$ , and when used in conjunction with the definition for the silhouette area in Equation 3.24, is defined as

$$h = 2\sqrt{2}\sigma_h. \quad (3.25)$$

### 3.3 Climatic sensitivity to surface type and orography over Greenland

It has been shown by previous studies that the climate over Greenland is sensitive to changes in elevation (e.g. Lunt *et al.*, 2004; Petersen *et al.*, 2004) and surface type (e.g. Crowley and Baum, 1995). Thus the following sections isolate and examine the sensitivity of the climate to changes in surface type and elevation over Greenland under preindustrial conditions. In this way, the impact and importance of the vegetation-snow-climate feedback and change in surface elevation on the Greenland climate can be independently quantified. Furthermore, when these two are varied together in Section 3.3.5, any synergy between them can be identified which may be important in understanding the response of the climate to a melted GrIS. Experimental methodology is outlined followed by climate model validation over Greenland. The effects of surface type and elevation on the climate over a melted GrIS are subsequently analysed. The final simulations assess the state of the climate on an ice-free, bedrock-rebounded Greenland. All experiments in this chapter are run with fixed vegetation over Greenland. Focus is on the mean climatic effect of a melted Greenland rather than transient effects such as the influence on individual cyclones. This type of analysis would be more appropriate using a higher resolution GCM (e.g. Kristjánsson and McInnes, 1999).

#### 3.3.1 Experimental setup

A total of 15 HadCM3 experiments were run for 100 model years, sufficient to spin up the atmosphere and soil moisture. The length of spin-up for the model was 70 model years with 30 years for averaging. The spin-up time in large-scale ocean models is governed by the slow processes in the deep ocean and is usually on the order of a few thousand years. However, due to computational expense this is not easily achievable. As such the ocean component of HadCM3 is treated like a slab ocean model (where the ocean is represented by a well-mixed layer of water typically 50 m thick) for all simulations in this thesis, while still including the non-linear behaviour related to ocean circulation change (which will not completely be spun-up). Typically, the most common measure of the strength of the North Atlantic MOC is the maximum of the zonally integrated transport stream function in the North Atlantic. Figure

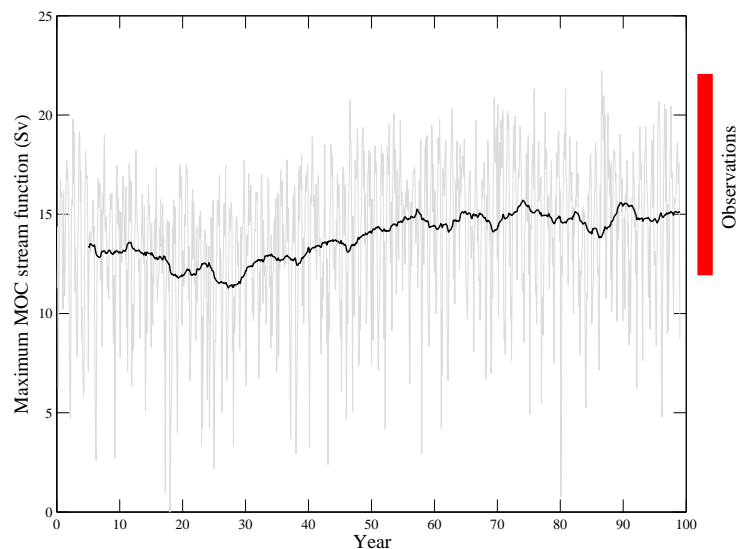


Figure 3.2: Evolution of the maximum Atlantic meridional overturning circulation (MOC) stream function at  $30^{\circ}\text{N}$  for the preindustrial HadCM3 MOSES 2 control. The black line shows the five-year running average superimposed on the monthly evolution of the maximum MOC stream function (light grey). Also shown by the red rectangle is the observational uncertainty from Talley *et al.* (2003).

3.2 shows a five-year running average of the maximum MOC stream function at  $30^{\circ}\text{N}$  in the Atlantic Ocean basin for the HadCM3 MOSES 2 control experiment representing the preindustrial (which is validated in Section 3.3.2). Over the final 30 years of averaging adequate spin-up has been achieved with values consistent with annual MOC observations from Talley *et al.* (2003) and also in agreement with other present day measurements (e.g. Smethie and Fine, 2001; Ganachaud, 2003; Lumpkin and Speer, 2007).

Twelve experiments were run where the GrIS is removed, six of which have the orographic height as modern and six where the orography is rebounded after removal of ice due to isostatic readjustment. In order to isolate the effects of changing surface type further, an additional experiment where surface roughness length is varied but albedo of the surface type is unchanged, is performed. Finally, an experiment investigating the effect of changing the elevation on the Greenland climate is simulated: GrIS is lowered to the height of the rebounded orography but with the surface remaining as ice.

$\text{CO}_2$  and other greenhouse gas concentrations are set at preindustrial values (see Table 3.4) for the control and the no GrIS experiments. This is primarily so that a clean comparison can be made between all of the experiments described above. In terms of the no GrIS experiments it is assumed that they represent a time in

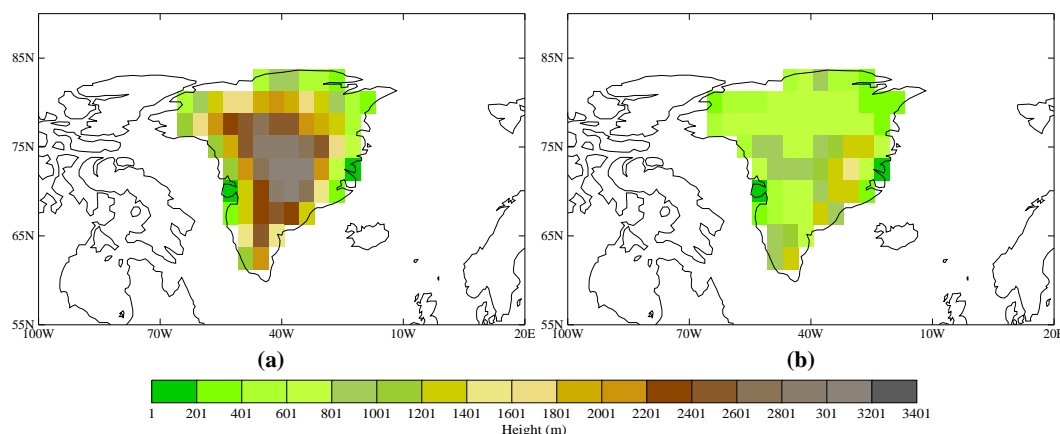


Figure 3.3: Greenland orographic height as seen by HadCM3 for (a) present day (with the ice-sheet) and (b) the rebounded orography after removal of the GrIS and isostatic readjustment.

the future when concentrations have decreased back to preindustrial values after increases in greenhouse gases resulted in complete melting of the ice-sheet.

The preindustrial control and the no GrIS experiments are initialised from a standard PMIP2 (Braconnot *et al.*, 2007) setup with orographic fields (see Section 3.2.4), soil and vegetation surface type parameters (see Section 3.2.3) modified over the Greenland region.

The Greenland orography for the preindustrial control corresponds to the combined height of the bedrock and ice thickness of Letreguilly *et al.* (1991b) (see Figure 3.3a). The fractional surface coverage is also modified as shown in Figure 3.4a to be consistent with Letreguilly *et al.* (1991b). Where there is no ice the surface is covered by bare soil. The no GrIS (henceforth referred to as noGrIS) experiments consist of six fixed fractional surface types: bare soil and the five PFTs defined in MOSES 2 (C3/C4 grasses, shrubs, broadleaf and needleleaf trees). Figure 3.4b shows that the entire Greenland land mass is covered by each surface type not just where the ice was present in the control (Figure 3.4a).

The noGrIS experiments were performed with modern day orography, noGrIS<sub>mod</sub> (Figure 3.3a), and also with a rebounded orography, noGrIS<sub>reb</sub> (Figure 3.3b), in order to estimate the effect land surface type has on the climate versus changing land

| CO <sub>2</sub> (ppm) | CH <sub>4</sub> (ppb) | N <sub>2</sub> O (ppb) | CFC11 (ppt) | CFC12 (ppt) |
|-----------------------|-----------------------|------------------------|-------------|-------------|
| 280                   | 760                   | 270                    | 0           | 0           |

Table 3.4: Concentrations of greenhouse gases for the preindustrial control used in HadCM3 MOSES 2.

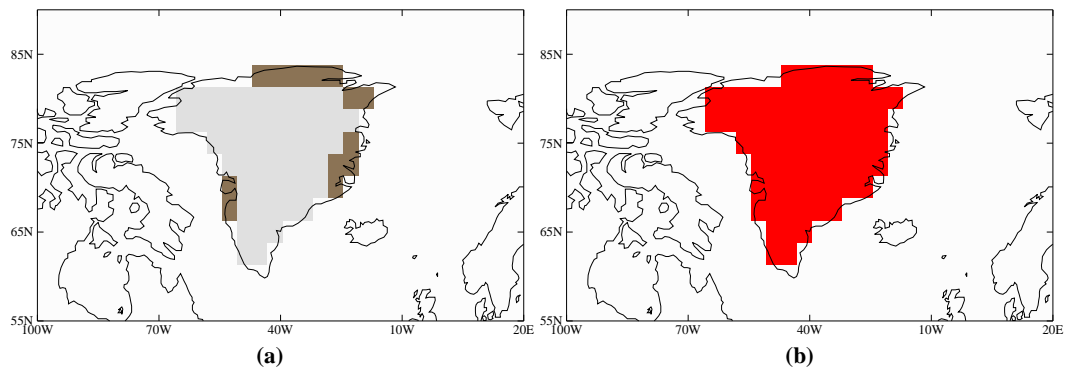


Figure 3.4: Greenland surface type as seen by HadCM3, MOSES 2 for (a) present day Greenland and (b) removal of ice from Greenland. Grey denotes the mask for ice, brown denotes the mask for bare soil and red represents the surface covered by any one of the PFTs or bare soil.

surface type and orography together. In order to produce the Greenland rebounded orography, Glimmer, initialised with the modern day ice-sheet, was forced with very high temperatures and no precipitation until all of the ice was melted. A new isostatic equilibrium without the GrIS was reached within 50,000 model years of simulation. The melting in this simulation has not been examined in detail since the main objective was to obtain a rebounded Greenland bedrock. This bedrock was then interpolated onto the HadCM3 grid in order to represent the orographic height in the GCM. Accordingly, the associated orographic parameters were calculated (see Section 3.2.4). This approach has been used by other studies (e.g Lunt *et al.*, 2004; Toniazzo *et al.*, 2004). No GCM simulations have been performed with the present day bedrock underlying the ice-sheet as a boundary condition. However, Toniazzo *et al.* (2004) performed such experiments and found no major differences between simulations when a rebounded bedrock or a present day bedrock were used.

The associated surface type parameters in Table 3.3 were also calculated for the preindustrial control and noGrIS experiments assuming that the soil properties in ice-free regions are those given for a medium type soil, which is the case for much of Siberia and Alaska at similar high latitudes. As previously discussed, in MOSES 2, a land surface gridbox cannot contain a partial covering of ice; it is either completely ice-covered or ice-free. However, the soil albedo is not so discretely defined. Around the margins of the GrIS the albedo can vary between the values for soil and ice depending on the fraction of soil ( $F_{soil}$ ) and ice ( $F_{ice}$ ) in each gridbox at a higher resolution than HadCM3. Thus a soil albedo on a  $1^\circ$  by  $1^\circ$  latitude-longitude resolution (global grid) is calculated according to the fractions of ice and

ice-free datapoints binned from the Letreguilly grid into the latitude-longitude boxes (similar to the method used to calculate the orography from a Cartesian to regular latitude-longitude grid in Section 3.2.4) according to

$$\alpha_{soil} = F_{soil}\alpha_{soil} + F_{ice}\alpha_{ice}. \quad (3.26)$$

The albedo is subsequently interpolated onto the HadCM3 land surface grid. Likewise, heat capacity was also calculated in this way. For the noGrIS experiments the soil albedo is set to the standard value of 0.17 and the heat capacity set to  $1.857 \times 10^6 \text{ J m}^{-3} \text{ K}^{-1}$ .

In addition, for the PFTs the LAI is defined for each surface according to Table 3.1 and the canopy height calculated according to Equation 3.1. Soil temperatures are left unchanged for all experiments since this is only an initial condition and will evolve as the experiments reach equilibrium. Finally, soil moisture and snow depth, also initial conditions, are modified for where there is ice or no ice. In terms of soil moisture, if ice is present this is set to zero at all soil layers since any moisture that may be present in soils underlying the ice mass will likely be frozen and therefore play no part in the hydrological cycle in MOSES 2. The snow depth is set to  $50,000 \text{ kg m}^{-2}$  where snow is present and zero in ice-free regions.

Freshwater fluxes which would arise from melting of the GrIS are not included in the simulations with HadCM3 discussed in this thesis. In reality, this freshwater input into the surrounding oceans could have implications for the MOC. However, since these simulations were only run for 100 years there would be insufficient time for the oceans to re-equilibrate fully with the modified climate. As such it is assumed that the simulations represent a time in the future after which a melted GrIS is once again in equilibrium with the oceans. This assumption is valid as various studies have indicated that although weakening of the thermohaline circulation could occur due to the melting of the ice-sheet it is likely to recover over a timescale shorter than it takes for the GrIS to fully rebound after removal of the ice (e.g Ridley *et al.*, 2005; Jungclaus, 2006). In addition, removal of the GrIS would raise sea-level by approximately 7 m. However, the land-sea mask in HadCM3 is not modified because this would make little difference to the land area at this resolution. This assumption was also made by Toniazzo *et al.* (2004) and Lunt *et al.* (2004).



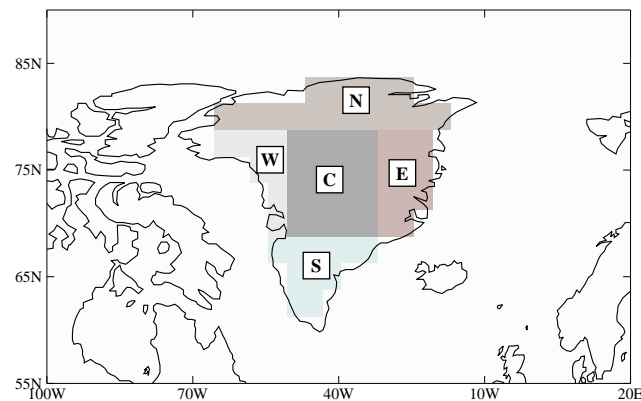


Figure 3.5: Shaded sections over Greenland define five regions: North (**N**), South (**S**), East (**E**), West (**W**) and Central (**C**).

In order to analyse certain regional aspects of the climate in detail, Greenland has been divided into five broad regions representing the North, South, East, West and Central areas (Figure 3.5). These account for the variation in orography. They are not the same as the divisions used in Toniazzo *et al.* (2004) and non-standard compared with Murphy *et al.* (2002), which were defined according to Era-40 data and HadAM3. This is because the rebounded orography is very different to the control so cannot be divided in the same way. Note also that any averages over all of Greenland combine all five regions.

### 3.3.2 Climate model evaluation

Evaluation of HadCM3 (with the land surface scheme MOSES 2) preindustrial control climate over Greenland is necessary since precipitation and temperature over this region are the forcings used to drive the ice-sheet model offline in Chapters 5 and 6. Previous work has shown that temperatures over Greenland in control runs for many AOGCMs, similar to HadCM3, perform poorly when compared with observations (Randall *et al.*, 2007). For example, Murphy *et al.* (2002) showed that winter Greenland temperatures are approximately  $5^{\circ}\text{C}$  too cold and summer temperatures are  $2$  to  $3^{\circ}\text{C}$  too warm compared with automatic weather station data at various locations over Greenland. However, they used the atmosphere only version of the Hadley Centre Model (HadAM3).

Although HadCM3 has been verified globally in terms of ocean variables, such as SSTs and ocean heat transport (Gordon *et al.*, 2000), the models' performance specifically in the Greenland region has not been published to date. The mean

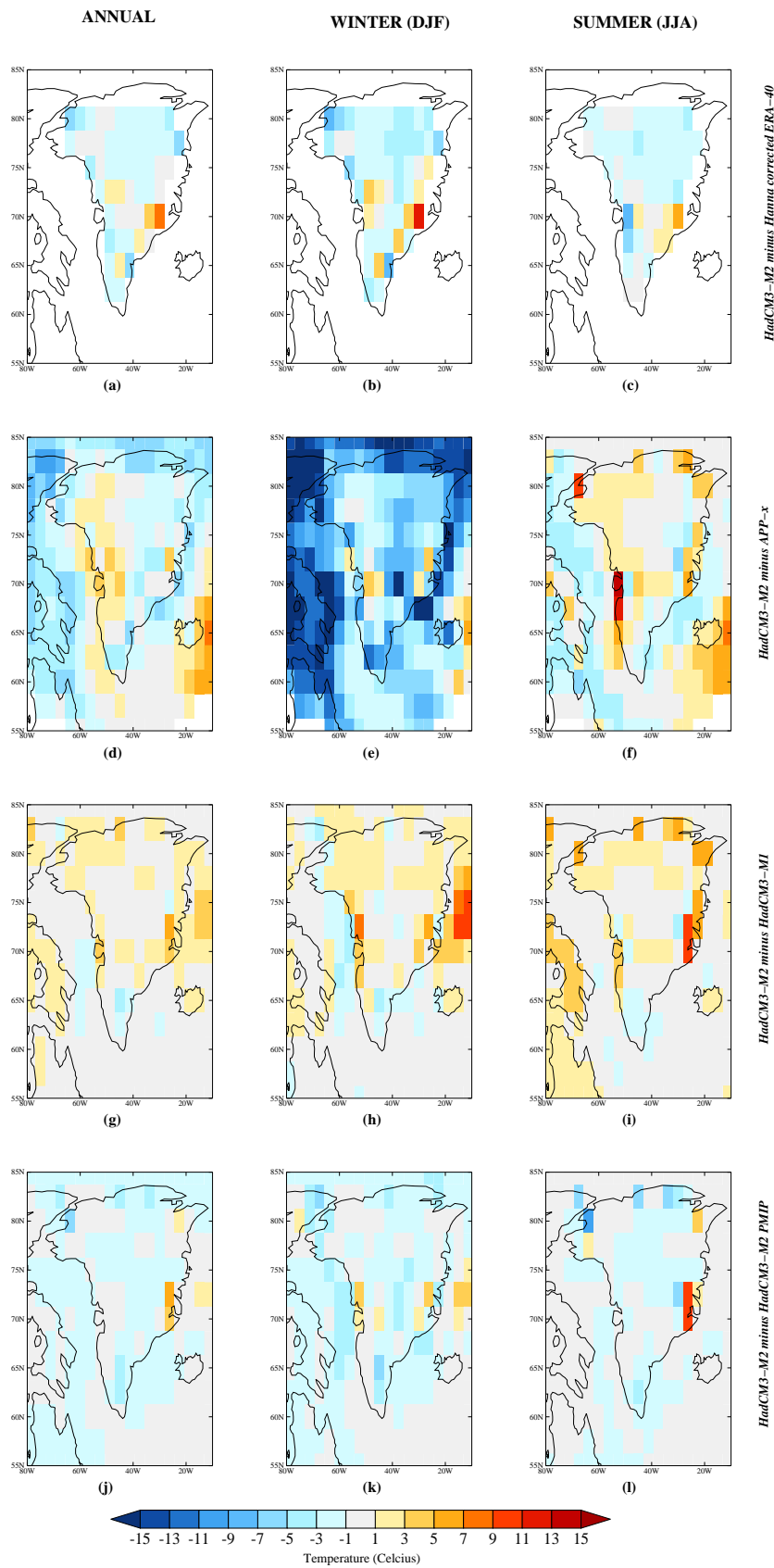


Figure 3.6: Annual, winter and summer near-surface temperature error for (a) to (c) HadCM3 control minus Hanna *et al.* (2005) temperature observation and (d) to (f) HadCM3 control minus AVHRR APP-x satellite observations. Note that (a) to (c) only show temperature bias over the GrIS.

|                    | ANN   | DJF   | JJA   | MAM   | SON   |
|--------------------|-------|-------|-------|-------|-------|
| <b><i>MD</i></b>   |       |       |       |       |       |
| Hanna et al.(2005) | -1.12 | -1.48 | -1.50 | 0.46  | -1.93 |
| AVHRR-APP-x        | -0.61 | -5.56 | 0.93  | 2.66  | -0.66 |
| HadCM3 M1          | 0.75  | 0.84  | 1.13  | 0.54  | 0.52  |
| HadCM3 M2, PMIP    | -1.11 | -1.15 | -0.78 | -1.11 | -1.38 |
| <b><i>MAE</i></b>  |       |       |       |       |       |
| Hanna et al.(2005) | 2.14  | 2.79  | 2.17  | 1.74  | 2.90  |
| AVHRR-APP-x        | 2.15  | 6.00  | 2.32  | 3.11  | 2.72  |
| HadCM3 M1          | 1.25  | 1.61  | 1.79  | 0.97  | 1.54  |
| HadCM3 M2, PMIP    | 1.57  | 1.72  | 1.72  | 1.34  | 2.07  |

Table 3.5: Mean difference (*MD*) and Mean Absolute Error (*MAE*) for near-surface temperature (in °C) for HadCM3 MOSES 2 preindustrial used in this thesis, compared with observations and other model versions of HadCM3 (HadCM3, MOSES 1 (M1) and HadCM3 MOSES 2 (M2), PMIP) discussed in the main text (DJF:winter, JJA:summer, MAM:spring, SON:autumn.)

difference (*MD*) and the mean absolute error (*MAE*) are used to compare HadCM3 MOSES 2 (M2) near-surface temperature with observational data and other versions of the Hadley Centre model. These measures are defined as

$$MD = \frac{1}{n} \sum_{i=1}^n f_i - y_i, \quad (3.27)$$

$$MAE = \frac{1}{n} \sum_{i=1}^n |f_i - y_i|, \quad (3.28)$$

where  $n$  is the number of HadCM3 gridboxes over which the temperature is averaged,  $f_i$  is the HadCM3 MOSES 2 temperature for each gridbox and  $y_i$  is the observational/HadCM3 model simulation temperature value. Table 3.5 shows the annual, winter, summer, spring and autumn 30 year average mean difference and mean absolute errors compared with corrected ERA-40 temperatures (Hanna *et al.*, 2005) and AVHRR APP-x satellite derived temperatures, both of which have been discussed in detail in Chapter 2, Section 2.4.3. Note that the Hanna temperatures are only used for comparison where there is an ice-sheet present. In addition, comparisons have also been made with other versions of HadCM3. These are a HadCM3 preindustrial control simulation but with the MOSES 1 (M1) land surface scheme and a standard HadCM3 MOSES 2 control simulation from the Paleoclimate Modeling Intercomparison Project (PMIP) (Braconnot *et al.*, 2007). In this way model

performance can be put into context with other versions of the Hadley Centre model. HadCM3 M1 has been chosen in order to ascertain any significant differences in climate model output that arise due to differences between the MOSES 1 and MOSES 2 land surface schemes. Excluding the Greenland region the HadCM3 M2 PMIP preindustrial simulation used the same model setup and boundary conditions, (i.e. prescribed vegetation cover, soil properties etc) as the HadCM3 M2 control used in this thesis. Thus any differences due to the modified Greenland orography and ice mask in the simulations presented here can be assessed.

Figure 3.6 shows the spatial distribution of temperature difference over Greenland for the annual, winter and summer 30 year means for comparison with ERA-40-corrected Hanna *et al.* (2005) GrIS temperatures (Figures 3.6a, b and c), satellite derived temperatures (Figures 3.6d, e and f), HadCM3 M1 preindustrial control temperatures (Figures 3.6g,h and i) and finally HadCM3 M2 PMIP preindustrial control temperatures (Figures 3.6j, k and l). Although mean annual temperature differences are relatively small compared with both observational datasets, there is larger variability in seasonal temperature differences, particularly during the winter months. Comparison with APP-x satellite derived temperatures results in a cold bias during the winter months of  $\sim 6^{\circ}\text{C}$  over Greenland. Differences with the Hanna Era-40 temperatures (Figure 3.6b) show a smaller winter negative bias ( $\sim 1.5^{\circ}\text{C}$ ), although this is complicated by some regions being warmer and others cooler (see Figure 3.6b). As a result, the mean absolute error ( $2.8^{\circ}\text{C}$ ) is somewhat larger than the mean difference. In eastern Greenland there is a warm bias in winter (and also summer) compared with both sets of observations. This is likely due to these regions being ice-free in the climate model (due to the resolution) while in fact they may partially be covered with ice in reality and therefore have a cooler surface temperature owing to the ice-albedo feedback. This demonstrates one limitation of the land surface scheme used here, such that there cannot be partial ice-cover in a land surface gridbox. In terms of comparison with the satellite derived temperatures part of the difference could be due to difficulties in accurately retrieving temperature as a result of the very cold, bright and reflecting surface of the ice-sheet, especially during the winter months (J. Box, Pers. Comm.)

Since ablation is most prevalent during spring and summer the temperature difference during these seasons is more important than winter when calculating

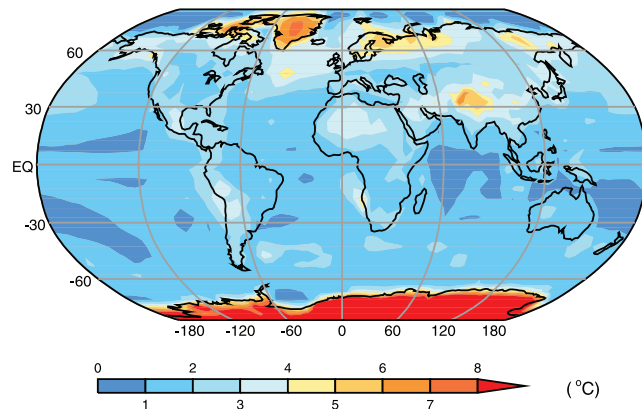


Figure 3.7: Multi-model root-mean-square error for simulated surface temperature compared with observed annual mean. This error is calculated over sea and land surface for the the multi-model dataset at the the Program for Climate Model Diagnosis and Intercomparison (PCMDI). The observational data are from The Hadley Centre Sea Ice and Sea Surface Temperature (HadISST) (Rayner *et al.*, 2003) climatology of SST for 1980 to 1999 and the Climatic Research Unit (CRU) climatology of surface air temperature over land for 1961 to 1990 (Jones *et al.*, 1999) (*from* Randall *et al.* (2007)). For results for individual AOGCMs see Randall *et al.* (2007).

surface mass balance using the PDD scheme in the ice-sheet model. Temperatures over the ice-sheet show a small, positive bias ( $0.46^{\circ}\text{C}$ ) for spring (MAM) compared with the ERA-40 Hanna temperatures. Over all of Greenland the spring and summer (JJA) average differences ranges from  $\sim 2$  to  $3^{\circ}\text{C}$  warmer compared with APP-x satellite derived temperatures. This result is similar to the summer bias observed by Murphy *et al.* (2002) although they compared summer temperatures with automatic weather station data. Comparisons with summer ERA-40 temperatures show a significant warm bias (over  $10^{\circ}\text{C}$ ) along the eastern margin of the ice-sheet (see Figure 3.6f).

For all seasons the *MAE* in temperature, when the HadCM3 preindustrial control in this thesis is compared with a HadCM3 MOSES 1 preindustrial control, is significantly smaller than the *MAE* derived from comparison with near-surface temperature observations (see Table 3.5). This is also the case for comparison with the standard HadCM3 M2 PMIP preindustrial control simulation. However, Figure 3.6 shows that for winter and summer there is a warm bias of  $0.8$  and  $1.1^{\circ}\text{C}$  respectively averaged over Greenland when compared with HadCM3 M1. While comparisons with HadCM3 M2 PMIP show a cold bias of  $-1.2$  and  $-0.8^{\circ}\text{C}$  during the winter and summer months respectively.

In order for these results to be put into context, it is also important to look at the error in temperature compared with observation for other AOGCMs over Greenland.

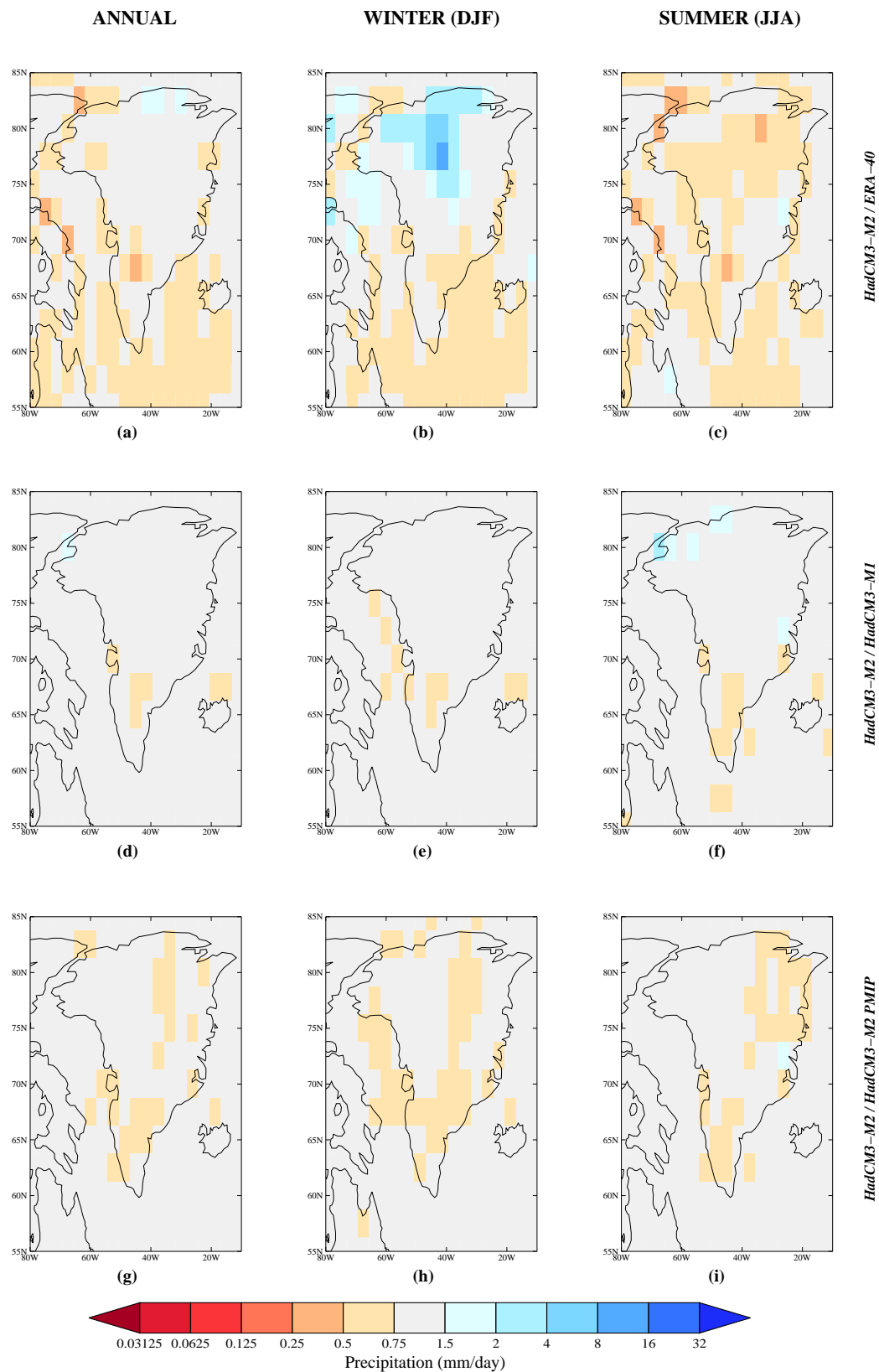


Figure 3.8: Annual, winter and summer precipitation error for (a) to (c) HadCM3 compared with ERA-40 precipitation, (d) to (f) HadCM3 M1 and HadCM3 M2 PMIP (g) to (i). Errors are expressed as a ratio of HadCM3 M2:obs/model version. Blue corresponds to the model being wetter than observation/model version and red, drier than observation/model version.

Figure 3.7 shows the root mean square error in annual temperature for a multi-model dataset compared with SSTs and land air temperature observations from HadISST and the Climate Research Unit (CRU) respectively. The Coupled Model Intercomparison Project (CMIP) (Meehl *et al.*, 2007) multi-model dataset (archived at the Program for Climate Model Diagnosis and Intercomparison) comprises 23 AOGCMs. Outside of the polar regions the root mean square error is less than 2°C. However, the root mean square error over Greenland is up to 8°C, which is significantly worse measure than the *MAE* for HadCM3 MOSES 2 shown in this thesis. It is, however, important to note that one of the caveats for comparing model simulations with observation at high latitudes is the scarcity of data.

Murphy *et al.* (2002) also showed HadAM3 compared well with ERA-40 total precipitation data. Annual winter and summer precipitation from HadCM3 M2 has been compared with ERA-40 precipitation (see Chapter 2 and Section 2.4.2 for more details of this dataset) and is shown in terms of ratios in Figures 3.8a, b and c. In addition, comparisons with HadCM3 M1 (Figures 3.8d, e and f) and HadCM3 M2 PMIP (Figures 3.8g, h and i) are also shown. Comparison with ERA-40 precipitation shows very good agreement for annual precipitation. However, during the winter HadCM3 is on average two to four times as wet compared with observation in the north of the island, while during summer months the model is twice as dry for much of northern, central Greenland. However, Hanna *et al.* (2006) show that ERA-40 is  $\sim 50\%$  too dry in the central northern parts of Greenland, when validated using ice core data. Consequently, the apparent wet bias of the model may in reality be less. Comparison with HadCM3 MOSES 1 shows generally very good agreement. There is no significant wet bias during either winter or summer with only an isolated region in the summer where precipitation is up to two times as dry in HadCM3 M2. Similarly, comparison with HadCM3 M2 PMIP shows better agreement than with ERA-40 precipitation although the regions of dryness are more extensive compared with HadCM3 M1.

In summary HadCM3 MOSES 2 is an adequate model to use for studies over Greenland since any biases are similar or even smaller to other AOGCMs. In order to reduce model bias and its effect on ice-sheet model results the anomaly coupling method will be used for both precipitation and temperature in later chapters.

| Surface type     | ANN  | DJF  | JJA   | MAM   | SON  |
|------------------|------|------|-------|-------|------|
| Bare soil        | 0.36 | 0.12 | 1.23  | -0.12 | 0.29 |
| C3 grasses       | 3.48 | 0.27 | 7.54  | 3.19  | 2.89 |
| C4 grasses       | 4.14 | 0.13 | 9.23  | 3.36  | 3.79 |
| Shrub            | 4.93 | 0.75 | 9.38  | 5.47  | 4.09 |
| Broadleaf trees  | 6.92 | 1.17 | 12.20 | 8.52  | 5.78 |
| Needleleaf trees | 6.41 | 0.99 | 11.06 | 8.43  | 5.16 |

Table 3.6: Near-surface average temperature anomaly over Greenland for noGrIS<sub>mod</sub> simulations minus preindustrial control.

### 3.3.3 Climatic sensitivity to surface characteristics over an ice-free Greenland

In order to understand how vegetation type effects the Greenland climate when the ice-sheet is removed and CO<sub>2</sub> concentrations are held at 280 ppmv it is necessary to isolate some of the potential feedback processes that take place. The primary changes by varying surface type are to alter the snow-free and snow-covered albedos and the roughness length. The LAI and canopy height are also altered for the PFTs. In this section all simulations have modern day orography as shown in Figure 3.3a. Any changes that occur in the climate system will therefore *not* be due to a change in altitude over Greenland.

#### Local changes in surface temperature and surface heat fluxes

Figure 3.9 shows the temperature anomaly when the GrIS is replaced with the five PFTs and bare soil. During winter temperature anomalies over Greenland are close to zero for bare soil (Figure 3.9a) and up to 10°C in central regions for the PFTs. Table 3.6 shows the annual and seasonal temperature anomalies relative to the control over the Greenland land surface defined by Figure 3.4b. The range in average winter temperature anomaly is relatively small and varies from 0.1 (bare soil) to 1.2°C (broadleaf trees). These small values can be explained by the insolation forcing received over Greenland during the winter months. The daily mean insolation received at the surface is close to zero (only about 0.2 W m<sup>-2</sup> during winter) and therefore any temperature change that is related to albedo change and the intensity of the insolation in the simulations will be small. However, bare soil still has a temperature change more than 1°C cooler than broadleaf tree. During summer a similar



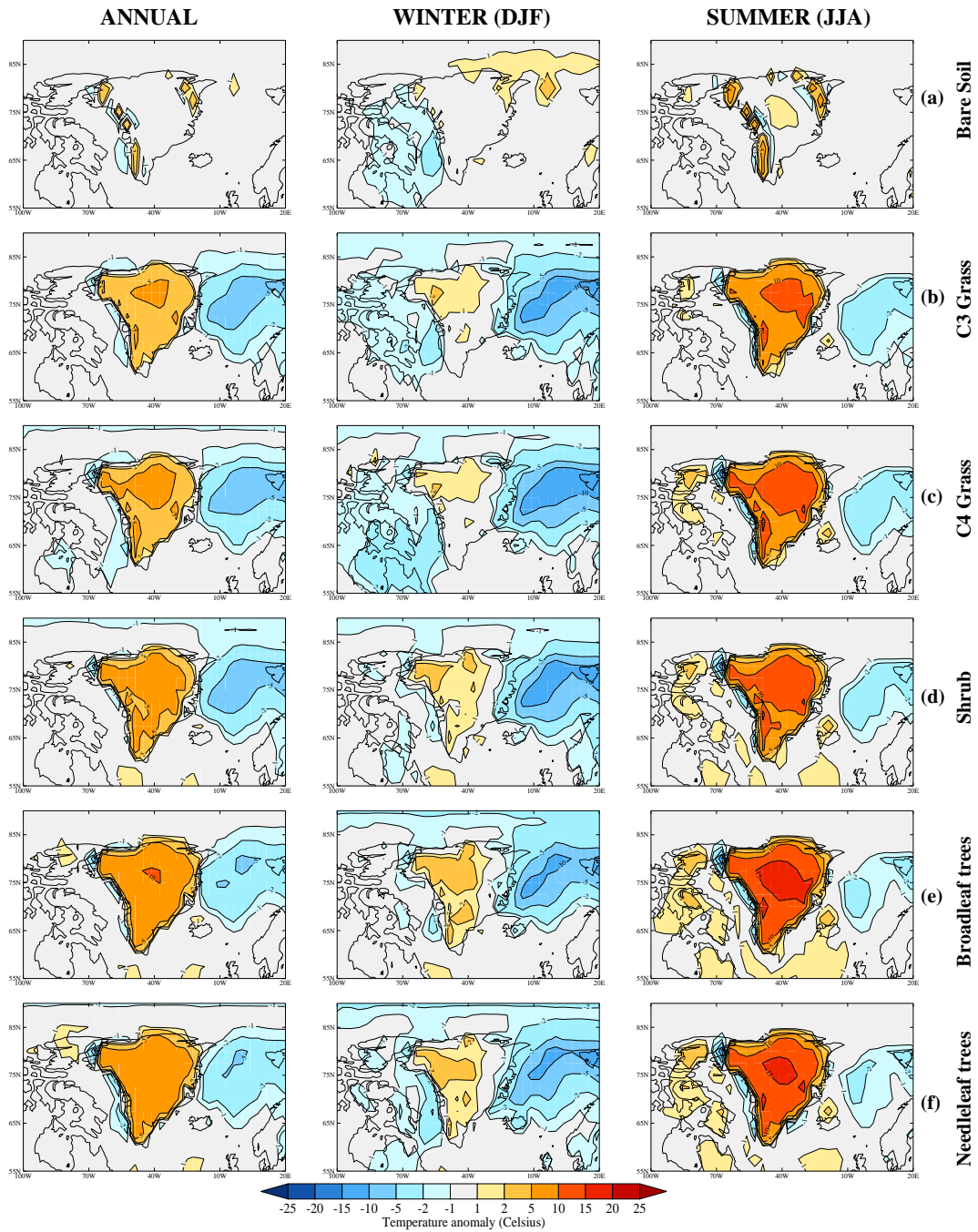


Figure 3.9: Near-surface temperature anomalies (in °C) for noGrIS<sub>mod</sub> simulations minus preindustrial control. Plots show annual, winter and summer anomalies averaged over the last 30 years of the simulations.

| Surface type     | Average surface albedo (0-1) |        |
|------------------|------------------------------|--------|
|                  | Winter                       | Summer |
| Ice              | 0.80                         | 0.74   |
| Bare soil        | 0.80                         | 0.65   |
| C3 grasses       | 0.64                         | 0.32   |
| C4 grasses       | 0.62                         | 0.29   |
| Shrubs           | 0.49                         | 0.23   |
| Broadleaf trees  | 0.15                         | 0.10   |
| Needleleaf trees | 0.16                         | 0.12   |

Table 3.7: Average Greenland surface albedo when Greenland is replaced with bare soil and each of the PFTs and orography is modern. Winter and summer values are shown.

pattern is shown with the least change in temperature for bare soil ( $1.2^{\circ}\text{C}$ ) and the largest for the needleleaf and broadleaf trees ( $11.1^{\circ}\text{C}$  and  $12.2^{\circ}\text{C}$  respectively). The mean July temperature in central Greenland is as high as  $6^{\circ}\text{C}$  and  $8^{\circ}\text{C}$  for needleleaf and broadleaf trees respectively. However, a bare soil surface has temperatures as low as  $-10^{\circ}\text{C}$  for the same month and region.

During winter almost all precipitation falls as snow resulting in surface characteristics for bare soil very similar to that of the control and therefore a temperature anomaly of almost zero. Broadleaf and needleleaf trees result in a surface with lower albedo as a result of the trees masking the high reflectivity of the snow surface and therefore any insolation that is received is more readily absorbed resulting in a small increase in temperature compared with the bare soil case. This is clearly observed in Table 3.7 and Figure 3.10 which show the surface albedo over Greenland for winter and summer. Broadleaf and needleleaf trees have low albedo values between 0.1 and 0.2 during both seasons while bare soil has an albedo values over Greenland very similar to the preindustrial control (i.e. has similar characteristics to an ice-sheet being present). Even during the summer the surface albedo for noGrIS<sub>mod</sub> with bare soil remains high. The combination of a snow-covered albedo of 0.8 for a bare soil surface in conjunction with a high altitude over much of Greenland, results in a melt season which is less vigorous due to a weaker snow-vegetation-climate feedback compared with the other PFTs, and as such most of the surface remains snow-covered throughout the season with a sustained highly reflective surface (see Figure 3.14). Grasses and shrubs have intermediate values of albedo between bare soil and trees and also show the largest differences in albedo between seasons (as high as 0.7 in winter and as low as 0.3 during summer).

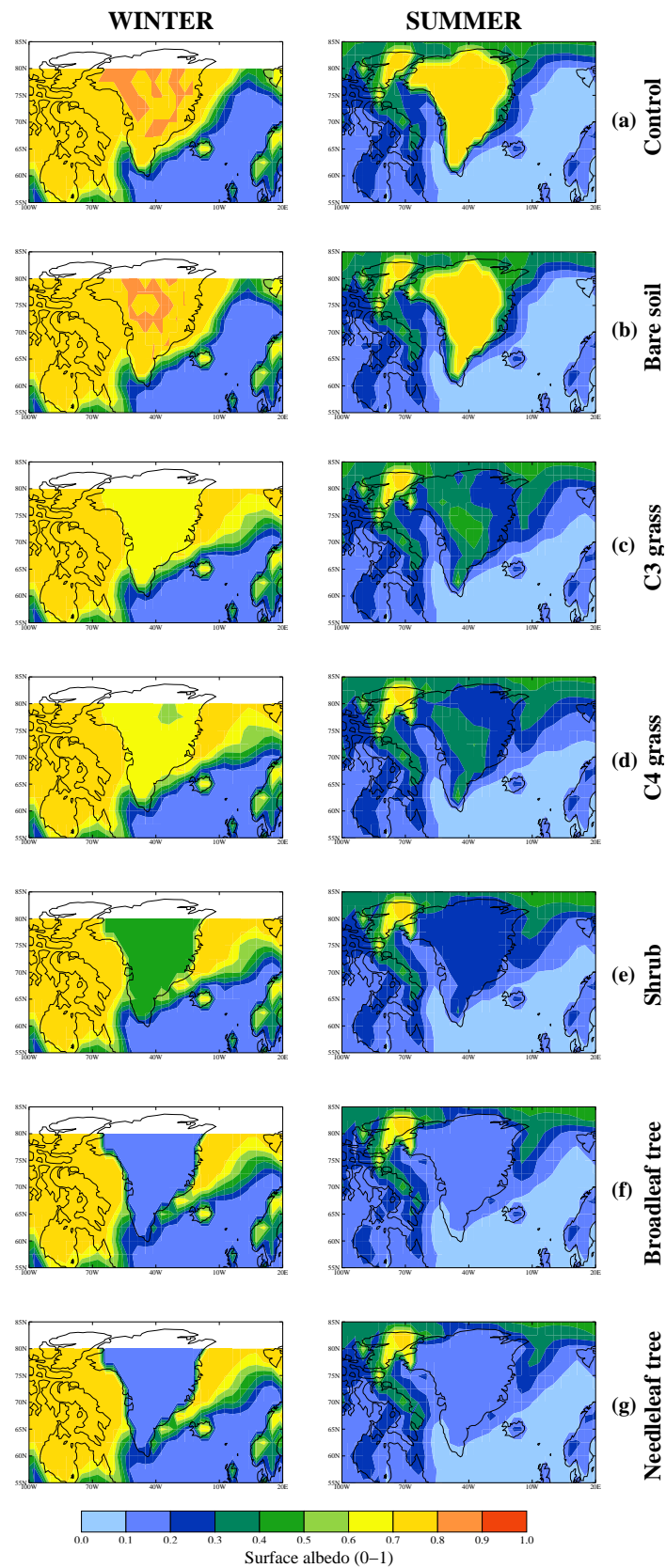


Figure 3.10: Average surface albedo over Greenland during winter and summer months for the preindustrial control, and noGrIS<sub>mod</sub> simulations.

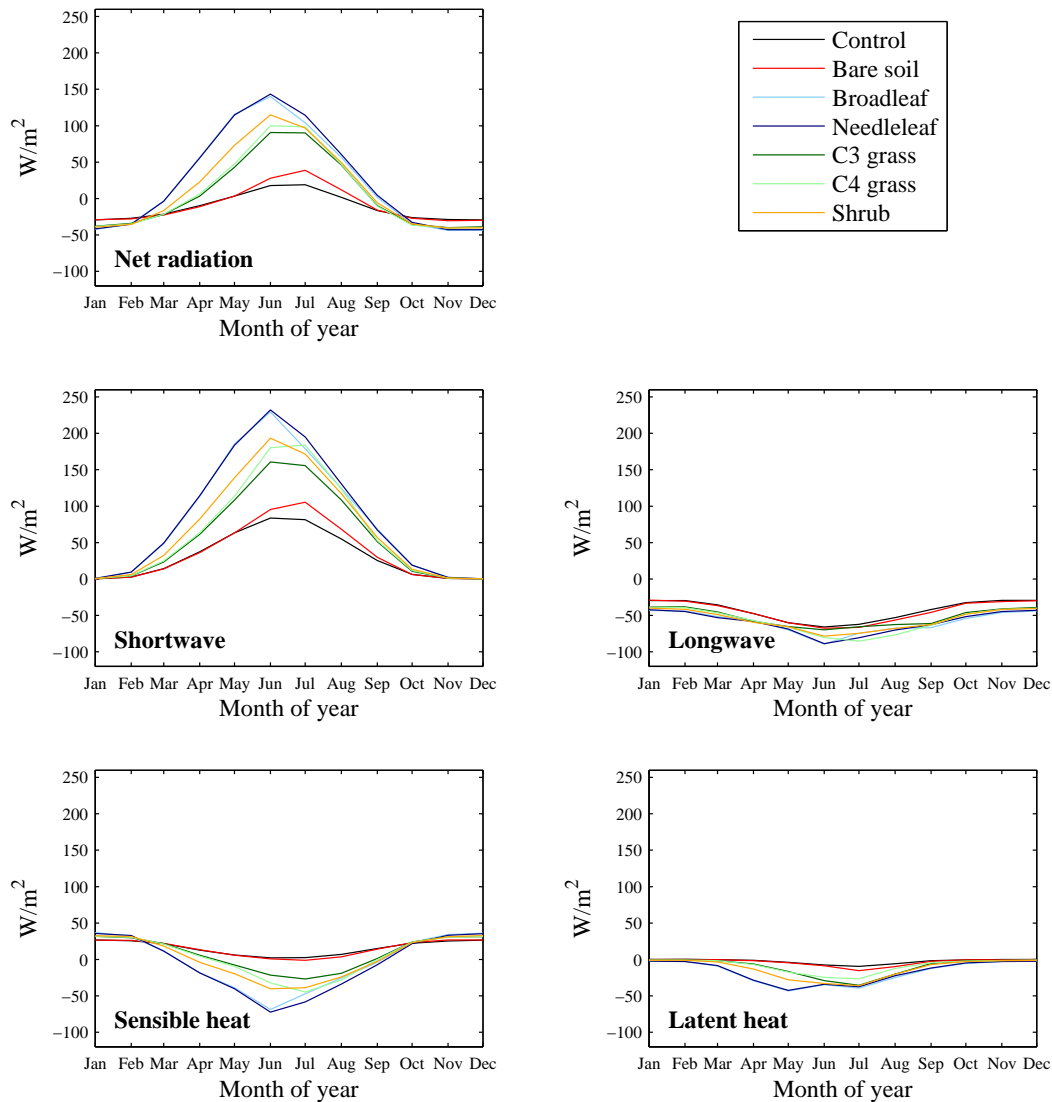


Figure 3.11: Annual cycle of heat fluxes averaged over all of Greenland for the control and noGrIS<sub>mod</sub> simulations. All fluxes are positive downwards toward the surface. Note that net radiation is the sum of net shortwave and net longwave radiation.

Figure 3.11 shows the average monthly variation in surface heat fluxes over all of Greenland. Note all surface heat fluxes are positive downwards. In order for comparison a brief summary is given for the annual heat fluxes of the control. In terms of net downward shortwave heat flux there is an increase in heat absorbed at the surface from  $0.2 \text{ W m}^{-2}$  in January to  $84 \text{ W m}^{-2}$  in June followed by a steady decrease toward near-zero values again in December. This compares well with  $80 \text{ W m}^{-2}$  in June observed in the control produced by Toniazzi *et al.* (2004) who did a similar analysis as the control case here. Longwave heat losses from the surface increase from  $29 \text{ W m}^{-2}$  in the winter to  $65 \text{ W m}^{-2}$  in the summer. This again

compares very well with Toniazzo *et al.* (2004). Throughout the year sensible heat fluxes remain positive decreasing toward the summer months from  $26 \text{ W m}^{-2}$  in January to around  $2 \text{ W m}^{-2}$  in June. Latent heat fluxes are very small but slightly positive during the winter and become negative as summer approaches reaching a maximum of  $9 \text{ W m}^{-2}$ . The trend observed in sensible heat is similar to Toniazzo *et al.* (2004). However, their latent heat flux remains small and negative throughout the year but close to  $10 \text{ W m}^{-2}$ .

First note that the noGrIS<sub>mod</sub> simulation with bare soil is very similar to the control for all surface heat fluxes. The largest deviation is observed in the summer months by about  $25 \text{ W m}^{-2}$  for the net downward shortwave flux. This is when the albedo of the surface is most reduced compared with the control increasing the amount of shortwave heat flux absorbed at the surface. During the winter months the noGrIS<sub>mod</sub> experiments are very similar to the control for the turbulent and net downward shortwave fluxes. However, the net longwave fluxes are marginally larger compared with the control.

During the summer months the most obvious difference in surface heat fluxes between the PFT noGrIS<sub>mod</sub> simulations and the control is a marked increase in net downward shortwave flux. This begins in early spring as any snow present begins to thaw exposing more of the lower albedo surface of the vegetation compared with the control. This in turn sets up a positive feedback loop between melting of the surface, albedo and the absorption of net shortwave flux at the surface. This increase in net downward shortwave flux is partly offset not only by the increase in emission of longwave flux from the surface but also by an increase in the turbulent fluxes of sensible and latent heat from the surface. The tree vegetation types have the largest sensible heat flux away from the surface out of all the PFTs. This also applies for latent heat flux although not to as large an extent. The timing of peak latent heat flux is also earlier for the needleleaf trees while the other surface types see a peak during July after sufficient moisture buildup during the spring.

The impact of LAI differences can be seen by comparing the results from a surface covered by C3 and C4 grasses since they have the same snow-free and snow-covered albedo parameterisations (see Table 3.2). The summer temperature difference between the C3 and C4 grasses of  $1.2^\circ\text{C}$  can be explained by the difference in snow-free albedo for these PFTs. Within MOSES 2 the snow-covered and snow-free albedos

are dependent on a weighting factor for albedo which in turn is dependent on the LAI of the PFT (see Equation 3.4). The LAI for C3 and C4 grasses are 3.0 and 4.0 respectively and therefore according to Equation 3.4 the corresponding snow-free albedos are 0.33 and 0.28. This is the equivalent to a 15 % change in albedo relative to C4 grasses. In summer the peak net shortwave heat flux for C3 grasses is  $161 \text{ W m}^{-2}$  and  $184 \text{ W m}^{-2}$  for C4 grasses; approximately 15 % greater.

### Snow amount and snow cover

Snow amount from the climate model has been used as a diagnostic for ice-sheet regrowth by previous studies in the absence of an ice-sheet model (Crowley and Baum, 1995; Toniazzo *et al.*, 2004). Figure 3.12 shows the timeseries of annual average snow cover (mm water equivalent or  $\text{kg m}^{-2}$ ) for the duration of the noGrIS<sub>mod</sub> simulations in the five regions over Greenland defined by Figure 3.5; note the logarithmic scale. If there is net accumulation, snow cover increases year-on-year. The amount of snow that has built up within the duration of the experiment corresponds to the snow amount after 100 years. An absence of any trend indicates no build-up of snow during the length of the experiments. For all regions except the north, the noGrIS<sub>mod</sub> bare soil simulation clearly shows an increase in snow amount with time suggesting the potential for a build up of ice. However, all other noGrIS simulations show a similar pattern of no clear trend in snow amount increase year on year for all Greenland regions. The largest accumulations occur for the southern region and the least in the northern region. This is mainly a reflection of local conditions where the accumulation is larger with increasing altitude and precipitation.

Figure 3.13 shows the snow cover in February and Figure 3.14 in August, averaged over the last 30 years of the simulations. There is a large variation in snow cover seasonally for the simulations replaced with vegetation but not for bare soil. The pattern observed for bare soil is similar in winter and summer which is corroborated by the persistent high albedo and cold surface temperatures throughout the year. However, the snow cover during August is significantly less with no more than 10 mm (water equivalent) of accumulation over the vast majority of Greenland. This compares with 700 mm during February. The absence of long-term accumulation for the PFT noGrIS<sub>mod</sub> experiments indicates that in some years the summer months could show complete melting of the snow in several GCM gridboxes. The

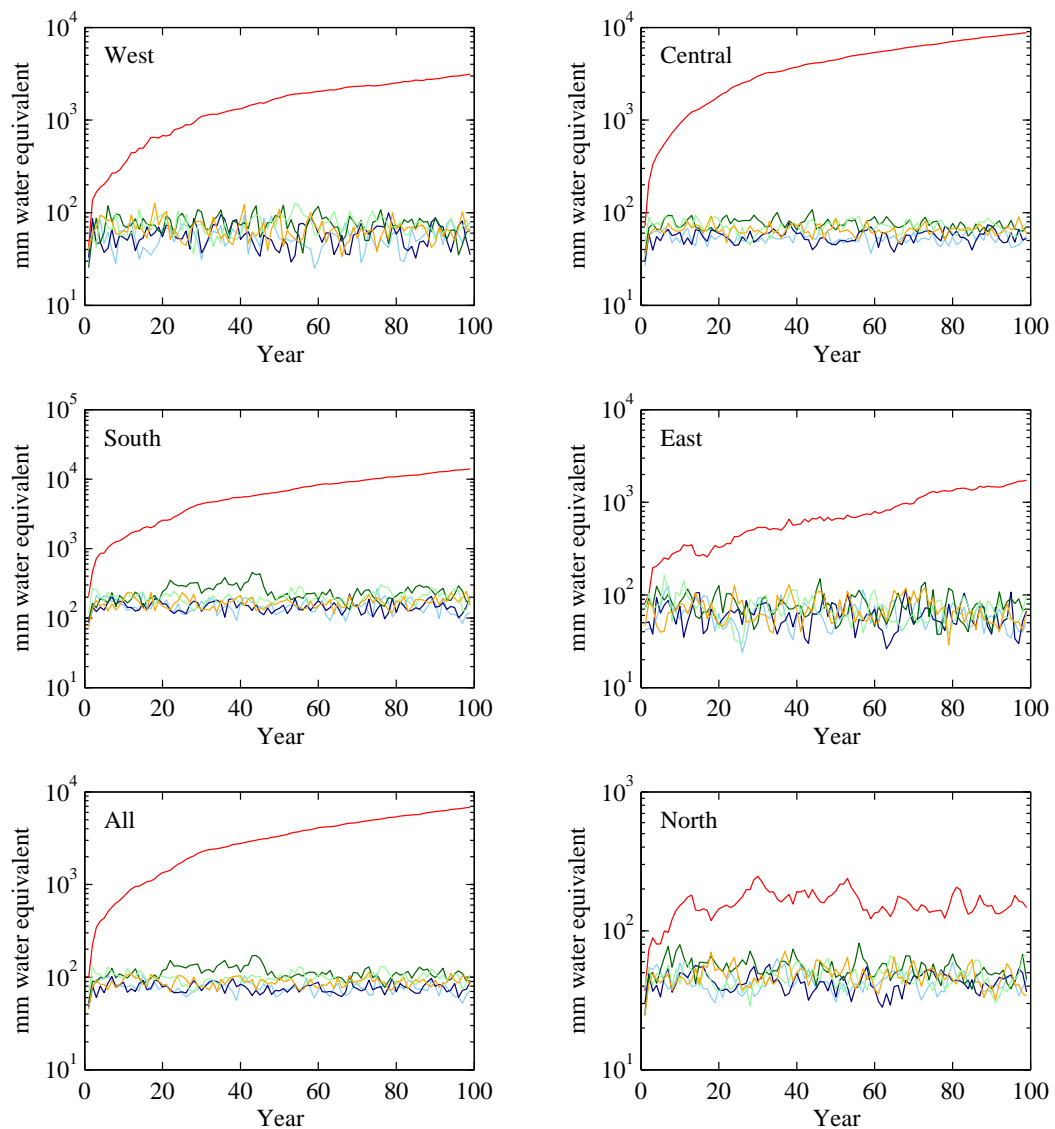


Figure 3.12: NoGrIS<sub>mod</sub> simulation cumulative mass balance (in  $\text{kg m}^{-2}$ ) for North, South, East, West and Central Greenland. Cumulative mass balance is also shown for all of Greenland. Time series spans the length of the simulations. All PFTs and bare soil are shown by the following: **bare soil**, **broadleaf trees**, **needleleaf trees**, **C3 grass**, **C4 grass**, **shrub**. The values plotted are annual averages of the snow cover, which rises year-on-year if there is net accumulation. Note difference in scale for each plot.

implication of this result suggests that changing surface type alone affects whether removal of the GrIS due to prolonged climatic warming would be reversible. Based on only this diagnostic, a surface covered by bare soil indicates that reversibility is possible while a surface covered by any of the PFT implies removal of the ice-sheet would be likely irreversible, even with modern day altitude.

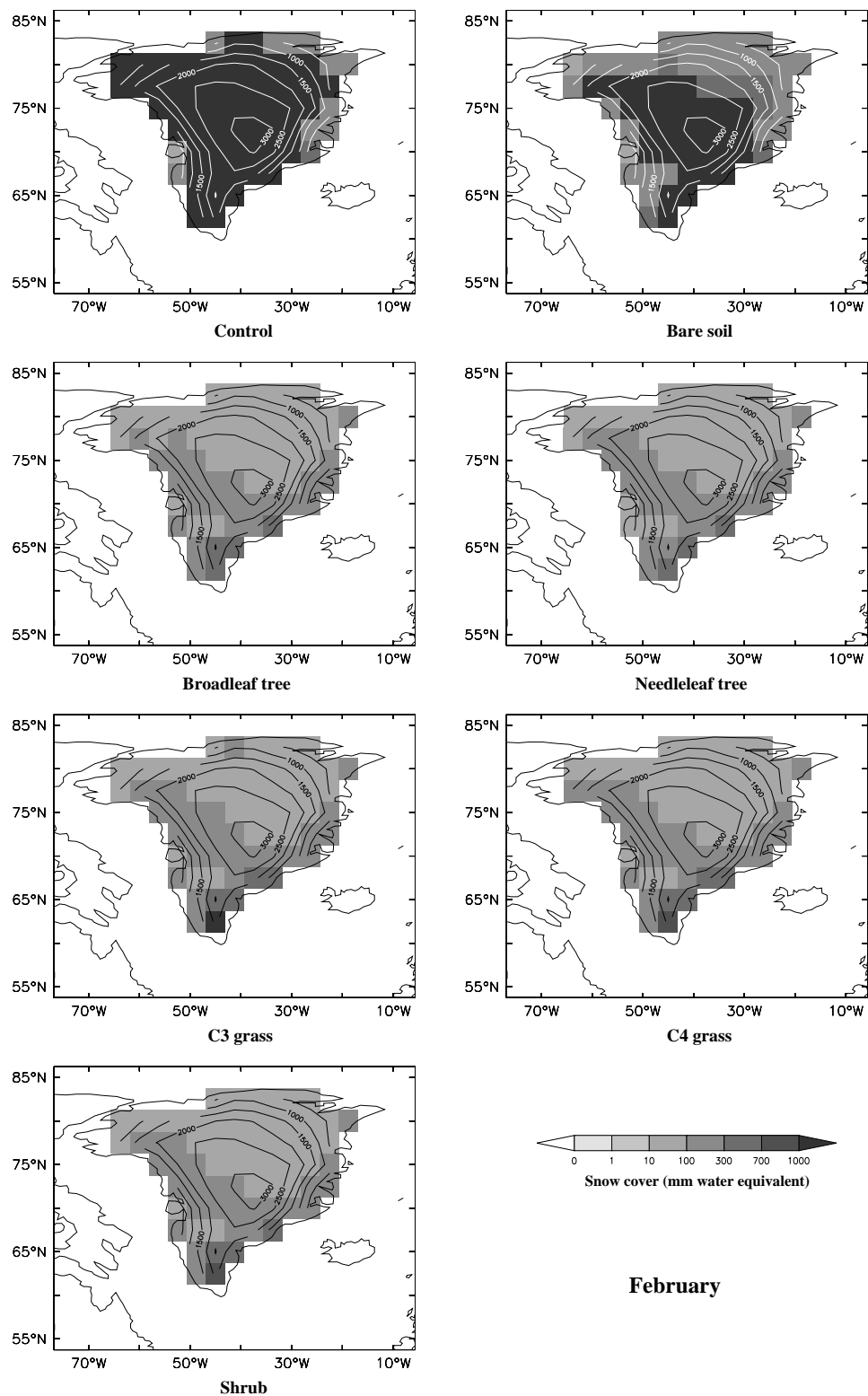


Figure 3.13: Average February snow cover over Greenland for the control and noGrIS<sub>mod</sub> simulations. Overplotted are levels of constant orographic height in metres at intervals of 500 m. The scale is based on Toniazzo *et al.* (2004) for direct comparison in later sections.



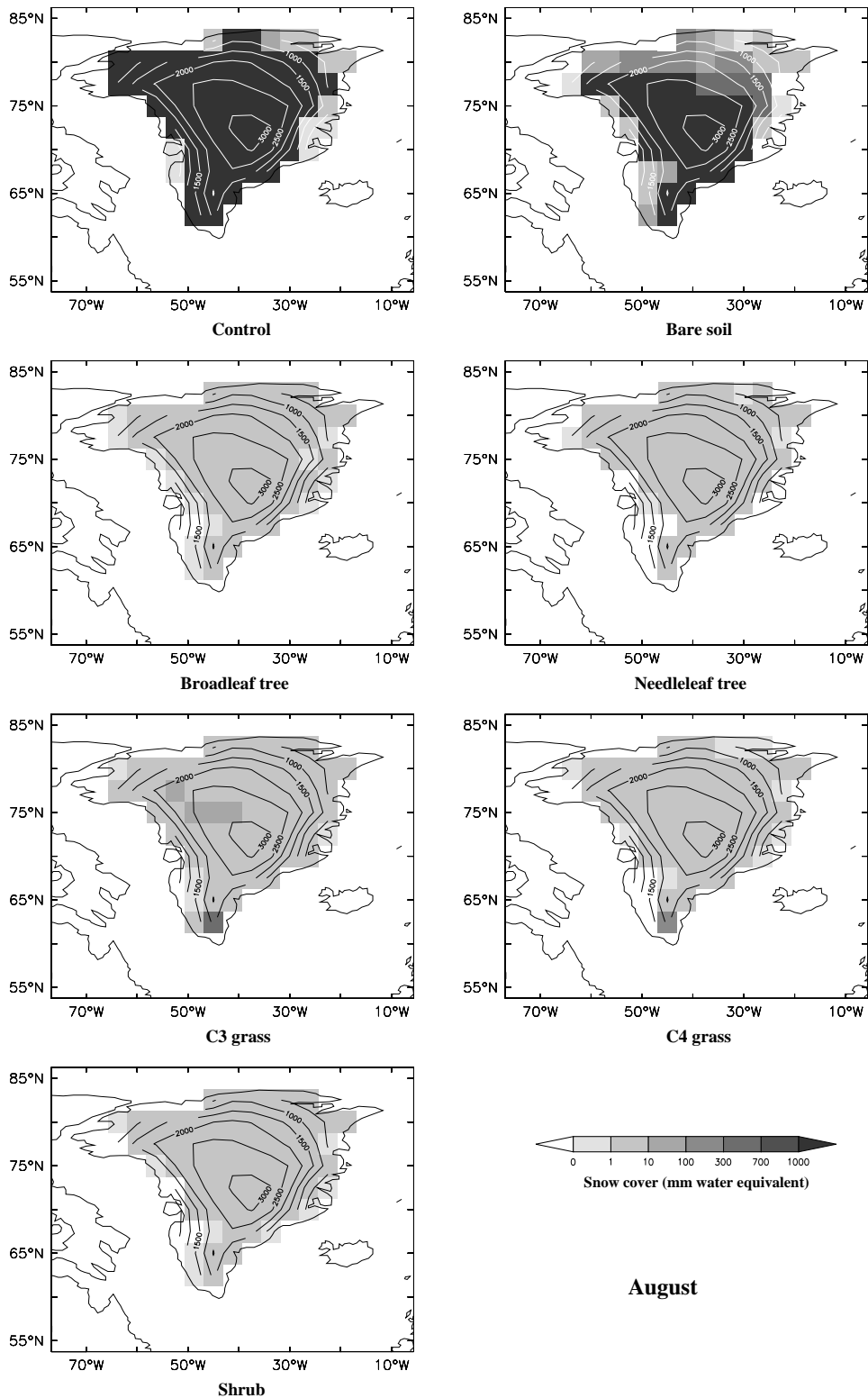


Figure 3.14: Average August snow cover over Greenland for the control and noGrIS<sub>mod</sub> simulations. Overplotted are levels of constant orographic height in metres at intervals of 500 m. The scale is based on Toniazzo *et al.* (2004) for direct comparison in later sections.

### Atmospheric circulation over Greenland

The impact of Greenland's orography on atmospheric circulation patterns has been investigated by several studies in terms of cyclone generation in the immediate vicinity of the island and changes to atmospheric circulation in areas further down stream from Greenland (e.g. Petersen *et al.*, 2004; Junge *et al.*, 2005; Kristjánsson *et al.*, 2009). This is also addressed using HadCM3 MOSES 2 in Section 3.3.4. The impact of simply changing the surface type over Greenland on the atmospheric circulation has not been examined in previous work.

During the winter months in the control there is a cold, strong anticyclone centred over Greenland (Figure 3.15a). There is a climatological minimum in the sea-level pressure to the south of Greenland, which is often referred to as the the Icelandic Low in the literature. This low-level wind pattern over Greenland and sea-level pressure minimum south of the island are also observed in the noGrIS<sub>mod</sub> experiments during winter (Figure 3.15b to g). Figure 3.16, left panel, shows the difference between the low-level winds for winter compared with the control. The bare soil noGrIS<sub>mod</sub> simulation shows no major difference in sea-level pressure or wind strength and direction at the 850 hPa pressure level during winter. However, for the PFT noGrIS<sub>mod</sub> simulations there is an increase in sea-level pressure of up to  $\sim 4$  hPa east of Greenland over the Barents Sea region north of Scandinavia, compared with the control. This is strongest for the grasses and shrubs. This increase coincides with an increase in sea-ice (see Section 3.3.3).

The low-level wind patterns and surface sea-level pressure observed in summer for the control and noGrIS<sub>mod</sub> experiments are shown in the right panel of Figure 3.15. The Icelandic Low in the control simulation (Figure 3.15a) has weakened and moved to the south of Iceland away from the southern tip of Greenland consistent with observations (Serreze *et al.*, 1997). There is also a weakening and shift of the the sea-level pressure minimum off the south coast of Greenland in all the noGrIS<sub>mod</sub> simulations (Figures 3.15b to g). In addition, the difference between the noGrIS<sub>mod</sub> and the control for these variables during the summer is shown in the right panel of Figure 3.16. For the case of bare soil (Figure 3.16a), similar to during the winter, there is marginal difference in sea-level pressure and low-level winds (which are also anticyclonic) compared with the control. However, the PFT noGrIS<sub>mod</sub> show low-

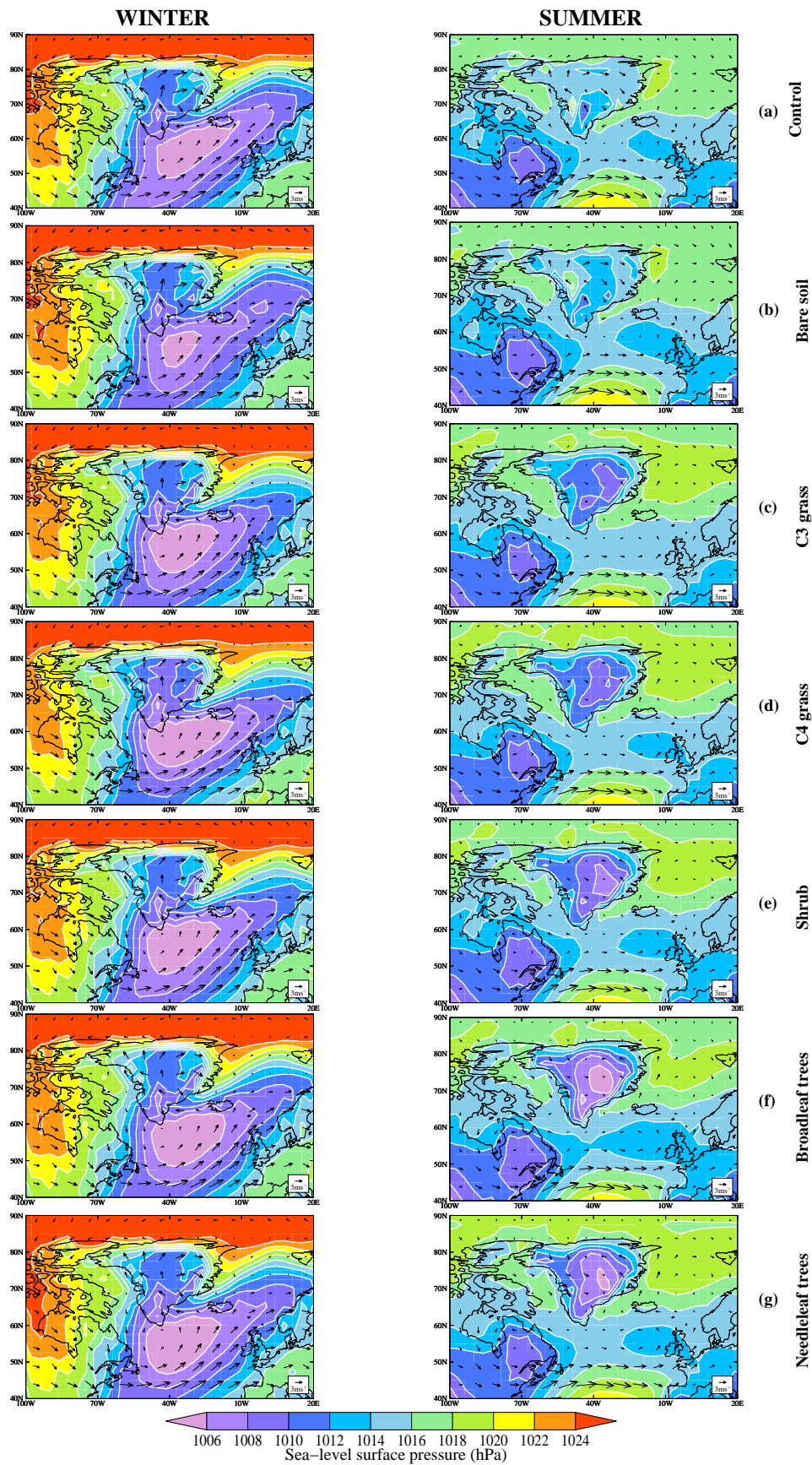


Figure 3.15: Wind speed and direction on pressure level 3 in HadCM3 (equivalent to 850 hPa over a surface at sea-level) for winter and summer months for the control and noGrIS<sub>mod</sub> simulations. Also shown by the filled contours is the surface sea-level pressure in hPa.

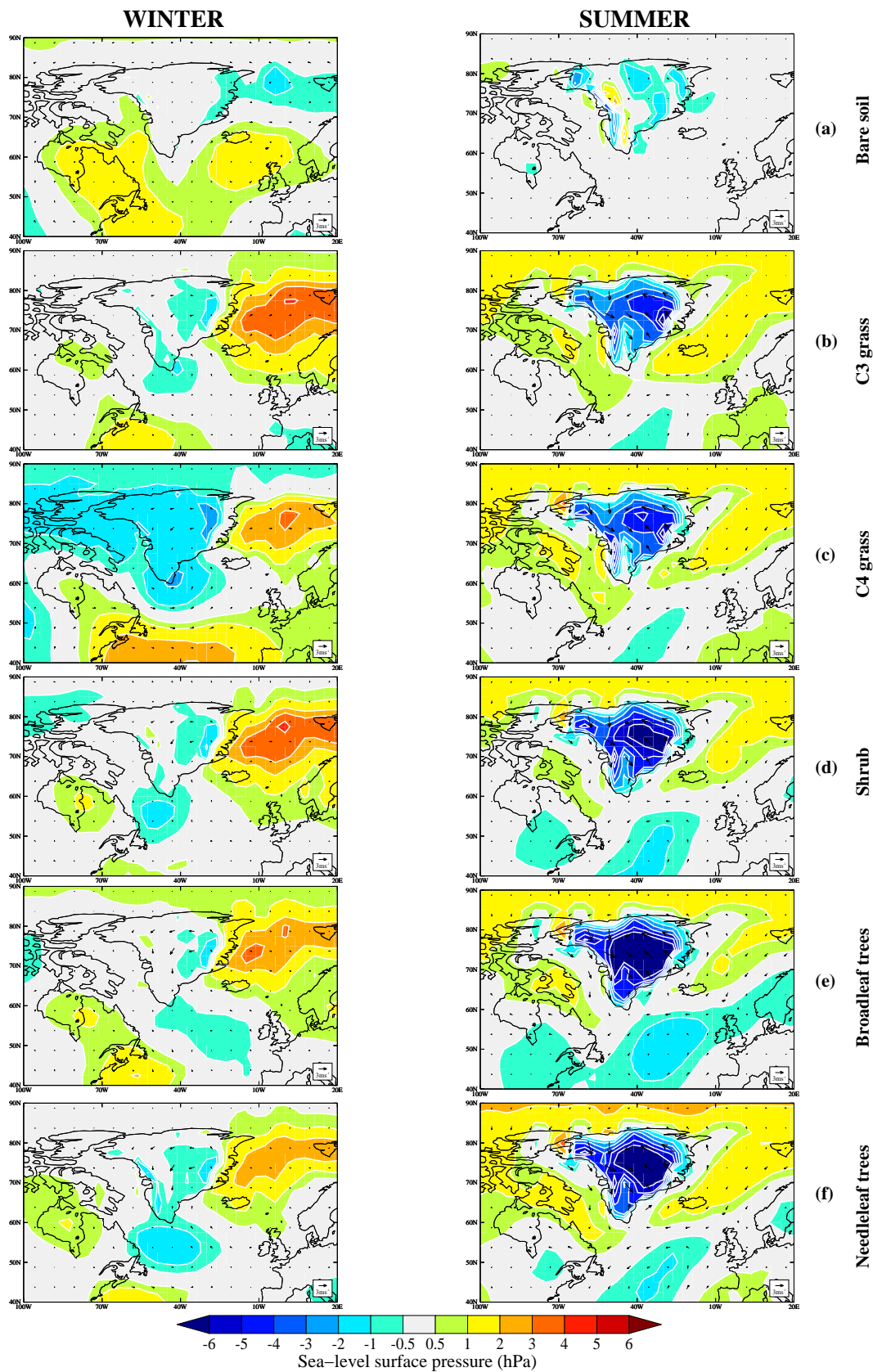


Figure 3.16: Difference in wind speed and direction on pressure level 3 in HadCM3 (equivalent to 850 hPa over a surface at sea-level) for winter and summer months between noGrIS<sub>mod</sub> experiment and the preindustrial control. Also shown by the filled contours is the difference in surface sea-level pressure in hPa.

level atmospheric cyclonic circulation over Greenland as opposed to the anticyclonic circulation for the control and bare soil noGrIS<sub>mod</sub>. This change in the wind pattern for the PFTs is also reflected in the reduction in the surface pressure over Greenland by more than 6 hPa. The cyclonic behaviour results from the increase in latent heat flux to the atmosphere (compared with the control), shown in Figure 3.11 over Greenland, for the noGrIS<sub>mod</sub> PFT experiments, which reduces the static stability in the atmosphere leading to the development of a lower pressure system centred over Greenland with cyclonic rotation of the low-level winds.

### **Precipitation, sea-ice and oceanic changes**

The precipitation (snowfall and rainfall) anomaly (relative to the control) for annual, winter and summer is shown in Figure 3.17 for the noGrIS<sub>mod</sub> simulations. A surface replaced with bare soil results in almost no change in precipitation throughout the year. During the winter all noGrIS<sub>mod</sub> precipitation anomalies over Greenland are no greater than 0.9 mm day<sup>-1</sup>, seen in the southern tip of Greenland for the grasses. However, over the Barents Sea region the maximum precipitation anomaly ranges from 1.2 to 1.8 mm day<sup>-1</sup> drier for the PFT noGrIS<sub>mod</sub> experiments compared with the control. This feature is not observed in the noGrIS<sub>mod</sub> bare soil experiment. The summer months see a marked increase in precipitation over central Greenland compared with the control for the PFT noGrIS<sub>mod</sub> simulations in association with the development of the low-level pressure system discussed in the previous section. The two tree types show the largest increase in wetness with more than 2 mm day<sup>-1</sup> falling within some regions of the interior of Greenland. Much of this precipitation falls as snow due to the high elevations. However, the summer months also see a significant amount of run-off and evaporation due to the build up of moisture in the canopy and in the soil surface top layer. Shrubs result in up to 1.5 mm day<sup>-1</sup> of snowfall precipitation in summer with grasses showing much smaller but positive amounts. Typically there is a decrease in snowfall in other regions over Greenland relative to winter (excluding the north) with an associated increase in rainfall as temperatures increase. The largest run-off is observed in the south for all simulations with an associated increase in the net snow loss.

The total cloud cover over Greenland varies between the noGrIS<sub>mod</sub> simulations (not shown). During winter there is no significant difference in cloud cover compared

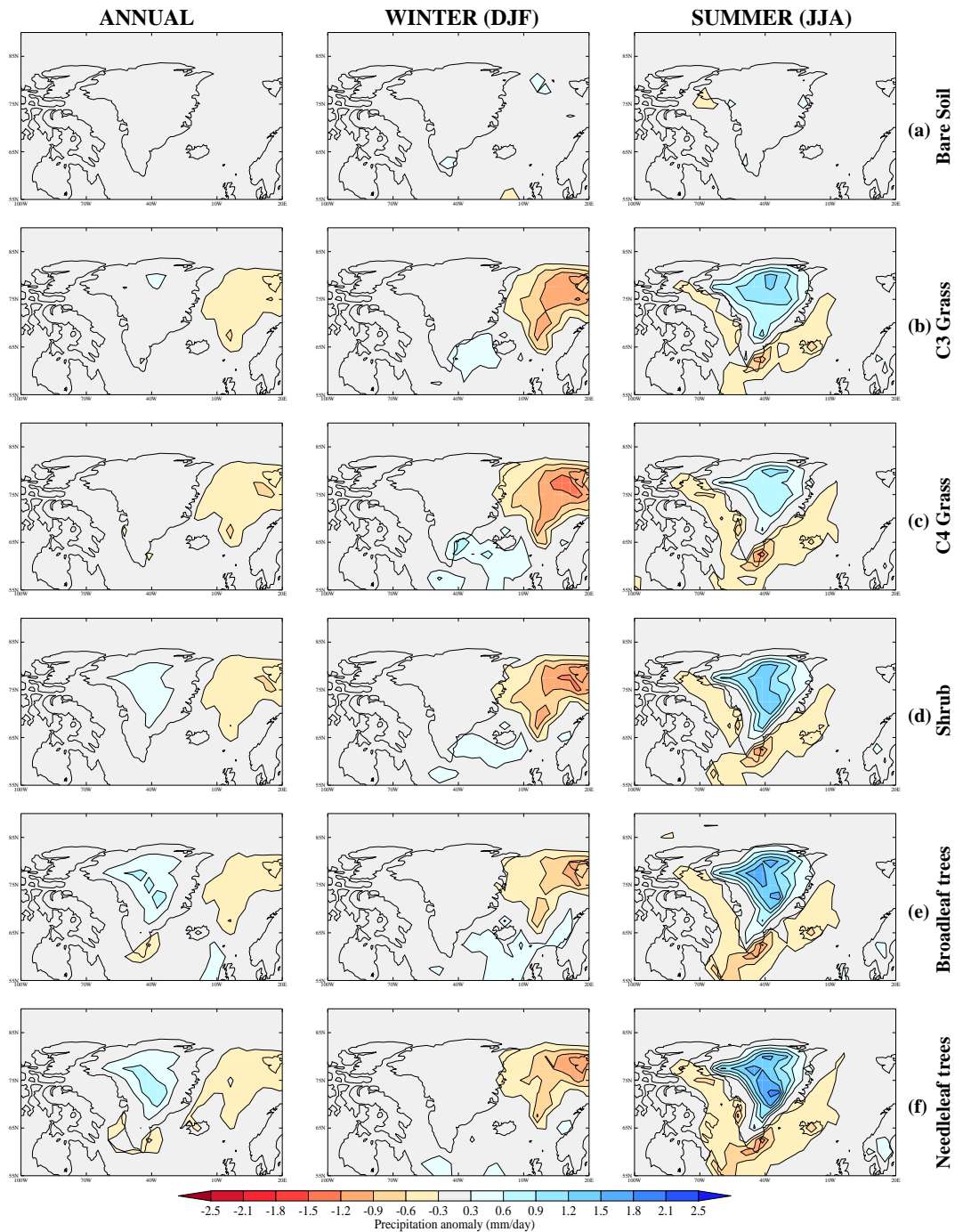


Figure 3.17: Total precipitation rate (snowfall and rainfall) in  $\text{mm day}^{-1}$  for noGrIS<sub>mod</sub> simulations minus preindustrial control. Plots show annual, winter and summer anomalies.

with the control consistent with no large differences in precipitation and latent heat flux. However, during the summer there is a cloud cover increase of more than 10 % over the majority of Greenland for the PFT noGrIS<sub>mod</sub> simulations. The cloud cover anomaly is much more variable for bare soil ranging from more than 10 % increase along sections of the coastline to less than 10 % in the interior compared with the control.

Since the orography remains unchanged any precipitation as a result of forced orographic lifting of moisture from the surface will not differ significantly. However, the type of vegetation will determine the quantity and spatial pattern of precipitation produced over Greenland. The interior no longer remains relatively dry with increases in evapotranspiration, evaporation from the canopy and evaporation from the soil surface decreasing the vapour-pressure deficit and enhancing the formation of clouds and therefore the potential for more precipitation. The warmer temperatures associated with the change in surface type will also enhance evaporation from the surface. This increase in moisture availability increases the surface latent heat flux and therefore increases the potential for further precipitation over Greenland which maintains a good moisture availability on the island. This increase in moisture availability is most significant for broadleaf and needleleaf trees, followed by shrubs then grasses. This in part is due to the ability of the more prominent canopy being able to intercept more water for free evaporation compared with grasses which lose more water to run-off. Evapotranspiration is also larger for trees, since trees have bigger roots which are able to access moisture from deeper soil layers, in part from infiltration of water from run-off, compared with grasses and shrubs.

The pattern of fractional sea-ice concentration anomalies (relative to the pre-industrial control) over the Greenland region is shown in Figure 3.18 for the noGrIS<sub>mod</sub> simulations. During winter there is an increase in sea-ice over the Barents Sea, which is strongest for the C3 and C4 grass simulations. There is a small negative change for the bare soil simulation. The change from an ocean surface to a sea-ice surface results in a positive sea-ice-albedo feedback mechanism being setup in the model leading to a further decrease in SST. This region of increased ice thus coincides with the colder near-surface air temperatures observed in Figure 3.9 and accounts for the drier regions in Figure 3.17. During the summer months the increase in sea-ice observed in winter is also present and reflected in the cooler near-surface air

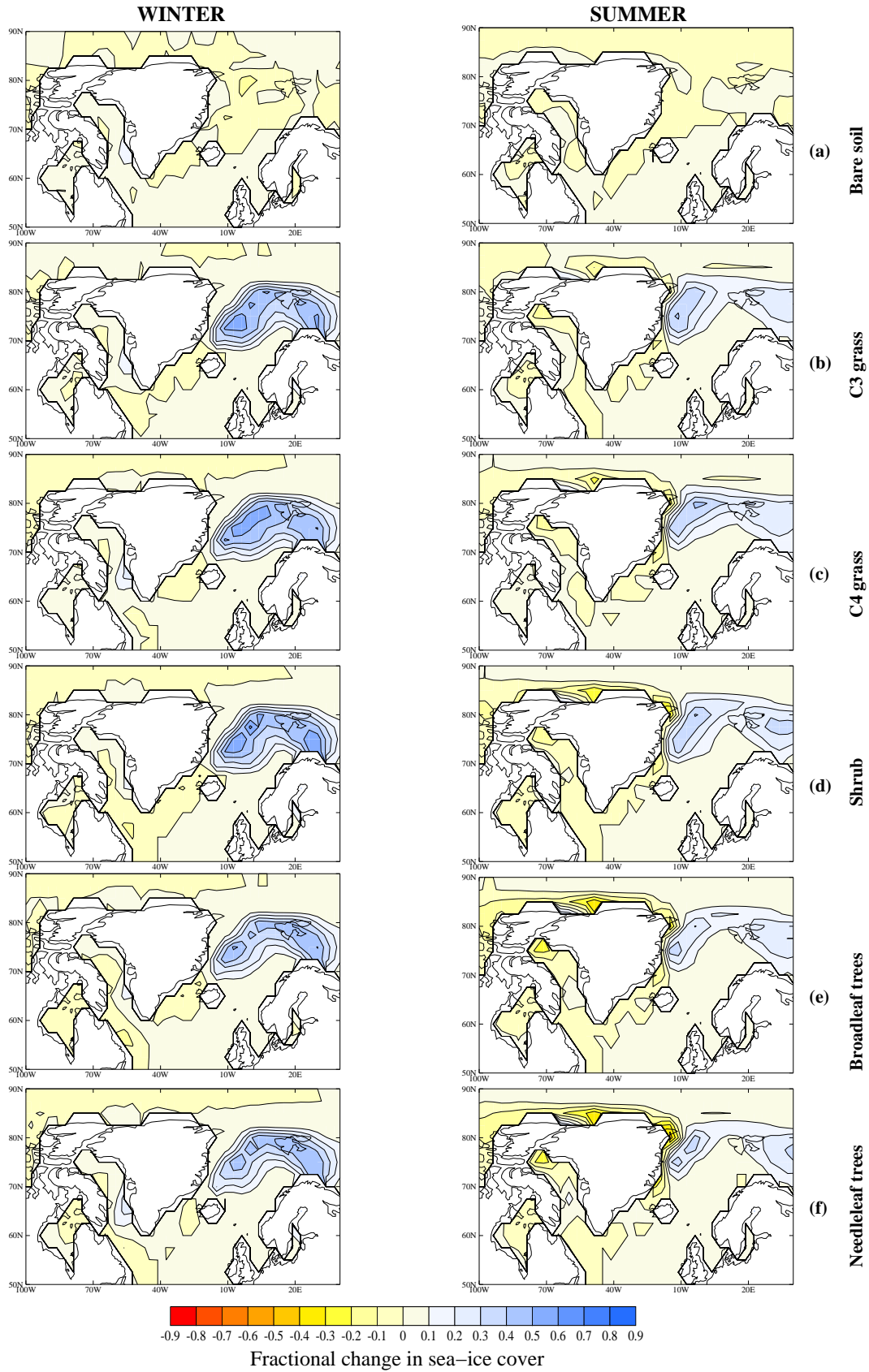


Figure 3.18: The fractional change in sea-ice cover for the winter and summer months for noGrIS<sub>mod</sub> simulations minus preindustrial control.



temperature anomalies and the ocean SST anomalies. However, the positive sea-ice anomalies are much reduced compared with winter. The turbulent fluxes are characteristically small over sea-ice (Serreze *et al.*, 2005) with latent heat flux essentially zero during the winter months and small but positive during the summer ( $\sim 10 \text{ W m}^{-2}$  for C3 grass where there is ice compared with up to  $20 \text{ W m}^{-2}$  in the control where it is ice-free in the same region). Therefore, there is a significant decrease in evaporation over the Barents Sea region where ice is present and a subsequent decrease in precipitation.

The increase in sea-ice concentration in the Barents Sea when the surface type is changed from ice to bare soil or a PFT is related to the transport of heat in the ocean. Ocean heat transport has a strong influence on the Barents Sea mean state (Mosby, 1962). The balance of heat in the ocean is controlled by heat transport from currents into the sea and heat loss via evaporation and sensible heat fluxes. However, it is important to realise that all the climate simulations in this thesis are only 100 years in duration which is insufficient time for the ocean to fully spin-up and equilibrate with the modified climate over Greenland. As a result only tentative conclusions concerning changes in ocean heat transport can be made. For the bare soil noGrIS<sub>mod</sub> the northwards heat transport is similar and even slightly greater than the control at latitudes greater than  $30^\circ\text{N}$  (not shown). This is reflected in the SSTs which show a  $1^\circ\text{C}$  warming in some regions east of Greenland. For all other surface types the heat transport is less than the control. At latitudes greater than  $60^\circ\text{N}$  (where sea-ice is present) the heat transport is reduced by up to 0.1 PW with the greatest reduction for C3 and C4 grass followed by shrubs and then trees, consistent with the pattern in sea-ice anomaly and SSTs (not shown). The reduction in total heat transport at latitudes greater than  $60^\circ\text{N}$  is essentially due to a reduction in heat transport by the wind-driven subpolar gyre system by up to 0.75 PW for grasses and shrubs. This is coincident with an increase in the sea-level surface pressure relative to the control. Therefore, the reduction in SSTs and increase in sea-ice concentration is primarily related to the reduction in wind-driven ocean heat transport.

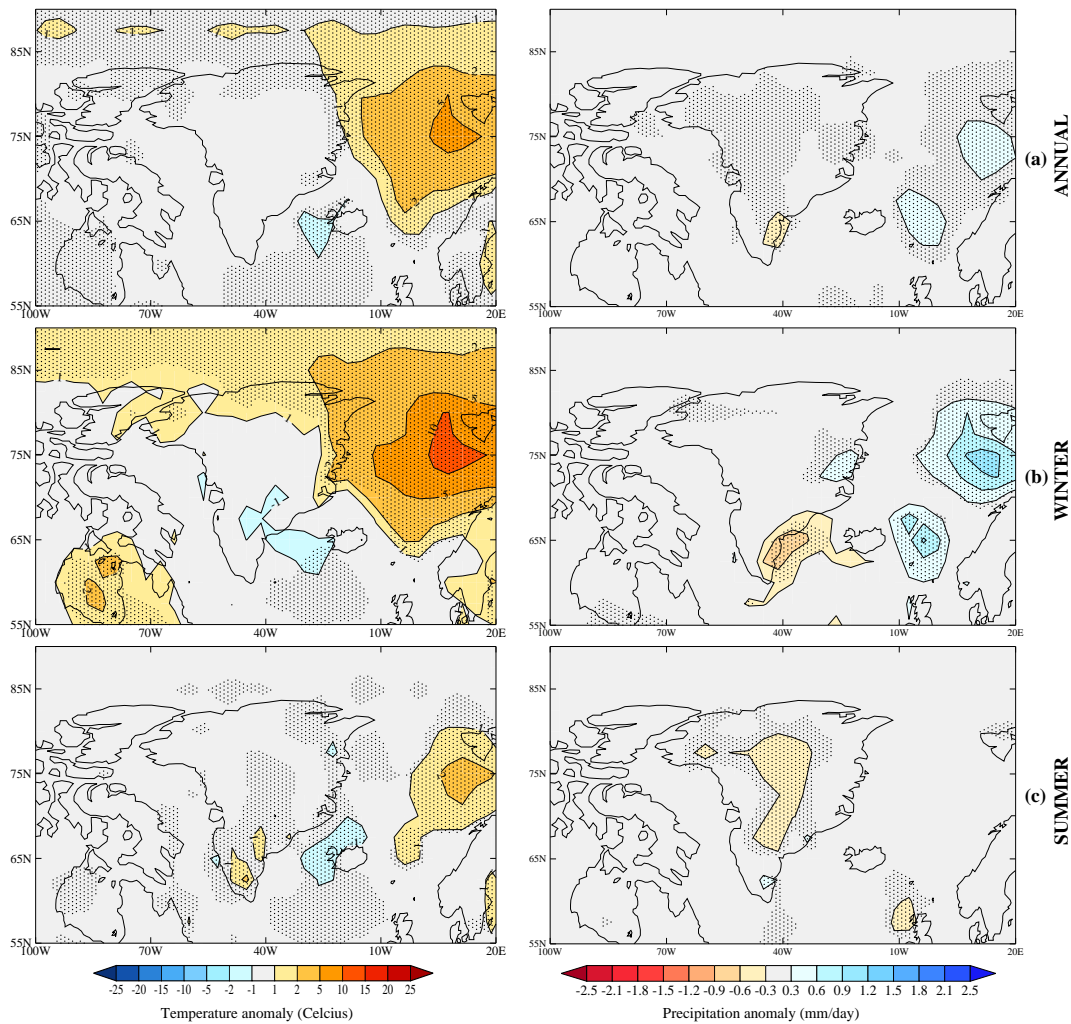


Figure 3.19: Temperature (*left*) and precipitation (*right*) sensitivity to surface roughness length,  $z_0$ , over Greenland. The plots show (a) annual, (b) winter and (c) summer near-surface temperature and precipitation anomalies for needleleaf:  $z_0^{ice}$  minus needleleaf:  $z_0^{nl}$ . In this case the orography is rebounded in both experiments. The stippled pattern denotes regions where differences are 95 % statistically significant using the Student T-test.

### Is roughness length important?

Previous regrowth/inception studies have attributed the temperature change over a melted Greenland as a result of the snow-vegetation-albedo feedback mechanism when the surface type is changed from ice to one with a lower snow-free and snow-covered albedo. It has already been shown that the vegetation-albedo feedback is also important in the study presented here when considering the climate over a melted GrIS. However, changing surface type also results in a change to the surface roughness length which primarily affects the turbulent fluxes of sensible and latent heat by modifying the surface exchange coefficient in Equation 3.11. In order to deduce whether surface roughness change contributes to the perturbed climate over

Greenland when the ice-sheet is removed and replaced with different surface types, the surface roughness length of noGrIS<sub>reb</sub> with needleleaf tree (needleleaf: $z_0^{nl}$ ) is modified to represent the surface roughness length of ice (needleleaf: $z_0^{ice}$ ). This is a change from 1 m to  $1 \times 10^{-4}$  m for  $z_0$ . A surface covered by needleleaf trees has been chosen to investigate the effect of roughness length on a melted GrIS climate because this PFT resulted in the largest change to the turbulent heat fluxes compared with the preindustrial control (see Figure 3.11).

Figure 3.19 shows the annual and seasonal temperature and precipitation sensitivity to changing roughness length (i.e. needleleaf: $z_0^{ice}$  minus needleleaf: $z_0^{nl}$ ). For completeness, the temperature and precipitation anomalies relative to the control are shown in Figure B.1 and Figure B.1 respectively in Appendix B. The stippled regions over and surrounding Greenland show where the temperature and precipitation changes, as a result of changing roughness length to ice values, are statistically significant. Annually, there is minimal difference over Greenland for the temperature anomalies. During winter, there is only a significant difference in the far north of Greenland. However, the region over the Barents Sea is significantly warmer for needleleaf: $z_0^{ice}$  as a result of less sea-ice coverage with a subsequent decrease in surface albedo of up to 20 %. During summer the south and interior of Greenland is marginally warmer by 1 to 5°C. Precipitation anomalies are shown in the right panel of Figure 3.19. Unlike the temperature diagnostic, the Student T-test indicates statistically significant differences in precipitation means over Greenland, albeit small. During winter it is up to 0.9 mm day<sup>-1</sup> drier along the east coast when the surface roughness length represents ice. The summer anomaly shows the interior of Greenland up to 0.6 mm day<sup>-1</sup> drier.

The effect of changing roughness length is not expected to have any influence on the surface shortwave flux but could affect the turbulent heat fluxes into the atmosphere of latent and sensible heat. Figure 3.20 shows the mean annual heat flux cycle over all of Greenland for noGrIS needleleaf: $z_0^{nl}$  (in red) and noGrIS needleleaf: $z_0^{ice}$  (in blue). The net radiation is balanced by the turbulent fluxes, snow melt and heat conduction into or out of the ground. The net radiation balance is similar during the winter months for both experiments. However, during the summer the net radiation at the surface is 27 W m<sup>-2</sup> larger for the needleleaf: $z_0^{nl}$  experiment. The net shortwave flux is very similar for both simulations as expected since no

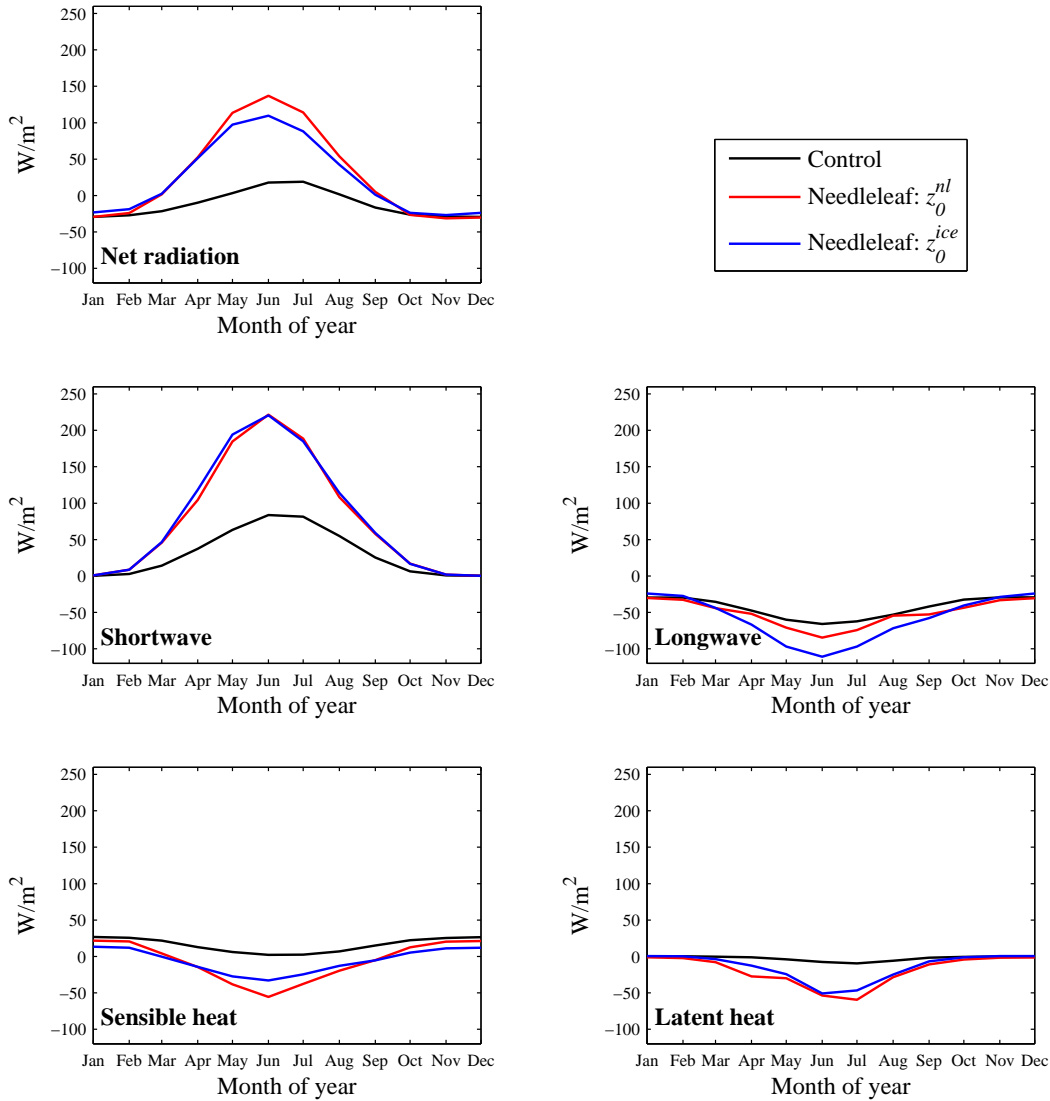


Figure 3.20: Annual cycle of surface heat fluxes (in  $\text{W m}^{-2}$ ) averaged over all of Greenland for the preindustrial control, noGrIS needleleaf:  $z_0^{nl}$  with rebounded orography and needleleaf:  $z_0^{ice}$  also with rebounded orography. Fluxes are positive toward the surface. Note that net radiation is the sum of net shortwave and net longwave radiation.

changes have been made to the albedo parameters which fundamentally determine the amount of shortwave radiation that is absorbed at the surface. However, there are notable differences in the net longwave and sensible heat fluxes during the summer months. When the roughness length is replaced with a value for ice the net longwave heat flux from the surface is increased by up to 25 to 30  $\text{W m}^{-2}$  while the the sensible heat flux reduced by up to 25  $\text{W m}^{-2}$  during June compared with needleleaf:  $z_0^{nl}$ . The differences in net longwave are due to differences in the upward longwave flux away from the surface rather than the downward flux toward the surface. The warmer surface in the needleleaf:  $z_0^{ice}$  in northern regions during summer

results in larger average upward longwave flux and thus reduces the net radiation balance. There is less difference in the latent heat flux but the needleleaf:  $z_0^{ice}$  is still marginally smaller throughout the year which accounts for the drier regions over Greenland shown in Figure 3.19. The ground heat flux and snow melt rate are similar for both experiments (not shown). Therefore, there is an increase in atmospheric heating via sensible heat flux as a result of an increase in roughness length in order to balance the increase observed in net radiation at the surface. During the winter sensible heat flux is positive (i.e. flux toward the surface) in both experiments similar to the control but reduced in the standard needleleaf experiment relative to the needleleaf:  $z_0^{ice}$ .

### Summary

The sensitivity of the climate over a melted GrIS when only the surface type is changed has been assessed in this section. Small positive temperature anomalies are observed during the winter months when insolation is low (0.1 to 1.2°C) while during the summer average Greenland temperature anomalies are significantly greater for the PFT simulations ranging from 7.5 to 12.2°C as a result of vegetation-snow-climate interactions. This is also reflected in the surface heat fluxes where there is an increase in shortwave radiation relative to the control absorbed at the surface. Isolating any feedbacks due to a change in surface roughness length does not have a major affect on the temperature or precipitation anomalies over Greenland. However, it changes the distribution of heat between sensible heat, latent and longwave heat fluxes. Increasing roughness length increases the flux of sensible heat (and to a lesser extent also the latent heat flux) from the surface during the summer months. A similar effect of changes to partitioning of energy at the surface was observed from measurement along a tundra to forest transect at high northern latitudes in Alaska where an increase in canopy height was associated with turbulent fluxes increasingly dominated by sensible heating (Beringer *et al.*, 2005). This transfer of turbulent heat energy upwards into the atmosphere weakens the static atmospheric stability of the boundary layer making the development of convective cells over Greenland more likely at the local scale during the summer. Although roughness length affects the partitioning of the surface energy balance it does not change the local climate over Greenland significantly. Therefore, this result supports the widely held as-

sumption that albedo of the surface is more important than surface roughness when considering feedbacks over a melted GrIS.

In terms of changes to the hydrological cycle over Greenland, there is only net accumulation of snow on the long-term average for a surface replaced with bare soil. The strong positive vegetation-snow-albedo feedback present in the PFT noGrIS<sub>mod</sub> simulations allows earlier snow melt during the spring months with large moisture build up into the summer months and concomitant increases in surface evaporation (also reflected in the increase in latent heat flux) and run-off.

Changing the surface type over Greenland results in no marked changes in low-level atmospheric circulation during the winter. However, during the summer there is a decrease in surface pressure associated with a change from anticyclonic to cyclonic motion of the low-level winds. This coincides with the increase in latent and sensible heat fluxes over Greenland which act to weaken the static stability of the atmosphere and initiate convection for the noGrIS<sub>mod</sub> PFT simulations. This is reflected in the increase in precipitation over much of Greenland and hence also an increase in cloud cover. The changes in atmospheric circulation particularly during the summer, result predominantly in a reduction in annual transport of heat by the oceanic subpolar gyres allowing an increase in the formation of sea-ice in the Barents Sea and an intensification of the sea-ice albedo feedback mechanism during the winter months.

### 3.3.4 Climatic sensitivity to elevation change over Greenland

In order to assess the seasonal changes in temperature observed over Greenland when the ice-sheet is removed, a simulation was performed where the orography was lowered to the level of the rebounded orography (see Figure 3.3) used in the noGrIS<sub>reb</sub> experiments described in Section 3.3.5 but the characteristics (e.g. snow-free and snow-covered albedo and surface roughness length) of the ice-sheet remained the same (this experiment is referred to as lowGrIS). Figure 3.21 shows the near-surface temperature and precipitation anomalies relative to the control. There are two main mechanisms which could change the temperature over Greenland when the orography is lowered: the lapse-rate correction for altitude change and orographically induced changes in atmospheric circulation. If the temperature change was only the result of the lapse rate correction, the average Greenland temperature anomaly between lowGrIS and the control should remain approximately the same throughout the year taking into account the temporal variability of the lapse rate parameter.

In the central regions over Greenland the temperature anomaly for all seasons is positive compared with the control with the temperature change as high as 13.5°C in both winter and summer. During the winter months in the lowGrIS experiment, however, the western coast of Greenland is flanked by temperatures more than 5°C colder compared with the control even though the orography is up to 400 m lower. This results in an average temperature anomaly (1°C) more than two times smaller than the summer and annual anomalies.

In order to approximately quantify how much of the temperature change is due to changes in the surface elevation, as a result of the lapse rate correction between elevations of lowGrIS and the control, and how much is due to atmospheric circulation changes, a simple lapse rate calculation is performed. The temperature change as a result of the lapse rate correction between surfaces of different elevation is related to height by

$$\Delta T = -\Gamma \Delta z, \quad (3.29)$$

where  $\Gamma$  is lapse rate and  $\Delta z$  is the change in altitude (in m). Since lapse rate varies spatially and temporally and can be somewhat complicated over ice-sheets (there is often a temperature inversion near the surface particularly during winter) a spatially and temporally varying (lowGrIS and control) mid-tropospheric lapse

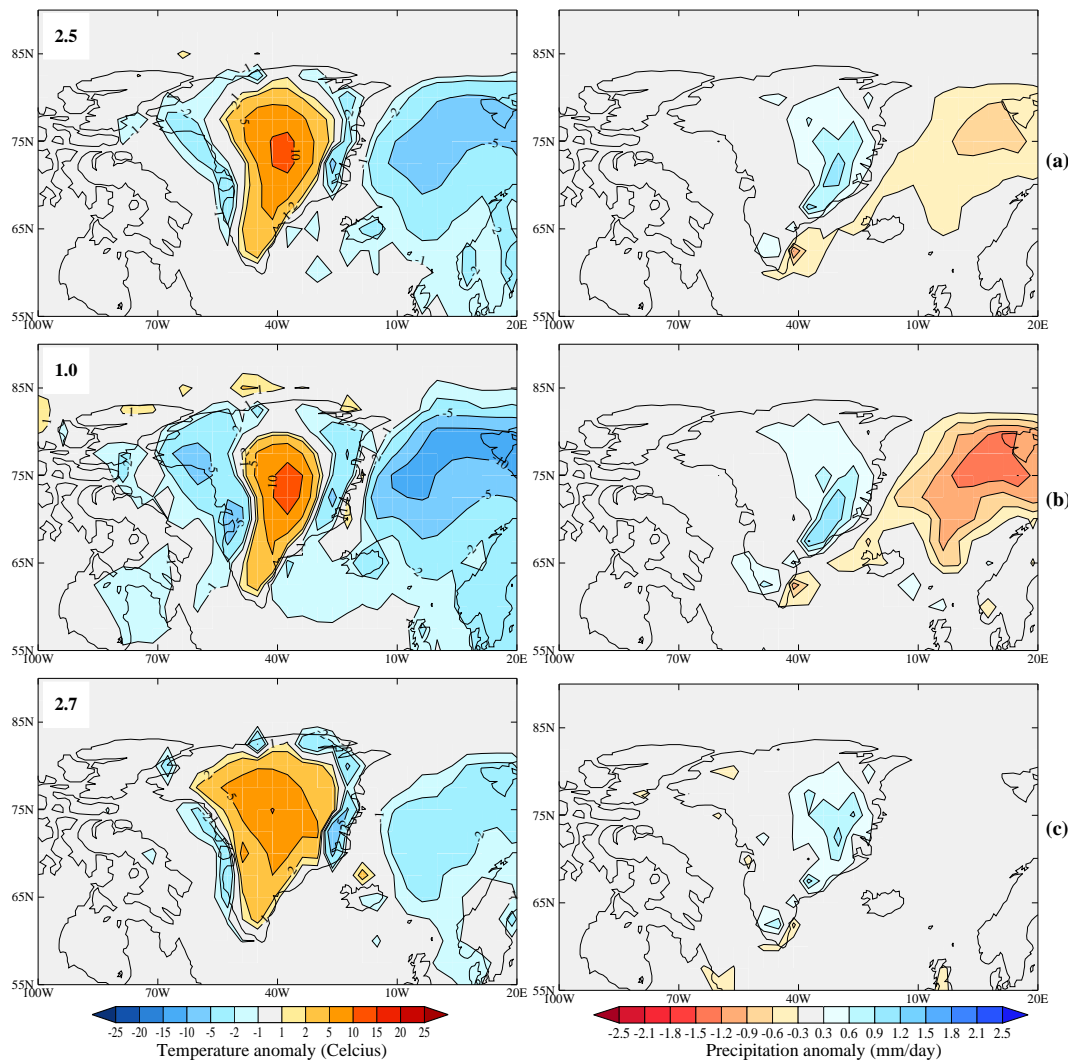


Figure 3.21: Near-surface temperature (*left*) and precipitation (*centre*) anomalies over Greenland and the surrounding Arctic for lowGrIS minus preindustrial control for (a) annual, (b) winter and (c) summer averages. The average temperature anomaly over Greenland land surface is given in the top left corner of the left panel.

rate has been calculated at the atmospheric 500 hPa pressure level in HadCM3 over Greenland. This lapse rate ranges from  $-5.7$  to  $-7.1^{\circ}\text{C km}^{-1}$  during winter and  $-6.6$  to  $-7.3^{\circ}\text{C km}^{-1}$  during Summer. Figure 3.22a shows the winter and summer temperature change over Greenland calculated from Equation 3.29. Also shown is the temperature anomaly over the same region for the lowGrIS experiment (Figure 3.22b) and the difference in temperature change over Greenland between (a) and (b) (Figure 3.22c). In central parts of Greenland there is reasonable agreement between the temperature anomalies for both seasons. However, this is not the case for much of western Greenland during the winter where temperature differences are up to  $14^{\circ}\text{C}$  cooler for the lowGrIS temperature anomaly. Comparisons for summer show better



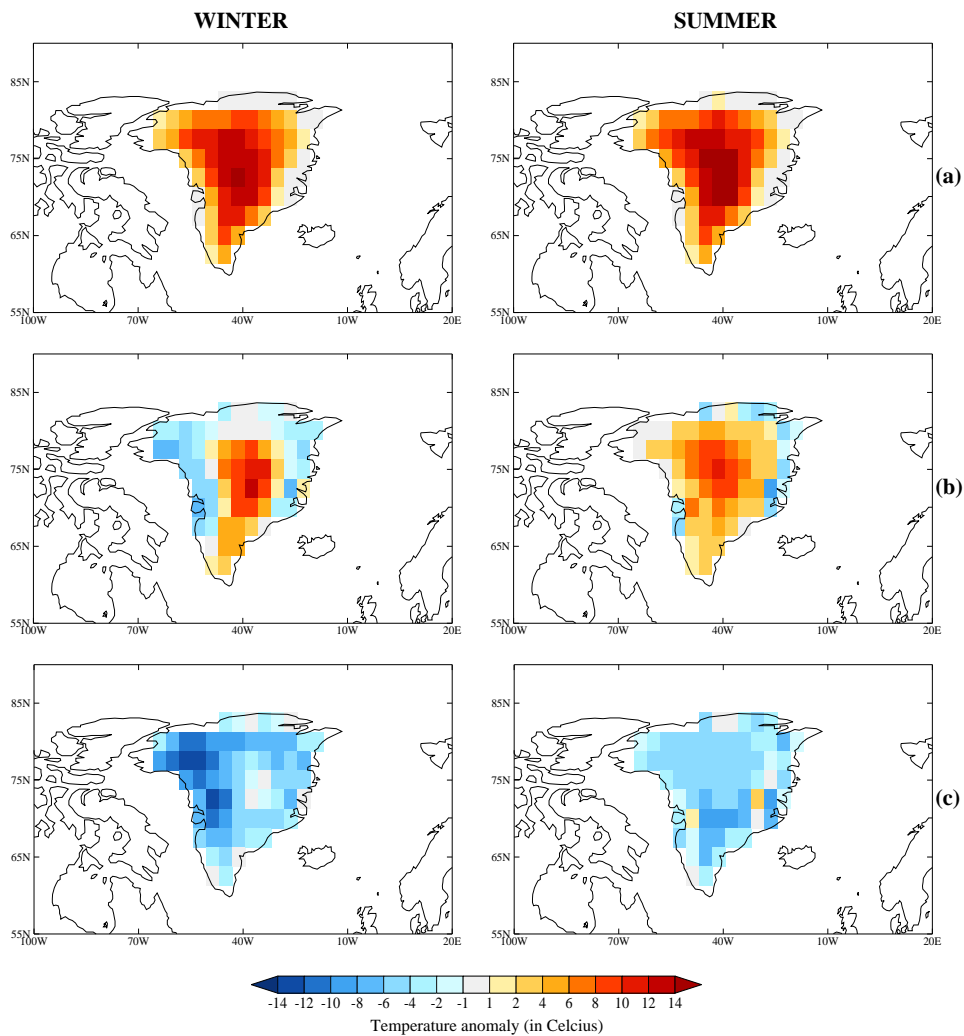


Figure 3.22: Winter and summer surface temperatures over Greenland for (a) calculated lapse rate temperature change (lapse rate used is an average mid-tropospheric value that is spatially and temporally varying), (b) lowGrIS minus preindustrial control and (c) calculated lapse rate temperature change minus lowGrIS (difference between (a) and (b)).

agreement but there is still a cold bias in the lowGrIS experiment compared with the control. Therefore, this result suggests that changes in atmospheric circulation are also important in determining temperature change over Greenland when the orography is lowered. This was not found to be the case in the study of Lunt *et al.* (2004). It is also possible that changes in cloud cover due to changes in the moisture availability could also affect the surface temperature over Greenland.

In order to understand what changes to atmospheric circulation have occurred over Greenland as a result of lowering the orography it is necessary to look at the low-level wind pattern change. Figure 3.23a shows the preindustrial control in winter and summer where Greenland is covered by an anticyclone with a positive tendency

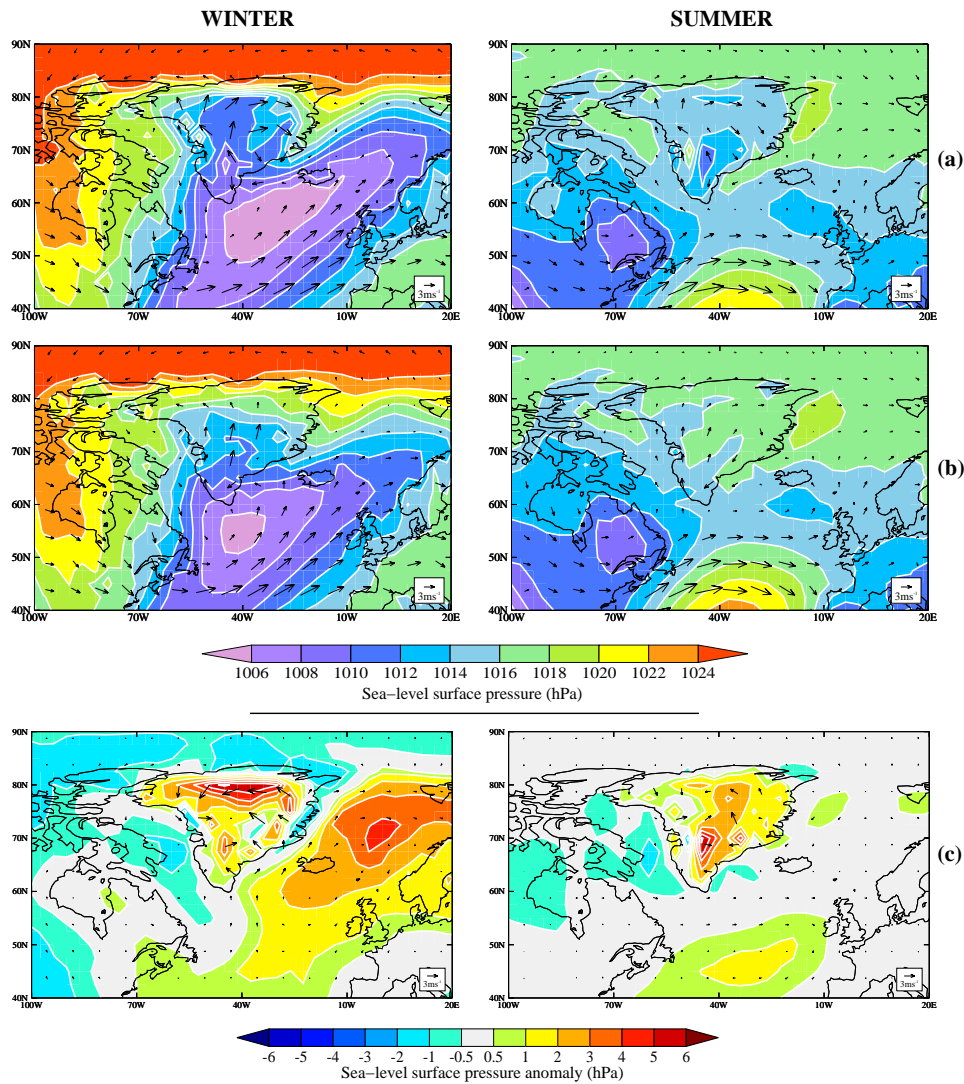


Figure 3.23: Winter and summer low-level (850 hPa) wind speed and direction over Greenland and the surrounding Arctic for (a) the preindustrial control, (b) lowGrIS and (c) lowGrIS minus preindustrial control. Also shown as filled contours is the surface sea-level pressure in hPa.

of the surface winds (at 850 hPa). During winter the Icelandic Low is positioned to the south east of Greenland demonstrated by the low surface pressure and cyclonic rotation of the low-level winds. When the ice-sheet is lowered this region of low pressure shifts westward with its cyclonic activity no longer as intense over the southern tip of Greenland (Figure 3.23b). There is a switch from anticyclonic to more cyclonic flow over Greenland.

Circulation changes caused by the reduction of height of the GrIS are also reflected in the change in precipitation pattern over parts of Greenland. The change in precipitation rate is observed in Figure 3.21 (right panel) for annual, winter and summer for lowGrIS relative to the control. There is an increase in precipitation

rate in eastern and central Greenland throughout the year which is more pronounced during the winter months. At the southern tip of Greenland there is a decrease in precipitation which was also observed in the study of Petersen *et al.* (2004). This decrease can partly be explained by the presence of orographic lifting of moisture along the steep-sided slopes of the ice-sheet in southeastern Greenland in the control which is reduced in the lowGrIS as a result of the lower orography. Also, onshore flow from the Icelandic Low with associated cyclonic activity results in a larger contribution of precipitation on the southeast coast in the control and is reduced in the lowGrIS simulation. The change in orography along the coasts of Greenland is less dramatic in the lowGrIS simulation resulting in less intense but a larger spatial distribution of precipitation over Greenland. There is also a distinct region over the Barents Sea which is up to  $1.5 \text{ mm day}^{-1}$  drier associated with an increase in sea-ice (not shown).

In order to explain the cold bias in temperatures observed in lowGrIS compared with the simple lapse-rate correction for altitude change, the impact of removing the orography on the mid-tropospheric atmospheric circulation patterns can be looked at more closely by examining the geopotential height difference and the 1000-500 hPa geopotential thickness difference. Similar experiments, which specifically analysed the impact of the GrIS on Northern Hemisphere circulation, were performed by Petersen *et al.* (2004) and Junge *et al.* (2005) where they lowered the orography to sea-level but kept the surface characteristics the same (i.e. as ice). The Petersen *et al.* (2004) simulation was run for 10 model years using the NCAR Community Climate Model (CCM3). It must be noted that the resolution of this model is more than twice as fine as HadCM3 (approximately  $1^\circ$  by  $1^\circ$ ) in order to resolve Greenland better. In contrast to the study in this thesis, Petersen *et al.* (2004) found that lowering the orography reduced the sea-level pressure to the east of Greenland while Figure 3.23 shows an increase by 4 hPa compared with the control. A reduction of sea-level pressure east of Greenland was also the case in the Junge *et al.* (2005) study which used the ECHAM4 climate model. Petersen *et al.* (2004) and Junge *et al.* (2005) performed atmosphere only simulations and therefore did not include any feedbacks between ocean, sea-ice and the atmosphere. In this thesis, however, changes in ocean circulation driven by changes in atmospheric circulation over Greenland lead to development of sea-ice east of Greenland which in turn

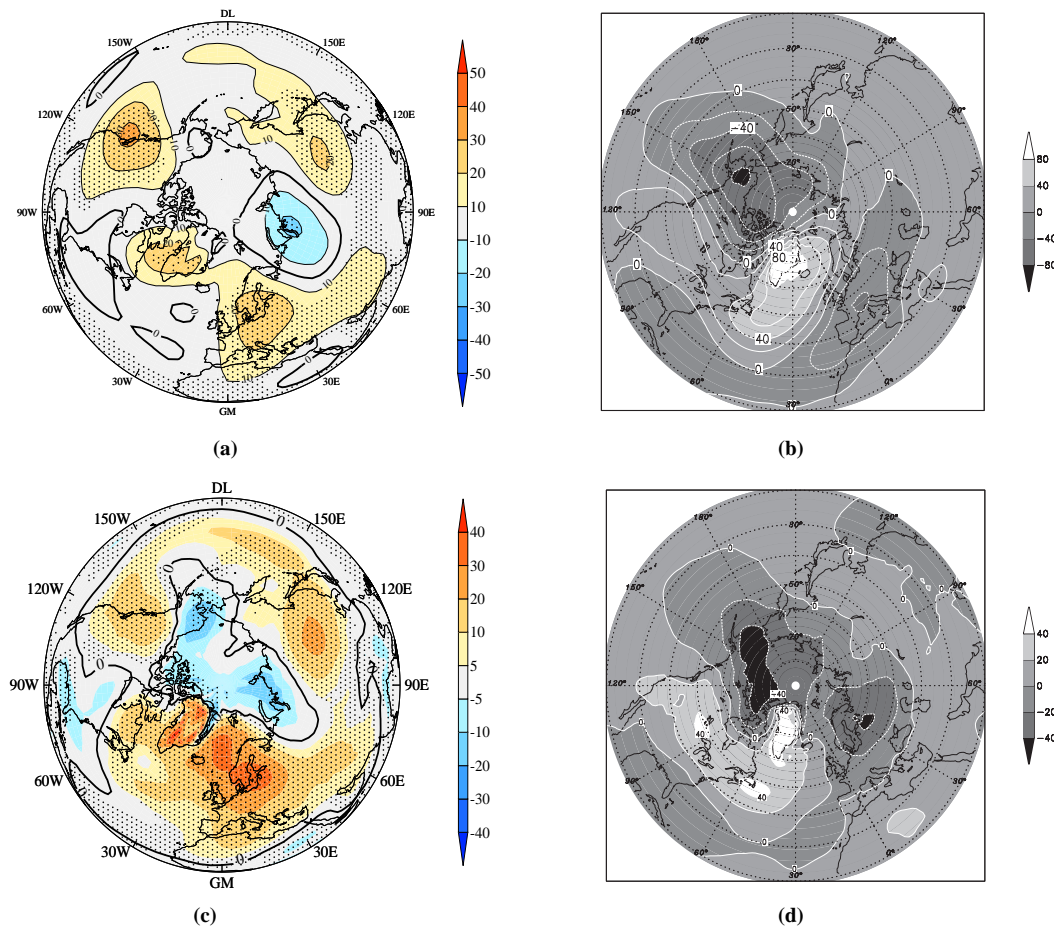


Figure 3.24: (a) The mean winter 500 hPa geopotential height difference minus zonal mean in metres: preindustrial control minus lowGrIS, (b) the mean winter 500 hPa geopotential height difference, preindustrial control minus noGrIS from Petersen *et al.* (2004), (c) the 500-1000 hPa thickness minus zonal mean in metres: preindustrial control minus lowGrIS and (d) the 500-1000 hPa thickness difference: preindustrial control minus noGrIS from Petersen *et al.* (2004). The stippled regions on (a) and (c) define regions where differences are 90 % statistically significant using the Student T-test. In the case of Petersen *et al.* (2004) any differences are 95 % significant.

weakens any possible cyclone activity and is reflected in the increase in sea-level pressure, which is absent in Petersen *et al.* (2004) and Junge *et al.* (2005).

Figure 3.24a shows the change in geopotential height at 500 hPa between the control and lowGrIS simulation and comparison with the result from Petersen *et al.* (2004) (Figure 3.24). Although there is an increase in geopotential height over the Greenland region, which is similar but smaller to Petersen *et al.* (2004), there is an increase rather than a decrease over North America. The pattern over much of Europe is also different. Reasons for the differences between these models are partly due to the CCM3 model resolution being able to more adequately resolve sharp changes in orography in the control. In fact, one of the main conclusions by the study of Junge *et al.* (2005) was that the effects of removing the GrIS on far-field

circulation was very sensitive to model resolution while local changes were relatively insensitive. From this, Junge *et al.* (2005) stated no firm conclusions on the impact of removing the GrIS on the atmospheric circulation further afield can currently be made.

The pattern in the 1000-500 hPa geopotential thickness for control minus low-GrIS (Figure 3.24c) is similar to Petersen *et al.* (2004) (Figure 3.24d). Over the very northern parts of Canada and Alaska the thickness is reduced by Greenland's presence. The thickness over the central part of North America, however, is significantly increased in both this study, Petersen *et al.* (2004) and Junge *et al.* (2005) (not shown). From the geopotential height diagnostic, Petersen *et al.* (2004) and Junge *et al.* (2005) proposed that the absence of the GrIS removes the mechanical blocking/damming of cold air on the western side of Greenland during the winter months. The air mass to the west of Greenland is cooled by radiative heat loss during the polar winter over the cold land mass and sea-ice in the Baffin bay region. This cooler air results in a reduction in the 1000-500 hPa geopotential thickness observed in Figure 3.24c. Thus the presence of Greenland acts as a barrier making it more difficult for the cold air to 'spread' out or be advected away by passing cyclones. Hence, removal of the ice-sheet would remove this 'damming' effect allowing the low-level cold air to penetrate over western Greenland accounting for the colder temperatures, in particular, on the west coast in the lowGrIS simulation compared with the control discussed above.

One final point should be taken into account to explain the differences that are observed between the lowGrIS simulation and those in previous work. The lowGrIS study uses a rebounded orography with a mountain range over eastern Greenland and an average elevation of 770 m above sea-level which will impact on the low-level wind patterns differently compared with a flat orography at sea-level used by the previous studies.

### Summary

The impact on the climate over Greenland and further afield by lowering the orography acts to increase the local temperature over Greenland (due to a lapse rate correction for altitude change) but also has an effect on the low-level atmospheric circulation and hence precipitation patterns over Greenland. An attempt has been

made to extract the contribution to temperature change from lapse rate feedbacks only by estimating an average mid-tropospheric lapse rate during the winter and summer months. The climate, however, simulated with HadCM3 and a rebounded orography (lowGrIS) is colder over Greenland than when only temperature change due to the lapse rate correction is assumed. This is particularly the case over western Greenland where temperature anomalies are more than  $10^{\circ}\text{C}$  cooler. Therefore, changes in atmospheric circulation as a result of lowering the orography also contribute to the change in near-surface temperature over Greenland. However, the effect of changing altitude is far less pronounced on mid-tropospheric temperature which vary by no more than  $1.4^{\circ}\text{C}$  at the 500 hPa pressure level between lowGrIS and the preindustrial control. Low-level cold air masses, once blocked by the high and steep elevation of the GrIS in the west, are able to spread over much of Greenland more readily. Furthermore, there is wider spread of precipitation into the interior of Greenland from the east which was once prevented by the blocking nature of the steep orography. The reduction in cyclogenesis off the south eastern coast of Greenland and over the Barents Sea due to a lowering of the orography results in the development of further sea-ice, due to a reduction in heat transport in the oceans by the wind-driven currents.

### 3.3.5 The impact on climate from a Greenland ice-sheet deglaciation

This section investigates the scenario whereby the GrIS is removed and replaced with the six different surface types and the bedrock is rebounded and reached isostatic equilibrium after unloading of the ice-sheet. Therefore, the feedback processes isolated in the previous sections are now allowed to interact together. The results shown here used similar methodology to previous regrowth studies discussed in Chapter 1 and a comparison will be made where similar experiments have been conducted.

#### Surface temperature and heat flux changes

During winter the average near-surface temperature over a melted Greenland ice-sheet ranges from  $-31^{\circ}\text{C}$  (for bare soil) to  $-30^{\circ}\text{C}$  (for needleleaf tree), not dissimilar from temperatures in eastern Siberia. Average summer temperatures are positive over Greenland for all surface types ranging from  $1.5$  (bare soil) to  $9.4^{\circ}\text{C}$  (needleleaf tree) which could have a significant impact on the potential growth and maintenance of an ice-sheet. Figure 3.25 shows winter, summer and annual anomalies (relative to the control) for all noGrIS<sub>reb</sub> simulations. In all cases the largest change in near-surface temperature occurs over Greenland itself. The annual mean near-surface temperature over Greenland in the noGrIS<sub>reb</sub> climates ranges from  $5^{\circ}\text{C}$  to  $10.2^{\circ}\text{C}$  higher than the control (see Table 3.8). During summer the average Greenland temperature increase is  $7.6^{\circ}\text{C}$  for bare soil with a maximum increase of  $18^{\circ}\text{C}$ . The average increase in temperature for needleleaf trees is  $15.5^{\circ}\text{C}$  with a maximum increase of  $26^{\circ}\text{C}$  in the Greenland interior. However, the temperature increase during winter is not only smaller but the range between different surface types is also reduced ( $1.15^{\circ}\text{C}$  difference) compared with the summer range. The maximum winter temperature change is  $15^{\circ}\text{C}$  for bare soil compared with  $17^{\circ}\text{C}$  for needleleaf tree in central Greenland.

There is also a significant decrease in temperature in the region previously described centered over the Barents Sea, north-east of Greenland and north of Scandinavia. This is similar but more pronounced compared with the noGrIS<sub>mod</sub> experiments and the lowGrIS experiment. This feature is also present during the summer months but several degrees warmer and does not extent as far east. Figure 3.26 shows

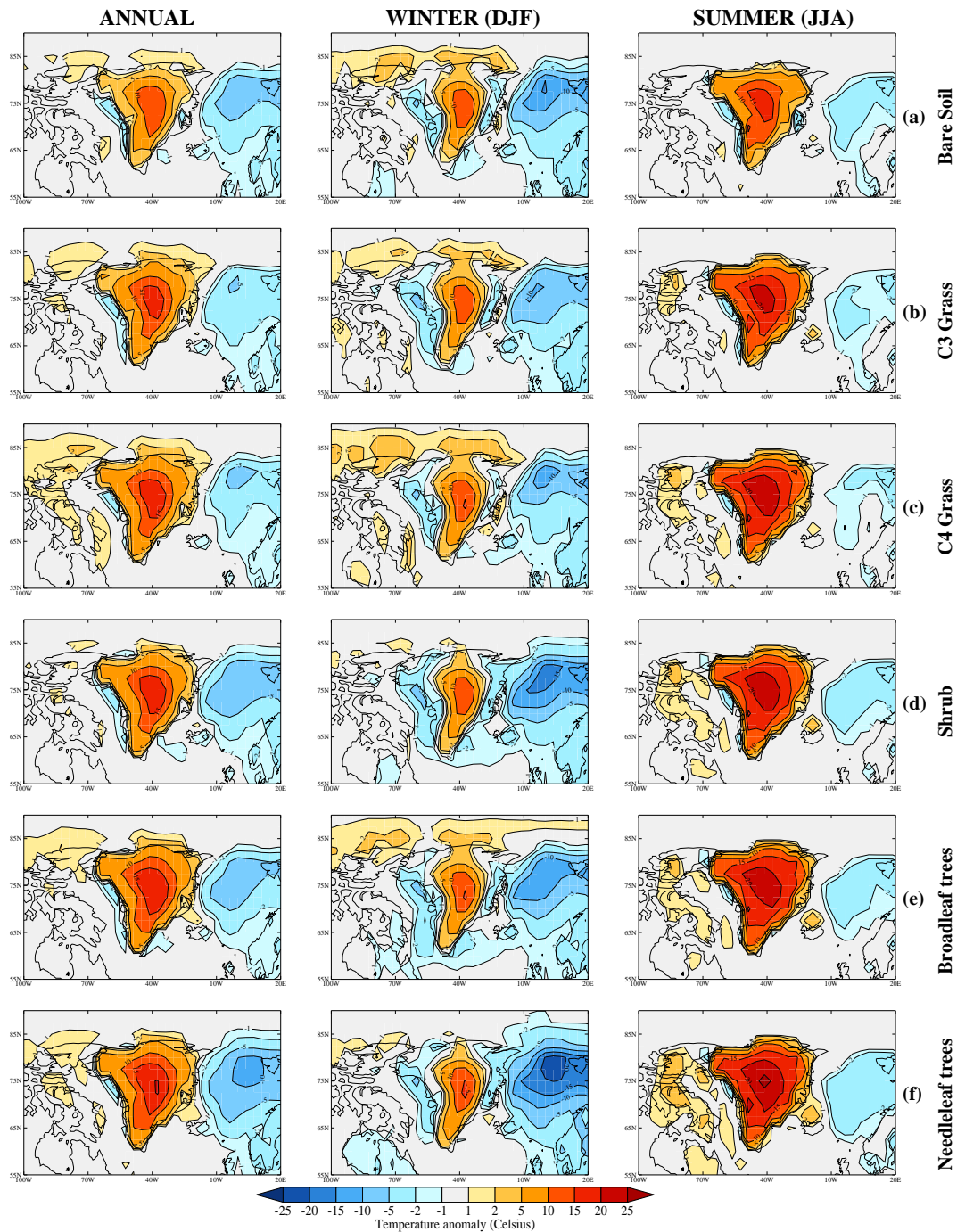


Figure 3.25: Near-surface temperature anomalies (in  $^{\circ}\text{C}$ ) for noGrIS<sub>reb</sub> simulations minus preindustrial control. Plots show annual, winter and summer anomalies.



| Surface type     | ANN   | DJF  | JJA   | MAM   | SON   |
|------------------|-------|------|-------|-------|-------|
| Bare soil        | 4.99  | 2.65 | 7.65  | 2.79  | 6.87  |
| C3 grasses       | 7.48  | 2.80 | 11.83 | 6.81  | 8.47  |
| C4 grasses       | 8.43  | 3.53 | 14.00 | 7.12  | 9.01  |
| Shrub            | 8.34  | 2.40 | 13.82 | 8.44  | 8.66  |
| Broadleaf trees  | 9.92  | 3.29 | 14.43 | 11.79 | 10.15 |
| Needleleaf trees | 10.19 | 3.38 | 15.54 | 11.84 | 10.06 |

Table 3.8: Near-surface average temperature anomaly over Greenland for noGrIS<sub>reb</sub> simulations minus preindustrial control.

the summer and winter temperature change over the Northern Hemisphere for the same set of experiments. Results from the other surface types are not shown but give a similar distribution in temperature between these two extremes. Statistically in both cases the effect of changing the surface type and modifying the orography results in a predominantly localised effect with respect to temperature change over Greenland and the surrounding Arctic region in the Northern Hemisphere.

The local temperature changes over a deglaciated Greenland can be compared with previous studies. The average winter temperature over a melted Greenland of  $\sim -30^\circ\text{C}$  for all surface types is comparable with  $-27^\circ\text{C}$  observed by Toniazzi *et al.* (2004) when they used a bare soil surface and HadCM3 but with the MOSES 1 land surface scheme. The maximum winter temperature anomaly range of  $14.5^\circ\text{C}$  to  $17^\circ\text{C}$  also compares well with Lunt *et al.* (2004); a study which used a rebounded bedrock with a tundra surface. They found a maximum increase of  $14^\circ\text{C}$  which is close to the bare soil and C3 grass maximum increase. The average winter temperature change of  $2.4$  (bare soil) to  $3.4^\circ\text{C}$  (needleleaf tree) is slightly smaller than the Lunt *et al.* (2004)  $4^\circ\text{C}$  average change. This is likely due to differences in the climate models, particularly the land surface schemes, and different areal regions for averaging over Greenland. Their average summer temperature anomaly ( $8.5^\circ\text{C}$ ) fits within the range deduced in this study from  $7.7$  to  $15.5^\circ\text{C}$ . However, the closest PFT to tundra is C3 grasses which showed a summer anomaly of more than  $11^\circ\text{C}$ .

Crowley and Baum (1995) and Toniazzi *et al.* (2004) examined the average absolute summer temperatures over Greenland. With topography at sea-level Crowley and Baum (1995) found summer temperatures on Greenland were around  $10^\circ\text{C}$  for bare soil and tundra surface types and up to  $14^\circ\text{C}$  for needleleaf trees. While a sim-

ulation with a rough representation of topography at 500 m above sea-level (based on rebounded bedrock from Letreguilly *et al.* (1991b)) produced a range from 2°C to 4°C lower than at sea-level for a Greenland surface covered by tundra. The July-August average temperatures for Toniazzo *et al.* (2004) range from 5°C to 13°C with a surface of bare soil. The average summer temperatures over all of Greenland for the noGrIS<sub>reb</sub> bare soil experiment in this study is somewhat lower at 1.5°C although this does not only take the central regions into account where temperatures are as high as 7.4°C. The average summer temperature for needleleaf trees of 9.4°C is more comparable with the temperatures observed by Crowley and Baum (1995) with a surface of tundra. However, in much of central Greenland temperatures are 12 to 14°C which compares well with the temperatures observed for a topography at sea-level with boreal forest coverage.

The annual cycle of surface heat fluxes is shown in Figure 3.27. During the winter months there is a reduction in heat loss via longwave emission for the bare soil noGrIS<sub>reb</sub> simulation compared with the control. This can be explained by the atmospheric layers over the lower surface being warmer than in the control where the ice-sheet is present. This in turn reduces the heat losses from the surface via longwave emission. This behaviour, however, is not the case for longwave emissions in the vegetated noGrIS<sub>reb</sub> simulations which are approximately the same as the control in winter. There is a small increase in heat loss via sensible heat flux during the winter months for all noGrIS<sub>reb</sub> simulations compared with the control and no notable difference in latent heat flux. Net shortwave fluxes are all close to zero as a result of low insolation at high latitudes during winter. The largest and most striking differences that occur between surface types and the control are observed during the summer. The thawing during early spring observed in the hydrological cycle (see next section) results in a marked increase in net downward shortwave heat flux. As the surface becomes exposed with the melting of overlying snow the albedo is reduced and absorption of shortwave radiation increases. The largest differences relative to the control are observed for needleleaf tree, followed closely by broadleaf tree, shrubs grasses and then bare soil, consistent with the noGrIS<sub>mod</sub> experiments. The difference in net shortwave heat flux relative to the control for needleleaf tree during June is 138 W m<sup>-2</sup> compared with only 20 W m<sup>-2</sup> for a surface with bare soil. The peak shortwave heat flux is also shifted later (July) for bare soil due to

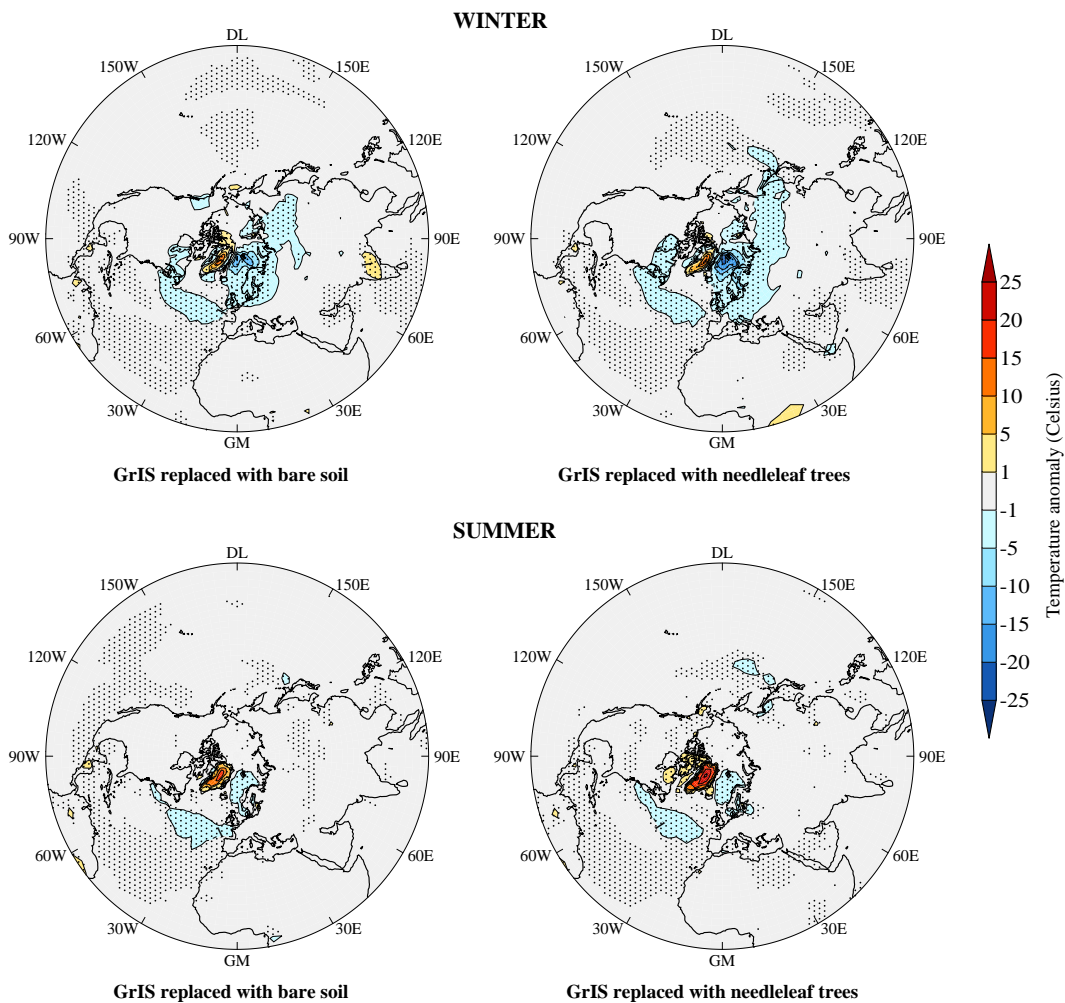


Figure 3.26: Near-surface temperature change over the Northern Hemisphere for the summer and winter months. *Left*: bare soil minus preindustrial control and *Right*: Needleleaf trees minus preindustrial control. Other surface types are not shown but show a similar pattern. The stippled pattern represents regions where the change in surface temperature is 95 % statistically significant using the Student T-test.

continued thawing of the snow-covered surface.

There is also a significant increase in heat losses from the surface in the form of turbulent fluxes during summer for the noGrIS<sub>reb</sub> simulations which partially offsets the large shortwave fluxes observed. Again the largest losses via sensible heat flux occur for the two tree types (needleleaf tree:  $58 \text{ W m}^{-2}$ ) followed by the grasses and shrubs. There is a substantially smaller increase for bare soil ( $4 \text{ W m}^{-2}$ ). A similar pattern is observed for latent heat flux with peak latent heat losses occurring in July. The difference for needleleaf trees and bare soil is  $50 \text{ W m}^{-2}$  and  $15 \text{ W m}^{-2}$  respectively. These results suggest that there is almost equal partitioning between the turbulent heat fluxes during the summer for the needleleaf noGrIS<sub>reb</sub> simulations while heat losses via latent heat flux are substantially larger for bare soil.

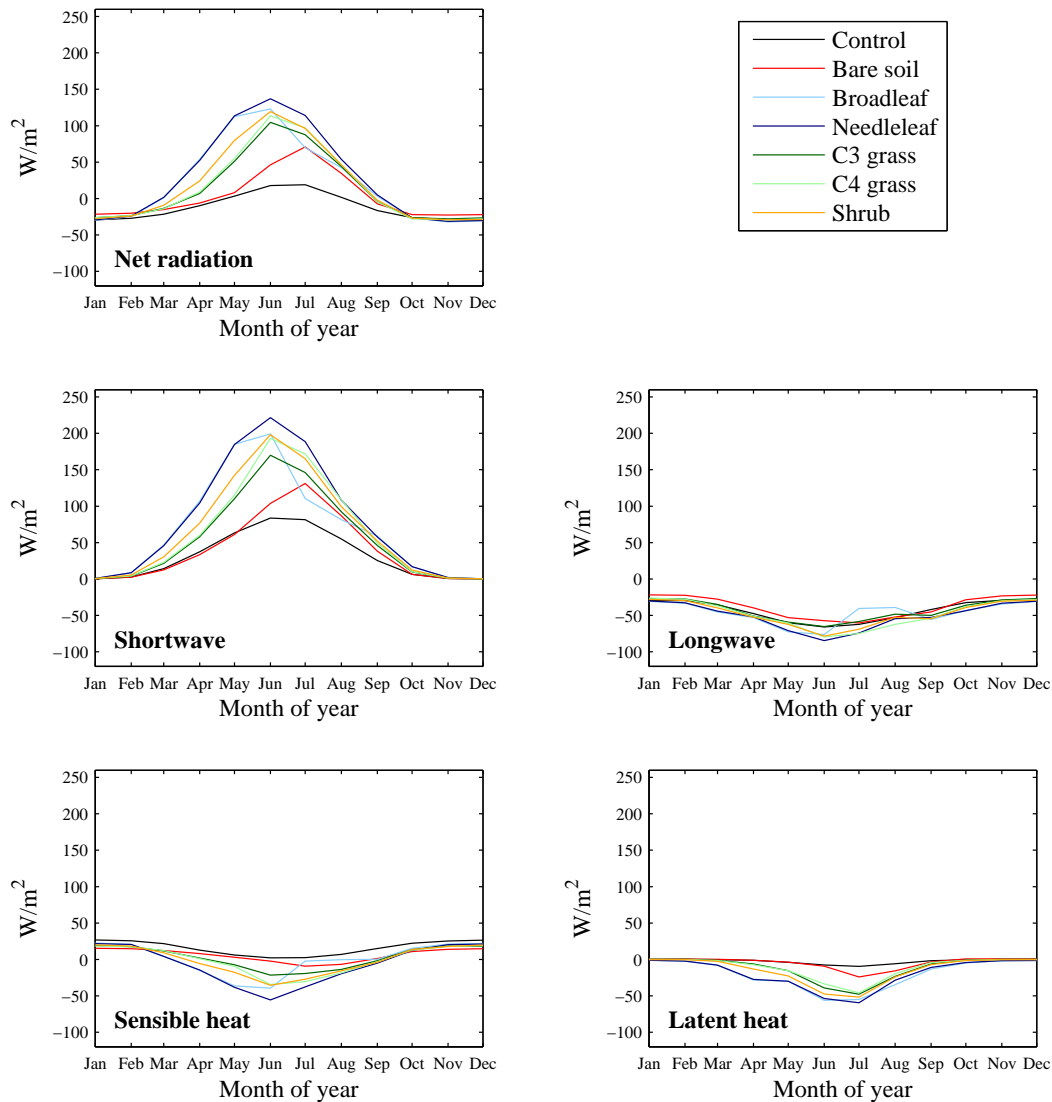


Figure 3.27: Annual cycle of heat fluxes averaged over all of Greenland for the control and noGrIS<sub>reb</sub> simulations. All fluxes are positive downwards toward the surface. Note that net radiation is the sum of net shortwave and net longwave radiation.

### Synergy between temperature response to altitude and surface type change

By performing the sensitivity studies in Section 3.3, interactions (in terms of temperature changes) between the snow-vegetation-climate feedback and change in elevation of the surface can be examined when they are varied together. For example, Table 3.9 shows the difference in temperature between the noGrIS<sub>reb</sub> simulations and the result when the temperature sensitivity to surface type, (noGrIS<sub>mod</sub>) and elevation change (lowGrIS) are linearly combined. If there was no synergy the difference would sum approximately to zero. Ideally, in order to perform a complete feedback analysis all possible feedback processes should be switched on and off in all possible

| Surface type     | synergy=noGrIS <sub>reb</sub> - (lowGrIS+noGrIS <sub>mod</sub> ) |        |
|------------------|--|--------|
|                  | Winter   | Summer |
| Bare soil        | 1.53   | 3.72   |
| C3 grasses       | 1.53   | 1.59   |
| C4 grasses       | 2.4  | 2.07   |
| Shrub            | 0.65   | 1.74   |
| Broadleaf trees  | 1.12   | -0.47  |
| Needleleaf trees | 1.39   | 1.78   |

Table 3.9: The difference in winter and summer mean near-surface temperature (in °C) averaged over all of Greenland between the rebounded noGrIS<sub>reb</sub> simulation and the linearly combined temperature response to only altitude change (lowGrIS) and surface type change (noGrIS<sub>mod</sub>).

combinations. This would require also investigating the impact of atmosphere-ocean interactions and sea-ice atmosphere-ocean interactions on the local climate when the ice-sheet is removed. Although this has not been performed the results do highlight the complexity of feedback processes in the Earth system and the synergy that exists in the local climate over Greenland. For all surface types, the difference in winter temperature is positive ranging between 0.65°C and 2.4°C. This is also shown for summer (excluding broadleaf trees) where the largest disparity is for bare soil. Using bare soil as an example, the interaction between elevation and surface type is clearly seen. When the elevation remains unchanged and the surface replaced with bare soil, the surface continues to behave very much like an ice-sheet, with large accumulations of snow cover and small amounts of snow melt in early spring in order to initiate the surface-albedo feedback (see Figure 3.12). However, when the elevation is lowered the temperature change due to the lapse-rate correction for change in altitude and atmospheric circulation changes is enough to cause considerable melt in early spring resulting in strengthening of the ice-albedo feedback mechanism as the albedo of the soil surface becomes exposed (which was absent when the elevation was high) warming the surface further.

### The hydrological cycle over a melted Greenland ice-sheet

Total precipitation anomalies relative to the control for annual, winter and summer are shown in Figure 3.28. For all of the noGrIS<sub>reb</sub> simulations there is an increase in precipitation on the east coast of Greenland in winter and summer with a decrease

in precipitation over the Barents Sea in winter. The increase seen in winter relative to the control is similar to the pattern observed in the lowGrIS experiment (see Figure 3.21b) which was absent from the surface-type sensitivity studies (see Figure 3.17). The southeastern tip of Greenland also shows a reduction in precipitation in the winter. During winter the anomalies observed are similar in spatial distribution for all vegetation types (up to  $1.5 \text{ mm day}^{-1}$  in some cases) but with an increase in precipitation change extending further south along the eastern coast for needleleaf tree. Table A.1 in Appendix A shows the average Greenland precipitation for winter for the noGrIS<sub>reb</sub> experiments are not only very similar ( $0.2$  to  $0.3 \text{ mm day}^{-1}$ ) for all surface types but also compare closely with the lowGrIS average anomaly. This result implies that the change in precipitation relative to the control from a deglaciated Greenland during winter is mainly attributed to a change in the Greenland orography from unloading of the ice-sheet. However, during the summer the distribution and intensity of precipitation change differs between surface type (see Table A.1). Maximum precipitation anomalies over Greenland are greater than  $2.5 \text{ mm day}^{-1}$  for needleleaf tree but no more than  $0.9 \text{ mm day}^{-1}$  for bare soil. The precipitation also penetrates further into the central and western regions of Greenland for needleleaf and broadleaf tree, into the central regions for shrubs and grasses and is mainly confined to the eastern coast of Greenland for bare soil. Furthermore, there is a continuation of the decrease in precipitation observed along the southern tip of Greenland in the vicinity of the Labrador Sea and into the Davis Strait for the PFT noGrIS<sub>reb</sub> simulations. Thus, average Greenland summer precipitation anomalies for the noGrIS<sub>reb</sub> simulations, in addition to the dependence on altitude change, are also dependent on the surface type.

The following discusses the hydrology over Greenland in more detail. The annual water cycle over Greenland is shown in Figure 3.29 for the five PFTs, bare soil and the control simulation. It is also divided into the different regions over Greenland as illustrated in Figure 3.5. Liquid precipitation (rainfall) dominates from late spring to early autumn for all noGrIS<sub>reb</sub> experiments. The control and bare soil are comparable in eastern Greenland but rainfall is greater in all other regions for bare soil. The five PFT noGrIS<sub>reb</sub> experiments show up to  $2 \text{ mm day}^{-1}$  in central and southern Greenland with marginally smaller amounts in the north and east.

Solid precipitation (snowfall) remains positive for all regions during the entire

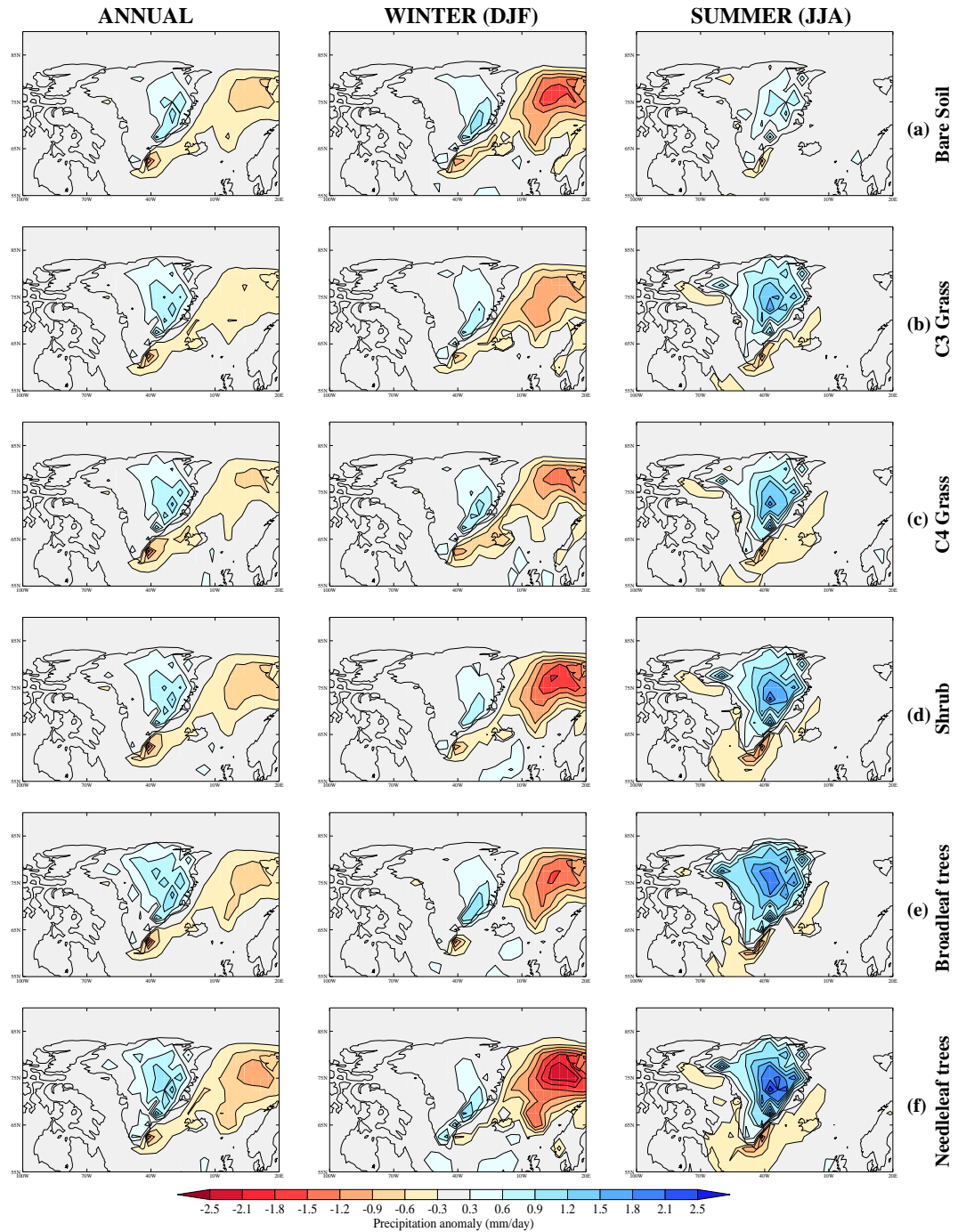


Figure 3.28: Total precipitation rate (snowfall and rainfall) in  $\text{mm day}^{-1}$  for noGrIS<sub>reb</sub> simulations minus control. Plots show annual, winter and summer anomalies.

year for the control simulation but decreases in the summer months. The largest snowfall amounts in all cases are observed in the south and east coinciding with the higher elevations of the rebounded orography. During autumn and spring precipitation is nearly all solid in all noGrIS<sub>reb</sub> simulations but is markedly reduced during the summer months coincident with the increase in rainfall amounts. Bare soil shows the least increase in rainfall compared with the other noGrIS<sub>reb</sub> simulations.

The increase in intensity of the melt season for the noGrIS simulations is clearly seen in terms of run-off amounts. Summer run-off for all noGrIS<sub>reb</sub> experiments is almost twice as large as that for the control. The timing for the initiation of the melt season is also important. For the trees, grasses and shrubs run-off begins to increase earlier in spring (April, May) compared with June for bare soil and the control.

The individual components that make up the evaporative flux in Equation 3.15 are examined more closely. Evaporation is negligible in the control simulation throughout the year with any small amounts occurring purely as evaporation from the soil surface. In the east and west regions it becomes slightly more significant as a result of ice-free regions where bare soil is present. It is zero in the central region of the ice-sheet as would be expected. However, small amounts of moisture flux from sublimation of snow during the summer months are prevalent in all regions, particularly in the central part of the ice-sheet. Where there is no vegetation in a gridbox evaporation from the surface is bare soil evaporation. Otherwise, it corresponds to transpiration from the vegetated fraction. In terms of the noGrIS<sub>reb</sub> simulations evaporation from the soil surface is significant ranging from 0 (during winter months) to 1.3 mm day<sup>-1</sup> during the summer. It is largest for the shrubs and trees due to an increase in moisture availability in the soil layers. This evaporation from the soil surface is a result of moisture build up during the summer months as observed in the noGrIS<sub>mod</sub> experiments. Evaporation from the canopy is greatest during the summer months for trees, followed by grasses and shrubs which would be expected since it is predominantly dependent on the fraction of the canopy which is saturated. In fact, evaporation from broadleaf trees is almost double that from needleleaf trees. Sublimation is greatest in the early spring for all noGrIS<sub>reb</sub> simulations coincident with the onset of the melting season when snow is still present over much of the surface with up to 1 mm day<sup>-1</sup> for trees in central and southern



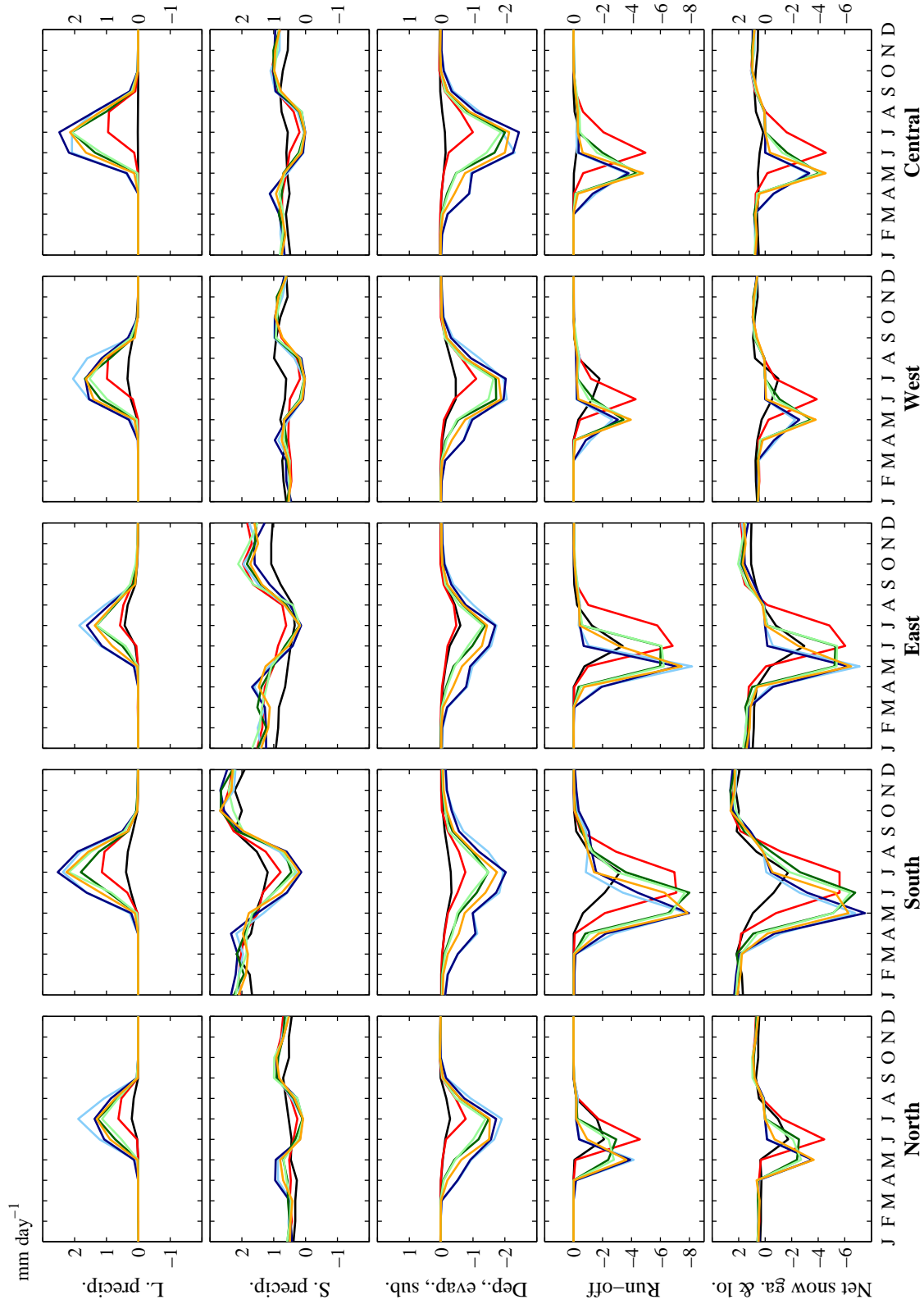


Figure 3.29: Annual hydrological cycle for five regions over Greenland as defined in Figure 3.5 for the noGrIS<sub>reb</sub> simulations. The diagnostics shown are net snow gain and loss (Net snow ga. & lo.), run-off, deposition, evaporation and sublimation (Dep., evap., sub.), solid precipitation (S. precip) and liquid precipitation (L. precip). All quantities are in millimeters per day water equivalent. Note that fluxes toward the surface are counted as positive. For each graph are shown the preindustrial control (black), bare soil (red) and the 5 PFTs: C3 grasses (dark green), C4 grasses (pale green), needleleaf trees (dark blue), broadleaf trees (light blue) and shrubs (orange).

Greenland. During the summer small but negative sublimation (deposition) ensues for all vegetation types and bare soil implying more atmospheric moisture in the near-surface atmospheric layer over Greenland.

The net snow gain and loss throughout the year averages close to zero for the control. However, the noGrIS<sub>reb</sub> simulations show substantially greater snow loss compared with gains made during the winter months. Snow loss is also observed earlier in Spring in accordance with the increase in run-off. The hydrological cycle for bare soil over Greenland is similar to the bare soil experiment of Toniazzo *et al.* (2004).

### Snow amount and cover

As previously mentioned the snow diagnostic has been used in the past to indicate the potential of regrowth of the GrIS under a preindustrial climate. Figure 3.30, in the same form as Figure 3.12, shows the annual amount of snow cover spanning the length of the simulations. As in the case of the noGrIS<sub>mod</sub> experiments, there is no accumulation on the long-term average for any of the PFT noGrIS<sub>reb</sub> simulations for all regions over Greenland. The annual amounts are also similar. However, the simulation where the ice-sheet is replaced with bare soil (solid red line) differs between the two orographic setups. Where orography is set at modern there is a positive trend in accumulation in all regions except the north. However, when the orography is lowered to the rebounded state this positive trend is no longer observed in the west. Furthermore, in central regions it is also far less pronounced and the annual amounts of accumulation are a factor of 10 lower. Any inference about ice-sheet regrowth from this timeseries suggests that this would be confined only to the southern and eastern regions of Greenland if the surface was replaced only with bare soil.

Seasonally, there are significant variations of snow cover over Greenland which are more pronounced than in the noGrIS<sub>mod</sub> simulations, especially for bare soil. Figures 3.31 and 3.32 show the average snow cover in February and August. Also included is the average snow cover for the noGrIS experiment in the study of Toniazzo *et al.* (2004). Since this study uses HadCM3 but with MOSES 1 it is suitable for a direct comparison to see what difference the land surface scheme makes. In the experiment shown the bedrock is unloaded and allowed to reach isostatic equilibrium similar to

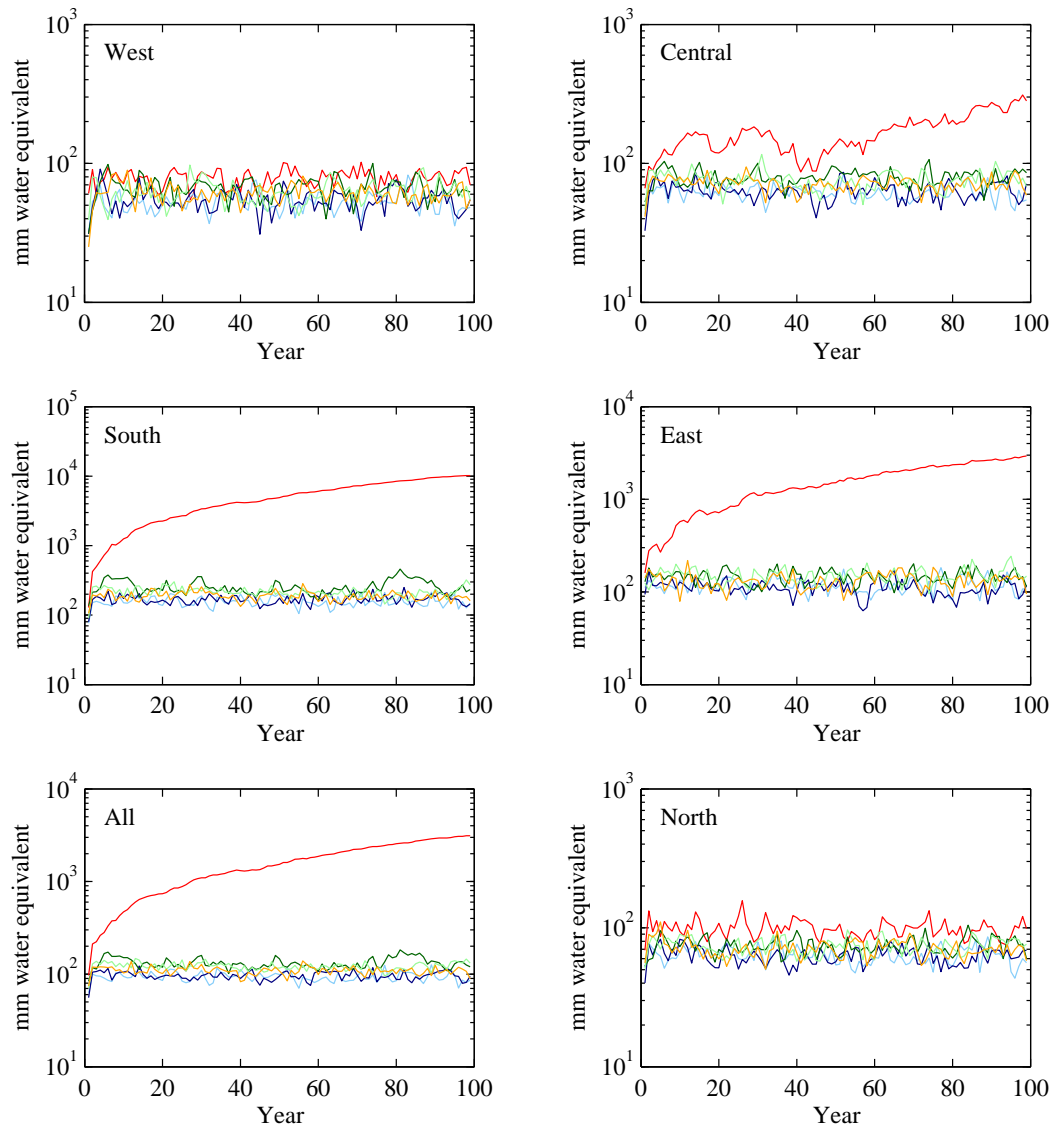


Figure 3.30: Cumulative mass balance (in  $\text{kgm}^{-2}$ ) for North, South, East, West and Central Greenland for all noGrIS<sub>reb</sub> simulations. Cumulative mass balance is also shown for all of Greenland. Time series spans the length of the simulation. All PFTs and bare soil are shown: **bare soil**, **broadleaf trees**, **needleleaf trees**, **C3 grass**, **C4 grass**, **shrub**. The values plotted are annual averages of the snow cover, which rises year-on-year if there is net accumulation.

the noGrIS<sub>reb</sub> simulations in this thesis. The surface is replaced with bare soil and the simulation run for 40 years and averaged over the last two decades.

As expected, snow accumulation is greater during winter than summer as shown for the annual hydrological cycle in Figure 3.29. During February the accumulation is greatest in the south and east with amounts larger than 1000 mm in places. The least accumulation occurs in the west and central-northern regions for all noGrIS<sub>reb</sub> simulations. The bare soil surface shows the accumulation in the east is more extensive than for the noGrIS<sub>reb</sub> PFT experiments, stretching north along the eastern

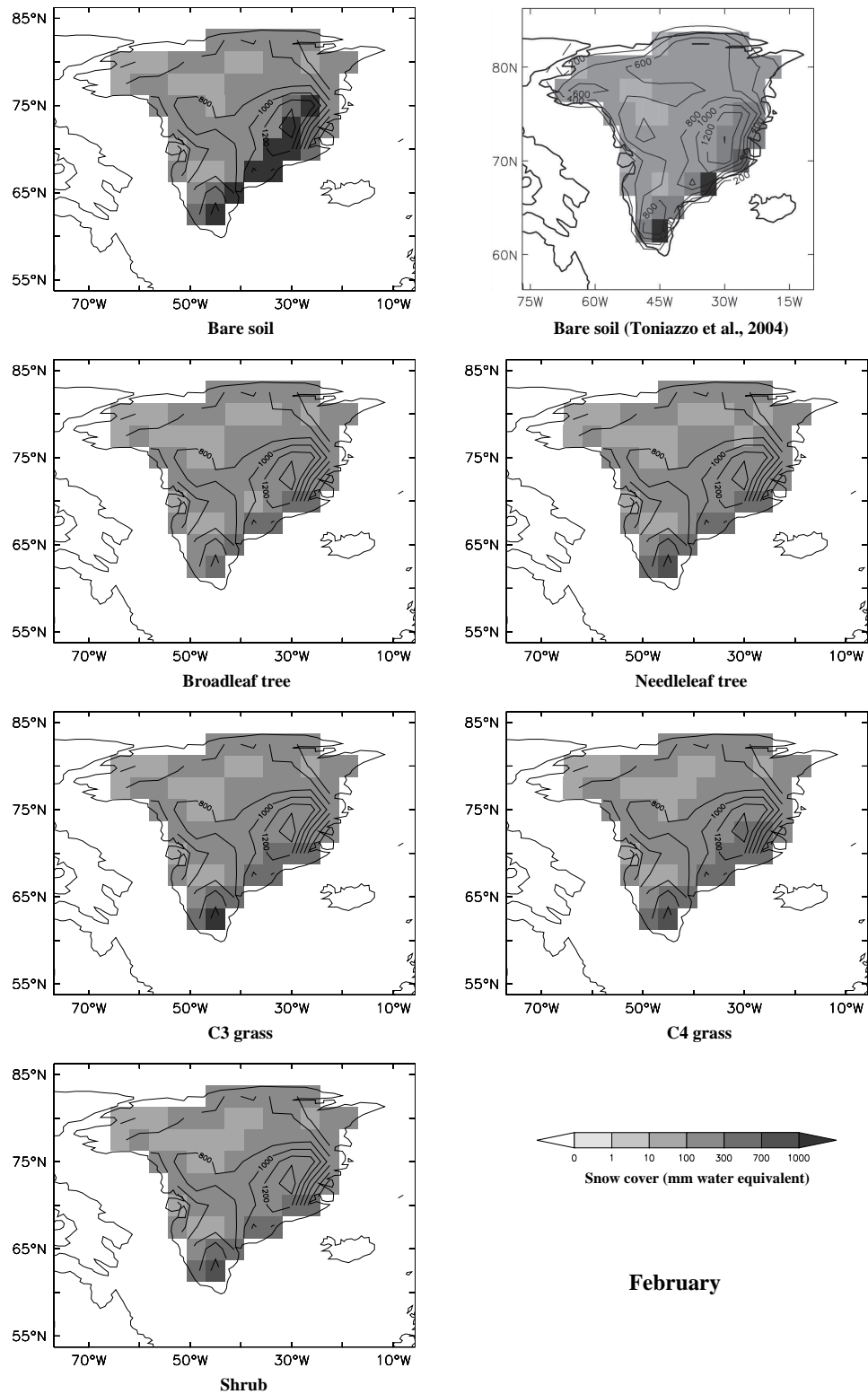


Figure 3.31: Average February snow cover over Greenland for the control and noGrIS<sub>reb</sub> simulations. Overplotted are levels of constant orographic height in metres at intervals of 200 m. The subfigure at the top-right is taken from Toniazzo *et al.* (2004) who performed a similar experiment with bare soil surface type.

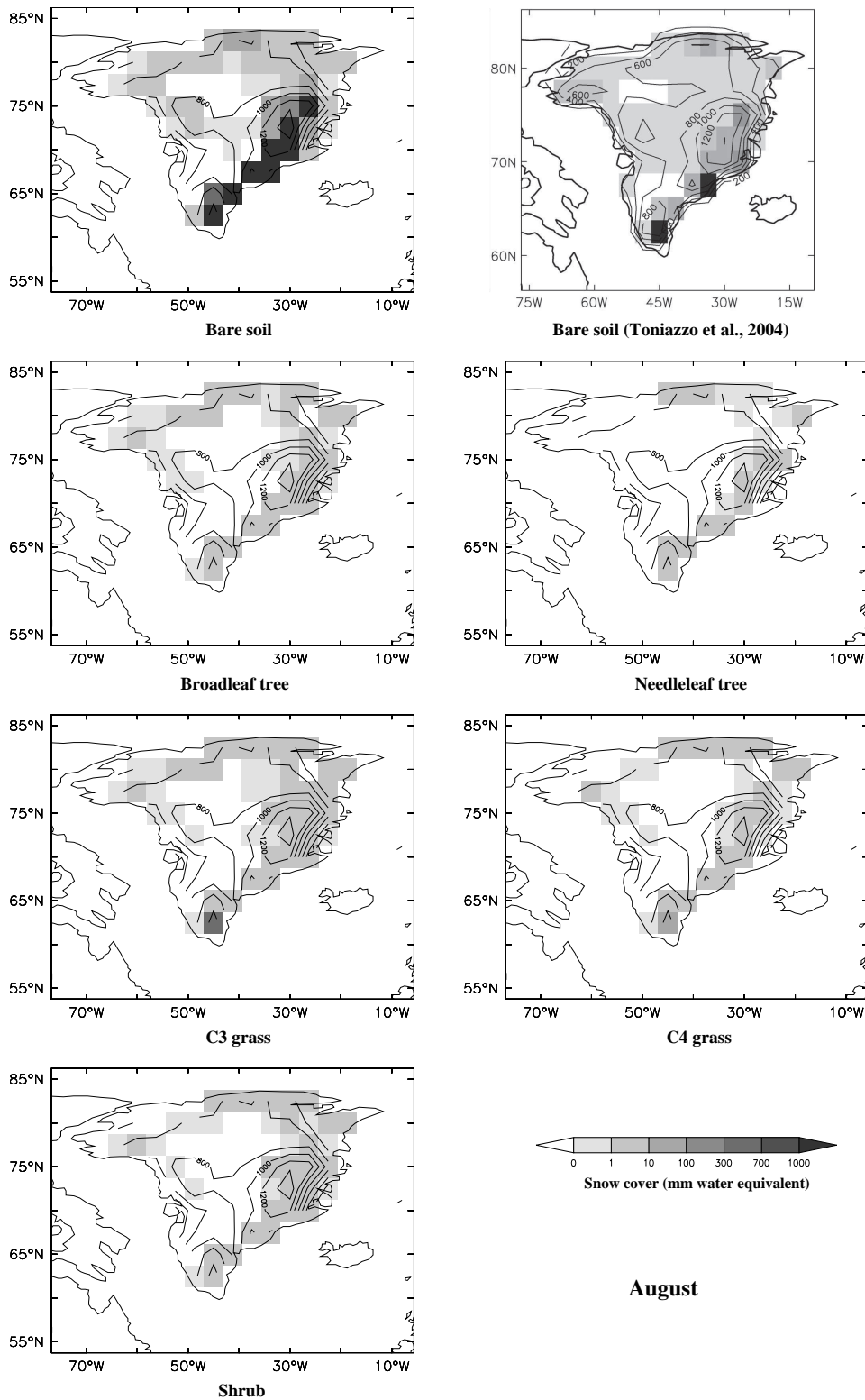


Figure 3.32: Average August snow cover over Greenland for the control and noGrIS<sub>reb</sub> simulations. Overplotted are levels of constant orographic height in metres at intervals of 200 m. The subfigure at the top-right is taken from Toniazzo *et al.* (2004) who performed a similar experiment with bare soil surface type.

coast in synchronicity with the eastern mountain range. This pattern is similar to that observed by Toniazzo *et al.* (2004). By summer, there is a substantial decrease in snow cover for all noGrIS<sub>reb</sub> experiments. In central, northern and western regions much of Greenland is snow-free similar to Toniazzo *et al.* (2004). For the PFT noGrIS<sub>reb</sub> simulations in this study much of the rest of Greenland is covered by no more than 1 mm of snow cover which is not significant in terms of longterm accumulation. Where the PFT simulations differ most from bare soil is the eastern regions of Greenland with snow cover in the PFT simulations no greater than 100 mm. For bare soil, however, a substantial part of this region has snow amounts not dissimilar to February. Needleleaf tree shows overall the least snowfall cover with no more than 10 mm in any region. There is a larger snow amount in the south for C3 grasses compared with the the other noGrIS<sub>reb</sub> simulations although this only occurs in one grid cell. This large variability in the south of Greenland could be explained by insufficient resolution of the orography as discussed in Toniazzo *et al.* (2004).

The snow diagnostic was also examined by Crowley and Baum (1995) for a surface covered with bare soil and a rough representation of mountains for the bedrock. They found that snow cover varied vastly throughout the year. Over the length of their simulation snow accumulated by over one metre each year, similar to that observed in winter in this study. However, during the summer the energy balance was enough to melt the snow completely leaving at least two snow-free months for the experiment of Crowley and Baum (1995). This variation, however, only reflects accumulation in the central region of Greenland. The inadequate resolution of the high mountainous regions in the Crowley and Baum (1995) study is likely the reason for the difference in snow accumulation compared with HadCM3 MOSES 2. Lunt *et al.* (2004) also found no accumulation in the final year of their regrowth study with only the possibility of ice growth development in Ellesmere Island northwest of Greenland.

### **Atmospheric circulation over a deglaciaded Greenland**

Significant differences in the low-level atmospheric circulation over Greenland, when only the surface type is changed to any one of the PFTs (discussed in Section 3.3.3), occurs during the summer months where cyclonic flow develops as opposed

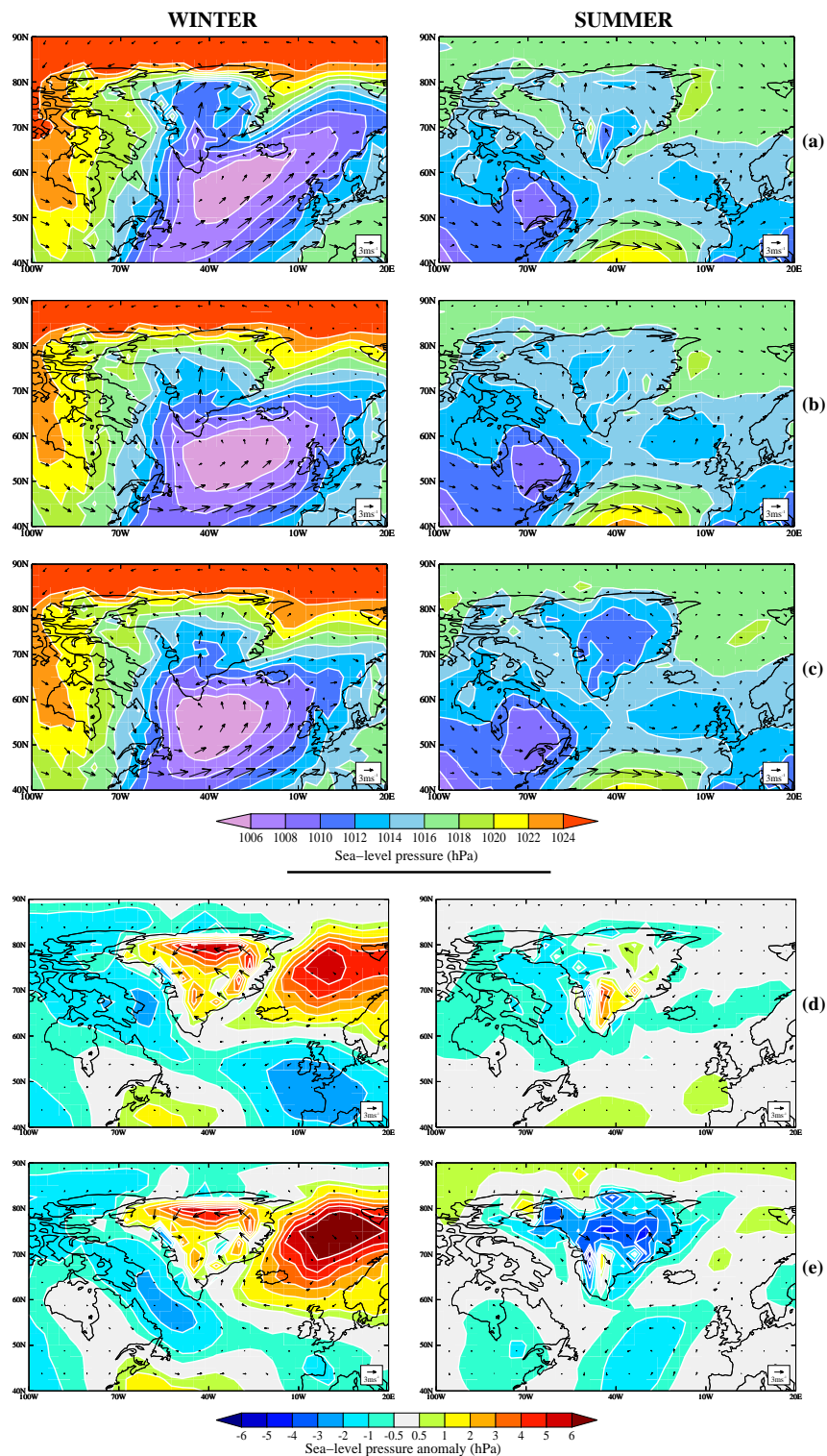


Figure 3.33: Winds at pressure level 3 corresponding to 850 hPa over a surface at sea-level (shown by arrows). Filled contours refer to sea-level surface pressure in hPa. (a) preindustrial control, (b) noGrIS<sub>reb</sub> bare soil, (c) noGrIS<sub>reb</sub> needleleaf tree, (d) noGrIS<sub>reb</sub> bare soil minus preindustrial control and (e) noGrIS<sub>reb</sub> bare soil minus preindustrial control.

to anticyclonic flow in the control. When the orography is lowered and surface type remains unchanged (lowGrIS) the flow is more cyclonic in both winter and summer with incomplete blocking of cold low-level air masses in the west of the island. Figure 3.33 shows the low-level circulation and surface pressure when the orography is lowered and the surface type changed together. Only the noGrIS<sub>reb</sub> bare soil and needleleaf simulations are shown but the other PFTs show similar wind and surface pressure patterns varying in intensity between these two. During the winter the difference in low-level circulation is similar for both surface types (left panel of Figures 3.33d and e) with a change from anticyclonic flow to more cyclonic flow. This is predominately the result from lowering the orography since it is similar to the wind pattern shown for the lowGrIS simulation. However, during the summer months the change in low-level winds compared with the control is dominated by changing the surface type of Greenland as result of enhanced thermal forcing. Note also that the changes in circulation in the summer are stronger for needleleaf trees as a result of more shortwave flux absorbed at the surface as well as larger sensible and latent heat fluxes away from the surface.

The high sea-level pressure region over the Barents Sea, observed in the lowGrIS simulation and the PFT noGrIS<sub>mod</sub> simulations during winter, is also observed in these noGrIS<sub>reb</sub> simulations as a result of a reduction in cyclogenesis in this region and off the southern coast of Greenland. Furthermore, during winter and summer, the changes in surface pressure exhibit non-linear behaviour where noGrIS<sub>reb</sub> needleleaf tree simulation has a surface pressure up to 3 hPa larger than when contributions from noGrIS<sub>mod</sub> needleleaf and lowGrIS are added together. During summer the opposite is found whereby noGrIS<sub>reb</sub> needleleaf tree has a surface pressure up to 3 hPa smaller over the Barents Sea compared with noGrIS<sub>mod</sub> linearly combined.

These results confirm changes in temperature during winter are not only the result of the lapse rate correction for altitude change but also due to local changes in atmospheric circulation. However, during the summer changes in temperature are dominated by increased absorption of shortwave radiation at the surface due to the change in surface albedo for the different surface types. A similar conclusion was also found by Toniazzo *et al.* (2004).



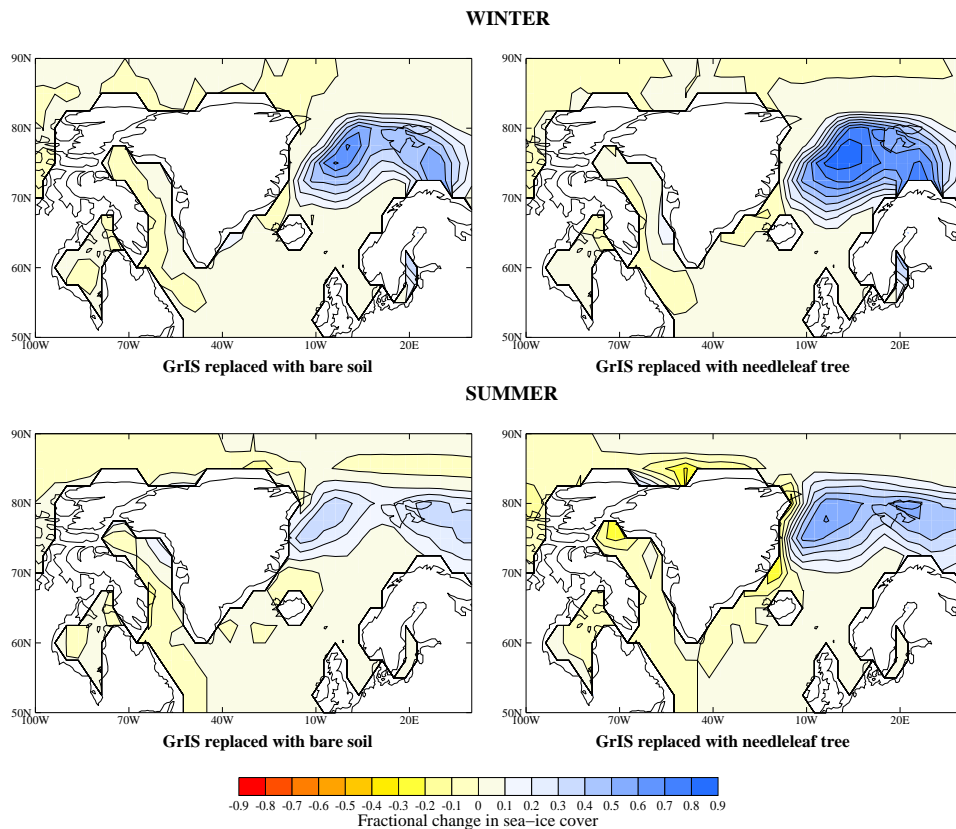


Figure 3.34: The fractional change in sea-ice cover for the winter and summer months for noGrIS<sub>reb</sub> bare soil and needleleaf tree simulations minus preindustrial control. Results from other surface types are not shown but show a similar pattern and magnitude.

### Sea-ice and oceanic circulation

The changes observed in sea-ice concentration, east of Greenland, for the noGrIS<sub>mod</sub> simulations (Figure 3.18) and also the lowGrIS simulation (not shown) occur when both the surface type and orography are changed together. Figure 3.34 shows the fractional change in winter and summer for a surface replaced with bare soil and needleleaf tree and the orography is rebounded. The other surface types (not shown) show a similar pattern ranging in intensity between these two extremes. Where there is an increase in sea-ice concentration there is also the concomitant decrease in the ocean mixed layer depth. Evaporation from the Barents Sea region is reduced by more than  $4 \text{ mm day}^{-1}$  for the noGrIS<sub>reb</sub> simulations with a more extensive region covered by this evaporative deficit for needleleaf trees relative to the preindustrial control.

For all simulations the ocean heat transport (not shown) is reduced throughout the North Atlantic compared with the control. Needleleaf tree shows the largest

change with a heat transport reduction of over 0.1 PW. The C3, C4 grasses and bare soil show the least reduction in poleward heat transport in accordance with a smaller change in sea-ice concentration compared with needleleaf trees. At latitudes greater than 60°N the reduced poleward heat transport is dominated by the reduction of subpolar gyre heat transport compared with the control for all surface types. The largest reduction in the subpolar gyre heat transport occurs for a surface covered by needleleaf trees by up to 0.125 PW.

When the surface is covered with a PFT, lowering the orography and changing the surface type enhances the reduction in heat transport primarily at high latitudes by the gyre ocean currents and results in an increase in sea-ice concentration in the Barents Sea. In contrast, the reduction in oceanic heat transport at high northern latitudes for the noGrIS<sub>reb</sub> experiment with a surface covered by bare soil, is primarily attributed to lowering of the orography with little influence from changing the surface type from ice to bare soil. There is no evidence of a significant change in the strength of the Atlantic MOC for any of the simulations consistent with the results found by Toniazzo *et al.* (2004).

### 3.4 Discussion and conclusions

This chapter focussed on describing and understanding the changes to the climate over Greenland when the ice-sheet is removed and replaced with different surface types and topography. Sensitivity to changing surface type showed that temperature changes over Greenland are controlled fundamentally by the albedo (as opposed to the surface roughness length) of the surface with broadleaf and needleleaf trees resulting in the largest anomalies during the summer months. During winter, only small changes in temperature and precipitation occur with insignificant changes to low-level circulation patterns. In the summer months the increase in thermal forcing results in changes to the hydrological cycle with an increase in moisture availability and hence latent heat flux and the potential for increased rainfall. Roughness length does not change the temperature over Greenland significantly or the precipitation pattern. However, the increase in turbulent surface fluxes when roughness length is increased results in cooler temperatures over the Barents Sea and an increase in sea-ice.

Lowering the orography of Greenland results in less precipitation at the south-eastern tip of Greenland but precipitation increases further north along the eastern coast spreading into the interior of the island. The decrease in altitude not only has the effect of increasing temperatures over Greenland compared with the control due to the temperature-altitude relationship but also changes the pattern of low-level atmospheric circulation during winter and summer with cooler temperatures over northwestern Greenland due to reduced blocking of cold air masses west of the island. Thus changes in atmospheric circulation patterns as a result of lowering the orography are important in controlling some of the temperature change observed over a melted, rebounded Greenland particularly during the winter months. This result contrasts with Lunt *et al.* (2004) which suggested that changes in circulation patterns were not important in controlling local temperature changes.

Simulations were subsequently performed where elevation was lowered to a rebounded state after removal of the GrIS and the surface type changed to bare soil and the PFTs. During the winter temperature anomalies are similar for all experiments and attributed to the change in altitude and also changes in local atmospheric circulation. However, summer temperatures are dominated by vegetation-snow-climate feedbacks as a result of increased absorption of shortwave radiation and sensible heat fluxes. However, non-linearity exists between noGrIS<sub>reb</sub> and noGrIS<sub>mod</sub> plus lowGrIS due to interactions between lowering the surface and changing the surface type. On average the temperature anomalies are greater for noGrIS<sub>reb</sub> than when the individual sensitivities are linearly combined.

The question of whether the GrIS could regrow has been addressed by others (e.g. Toniazzo *et al.*, 2004; Crowley and Baum, 1995) using diagnostics such as snow amount in the absence of any ice-sheet model. From this study, a surface covered by bare soil indicates that there is the possibility of regrowth of an ice-sheet based on snow cover accumulations in the elevated bedrock regions of eastern Greenland. This pattern, however, is not observed for any of the PFTs. Changing to a vegetated surface also acts to alter the hydrological cycle considerably with increases in evaporation and surface run-off due to increased moisture availability from transpiration and retention of water in the canopy available for evaporation. This results in larger latent heat fluxes during the summer months which provides the moisture for the observed increase in cloud formation and precipitation over the

Greenland region. Changes in atmospheric circulation due to changes in orographic height and enhanced thermal forcing over Greenland during the summer result in a reduction in ocean gyre poleward heat transport in the vicinity of the Barents and Norwegian sea regions by reducing the cyclogenesis occurring off the south eastern coast. An outcome of this is an increase in sea-ice development and associated cooling of sea surface and near-surface air temperatures during the winter. The reason for the increase in sea-ice in the study of Lunt *et al.* (2004) was attributed purely as an atmospheric circulation feedback. They noted in their model an increase in meridional atmospheric heat transport from the poles southwards over the Barents Sea resulting in colder air near the surface and therefore an increase in sea-ice coverage relative to the control. Although changes in atmospheric circulation also occur in this study it is the transport of heat in the ocean rather than the atmosphere that controls the increase in sea-ice east of Greenland. A reduction in cyclone development south east of Greenland as a result of a shift in the wind-driven ocean currents reduces the heat transport into the ocean basins near Greenland. A similar result was also found by Toniazzo *et al.* (2004) and Ridley *et al.* (2005).

Clearly, vegetation type has a profound effect on the climate over Greenland and its close surroundings increasing summer temperatures on average by as much as 16°C relative to the control, reducing ocean heat transport at high latitudes in the North Atlantic and changing low-level atmospheric circulation and precipitation patterns. According to the snow cover diagnostic it is likely that unless the surface type remains as bare soil the GrIS could not regrow. However, it is highly unrealistic that only one surface type would be present over a melted Greenland. Furthermore, although it is possible that bare soil, C3 grasses, shrubs and needleleaf trees might be found on Greenland if it were to completely melt, the development of C4 grasses and broadleaf trees would be highly unlikely since these are generally found in mid to low latitude regions of the Earth. The next chapter builds on this work by allowing the vegetation over Greenland to dynamically evolve and equilibrate with the climate by letting interactions between land surface, atmosphere and ocean to take place.

# The response of vegetation to a melted Greenland ice-sheet

## 4.1 Introduction

Many studies over the last few decades have considered the importance of vegetation-atmosphere interactions at various temporal and spatial scales ranging from microclimates (e.g. Aussenac, 2000) to global climate dynamics (Crucifix *et al.*, 2005). In order to realistically model the impact of vegetation on the climate over a deglaciated Greenland and its irreversibility, it is necessary to allow the vegetation to evolve and feedback on the atmosphere. Although several studies have examined the role of vegetation feedbacks on the inception of Northern Hemisphere ice-sheets at the beginning of the last glacial period using interactive vegetation models (e.g. Meissner *et al.*, 2003; Calov *et al.*, 2005b; Kubatzki *et al.*, 2006), few have examined the importance of vegetation feedbacks on the future regrowth of the GrIS if it were to completely melt in the future. Only one study has looked at the potential for regrowth over Greenland with a fully coupled climate - vegetation - ice-sheet model (Vizcaíno *et al.*, 2008) but this used an Earth System Model with a lower horizontal resolution ( $\sim 5.6^\circ$  by  $5.6^\circ$ ) than HadCM3 and the result in terms of vegetation response was not examined in detail. Offline forcing of a vegetation model using output from a full GCM (Lunt *et al.*, 2004) found that there was the potential for tree growth in southern Greenland with other regions covered predominantly by grasses. This led to the conclusion that the climatology used to force their ice-sheet model offline would have been more appropriate if the surface in the climate model had represented a mixture of trees and grasses rather than the prescribed tundra surface that was actually implemented.

Chapter 3 examined the sensitivity to *fixed* surface type over Greenland and change in orographic height as a result of the GrIS melting. This chapter builds on previous GrIS regrowth studies which considered vegetation feedbacks (Crowley and

Baum, 1995; Lunt *et al.*, 2004) by simulating the climate with a fully coupled interactive vegetation-climate model. The first section of this chapter briefly compares a number of Dynamic Global Vegetation Models (DGVMs) that are currently in use, followed by a model description and validation of the TRIFFID DGVM, used in conjunction with HadCM3 in this thesis. Sensitivity of the model to initial surface conditions over Greenland is explored and the impact of vegetation on the climate over Greenland and the potential for ice inception discussed.

## 4.2 Vegetation model description and evaluation

In order to assess the importance of climate vegetation feedbacks it is necessary to include an interactive vegetation component within a coupled AOGCM. This section begins by describing some of the aspects of the various DGVMs in the current literature in order to put into context the one used in this thesis. A range of DGVMs exist with varying degrees of complexity and computational efficiency. An example of a relatively simple DGVM is VECODE (Bromwich *et al.*, 1998; Brovkin *et al.*, 2002) which predicts the fractional contribution of grasses, trees and bare soil and the Net Primary Productivity (NPP) of a particular gridbox. This is based on an empirically derived function of precipitation and temperature. Vegetation structure is updated every year. Due to its computational efficiency it can be included within EMICs such as CLIMBER and LOVECLIM, which allows simulations of long time integrations to be performed. The future GrIS melting study by Driesschaert *et al.* (2007) discussed in Section 1.4 used this DGVM.

More recent DGVMs have either used the ‘bottom up’ approach which explicitly model the growth, death and competition of individual plants or the ‘top down’ approach which models the relevant land surface characteristics such as vegetated fraction and LAI directly.

Hybrid (Friend *et al.*, 1997) is an example of a DGVM that uses the ‘bottom up’ approach. It simulates individual trees and layers of grass competing for moisture, nitrogen and light. The model is run several times for each gridbox and then scaled up to gridbox size. The vegetation structure is updated every year. This is a very computationally expensive method of vegetation modelling and therefore this type of DGVM cannot easily be included interactively in full GCMs. Furthermore, on

such a small, detailed scale, GCMs are unlikely to be sensitive to any changes in individual species and the age composition of the landcover. LPJ (Sitch *et al.*, 2003) is another such DGVM that uses the ‘bottom up’ approach but in order to overcome the computational inefficiency that Hybrid experiences it simulates PFTs rather than individual plants and can therefore be included interactively in GCMs such as the one used by Vizcaíno *et al.* (2008). Vegetation is also updated every year. ORCHIDEE (Krinner *et al.*, 2005) used in the study of Lunt *et al.* (2004) is another example of the ‘bottom up’ approach where its parameterisation of vegetation dynamics (e.g. climatic criteria for the introduction/elimination of PFTs) is based on LPJ. It is designed to be interactively coupled with the IPSL-CM4 coupled atmosphere-ocean-vegetation model although can also be run offline. The land-surface is described as a mosaic of 12 PFTs and bare soil and each of these 13 surface descriptors can simultaneously occupy the same grid box.

IBIS (Foley *et al.*, 1996; Kucharik *et al.*, 2000) is an example of a ‘top down’ DGVM. It simulates gridbox vegetation in two layers: tree layer canopy and grass layer canopy where the PFTs compete for light and moisture. Vegetation is updated annually depending on the annual mean carbon fluxes. A second example, and the one used here is TRIFFID (Top-down Representation of Interactive Foliage and Flora including Dynamics) and is coupled to HadCM3 (Cox *et al.*, 2000). In this model PFTs compete horizontally where shrubs displace grasses and trees displace grasses and shrubs. Competition between species (i.e. different tree and grass types) is also modelled explicitly. Vegetation structure is updated every 10 days based on carbon fluxes from the land surface scheme, MOSES 2, in HadCM3. This version of HadCM3 has been used to simulate vegetation cover in several palaeostudies related to the mid-Pliocene and adequately supports palaeoenvironmental reconstructions and geological proxy data (Haywood and Valdes, 2006; Francis *et al.*, 2007; Salzmann *et al.*, 2008). It has also previously been used to assess the importance of vegetation atmospheric interactions in order to direct future efforts in model development (Crucifix *et al.*, 2005).

The following sections outline the mechanisms of the TRIFFID DGVM and the coupling with the MOSES 2 land surface scheme. For a complete description the reader is referred to Cox (2001).

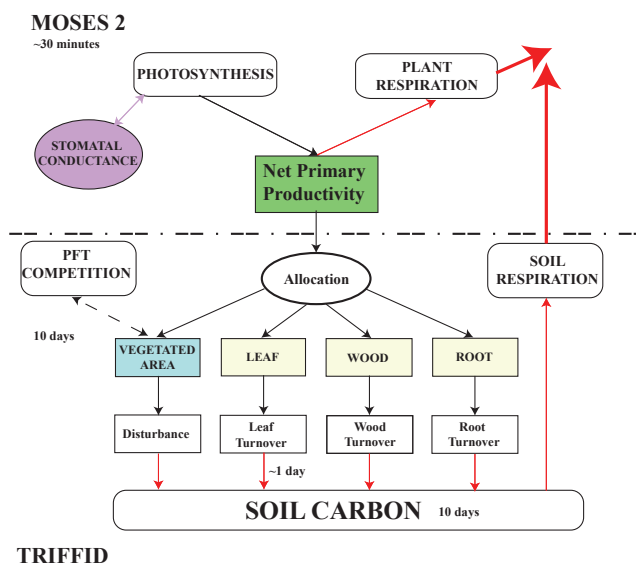


Figure 4.1: Schematic illustrating the flow of carbon for each vegetation type in the TRIFFID vegetation model. The processes shown above the dotted line are the fluxes calculated in the MOSES 2 land surface scheme for each atmospheric timestep. Under the fully coupled dynamic mode the vegetation and soil are updated every 10 days in TRIFFID (*modified from Cox (2001)*).

#### 4.2.1 Coupling to the land surface scheme, MOSES 2

The terrestrial biosphere is defined in terms of the structure and coverage of the five PFTs (broadleaf trees, needleleaf trees, C3 grasses, C4 grasses and shrubs) discussed in Chapter 3. Within TRIFFID, the coverage, LAI and canopy height of each PFT are updated using a ‘carbon balance approach’. Vegetation change is ultimately driven by net carbon fluxes calculated within the MOSES 2 land surface scheme (Cox *et al.*, 1999). A coupled photosynthesis-stomatal conductance model (Cox *et al.*, 1998) is used to derive the carbon fluxes for each PFT with the resultant rates of photosynthesis and plant respiration being dependent on climate and atmospheric CO<sub>2</sub> concentration. Thus, the response of vegetation to climate occurs via the climate-induced changes in the vegetation to fluxes of atmospheric carbon. Figure 4.1 shows a schematic of the coupling between TRIFFID and MOSES 2 for each vegetation type. The processes above the dotted line are fluxes calculated in MOSES 2 at every atmospheric timestep (every 30 minutes in HadCM3) and are time-averaged before being passed to TRIFFID (usually every 10 days in fully dynamic mode) where the average NPP is allocated between the growth of the existing vegetation (leaf, root and wood biomass) and the expansion of the ‘vegetated area’. In addition, leaf phenology is updated on an intermediate timescale of about one day using accumulated temperature dependent leaf turn-over rates. The final stage



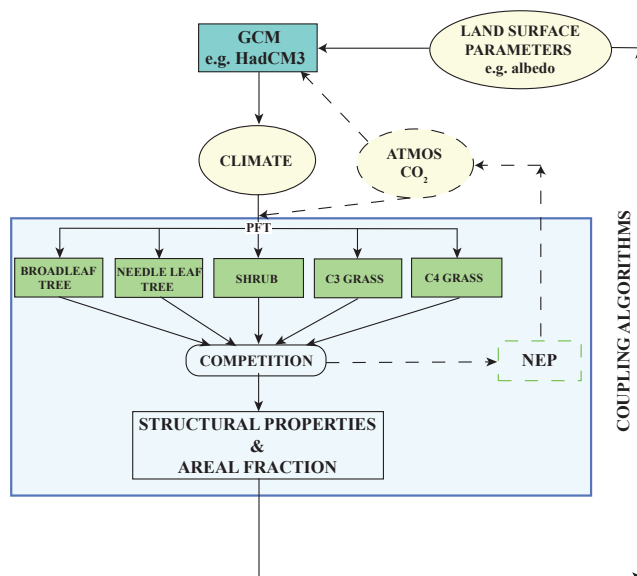


Figure 4.2: Schematic illustrating the coupling between TRIFFID and a GCM (in this case HadCM3). The region highlighted in blue describes the processes occurring within the TRIFFID model. Changes in the distribution and structure of the five PFTs provide a feedback to the climate via two routes. The first highlighted with solid arrows determines the biophysical land-surface parameters which in turn affects the the land-atmosphere heat fluxes. The second, highlighted with dashed arrows, results by changes in carbon stored in the vegetation and soil which can change the evolution of atmospheric  $\text{CO}_2$  and therefore the climate through the greenhouse effect. (*modified from Cox (2001)*). In this study the second route that feeds back on  $\text{CO}_2$  is switched off.

in the coupling between TRIFFID and the land surface scheme involves updating the land-surface parameters required by MOSES 2 (e.g. surface roughness length and albedo) based on the new vegetation state. This ensures that changes in the biophysical properties of the land surface, as well as changes in terrestrial carbon are fed back to the atmosphere. The structure depicted in Figure 4.2 ensures that there is a consistency between surface hydrological states ‘observed’ by the atmosphere and the vegetation.

### 4.2.2 Vegetation dynamics

The following equations describe how the vegetation carbon density,  $C_v$  (Equation 4.1), and fractional coverage,  $\nu$  (Equation 4.2), of a given PFT are updated based on carbon balance of the PFT and on competition with other PFTs:

$$\frac{dC_v}{dt} = (1 - \lambda)\Pi - \Lambda_l, \quad (4.1)$$

$$C_v \frac{d\nu}{dt} = \lambda \Pi \nu_* \left\{ 1 - \sum_j c_{ij} \nu_j \right\} - \gamma_v \nu_* C_v, \quad (4.2)$$

where  $\nu_*$  is the fractional coverage of a PFT if  $\nu$  is greater than 0.01 otherwise it is equal to 0.01,  $\Pi$  is the NPP per unit vegetated area of the PFT being analysed,  $\Lambda_l$  is the litterfall rate on a PFT and represents the loss of carbon matter resulting from the natural life cycle of the vegetation and makes up contributions from leaf, root and stem carbon. In Equation 4.2,  $\gamma_\nu$  is a disturbance parameter and incorporates the effects of mortality arising from processes other than competition with other PFTs, e.g. fire. This is calculated in the MOSES 2 land surface scheme. The NPP is split (according to the fraction  $\lambda$  and  $1-\lambda$  respectively) between increasing the fractional coverage in Equation 4.2 and increasing the carbon content of the existing vegetated area in Equation 4.1. This partitioning coefficient,  $\lambda$ , is assumed to be piecewise linear in the LAI with all NPP used for *growth* for small LAI values and all NPP being used for *spreading* for large LAI values. It is defined as

$$\lambda = \begin{cases} 1 & \text{for } L_b > L_{max} \\ \frac{L_b - L_{min}}{L_{max} - L_{min}} & \text{for } L_{min} < L \leq L_{max}, \\ 0 & \text{for } L \leq L_{min} \end{cases} \quad (4.3)$$

where  $L$  is the LAI and  $L_{min}$  and  $L_{max}$  are minimum and maximum values specified for each PFT. Finally,  $L_b$  is the ‘balanced’ LAI which would be reached if the plant was in full leaf.

Although Equation 4.1 represents carbon balance, found in most terrestrial carbon cycle models, TRIFFID is different in that it is also coupled to Equation 4.2 based on the Lotka-Volterra approach to interspecies and intraspecies competition (Gotelli, 2001). The competition coefficients,  $c_{ij}$ , describe the impact of vegetation type ‘ $j$ ’ on vegetation type ‘ $i$ ’ (vegetation type of interest). Their coefficients lie between zero and one and are shown in Table 4.1. Intraspecies competition also occurs for each PFT such that vegetation fraction is always limited to be less than one. Intraspecies competition between natural PFTs is dependent on a tree-shrub-grass dominance hierarchy where dominant types ‘ $i$ ’ act to limit the expansion of subdominant types ‘ $j$ ’ (i.e.  $c_{ji}=1$  and  $c_{ij}=0$ ). As such shrubs automatically displace grasses, and trees displace grass and shrubs. There is also competition between the tree types (broadleaf and needleleaf) and the grass types (C3 and C4) where competition coefficients are dependent on their relative heights according to

|             | <b>i=BL</b> | <b>i=NL</b> | <b>i=C3</b> | <b>i=C4</b> | <b>i=SH</b> |
|-------------|-------------|-------------|-------------|-------------|-------------|
| <b>j=BL</b> |             | *           | 1           | 1           | 1           |
| <b>j=NL</b> | *           |             | 1           | 1           | 1           |
| <b>j=C3</b> | 0           | 0           |             | *           | 0           |
| <b>j=C4</b> | 0           | 0           | *           |             | 0           |
| <b>j=SH</b> | 0           | 0           | 1           | 1           |             |

Table 4.1: Intraspecies competition between the PFTs in TRIFFID. The entry “\*” is given by Equation 4.4 and relates to competition within species. A value of 0 indicates that PFT,  $i$ , dominates PFT,  $j$ , and a value of 1 indicates PFT,  $j$ , dominates PFT,  $i$ .

$$c_{ij} = \frac{1}{1 + \exp \{20 (h_i - h_j) / (h_i + h_j)\}}, \quad (4.4)$$

where  $h_i$  is the vegetation height of PFT  $i$ .

### 4.2.3 Leaf phenology

Mortality rates of tree-type leaves are assumed to be a function of temperature increasing from a minimum value as the leaf temperature drops below a threshold value of 0°C for broadleaf trees and −30°C for needleleaf trees. However, this is not sufficient to produce a realistic phenology. A parameter which is updated daily,  $p$ , describes the phenological status assuming leaves are dropped at a constant rate when daily mean value of leaf mortality rate is twice its minimum value and budburst occurs at the same rate when leaf mortality rates drop below this threshold and ‘full leaf’ is approached. To ensure conservation of carbon the effective leaf mortality rate should also be updated when the phenological changes are occurring.

### 4.2.4 Soil carbon storage

The soil carbon storage,  $C_s$ , in each gridbox is increased by total litterfall ( $\Lambda_c$ ) and decreased by microbial soil respiration ( $R_s$ ). The total litterfall is determined by the local litterfall from each PFT, litterfall due to large-scale disturbance and PFT competition. The soil respiration is dependent on soil temperature, volumetric soil moisture concentration and soil carbon content.

### 4.2.5 Updating biophysical parameters

In order to feedback on the MOSES 2 land surface scheme and therefore close the feedback loop in Figure 4.2 it is necessary to update the land-surface parameters required by MOSES 2. These include aerodynamic roughness lengths, the snow-free

albedos of the vegetation types and the canopy water capacity described in Section 3.2.3. They are recalculated directly from the canopy height and the LAI of each PFT respectively each time the vegetation cover is updated. The values of canopy height,  $h$ , are determined by the total stem biomass. The canopy water capacity,  $C_m$ , which determines the amount of water that is freely available for evaporation, varies linearly with the LAI

$$C_m = 0.5 + 0.05L, \quad (4.5)$$

where the offset 0.5 represents interception by leafless plants and puddling of water on the soil surface. Other hydrological land-surface parameters are PFT dependent but do not depend on LAI or canopy height. Instead, root density falls off exponentially with depth such that it is  $e^{-2}$  of its surface value at a specified rootdepth. Rootdepths are 3.0 m for broadleaf trees, 1.0 m for needleleaf trees and 0.5 m for grasses and shrubs. The roots themselves are assumed to enhance the maximum surface infiltration rate for water by a factor of 4 for trees and 2 for the other PFTs.

#### 4.2.6 Spinning up TRIFFID

Soil carbon and forest area require timescales on the order of millennia to reach equilibrium resulting in it not being computationally feasible to spin-up TRIFFID using a fully coupled GCM. TRIFFID has therefore been designed to operate in both an ‘equilibrium’ and ‘dynamic’ mode. In equilibrium mode TRIFFID is coupled asynchronously to the atmospheric component of HadCM3. Accumulated carbon fluxes are passed from MOSES 2 every five years to TRIFFID (coupling period). The vegetation and soil variables are updated iteratively with a long internal timestep (50 years in this case). Thus a HadCM3 simulation of 100 years with TRIFFID in equilibrium mode is equivalent to 1,000 years of interactive vegetation. This approach is effective in producing equilibrium states for the slowest variables (soil carbon and forest cover) (Cox *et al.*, 2000). In dynamic mode the TRIFFID-GCM coupling period is typically 10 days. Although the equilibrium mode allows the slow components of the system to equilibrate it is often necessary to continue a simulation using dynamic mode in order to bring the faster varying components (e.g. grasses) into equilibrium with the seasonally varying climate.

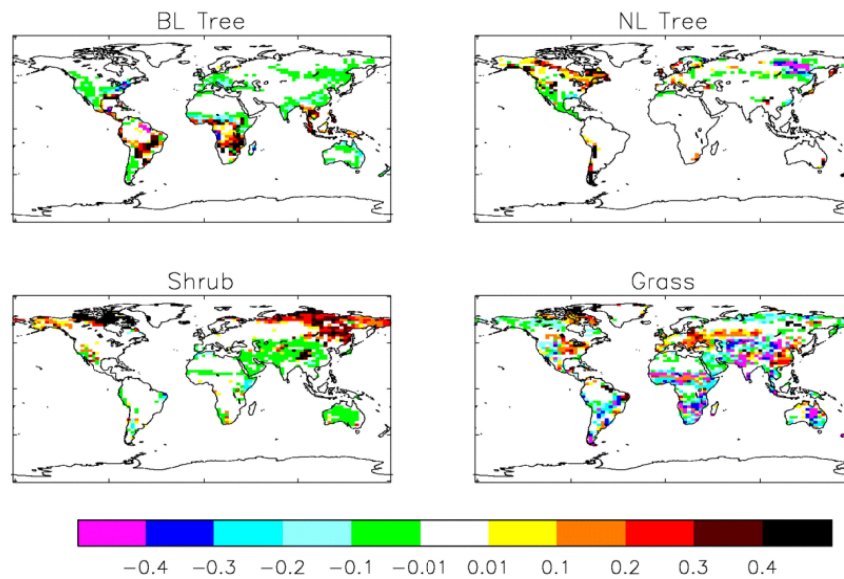


Figure 4.3: Comparison of modelled vegetation fractions with the IGBP-DIS land cover satellite observations (Loveland *et al.*, 2000). The plots show differences in the fractional coverage (model PFT minus IGBP observation) for each PFT in each land gridbox of HadCM3. Note that C3 and C4 grasses have been combined into a single prediction of grass distribution. This figure is reproduced from Betts *et al.* (2004).

#### 4.2.7 Model evaluation

Previous work has assessed the ability of MOSES 2 coupled to TRIFFID to predict global present day vegetation distributions adequately (Betts *et al.*, 2004). Figure 4.3 shows present day vegetation fractions compared with satellite observations (Loveland *et al.*, 2000) using HadCM3LC, a low resolution ocean (equivalent to the resolution of the atmosphere component of HadCM3) version of HadCM3 with the carbon-cycle included. Betts *et al.* (2004) concluded that MOSES 2 does a reasonable job at reproducing present day vegetation. However, this study focussed on differences between model observation at low latitudes, specifically a dry bias in the Amazon Forest preventing the growth of trees and a southward shift of the Sahara-Sahel interface by  $3^\circ$  to  $5^\circ$  hypothesised to be due to an under representation of vegetation feedbacks in this region. This latter deficiency in the model is present in several GCMs when modelling the vegetation in the Sahara for the mid-Holocene 6,000 years ago (Joussaume *et al.*, 1999). This thesis, however, is concerned with vegetation feedbacks at northern high latitudes which is a different issue.

A preindustrial control simulation has been performed initiated from the end of the fixed vegetation preindustrial control simulation with the Letreguilly GrIS dataset included and is described in Chapter 3, Section 3.3.1. TRIFFID was first

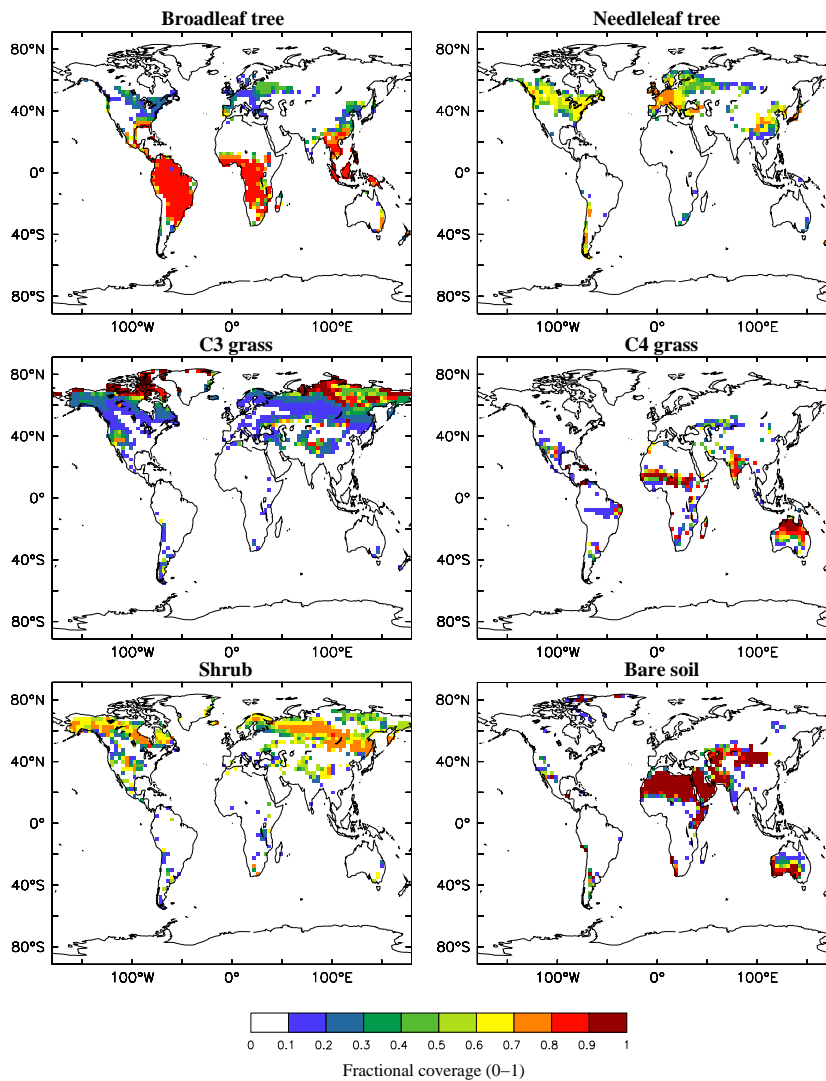


Figure 4.4: The average annual fractional coverage of the PFTs and bare soil in the preindustrial control simulation using HadCM3 and TRIFFID in dynamic mode.

run for 200 years in equilibrium mode which is equivalent to 2,000 years of vegetation simulation. The simulation was then switched to dynamic mode for a final 200 years in order for the faster varying components to equilibrate with the seasonally varying climate. Figure 4.4 shows the average vegetation fractions for the PFTs and bare soil for the last thirty years of this experiment. C3 grasses, although scattered across the globe, are dominant mainly in the high latitude regions of the Northern Hemisphere. C4 grasses are dominant in a very much warmer climate particularly over much of Australia and at the Sahara-Sahel interface in Africa and in the Sahel itself. Shrub distribution is found isolated in various regions across the Earth but dominates in the mid-high latitudes. Where shrubs and grasses are not present these regions are dominated by bare soil or trees. For example, much of North Africa is

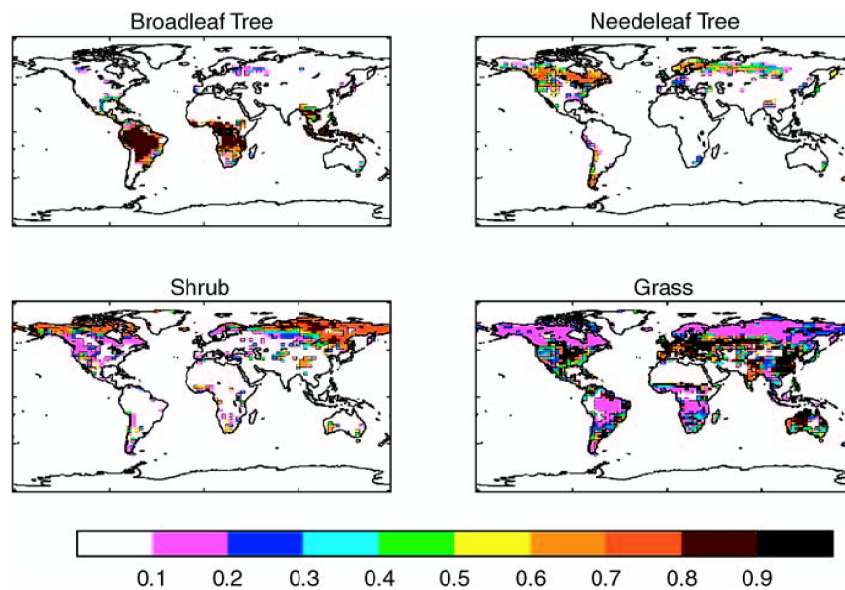


Figure 4.5: The average (30 years) annual fractional coverage of PFTs simulated by the HadCM3LC preindustrial control simulation of Betts *et al.* (2004). Note that C3 and C4 grasses have been combined into one grass vegetation distribution. Figure reproduced from Betts *et al.* (2004).

covered by bare soil consistent with the arid conditions of the Sahara. Broadleaf trees are found in tropical regions particularly over South America. The needleleaf trees are restricted to the boreal regions of the Northern Hemisphere. These results can be compared with the vegetation distribution for Betts *et al.* (2004) in Figure 4.5. The broadleaf tree distribution is similar in Africa, South America and Australia. However, the simulation presented here predicts more of this vegetation type in Europe, North America and the Far East. A greater fraction of needleleaf trees are predicted in Europe compared with Betts *et al.* (2004) and the Far East but there is a similar pattern over North America. Spatially, the distribution of shrubs is comparable between this study and Betts *et al.* (2004). However, Betts *et al.* (2004) predicted large fractions of shrubs in high latitude regions of Siberia. As a result of this under prediction of shrub the hierarchy system of TRIFFID results in C3 grass domination in these regions in this study compared with Betts *et al.* (2004). The region of grasses observed in northeast Amazonia which did not agree with observations in the Betts *et al.* (2004) study is also present in this simulation. The difference in vegetation coverage between the preindustrial control simulation in this thesis and the one in Betts *et al.* (2004) could be attributed to different land-use representations. Betts *et al.* (2004) used near-current agricultural land-use with an anthropogenic disturbance mask imposed. Anthropogenic disturbance in the model

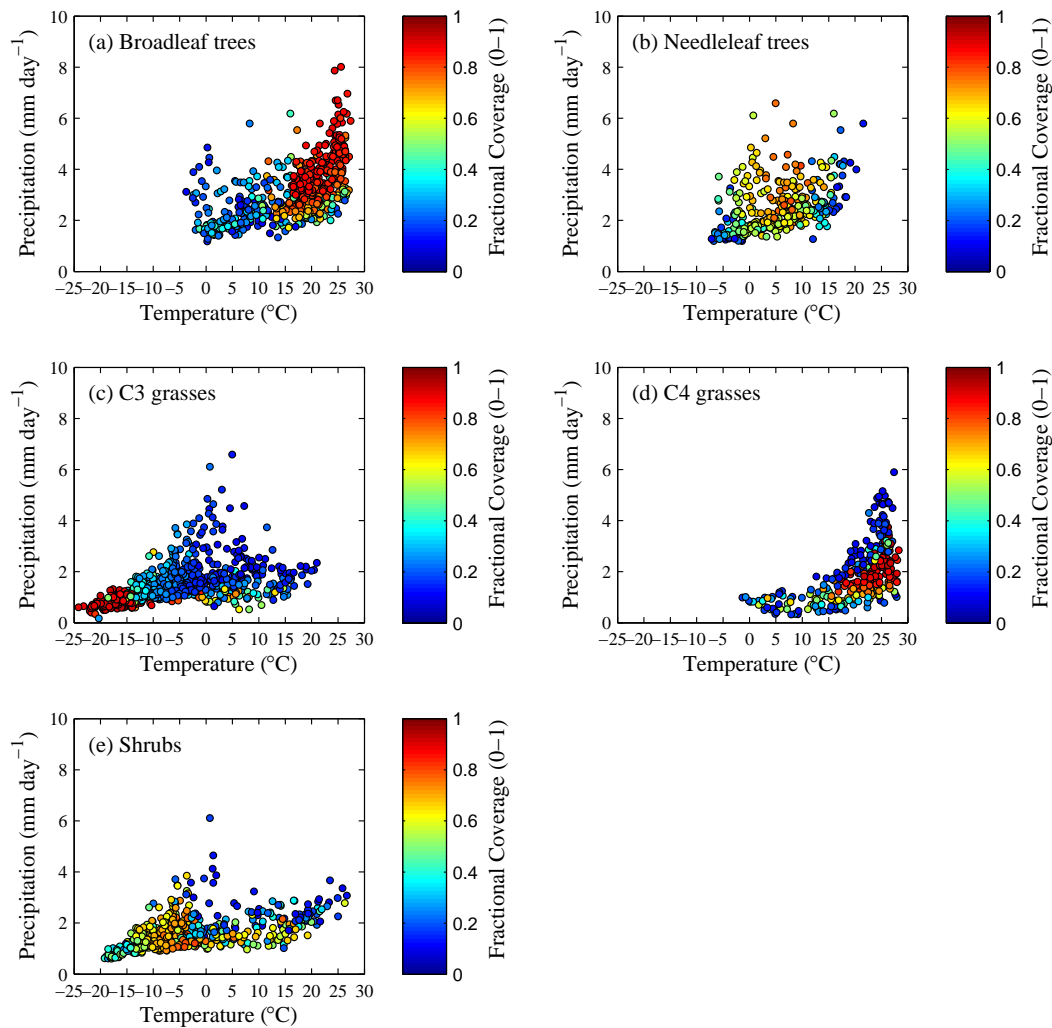


Figure 4.6: The annual tolerance of the PFTs in terms of near-surface air temperature and precipitation for all gridboxes where the PFT has a fractional coverage of 10 % or more. This is the annual vegetation distribution for the control simulation. The colorbar shows the fractional coverage. The PFTs and their maximum fractional coverage for the different PFTs are (a) broadleaf trees (0.89), (b) needleleaf trees (0.80), (c) C3 grasses (0.94), (d) C4 grasses (0.96) and (e) shrubs (0.81).

is represented with a land-use mask as a constraint on the vegetation dynamics. As a result trees and shrubs are excluded from the deforested or cultivated fraction of the gridbox, and only grasses are permitted. Thus grasses can implicitly also represent crops. However, no disturbance mask is used in the version of HadCM3 MOSES 2 in this thesis and therefore distribution of trees and shrubs will differ with the Betts *et al.* (2004) study. It is also worth noting that different versions of HadCM3 (i.e. the low resolution of the ocean model in Betts *et al.* (2004)) are used.

Figure 4.6 shows where each PFT in climate space is predicted more than 10 % fractional coverage. This climate space is defined in terms of near-surface air temperature (in °C) and precipitation (in mm day<sup>-1</sup>) at all HadCM3 gridboxes



for a preindustrial climate, similar to the approach used by Hughes (2003). Each PFT occupies a relatively unique region of climate space in this preindustrial control simulation. Figure 4.6a shows that broadleaf trees are abundant in warm (greater than  $15^{\circ}\text{C}$ ) and wet conditions. Needleleaf trees (Figure 4.6b) are more abundant however at much colder temperatures (generally between  $-5$  and  $10^{\circ}\text{C}$ ) and drier conditions compared with broadleaf trees. The C3 grasses (Figure 4.6c) cover a large proportion of the climate space but are most abundant at very cold (as low as  $-25^{\circ}\text{C}$ ), dry conditions. In contrast the C4 grasses are clustered mainly in the very warm and dry part of the climate space (Figure 4.6d). Finally, shrubs (Figure 4.6e) show less clustering than the other PFTs but are most abundant for temperatures between  $-5$  and  $5^{\circ}\text{C}$ . These results are similar to Hughes (2003) who performed a preagricultural simulation with HadSM3 (slab ocean version of HadCM3) with interactive vegetation. The tolerances of the PFTs in terms of precipitation and temperature also coincide with the dominant PFT environmental niches shown in Figure 4.4. For example, C4 grasses are predominantly found in low latitude regions where temperatures are very warm.

The final part of the validation of vegetation fraction for the control simulation is shown in Figure 4.7 by comparing the end of the simulation spin-up with the initial PFT fractional distribution based on the IGBP-DIS land cover satellite observations (Loveland *et al.*, 2000). Differences in each PFT and bare soil are shown between the average annual fraction and the IGBP-DIS dataset. This discussion focusses on the change in vegetation types at high latitudes as this is the focus of this thesis. There are no major differences in broadleaf tree between IGBP-DIS and the spun-up fractional distribution with only a slight reduction in North America. This is expected since this tree type is confined to warmer and wetter conditions. Needleleaf trees, however, shows a significant reduction at high northern latitudes in North America and Northern Europe and expansions of this tree type at mid-latitudes for Europe and North America. C3 grasses show a significant expansion of grasses (between 50 and 100 %) at high latitudes with no differences in C4 grasses. Finally, the shrubs show a decrease in northern Canada and increase in mid-latitude America and Europe. Specifically, in the ice-free regions of Greenland in HadCM3, vegetation evolves to include fractions of shrub and C3 grasses which is consistent with the types of vegetation found in the ice-free regions of modern day Greenland (Funder, 1989;

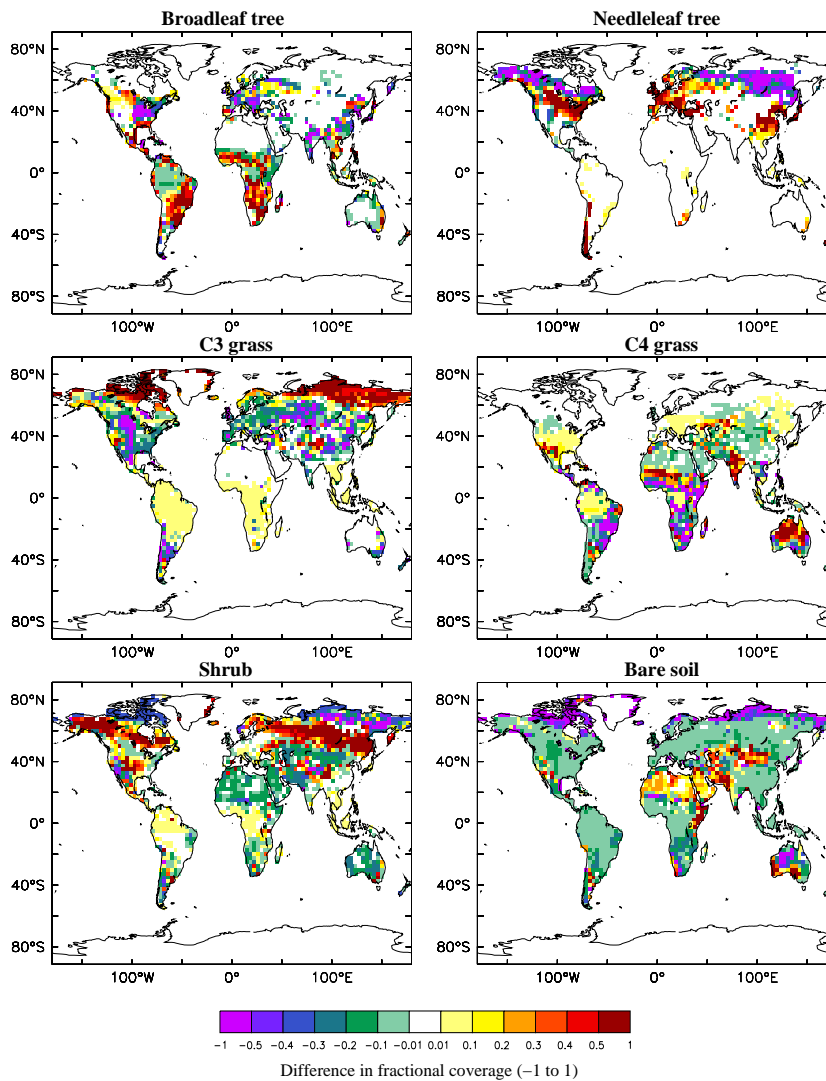


Figure 4.7: The average annual fractional coverage differences of PFTs and bare soil for the pre-industrial control simulation minus initial condition.

Drees and Daniels, 2009).

Figure 4.8 shows the  $MD$  and  $MAE$  (see Equations 3.27 and 3.28 respectively) in the mean global near-surface temperature field and the CRU climatology land observations from Jones *et al.* (1999). The  $MAE$  during winter and summer, outside the polar regions is less than  $3^{\circ}\text{C}$  over much of the Earth's land surface. The Greenland climate is evaluated separately below with the datasets discussed in Section 2.3 because of the lack of data over this region in the CRU climatology. Some of the larger errors occur in regions of sharp elevation changes and may result simply from mismatches between the model topography (typically smoothed) and the actual topography. The large negative bias in model temperature at mid to high northern latitudes, particularly during winter (see Figure 4.8), can partly explain

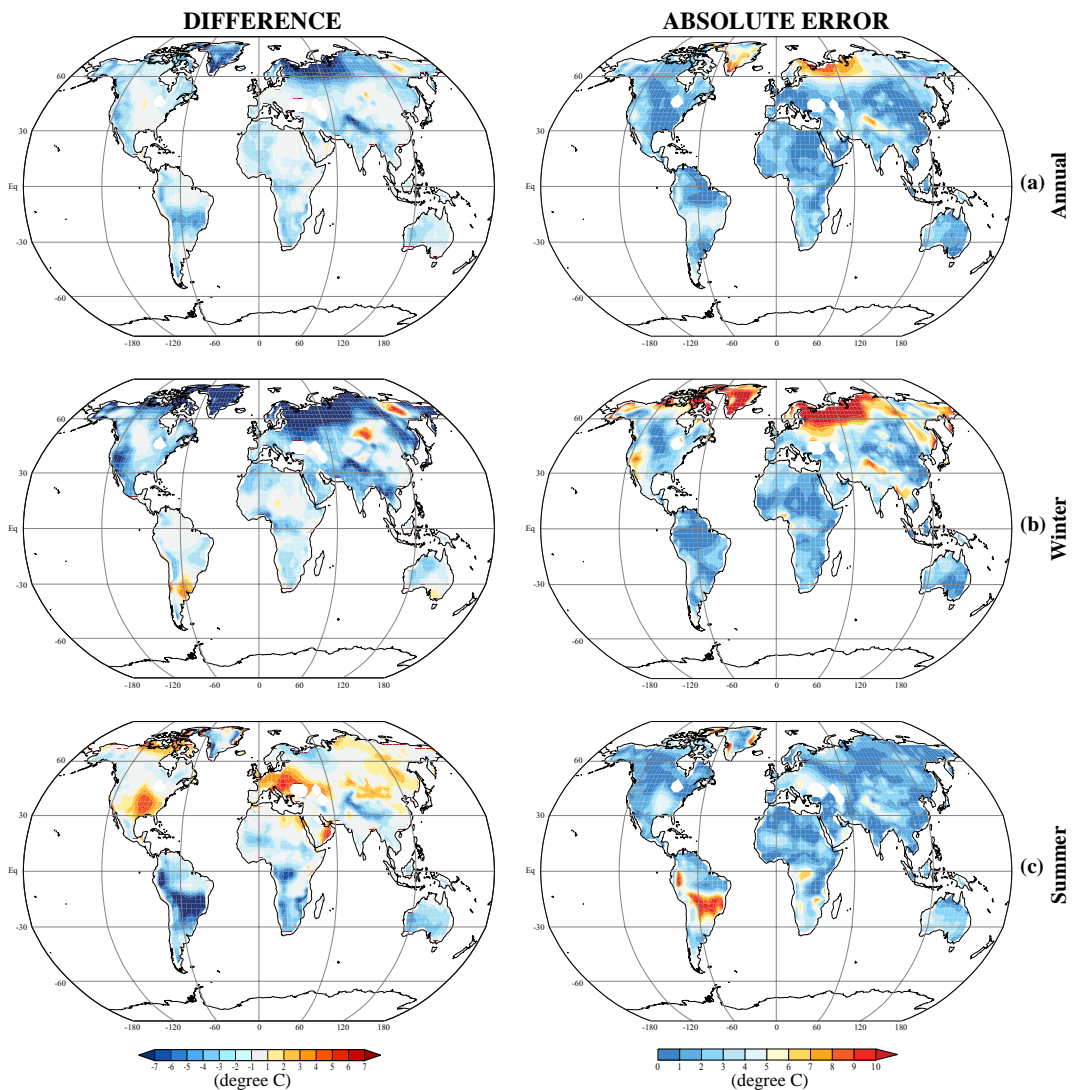


Figure 4.8: Global near-surface temperature difference and mean absolute error (in  $^{\circ}\text{C}$ ) in HadCM3 MOSES 2 TRIFF compared with CRU for (a) annual (b) winter and (c) summer.

the under representation of needleleaf trees and shrubs in Figure 4.7 compared with the IGBP-DIS landcover dataset. In turn this leads to an increase in the expansion of tundra-type C3 grasses which can tolerate the very cold winter temperatures in the modelled preindustrial climate at high latitudes.

Table 4.2 shows the mean difference and mean absolute error for near-surface temperature (in  $^{\circ}\text{C}$ ) for the Greenland region (Figure 3.4) compared with observed temperatures over the ice-sheet from Hanna *et al.* (2005) and satellite temperatures (APP-x) over all of Greenland. There is a significant winter cold bias in the model, at least at high latitudes, by up to  $7.5^{\circ}\text{C}$  compared with satellite data and  $\sim 4^{\circ}\text{C}$  with Hanna *et al.* (2005) temperatures over the ice-sheet. This is also shown in Figure

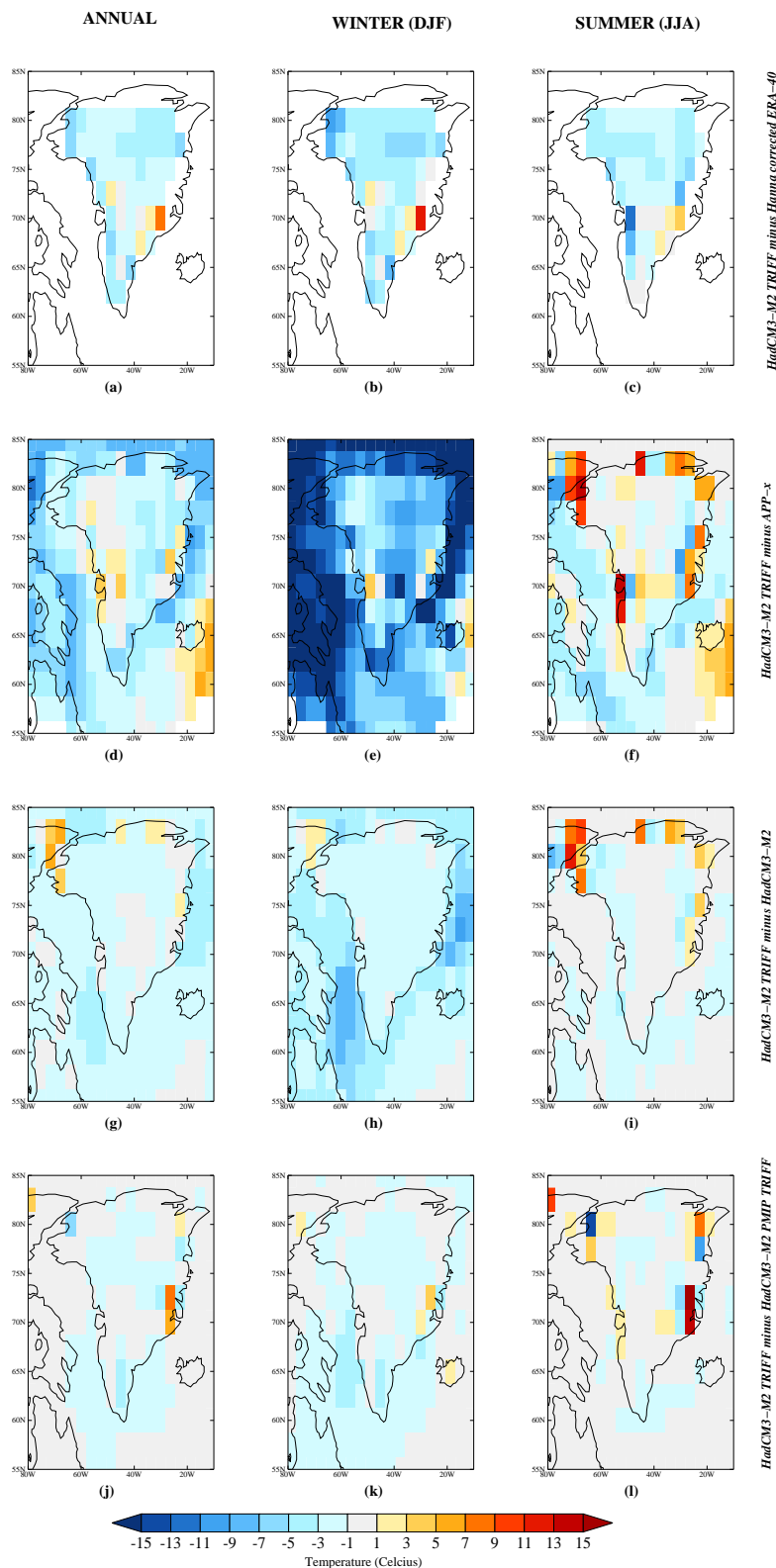


Figure 4.9: Annual, winter and summer surface temperature error (in °C) for (a) to (c) HadCM3 MOSES 2 TRIFFID minus Hanna *et al.* (2005) temperature observations, (d) to (f) HadCM3 MOSES 2 TRIFFID minus AVHRR APP-x satellite observation, (g) to (i) HadCM3 MOSES 2 TRIFFID minus HadCM3-MOSES 2 fixed vegetation preindustrial control and (j) to (l) HadCM3 MOSES 2 TRIFFID minus PMIP HadCM3 MOSES 2 TRIFFID preindustrial control. Note that (a) to (c) only show temperature bias over the GrIS.

|                            | ANN   | DJF   | JJA   |
|----------------------------|-------|-------|-------|
| <b><i>MD</i></b>           |       |       |       |
| Hanna <i>et al.</i> (2005) | -2.48 | -3.24 | -2.46 |
| AVHRR-APP-x                | -1.72 | -7.28 | 0.28  |
| HadCM3 M2                  | -1.11 | -0.66 | -1.72 |
| HadCM3 M2 PMIP TRIFF       | -0.68 | -0.17 | -1.19 |
| <b><i>MAE</i></b>          |       |       |       |
| Hanna <i>et al.</i> (2005) | 2.87  | 3.74  | 2.98  |
| AVHRR-APP-x                | 2.54  | 7.46  | 2.87  |
| HadCM3 M2                  | 1.29  | 1.32  | 1.72  |
| HadCM3 M2 PMIP TRIFF       | 1.36  | 1.92  | 1.49  |

Table 4.2: Mean Difference (*MD*) and Mean Absolute Error (*MAE*) for near-surface temperature (in °C) for HadCM3 M2 TRIFF compared with observation and alternative versions of HadCM3 over the Greenland region. AVHRR-APP-x refers to satellite temperature data and Hanna *et al.* (2005) refers to ERA-40 temperature data only over the ice sheet (both discussed in section 2.3.2). Comparisons are made with HadCM3-M2 fixed vegetation preindustrial control described in Chapter 3 and the PMIP HadCM3-M2 TRIFFID preindustrial simulation. For comparison with Hanna *et al.* (2005) averages are performed over the ice-mask in Figure 3.4a. For all other comparisons averages are performed over all of Greenland according to Figure 3.4b.

4.9b and e. During summer there is also a cold temperature bias ( $\sim 3^\circ\text{C}$ ) over the ice-sheet (Figure 4.9c) similar to the winter *MAE*, but biases are considerably larger around the margins of the ice-sheet (Figure 4.9f).

Temperature comparisons for the HadCM3 M2 TRIFF preindustrial control are also made with the HadCM3 M2 preindustrial control simulation where vegetation is not interactive (described in Chapter 3, Section 3.3.1). During winter, on average, HadCM3 M2 TRIFF is  $\sim 1^\circ\text{C}$  colder than when interactive vegetation is not included (see Figure 4.9h). During the summer months there is again a similar cold temperature bias for HadCM3-M2 TRIFF compared with HadCM3 M2. The most notable differences in temperature occur around the margins of the GrIS (Figure 4.9i). This is attributed to vegetation growing in the ice-free regions of Greenland in the interactive vegetation preindustrial control while the equivalent gridboxes remain covered by bare soil for the fixed preindustrial control.

In Chapter 3, Section 3.3.2, the HadCM3 M2 preindustrial control with fixed vegetation was compared with a standard HadCM3 MOSES 2 PMIP (fixed vegetation) preindustrial simulation in order to assess what differences the modified orography and ice-mask over Greenland made to the average climatology. Likewise, a similar evaluation can be made when vegetation is interactive by comparing the HadCM3

M2 TRIFF simulation in this thesis with a standard HadCM3 M2 PMIP interactive vegetation preindustrial control. During winter, Figure 4.9k shows a small cold bias for HadCM3-M2 TRIFF minus HadCM3-M2 PMIP TRIFF. The largest temperature differences during the summer occur on the eastern margin where the GrIS mask was modified in this thesis to be ice-free (compared with ice-covered in the standard PMIP simulation) and therefore results in temperatures more than 10°C warmer due to the development of grasses and shrubs. These results, however, show that comparison with other similar HadCM3 model simulations result in significantly smaller errors over Greenland than comparison with observation data for both winter and summer seasons (see Table 4.2).

Precipitation anomalies (relative to ERA-40 data, HadCM3 M2 preindustrial control and HadCM3 M2 PMIP TRIFF) are shown in Figure 4.10. Like temperature the difference between HadCM3 model versions over Greenland is less pronounced than the difference between HadCM3 M2 TRIFF and observation. Precipitation is up to 16 times too wet in central northern Greenland during winter (see Figure 4.10b), although this is partly an artifact of the ERA-40 dataset being too dry in this region (discussed in Section 2.4.2) compared with ice core data. During winter and summer the control used in this Chapter is up to two times as dry in isolated regions compared with other HadCM3 model versions. There is though a wet bias along the northeast coast compared with HadCM3-M2 PMIP TRIFF (Figure 4.10i) during summer, associated with the change in ice mask.

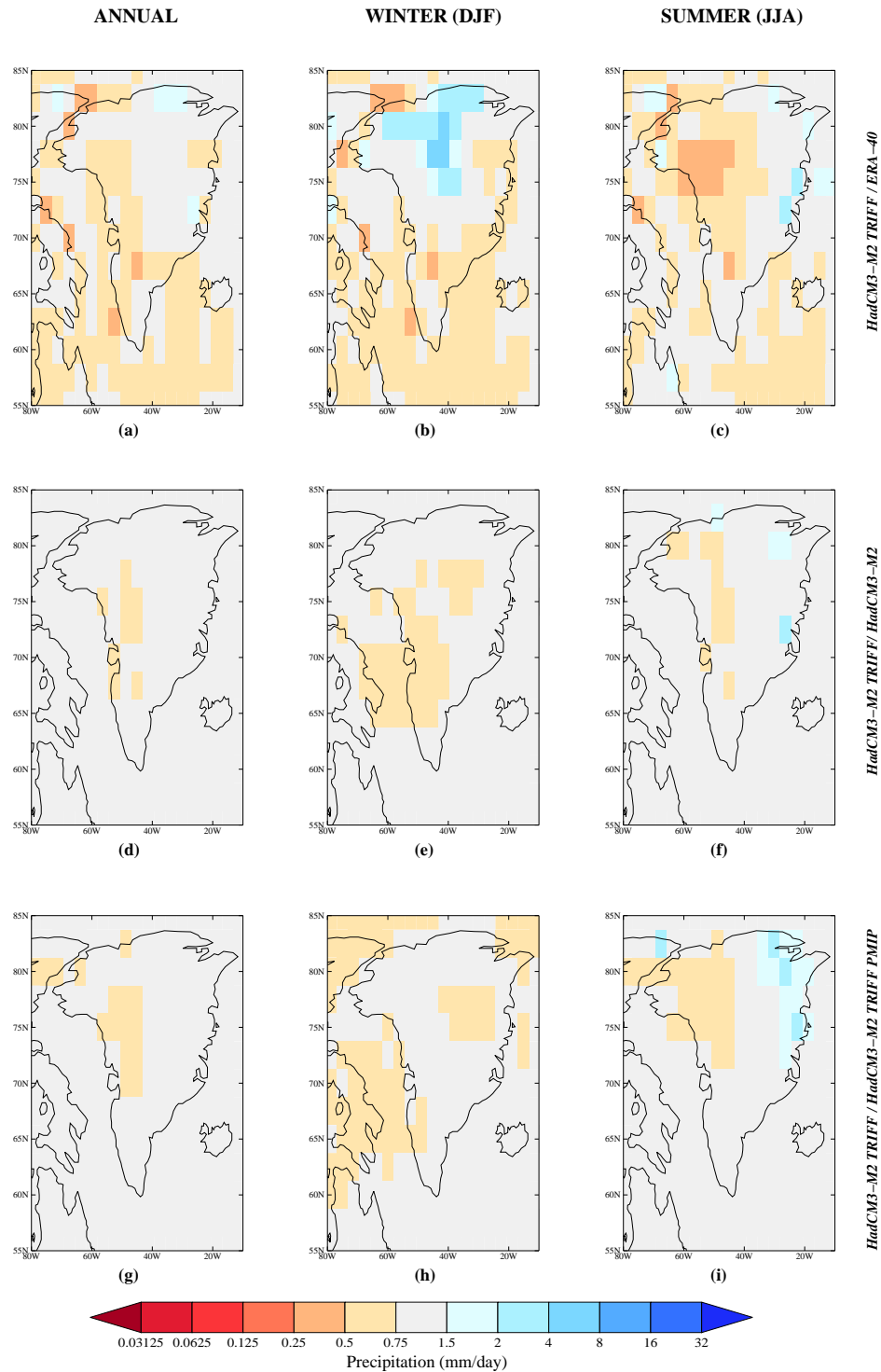


Figure 4.10: Annual, winter and summer precipitation error (expressed as ratios) for (a) to (c) HadCM3 MOSES 2 TRIFFID / ERA-40 precipitation observation, (d) to (f) HadCM3 MOSES 2 TRIFFID / HadCM3-MOSES 2 fixed vegetation preindustrial control and (g) to (i) HadCM3 MOSES 2 TRIFFID / PMIP HadCM3 MOSES 2 TRIFFID.

### 4.3 The influence of interactive vegetation on the climate of a melted GrIS

Two experiments have been performed to explore the impact of interactive vegetation on the climate over a deglaciated and fully rebounded Greenland. A new control has already been discussed in Section 4.2.7. The noGrIS simulations were initialised either with a surface covered by bare soil (noGrIS<sub>bsi</sub>) or needleleaf trees (noGrIS<sub>nli</sub>) in order to explore the impact of the initial surface type properties on the resultant vegetation distribution and climatology over Greenland and to determine whether more than one stable vegetated state exists under preindustrial conditions. These surface types were chosen because they produced the most contrasting climates in Section 3.3.5, in terms of temperature and precipitation anomalies (relative to preindustrial), which are the forcings used to drive the ice-sheet model. Each simulation was run as a continuation from the fixed bare soil and needleleaf tree noGrIS<sub>reb</sub> experiments with TRIFFID in equilibrium mode for 200 years (equivalent to 2,000 years of vegetation simulation) followed by a further 200 years in dynamic mode.

Although starting from needleleaf tree is likely very unrealistic it allows the sensitivity of the model to initial surface condition to be assessed. A surface covered with bare soil is a more realistic scenario for simulating the influence of vegetation feedbacks and on the potential for ice regrowth over a deglaciated Greenland. Melting of the GrIS under a future warming scenario would expose the bare rock surface under the ice-sheet. An analogy for the evolution of soil development can be made with advancement and retreat of ice during the last interglacial-glacial cycle in the Northern Hemisphere. At the end of the LIG soil present on ice-free surfaces would have been eroded away as the climate cooled and the ice advanced over much of the high latitude regions of the Northern Hemisphere. Therefore, once the ice retreated as the climate began to warm again, soils would need to reform before any potential vegetation could grow on the exposed surfaces. The soils of the Canadian Shield provide a good example of a possible timescale for soil development on a deglaciated Greenland. The Canadian Shield forms the stable cratonic core of North America, stretching north from the Great Lakes to the Arctic Ocean. It covers more than half of Canada, includes much of the Greenland bedrock and extends into the United States as the Adirondack Mountains and the Superior Highlands. During the last



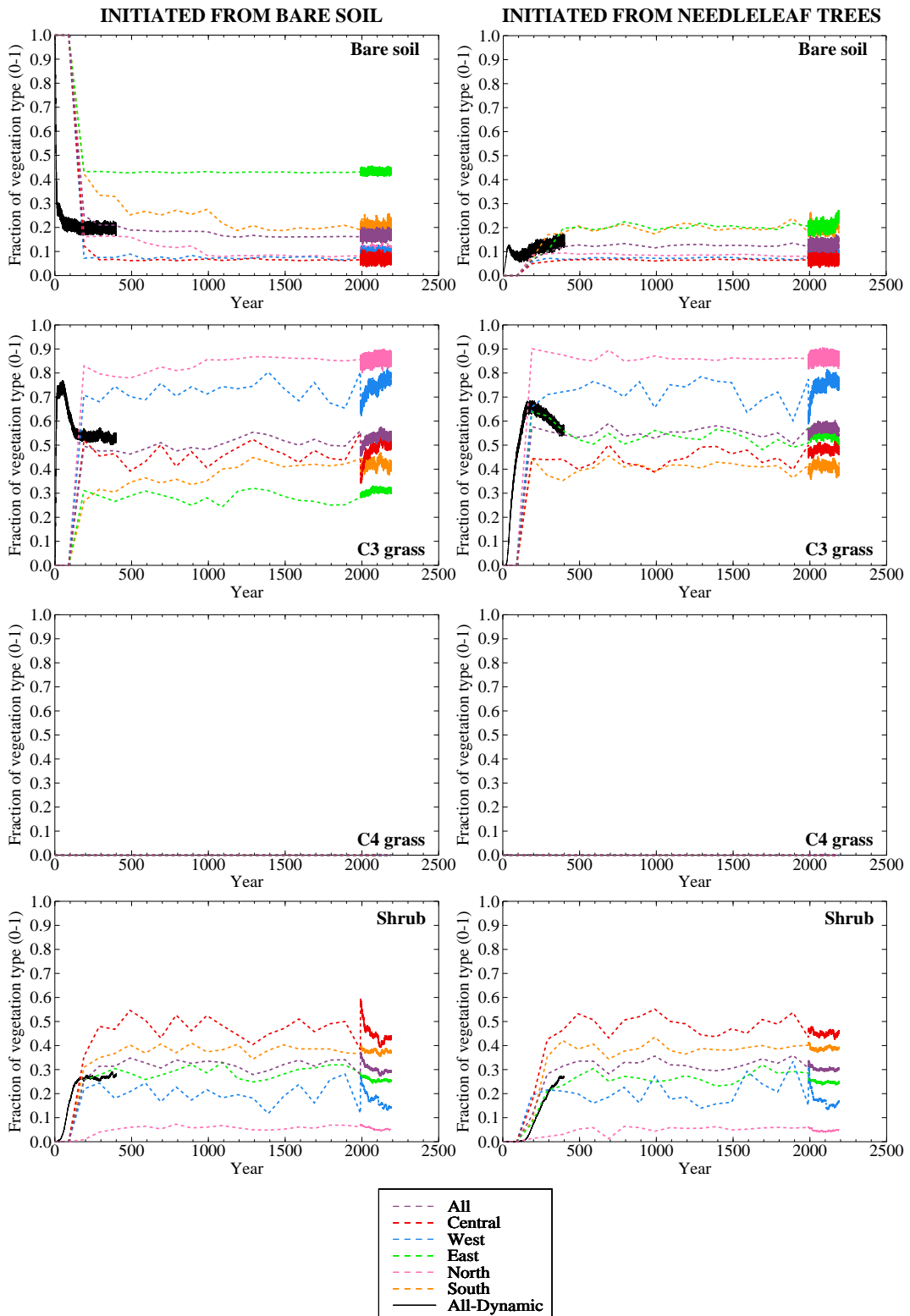


Figure 4.11: Spin-up of vegetation type for bare soil, C3 and C4 grasses, shrubs, broadleaf and needleleaf trees over Greenland using TRIFFID. Each experiment is initialised with a rebounded orography and no ice. *Left* noGrIS<sub>bsi</sub> and *right* noGrIS<sub>nli</sub>. The fraction of each vegetation type is averaged over the different regions of Greenland given in Figure 3.5. For the case of the Greenland experiments where vegetation is spun up in fully coupled dynamic mode from the beginning, 400 model years of elapsed time are shown (solid black lines); these experiments will not be discussed any further. All other cases show spin-up in equilibrium mode for 2,000 years (200 HadCM3 climate years) and continuation in dynamic mode for a further 200 years. *Continued on next page...*

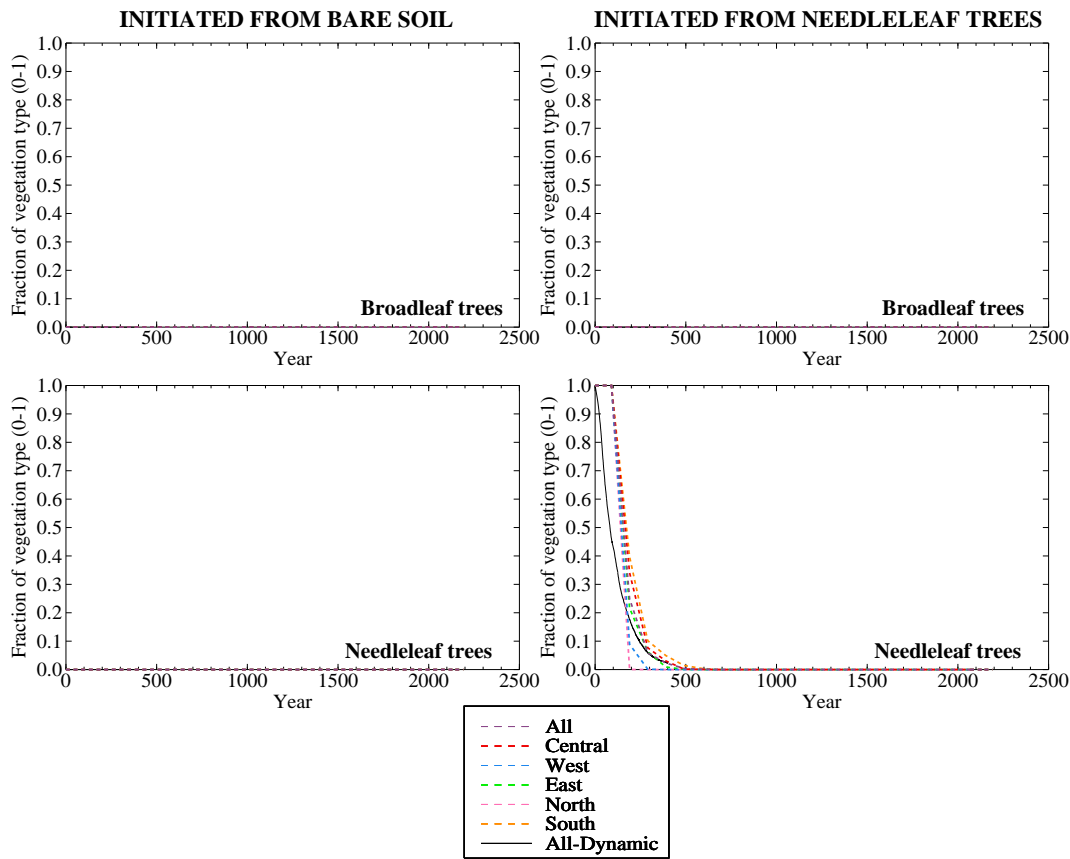


Figure 4.11: ...continued from previous page.

ice age the soils in this region were removed as the Laurentide ice-sheet advanced southwards. However, the retreat of the ice at the end of this glacial period subsequently re-exposed the bare rock which has now been ice-free for approximately 10,000 years. Although the soils are thin they have developed such that south of the treeline, forests are supported and north of the treeline tundra vegetation is abundant (Acton, 1989; Tarnocai, 1989). Since this simulation uses a rebounded bedrock, it is assumed that the time it takes to rebound (several thousand years) as the ice melts is sufficient for soil development over Greenland. These simulations begin from a condition where the bedrock is in equilibrium and the climate is similar to preindustrial conditions as was the case for the fixed vegetation simulations.

### Vegetation growth over a melted Greenland ice-sheet

Figure 4.11 shows the surface type coverage spin-up for the five PFTs and bare soil over all of Greenland as well as the predefined regions shown in Figure 3.5. Initiation from bare soil is shown on the lefthand panels and initiation from needleleaf tree

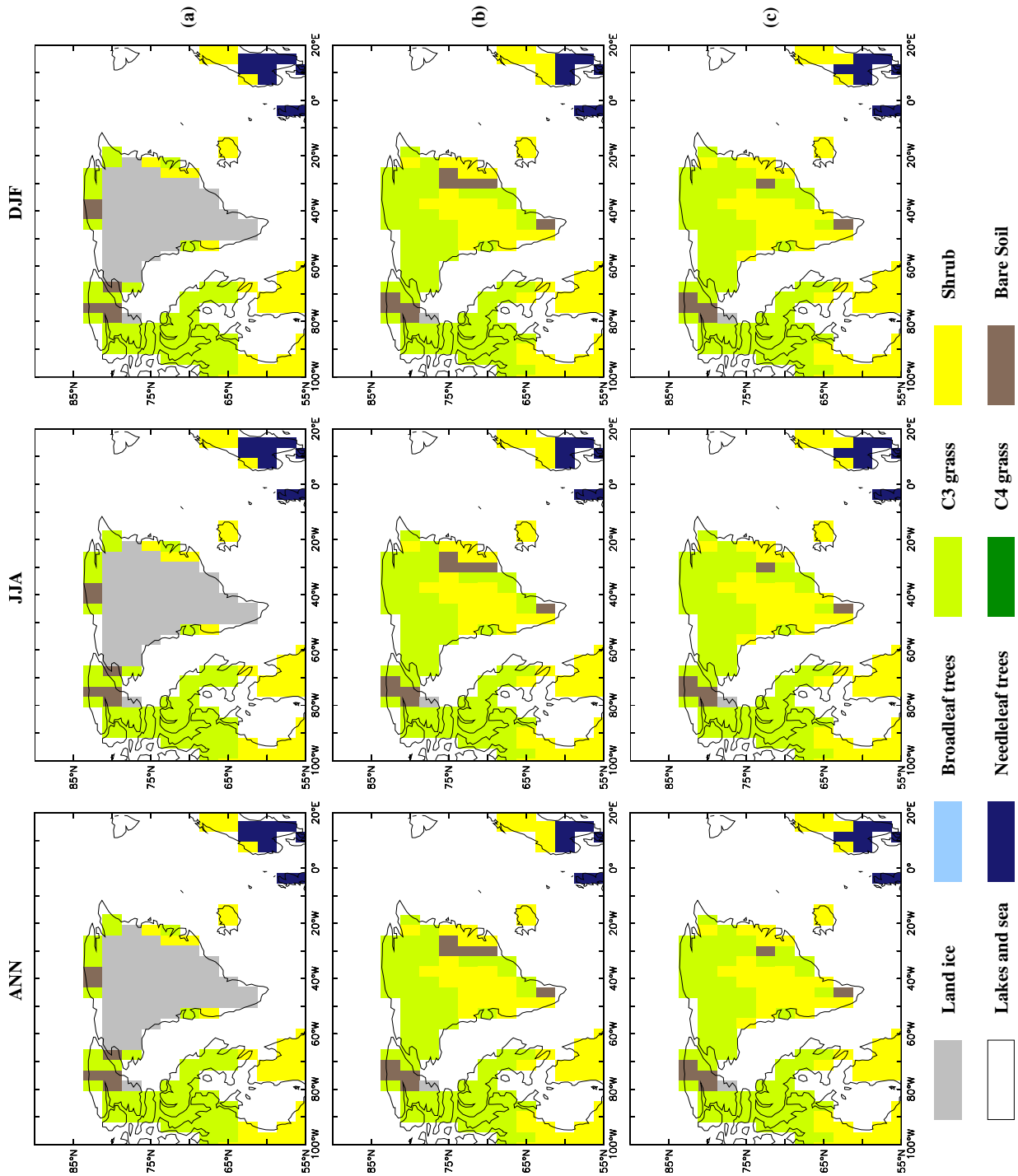


Figure 4.12: Dominant vegetation coverage over Greenland after running TRIFFID in equilibrium mode for 2,000 years (200 equivalent years for GCM run-time) followed by 200 years of TRIFFID in dynamic mode. Within each grid-cell the dominant PFT/other land surface type is shown for (a) GrIS present (b) noGrIS<sub>bsi</sub> and (c) noGrIS<sub>run-time</sub> for preindustrial conditions. The bedrock is rebounded in the noGrIS simulations.

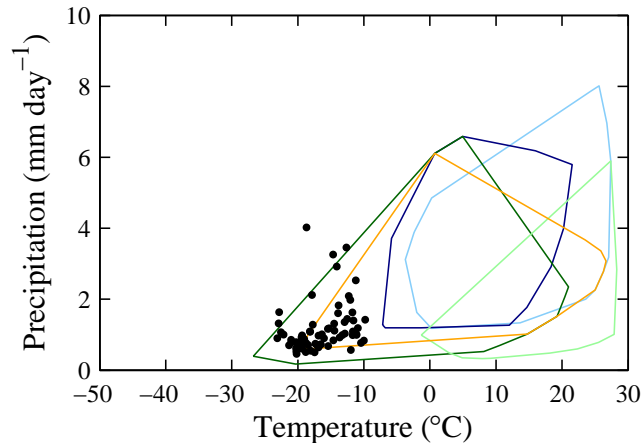


Figure 4.13: Average annual near-surface air temperature versus precipitation for all gridboxes (represented by black circles) over all of Greenland in noGrIS<sub>bsi</sub>. Also shown is the parameter space tolerated by the five PFTs (broadleaf trees, needleleaf trees, C3 grass, C4 grass, shrub) as illustrated in Figure 4.6.

on the righthand panels. In addition, simulations were performed in fully dynamic TRIFFID mode from the start for 400 years in order to assess how close they match the trend obtained using equilibrium mode. These are shown as black lines for averages over all of Greenland as an example. It is evident that these experiments begin to track the average Greenland equilibrium mode fraction (purple dotted line) for all surface types and demonstrate that it is feasible to run the simulations in equilibrium rather than dynamic mode in order to gain sufficient model spin-up. The final 200 years of the simulations show no major difference in the trend of fractional vegetation type from equilibrium mode. However, for the faster varying vegetation components that adapt to the seasonally changing climate such as C3 grasses, fractional coverage can vary by as much as 10 % between winter and summer.

There is no broadleaf tree growth over Greenland for either of the noGrIS simulations. This is also the case for C4 grasses. This result is consistent with the environmental niches where one would expect to find these PFTs. There is also no growth of needleleaf trees over Greenland. NoGrIS<sub>nli</sub> shows complete disappearance of needleleaf trees over Greenland within 500 vegetation model years. C3 grasses show the largest fractional coverage in the north of Greenland ranging from 80 to 90 % for both noGrIS simulations. However, the least coverage of C3 grass is found in the south for the noGrIS<sub>nli</sub> experiment and in the east for noGrIS<sub>bsi</sub>. In terms of bare soil coverage, there is a reduction in all regions for noGrIS<sub>bsi</sub> with less than 10 % coverage in the north, west and central regions. The largest fraction is found in

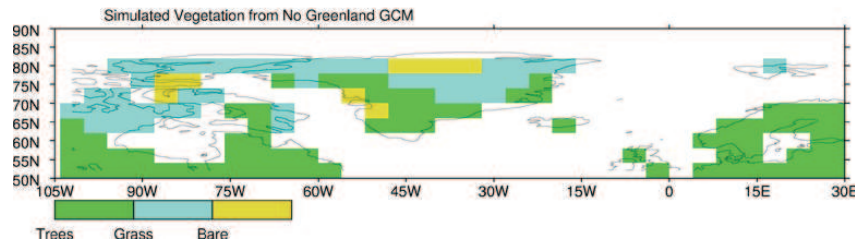


Figure 4.14: Vegetation cover with a melted GrIS, simulated by ORCHIDEE, forced offline by a noise sheet climatology (from Lunt *et al.* (2004)).

the east coincident with the high altitude of the bedrock. NoGrIS<sub>nli</sub> sees an increase in bare soil in all regions but has a much lower coverage in the east ranging from 20 to 30 % compared with noGrIS<sub>bsi</sub> (~ 45 %). The seasonal variation observed for the bare soil fraction when the experiments are switched to dynamic mode is simply a response to the expansion and contraction of grasses and or shrubs throughout the year. Finally, the evolution of shrubs on Greenland is very similar for both initial conditions with the largest fractions in central Greenland (40 to 50 % coverage) coincident with the warmest temperatures (see Figure 4.15). The least coverage is observed for the north and west (less than 10 %).

Figure 4.12 shows the average dominant surface type in each gridbox over the Greenland region for annual, winter and summer months. The control and noGrIS experiments are shown. The dominant distribution of vegetation throughout the year does not appear to change for either of the noGrIS experiments. The coverage of shrubs in central and southern Greenland and C3 grasses in the north and west is identical for both with the main but localised differences in the east where noGrIS<sub>bsi</sub> results in a larger proportion of bare soil coverage compared with noGrIS<sub>nli</sub>. Outside of Greenland there are no significant changes in vegetation distribution compared with the control for either experiment. Since there is very little evidence of hysteresis in the system when spinning up from different surface types, further discussion will only refer to the noGrIS<sub>bsi</sub> simulation since this is the most likely realistic scenario.

The noGrIS<sub>bsi</sub> simulation results in no growth and maintenance of any trees over Greenland. Figure 4.13 shows the average annual precipitation-temperature climate space representing the gridboxes over Greenland for the noGrIS<sub>bsi</sub> experiment. Also overlain are the broad climate space regions defined by the different PFTs for the control according to Figure 4.6. Clearly, no region over Greenland is suitable to grow any type of tree in terms of precipitation or temperature. However, much

|         | NPP ( $\text{gC m}^{-2} \text{ yr}^{-1}$ ) |            |          |          |       |
|---------|--|------------|----------|----------|-------|
|         | Broadleaf                                  | Needleleaf | C3 grass | C4 grass | Shrub |
| All     | 59.1                                       | 124.0      | 313.7    | 78.4     | 130.4 |
| North   | 44.8                                       | 111.7      | 311.2    | 54.2     | 98.1  |
| South   | 56.3                                       | 118.3      | 273.2    | 78.9     | 129.3 |
| East    | 43.2                                       | 88.1       | 216.8    | 60.7     | 100.9 |
| West    | 59.9                                       | 130.3      | 341.2    | 85.7     | 120.8 |
| Central | 77.5                                       | 152.4      | 389.7    | 98.1     | 168.1 |

Table 4.3: The average annual potential NPP (in  $\text{gC m}^{-2} \text{ yr}^{-1}$ ) (supplied to TRIFFID) which represents the difference between photosynthesis and photorespiration for each PFT over different regions of Greenland. Results are only shown for noGrIS<sub>bsi</sub> since noGrIS<sub>nli</sub> are similar.

of Greenland falls into the annual temperature-precipitation climate space for C3 grasses and to a lesser extent shrubs. This result contrasts with Lunt *et al.* (2004). Figure 4.14 shows the dominant vegetation types over Greenland when their noGrIS simulation was used to force the DGVM, ORCHIDEE, offline. The locations of trees in this simulation were found in the south and west and along the eastern coast of Greenland. The south and west tree distribution coincides with shrub distribution found in this study. There is general agreement in grass distribution between the two studies but not for bare soil distribution. Lunt *et al.* (2004) found bare soil dominated in the north while this study finds bare soil dominance is mainly confined to the east. Their winter temperatures over Greenland are sufficient to maintain trees throughout the year. Although summer temperature ( $-9^{\circ}\text{C}$  to  $11^{\circ}\text{C}$ ) and moisture conditions over Greenland for the simulations presented in this thesis are sufficient for the expansion/growth of needleleaf trees this is not the case during winter when temperatures reach as low as  $-40^{\circ}\text{C}$  and no higher than  $-22^{\circ}\text{C}$ , well below the temperature thresholds for leaf mortality.

The boundary between forest and tundra at high latitudes can be expressed as a function of NPP. This reflects the requirement for a minimum carbon balance to sustain the growth and reproduction of trees and can be thought of as describing the vegetation ‘health’ (Cox *et al.*, 1999). Since  $\text{CO}_2$  must be diffused through stomata before it can be fixed by the plant, a relationship is used between net photosynthesis and stomatal conductance to water vapour by the plant in MOSES 2. The NPP is the difference between gross productivity (equivalent to the canopy photosynthesis) that depends on temperature, solar irradiance, humidity deficit, soil moisture concentrations, canopy LAI and atmospheric  $\text{CO}_2$  concentration.

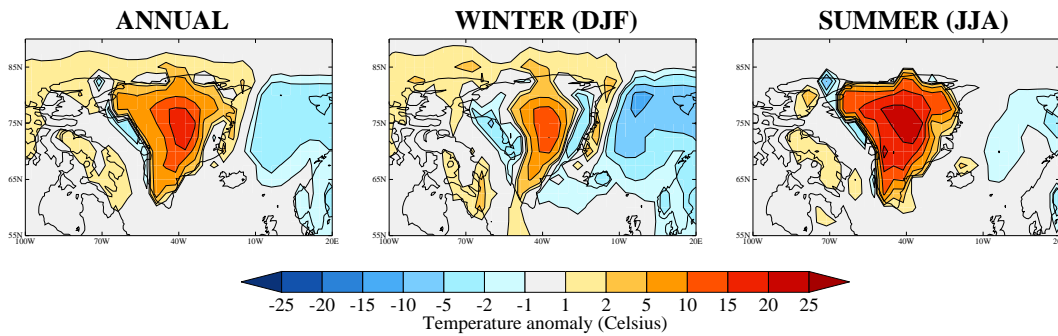


Figure 4.15: Near-surface temperature anomaly (in  $^{\circ}\text{C}$ ) for noGrIS<sub>bsi</sub> simulation minus TRIFFID control. Plots show annual, winter and summer anomalies. This plot can be compared with Figure 3.25 for the fixed surface noGrIS<sub>reb</sub> simulations in Chapter 3.

According to Kaplan *et al.* (2003) the minimum NPP required for trees at high latitudes is  $140 \text{ gC m}^{-2}\text{yr}^{-1}$ . The study of Lunt *et al.* (2004) found that the NPP of trees on Greenland in their simulation ranged between  $350$  and  $500 \text{ gC m}^{-2} \text{ yr}^{-1}$ , well above this minimum threshold. In mid-latitude regions where needleleaf trees dominate in the TRIFFID control simulation, NPP is also sufficiently above this threshold. TRIFFID takes as input NPP for each PFT and based on this provides fractional vegetation cover and LAI of each PFT as output, required to determine the physical characteristics of the land surface such as the albedo, moisture availability and aerodynamic roughness. Thus, the average NPP which would be available for each of the PFTs over Greenland is shown in Table 4.3. It is evident that the NPP associated with needleleaf trees anywhere on Greenland is generally not sufficient to maintain and expand this vegetation type. However, C3 grass average NPP ranges between  $217$  and  $319 \text{ gC m}^{-2} \text{ yr}^{-1}$  which is comparable with tundra biomes for present day and field measurements (Kaplan *et al.*, 2003). NPP for the shrub PFT are similar to measurements in high latitude regions which record up to  $160 \text{ gC m}^{-2}\text{yr}^{-1}$  (Shaver *et al.*, 2001) but in many cases NPP is usually lower (Gilmanov and Oechel, 1995; Shaver and S., 1999).

### Local temperature and heat flux changes

Figure 4.15 shows the annual, winter and summer near-surface temperature anomaly over the Greenland region for the noGrIS<sub>bsi</sub> experiment. First note that during winter the anomaly in central Greenland is positive and the island margins flanked by negative temperature anomalies. This is especially the case in the east. The decrease in near-surface temperatures over the Barents Sea region east of Greenland

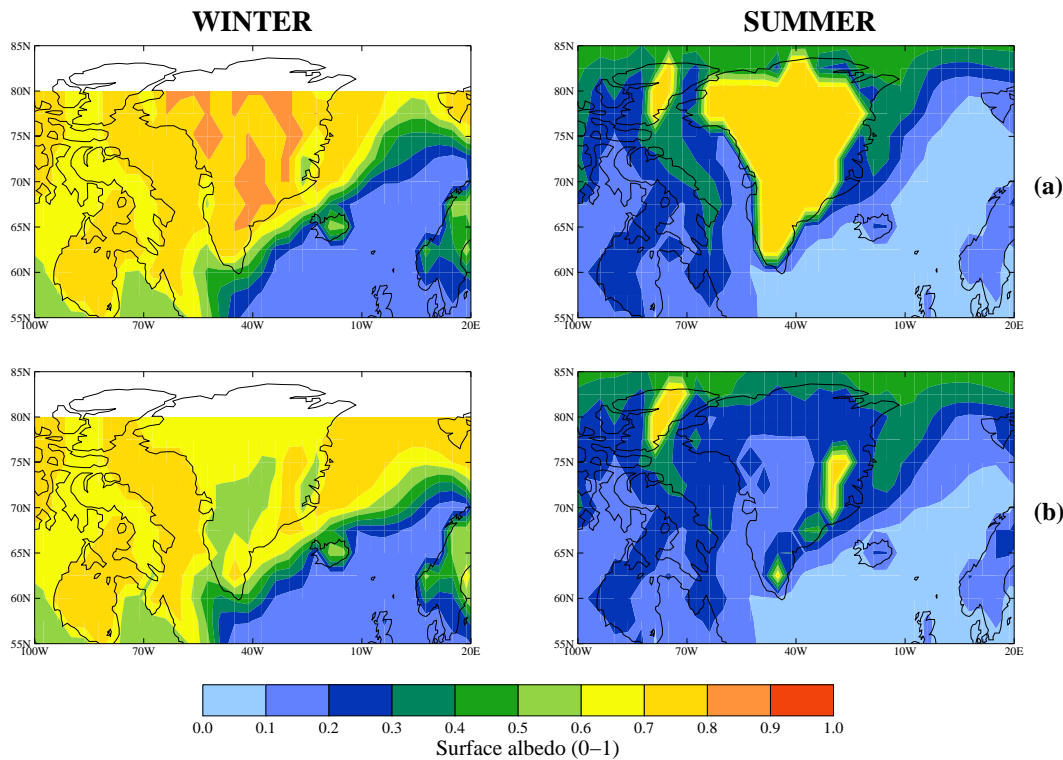


Figure 4.16: Average surface albedo over Greenland during winter and summer months for (a) TRIFFID preindustrial control and (b) noGrIS<sub>bsi</sub>.

during winter, observed in all the fixed vegetation noGrIS<sub>reb</sub> experiments (see Figure 3.25), is also evident when interactive vegetation is included. The average annual anomaly over the Greenland region is 7.3°C for noGrIS<sub>bsi</sub>. This is similar to averages obtained for surface covered with fixed C3 grasses and shrubs respectively (see Table 3.8 and Figures 3.25b and d). During winter the temperature increase is 2.8°C for noGrIS<sub>bsi</sub> and falls within the fixed vegetation noGrIS<sub>reb</sub> winter temperature anomaly range from 2.7 to 3.4°C (see Table 3.8). During summer, the average Greenland positive temperature anomaly is 12.2°C for noGrIS<sub>bsi</sub> and is comparable with the value obtained for noGrIS<sub>reb</sub> with a surface covered by C3 grasses (see Table 3.8 and Figure 3.25b).

The impact of vegetation growth on the average surface albedo of Greenland is shown in Figure 4.16 for winter and summer. The interactive vegetation HadCM3 preindustrial control (Figure 4.16a) shows a similar pattern in surface albedo for winter and summer over Greenland ranging between 0.7 and 0.9 where there is ice cover. During the summer months snow melt in the east exposes a lower albedo surface in the ice-free regions. There is also a lower surface albedo in the Baffin Bay



and Davis Strait region during this season due to a decrease in sea-ice concentration (positive sea-ice-albedo feedback due to enhanced high latitude warming). The albedo of the surface over Greenland when the ice-sheet is removed is reflected by the different vegetation types over Greenland, which have evolved under preindustrial conditions (see Figure 4.16b). This is particularly the case for the summer months. During winter the albedo ranges from 0.5 in the west to 0.8 in the east. This is explained by the vegetation-snow-albedo feedback. Where the surface is covered predominantly by bare soil in the east the albedo is high due to winter snowfall sufficiently covering the surface such that a highly reflective surface ensues. However, in the west where shrubs dominate, the albedo is lower due to the canopy masking the high-albedo surface and therefore lowering the surface albedo. During summer this effect is further enhanced with high albedos (0.8) confined to the high altitude regions of the east where bare soil dominates and insufficient melting of snow occurs. The average surface albedo in the west of Greenland is as low as 0.1, coincident with dominance by the shrub PFT. In the north the albedo is higher than in the west with a range between 0.2 and 0.3 where C3 grasses are prevalent. This range in albedo values during the summer is reflected in the near-surface temperature anomalies in Figure 4.15 and the net shortwave heat flux at the surface (Figure 4.17).

Since surface energy balance results from Chapter 3 showed that vegetation type had the most profound effect on average summer heat fluxes (see Figure 3.27 for more detail), these are shown in Figure 4.17 for noGrIS<sub>bsi</sub>. Net downward shortwave heat flux is close to zero during much of the winter as expected since insolation values are low. However, the summer anomaly relative to the control is as high as 120 W m<sup>-2</sup> in central Greenland due to the low albedo surface and falls within the range deduced from the fixed vegetation noGrIS simulations (20 to 138 W m<sup>-2</sup>). The region in the east of Greenland, however, shows very small net shortwave anomalies due to the surface albedos between control and noGrIS<sub>bsi</sub> simulation being similar (less than 10 W m<sup>-2</sup> different, compare summer albedos in Figure 4.16a and b). This coincides with the bare soil dominance observed in Figure 4.12b where some snow cover still persists throughout the summer months resulting in maintenance of a high albedo surface and therefore reduced absorption of shortwave flux at the surface. In terms of turbulent heat fluxes there is a marked increase in heat losses away from the surface during the summer months similar to the result from the

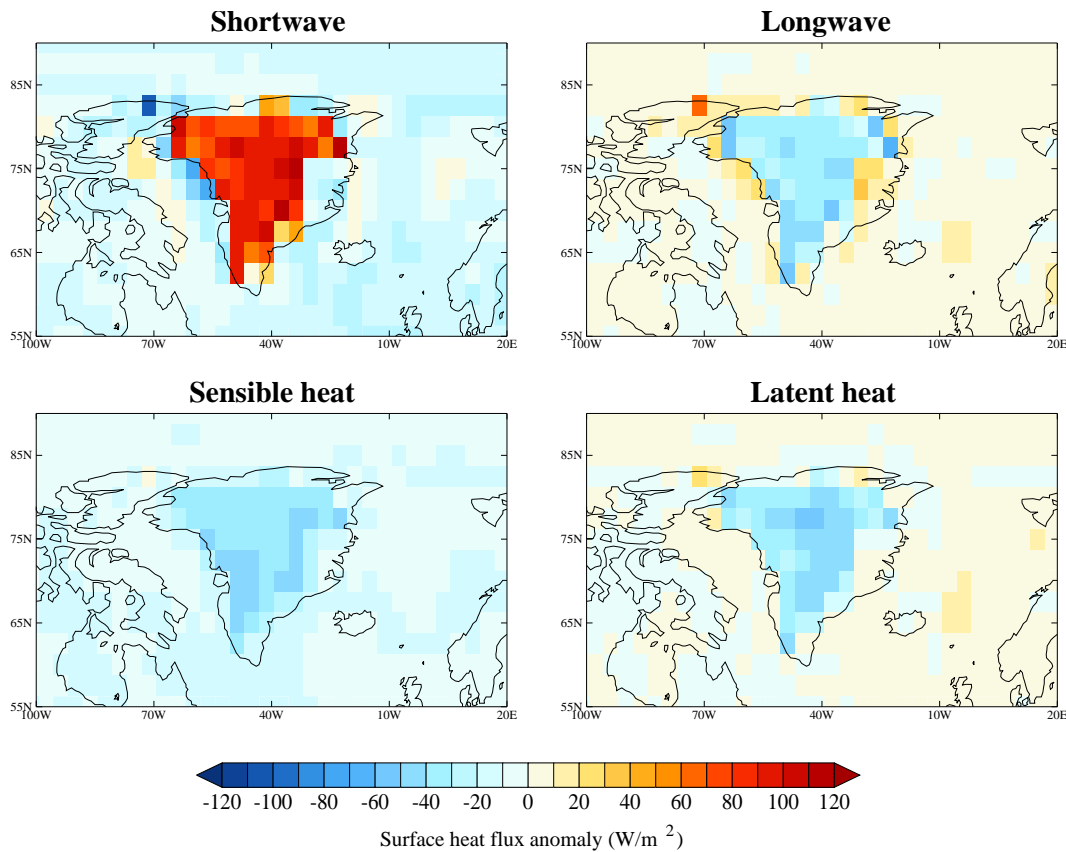


Figure 4.17: Average summer heat flux anomalies (in  $\text{W m}^{-2}$ ) for noGrIS<sub>bsi</sub> minus preindustrial TRIFFID control. Heat fluxes toward the surface are positive.

noGrIS<sub>reb</sub> fixed vegetation experiments. Latent heat flux values reach up to  $60 \text{ W m}^{-2}$  greater than the control, similar to values for a surface covered in fixed needleleaf tree, over much of Greenland, coincident with the spatial distribution of C3 grass and shrub vegetation dominance. However, fluxes are much smaller (up to a factor of 4) and even slightly positive where bare soil dominates due to less evapotranspiration (from the smaller amounts of vegetation present) from the surface taking place in those gridboxes. Similarly, sensible heat flux also increases over a vegetated Greenland during the summer by comparable amounts to latent heat. The longwave heat fluxes are also larger as a result of the warmer surface, due to increase shortwave absorption and lowered elevation of the orography, compared with the ice-covered control.

### The hydrological cycle and snow cover over a vegetated Greenland

Precipitation anomalies over the Greenland region for annual, winter and summer are shown in Figure 4.18. During winter there is an increase in precipitation by up

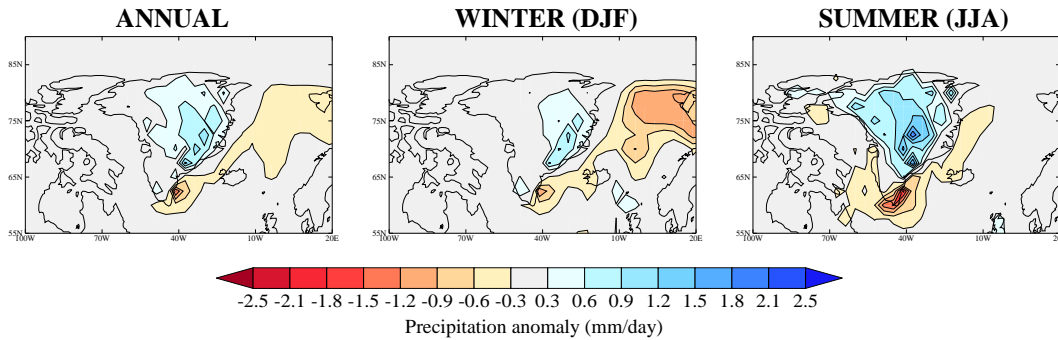


Figure 4.18: Total precipitation rate (snowfall and rainfall) in  $\text{mm day}^{-1}$  for  $\text{noGrIS}_{bsi}$  minus preindustrial TRIFFID control. Plots show annual, winter and summer anomalies. This plot can be compared with Figure 3.28 for the fixed surface  $\text{noGrIS}_{reb}$  simulations in Chapter 3.

to  $1.5 \text{ mm day}^{-1}$  on the eastern coast of Greenland with a small decrease at the southern tip. The Barents Sea also sees a decrease in precipitation by up to  $1.2 \text{ mm day}^{-1}$ . The pattern observed in the winter over Greenland is similar to that observed when vegetation type is fixed (compare Figure 4.18 and Figure 3.28). In particular, the spatial distribution and intensity of precipitation in the Barents Sea compares reasonably with the fixed C3 grass experiment (Figure 3.28b).

During the summer months there is an intensification and expansion of precipitation from the east of Greenland and into the interior relative to the control with precipitation anomalies up to  $2 \text{ mm day}^{-1}$  higher. The region of drier conditions in the south intensifies and extends further west into the Davis Strait and onto the west coast of Greenland, which was also observed when vegetation was not interactive.

The hydrological cycle is shown in more detail in Figure 4.19. During the winter months there is no liquid precipitation in any region over Greenland. As spring approaches and the melt season begins, rainfall increases and peaks in July for all regions followed by a decrease as temperatures begin to decline as the winter months approach. This increase in rainfall is associated with a decrease in solid precipitation amounts. The amount of liquid precipitation varies between regions in summer from only  $1 \text{ mm day}^{-1}$  in the east to  $2 \text{ mm day}^{-1}$  in central and southern Greenland. In the north snow falls throughout the year although decreases during the summer months. The south of Greenland is the most variable in terms of solid precipitation but is positive throughout the year with the largest accumulation during winter (up to  $3 \text{ mm day}^{-1}$ ). In the east the snowfall amount is also positive throughout the year and although there is a decrease in the summer similar to the control in July (with up to  $2 \text{ mm day}^{-1}$ ), more solid precipitation falls during autumn compared with the

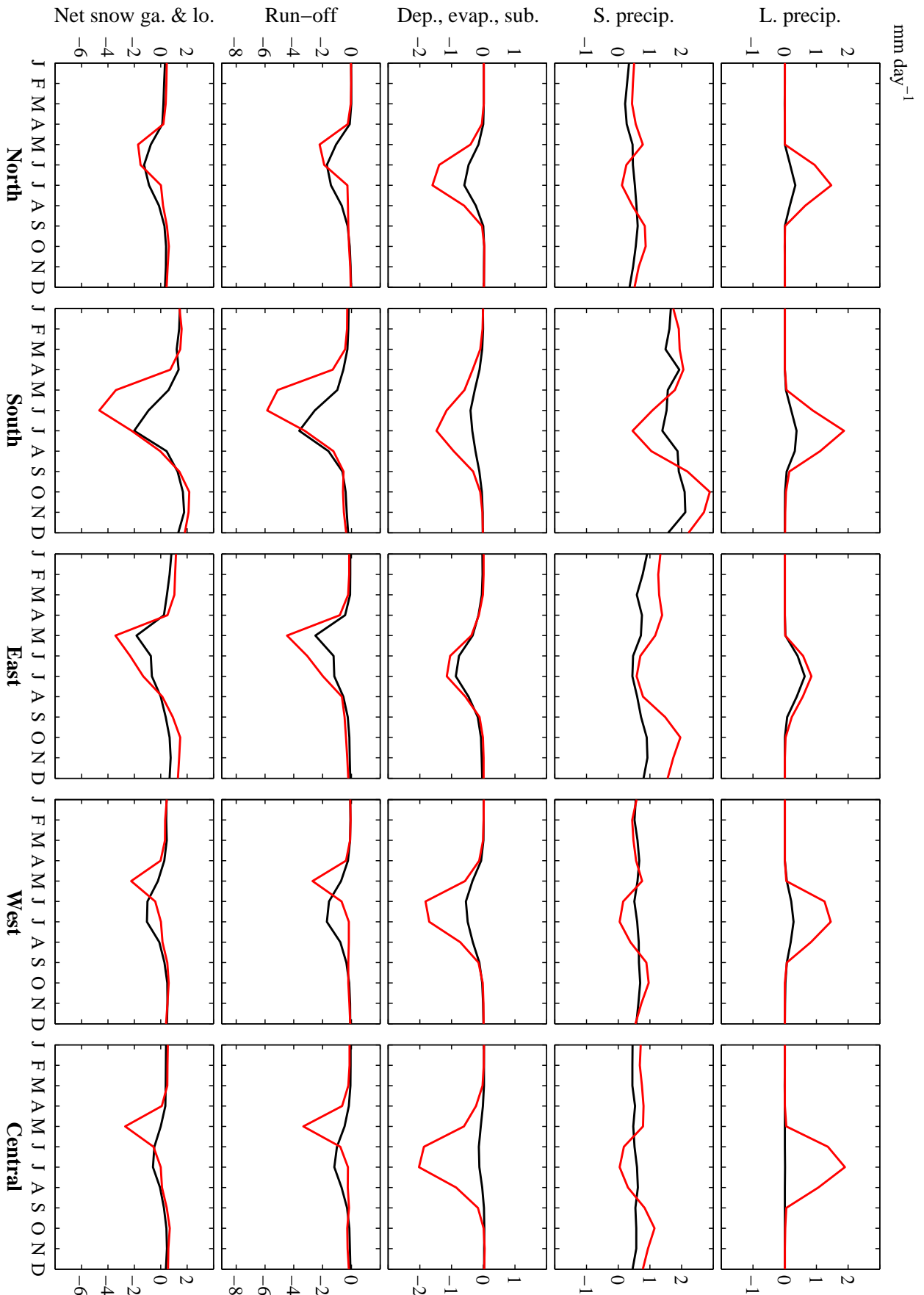


Figure 4.19: Annual hydrological cycle for five regions over Greenland as defined in Figure 3.5. The diagnostics shown are net snow gain and loss (Net snow ga. & lo.), run-off, deposition, evaporation and sublimation (Dep., evap., sub.), solid precipitation (S. precip) and liquid precipitation (L. precip). All quantities are in millimeters per day water equivalent. Note that fluxes toward the surface are counted as positive. For each graph the preindustrial TRIFID control (black) and noGrISbsi (red) are shown.

control. The west and central locations show a similar pattern to the north with the least snowfall in summer compared with all other regions. Run-off amounts are small and comparable to the control for the winter months over Greenland. However, all regions apart from the east show an increase in run-off earlier in the melting season due to intensification of the vegetation-snow-albedo feedback mechanism. South and central Greenland sees the largest run-off amounts of up to  $6 \text{ mm day}^{-1}$  and  $4 \text{ mm day}^{-1}$  respectively and the west the least ( $3 \text{ mm day}^{-1}$ ). The east experiences up to  $1 \text{ mm day}^{-1}$  more run-off than the control but the onset of increased run-off is similar (in contrast to the rest of Greenland). Evaporation water fluxes during winter are close to zero. In the west, south and north evaporation increases and peaks in July/August after sufficient moisture buildup with similar fluxes (up to  $2 \text{ mm day}^{-1}$ ). The east experiences the smallest amount of evaporation in the summer in accordance with the low latent heat flux values shown in Figure 4.17. The dominance of bare soil results in less evaporation from the canopy or via transpiration. Central Greenland has the largest evaporation rates and the largest contrast compared with the control. This is because this region is now dominated by shrubs and grass, which have the ability to access moisture content in soil layers below the surface. Finally, the net snow gain and loss shows that although the south observes the largest increases in snow in autumn/winter it also experiences the largest losses in the summer. In general, the hydrological cycle in the east throughout the year most closely resembles the fixed noGrIS<sub>reb</sub> bare soil experiment in Figure 3.29. All other regions closely match the cycles for shrubs and grasses.

The snow cover for February and August in Figure 4.20 mainly reflects the local altitude in the noGrIS<sub>bsi</sub> simulations as well as the surface type present. The elevated regions in the south and east are conducive for greater solid precipitation (as observed in the hydrological cycle). There is significant variation between the seasons consistent with the fixed vegetation experiments. During winter most of Greenland is covered by more than 100 mm of snow with more than 1000 mm in the east. This compares with the snow cover in the fixed noGrIS<sub>reb</sub> bare soil experiment (see Figure 3.31). In summer a substantial part of central Greenland becomes snow-free. Only the east and south sees locations where snow cover is as high as during winter. This is because snow continues to fall at these high elevations and a surface of bare soil results in a higher snow-covered albedo compared

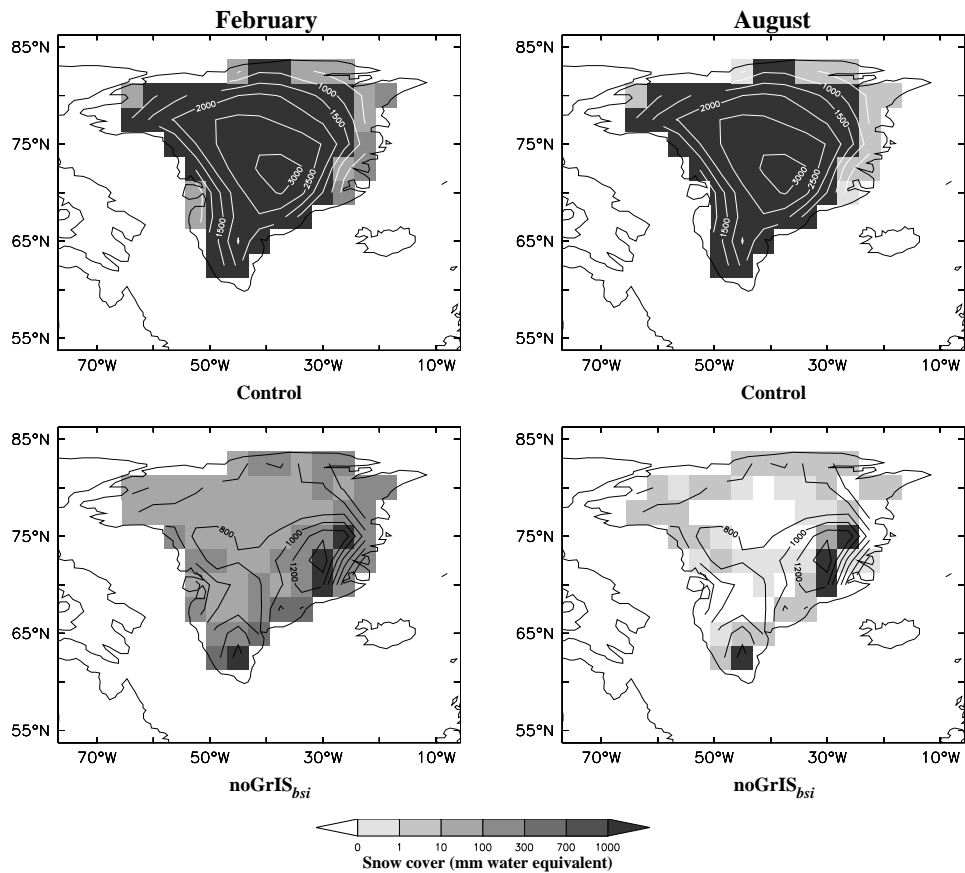


Figure 4.20: Average August and February snow cover over Greenland for the TRIFFID preindustrial control and noGrIS<sub>bsi</sub> simulations. Overplotted are levels of constant orographic height in metres at intervals of 500 m for the control and 200 m for the noGrIS<sub>bsi</sub> simulation. These plots can be compared with Figures 3.31 and 3.32 for fixed surface vegetation in Chapter 3. The non-linear snow cover scale is from Toniazzo *et al.* (2004).

with other regions. Again this most closely resembles the bare soil noGrIS<sub>reb</sub> fixed experiment in Figure 3.32. Although the average summer temperature anomalies in these TRIFFID simulations are comparable to a surface covered by C3 grasses the distribution of snow cover resembles a surface covered by bare soil and therefore has implications for the potential of ice-sheet regrowth.

### Atmospheric circulation

The low-level atmospheric circulation over Greenland and its neighbouring seas is shown in Figure 4.21 for the control, and noGrIS<sub>bsi</sub> simulations. The TRIFFID control shows similar low-level atmospheric circulation patterns as the control used in Chapter 3 during winter and summer (compare with Figure 3.33a). During winter there is anticyclonic flow with the Icelandic low positioned to the south of Greenland. When the orography is lowered the Icelandic low shifts southwards and weak-

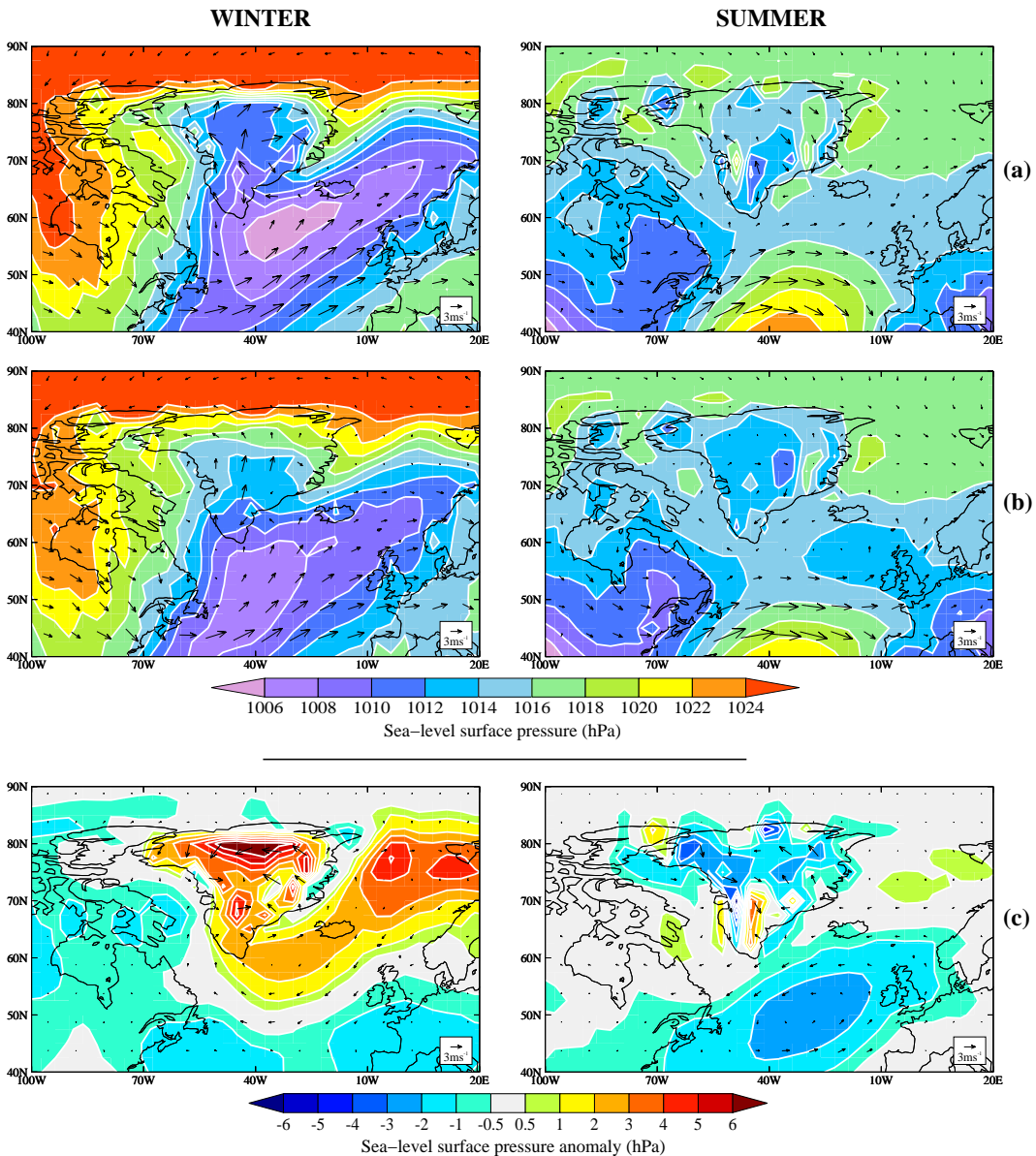


Figure 4.21: Winds at pressure level 3 in HadCM3 corresponding to 850 hPa over a surface at sea-level (shown by arrows). Filled contours show sea-level surface pressure in hPa. (a) Control (TRIFFID preindustrial) and (b) noGrIS<sub>bsi</sub>. The bottom panel shows the difference in wind patterns at pressure level 3 and sea-level pressure for (c) noGrIS<sub>bsi</sub> minus preindustrial TRIFFID control.

ens (compare with Figure 3.33c). The differences in low-level circulation in winter between the control and noGrIS<sub>bsi</sub> simulations are reflected in the precipitation distribution in Figure 4.18 as a result of reduced blocking and orographic lift of moisture along the eastern coast. As discussed in Chapter 3 (section 3.3.5) the changes in low-level circulation during winter are mainly accounted for by the changes in orography. However, during summer, surface type has a significant effect on the circulation as a result of an increase in shortwave flux absorbed at the surface and subsequent

increases in latent and sensible heat flux driving the ascent of warm air from the surface and therefore the potential for localised cyclonic flow. The low-level circulation observed here in the summer is again comparable with that found for fixed C3 grass and shrubs. This is expected since much of Greenland is covered with these types of vegetation.

## 4.4 Discussion and conclusions

In order to determine the influence of vegetation growth on the potential irreversibility of a deglaciated Greenland, simulations have been performed using the DGVM, TRIFFID, fully coupled to HadCM3. First the model was evaluated, specifically at high latitudes, in terms of temperature and precipitation over Greenland and global vegetation distribution. There is a cold bias over the Greenland region, particularly during winter, by approximately  $-3^{\circ}\text{C}$  compared with observations over the GrIS and  $-7.5^{\circ}\text{C}$  with satellite data over all of Greenland. As a consequence there is an underestimation of needleleaf trees at mid to high northern latitudes compared with the observed vegetation distribution, derived from satellite observation, used to initiate the experiments in the model. However, comparisons with other HadCM3 model versions show smaller differences than with observation data.

The impact of surface type initial condition on the interactive vegetation distribution and climate over Greenland has been investigated by using the two most contrasting climates in Chapter 3: a surface covered by bare soil and a surface covered with needleleaf trees. Although starting from a surface covered with needleleaf tree is highly unrealistic, the results showed the eventual vegetation growth and associated climate was predominantly insensitive to initial condition in terms of vegetation distribution, local temperature changes, hydrological changes and ocean heat transport. Therefore, from these simulations there appears to be only one stable vegetated state on a deglaciated, fully rebounded Greenland with preindustrial  $\text{CO}_2$  concentrations.

Vegetation growth over a deglaciated Greenland comprises a mixture of C3 grasses, shrubs and bare soil. C3 grasses dominate in the north and west while shrubs dominate in the warmer central and southern parts of Greenland. The high altitude of the eastern region is predominantly covered by bare soil. There are



no significant changes to vegetation outside of Greenland consistent with the conclusion from Lunt *et al.* (2004). However, no trees are predicted over Greenland in contrast to Lunt *et al.* (2004) and Driesschaert *et al.* (2007) who showed the development of trees in the south and east of a melted Greenland. In the case of Driesschaert *et al.* (2007) the VECODE DGVM was used which is a simplified vegetation model as described in Section 4.2 with only two PFTs modelled. The resolution of the atmosphere-vegetation component is also nearly twice as coarse as HadCM3-TRIFFID and is therefore unlikely to resolve the high elevation regions over Greenland particularly well. Furthermore, that study simulates the melting of the GrIS and described the vegetation distribution at the end of a 2,000 year simulation. The bedrock may not have been fully rebounded in that case and therefore have provided climate conditions more favourable for tree growth. In the study of Lunt *et al.* (2004) only one-way coupling between vegetation and climate was performed and therefore changes in vegetation were not able to feedback on the climate. Furthermore, the rebounded orography they used was far less complex than that used in this study. The majority of Greenland was between 500 and 1000 m with a small region in the east up to 1500 m in Lunt *et al.* (2004). Figure 3.3 shows much of eastern Greenland is above 1200 m and as high as 1600 m in this study providing conditions less favourable for vegetation growth. The difference in elevation between the study of Lunt *et al.* (2004) and this study could be sufficient to prevent tree growth in the south and east in TRIFFID as a result of near-surface temperatures being too cold for needleleaf tree to expand and maintain growth and productivity. The cold bias in MOSES 2-TRIFFID is also a factor and cannot be excluded as a reason for why there is no tree growth over Greenland using HadCM3. These results suggest that vegetation type is largely determined by the conditions in the coldest months since temperature and precipitation during the summer would potentially be tolerated by needleleaf tree.

In terms of changes to the local climate over a deglaciated and vegetated Greenland, precipitation patterns during the winter are similar to the fixed noGrIS<sub>reb</sub> vegetation experiments in Chapter 3, Section 3.3.5, and are largely orographically induced during this season. During summer, there is an intensification and expansion of precipitation over Greenland as a result of an increase in surface moisture flux as well as the orographic enhancement along the eastern margin. The hydrolog-

ical cycle over much of Greenland resembles that of fixed noGrIS<sub>reb</sub> C3 grass/shrubs consistent with the interactive vegetation distribution. It is somewhat different in the east and to some extent in the south where bare soil is prevalent. The contrast in surface temperature and snow cover over a vegetated Greenland reflects the effect of the vegetation-snow-albedo feedback mechanism where shrubs and grasses have a lower surface albedo due to the ability of the canopy to mask any snow at the surface which increases the absorption of shortwave heat flux at the surface (see Section 1.3.2).

Changes in atmospheric circulation in winter are consistent with the change in orographic forcing discussed in Chapter 3. Likewise, changes in summer are driven more by increased heat flux at the surface via absorption of shortwave radiation and subsequent increases in heat losses via the turbulent heat fluxes. This is consistent with Crucifix *et al.* (2005) which showed that growth of vegetation increased fluxes of evapotranspiration and therefore the latent heat flux. Winter near-surface temperature anomalies are comparable with the winter fixed vegetation noGrIS<sub>reb</sub> anomalies and therefore attributed to the lapse rate correction in temperature between different elevations and changes in low-level atmospheric circulation. During summer the average temperature anomaly is similar to the noGrIS<sub>reb</sub> fixed C3 grass experiment. Although much of Greenland is covered by shrubs, the average anomaly is lower than that for noGrIS<sub>reb</sub> fixed shrubs because the east and southern regions are represented by bare soil where the surface temperature is several degrees cooler.

Since the distribution of vegetation has a significant impact on snow cover it therefore has a strong influence on inferring the possibility of ice-sheet regrowth where an ice-sheet model is not used. Where there are shrubs and grasses, snow cover is small and even snow-free in central Greenland during the summer. However, regions dominated by bare soil are favourable for snow accumulation with insufficient melting during spring and early summer and therefore maintain snow cover throughout the year. It is possible that this region could provide suitable conditions for ‘seeding’ of an ice-sheet.

Removing the GrIS does not have a significant far-field impact on the climate when interactive vegetation is included compared with the control. Only over Greenland and the surrounding seas is the near-surface temperature statistically different from the control mean at the 95 % level of confidence using the Student T-test.

There is an increase in sea-ice to the east of Greenland and therefore a decrease in near-surface and SSTs consistent with the noGrIS<sub>reb</sub> fixed vegetation experiments and previous studies (Lunt *et al.*, 2004; Toniazzo *et al.*, 2004; Ridley *et al.*, 2005). This is caused by a reduction in gyre ocean heat transport as a result of shifting of the North Atlantic storm tracks and a reduction in cyclogenesis off the southern tip of Greenland.

Although inferences about ice-sheet regrowth (under a preindustrial climate with a rebounded orography) from diagnostics such as snow cover can be made, it is necessary to determine whether the high ground in the east and south is sufficient to provide a suitable location for the development of an ice cap and subsequent dynamic ice-sheet regrowth over much of the Greenland landmass. This question can be addressed using a dynamic ice-sheet model such as Glimmer. Chapter 5 explores the possibility of ice-sheet regrowth and whether the inclusion of vegetation feedbacks in HadCM3 is important for the inception of ice over a deglaciated and fully rebounded Greenland.



# The response of a dynamic ice-sheet model to the climate of a melted Greenland ice-sheet

## 5.1 Introduction

Previous studies (Crowley and Baum, 1995; Lunt *et al.*, 2004; Toniazzo *et al.*, 2004) have used the snow cover amount variable, derived from GCMs, as an indicator of ice-sheet regrowth. From interpretation of this diagnostic they concluded that an ice-sheet was unlikely to regrow if it had completely melted due to a sustained greater than 3°C annual warming over Greenland and a subsequent return to a preindustrial climate. However, the study of Lunt *et al.* (2004) also used their GCM climate to force an ice-sheet model offline and found regrowth of a substantial ice-sheet in central and eastern Greenland at the end of their simulation. They attributed the difference in results between climate and ice-sheet model diagnostics to the high-resolution used in ice-sheet models (compared with typical GCM resolutions) resolving regions of very high altitude that are not represented by a typical GCM resolution such as HadCM3. A further study (Vizcaíno *et al.*, 2008) used a low resolution GCM (with the DGVM, LPJ included) coupled to an ice-sheet model and found no significant ice-sheet growth at the end of their 1,000 year simulation.

In addition to future regrowth, the anthropogenic influence on GrIS melting behaviour has been examined by others. Ridley *et al.* (2005) used two way-coupling between HadCM3 (MOSES 1) and an ice-sheet model under four times elevated CO<sub>2</sub> concentrations and found almost complete disintegration of the ice-sheet within 3,000 years with no recovery or new stable state achieved. Experiments performed by Charbit *et al.* (2008) using an EMIC coupled to an ice-sheet model examined the impact of evolving carbon emissions on the irreversible melting of the GrIS. They found that for complete and irreversible melting of the GrIS to be avoided, total

CO<sub>2</sub> emissions should not overcome 2,500 GtC in the future. However, the impact of CO<sub>2</sub> on the irreversibility of a melted GrIS is not investigated in this thesis.

The contrasting results between GCM diagnostic and ice-sheet model for future regrowth of the GrIS indicate that it is necessary to use a dynamic ice-sheet model in conjunction with a GCM in order to address the question of whether regrowth of the GrIS is possible under a preindustrial climate. In particular, this Chapter will evaluate the importance of including vegetation feedbacks in the GCM simulation on the future inception of ice on Greenland using the ice-sheet model Glimmer. Lunt *et al.* (2004) acknowledge that the lack of vegetation feedbacks in their GCM noGrIS simulation could result in a smaller equilibrium ice-sheet as a result of tree and grass growth over Greenland decreasing the summer albedo and raising the local near-surface temperature.

Ice-sheet forcing methodology is first described followed by offline forcing of Glimmer using the *fixed* vegetation noGrIS simulations described in Chapter 3 and the *dynamic* vegetation noGrIS simulations described in Chapter 4. The ice-sheet model description can be found in Section 2.2.

## 5.2 Ice-sheet regrowth over a melted, rebounded Greenland

Offline ice-sheet model forcing has been used in this study in order to overcome the computational expense of running HadCM3 synchronously coupled to Glimmer. Since higher order physics is not included in Glimmer it can be run for long model time periods relatively quickly. However, it is not currently possible to run a full GCM, such as HadCM3, on the timescales of ice-sheet growth and decay (typically several thousands of years). Although previous work (e.g. Vizcaíno *et al.*, 2008) has used two-way coupling for GrIS regrowth experiments they used a lower resolution GCM and therefore were not so constrained by the climate model time integrations. It is therefore important to realise that the simulations presented in this chapter do not include the ice-albedo feedback or the vegetation-snow-climate feedback mechanisms between ice-sheet model and climate model. The implication of this is that a growing ice-sheet does not influence the surface energy budget in the GCM through albedo changes which in turn modifies the climate over Greenland. However, the

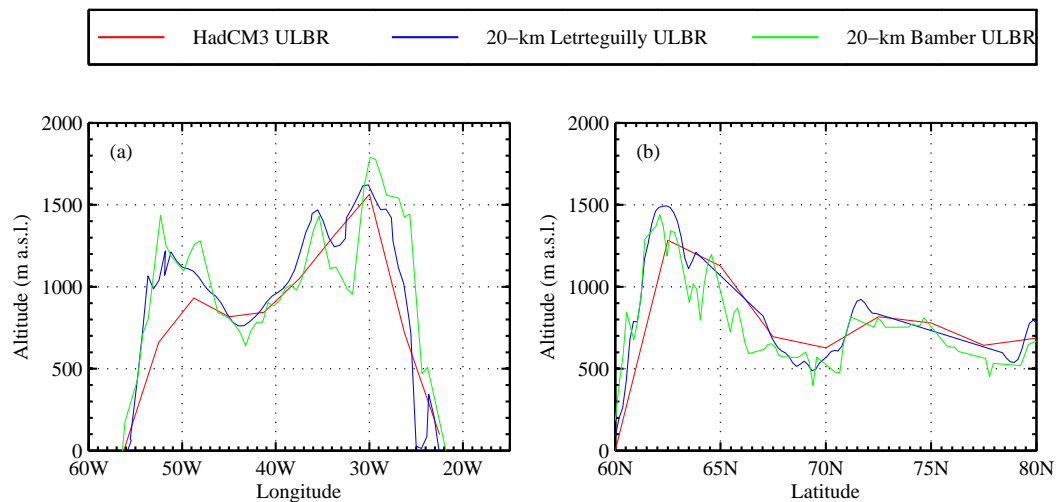


Figure 5.1: Transects of Greenland bedrock topography at 20 km resolution from the Letreguilly and Bamber datasets and the Letreguilly dataset interpolated to the HadCM3 resolution for the noGrIS simulations. (a) an east-west transect at  $72.58^{\circ}\text{N}$  and (b) a south-north transect at  $45^{\circ}\text{W}$  passing through the southern tip of Greenland (ULBR=Unloaded BedRock).

ice-elevation feedback is taken into account via a lapse rate correction as the ice-sheet grows/decays. For example, the surface temperature of the ice-sheet decreases as the ice-sheet grows and increases in altitude.

Figure 5.1 shows east-west and south-north transects of the rebounded bedrock topography at the 20 km resolution for the Bamber and Letreguilly datasets and also at the resolution of HadCM3. First note that the detail in bedrock topography at the 20 km resolution is largely absent at the comparatively coarse HadCM3 resolution. It is this detail which could make it possible to model the effect of seeding an ice-sheet at high elevations and justifies the need to use a dynamic ice-sheet model. For the east-west transect (Figure 5.1a) the coastal eastern mountain range shows a reduced altitude for HadCM3 by several hundred metres compared with the Bamber 20 km dataset. It is significantly closer in altitude to the Letreguilly dataset since this is the data that the HadCM3 rebounded orography was derived from. Along the western coast the mountains in HadCM3 are at an altitude at least 300 m lower compared with the 20 km resolution datasets. In terms of the south-north transect (Figure 5.1b) there is less difference in altitude between HadCM3 and the Glimmer resolution datasets apart from the altitude of the southern mountain range. These differences between datasets could determine whether ice regrows or not and illustrate the caution needed in predicting ice regrowth from climate model diagnostics alone.

### 5.2.1 Forcing methodology

In order to force Glimmer offline an anomaly method has been used in accordance with previous modelling studies (e.g. Huybrechts and T'Siobbel, 1997; Huybrechts and de Wolde, 1999; Ridley *et al.*, 2005; Driesschaert *et al.*, 2007; Lunt *et al.*, 2008, 2009). By using an anomaly forcing method it acts to minimise systematic errors in the climate model. Validation of HadCM3 preindustrial controls (with and without interactive vegetation) showed a cold temperature bias over Greenland during the winter months. Consequently, the use of temperature anomalies rather than absolute temperatures are used to force the ice-sheet model in order to eliminate these climate model biases. Thus, monthly mean changes in precipitation and near-surface temperature are superimposed onto a present day reference climatology used by the surface mass balance model in Glimmer. This chapter uses present day reference climatologies and model parameterisations based on the EISMINT-3 exercise setup (discussed in detail in Chapter 2, Section 2.3.1) and the ‘tuned’ more realistic boundary conditions and forcings (five optimal tuned parameter sets) derived in Chapter 2, Section 2.5.3.

In addition, the coarse resolution of HadCM3 relative to Glimmer results in a poor representation of topography (shown in Figure 5.1) and therefore it is not meaningful to use absolute values for temperature. In order to combat this problem a lapse rate correction is applied to the near-surface air temperature to account for the differences in altitude between the lower resolution HadCM3 grid and the higher resolution Glimmer grid.

As a result of these issues, all experiments were forced by monthly mean temperature anomalies ( $T^{ice}$ ) as follows

$$\begin{aligned}
 T^{ice} &= T^{REF} + \Delta T^{GCM} + L_G \cdot \Delta H^{GCM}, \\
 \Delta T &= (T_{expt}^{GCM} - T_{cnt}^{GCM}), \\
 \Delta H &= (H_{expt}^{GCM} - H_{cnt}^{GCM}),
 \end{aligned}
 \tag{5.1}$$

where  $T^{REF}$  is the present day monthly observed near-surface temperature,  $\Delta T^{GCM}$  (in °C) is the monthly mean change in temperature between a GCM perturbed climate experiment and the GCM preindustrial control and ‘ $L_G \cdot \Delta H$ ’ is the temperature change from a lapse rate correction as a result of any change in elevation



between the perturbed climate GCM simulation and the GCM control. Downscaling of  $T^{ice}$ , in order to account for the difference in altitude between the low resolution topography associated with the baseline observed temperatures (i.e.  $T^{REF}$ ) and the high-resolution of the Glimmer bedrock, is subsequently performed according to Equation 2.14.

Changes in precipitation are often more difficult to address using the anomaly approach due to the large uncertainties in GCM model simulations (Randall *et al.*, 2007). There are several possible methods to calculate the precipitation anomaly including superimposing *ratios* of precipitation or *absolute differences* in precipitation onto the reference precipitation. Other methods such as setting the precipitation rate proportional to the moisture holding capacity of an air column with a known sensitivity per °C (Huybrechts and T'Siobbel, 1995) have been used but are not described here. Huybrechts and T'Siobbel (1997) performed a series of Last Glacial Maximum simulations using the anomaly method and tested the sensitivity of applying precipitation ratios compared with absolute differences. They found that the anomaly method used made little difference to the final result with absolute differences giving a smaller ice area and volume of  $\sim 4\%$  and  $\sim 7\%$  respectively compared with the ratios method. In this thesis the absolute difference in precipitation method is used for consistency with previous, related work (Lunt *et al.*, 2009; Irvine *et al.*, 2009; Stone *et al.*, 2010). Therefore, the monthly precipitation anomaly is calculated according to

$$P^{ice} = P^{REF} + \Delta P^{GCM}$$

$$P^{ice} = \begin{cases} P^{REF} + (P_{expt}^{GCM} - P_{cnt}^{GCM}) & \text{if } P^{REF} + \Delta P^{GCM} \geq 0 \\ 0 & \text{if } P^{REF} + \Delta P^{GCM} < 0 \end{cases} \quad (5.2)$$

where  $P^{REF}$  is the monthly present day precipitation rate (in  $\text{mm s}^{-1}$ ),  $\Delta P^{GCM}$  is the monthly mean change in precipitation rate between a perturbed GCM climate and the GCM control. When  $P^{ice}$  becomes negative it is set to zero since negative precipitation is not possible.

The following sections address the question of whether the GrIS is likely to reglacierate, following a melting driven by greenhouse gas increases, and how sensitive this potential reglacieration might be to surface type over Greenland in the climate

model. This is tested first by forcing Glimmer offline with the fixed vegetation noGrIS<sub>reb</sub> simulations (from Chapter 3, Section 3.3.5). This allows the sensitivity of ice-sheet regrowth to individual surface type to be assessed and indicates whether the snow cover and amount variables from the GCM are adequate in predicting future ice-sheet behaviour. In addition to these idealised experiments, the sensitivity of ice-sheet behaviour to the likely predicted vegetation distribution over an ice-free Greenland is addressed when the ice-sheet model is forced with the interactive vegetation climatologies discussed in Chapter 4.

In order to perform such experiments the initial boundary condition used was a rebounded, high-resolution bedrock of the Letreguilly and Bamber datasets (discussed in Sections 2.3 and 3.3.1) with no ice. Simulations were run for 50,000 years in order for the ice-sheet to reach equilibrium.

### 5.2.2 Fixed vegetation climate simulations

The evolution in ice volume and ice surface extent is shown in Figure 5.2 and Figure 5.3 respectively when Glimmer is forced with monthly temperature and precipitation anomalies from the six noGrIS<sub>reb</sub> fixed surface type experiments discussed in Chapter 3, Section 3.3.5. The diagnostics of resultant equilibrium ice volume, ice surface extent, equivalent global sea-level height and maximum ice thickness are also given in Table C.1 in Appendix C. In addition, also included in Table C.1, are the ice-sheet diagnostics for present day simulations under the different Glimmer model parameter sets described in Chapter 2. Note that all ice-sheet model parameter sets overestimated the present day form of the GrIS, including the tuned parameter sets, with the error, for instance, in sea-level equivalent height ranging from 4.1 to 19.2 %. Thus, all comparisons are made with modelled present day GrIS volume rather than the observed ice-sheet data. All simulations result in some ice inception growth over Greenland after 50,000 years. However, there is a distinct threshold in ice volume between a surface covered by bare soil and a surface covered with one of the five PFTs. Figure 5.2a shows the evolution in ice volume for the noGrIS<sub>reb</sub> bare soil experiment. The equilibrium ice volume ranges from  $0.76 \times 10^6$  to  $3.0 \times 10^6 \text{ km}^3$  depending on Glimmer model setup. The largest growth of ice occurs for the EISMINT-3 setup with an ice surface extent only 7.6 % smaller than the EISMINT-3 modelled present day GrIS. However, the tuned model parameter sets

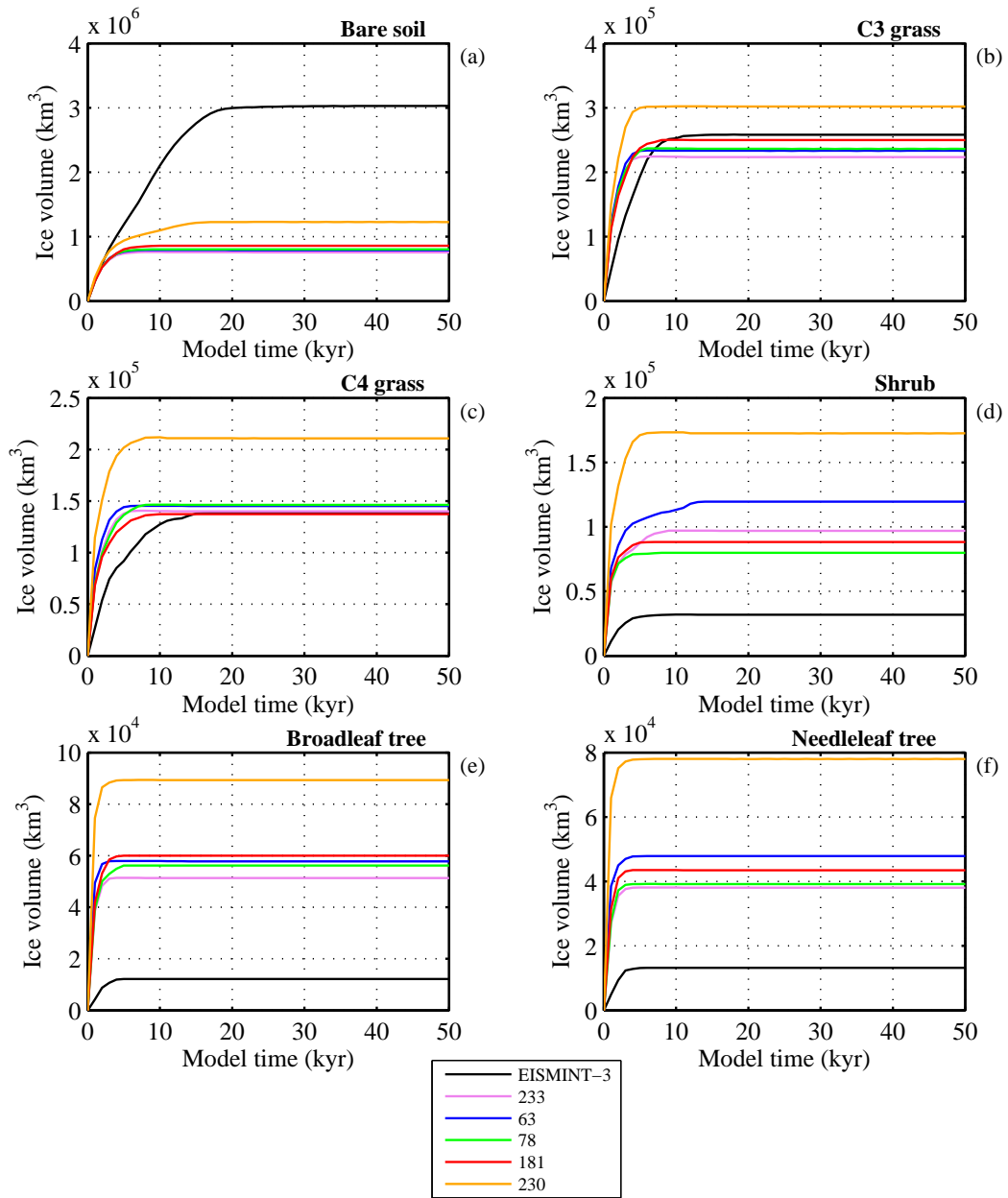


Figure 5.2: Evolution of ice-sheet volume when Glimmer is forced with *fixed* (a) bare soil, (b) C3 grass, (c) C4 grass, (d) shrub, (e) broadleaf tree and (f) needleleaf tree noGrIS<sub>reb</sub> climatologies. On each subfigure the ice-sheet evolution for the tuned Glimmer model parameter sets discussed in Section 2.5.3 and the EISMINT-3 setup are shown. Note that the scales are different on each subfigure in order to compare the results from different ice-sheet model parameter sets clearly.

result in ice volumes substantially smaller when forced with noGrIS<sub>reb</sub> fixed bare soil climatology (greater than 92 % smaller compared with EISMINT-3).

When the surface is replaced with any one of the PFTs and Glimmer is forced offline, the ice volume is at least ten times smaller compared with when the surface was covered with bare soil (Figures 5.2b to f). The smallest ice volume and ice surface extent occurs for the broadleaf and needleleaf tree PFTs, followed closely

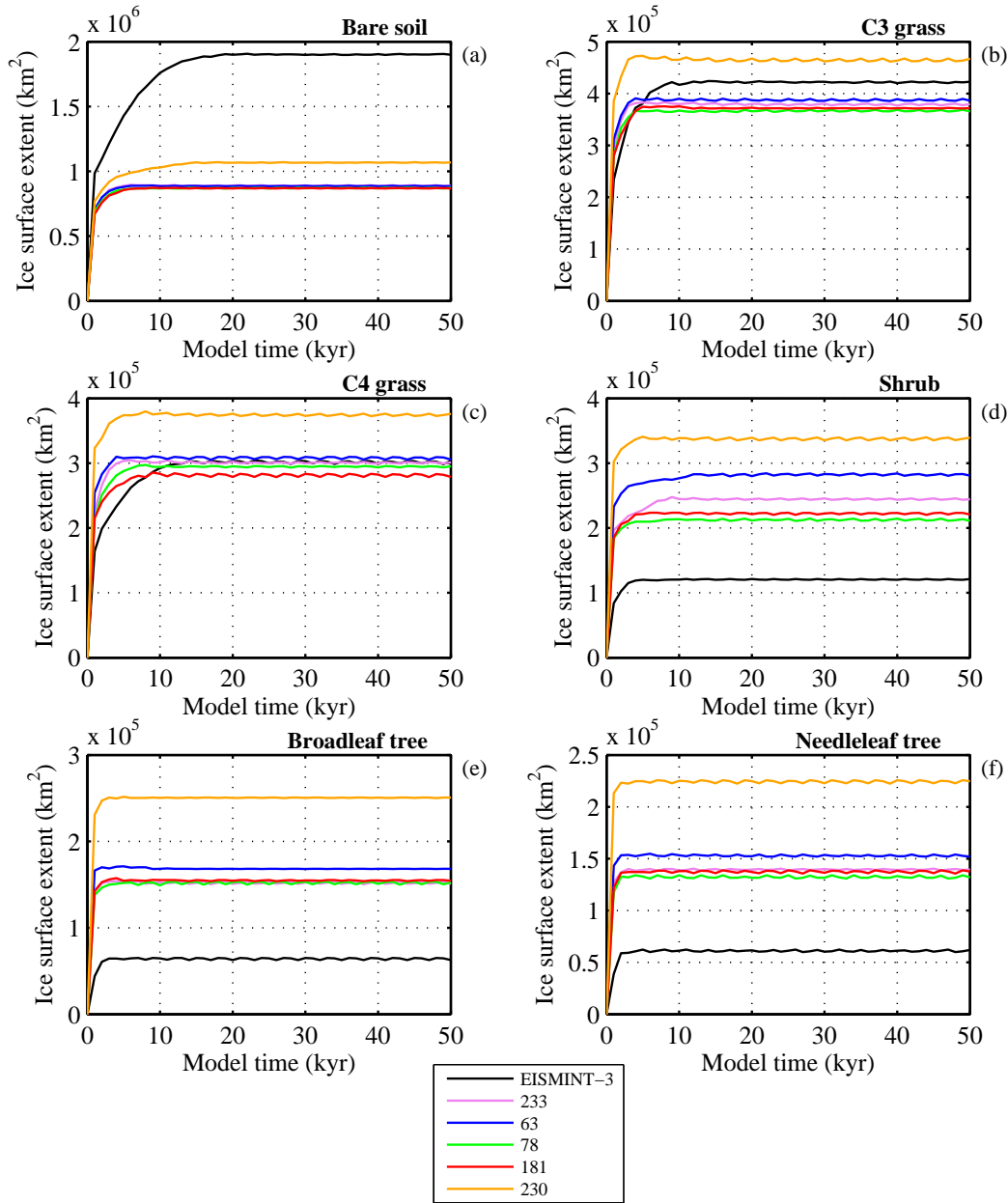


Figure 5.3: Evolution of ice surface extent when Glimmer is forced with *fixed* (a) bare soil, (b) C3 grass, (c) C4 grass, (d) shrub, (e) broadleaf tree and (f) needleleaf tree noGrIS<sub>reb</sub> climatologies. On each subfigure the ice-sheet evolution for the tuned Glimmer model parameter sets discussed in Section 2.5.3 and the EISMINT-3 setup are shown. Note that the scales are different on each subfigure in order to compare the results from different ice-sheet model parameter sets clearly.

by shrubs and C4 grasses and finally C3 grasses. The largest ice volume for a surface covered by one of the five PFTs is consistently found for the tuned setup, expt 230. However, in contrast with the results for noGrIS<sub>reb</sub> with bare soil, the EISMINT-3 setup results in the smallest ice volume and ice surface extent for the PFT climatologies. Figures 5.3b to f show cyclic behaviour of the ice surface extent about a mean equilibrium trend. However, this cyclic behaviour is not seen in the

evolution of ice volume in Figure 5.2. This can be explained by the ice-free/ice-covered threshold determined from the derived ice thickness at each gridpoint on the Glimmer grid. If ice thickness is greater than zero for any gridpoint it is counted as being ice-covered which ultimately results in small fluctuations in the ice surface extent since growth of even less than 1 m is counted as ice-covered.

The time at which it takes to reach equilibrium in terms of ice surface extent and ice volume varies between surface type and also Glimmer model parameter sets. The largest disparity between model parameter sets occurs for a bare soil surface. When the surface is covered in bare soil (Figure 5.2a and Figure 5.3a) equilibrium is reached after approximately 20,000 years for the EISMINT-3 setup. However, for four out of the five tuned parameter sets equilibrium is reached by approximately 5,000 years. While tuned setup expt 230 takes about 10,000 years longer than the other tuned parameter sets. In terms of the PFTs, equilibrium is reached significantly quicker with smaller differences between model parameter sets. For instance, a surface covered by needleleaf tree (Figure 5.2f and Figure 5.3f) results in ice equilibrating within approximately 4,000 years for all model parameter sets. A surface covered by C3 grass (Figure 5.2b) shows equilibration by 15,000 years under an EISMINT-3 setup and just under 10,000 years for all other tuned parameter sets. The range in equilibrium times merely reflects the fact that more ice grows for a surface covered by bare soil followed by a surface covered by C3 grasses and therefore takes longer to reach an equilibrium state.

Figure 5.4 shows the ice-sheet geometry for the six fixed surface type climatologies when Glimmer is configured with the EISMINT-3 and five tuned parameter sets at the end of 50,000 years of simulation. It is clear that any significant regrowth of ice over Greenland only occurs for a surface covered by bare soil for all ice-sheet model setup scenarios. In particular, the EISMINT-3 setup results in almost complete reglaciation of Greenland with only western regions remaining ice-free. Maximum ice thickness at the ice-sheet divide in central Greenland is comparable to the present day modelled ice-sheet (3.3 km compared with 3.1 km). The tuned parameter sets, however, result in only partial regrowth with ice confined to the high altitude regions of the east and south of the island. Any ice-sheet coverage present for all Glimmer model parameter sets is not dissimilar for the five PFTs. When the surface is covered by C3 grass a persistent ice dome forms in the south with another

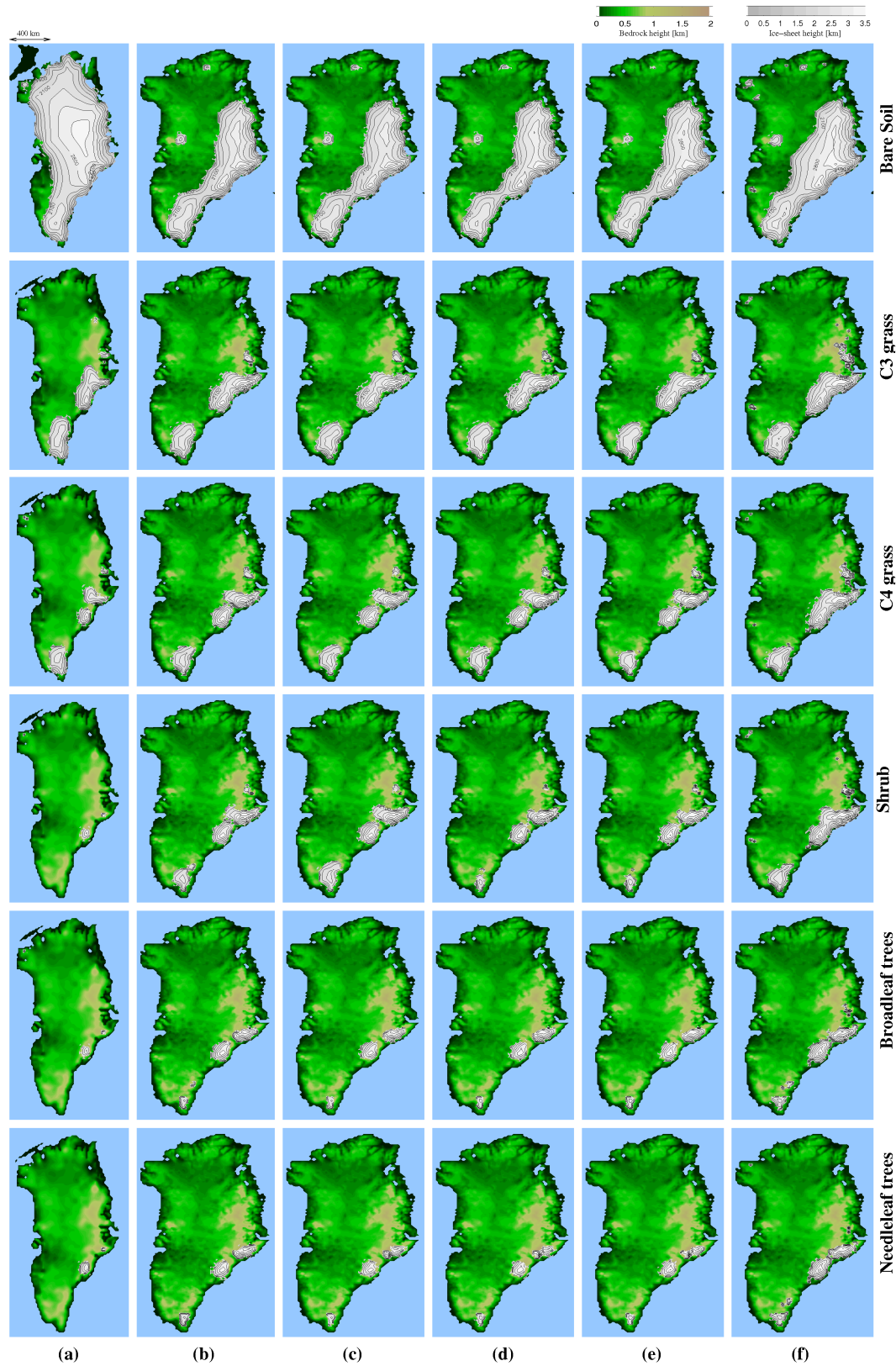


Figure 5.4: Ice-sheet geometries after 50,000 years of simulation for the noGrIS<sub>reb</sub> fixed vegetation climatologies discussed in Chapter 3, Section 3.3.5. Geometries are shown for the different Glimmer model parameter sets: (a) EISMINT-3 and the 5 optimal tuned parameter sets derived in Section 2.5.3 (b) expt 233, (c) expt 63, (d) expt 78, (e) expt 181 and (f) expt 230. Glimmer simulations begin from an initial condition of no ice and rebounded bedrock.

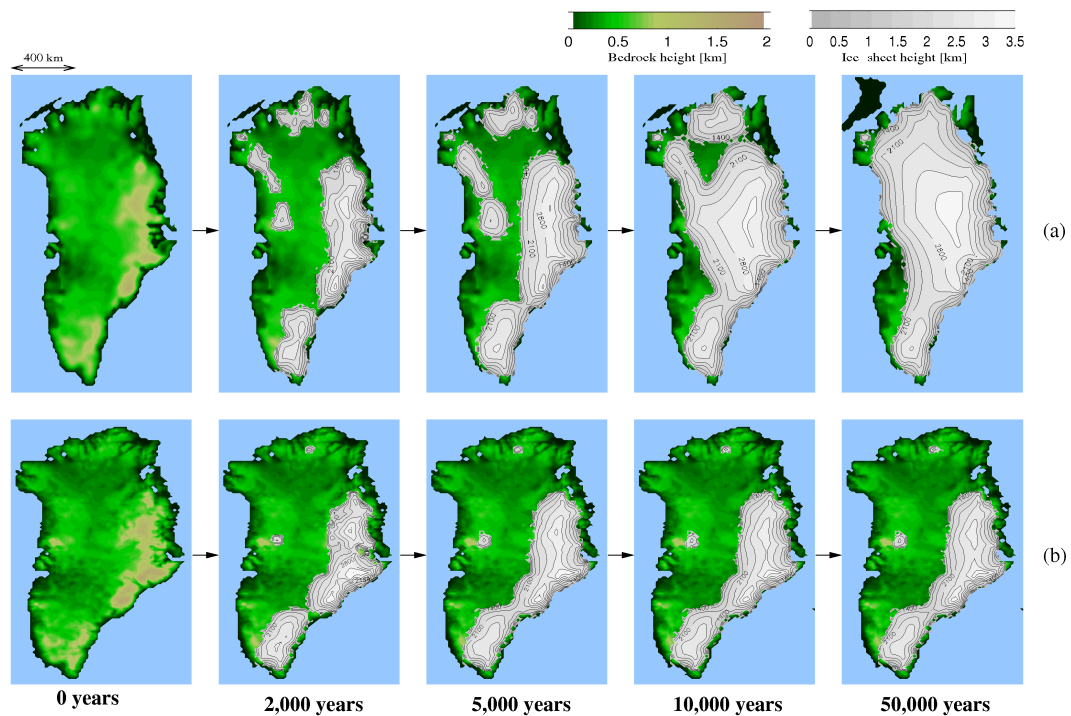


Figure 5.5: Snapshots through time of GrIS extent when Glimmer is forced offline with a fixed bare soil noGrIS<sub>reb</sub> climatology for Glimmer model parameter sets (a) EISMINT-3, (b) tuned expt 230 and (c) tuned expt 233. The tuned experiments represent the extremes in ice volume evolution for the optimal tuned parameter sets (see Figure 5.2a).

isolated ice cap in the east. For trees and shrubs ice is only found in the highest mountainous regions of Greenland as small, isolated ice caps with ice mass no more than the equivalent of 0.2 m of sea-level height.

A series of snapshots through time for the development of ice on Greenland when the surface is covered with bare soil is shown in Figure 5.5. Accumulation of snow and ice are controlled by local climate which is particularly sensitive to topographic features. Accordingly, large ice-sheets will begin as small mountain glaciers and ice caps at high altitudes. If the climate is sufficiently cool these will thicken and coalesce and their increased surface altitude will cool the local surface climate further. In turn, the ice will become thick enough to flow to lower altitudes where the ice-elevation feedback lowers the temperature adequately to ensure no melting of the ice (Marshall and Clarke, 1999). In terms of the EISMINT-3 model simulation (Figure 5.5a) after 2,000 years ice has begun to nucleate in the high altitude regions of the east and south of the island. There is also some growth in the north and northwest. By 5,000 years ice nucleation in the east has expanded westward with the flow of glaciers into regions of relatively low bedrock. This gradual build up of ice

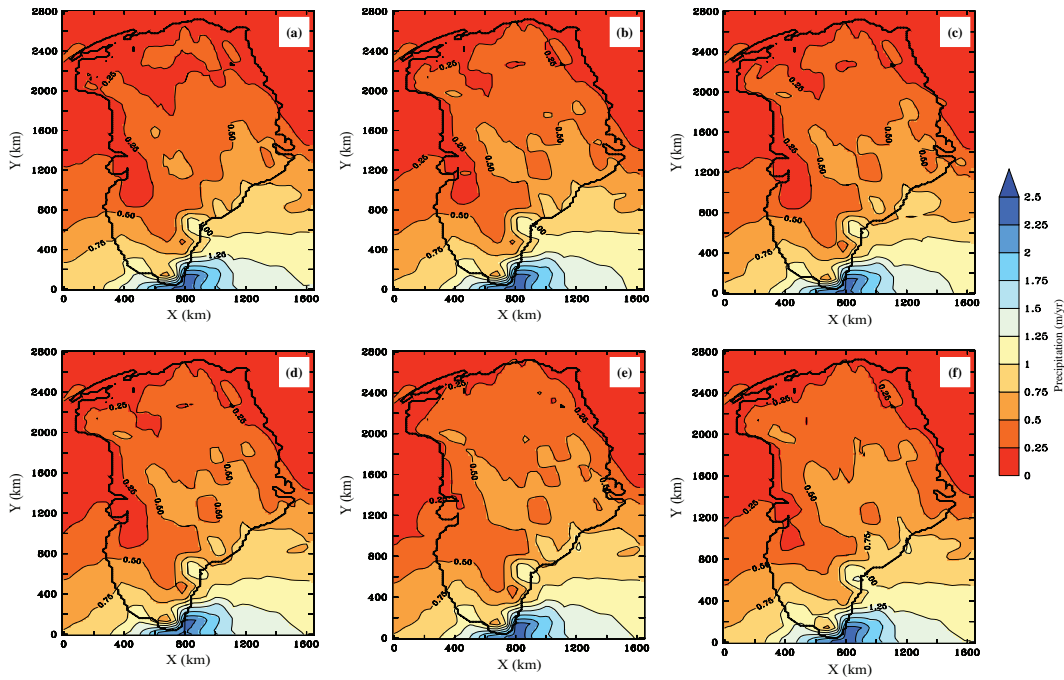


Figure 5.6: Annual accumulation (in m/yr) over Greenland when Glimmer is forced with noGrIS<sub>reb</sub> climatologies where the surface type is fixed as (a) bare soil, (b) C3 grass, (c) C4 grass, (d) shrub, (e) broadleaf tree and (f) needleleaf tree.

via the ice-temperature-elevation feedback mechanism allows an extensive ice-sheet to form over much of Greenland. By 10,000 years the isolated regions of ice growth in the north and north-west have coalesced with the expanding ice from the east. As a consequence of this ice formation much of the bedrock in central Greenland is several hundred metres below sea-level similar to present day observations (Bamber *et al.*, 2001).

Figure 5.5b shows the minimum ice growth for the tuned expt 233 Glimmer parameter set (when the surface is covered with bare soil), consistent with the ice volume evolution in Figure 5.2. All other tuned ice-sheet configurations show a similar pattern. Unlike ice-sheet development for the EISMINT-3 setup, much of the ice-sheet regrowth has occurred by 2,000 years and confined to the high altitude regions of the east and south. There is little or no separate nucleation of ice in the relatively high regions of the west and north.

These differences between Glimmer model parameter sets and noGrIS surface types can be examined in terms of both the differences in parametric uncertainty and boundary conditions in Glimmer as well as the difference in precipitation and temperature forcing from the noGrIS<sub>reb</sub> climate simulations. Precipitation from HadCM3 downscaled onto the Glimmer dataset is not altered by any of the tuned



ice-sheet model parameters (lapse rate, PDD factors for ice and snow, geothermal heat flux, and flow enhancement factor). Figure 5.6 shows the annual precipitation (assumed potentially all to lead to accumulation) in  $\text{m yr}^{-1}$  for all noGrIS<sub>reb</sub> fixed surface types. The precipitation for a surface covered in bare soil is shown by Figure 5.6a. The inception of ice in the east (with up to  $1.25 \text{ m yr}^{-1}$  of accumulation in the southeast) is seeded by the increase in precipitation throughout the year relative to the preindustrial, in combination with surface temperatures below zero throughout the year. The precipitation is substantially lower in the west where Greenland remains ice-free for all ice-sheet model setup scenarios and temperatures are above zero during the summer months.

There is an increase in annual precipitation rate over Greenland as the surface is modified from grasses (Figure 5.6b and c) to a surface covered in shrubs and trees (Figure 5.6d, e and f). When the surface is covered by needleleaf tree vegetation (Figure 5.6f), annual precipitation is up to  $0.5 \text{ m yr}^{-1}$  larger than for a bare soil surface in central Greenland. Precipitation in northern and western parts of the island is also larger but less pronounced.

In contrast to precipitation, temperature forcing from HadCM3 is affected by parametric uncertainty in the downscaling procedure from the low resolution of the climate model to the high-resolution of the ice-sheet model. The lapse rate used in this downscaling differs between the Glimmer model parameter sets ranging from  $-7.4$  to  $-4.1^\circ\text{C km}^{-1}$ . Figure 5.7 shows the summer temperature distribution over Greenland from Glimmer at the beginning and end of the fixed bare soil noGrIS<sub>reb</sub> simulation. Also shown is the annual mass balance after 50,000 years. Summer temperatures are shown here because this is the season when ablation is most prominent and indicates whether any ice present can survive into the winter months. Initially the summer temperature for model setup expt 230 (not shown), particularly in the east, is several degrees Celcius colder compared with EISMINT-3. This is because not only is the bedrock higher in coastal regions for the Bamber rebounded bedrock dataset (see Figure 2.5c and Figure 5.1) compared with the Letreguilly dataset but the lapse rate correction is also almost  $1^\circ\text{C}$  more negative ( $-7.4^\circ\text{C km}^{-1}$  compared with  $-6.3^\circ\text{C km}^{-1}$ ). Likewise, the higher bedrock of the Bamber dataset, even though the lapse rate correction magnitude is far less negative ( $-4.3^\circ\text{C km}^{-1}$ ), results in marginally cooler temperatures for expt 233 compared with the EISMINT-3 setup

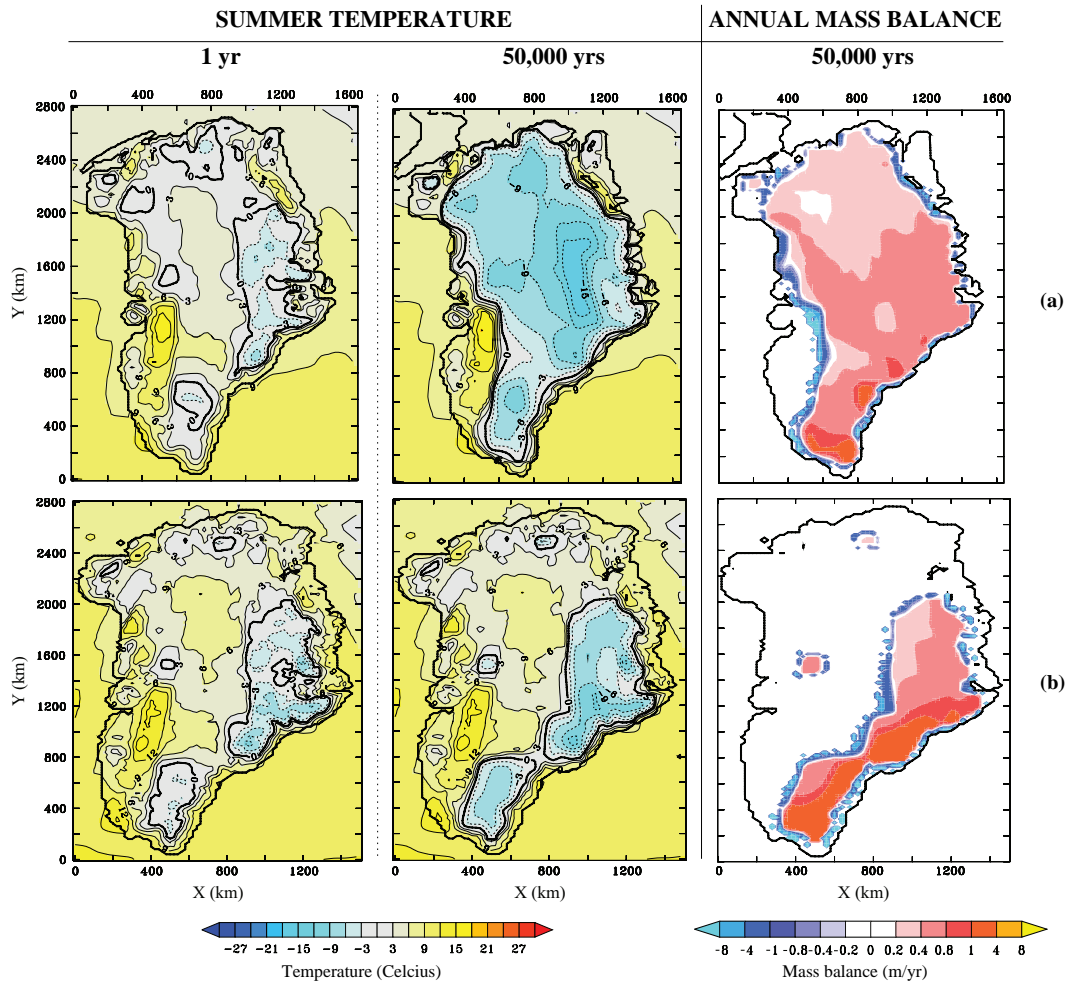


Figure 5.7: Evolution of summer surface temperature from 1 year to 50,000 years when Glimmer is forced with noGrIS<sub>reb</sub> (fixed bare soil) climatology. Annual surface mass balance is also shown at 50,000 years. Glimmer model parameter sets are (a) EISMINT-3 and (b) tuned expt 233. All other tuned experiment parameter sets are similar to (b). Note the different x-scale between EISMINT-3 and the tuned parameter sets due to the different projections.

(see Figure 5.7b). However, the initial cooler temperatures in the east for these Glimmer tuned parameter sets do not result in the growth of an extensive ice-sheet in Figure 5.5b. This is because the effect of the lapse rate parameter and the bedrock is more than compensated by the high PDD factors for ice (see Table 2.5) which increases the potential melting rate and therefore alters the width and extent of the GrIS preventing expansion into central regions. Apart from in the high elevation regions of the east, summer temperatures for the tuned Glimmer parameter sets are significantly above zero in the central interior of Greenland and greater than  $10^{\circ}\text{C}$  in the west for a surface covered by bare soil. A similar temperature distribution

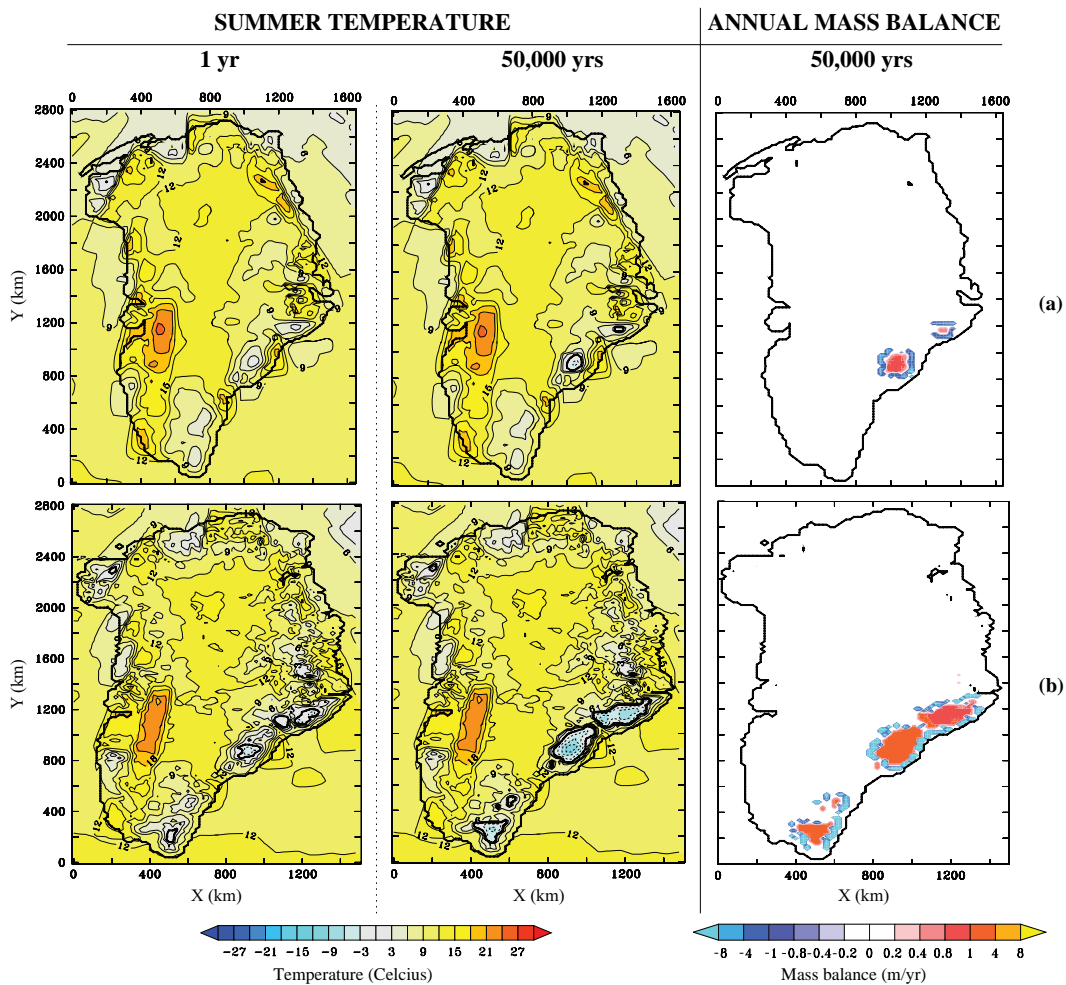


Figure 5.8: Evolution of summer surface temperature from 1 year to 50,000 years when Glimmer is forced with noGrIS<sub>reb</sub> fixed needleleaf tree vegetation climatology. Annual surface mass balance is also shown at 50,000 years. Glimmer model setups are (a) EISMINT-3 and (b) tuned expt 230. All other tuned experiment parameter sets are similar to (b). Note the different x scale between EISMINT-3 and the tuned setup due to the different projections.

is shown for EISMINT-3 although temperatures in central regions are on average several degrees cooler. With lower PDD factors ice-sheet growth during the winter months can slowly advance and be maintained during the summer as a result of decreasing the surface temperatures due to the ice-elevation feedback mechanism.

After 50,000 years of simulation the summer temperature distribution in Figure 5.7 shows temperatures as low as  $-12$  to  $-15^{\circ}\text{C}$  over eastern regions with temperatures in the west greater than  $12^{\circ}\text{C}$ . This is also the case for the other Glimmer model parameter sets not shown. Annually, temperatures in the east range from  $-25$  to  $-27^{\circ}\text{C}$  and just above zero in the west. The decrease in temperature in the

east over the timespan of the simulation is a result of the positive ice-temperature-elevation feedback mechanism and is observed for all the Glimmer model parameter sets with ice reaching maximum thicknesses of approximately 2 to 3 km.

The annual surface mass balance indicates accumulation of up to  $8 \text{ m yr}^{-1}$  (consistent with the precipitation pattern in Figure 5.6a) in the southeast with mass loss more than  $8 \text{ m yr}^{-1}$  in the ablation zones. In terms of the ice-sheet evolution in Figure 5.7b (Glimmer model parameter set expt 233) the high flow enhancement factor results in the lowest maximum ice thickness of all the Glimmer parameter sets. Although the PDD factors are marginally lower than for expt 230 the faster flow delivers a larger flux of ice to the ablation zone at lower elevations and prevents the ice-elevation feedback from intensifying. In this way the ice-sheet does not expand into the interior of Greenland.

From Figure 5.4 the smallest inception of ice over Greenland occurs when the surface is covered by trees. Since the growth of broadleaf trees is highly unrealistic at high northern latitudes, the focus will be on the response of the ice-sheet model to the climate where the surface is covered by needleleaf trees. This provides the most contrasting scenario to the noGrIS<sub>reb</sub> bare soil experiment which was also the case in terms of the climate response in Chapter 3. The inception growth is similar for all Glimmer model parameter sets with the development of small ice caps over the highest ground in the east and south. For the case of the EISMINT-3 setup (Figure 5.4a) there is no ice growth in the south which is present in the tuned model parameter sets (Figure 5.4c to f). Although precipitation on the eastern coast (Figure 5.6f) would be sufficient to maintain the growth of ice in the east and the subsequent possible expansion into low-level bedrock regions as seen for a surface covered by bare soil, it is the surface temperatures over most of Greenland which prevent any substantial ice regrowth. Figure 5.8 shows the summer surface temperature and annual mass balance for EISMINT-3 setup and the tuned expt 230 parameter set for a surface covered by needleleaf tree. Summer temperatures over most of Greenland are significantly above zero. In the west temperatures are greater than  $20^\circ\text{C}$  for all Glimmer parameter sets. Only in isolated, elevated bedrock regions in the east and south are temperatures a few degrees below zero. For the EISMINT-3 setup (Figure 5.8a) much of southern Greenland experiences summer temperatures above zero throughout the simulation with no seeding of ice and the

subsequent initiation of a positive ice-elevation feedback to slowly increase the ice mass. The additional ice that develops in this region for the tuned parameter sets is maintained by the marginally colder temperatures from onset as a result of the higher altitude of the Bamber bedrock dataset. However, there is no intensification of the ice-elevation feedback mechanism. This is also reflected in the annual surface mass balance where accumulation is confined to the east and south.

### Comparison of the snow diagnostic with dynamic ice regrowth

Since previous studies (Crowley and Baum, 1995; Toniazzi *et al.*, 2004) have used the diagnostic of snow cover as an indicator of ice regrowth on a melted Greenland a comparison has been made (Figure 5.9) between ice surface extent predicted by Glimmer and the minimum snow cover at each gridbox over Greenland, as predicted by HadCM3 for each of the noGrIS<sub>reb</sub> simulations. On each ice surface extent plot all ice configurations after 50,000 years of simulation from EISMINT-3 and the optimal tuned Glimmer model parameter sets are shown (a to f). As previously discussed in Section 3.3.5, a surface covered by bare soil shows persistent snow cover only in the east and southeast of Greenland and therefore inferred the potential for ice regrowth in this region. Indeed, Figure 5.9 shows that for all parameter sets of Greenland there is growth of ice in the east where the high elevations of the mountainous regions resolved by the Glimmer resolution provides a prime location for ice-sheet seeding. However, the extent of ice into central, north and northwestern Greenland for the EISMINT-3 setup is not in agreement with the minimum snow amount indicating no accumulation of snow. The tuned parameter sets agree more closely with the spatial pattern of the snow cover diagnostic although the ice flows further into central regions of Greenland, especially for tuned setup (f) (expt 230) in Figure 5.9.

For the case of C3 grass the minimum snow cover over Greenland amounts to no more than 100 mm water equivalent in the east, with central and western regions snow-free. However, there is nucleation of ice in the south (coincident with an isolated region where snow cover is up to 300 mm of water equivalent in HadCM3) and the east for all model parameter sets where maximum ice thickness ranges between 1.57 to 1.94 km. A similar situation exists for a surface covered by shrubs or C4 grasses where some ice incepts to form isolated ice caps while the minimum

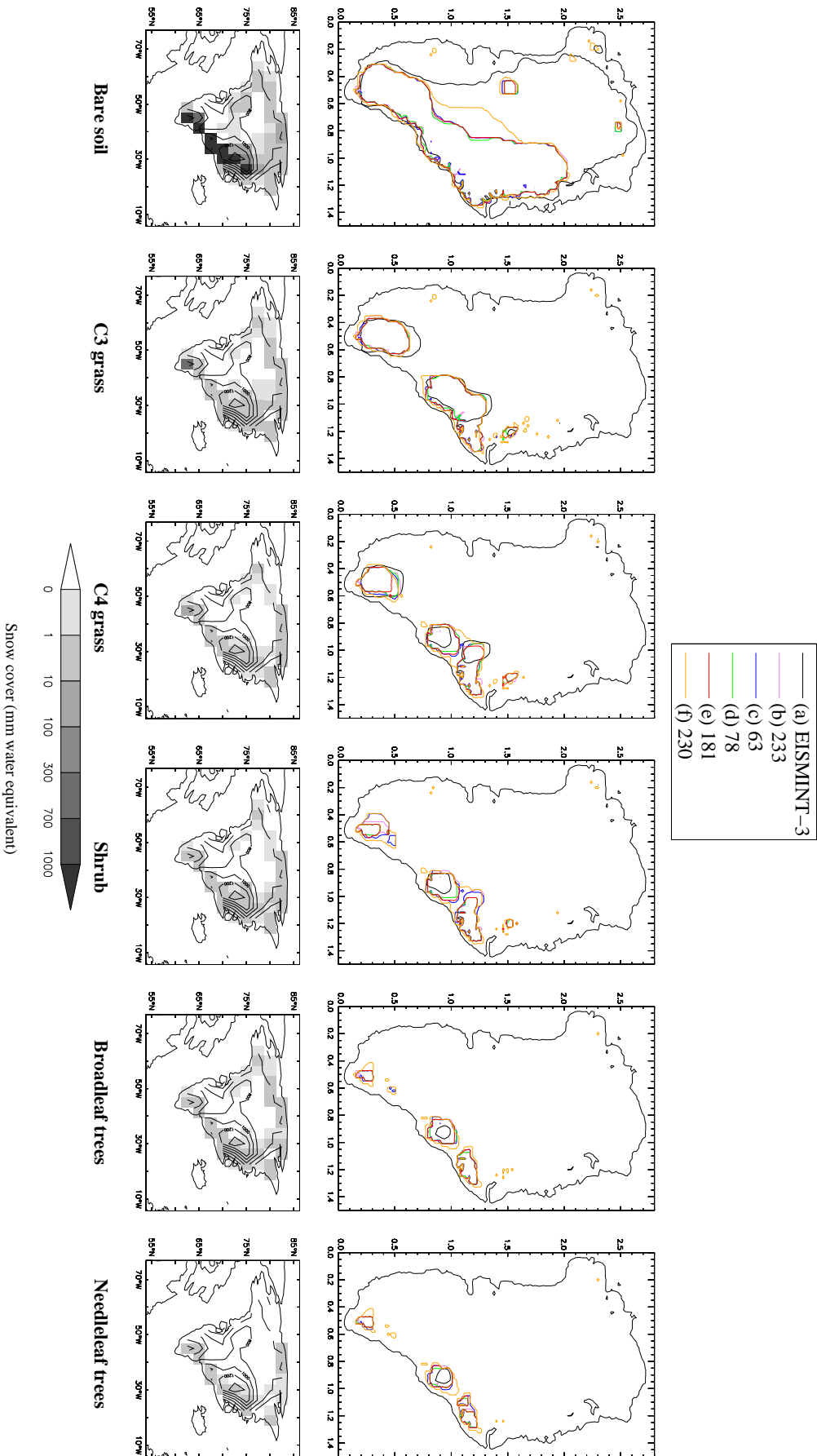


Figure 5.9: Combined figure of ice-sheet extent for all the different ice-sheet model parameter sets (a) to (f) for each of the noGrIS<sub>reb</sub> fixed vegetation climatologies shown in Chapter 3. Also shown is the average minimum snow cover diagnostic in each gridbox for the noGrIS<sub>reb</sub> fixed vegetation simulations.

snow cover amounts to no more than 10 mm water equivalent. For the broadleaf and needleleaf tree simulations the lack of any persistent snow cover in HadCM3 agrees with the almost ice-free Greenland predicted by Glimmer with the EISMINT-3 setup (a). However, the tuned parameter sets (b to f) predict some ice inception in the south and east (amounting to 0.1 to 0.2 m equivalent sea-level height) which would not have been inferred from the snow cover diagnostic.

The higher resolution of the Glimmer grid and the inclusion of the ice-elevation feedback mechanism, which are absent from HadCM3, suggests that potential regrowth of the GrIS cannot be solely determined from the snow cover amount and the average long-term trend from GCMs. Furthermore, the exclusion of the ice-albedo missing feedback, suggests it is possible, particularly in the case of a bare soil surface type, that a further iteration of HadCM3 with the new predicted ice-sheet would result in a cooler climate over Greenland by altering the surface energy budget and therefore promote more extensive ice growth in Glimmer.

These results suggest that the potential for extensive ice-sheet regrowth after complete melting of the GrIS is extremely sensitive to surface type. Although ice-sheet seeding in the high altitude regions is largely independent of the surface type, a surface dominated by bare soil results in extensive ice growth at lower elevations in the east under all Glimmer model parameter sets while a surface covered by needleleaf tree results in almost no regrowth of ice. Therefore, the behaviour of the GrIS under preindustrial conditions is highly dependent on surface type. A surface covered by bare soil indicates that under preindustrial conditions the behaviour of the GrIS shows some recovery while a surface covered by trees indicates inception of any significant GrIS is unlikely.

These contrasting results reinforce the need to force Glimmer with the climatologies from the interactive noGrIS vegetation climate simulations discussed in Chapter 4, since this likely represents a more realistic surface coverage for a future melted and rebounded Greenland, as long as sufficient time has elapsed for soil and vegetation development.

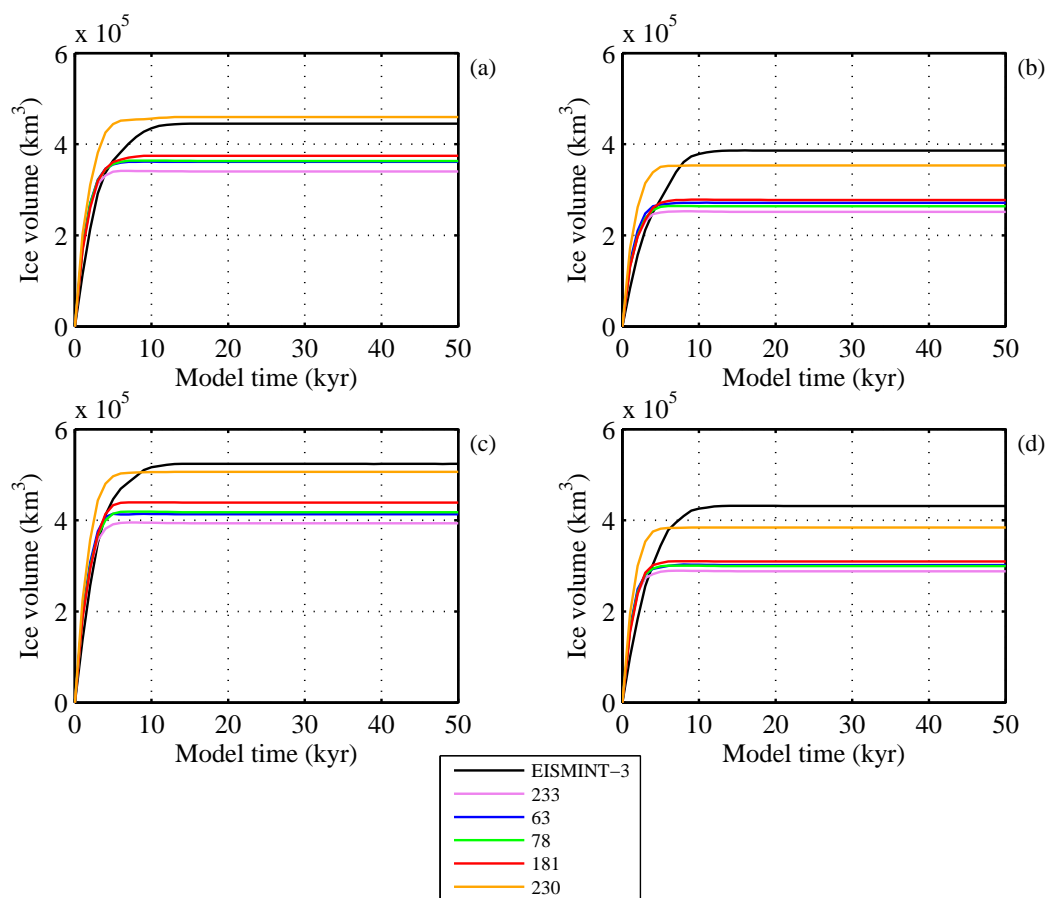


Figure 5.10: Evolution of ice-sheet volume when Glimmer is forced with *interactive* vegetation noGrIS climate simulations initiated from (a) bare soil in equilibrium mode, (b) needleleaf tree in equilibrium mode, (c) bare soil in dynamic mode and (d) needleleaf tree in dynamic mode. On each subfigure the ice-sheet evolution for the tuned Glimmer model parameter sets discussed in Section 2.5.3 and the EISMINT-3 setup are shown. Note that the scales are different on each subfigure in order to compare the results from different ice-sheet model parameter sets clearly.

### 5.2.3 Interactive vegetation climate simulations

The evolution of ice volume with time when Glimmer is forced with interactive vegetation noGrIS climatologies is shown in Figure 5.10. Table C.2 (Appendix C) also shows the ice volume, sea-level equivalent height, ice surface extent, and maximum ice thickness diagnostics. It is first interesting to evaluate the sensitivity of GrIS regrowth in response to seasonally varying vegetation by comparing simulations where TRIFFID is in equilibrium mode (no seasonality) with those in dynamic mode (seasonally varying). For all Glimmer model parameter sets the resultant equilibrium ice volume is consistently higher when TRIFFID is in dynamic mode compared with equilibrium mode. For instance, when the simulation is initiated from bare soil coverage over Greenland the ice volume ranges from 10.9 to 16.7 % higher (Figure 5.10a



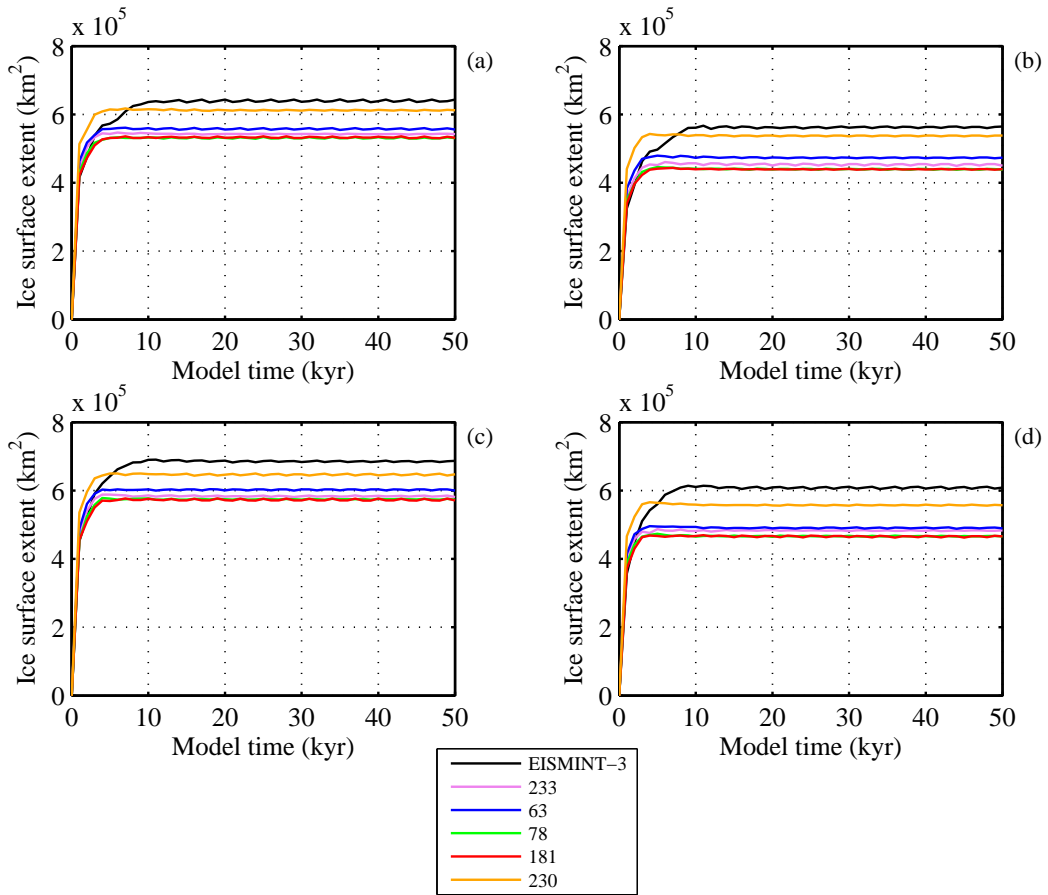


Figure 5.11: Evolution of ice surface extent when Glimmer is forced with *interactive* vegetation noGrIS climate simulations initiated from (a) bare soil in equilibrium mode, (b) needleleaf tree in equilibrium mode, (c) bare soil in dynamic mode and (d) needleleaf tree in dynamic mode. On each subfigure the ice-sheet evolution for the tuned Glimmer model parameter sets discussed in Section 2.5.3 and the EISMINT-3 setup are shown. Note that the scales are different on each subfigure in order compare the results from different ice-sheet model parameter sets clearly.

and c). Likewise, initiation from needleleaf tree shows a range from 8.6 to 16.0 % higher when TRIFFID is in dynamic rather than equilibrium mode (Figure 5.10b and d). A similar pattern is shown for ice surface extent (see Figure 5.11). These differences between the TRIFFID coupling modes are predominantly dependent on the amount of accumulation in the east of Greenland rather than any differences in near-surface air temperature. Where the surface mass balance is greater than zero it is on average  $+0.62 \text{ m yr}^{-1}$  for TRIFFID in dynamic mode compared with  $0.58 \text{ m yr}^{-1}$ .

However, the difference in equilibrium ice volume between  $\text{noGrIS}_{bsi}$  and  $\text{noGrIS}_{nli}$  is more significant and ranges from 20.9 to 41.9 % larger for TRIFFID in equilibrium coupling mode (Figure 5.10a and b). A similar range (21.4 to 41.7 %) is observed for TRIFFID in dynamic mode. On average over eastern Greenland the annual near-

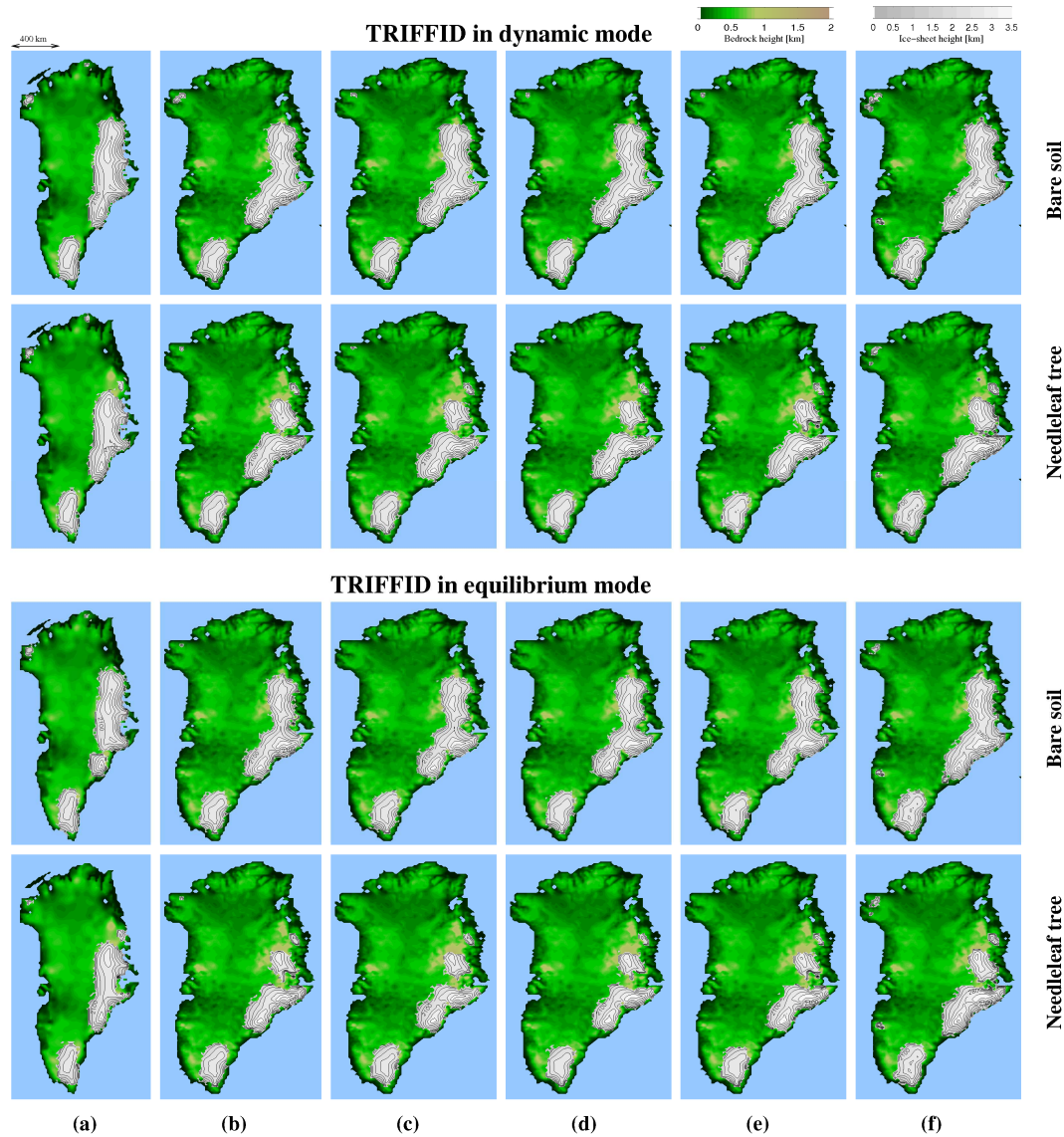


Figure 5.12: Ice-sheet geometries after 50,000 years of simulation for the noGrIS *interactive* vegetation climatologies with rebounded bedrock shown in Chapter 4. Ice-sheet geometries are shown for Glimmer model setup: (a) EISMINT-3 and also the 5 optimal parameter sets derived in Section 2.5.3: (b) expt 233, (c) expt 63, (d) expt 78, (e) expt 181 and (f) expt 230. Ice simulations begin from an initial condition of no ice and rebounded bedrock. Bare soil and Needleleaf refer to the initial condition for surface type in HadCM3 (noGrIS<sub>bsi</sub> and noGrIS<sub>nli</sub>).

surface air temperature is  $\sim 1^\circ\text{C}$  warmer for noGrIS<sub>nli</sub> compared with noGrIS<sub>bsi</sub>. During the summer regions in the east above  $0^\circ\text{C}$  for noGrIS<sub>nli</sub> prevent expansion of ice into this area. These cooler temperatures in noGrIS<sub>bsi</sub> are associated with the small increase in bare soil distribution compared with noGrIS<sub>nli</sub> (see Figures 4.12b and c) which increases the surface albedo and therefore reduces the amount of heating at the surface.

The ice mass grown on Greenland is equivalent to 0.7 to 1.3 m of sea-level height

depending on Glimmer model setup, surface type initial condition and the TRIFFID coupling mode. EISMINT-3 and tuned parameter set expt 230 result in the largest ice-sheet regrowth in terms of ice volume and ice surface extent. The time to reach equilibrium for all dynamic vegetation HadCM3 simulations in Figure 5.10 takes approximately 5,000 years for the optimal tuned parameter sets and 15,000 years for the EISMINT-3 setup. This is comparable to the time taken to reach equilibrium when the surface was covered only with C3 grasses.

The geometry of the GrIS regrowth when Glimmer is forced with noGrIS<sub>nl</sub> and noGrIS<sub>bsi</sub> in TRIFFID dynamic and equilibrium modes is shown in Figure 5.12. The general pattern of regrowth is largely insensitive to differences Glimmer model setup, surface initial condition in the interactive vegetation climate simulations and the coupling TRIFFID mode used. Ice inception only occurs as isolated events in the south and east of the island. The following discusses the minor differences between these Glimmer simulations in detail.

For noGrIS<sub>bsi</sub> the ice-sheet is confined to the eastern and southern mountains as two distinct ice masses for all Glimmer model parameter sets. A similar pattern is also observed for noGrIS<sub>nl</sub> although the ice-sheet is split into three smaller ice domes. There is no expansion of ice into central regions of Greenland or any growth in the north or west of the island for any of the HadCM3 TRIFFID simulations. Within 2,000 model years most of the ice-sheet inception and development in response to the perturbed climates has taken place.

The annual precipitation for all four noGrIS TRIFFID GCM simulations is shown in Figure 5.13. Although differences in the precipitation between TRIFFID coupling modes can explain the differences in ice volume observed in Figure 5.10a and c the the similar general pattern in ice-sheet geometry observed for all four climate simulations means further discussion will focus on the noGrIS<sub>bsi</sub> climate with TRIFFID in dynamic mode since this is realistically the most likely scenario for ice-sheet regrowth in the future. Comparable to the fixed vegetation experiments in Section 5.2.2 the greatest precipitation amounts are found on the eastern coast due to orographic lifting of moisture which aids in maintaining ice growth in this region. However, the increases in precipitation in central Greenland relative to the preindustrial control, particularly during the summer, does not result in any ice regrowth in central Greenland. Figure 5.14 shows the summer temperature distribution over the Greenland

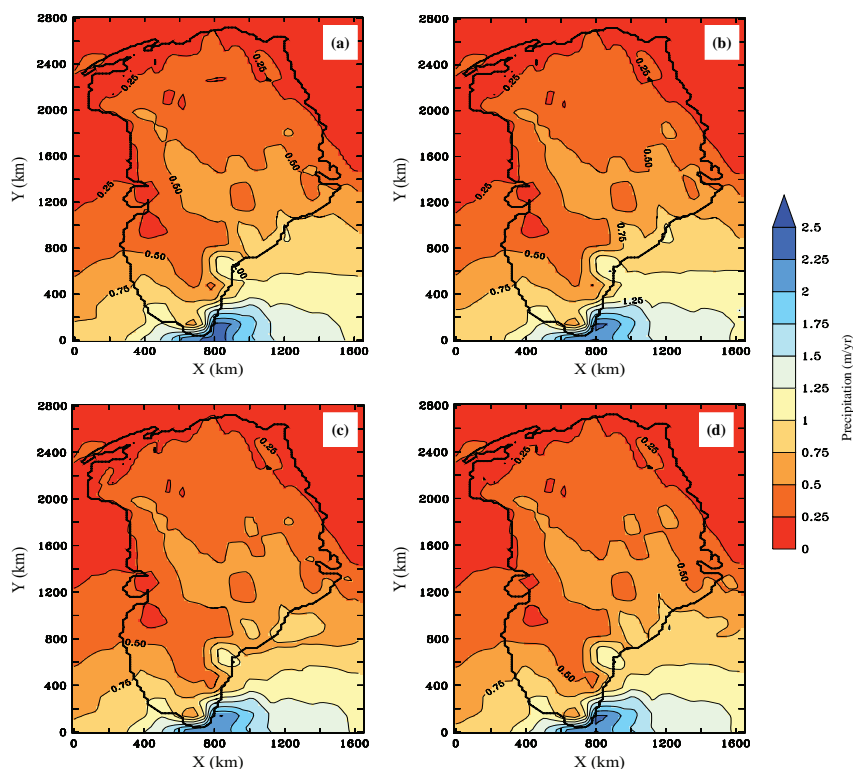


Figure 5.13: Annual accumulation (in m/yr) over Greenland when Glimmer is forced with a noGrIS climatology where the surface type is interactive in (a) dynamic TRIFFID mode initialised from bare soil, (b) dynamic TRIFFID mode initialised from needleleaf tree, (c) equilibrium mode initialised from bare soil and (d) equilibrium mode initialised from needleleaf tree.

region at the beginning and end of the simulation for the EISMINT-3 setup and the tuned expt 233 parameter set. Mass balance of the ice-sheet is also shown at the end of 50,000 years. Summer temperatures in the west are greater than  $18^{\circ}\text{C}$  for all Glimmer simulations while temperatures in central regions are approximately twice as small. Annual average temperature in the west of Greenland are close to zero for all simulations while central Greenland observes annual temperatures just below zero. In the east and south summer temperatures are as low as  $-6$  to  $-12^{\circ}\text{C}$ . As ice begins to develop in this region the temperature decreases further as a result of the positive ice-elevation feedback. This region of coldest summer temperatures coincides with where the surface type is dominated by bare soil predicted by TRIFFID. Although ice can grow at these high elevations, the temperatures in central Greenland where shrubs and grasses are present are warm enough during the summer months to prevent further growth of the ice-sheet with ablation dominating on the margins of the high altitude eastern regions, particularly in the Glimmer experiments where PDD factors are high (i.e. Figure 5.14b).

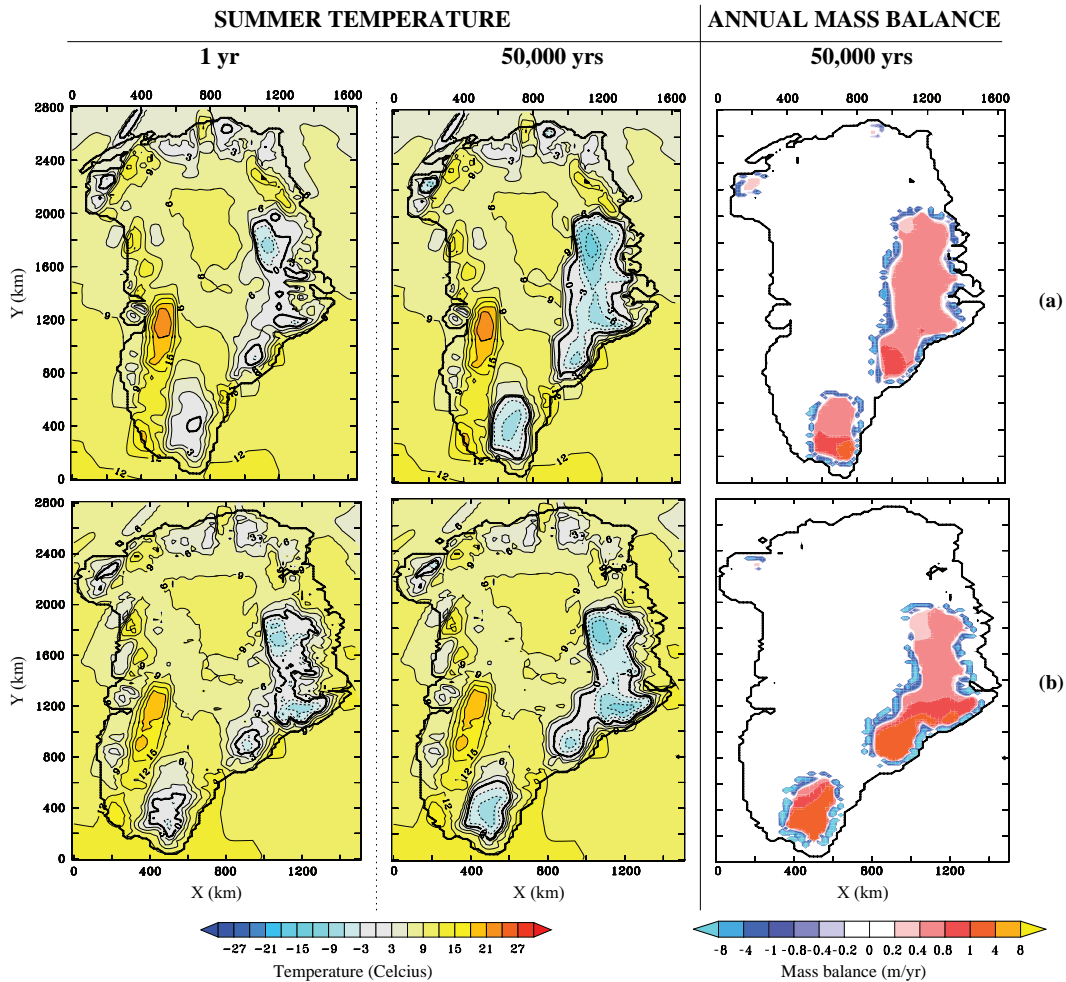


Figure 5.14: Evolution of summer surface temperature from 1 year to 50,000 years from Glimmer forced with noGrIS<sub>bsi</sub> (interactive vegetation initialised from bare soil and in dynamic mode) climatology. Annual surface mass balance is also shown at 50,000 years. Glimmer model setups are (a) EISMINT-3 and (b) tuned expt 233. All other tuned experiment parameter sets are similar to (b). Note the different x-scale between EISMINT-3 and the tuned setup.

### 5.3 Discussions and conclusions

Offline forcing of Glimmer with the noGrIS<sub>reb</sub> fixed vegetation climatologies has shown a distinct threshold between little or no regrowth for the PFTs and substantial ice-sheet regrowth for bare soil surface type. In addition, the amount of regrowth is largely robust to the ice-sheet model setup and the PFT surface type; for instance equivalent sea-level heights are all less than 1 m. However, for a surface covered with bare soil, sea-level equivalent height ranges from 1.9 to 7.6 m for all Glimmer model parameter sets. When the EISMINT-3 setup is used there is almost complete coverage of ice over Greenland as it flows from regions of high altitude

to lower levels where the ice-elevation feedback is able to sustain the slow growth of ice. This arises for the EISMINT-3 setup because of a combination of lower ablation parameters and summer surface temperatures in central Greenland several degrees cooler and closer to the 0°C threshold compared with the tuned Glimmer parameter sets. However, a surface covered by broadleaf and needleleaf trees results in the least amount of ice regrowth, amounting to no more than 0.2 m of sea-level equivalent height. Likewise, shrubs and C4 grasses result in marginally larger regrowth (equivalent sea-level height up to 0.8 m) but still at least twice as small as that for a surface covered by bare soil. These results indicate that the surface type is indeed important in predicting inception of ice and subsequent regrowth of the GrIS if increases in greenhouse gases were sufficient to alter the climate and melt the GrIS. These experiments, however, are highly idealised and it is unlikely that an ice-free Greenland would be covered by one surface type. Since palaeobotanical evidence suggests that vegetation (in particular shrubs and trees) may have existed on Greenland in the past (Willerslev *et al.*, 2007a) it is important that Glimmer is forced with a climatology where the vegetation is allowed to grow and feedback on the climate over Greenland. The presence of trees and shrubs could be sufficient to prevent any regrowth of ice due to the low albedo surface and therefore increased summer warming and melting of any lying snow remaining from the winter months.

Forcing Glimmer with dynamic vegetation noGrIS climatologies has shown that any ice regrowth depends more on the surface type initial condition than whether TRIFFID is in equilibrium or dynamic coupling mode. Nevertheless, ice regrowth is more substantial for dynamic rather than equilibrium TRIFFID mode, consistent with cooler summer and winter temperatures especially in the east (by up to 1°C in summer and 2°C in winter). Although ice-sheet volume varies from  $2.9 \times 10^5$  to  $5.2 \times 10^5$  km<sup>3</sup> between noGrIS<sub>bsi</sub> and noGrIS<sub>nli</sub>, the overall geometry of the ice-sheet is similar, confined to the southern and eastern mountain ranges for all Glimmer model parameter sets. Therefore, only partial regrowth of the GrIS is possible under preindustrial conditions and is dependent on the distribution of vegetation type over Greenland. The presence of bare soil dominance in the east and south, in conjunction with high-resolution mountainous topography, provides favourable conditions for ice-sheet nucleation with sufficiently cold surface temperatures and adequate precipitation to sustain the growth. At lower bedrock elevations, the

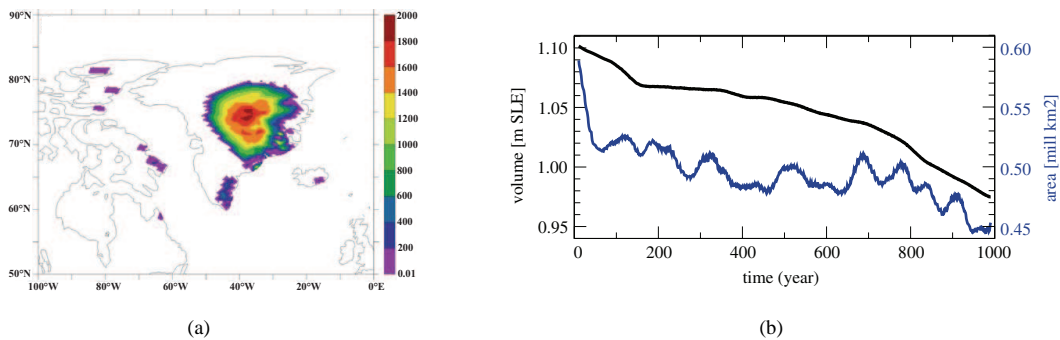


Figure 5.15: Prediction of ice regrowth on a melted Greenland from previous modelling studies. (a) Ice-sheet thickness after forcing the GREMLINS ice-sheet model offline with a no-ice climate (from Lunt *et al.* (2004)), (b) ice-sheet volume (in black) and area (evolution in blue) for a no-GrIS simulation using a two-way coupled climate ice-sheet model simulated for 1,000 years and initiated from a small ice cap in the south of the island (from Vizcaíno *et al.* (2008)).

growth of shrubs and grasses and the associated warmer climate prevents any flowing ice into these regions from coalescing and expanding further into the interior of the island, therefore preventing complete deglaciation of Greenland.

This partial regrowth can be compared with previous similar ice-sheet modelling studies. Letreguilly *et al.* (1991b) showed the GrIS could reform on a bare rock surface under present-day and even warmer conditions, similar to the noGrIS<sub>reb</sub> fixed bare soil simulation here. However, they only used precipitation parameterised according to temperature with no inclusion of the effect of orographic or atmospheric circulation changes on precipitation amounts. For a better comparison simulations which utilise a full GCM are discussed. Figure 5.15a shows the ice-sheet thickness from the study of Lunt *et al.* (2004) where the GREMLINS ice-sheet model was forced offline using their no-ice Greenland climatology with a fixed surface of tundra in the GCM. A substantial ice-sheet in eastern and central Greenland was simulated with a maximum ice thickness up to 2,000 m. This thickness is comparable with those simulations where the surface was covered by bare soil and C3 grass in this study although expansion into central Greenland is only observed for bare soil coverage. Lunt *et al.* (2004) also found that the snow cover diagnostic from their GCM did not indicate any potential for ice-sheet regrowth, contrary to the result found from using a dynamic ice-sheet model. This implied that snow cover was a poor representation of ice-sheet regrowth. They did, however, acknowledge that a better representation of precipitation in the GCM could have resulted in a smaller equilibrium ice-sheet. Furthermore, their prediction of trees in the south of Greenland from forcing a DGVM offline could have altered the result substantially

with smaller regrowth of the GrIS. This hypothesis is reinforced by the results in this thesis using TRIFFID which produced a smaller equilibrium ice-sheet than that observed in Lunt *et al.* (2004) without vegetation feedbacks included. Contrary to Lunt *et al.* (2004), the snow diagnostic in HadCM3 suggested potential regrowth could occur but only in the east of Greenland for the fixed bare soil noGrIS<sub>reb</sub> and the TRIFFID noGrIS experiments.

Figure 5.15b shows the evolution in sea-level equivalent height and ice surface extent from the study of Vizcaíno *et al.* (2008). This study used two-way coupling between ice-sheet model and climate model and simulated 1,000 years starting from a small initial ice-cap and preindustrial conditions. Vegetation feedbacks were also included using the LPJ DGVM. They found no expansion of ice over Greenland and even a slight decay of the existing ice in their simulation attributed to the absence of a regional cooling signal from collapse of the North Atlantic MOC (which was not included in the GCM experiments in this thesis). However, the range in the sea-level equivalent height for the duration of the experiment (1.1 to 0.98 m) compares well with the equilibrium sea-level equivalent height range of 0.7 to 1.3 m predicted when Glimmer was forced offline with the interactive vegetation noGrIS climatologies in dynamic TRIFFID coupling mode. The area extent in Figure 5.15b ranges from  $6 \times 10^5$  to  $4.8 \times 10^5$  km<sup>2</sup> which also agrees closely with the equilibrium ice surface extent range of  $4.7 \times 10^5$  to  $6.0 \times 10^5$  km<sup>2</sup> for the TRIFFID noGrIS simulations in dynamic coupling mode. It would be interesting to know if the Vizcaíno *et al.* (2008) simulation was continued for a further 1,000 years whether an equilibrium GrIS would be reached. This would then be similar to the timescale for equilibration of ice regrowth for simulations with vegetation feedbacks used in this thesis ( $\sim 2,000$  years). Also, a simulation without the collapse of the NAMOC would be more informative.

In conclusion, these results suggest that including vegetation feedbacks is important for determining the reversibility of a Greenland deglaciation. Only for a surface covered by bare soil was there almost complete reglaciation and this was heavily dependent on the parameterisation of Glimmer and the boundary conditions and reference climate used. Previous work also (Letreguilly *et al.*, 1991b; Lunt *et al.*, 2004) using a dynamic ice-sheet model in offline mode, which did not include the influence of vegetation feedbacks on the Greenland climate, produced significant



reglaciation similar to the noGrIS<sub>reb</sub> bare soil experiment in this thesis.

However, inclusion of vegetation feedbacks gave contrasting results. Only a small regrowth in the high mountainous regions occurred when vegetation was interactive and this was largely insensitive to the parametric uncertainty in the ice-sheet model. The lack of complete regrowth, in agreement with previous studies (Crowley and Baum, 1995; Toniazzo *et al.*, 2004; Vizcaíno *et al.*, 2008), suggests that it is possible that the GrIS can be almost ice-free and ice-covered under preindustrial conditions and that the present GrIS could be a relict ice mass left over from the last glacial period. Although the mountains are responsible for initiation of an ice-sheet in all Glimmer simulations, the slow expansion of ice to low-level regions via dynamic ice flow in combination with the ice-elevation feedback mechanism is insufficient to grow an ice-sheet if grasses and shrubs are present. This confirms the initial hypothesis by Crowley and Baum (1995) that even if high elevations could be adequately resolved, ice may not develop in central Greenland due to higher temperatures at lower altitudes enhanced by vegetation feedbacks.

One major caveat in this study, however, is that two-way coupling between climate and ice-sheet model is absent and so neglects the ice-albedo feedback. It is possible a further iteration of HadCM3 with this new small ice-sheet geometry would result in the local summer climate being sufficiently cooler than the noGrIS climates due to the albedo effect (with an associated reduction in the ‘warmer’ vegetation types over Greenland). This new climate could then support the development of a larger ice-sheet resulting in a very different climate. This remains a topic for future work although a simpler methodology which is not computationally expensive is developed in the next Chapter.



# Modelling the impact of vegetation feedbacks on the minimum extent of the GrIS during the Last Interglacial

## 6.1 Introduction

This chapter builds on the previous chapters in this thesis by using the methodology developed for ice-sheet model parametric uncertainty (Chapter 2) and for assessing the impact of vegetation feedbacks on the climate over a melted GrIS (Chapters 3 to 5), to investigate vegetation and ice-sheet evolution at a time in the past when Greenland was thought to be at least partially ice-free. It further provides an opportunity to test model results against actual data and indicate where the methodology might be improved and developed.

The Last Interglacial (LIG), lasting from  $130\pm 1$  to  $116\pm 1$  thousand years ago (ka), represents a time in the past when, at least regionally, the Arctic was up to  $5^\circ\text{C}$  warmer than present determined from a range of proxy and model data (e.g. Montoya *et al.*, 2000; Kaspar *et al.*, 2005; Otto-Bliesner *et al.*, 2006a). Furthermore, evidence suggests that sea-level was anywhere from 2 to 8 m higher than present, indicating less glacial ice on Earth at that time (Stirling *et al.*, 1998; Kopp *et al.*, 2009). The LIG, therefore, provides a potential analogue for future global warming and the implications melting of the GrIS would have on future sea-level and Arctic climate. The reader is referred to Chapter 1, Section 1.5, for a detailed account of the LIG climate and the primary mechanisms (changes in the orbital parameters of the Earth and greenhouse gas changes) which caused the warming observed at this time.

Several studies, which have been outlined in in Chapter 1, Section 1.5.3, have at-

tempted to quantify the contribution from the GrIS to this estimated sea-level highstand with values ranging from 1.5 to 5.5 m sea-level equivalent height (Letreguilly *et al.*, 1991a; Cuffey and Marshall, 2000; Tarasov and Peltier, 2003; Lhomme *et al.*, 2005; Otto-Bliesner *et al.*, 2006a). However, most of these studies relied heavily on palaeothermometry where LIG temperatures were derived from the oxygen isotope record from various ice cores over Greenland. This has large uncertainties concerning the interpretation of the oxygen isotope proxy signal in terms of temperature and precipitation relationships, age-depth analysis of the ice core and representation of the climate state over Greenland by only one or two ice core locations (e.g. Letreguilly *et al.*, 1991a; Ritz *et al.*, 1997; Cuffey and Marshall, 2000; Tarasov and Peltier, 2003; Lhomme *et al.*, 2005). One further study used offline forcing of an ice-sheet model with AOGCM output but did not include a transient climate, or any vegetation feedbacks. Furthermore, they used palaeodata to constrain the size of the ice-sheet by terminating the simulation when the Dye-3 ice core location became ice-free in the simulation. However, the robustness of whether this core represents ice from the LIG is still a matter for contention (Otto-Bliesner *et al.*, 2006a).

This chapter builds on the study of Otto-Bliesner *et al.* (2006a) by performing simulations with and without vegetation feedbacks included. Furthermore the climate is allowed to evolve between 130 to 120ka in conjunction with offline ice-sheet evolution. Consequently, ice-sheet geometry is predicted throughout the LIG and compared with rather than constrained by the palaeo ice-surface extent data from various ice cores on Greenland. The impact of ice-sheet model parametric uncertainty on the evolution of the GrIS through the LIG is also investigated. The chapter begins with experimental climate methodology, followed by an assessment of the HadCM3 MOSES 2 LIG climate, a description of the climate ice-sheet matrix coupling methodology and a prediction of the minimum extent of the GrIS during this time period. Finally, the chapter ends with discussion and conclusions.

## 6.2 Experimental methodology

Three snapshot timeslices were chosen to represent the global LIG climate state at 130, 125 and 120ka and run for 100 model years *with* and *without* a modern-day GrIS present using HadCM3, MOSES 2. A total of six HadCM3 experiments where

vegetation was fixed and six where it fed back on the climate (interactive) were performed. The simulations where vegetation was interactive were run in TRIFFID equilibrium mode since seasonality in the vegetation distribution was shown not to make a significant difference to the resultant ice-sheet geometry in Section 5.2.3 of Chapter 5.

One caveat of these simulations concerns those where there is no GrIS and the orography has rebounded. Obviously, if there was a substantial ice-sheet present before the start of the LIG, as inferred from the eustatic sea-level curve in Figure 1.7, there would have been insufficient time for all the ice to melt, the bedrock to rebound fully, soil to develop on the bare rock surface and vegetation to grow. However, it provides the most contrasting climate scenario to a fully glaciated Greenland being present throughout the LIG (also unlikely). This gives a range in climate between which the ‘expected’ climate over a partially melted GrIS during the LIG might lie.

### 6.2.1 Climate model boundary conditions

The changed forcings from present day for the LIG are the modified trace gas concentrations and the large seasonal and latitudinal insolation changes at the top of the atmosphere associated with the Milankovitch orbital forcing discussed in Section 1.5.2. Figure 6.1 shows the variation in insolation from 140 to 110ka for the spring and summer months at three latitudes over Greenland: 65°N, 74°N and 80°N. Insolation anomalies over Greenland relative to present day (Figure 6.1b) are at a maximum at ~130ka for May and June and decrease thereafter. Smaller anomalies for July and August peak from ~120 to 125ka. Orbital parameters were taken from Berger and Loutre (1991) for the three time snapshots at 130, 125 and 120ka. Table 6.1 shows the obliquity, eccentricity and perihelion for these three timeslices. A further experiment at 136ka is also included in order to spin-up the ice-sheet model sufficiently and is described in more detail in Section 6.4.2. Comparison with present day shows that at the beginning of the LIG the eccentricity was greater, the obliquity slightly greater and the perihelion coinciding with the northern summer instead of northern winter.

Also shown in Figure 6.1 is the derived proxy reconstructed CO<sub>2</sub> concentration from 140 to 110ka based on Luthi *et al.* (2008). All CO<sub>2</sub> values are on the EDC3\_gas age scale (Loulergue *et al.*, 2007). There is a sharp rise in CO<sub>2</sub> con-

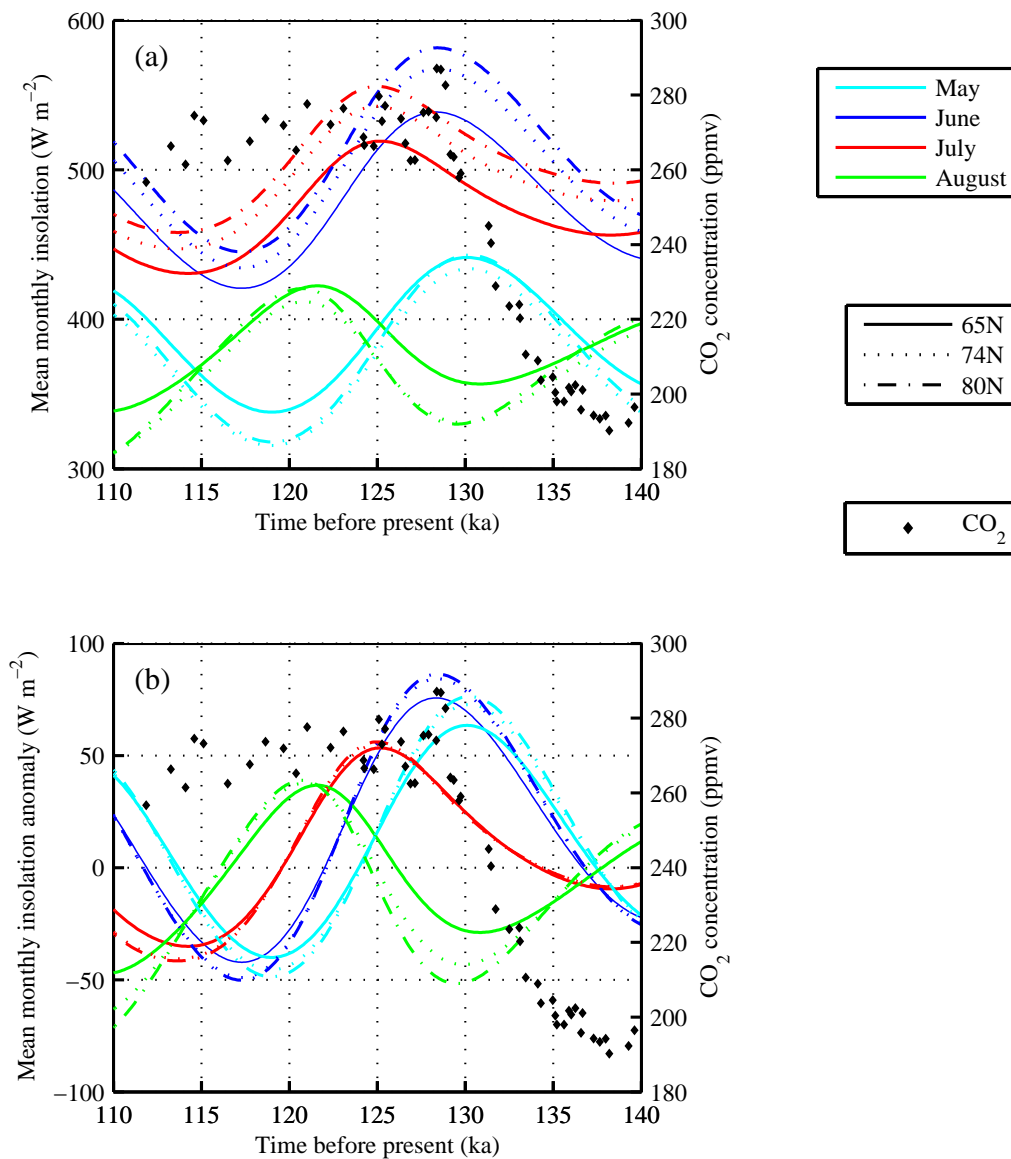


Figure 6.1: Timeseries of LIG (a) insolation and (b) insolation anomaly relative to present over Greenland for the period 140 to 110ka. Insolation values are calculated using the numerical solution of Laskar *et al.* (2004) (see <http://www.imcce.fr/Equipes/ASD/insola/earth/online/> accessed on [06/01/10]). Also overlain is CO<sub>2</sub> concentration (ppmv) from the composite record of Luthi *et al.* (2008) based on data from Petit *et al.* (1999) and Pépin *et al.* (2001) for the LIG (they are on the EDC3\_gas a age scale (Loulergue *et al.*, 2007)). The colours correspond to the following months: May (light blue), June (blue), July (red) and August (green). Linesyles refer to different latitudes over Greenland.

centration between 140 and 130ka from  $\sim 200$  to 260 ppmv. Thereafter, this trace gas concentration stabilises between 260 and 290 ppmv. Since the greenhouse gases do not markedly vary from preindustrial during the LIG (Luthi *et al.*, 2008) and it has been shown that climate perturbations were predominantly orbitally driven at this time (e.g Kutzbach *et al.*, 1991; Crowley and Kim, 1994; Slowey *et al.*, 1996; Montoya *et al.*, 2000; Loutre *et al.*, 2007), they remain constant and unchanged

from the values used in the preindustrial simulations. In this way any changes in LIG climate from the preindustrial are due to changes in the orbital parameters of the Earth and in the case of interactive vegetation also changes in vegetation distribution. CO<sub>2</sub> was therefore held constant at 280 ppmv for all experiments performed using HadCM3 between 130 and 120ka (see Table 6.1). All other trace gases were equivalent to preindustrial values given in Table 3.4. The exception was at 136ka where CO<sub>2</sub>, methane (CH<sub>4</sub>) and nitrous oxide (N<sub>2</sub>O) are lower compared with preindustrial at 200ppmv, 413 ppbv and 229 ppbv respectively. This is because differences in the trace gases compared with preindustrial are the driving mechanism for the perturbed climate rather than changes in the orbital parameters compared with preindustrial (see Figure 6.1b where summer high latitude insolation anomalies are small at 136ka).

Outside of Greenland, global vegetation coverage was prescribed at present-day distributions used in Chapters 3 and 4. The simulations without interactive vegetation and where the GrIS is removed were prescribed a bare soil coverage in place of Greenland ice while the simulations where the GrIS was present used the present-day ice-sheet mask with bare soil in ice-free regions. The fixed vegetation LIG simulations were initiated from the end of the fixed noGrIS<sub>reb</sub> bare soil simulation from Chapter 3 and the preindustrial control also described in Chapter 3. The interactive vegetation LIG simulations were initiated from the noGrIS<sub>bsi</sub> simulation from Chapter 4. The interactive vegetation preindustrial control corresponds to the one used in Chapter 4. Interactive vegetation experiments were run with TRIFFID in equilibrium coupling mode. This was not only computationally less intensive but it has also been shown in Chapter 4 that the mode of TRIFFID does not make a significant difference to the vegetation distribution nor the climate over Greenland. Further, the ice-sheet modelling results in Chapter 5 showed that the TRIFFID mode did not make a major difference to the geometry of any resultant ice-sheet. It was also shown that the equilibrium mode results in Figure 5.10 gave a smaller ice-sheet than dynamic mode. Thus, it is likely that using the equilibrium mode will predict the smallest GrIS during the LIG.

For the noGrIS LIG simulations the bedrock was rebounded and in isostatic equilibrium. Likewise, the simulations where the GrIS is included used modern day orography. Finally, the land-sea mask remained unchanged from modern since there

| Time (ka) | Obliquity (°) | Eccentricity | Perihelion (day of yr) | CO <sub>2</sub> (ppmv) |
|-----------|---------------|--------------|------------------------|------------------------|
| 136       | 23.97         | 0.0367       | 35.1                   | 200                    |
| 130       | 24.25         | 0.0401       | 121.8                  | 280                    |
| 125       | 23.82         | 0.0423       | 200.0                  | 280                    |
| 120       | 23.04         | 0.0436       | 287.6                  | 280                    |
| 0         | 23.45         | 0.01724      | 2.6                    | 280                    |

Table 6.1: The orbital parameters (from Milankovitch theory) for four time snapshots between 140 and 120ka (Berger and Loutre, 1991). Also given is the CO<sub>2</sub> concentration (Luthi *et al.*, 2008) used in HadCM3 which is held constant. Preindustrial values are shown for comparison.

were no significant tectonic changes to the continents between 130ka and present.

## 6.3 The climate of the LIG

### 6.3.1 Temperature changes during the LIG

Previous studies using AOGCMS have simulated the LIG climate but as yet no standard intercomparison simulations have been performed. This will feature as one of the main aims of the European Union project Past4Future, and PMIP3. Figure 6.2a shows the average summer temperature anomaly for 130ka with greatest warming over Eurasia and the Baffin Island/northern Greenland region from a multi-model synthesis produced by Jansen *et al.* (2007). Also shown in Figure 6.2 are the HadCM3 fixed vegetation 130ka anomaly (Figure 6.2b) and the HadCM3 interactive vegetation 130ka anomaly (Figure 6.2c) from this study. Note that all anomalies are relative to preindustrial. Overlain on each plot are proxy temperature reconstructions from the LIG (Kaspar *et al.*, 2005; Anderson *et al.*, 2006). There is general agreement in maximum Arctic summer warmth although the HadCM3 plots show an underestimation in temperature over the Greenland region even when vegetation feedbacks are included. Jansen *et al.* (2007) attributed the underestimated warmth in Siberia (Figure 6.2a) as a result of no vegetation feedbacks being included in the models. The underestimation in near-surface summer temperature anomaly over Greenland by HadCM3 with TRIFFID switched on is partly due to the cold bias observed at high latitudes in the model (see Section 4.2.7) and also perhaps because less ice was present over Greenland than is used in the 130ka simulation shown in Figure 6.2.

The global annual mean anomaly for fixed and interactive vegetation is 0.13°C



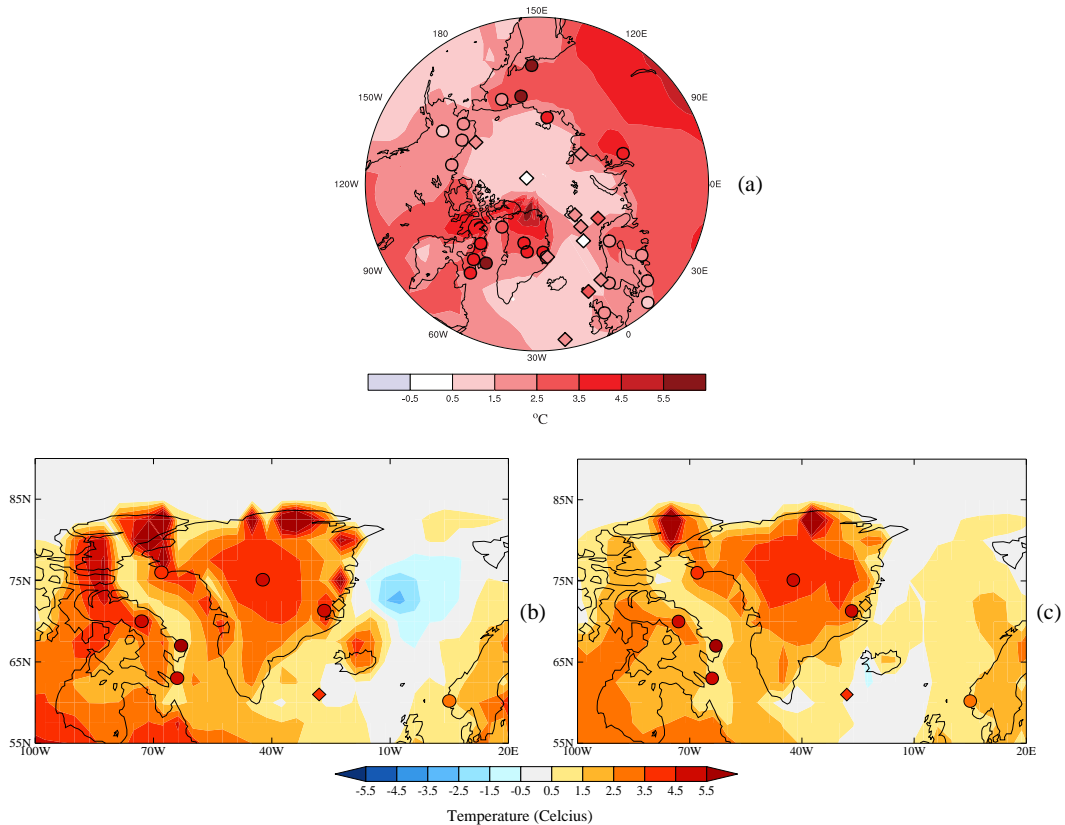


Figure 6.2: Summer near-surface temperature change over Greenland and the surrounding region for the LIG compared with preindustrial. (a) Multi-model warming simulated by National Center for Atmospheric Research (NCAR) Community Climate Model (CCSM), 130ka minus present (Otto-Bliesner *et al.*, 2006a) and the ECHAM4 HOPE-G model, 125ka minus preindustrial (Kaspar *et al.*, 2005) (from Jansen *et al.* (2007)), (b) 130ka HadCM3 with fixed vegetation and GrIS present simulation minus preindustrial control and (c) 130ka HadCM3 with interactive vegetation and GrIS present simulation minus preindustrial TRIFFID control. Overlain on all plots are proxy estimates of maximum summer warming from terrestrial (circles) and marine (diamonds) sites as compiled in the synthesis by Anderson *et al.* (2006) and Kaspar *et al.* (2005).

and  $0.15^{\circ}\text{C}$  respectively. This shows the LIG global annual temperatures were not notably higher than preindustrial, consistent with the orbital forcing. The average summer temperature warming at 130ka over Greenland when an ice-sheet is present and vegetation is fixed is  $3.3^{\circ}\text{C}$  and when vegetation is interactive  $3.0^{\circ}\text{C}$ .

Figure 6.3 and Table 6.2 show the temperature anomalies over the Greenland region for 130, 125 and 120ka with and without the GrIS present and with and without vegetation feedbacks included. Only summer temperature anomalies are shown in Figure 6.3 since this is when changes in surface energy balance and ablation of ice are most pronounced. As discussed above, there is an increase in temperature during the summer months from  $3$  to  $4^{\circ}\text{C}$  due to the orbital forcing of the LIG alone. When the GrIS is removed and the bedrock is rebounded and in isostatic equilibrium, the temperature over Greenland increases for all time periods with

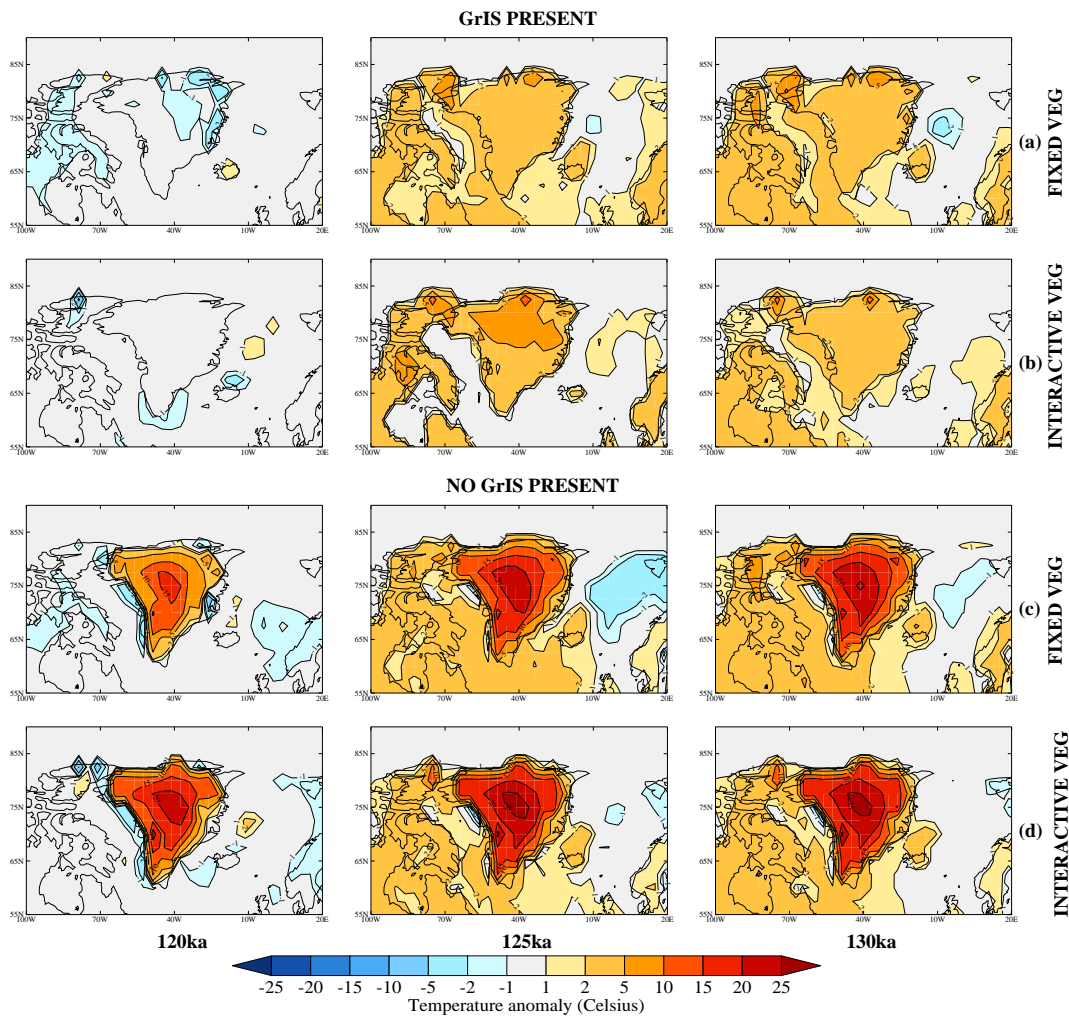


Figure 6.3: Near-surface summer temperature anomaly (LIG simulation minus preindustrial) for the three time snapshots: 130, 125 and 120ka. (a) GrIS present and vegetation fixed, (b) GrIS present and vegetation interactive, (c) no GrIS, rebounded bedrock and fixed vegetation and (d) no GrIS, rebounded bedrock and interactive vegetation.

and without vegetation feedbacks included as a result of the temperature lapse rate correction due to a change in altitude, changes in atmospheric circulation and the increase in shortwave heat flux absorption owing to the lower albedo of the surface in the summer. First note for Figures 6.3a to d the temperature anomaly for the LIG peaks between 125 and 130ka and decreases substantially by 120ka, in accordance with the reduction in solar insolation in the summer months relative to present (see Figure 6.1b). This insolation anomaly even becomes negative in June by approximately  $36 \text{ W m}^{-2}$ . At 130ka and 125ka there is significant warming (2 to  $5^\circ\text{C}$ ) over the Hudson Bay/Baffin Island and Labrador sea region with and without a GrIS present as well as if vegetation feedbacks are included or not. By 120ka, the simulations where the GrIS is present show a much reduced positive temperature

| Experiment                     | ANN   | DJF   | JJA   |
|--------------------------------|-------|-------|-------|
| <i>130ka</i>                   |       |       |       |
| GrIS present (fixed veg)       | 0.32  | -0.93 | 3.27  |
| GrIS present (interactive veg) | 0.14  | -1.54 | 3.00  |
| No GrIS (fixed veg)            | 6.97  | 1.93  | 14.68 |
| No GrIS (interactive veg)      | 8.05  | 1.43  | 15.95 |
| <i>125ka</i>                   |       |       |       |
| GrIS present (fixed veg)       | 0.74  | 0.53  | 3.31  |
| GrIS present (interactive veg) | 0.42  | -0.19 | 3.04  |
| No GrIS (fixed veg)            | 7.13  | 4.23  | 13.66 |
| No GrIS (interactive veg)      | 8.16  | 2.84  | 15.9  |
| <i>120ka</i>                   |       |       |       |
| GrIS present (fixed veg)       | 0.19  | 1.20  | -0.96 |
| GrIS present (interactive veg) | -0.09 | -0.40 | -0.18 |
| No GrIS (fixed veg)            | 5.53  | 4.90  | 6.76  |
| No GrIS (interactive veg)      | 7.67  | 3.78  | 11.73 |

Table 6.2: Table showing the average near-surface temperature anomalies (in °C) for the three LIG snapshots:130,125 and 120ka over Greenland with and without the GrIS present and with and without interactive vegetation.

anomaly with regions over Greenland even becoming slightly negative. There is no longer any significant warming of the land surface west of Greenland nor in northern Europe.

Figure 6.3c and d show the summer warming when the GrIS is removed and replaced with fixed bare soil and interactive vegetation respectively. Both show additional summer warming primarily over Greenland when the GrIS is present due to the reduced surface albedo and the lowered orography. However, Figure 6.3 shows a reduction in temperatures over the Barents Sea region similar to the results found in Section 3.3.5 for the future melted GrIS experiments under preindustrial climate conditions. This feature is less pronounced when vegetation feedbacks are included. Inclusion of vegetation growth on a Greenland with no ice increases the temperature on average by up to 1.3, 2.2 and 5.0°C compared without vegetation feedbacks for 130, 125 and 120ka respectively. This is because the summer albedo is 0.04, 0.10 and 0.24 lower for 130, 125 and 120ka respectively when vegetation develops over Greenland, compared with when the surface is fixed as bare soil. There is a much smaller difference in temperature when the GrIS is present with and without vegetation feedbacks because the average albedo of the surface remains similar throughout the year (0.7 to 0.8).

At the location of the NGRIP (see Figure 1.11) ice core simulated temperature

anomalies from the noGrIS experiments are in excess of 20°C (for fixed and interactive vegetation) and the average summer Greenland anomaly ranges from 13.7 to 16.0°C for 125 to 130ka. These are clearly an over estimate compared with the proxy palaeodata estimate of only 5°C warming shown in Figure 6.2 and described by Andersen *et al.* (2004). This disparity between data and model simulation suggests that it is very likely the GrIS did not completely disappear but retreated to become a smaller ice-sheet. At 120ka there is a reduction in summer warming when the GrIS is removed by 7.9°C compared with at 130ka. Likewise when vegetation feedbacks are included there is also a reduction but smaller by 4.2°C.

Winter temperature anomalies are less significant than the summer anomalies and even slightly negative when the GrIS is present (see Table 6.2). Inclusion of vegetation feedbacks during the winter actually results in average Greenland temperatures lower than when vegetation is fixed contrary to the suggestion by Anderson *et al.* (2006) which inferred vegetation feedbacks could contribute to winter warmth as well as the summer warmth discussed. However, there are notable winter temperature biases in HadCM3 MOSES 2 with TRIFFID as discussed in Section 4.2.7 and therefore this result is far from conclusive. The positive winter anomalies observed at all time snapshots when the GrIS is removed are mainly a result of changes in elevation and atmospheric circulation, as observed for the future regrowth experiments in Section 3.3.4, rather than changes in surface type.

### 6.3.2 Hydrological changes during the LIG

Over much of the Greenland region annual precipitation rate anomalies shown in Figure 6.4 are insignificant (at the 95 % level of confidence using the Student T-test) when the GrIS is present in HadCM3 simulations throughout the LIG. The result is also similar whether vegetation feedbacks are included or not. This result is consistent with Otto-Bliesner *et al.* (2006a) although they find marginal increases in precipitation in northwest and central Greenland and southeast Iceland. However, the fixed vegetation simulations are consistently drier over Iceland using HadCM3 for all three time snapshots. This is because the north of Iceland SSTs are several degrees cooler as a result of an increase in sea-ice coverage which acts to cool the sea-surface further via the sea-ice-albedo feedback. Hence, the presence of sea-ice reduces the moisture availability over this region relative to the preindustrial.

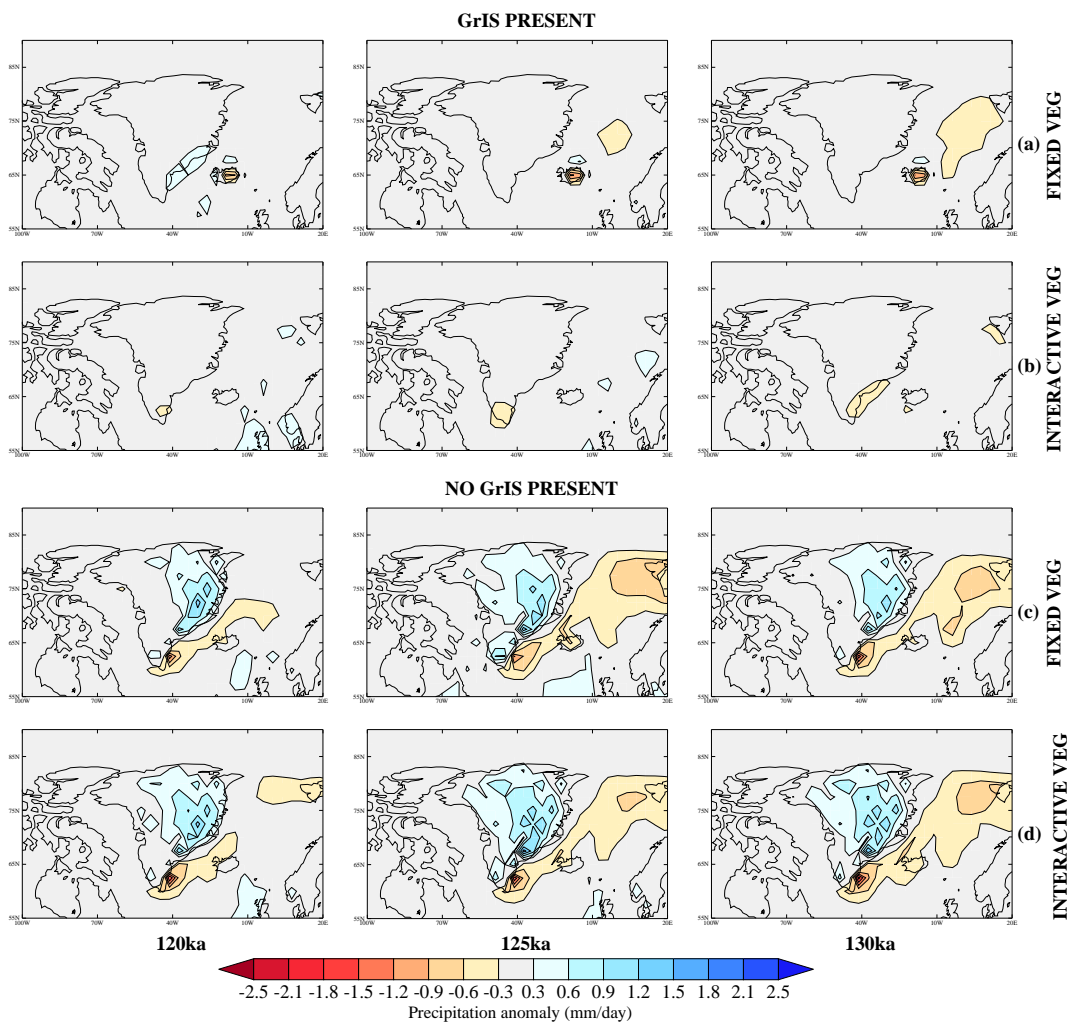


Figure 6.4: Annual precipitation rate anomalies (in  $\text{mm day}^{-1}$ ) relative to preindustrial for the three time snapshots: 130, 125 and 120ka. (a) GrIS present and vegetation fixed, (b) GrIS present and vegetation interactive, (c) no GrIS, rebounded bedrock and fixed vegetation and (d) no GrIS, rebounded bedrock and interactive vegetation.

When the GrIS is removed (Figures 6.4c and d) there is a significant increase in precipitation by up to  $1.2 \text{ mm day}^{-1}$  along the eastern coast of Greenland regardless of vegetation feedbacks. This is similar to the precipitation pattern observed in Figure 3.28 when vegetation is fixed and the GrIS removed under preindustrial conditions. This precipitation is associated with the enhanced orographic lifting of moisture along the east coast of the island. The drier region at the southern tip of Greenland, present in the fixed and interactive simulations for the future regrowth experiments, is also evident during the LIG. With vegetation feedbacks included the region of precipitation increase in the east expands further into central Greenland associated with the increase in moisture flux during the summer months. This is due to increased evapotranspiration from the growth of vegetation in this region.

At 120ka there is a slight decrease in the area covered by positive precipitation anomalies associated with a reduction in shrub type vegetation (see next section).

When the GrIS is present and the vegetation is fixed there is a reduction in annual snow cover along the north and east margins of the ice-sheet (including the ice-free regions) by at least 600 mm (water equivalent) compared with the preindustrial for 125ka and 130ka. However, by 120ka the snow cover is once again similar to the preindustrial associated with the reduction in near-surface temperatures over Greenland (see Figure 6.3). Similar losses in snow depth at 130ka are shown by Overpeck *et al.* (2006) where there is a net annual reduction in snowfall by as much as 600 mm along the north, south and western edges of the ice-sheet. A similar pattern is observed with interactive vegetation. However, as shown in Chapters 2 and 3, the snow cover and amount diagnostic is not a particularly good indicator of ice-sheet evolution and will not be discussed any further.

### 6.3.3 Changes in vegetation during the LIG

The dominant global land surface type is shown at 130, 125 and 120ka for the TRIFFID simulations in Figure 6.5, where the GrIS is present (Figure 6.5a) and removed (Figure 6.5b). Since the land surface at high latitudes has been shown to be warmer than the preindustrial climate (see Section 6.3.1) for the early to mid-LIG, it is expected that the vegetation changes accordingly in response to this warming. In turn the growth of vegetation over Greenland acts to amplify this warming signal produced primarily by changes in the orbital parameters of the Earth. The impact of removing the GrIS is predominately localised on the distribution of vegetation type at high northern latitudes (compare vegetation distribution outside of Greenland in Figures 6.5a and b). However, compared with the preindustrial there is an advancement of shrubs northward into regions previously occupied by the 'cold' C3 grasses, between 130 and 125ka. Broadleaf tree also becomes more dominant in northern Europe by 125ka as the climate warms in response to the orbital forcing. By 120ka, however, shrubs have begun to retreat southwards again replaced by the C3 grasses and temperate forests at 60°N in Europe have died back. There is no obvious northward shift of the boreal treeline at any time during the LIG simulated here using TRIFFID in contrast to the LIG simulations of Schurgers *et al.* (2007) and Gröger *et al.* (2007).

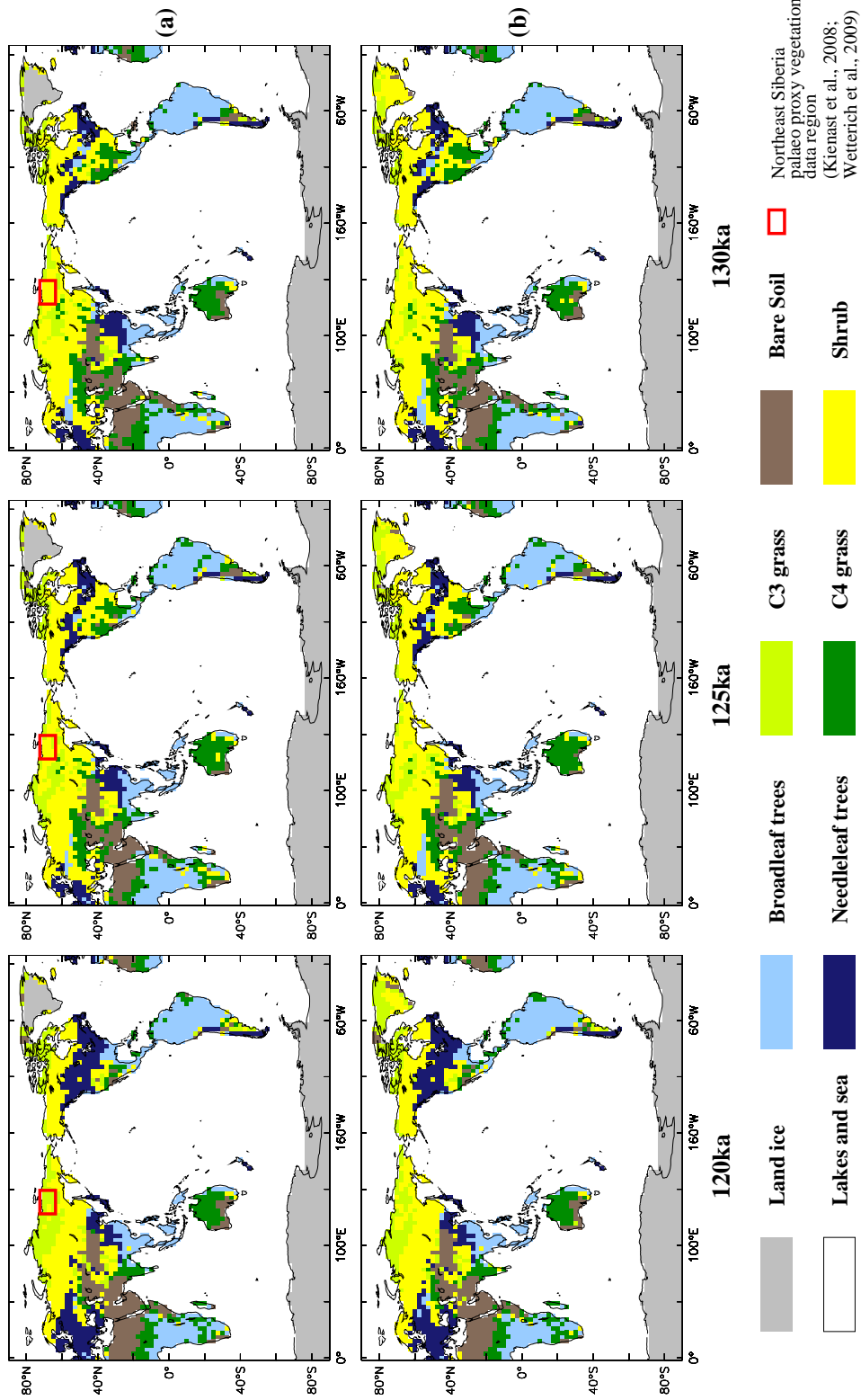


Figure 6.5: Dominant global vegetation coverage after running TRIFFID in equilibrium mode for 1,000 years (100 equivalent years for GCM run-time) at 130, 125 and 120ka for (a) GrIS present and (b) GrIS removed with a rebounded bedrock. Within each grid-cell the dominant PFT/other land surface type is shown. The square red boxes correspond to the approximate location of LIG vegetation proxy data from the study of Wetterich *et al.* (2009).

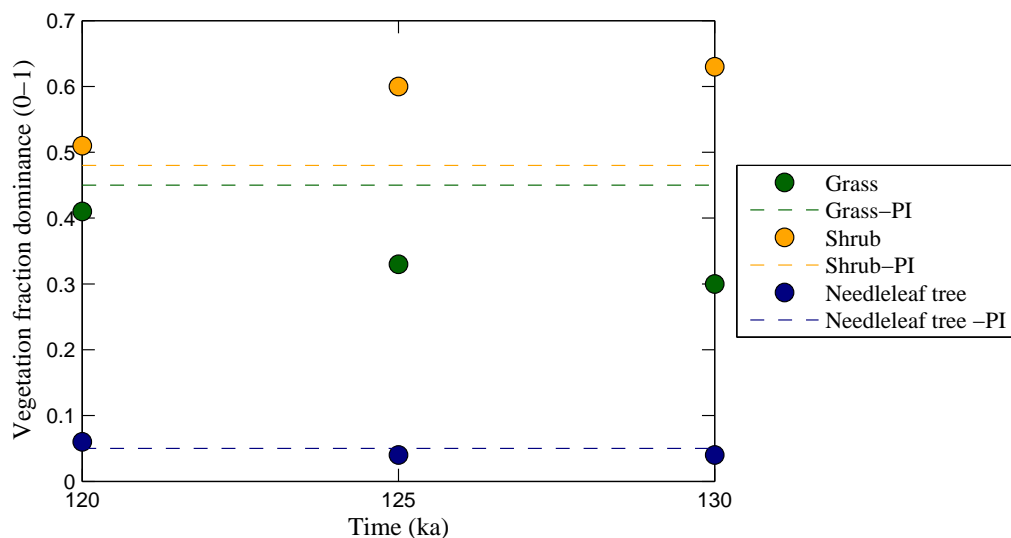


Figure 6.6: Annual average vegetation dominance fraction for the land surface between 60 to 90° N through the LIG when TRIFFID is in equilibrium mode and the GrIS is present. The GrIS gridboxes have been excluded because vegetation cannot develop there in the MOSES 2 land surface scheme. The PFTs shown are grass, shrub and needleleaf tree and the preindustrial (PI) TRIFFID control fraction for each of these PFTs for comparison.

A comparison in fractional annual vegetation dominance (when the GrIS is present) at high Northern Hemisphere latitudes at different times during the LIG snapshots and the preindustrial control is shown in Figure 6.6. The area covered by the GrIS is removed from calculations since vegetation is not able to develop in gridboxes that contain ice in MOSES 2. Needleleaf tree dominance at high latitudes is particularly small and does not differ much from the preindustrial simulation. However, the proportion of land surface covered by shrubs is on average higher than during the preindustrial throughout the LIG although it steadily decreases from 0.63 to 0.51 over the 10,000 years assuming a linear response. The tundra grasses that occupy much of the Arctic region are somewhat less dominant during the LIG compared with preindustrial due to the increase in occupation by shrubs. There is, however, an increase in C3 grass dominance from 0.3 at 130ka to 0.41 by 120ka approaching the preindustrial value of 0.45. The changes in vegetation are associated with the average 3°C cooling on land observed in the summer months between 130 and 120ka for 60 to 90°N. Comparisons with palaeo proxy vegetation data show agreement in northeast Siberia where areas now occupied by tundra (C3 grasses in TRIFFID) are replaced by shrubs at the peak warmth of the LIG with a return to grasses by the end of the LIG (Kienast *et al.*, 2008; Wetterich *et al.*, 2009) (see square red boxes on Figure 6.5a). However, the extension of boreal forest into the interior



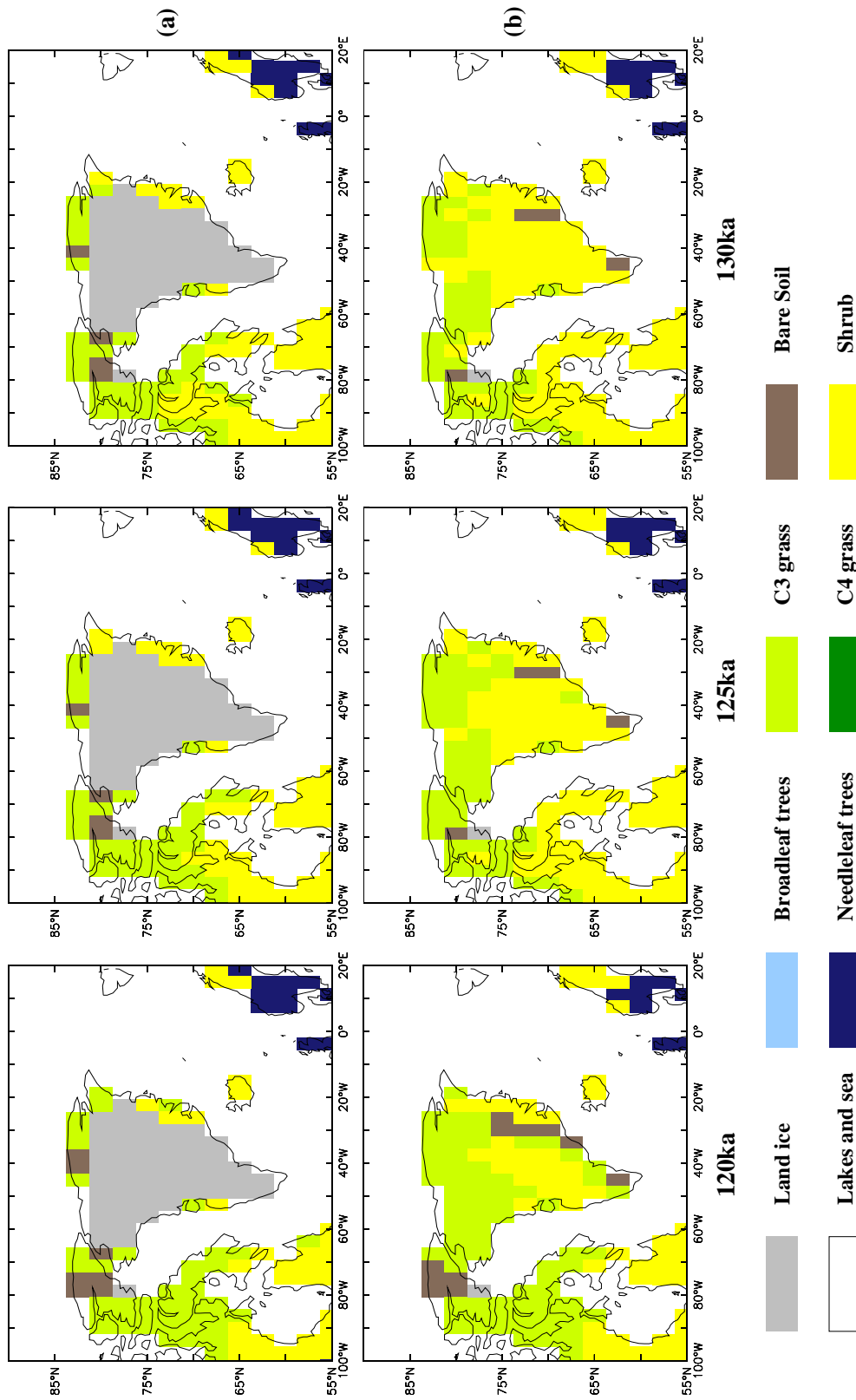


Figure 6.7: Dominant vegetation coverage over the Greenland region after running TRIFFID in equilibrium mode for 1,000 years (100 equivalent years for GCM run-time) at 130, 125 and 120ka for (a) GrIS present and (b) GrIS removed with a rebounded bedrock. Within each grid-cell the dominant PFT/other land surface type is shown.

of Alaska suggested by Anderson *et al.* (2006) is not present in the interactive LIG vegetation simulations from this study.

When the GrIS is removed and the bedrock is rebounded, vegetation develops over Greenland as shown in Figure 6.7b. The snapshots chosen are separated by 5,000 years which is sufficient for vegetation growth to respond to any change in climate forcing. At 130ka central, western and much of eastern Greenland is dominated by shrubs. C3 grasses are confined to the northern parts of the island. Only at the very highest altitudes in the east does no vegetation develop, similar to the results from the future GrIS regrowth simulations (see Figure 4.12b). Compared with when the surface type is fixed as bare soil this surface results in very similar average summer and winter albedos, which are only 0.04 and 0.02 lower respectively. A similar pattern of vegetation dominance is shown at 125ka but with some advancement of grasses further south into central Greenland. By 120ka only some central and western parts of Greenland are dominated by shrubs. Regions to the north and east are occupied by C3 grasses. Furthermore, die-back of shrubs and grasses to expose bare soil as the dominant land surface type is found in the east. This is reflected in the higher average summer albedo of 0.30 compared with 0.22 and 0.23 at 125 and 130ka respectively. During the peak LIG warmth, the advancement of shrubs over much of Greenland in HadCM3 agrees with plant macrofossil assemblages indicating the presence of dwarf shrubs in central and eastern Greenland during this time (Bennike and Bocher, 1994). However, there is no evidence of the tentative suggestion of boreal forest in southern Greenland within the last one million years (Willerslev *et al.*, 2007a).

#### 6.3.4 Sea-ice changes during the LIG

The increased insolation anomalies during the early part of the LIG result in spring/summer melting of the Arctic sea-ice with reduced concentrations compared with preindustrial throughout the summer months. Figure 6.8 shows the summer average sea-ice concentration for the three snapshots through the LIG, with and without a GrIS present and with and without interactive vegetation included. The preindustrial sea-ice concentration with and without vegetation feedbacks is also included for comparison. When the GrIS is present the pattern of sea-ice concentration is similar with and without vegetation feedbacks included (see Figure 6.8a and b). At

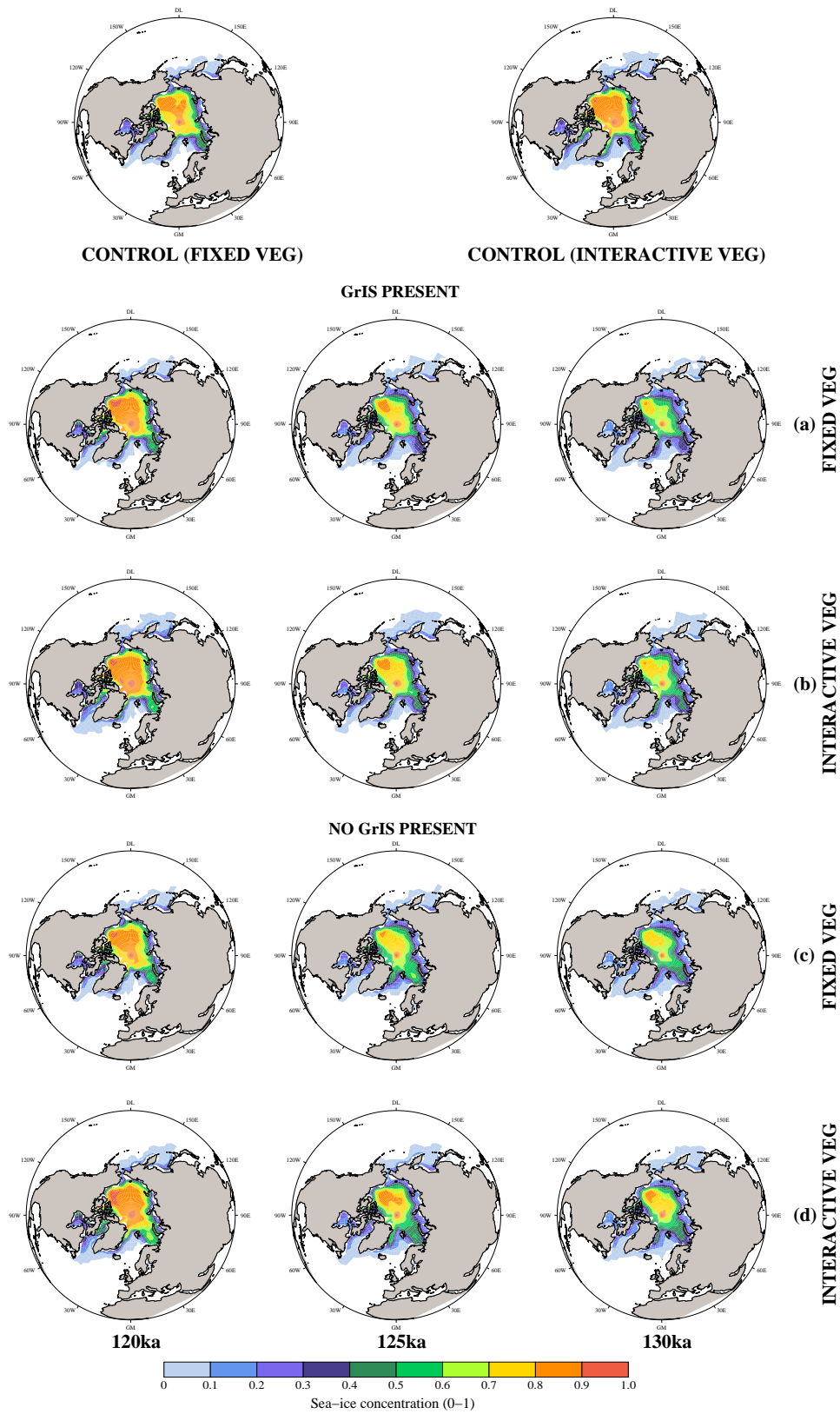


Figure 6.8: Average summer sea-ice concentrations (0-1) during the LIG for the Arctic for the fixed and interactive vegetation controls, (a) fixed vegetation-GrIS present, (b) interactive vegetation-GrIS present, (c) fixed vegetation-no GrIS and (d) interactive vegetation-no GrIS.

130ka sea-ice concentration is reduced by up to 40 % compared with the preindustrial control in the central part of the Arctic Ocean. This is similar to the result found by Otto-Bliesner *et al.* (2006a) where reduction in sea-ice concentration was as high as 50 % compared with present. This reduction of summer sea-ice around the margins of Greenland results in a positive sea-ice-albedo feedback and contributes to the warming observed in this region, particularly in the Labrador Sea. At 125ka there is still a reduction in sea-ice in the Arctic compared with the preindustrial but only up to 20 % over the majority of the region. By 120ka the pattern in summer sea-ice concentration is similar if not greater than the preindustrial with over 50 % sea-ice present again in the Labrador Sea. This increase in sea-ice is attributed to the cooler climate as a result of reduced summer insolation forcings towards the termination of the LIG.

When the GrIS is removed and forced with the insolation forcings of the LIG there is more difference in terms of summer sea-ice concentration between fixed and interactive vegetation surface types (Figures 6.8c and d) compared with when the GrIS was present. As was the case for the GrIS present experiments, there is a reduction in Arctic sea-ice during the summer months compared with the preindustrial during the early to mid LIG period. By 120ka, however, the sea-ice concentration is comparable with the preindustrial. The main difference that exists is an increase of sea-ice on the eastern coast of Greenland and the Barents Sea region by up to 40 % which is even more pronounced during the winter months, especially for the interactive vegetation experiments. This change in sea-ice concentration east of Greenland was also found with the future regrowth experiments in Chapters 3 and 4 and was attributed to changes in ocean heat transport caused by atmospheric circulation changes from lowering of the orography and more intense thermal heating over Greenland during the summer.

## 6.4 The minimum extent of the GrIS during the LIG

In order to predict the minimum extent of the GrIS during the LIG a number of palaeoclimatic observations criteria should be met in order to deem a LIG GrIS simulation acceptable. Such observational evidence, some of which is based on interpretation of age estimates of ice cores in Greenland, and its limitations have

been discussed in Chapter 1, Section 1.5.3. The following criteria are hence used in obtaining acceptable estimates of the minimum GrIS:

1. Equivalent sea-level height of ice loss from the GrIS not to exceed the *upper* bound estimate of the LIG sea-level highstand: 6 to 8 m (Kopp *et al.*, 2009).
2. Timing of the minimum extent of the GrIS to coincide with the peak in the sea-level highstand between 124 and 127ka (Kopp *et al.*, 2009).
3. The presence of ice in the vicinity of the central Summit and NGRIP ice core locations (see Figure 1.11) throughout the LIG time period simulated (Raynaud *et al.*, 1997; Andersen *et al.*, 2004).
4. The presence of ice in the east of Greenland in the vicinity of the Renland core throughout the LIG (Johnsen *et al.*, 1992; Hansson and Holmen, 2001).
5. Lowering of the ice-sheet surface at the palaeodivide by no more than  $\sim 500$  m (Raynaud *et al.*, 1997).

The following two criteria are more controversial:

1. Possible ice at the location of the Camp Century ice core (see Figure 1.11) (Koerner, 1989).
2. Dye-3 is equivocal with some studies tentatively concluding it was ice-covered and ice cores predated the LIG (e.g. Dansgaard *et al.*, 1985; Andersen *et al.*, 2004; Willerslev *et al.*, 2007a) while others suggested it was ice-free (e.g. Koerner and Fischer, 2002; Lhomme *et al.*, 2005; Otto-Bliesner *et al.*, 2006a) during the peak LIG warmth.

#### 6.4.1 Offline forcing with a 130ka climatology

In order for a close comparison with the Otto-Bliesner *et al.* (2006a) modelling study, Glimmer was first forced offline with the fixed vegetation GrIS present 130ka climate for 10,000 years of model simulation. The initial ice-sheet configuration was a spun-up, equilibrated modern day ice-sheet for each of the selected Glimmer model parameter sets described in Chapter 2. Figure 6.9a shows the ice evolution and equivalent sea-level height of the remaining ice for the five recent tuned and

EISMINT-3 parameter sets. After 127ka the GrIS evolution is shown as dashes. The modelling study by Otto-Bliesner *et al.* (2006a), shown in Figure 6.9b, assumed the minimum GrIS configuration during the LIG occurred at 127ka and stopped their simulations at this point. This timing was constrained by the Dye-3 ice core location becoming ice-free in the model and the drawdown of the ice surface at the palaeodivide ( $\sim 570$  m) being in general agreement with ice core data from central Greenland (Raynaud *et al.*, 1997). They estimated the maximum contribution to LIG sea-level rise from the GrIS was subsequently 3.0 m. However, after 3,000 years of ice-sheet model simulation the results from the Glimmer model parameter sets used in this study give a range between 1.1 to 2.0 m of LIG sea-level rise from melting of the GrIS (see Figure 6.9a). Table 6.3 shows that none of the simulations in this study result in Dye-3 becoming ice-free by 127ka. Nor is there a significant lowering by several hundred metres at the palaeodivide of the ice-sheet. However, all other criteria outlined above are met. This is shown by the 127ka GrIS geometry in Figures 6.9c to h for the five tuned Glimmer parameter sets and EISMINT-3. Continuation of the simulations past 127ka, results in Dye-3 becoming ice-free only for the EISMINT-3 simulation at  $\sim 124$ ka without compromising the acceptable criteria for a minimum LIG GrIS. The maximum contribution to sea-level rise during the LIG ranges from approximately 1.5 to 3.8 m. Although the maximum contribution from the tuned expt 230 simulation is 7.0 m by 124ka, the central ice core location becomes ice-free and therefore violated the Summit and NGRIP acceptable criteria. Therefore, in order for this criteria to be satisfied the maximum contribution to the sea-level highstand occurs after 4,000 years of model simulation. In all cases the surface of the ice-sheet lowers in response to the orbitally induced warming. However, the GrIS ice divide remains significantly higher than the ice core constraint of a 500 m lowering.

Since none of these GrIS configurations are in equilibrium, continued warmth would drive a smaller and lower ice-sheet and therefore result in continued sea-level rise (as shown in Figure 6.9a). However, aside from compromising the palaeodata constraints on the size and timing of the minimum GrIS ice-sheet, this would also not agree with the changing Arctic climate which had begun to cool once more by 120ka due to a large reduction in insolation anomalies during the spring/summer months (see Figure 6.1).

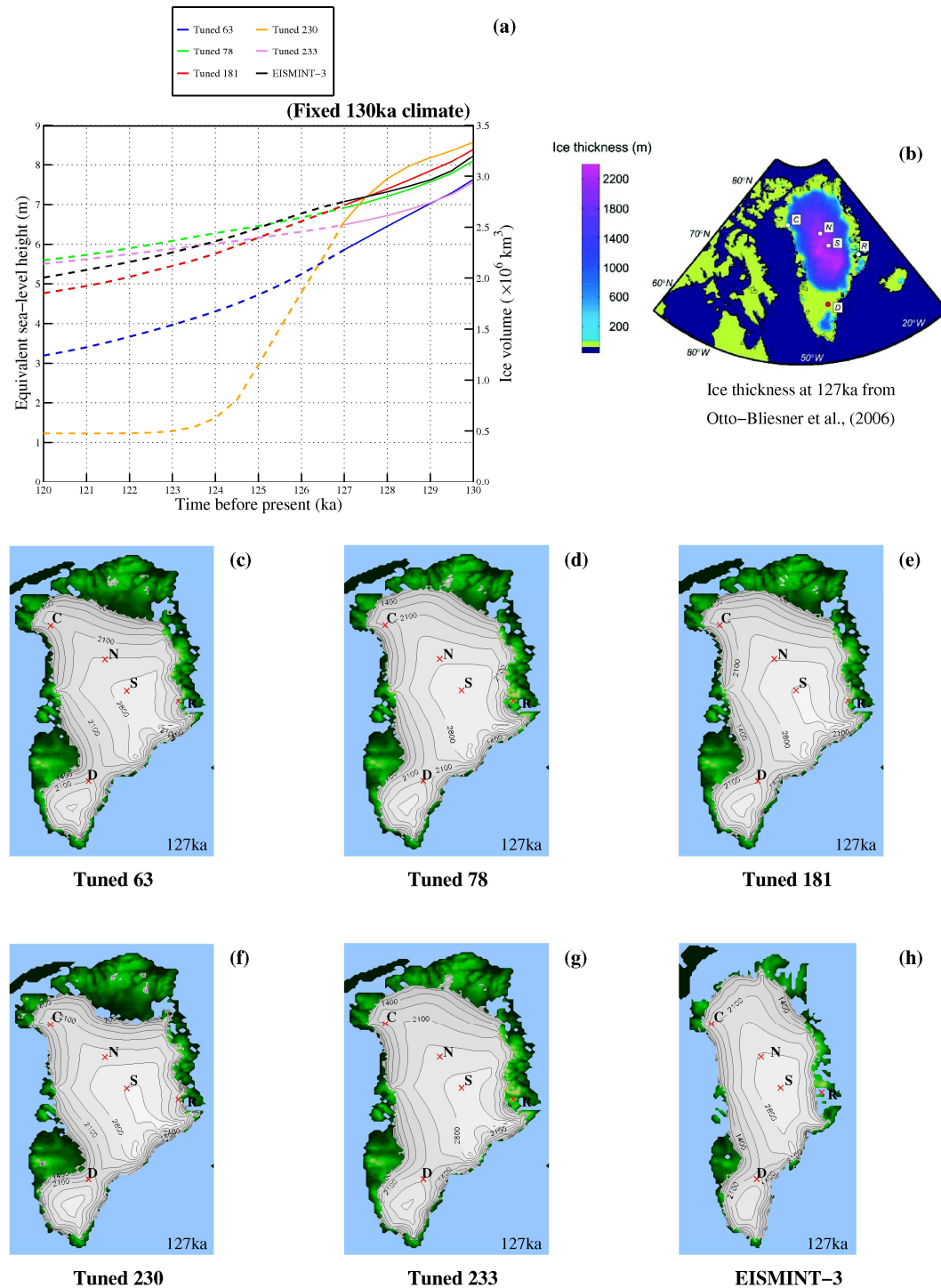


Figure 6.9: Offline forcing of Glimmer with a 130ka fixed vegetation HadCM3 climate with the GrIS present. (a) Ice volume and equivalent sea-level height for 10,000 model years. All Glimmer model parameter sets are shown. The dashed line sections correspond to ice evolution after 127ka which corresponds to the timing of the minimum GrIS extent and ice volume deduced by Otto-Bliesner *et al.* (2006a). (b) The GrIS geometry at 127ka for Otto-Bliesner *et al.* (2006a) simulation. (c) to (h) Also shown are the GrIS geometry at 127ka for tuned 63 (c), tuned 78 (d), tuned 181 (e), tuned 230 (f), tuned 233 (g) and EISMINT-3 (h) parameter sets. Ice core observations indicate LIG ice at Renland (R), NGRIP (N), Summit (S) and possibly Camp Century (C). Evidence for LIG at Dye-3 (D) is equivocal.

| Glimmer setup                          | EISMINT-3    | Recent tuning expts |       |       |       |       | Otto-Bliesner <i>et al.</i> (2006a) study |
|--|--------------|---------------------|-------|-------|-------|-------|---|
|  |              | 63                  | 78    | 181   | 230   | 233   |   |
| 127ka                                  |              |                     |       |       |       |       |   |
| Sea-level (m)                          | 1.2          | 1.8                 | 1.2   | 1.4   | 2.0   | 1.1   | 3.0                                       |
| Palaeodivide lowering (m)              | 28           | 79                  | 59    | 54.0  | 50.0  | 59.0  | ~570                                      |
| Dye-3 ice-free?                        | no           | no                  | no    | no    | no    | no    | yes                                       |
| Dye-3 ice-free timing                  | 124 to 125ka | never               | never | never | never | never | -   |
| Max. sea-level (between 124 and 127ka) | 1.9          | 3.3                 | 1.8   | 2.6   | 3.8   | 1.54  | -   |

Table 6.3: Summary of GrIS evolution when Glimmer is forced offline with a 130ka fixed vegetation climatology for 10,000 years and the GrIS present. All simulations begin from an equilibrated modern day GrIS. The top half of the table compares the results from this study with Otto-Bliesner *et al.* (2006a). The lower half summarises the minimum extent of the GrIS during the 10,000 years of model simulation constrained by ice core data and the criteria outlined at the beginning of this section. When Dye-3 remains ice-covered the minimum GrIS occurs when all other palaeodata can still be satisfied (i.e. maximum sea-level contribution should be between 124 and 127ka). Note that none of the simulations satisfy the lowering of the ice-sheet at Summit by 500 m within the 10,000 years.

Although the palaeodata can be used in the way described above to constrain the minimum extent of the GrIS during the LIG, a more robust approach would be to allow the ice-sheet to evolve through the LIG as the climate evolves, in response to changes in the orbital parameters, and then compare the GrIS geometry independently with the ice core data. The offline forcing method shows that very different GrIS geometries and contribution to LIG sea-level rise can occur due to parametric uncertainties from the ice-sheet model and differences in the boundary conditions and the reference climate. Furthermore, forcing the GrIS offline with the 130ka climate is insufficient to melt the ice-sheet in accordance with palaeodata constraints within the first few millennia for all of the tuned parameter sets if Dye-3 is believed to be ice-free. The next section uses a ‘matrix coupling’ methodology (based on Pollard and DeConto (2009)) which accounts for the response of the GrIS to an evolving climate during the LIG. The impact of vegetation feedbacks on GrIS behaviour is also addressed to deduce whether this missing feedback in previous studies significantly alters the response of the GrIS to the insolation perturbations of the LIG.

### 6.4.2 Transient forcing of the GrIS during the LIG

It is not known exactly how big the GrIS was at 130ka (or at any other point during the LIG), although sea-level was approximately similar to present day (Siddall *et al.*, 2007; Kopp *et al.*, 2009) implying a substantial amount of ice must have been present at high northern and southern latitudes.



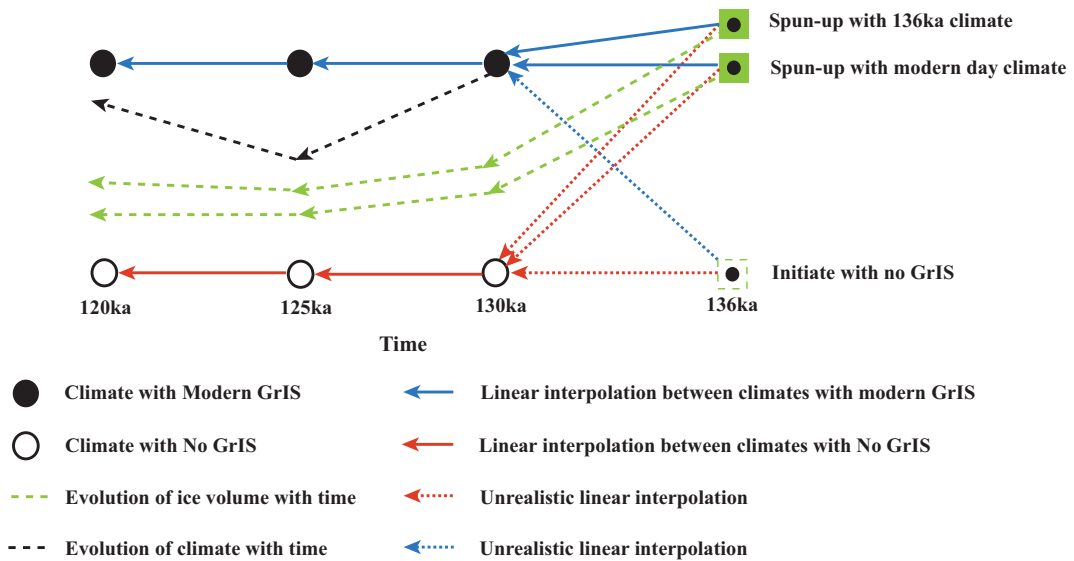


Figure 6.10: Diagram illustrating the coupling methodology between climate and ice-sheet for the LIG. Simulations are run for a total of 16,000 model years, initiated with a climate representative of 136ka (GrIS included). The transient climate evolves simultaneously with the ice-sheet model. Three possible initial conditions are shown for the ice-sheet model by the green squares: ice-sheet in equilibrium with 136ka climate, ice-sheet in equilibrium with modern day climate and no ice-sheet but rebounded bedrock. Climate is linearly interpolated from 136ka to 130ka via six possible routes (probable unrealistic ones are shown as dotted blue and red arrows). From 130 to 120ka the climate evolves (black dashed arrow shows an example) according to a weighting towards either a transient climate where there is a modern day GrIS (black filled circles) and one where there is noGrIS (black open circles). The weighting is based on the ratio of the previous years' ice volume relative to the ice volume at 130ka. The green dashed arrow shows schematically the evolution of the ice-sheet volume starting from 2 of the three initial conditions. See main text for more details and equations.

Since it is not possible to spin-up the ice-sheet model configuration at 130ka using HadCM3 coupled to Glimmer for several glacial-interglacial cycles, an approach has been used that assumes the ice-sheet is in equilibrium at the start of the transient ice-sheet model simulation. In order that changes in the ice-sheet response to climate at 130ka are not a result of inadequate spin-up of the ice-sheet model, simulations began at 136ka when the climate was substantially colder. A previous experiment run with HadCM3 but MOSES 1 (no interactive vegetation component) was used for the climatology at 136ka and its orbital parameters and trace gas concentrations are given in Section 6.2.1 and Table 6.1. This simulation was run for 500 model years with an averaging time of 30 years. As a result, the ice sheet model was initiated with an ice-sheet in equilibrium with the 136ka climate (Glimmer spun-up for 50,000 years in anomaly mode using a 136ka climatology).

### ‘Coupling’ methodology

Computationally, it is not yet feasible to run HadCM3 fully coupled (two-way) with Glimmer for the timescales of thousands of years such as the LIG. A methodology has been developed based on Pollard and DeConto (2009) in order to account for a transient climate which evolves as the ice-sheet volume evolves without this computational expense in time. Although it does not include some direct feedbacks between ice-sheet and climate (such as surface albedo change) it at least takes into account a changing climate as a result of the ice-sheet geometry changing and includes the ice-elevation feedback discussed in Chapter 5. The anomaly forcing method for precipitation and temperature (described in Chapter 5, Section 5.2.1) used to remove climate model biases in the future regrowth experiments, is also used here. A total of 16,000 years were modelled in this way, representing the time period from 136ka to 120ka. Figure 6.10 shows a diagrammatic of the coupling process, which is outlined in detail below.

The monthly average climate,  $CL(t)$ , is linearly interpolated along the time-axis from 136ka to 130ka. The linear interpolation can happen one of two ways:

$$CL(t) = \frac{cl_{130}^{ice} - cl_{136}^{ice}}{t_1}t + cl_{136}^{ice}, \quad (6.1)$$

where the interpolation is between the 136ka climate,  $cl_{136}^{ice}$ , and the 130ka climate *with* a GrIS,  $cl_{130}^{ice}$ , or

$$CL(t) = \frac{cl_{130}^0 - cl_{136}^{ice}}{t_1}t + cl_{136}^{ice}, \quad (6.2)$$

where the interpolation is between the 136ka climate and the 130ka climate *without* a GrIS,  $cl_{130}^0$ . In both cases  $t_1$  is 6,000 years. Glimmer is initiated with the equilibrated ice-sheet geometry which was obtained by forcing Glimmer offline with a constant 136ka climate.

At 130ka the climate is allowed to evolve each year between the two climate parameter sets (with and without a GrIS) according to a weighting function defined by the ratio of the ice volume ( $vol(t)$ ) at time  $t$  and the ice volume predicted at 130ka ( $vol(130)$ ) by the ice-sheet model. Between 130ka and 125ka the following linear interpolations are performed (represented by the solid blue and red arrows

respectively in Figure 6.10) similar to Equations 6.1 and 6.2

$$cl^{ice}(t) = \frac{cl_{125}^{ice} - cl_{130}^{ice}}{t_2}t + cl_{130}^{ice}, \quad (6.3)$$

and

$$cl^0(t) = \frac{cl_{130}^0 - cl_{125}^0}{t_2}t + cl_{130}^0, \quad (6.4)$$

where  $cl_{125}^{ice}$  is the 125ka climate with the GrIS present,  $cl_{125}^0$  is the 125ka climate with no GrIS and  $t_2$  is equal to 5,000 years. Likewise, a similar linear interpolation is also performed from 125 to 120ka.

The climate,  $CL(t)$ , at each year is now also weighted either towards the noGrIS climate,  $cl^0(t)$ , or the GrIS climate,  $cl^{ice}(t)$ , according to

$$CL(t) = \frac{vol(t)}{vol(130)}(cl^{ice}(t) - cl^0(t)) + cl^0(t). \quad (6.5)$$

This methodology is run for the EISMINT-3 Glimmer setup and the optimal tuned parameter sets for the more recent boundary conditions and forcings described in Section 2.5.3. In addition to using the ice-sheet model initial condition of a 136ka spun-up ice-sheet, two further initial conditions are investigated due to uncertainty in the 136ka climate and the size of the ice-sheet at this time:

1. Glimmer simulations initialised at 136ka with an ice-sheet in equilibrium with a present day climate (Glimmer spun-up for 50,000 years by forcing the model offline with the base line reference climatologies).
2. Simulations initialised at 136ka with no ice-sheet and a rebounded bedrock.

These initial conditions are also shown in Figure 6.10 as green squares. As a result there are an additional four simulations, using the linear interpolation between 136ka and 130ka given by Equations 6.1 and 6.2. This resulted in a total of 12 possible outcomes for each Glimmer model setup where half of these simulations included interactive vegetation in HadCM3.

Finally, simulations are performed without the weighting function towards the noGrIS experiments. Linear interpolation is performed only between the GrIS present simulations at 130ka, 125ka and 120ka, with and without vegetation feed-

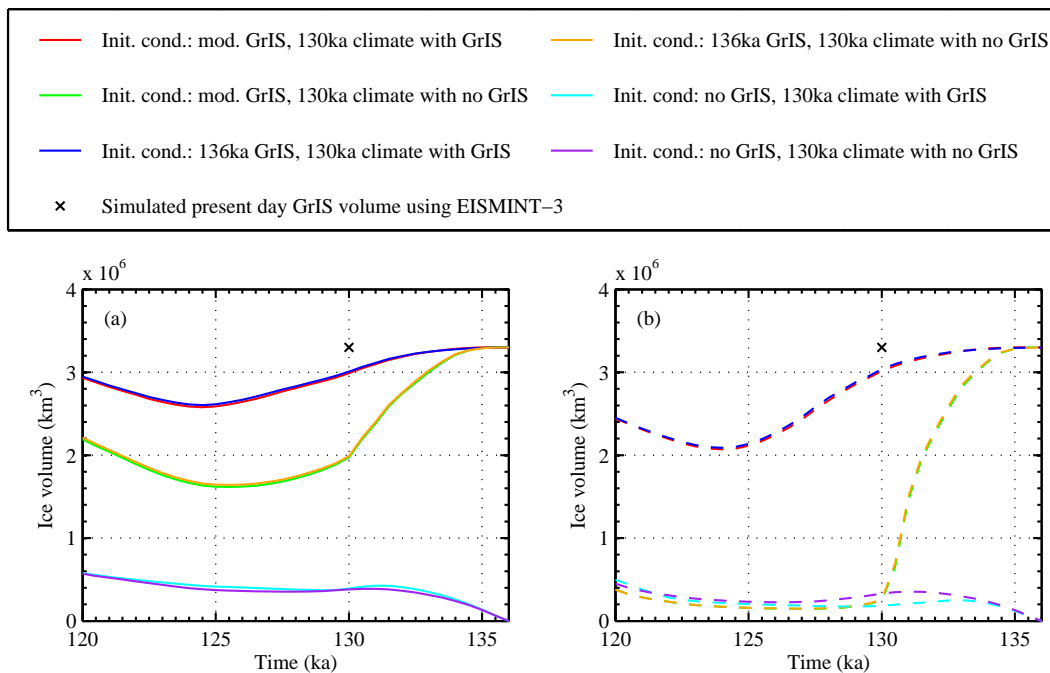


Figure 6.11: Evolution of GrIS volume from 136 to 120ka using the coupling methodology when Glimmer is setup in EISMINT-3 mode. (a) GrIS volume when vegetation is fixed and (b) GrIS volume when vegetation is interactive. The three different initial conditions are shown: spun-up modern day ice-sheet, spun-up 136ka ice-sheet and no ice-sheet. Interpolation from 136ka to 130ka GrIS present climate and 130ka no GrIS present climate is also shown. This results in a total of twelve scenarios (see Figure 6.10).

backs included (see Equation 6.3). In this way it is possible to see how much difference this matrix coupling methodology makes to the prediction of the minimum GrIS during the LIG. Furthermore, the Glimmer tuning exercise performed in Chapter 2 involved a tuning method for complete offline forcing of Glimmer with climate and, therefore, there is an argument that removal of the weighting function is the ‘correct’ way to perform the experiments with the selected tuned parameter sets.

### Changes in ice volume and sea-level

Figure 6.11 shows the 12 possible outcomes in this study for fixed vegetation (Figure 6.11a) and interactive vegetation (6.11b) for the EISMINT-3 setup of Glimmer. When vegetation feedbacks are not included four of the six simulations result in a realistic change in ice volume for the 16,000 year model simulation according to the criteria deeming a LIG simulation as acceptable, outlined at the beginning of Section 6.4. First note that a modern day spun-up GrIS and a 136ka spun-up GrIS result in very similar trajectories in terms of ice volume whether interpolated to a 130ka climate with a GrIS (red and blue lines) or without (orange and light blue

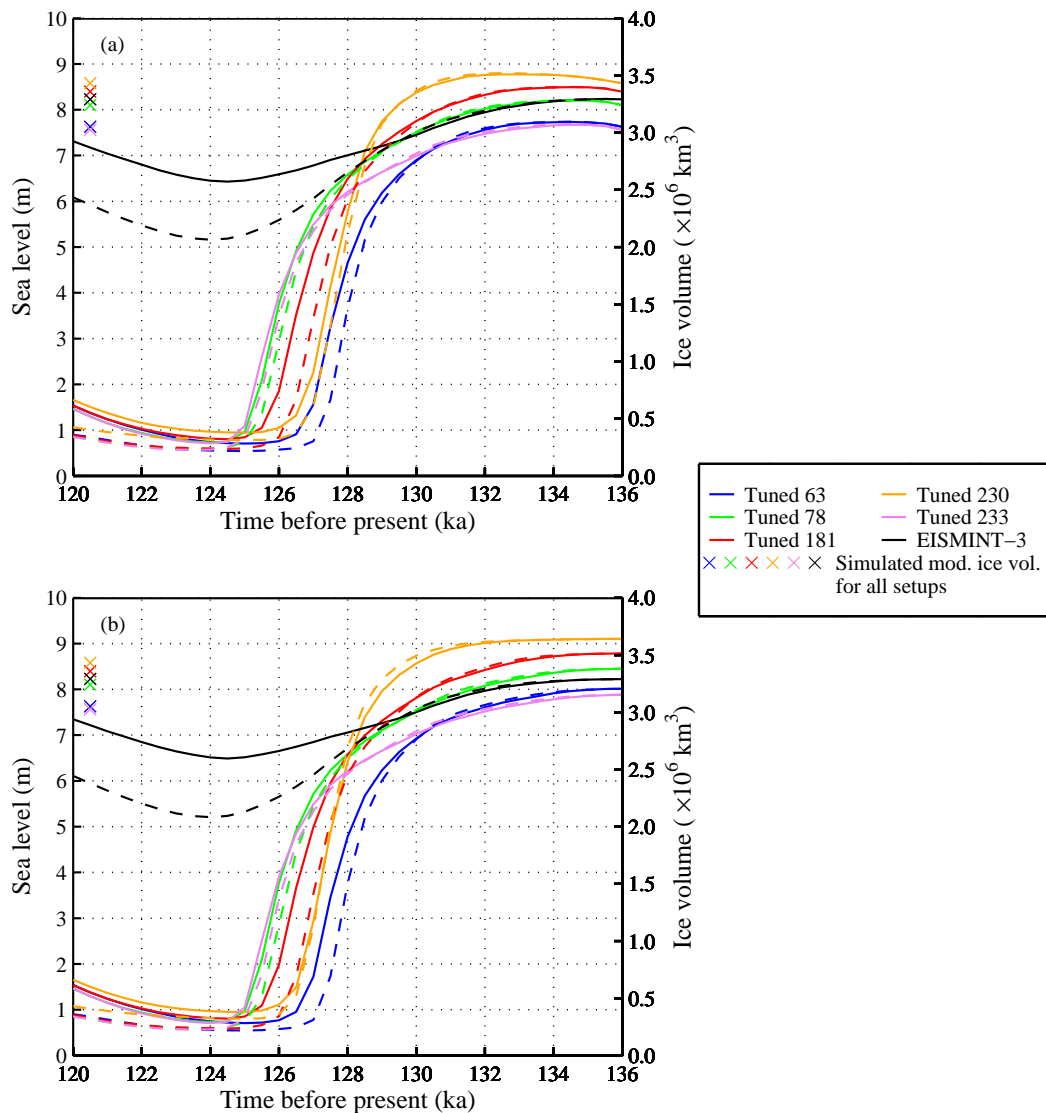


Figure 6.12: Ice volume and equivalent sea-level height through the LIG for the Glimmer EISMINT-3 and tuned parameter sets for initial ice-sheet conditions (a) modern day spun-up GrIS and (b) 136ka spun-up GrIS. The solid lines refer to fixed vegetation and the dashed lines refer to interactive vegetation. Also shown near the left y-axis for each Glimmer setup is the present day simulated equilibrium ice volume/sea-level equivalent height.

lines). The air temperature and precipitation for the spun-up GrIS simulation forced with a 136ka climate is  $\sim 2^{\circ}\text{C}$  colder and accumulation  $0.04\text{ m yr}^{-1}$  less than the modern day spun-up GrIS. However, these differences do not significantly alter the ice volume and shape of the ice-sheet. There is a steady decrease in ice volume between 136 and 130ka consistent with the rise in  $\text{CO}_2$  to 280 ppmv and an increase in summer insolation relative to present. Ice volume continues to steadily decrease until a minimum is reached at about 124ka when it begins to increase again in accordance with the cooler climate at 120ka relative to 130ka.

The simulations where the 136ka climate is interpolated to a noGrIS climate at 130ka result in a significantly lower minimum GrIS volume but still within palaeo-data constraints from LIG sea-level rise and ice-sheet extent. However, initialising with no ice results in a slow build up of ice mass between 136ka and 130ka and then a subsequent small decrease towards 125ka followed again by a slow increase in ice volume. Since the GrIS reaches an ice volume of  $\sim 4 \times 10^5 \text{ km}^3$  at 130ka this result is not consistent with sea-level at this time, which is estimated to be similar to present day (Siddall *et al.*, 2007; Kopp *et al.*, 2009) (see Figure 1.8).

Ice-sheet volume evolution when interactive vegetation is included are shown in Figure 6.11b. In this case the only simulations which show a realistic trajectory in ice volume are those which interpolate to a GrIS climate at 130ka and are initialised from a fully glaciated Greenland configuration. The other four simulations either do not build up enough ice at the start or result in almost complete collapse of the ice-sheet by 130ka and therefore do not satisfy the acceptable criteria for LIG GrIS in terms of ice coverage at the central ice core locations and the timing of the predicted minimum LIG GrIS. The ice-sheet model is therefore sensitive to contrasting initial conditions and climates at 130ka. Hereafter, only the two simulations (which were acceptable with and without vegetation feedbacks) starting from an initial condition of ice with climates interpolated from the 136ka climate to a GrIS present climate at 130ka will be discussed and referred to as  $\text{GrIS}_{mod}^{glim-setup}$  and  $\text{GrIS}_{136ka}^{glim-setup}$ ; ‘glim-setup’ refers to the EISMINT-3/tuned Glimmer setup, ‘mod’ refers to the spun-up modern day GrIS and ‘136ka’ refers to the spun-up 136ka GrIS. These are also the most likely to represent the transition between the penultimate glacial and the last interglacial periods since predicted ice volume at 130ka is close to the simulated present day value and therefore consistent with the estimated sea-level data (shown by the cross symbol on Figure 6.12).

The two selected experiments are now analysed in terms of the new tuned versions of Glimmer. EISMINT-3 is also included on the all Figures for direct comparison. Figure 6.12 shows ice-sheet evolution for all Glimmer model parameter sets (tuned and EISMINT-3) when vegetation is fixed (solid lines) and when it is interactive (dashed lines). Sea-level equivalent height and present day simulated ice volume for each model setup is shown by crosses close to the left hand y-axis. Figure 6.12a corresponds to  $\text{GrIS}_{mod}^{glim-setup}$  and Figure 6.12b corresponds to  $\text{GrIS}_{136ka}^{glim-setup}$ . In all

| Expt                  | Glimmer setup   | EISMINT-3 | Recent tuning expts |        |        |        |        |
|-----------------------|---|-----------|---------------------|--------|--------|--------|--------|
|                       |   |           | 63                  | 78     | 181    | 230    | 233    |
|                       | <i>Ice volume (<math>\times 10^6</math> km<sup>3</sup>)</i> |           |                     |        |        |        |        |
| GrIS <sub>mod</sub>   | Fixed veg   | 2.58      | 0.28                | 0.29   | 0.32   | 0.38   | 0.28   |
|                       | Interactive veg   | 2.07      | 0.22                | 0.24   | 0.24   | 0.31   | 0.23   |
| GrIS <sub>136ka</sub> | Fixed veg   | 2.60      | 0.28                | 0.29   | 0.32   | 0.38   | 0.28   |
|                       | Interactive veg   | 2.09      | 0.22                | 0.24   | 0.24   | 0.32   | 0.23   |
|                       | <i>Sea-level rise (m)</i>                                   |           |                     |        |        |        |        |
| GrIS <sub>mod</sub>   | Fixed veg   | 1.7       | 6.9                 | 7.4    | 7.6    | 7.6    | 6.8    |
|                       | Interactive veg   | 3.0       | 7.1                 | 7.5    | 7.8    | 7.8    | 7.0    |
| GrIS <sub>136ka</sub> | Fixed veg   | 1.7       | 6.9                 | 7.4    | 7.6    | 7.6    | 6.8    |
|                       | Interactive veg   | 3.0       | 7.1                 | 7.5    | 7.8    | 7.8    | 7.0    |
|                       | <i>Palaeodivide lowering (m)</i>                            |           |                     |        |        |        |        |
| GrIS <sub>mod</sub>   | Fixed veg   | 82        | no ice              | no ice | no ice | no ice | no ice |
|                       | Interactive veg   | 250       | no ice              | no ice | no ice | no ice | no ice |
| GrIS <sub>136ka</sub> | Fixed veg   | 69        | no ice              | no ice | no ice | no ice | no ice |
|                       | Interactive veg   | 243       | no ice              | no ice | no ice | no ice | no ice |

Table 6.4: Minimum GrIS volume, maximum LIG sea-level rise and ice surface drawdown at the Summit drilling core site for all Glimmer model parameter sets. Data for GrIS<sub>mod</sub> and GrIS<sub>136ka</sub> are shown.

cases, the inclusion of interactive vegetation results in a lower ice volume throughout the LIG compared with fixed vegetation. Furthermore, all show a decrease in ice volume with a minimum reached between 124 and 125ka, the time at which LIG sea-level rise peaked relative to present day according to Kopp *et al.* (2009) (see Figure 1.8a). Table 6.4 shows the minimum ice volume and maximum contribution to sea-level rise for all ice-sheet model parameter sets. It also shows the amount of ice surface lowering of the ice-sheet relative to present at the Summit ice core drilling site for the minimum ice-sheet configuration. First note that the results between GrIS<sub>mod</sub> and GrIS<sub>136ka</sub> are very similar. When vegetation is fixed the minimum ice volume for the GrIS occurs for GrIS<sup>63</sup> and GrIS<sup>233</sup> with almost complete collapse of the ice-sheet. The other Glimmer tuned parameter sets give similar results in between these. Sea-level contributions are estimated to be between 6.8 and 7.6 m, within the estimated sea-level highstand range given by Kopp *et al.* (2009). In contrast, GrIS<sup>EIS</sup> results in a substantially larger minimum ice-sheet volume with a contribution of 1.7 m to LIG sea-level rise relative to present day. Furthermore, surface drawdown in the Summit region also gives contrasting results. For GrIS<sup>EIS</sup> the surface only lowers between 69 (modern spun-up GrIS as initial condition) and 82 m (136ka spun-up GrIS as initial condition) well short of the constraint provided

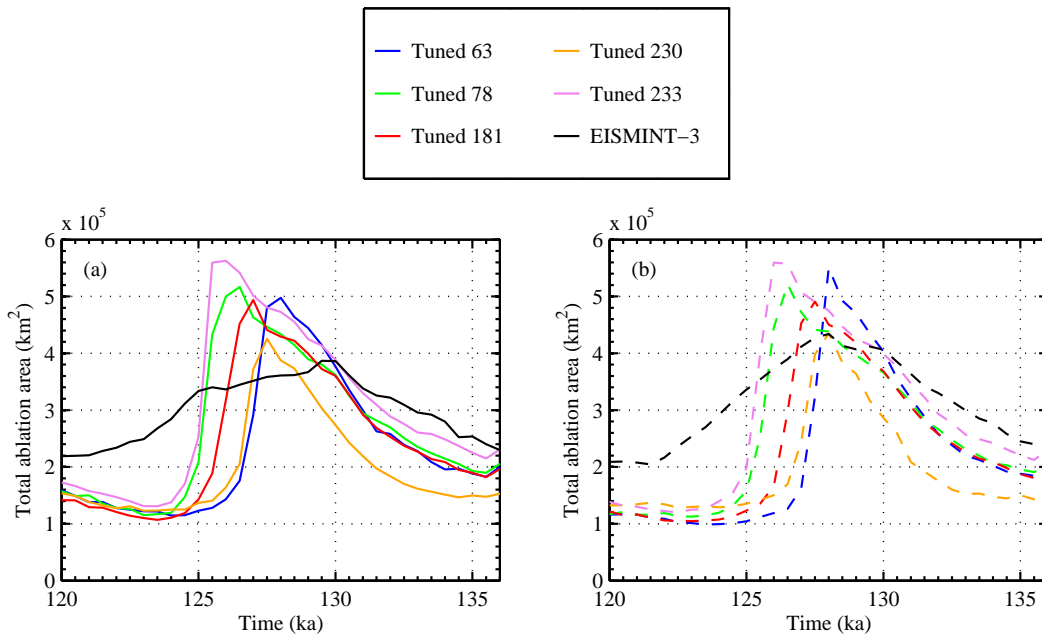


Figure 6.13: The total icefield ablation area over Greenland from 136 to 120ka (in  $\text{km}^2$ ) for (a) fixed vegetation and (b) interactive vegetation. Shown are the EISMINT-3 and new tuned Glimmer parameter sets.

by Summit (Raynaud *et al.*, 1997) which suggested an ice surface  $\sim 500$  m lower than present. In contrast, the modelled GrIS's using the tuned parameter sets result in complete melting of ice in this region contradicting the palaeoevidence that the central regions of Greenland were ice-covered throughout the LIG (see Figure 6.14)(Chappellaz *et al.*, 1997; Raynaud *et al.*, 1997; Andersen *et al.*, 2004).

When interactive vegetation feedbacks are included in the climate simulations, results for the tuned Glimmer parameter sets do not change significantly because most of the GrIS has already melted due to the weighting towards the 'cooler' noGrIS fixed surface climates compared with the interactive vegetation noGrIS climates (as a result of enhanced vegetation feedbacks). However, for GrIS<sup>EIS</sup> the contribution to the LIG sea-level highstand almost doubles compared with fixed vegetation to 3.0 m. In addition, the surface drawdown of the ice-sheet increases considerably to between 243 and 250 m, closer but still short of the  $\sim 500$  m lowering constraint provided by Raynaud *et al.* (1997).

The total icefield ablation area (all regions of Greenland where the annual surface mass balance is less than zero) throughout the LIG simulations performed here are shown in Figure 6.13. For GrIS<sub>mod</sub><sup>EIS</sup> when vegetation is fixed (Figure 6.13a) the ice-sheet immediately begins to respond to the warmer spring and summer temperatures



of the early to mid-LIG with the total ablation area increasing from  $2.3 \times 10^5 \text{ km}^2$  to  $3.8 \times 10^5 \text{ km}^2$  by 129.5ka followed by a slow decrease back to  $\sim 2.2 \times 10^5 \text{ km}^2$  at 120ka. Otto-Bliesner *et al.* (2006a) found an increase from  $2.64 \times 10^5 \text{ km}^2$  to  $5.25 \times 10^5 \text{ km}^2$  during the LIG with their simulation. For the tuned Glimmer parameter sets, there is a marked increase in ablation area over Greenland peaking between  $4.2 \times 10^5 \text{ km}^2$  (GrIS<sub>mod</sub><sup>230</sup>) and  $5.6 \times 10^5 \text{ km}^2$  (GrIS<sub>mod</sub><sup>233</sup>) from 125.5ka to 128ka and decreasing sharply to values between  $1.0 \times 10^5 \text{ km}^2$  and  $1.4 \times 10^5 \text{ km}^2$ . This agrees with the almost complete collapse of the GrIS by 125ka for the tuned Glimmer parameter sets. The low total ablation area from 125ka to 123ka compared with GrIS<sub>mod</sub><sup>EIS</sup> is a consequence of ice confined only to the high altitude regions much of which is above the equilibrium line between ablation and accumulation. There is a slow increase in ablation area for the tuned parameter sets as 120ka is approached due to increases in ice growth in eastern regions which become thick enough to flow to lower altitudes below the equilibrium line where ablation dominates. When vegetation feedbacks are included (Figure 6.13b) the GrIS<sub>mod</sub><sup>EIS</sup> total ablation area increases and peaks at  $4.2 \times 10^5 \text{ km}^2$  (11 % greater than when vegetation feedbacks are fixed) within 2,000 years from the start of the LIG and decreases thereafter back to modern day values. The Glimmer tuned parameter sets result in a similar pattern in total ablation area evolution compared with when vegetation is fixed, consistent with the ice-sheet evolution in Figure 6.12.

### Minimum extent of the GrIS

As already described, the GrIS retreats over several millennia in response to the orbitally induced Arctic summer warming, leading to surface lowering and a reduction in ice volume peaking around 124 to 125ka consistent with other modelling studies (Cuffey and Marshall, 2000; Tarasov and Peltier, 2003; Otto-Bliesner *et al.*, 2006a). Figure 6.14 shows the minimum extent of the GrIS from previous work (Figure 6.14a), GrIS<sub>mod/136ka</sub><sup>EIS</sup>, GrIS<sub>mod/136ka</sub><sup>63</sup> and GrIS<sub>mod/136ka</sub><sup>230</sup> (Figures 6.14b to d respectively). The minimum extent of the other three tuned parameter sets are not shown but fall between the range depicted for GrIS<sup>63</sup> and GrIS<sup>230</sup>. Overlain are the locations of the ice core drilling sites described in Section 1.5.3. Vegetation feedbacks are not included in these simulations. In all cases the Renland ice core location is ice-covered consistent with the palaeoevidence of pre-LIG ice surviving

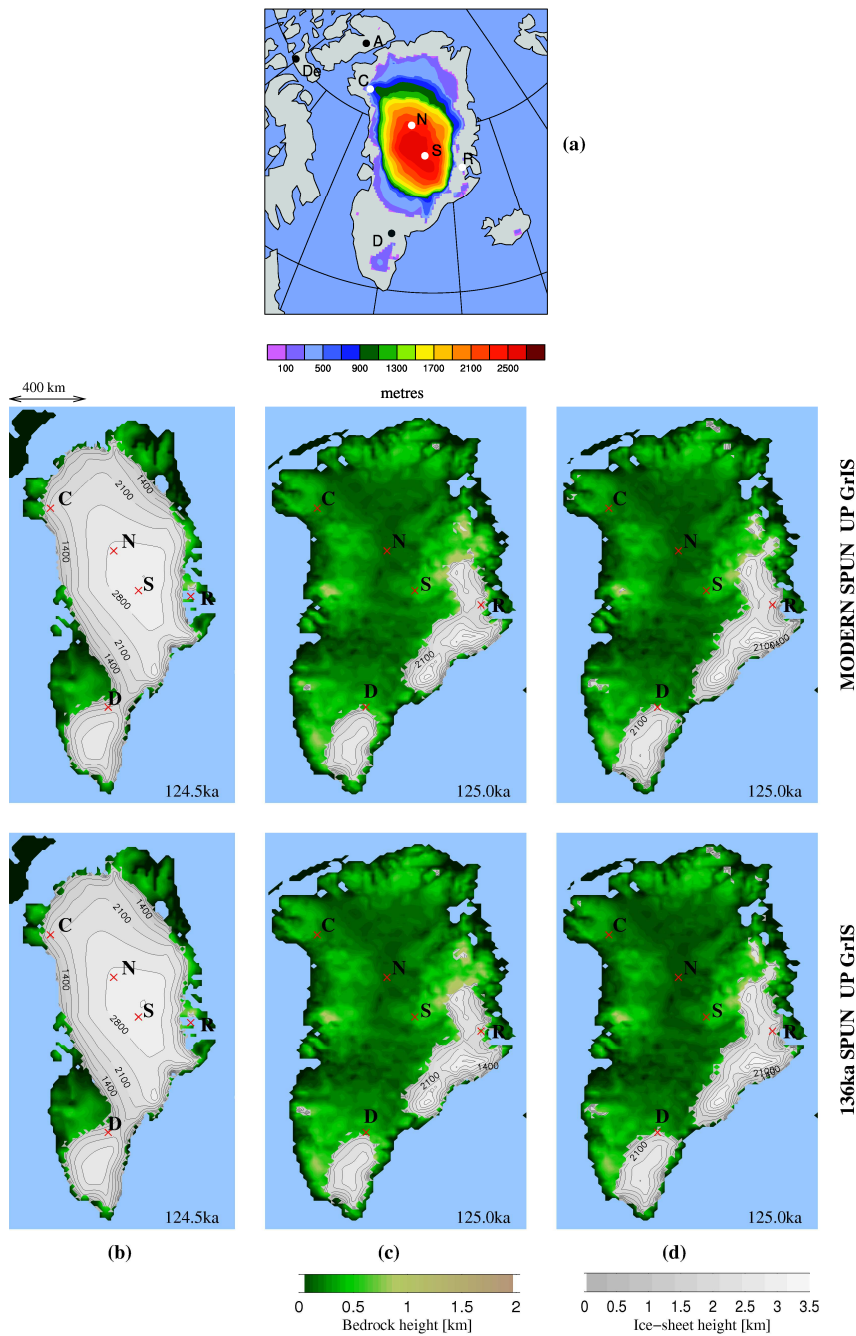


Figure 6.14: Minimum (approximate year shown underneath subfigures) simulated ice thickness and extent of the GrIS during the LIG initiated from a modern spun-up and a 136ka spun-up equilibrium GrIS forced with *fixed* vegetation climatologies. Results are shown for (a) multi-model average from three ice-sheet models, (Tarasov and Peltier, 2003; Lhomme *et al.*, 2005; Otto-Bliesner *et al.*, 2006a), reproduced from Jansen *et al.* (2007), (b) Glimmer EISMINT-3 model setup in this study, (c) Glimmer model setup for tuned experiment 63 in this study and (d) Glimmer model setup for tuned experiment 230 in this study. The other three tuned experiments are not shown but fall with the range deduced from (c) and (d). Ice core observations indicate LIG ice at Renland (R), NGRIP (N), Summit (S) and possibly Camp Century (C). Evidence for LIG at Dye-3 (D) is equivocal. Additional observations in the eastern Canadian Arctic are shown in (a) at Devon (De) and Agassiz(A) where no LIG ice is present. These locations are not shown in this study because the Arctic icefields outside of Greenland were not modelled.

the peak LIG warmth. However, the Summit and Camp Century core locations are only ice-covered for  $\text{GrIS}^{EIS}$  and the previous modelling studies. For the tuned Glimmer parameter sets the GrIS has retreated to the eastern and southern margins of Greenland leaving central and western regions completely ice-free and therefore inconsistent with the current palaeoevidence that these locations were covered by ice during the LIG. Furthermore, the equivocal core, Dye-3, remains ice-covered for  $\text{GrIS}_{mod}^{EIS}$  and  $\text{GrIS}_{136ka}^{EIS}$  in contrast to previous modelling work. It is depicted as ice-free in the multi-model synthesis in Figure 6.14a. Dye-3, however, is positioned on the margin of the isolated southern ice domes in Figures 6.14c and d.

When vegetation feedbacks are included in the climate simulations the timing of the minimum GrIS configuration is similar to the fixed vegetation experiments (124 to 125ka). However, the extent of the GrIS differs significantly in the south for  $\text{GrIS}^{EIS}$ . Figure 6.15 has a similar form to Figure 6.14 showing the GrIS minimum extent for (a) previous modelling studies, (b)  $\text{GrIS}_{mod/136ka}^{EIS}$  (c)  $\text{GrIS}_{mod/136ka}^{63}$  and (d)  $\text{GrIS}_{mod/136ka}^{230}$ . All Glimmer experiments show an ice-free Dye-3 consistent with recent previous ice-sheet modelling work (Cuffey and Marshall, 2000; Tarasov and Peltier, 2003; Lhomme *et al.*, 2005; Otto-Bliesner *et al.*, 2006a). However, again, only  $\text{GrIS}^{EIS}$  shows central Greenland ice-covered in agreement with the Summit cores. Since vegetation feedbacks, at least in the noGrIS simulations, result in intensification of the vegetation-snow-climate feedback mechanism and therefore enhanced local warming, particularly in the summer months over Greenland, they act to amplify the orbitally induced warming. This results in further retreat and lowering of the ice-sheet compared with when vegetation remained fixed due to increased weighting of the climate towards these ‘warmer’ noGrIS simulations. However, because the ice-sheet had already retreated to the high altitude regions of the east and south when vegetation was fixed for the tuned Glimmer parameter sets, the increased warming (and also precipitation) due to vegetation growth in the noGrIS experiments does not have a significant impact on further ice-sheet retreat.

Although the Glimmer tuned parameter sets result in a good approximation to the present day GrIS, they are clearly overly sensitive to a transient LIG climate with accelerated ice loss inconsistent with the palaeoevidence available. Only the EISMINT-3 setup results in an ice-sheet that is consistent, at least in terms of areal extent, with observations of early LIG ice present/absent at the drilling core sites.

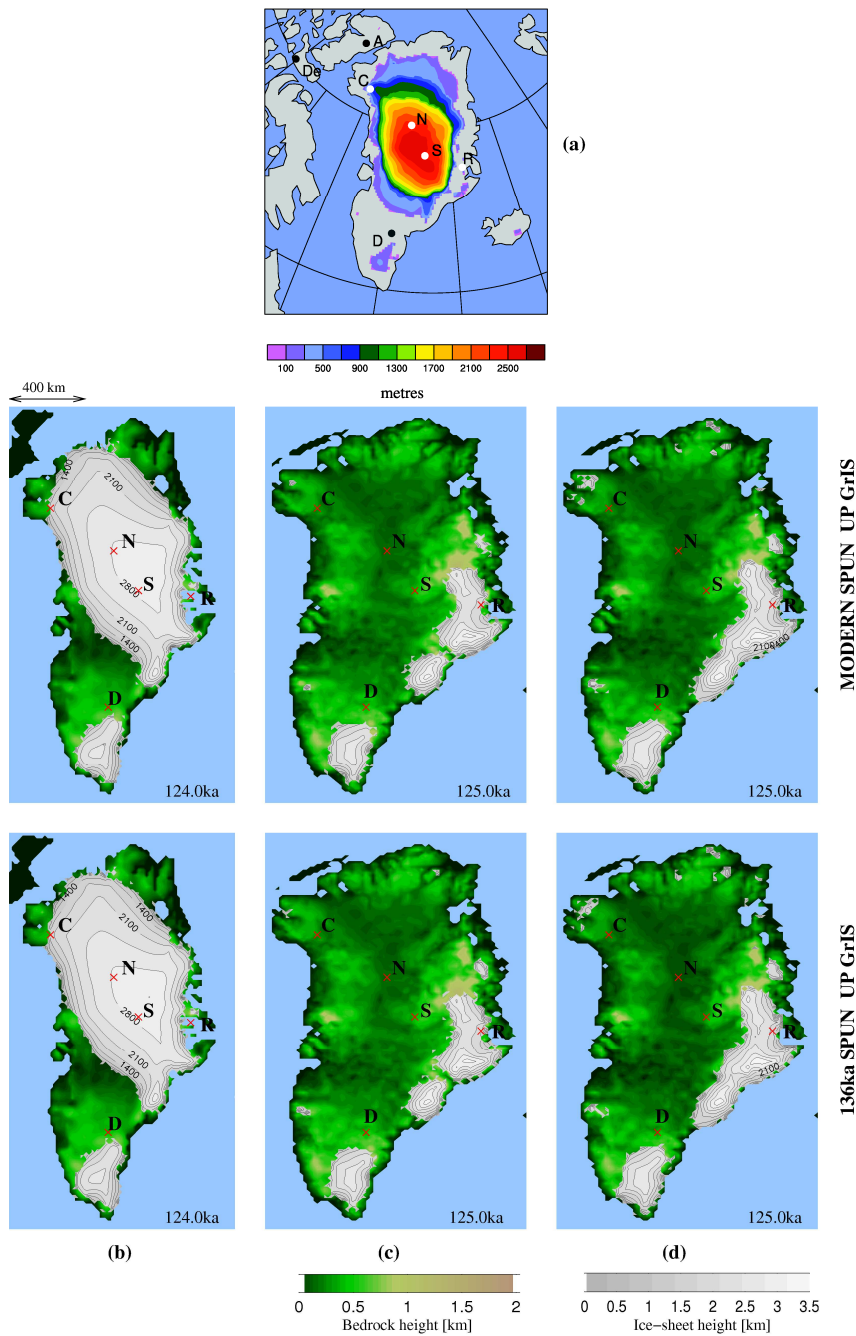


Figure 6.15: Minimum (approximate year shown) simulated ice thickness and extent of the GrIS during the LIG initiated from a modern spun-up and a 136ka spun-up equilibrium GrIS forced with *interactive* vegetation climatologies. Results are shown for (a) multi-model average from three ice-sheet models, (Tarasov and Peltier, 2003; Lhomme *et al.*, 2005; Otto-Bliesner *et al.*, 2006a), reproduced from Jansen *et al.* (2007), (b) Glimmer EISMINT-3 model setup in this study, (c) Glimmer model setup for tuned experiment 63 in this study and (d) Glimmer model setup for tuned experiment 230 in this study. The other three tuned experiments are not shown but fall with the range deduced from (c) and (d). Ice core observations indicate LIG ice at Renland (R), NGRIP (N), Summit (S) and possibly Camp Century (C). Evidence for LIG at Dye-3 (D) is equivocal. Additional observations in the eastern Canadian Arctic are shown in (a) at Devon (De) and Agassiz(A) where no LIG ice is present. These locations are not shown in this study because the Arctic icefields outside of Greenland were not modelled.

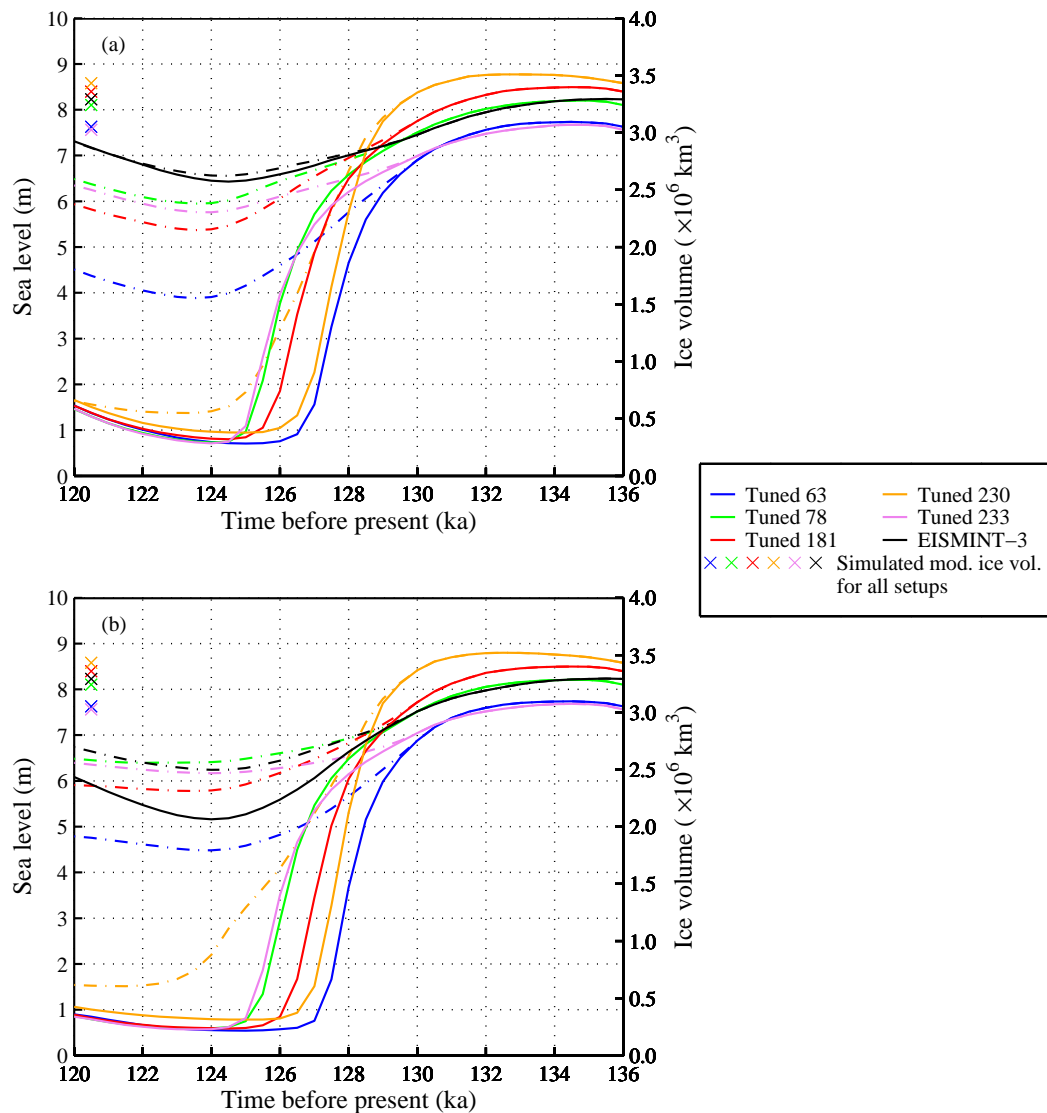


Figure 6.16: Comparison between ice volume evolution when the model is initiated with a spun-up modern GrIS with and without the weighting function included in the coupling methodology (i.e. without weighting function Glimmer is forced only with the GrIS present climatologies) for EISMINT-3 and Glimmer tuned parameter sets. (a) Fixed vegetation climate and (b) interactive vegetation climates. The dot-dash lines correspond to when the weighting function is absent and the solid lines correspond to when it is included. Also shown on the left y-axis for each Glimmer setup is the present day simulated equilibrium ice volume/sea-level equivalent height.

### How much difference does the ‘coupling’ methodology make?

In order to partially overcome the difficulty of performing a transient 16,000 year fully coupled HadCM3 Glimmer simulation, the previous section described a matrix coupling methodology where the climate each year was weighted towards equilibrium climates with and without a GrIS included, according to the previous years’ ice volume to initial (at 130ka) ice volume ratio. However, it is important to assess how much difference this method made to the overall GrIS evolution with and without

vegetation feedbacks included, especially as the tuning did not include this effect of matrix coupling. Thus, simulations were also performed where Glimmer was forced only with the GrIS present climatologies linearly interpolated between 130ka, 125ka and 120ka according to Equation 6.3. Figure 6.16 shows ice volume evolution for  $\text{GrIS}_{mod}$  for all Glimmer parameter sets with (solid lines) and without (dash-dot lines) the weighting function included. The result for  $\text{GrIS}_{136ka}$  shows very similar ice volume trajectories and is shown by Figure D.1 in Appendix D. When vegetation is fixed (Figure 6.16a)  $\text{GrIS}_{mod}^{EIS}$  shows similar ice volume trajectories whether the weighting function is included or not. In contrast, four of the five tuned Glimmer parameter sets (63, 78, 181 and 233) result in very different ice volume trajectories when the weighting function is excluded. They produce a range in LIG sea-level rise relative to present between 1.7 and 3.7 m, which falls within the range deduced by previous modelling studies. However,  $\text{GrIS}_{mod}^{233}$  still results in almost complete collapse of the ice-sheet by 124ka. Figure 6.17a shows the minimum extent of the GrIS for all Glimmer model parameter sets when the vegetation is fixed. The EISMINT-3 setup satisfies the ice core criteria which is not equivocal and is very similar in form to 6.14b as expected from the ice evolution curves shown in Figure 6.16. However, the tuned Glimmer parameter sets show more contrasting results in terms of minimum extent. Three of the five tuned simulations (78, 181, 233) satisfy the ice cover at the central ice cores. However, tuned parameter sets 63 and 230 show no ice-cover at NGRIP, with almost complete collapse of the ice-sheet for 233. Furthermore, the newly tuned experiments lose ice in the north which is not so apparent in the EISMINT-3 case.

Figure 6.16b shows the case when vegetation feedbacks are included in the climate simulations. Unlike the fixed vegetation experiment for  $\text{GrIS}_{mod}^{EIS}$ , the inclusion of the weighting function results in a smaller GrIS volume than if it were not included at all. In fact, the result when forced only with the GrIS present climatologies is closer to the fixed vegetation simulations in Figure 6.16a than the interactive simulation with the weighting function included. Figure 6.17 shows the minimum ice surface extent of the GrIS where Dye-3 still becomes ice-free without the weighting function. Therefore, the weighting function does not affect the geometry of the GrIS in relation to the ice core locations, but increases the contribution from the GrIS to the LIG sea-level highstand by  $\sim 1$  m.

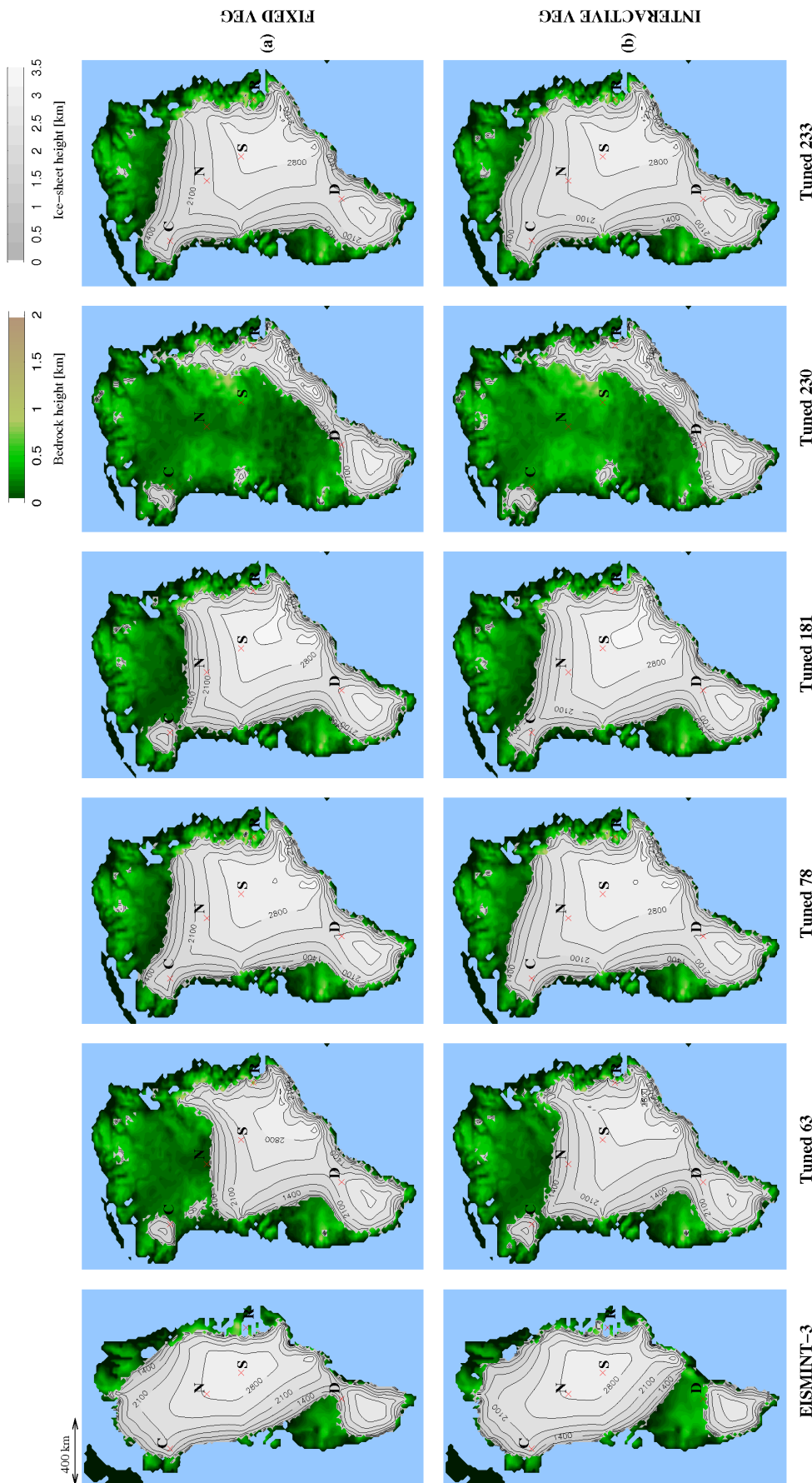


Figure 6.17: Minimum simulated ice thickness and extent of the GrIS during the LIG initiated from a modern day spun-up equilibrium GrIS forced with (a) the *fixed* vegetation climatologies and (b) the *interactive* vegetation climatologies, with the GrIS present and no weighting function included. All Glimmer parameter sets are shown. Ice core observations indicate LIG ice at Renland (R), NGRIP (N), Summit (S) and possibly Camp Century (C). Evidence for LIG at Dye-3 (D) is equivocal.

Similar to the fixed vegetation simulations, the same four tuned parameter sets (63,78,181 and 233) do not result in complete collapse of the GrIS when the weighting function is removed producing a range in sea-level rise relative to present between 1.3 and 3.1 m. Figure 6.17b shows that the results of these four simulations are acceptable according to the ice core criteria but with Dye-3 ice-covered in these cases. Tuned expt 230 results again in near collapse of the ice-sheet and is not an accepted scenario for the minimum extent of the GrIS according to the palaeodata. These results suggest that although the EISMINT-3 setup produces acceptable results using the ‘coupling’ methodology described in this thesis, the tuned Glimmer parameter sets for more realistic and up-to-date boundary conditions and reference climate forcings are overly sensitive to the increase in temperature that arises from partially weighting the climatology towards the noGrIS climates, whether the vegetation is fixed or not. Therefore the increase in near surface temperature by including the noGrIS climatologies (due to positive temperature changes as a result of a decrease in altitude and vegetation-snow-climate feedback mechanisms) in combination with generally high PDD factors, results in a ‘tipping point’ being reached whereby the ice-temperature-elevation feedback results in ablation increasing relative to accumulation as the ice-sheet lowers and the temperature increases. This results in weighting of the transient climate seen by Glimmer towards the noGrIS climatologies and therefore accelerating the ice loss further until local summer temperatures begin to decrease again after 125ka.

During ice-sheet retreat for  $\text{GrIS}_{mod}^{230}$ , where there is almost complete collapse whether the weighting function is included or not, the more negative lapse rate will act to warm the region further and cause more surface melt (in combination with the high PDD factors) than a less negative lapse rate via the positive ice-temperature-elevation feedback mechanism. A warmer climate compared with preindustrial results in increased melting during summer months and almost complete collapse of the GrIS.



## 6.5 Discussion and conclusions

The LIG provides a useful test of the climate and ice-sheet models since it allows a direct comparison between model results and actual data. This time period is particularly interesting since it is thought to be the last time the Arctic experienced warmer conditions than present along with estimated sea-level several metres higher. Therefore, it could give important insights into the effects of future predicted Arctic warming on the cryosphere at high northern latitudes. Few studies have looked at the impact of vegetation growth on the LIG climate and the impacts this could have on GrIS evolution.

From this study a summer Arctic warming in the early part of the LIG resulted in  $\sim 3^{\circ}\text{C}$  increase in temperature over Greenland compared with preindustrial with and without vegetation feedbacks included, consistent with previous AOGCM studies (Montoya *et al.*, 2000; Kaspar *et al.*, 2005; Otto-Bliesner *et al.*, 2006a). However, comparison with proxy data showed an underestimation of summer LIG temperature anomalies suggesting that the GrIS very likely retreated to a smaller and lower ice-sheet and therefore contributed to the LIG sea-level highstand of 4 to 8 m currently estimated. Simulations without the GrIS present at all (with and without vegetation feedbacks included), however, show an overestimation of central Greenland temperatures compared with proxy estimates from the NGRIP core. This suggests that it was very unlikely the GrIS completely disappeared during the LIG. Annual precipitation anomalies are insignificant throughout the LIG consistent with Otto-Bliesner *et al.* (2006a). However, removal of the ice-sheet and rebounding of the bedrock increases the intensity and distribution of precipitation due to orographic lifting of moisture into the atmosphere on the east coast and for the case where vegetation feedbacks were included, an increase in moisture flux from the growth of shrubs and grasses over the majority of Greenland in response to the orbitally induced warming and a reduction in orographic height. Similar to Otto-Bliesner *et al.* (2006a), there was a reduction in sea-ice concentration by up to 40 % in the summer months from 130ka to 125ka with a subsequent increase due to the marked reduction in orbitally induced summer warming by 120ka. Vegetation changes outside of Greenland showed a transition in the high northern latitudes from C3 tundra type grasses to shrubs at the peak of LIG warmth consistent with palaeo vegetation

proxy data in Siberia. However, there are no obvious shifts in the boreal treeline as observed by a previous climate modelling study of the early LIG (Schurgers *et al.*, 2007).

Offline forcing of Glimmer, in order to replicate as closely as possible the Otto-Bliesner *et al.* (2006a) study, was initiated from a spun-up modern day GrIS and forced with a fixed vegetation 130ka climatology for 10,000 years. The six Glimmer model parameter sets produced a more conservative range of estimated LIG sea-level rise relative to present between 1.1 m and 2.0 m (compared with 3.4 m from Otto-Bliesner *et al.* (2006a)) by 127ka. Furthermore, unlike the Otto-Bliesner *et al.* (2006a) study the Dye-3 ice core location did not become ice-free at this time and neither was there any significant lowering of the ice-sheet at the Summit ice core locations. The EISMINT-3 setup resulted in Dye-3 only becoming ice-free around 124ka to 125ka while this location remained ice-covered, without compromising data from the other ice core locations, for the tuned Glimmer parameter sets for the duration of the simulation. This suite of experiments neither included vegetation feedbacks nor predicted the ice-sheet evolution with a transient LIG climate.

Since a fully coupled HadCM3 Glimmer simulation for the timescales involved in this study is computationally time intensive and expensive, a new climate ice-sheet modelling methodology has been developed based on Pollard and DeConto (2009) which allows the ice-sheet to evolve and respond to the changing climate through the LIG by weighting the GrIS volume each year towards one of two climatologies: with and without a GrIS present. All simulations with and without vegetation feedbacks showed a decrease in ice-sheet volume from 130ka reaching a minimum around 125ka followed by slow increase thereafter, broadly consistent with palaeo sea-level curves for this time period (see Figure 1.8 a and b). This ice-sheet evolution is associated with an increase in total ablation area followed by a decline in response to the orbitally induced positive summer temperature perturbations of the LIG.

In terms of initial ice-sheet condition only two scenarios resulted in realistic ice-sheet volume trajectories for the EISMINT-3 setup: initiation from a spun-up modern day and a spun-up 136ka GrIS, with the 136ka climate interpolated to a GrIS present climatology at 130ka. The ice-sheet behaviour, however, was insensitive between these two initial conditions producing very similar trajectories for the different Glimmer parameter sets and boundary conditions.

Without vegetation feedbacks, the GrIS<sup>EIS</sup> setup results in a maximum LIG sea-level rise of 1.7 m and a minimum extent of the ice-sheet where Dye-3 remained ice-covered along with the other ice core locations, which appears to corroborate the presence of early LIG ice suggested by some (e.g. Dansgaard *et al.*, 1985; Andersen *et al.*, 2004; Willerslev *et al.*, 2007a). In the Summit region surface drawdown is only about 80 m, far short of the 500 m lowering estimated from Summit (GRIP) by Raynaud *et al.* (1997). However, when vegetation feedbacks are included in the climate model the amplification of the orbitally induced summer warming from vegetation growth in the noGrIS runs results in a LIG sea-level rise of 3.0 m similar to the 3.4 m sea-level contribution predicted by Otto-Bliesner *et al.* (2006a). In addition, the Dye-3 core location becomes ice-free and the surface drawdown at Summit is significantly larger (250 m) although still an underestimation compared with the proxy data. Only for the EISMINT-3 ice-sheet model setup, did HadCM3 MOSES 2 simulations of the LIG where interactive vegetation is included result in a maximum sea-level rise that falls within the range of 1.9 to 5.5 m compiled from previous recent modelling studies outlined in Table 1.1 (Cuffey and Marshall, 2000; Tarasov and Peltier, 2003; Lhomme *et al.*, 2005; Otto-Bliesner *et al.*, 2006a). It also agrees reasonably with the minimum 2.5 m sea-level rise attributed to Northern Hemisphere icefields from the probabilistic assessment of sea-level by Kopp *et al.* (2009).

In contrast, the tuned Glimmer parameter sets in conjunction with the more recent boundary conditions and reference climate datasets, produced a rise in sea-level between 6.8 and 7.6 m when vegetation was fixed and between 7.0 and 7.8 m when vegetation feedbacks were included. Both these ranges fall with the recent estimated likely LIG sea-level highstand range of 6.6 and 8.0 m (Kopp *et al.*, 2009). However, none of these simulations' minimum GrIS configuration agree with the observation of early LIG ice at Camp Century, Renland, NGRIP and Summit with the central and northern regions of Greenland becoming entirely ice-free. Although an attempt has been made here to assess the impact of parametric uncertainty in the ice-sheet model on the importance of vegetation feedbacks on the minimum extent of the GrIS, results have shown that the model setup is overly sensitive to a transient warmer than present climate. The lack of agreement with palaeoevidence reiterates the need to tune the ice-sheet model with more than just a present day

equilibrium climate. In the future, the LHS methodology described in Section 2.5 should be applied to the transient LIG climate in conjunction with the coupling method developed here. This would determine a new set of parameters for the LIG time period that result in ice surface extent and volume that agrees more closely with the ice core palaeodata and estimates of sea-level rise.

Since the tuning of Glimmer was performed using an entirely offline approach (it did not include the weighting function used in this Chapter) perhaps it is more appropriate to focus on results where this weighting methodology is not implemented. Forcing Glimmer with a transient climate where the GrIS is present throughout the LIG in HadCM3 produced interesting results. For the case of the EISMINT-3 setup the weighting function makes little difference to the size of the minimum GrIS when vegetation was fixed. However, four of the five new tuned parameter sets do not result in collapse of the ice-sheet during the LIG when vegetation was fixed. Three of these simulations produced minimum GrIS's that are acceptable in terms of the palaeodata criteria. When vegetation feedbacks are included the EISMINT-3 setup results in a reduced GrIS by  $\sim 1$  m of sea-level compared with fixed vegetation but there is little difference in the geometry of the GrIS with the Dye-3 ice core remaining ice free. Likewise, the tuned parameter sets produced similar results to when vegetation is fixed in this suite of experiments. In fact, the simulated minimum GrIS is slightly larger as a result of the marginally cooler interactive vegetation climate. Four out of the five simulations were satisfactory according to the ice core data. Hence, without the weighting function included the accepted simulations produce a range in sea-level contribution from 1.7 to 3.7 m for fixed vegetation and 1.9 to 3.1 m for interactive vegetation. Both ranges fall within that deduced from previous modelling studies.

Although it is feasible that much of the estimated LIG sea-level highstand (4 to 8 m) could come from extensive melting of the GrIS, the results, which included the weighting function, are not acceptable in terms of palaeoevidence of ice-cover from ice cores. Furthermore, estimation of surface temperature using HadCM3 (with and without vegetation feedbacks) over central regions of an ice-free Greenland do not agree with proxy data. Only the GrIS<sup>EIS</sup> produced results that were in agreement with most of the palaeodata. This simulation showed that ice in southern Greenland persisted throughout the LIG (in contrast to the result of Lhomme *et al.*

(2005)) but isolation of this ice from the main central ice dome was dependent on whether vegetation feedbacks were included or not. However, the weighting function acted only to reduce the volume of the GrIS further when vegetation feedbacks were included. It did not alter the fact that Dye-3 become ice-free with and without its inclusion.

Without the weighting function the tuned parameter sets produced results which were in agreement with palaeodata. However, the inclusion of interactive vegetation did not make any significant difference to the overall result. Ice persisted in central and southern Greenland with only substantial ice loss in the north. In all cases Dye-3 remained ice-covered in contrast to recent modelling studies where Dye-3 was ice-free (Cuffey and Marshall, 2000; Tarasov and Peltier, 2003; Lhomme *et al.*, 2005; Otto-Bliesner *et al.*, 2006a).

If the Dye-3 core was indeed ice-free as indicated by Koerner and Fischer (2002) then vegetation feedbacks, at least for the EISMINT-3 setup, are required in order for this condition to be satisfied implying that this additional feedback on the climate system is more important than Otto-Bliesner *et al.* (2006a) originally thought for estimating the minimum extent of the GrIS during the LIG. However, the tuned parameter sets without the weighting function resulted in persistent ice cover throughout the LIG over Dye-3 consistent with the evidence provided by Dansgaard *et al.* (1985), Andersen *et al.* (2004) and Willerslev *et al.* (2007a). The interpretation of pre-LIG ice at Dye-3 can be examined in several ways and is not conclusive. However, the evidence provided by Dansgaard *et al.* (1985) does not necessarily indicate ice in the south survived the peak interglacial warmth in the period 130 to 125ka; no ice was present from the previous glaciation. It is possible that this ice at the base of Dye-3 merely represents late growth of ice during the LIG when the GrIS reestablished itself fully in the south of the island in response to the cooling climate at the end of the LIG. The EISMINT-3 simulations with vegetation feedbacks indicated ice was once again present by 123ka making this explanation plausible. Equally, ice could have persisted throughout the LIG consistent with the results for the tuned parameter sets without the weighting function. Until an ice core that penetrates the entire LIG on Greenland is realised it is difficult to fully determine the ‘correct’ behaviour of the GrIS during the LIG and the results presented here are unable to confirm the presence/absence of LIG ice at Dye-3.

Based on current estimates of the LIG sea-level highstand from a various range of sources (Siddall *et al.*, 2007; Kopp *et al.*, 2009), the GrIS<sup>EIS</sup> setup with the weighting function contributes a maximum of 75 % to this range in sea-level increase relative to present, and therefore indicates other water sources on land are required to account for this high sea-level. Examples of such sources could come from the West Antarctic ice-sheet (e.g. Scherer *et al.*, 1998; Oppenheimer and Alley, 2005) and the Canadian icefields (Otto-Bliesner *et al.*, 2006a) which were not modelled here. Although the mechanisms for the high latitude summer warmth in the LIG are very different to those which are associated with predictions of future global warming (namely significant increases in CO<sub>2</sub> above preindustrial values of 280 ppmv), this work highlights the impact of such increases in high latitude Arctic summer temperatures on the extent of the GrIS and associated global sea-level change. Furthermore, this study emphasises the importance of including vegetation feedbacks in climate simulations and parametric uncertainty in the ice-sheet models for modelling the future climate of the Arctic. It also demonstrates that caution should be taken with conclusions that are drawn from those experiments which are not robust.

# Conclusions

The aim of this thesis was to better understand and quantify the impact of vegetation feedbacks on perturbed climates over Greenland and the interactions these feedbacks have with the climate and cryosphere of the Arctic. A review of current literature on the state of the GrIS under future melting as a response to anthropogenic forcing and subsequent potential regrowth is given in Chapter 1. This review highlighted the methodologies used, results obtained and where improvements could be made. The literature, with regard to the LIG, was also discussed. This period of time in the past provided a good test of the climate, vegetation and ice-sheet models. It is of interest because it represented a time when sea-level was significantly higher (4 to 8 m) and the GrIS likely smaller than today.

This chapter summarises the achievements and principal findings of the thesis with respect to the aims and objectives outlined in Section 1.6. It also identifies where further development and improvements can be made to this research, how this might be achieved and the future direction this work should take.

## 7.1 Summary of results and principal findings

This section considers the objectives in Section 1.6 and how these were achieved in the thesis. Since each Chapter contains a discussion and conclusions section only the main results will be summarised here.

### 7.1.1 Evaluation of the Glimmer ice-sheet model

The vast majority of climate ice-sheet modelling studies have used boundary condition and forcings that are nearly two decades old. The advent of new bedrock and ice thickness datasets with new temperature and precipitation forcing data provided a new up-to-date baseline reference climate for GrIS modelling studies. Comparisons between the older and newer datasets showed that for a standard set of model parameters, the recent datasets gave a poor representation of the modern ice-sheet, with an ice-sheet volume 25 % larger than observation. In order to improve on

this, a new approach to ice-sheet model tuning was attempted. Latin-Hypercube Sampling was performed to efficiently tune the model for present day conditions by simultaneously varying five poorly constrained model parameters: PDD factors for ice and snow, flow enhancement factor, geothermal heat flux and the near-surface lapse rate. Two hundred and fifty simulations were sufficient to cover parameter space. The maximum ice thickness and ice volume were shown to depend on the factors affecting ice flow while the surface extent was predominantly dependent on the PDD factors and the atmospheric lapse rate. Although geothermal flux can affect ice flow since it acts to melt the ice, which is a prerequisite for basal sliding, this had a minimal effect on the simulations presented here because basal sliding was switched off. This resulted in five optimal parameter sets which were used to give a representation of parametric uncertainty in ice-sheet model simulations for future and past Greenland climates. In all cases high PDD factors were required to simulate a more realistic modern GrIS. It is important to note that inclusion of basal sliding parameterisation and basal hydrology could compensate for these high PDD factors. Furthermore, caution should be taken when tuning the ice-sheet model to only one climate/set of boundary conditions since different sensitivities to different climate scenarios are possible.

### **7.1.2 Climatic sensitivity to surface type and altitude change over a melted GrIS**

Evaluation of the climate model, HadCM3 MOSES 2, over the Greenland region for the preindustrial showed reasonable agreement with observational temperature and precipitation data and errors not dissimilar from other AOGCMs at high latitudes. In order to understand changes in local climate over a melted GrIS, sensitivity experiments were performed with respect to land surface type and altitude change. When only surface type was changed, the response in near-surface temperature during the summer months was predominantly a result of the snow-vegetation-climate feedback where the lower albedo of vegetated surfaces resulted in an increase in absorption of shortwave heat flux and thus an increase in local temperature. The largest difference occurred for broadleaf and needleleaf trees (12.2°C and 11.1°C respectively) and the smallest for bare soil coverage (1°C). During the winter months temperature anomalies were close to zero for all surface types due to the low insolation at



this time of the year at high northern latitudes. Although surface roughness change resulted in changes in the way the surface energy budget is partitioned, it did not have a significant effect on the precipitation and temperature changes during the winter and summer months. Surface temperature change as a result of lowering the GrIS during the winter was not only due to the decrease in altitude but also the result of altered low-level atmospheric circulation due to the reduced blocking of cold air masses to the west of Greenland, over the Baffin Bay region, as a result of the lower and less steep orography. The increased precipitation in the east during winter and summer was attributed to this lowered orography.

Changing the surface type and lowering the orography together resulted in enhanced precipitation during the summer months as a result of orographic lifting of moisture and the increase in moisture availability at the surface for the vegetated surface types. Contrary to previous work (Lunt *et al.*, 2004), winter temperature changes were dominated by a decrease in altitude and also changes in atmospheric circulation, while summer temperature changes were dominated by the increase in thermal forcing at the surface as a result of the lower surface albedo of the PFTs. These results also highlighted the synergy that exists between changing altitude and surface type together shown by the non-linearity in the temperature response.

The impact of a melted GrIS was largely a localised effect on the climate. However, outside of Greenland winter temperature decreases observed over the Barents Sea were due to interactions with the sea-ice cover likely attributed to a decrease in northward ocean heat transport by the subpolar gyres as a result of changes in atmospheric circulation and a shift in the stormtracks. This resulted because of the change in orography and surface energy balance over Greenland due to surface type change. The greatest increase in sea-ice cover occurred for a rebounded Greenland covered with needleleaf trees.

### 7.1.3 Response of an ice-free Greenland climate to interactive vegetation

Chapter 4 examined the growth of vegetation on a rebounded bedrock and melted GrIS. Two simulations were performed with initial contrasting surface conditions: bare soil and needleleaf tree. However, the absence of any significant hysteresis indicated only one stable vegetated state on a deglaciated, fully rebounded Greenland

with preindustrial CO<sub>2</sub> concentrations. The vegetation distribution consisted of a mixture of shrubs, grasses and bare soil but no needleleaf tree growth in contrast to the offline vegetation simulation by Lunt *et al.* (2004). Outside of Greenland, there were no changes in dominant vegetation types caused by this growth over Greenland. The type of dominant vegetation on Greenland was controlled most closely by the temperature of the coldest month and the amount of carbon available to maintain and sustain growth. The distribution of vegetation had a significant impact on snow cover and amount. Where there were shrubs and grasses, snow cover was very small or even snow-free in central Greenland during the summer. However, regions dominated by bare soil were favourable for snow accumulation with insufficient melting during the spring and early summer months and therefore snow cover was able to survive throughout the year due to the persistent high albedo of the surface.

Temperature anomalies during winter and summer relative to the preindustrial were 2.8°C and 12.2°C respectively and were close to or above the annual  $\sim 3^\circ\text{C}$  warming threshold required for irreversible melting of the GrIS (Huybrechts *et al.*, 1991; Gregory *et al.*, 2004). Precipitation anomalies during the winter were similar to the simulation where the GrIS was lowered in the sensitivity experiments in Chapter 3. During summer there was an increase in precipitation over much of Greenland with a decrease along the southern tip associated with a decrease in cyclonic activity due to changes in the atmospheric circulation induced by the change in Greenland orography.

Based on climate diagnostics alone it is not possible to conclude whether an ice-sheet could regrow on Greenland, since it is possible that the high altitude regions dominated by bare soil could provide suitable conditions for ‘seeding’ of an ice-sheet if the altitude is adequately resolved in an ice-sheet model.

#### 7.1.4 Potential regrowth of the GrIS forcing Glimmer offline

Chapter 5 highlighted that the snow cover diagnostic from the GCM was a poor indicator of ice-sheet growth, similar to the conclusion by Lunt *et al.* (2004). Although there was sufficient snow build up in the east for a bare soil surface, there was no indication of buildup anywhere else on Greenland. However, when Glimmer was forced offline for the different parameter sets deduced in Chapter 2, there was almost complete regrowth for the EISMINT-3 standard and partial regrowth for

the other recent tuned parameter set combinations and boundary conditions. The mechanism for this ice growth was a result of ‘seeding’ of ice in high altitudes in eastern Greenland, which subsequently dynamically flowed into the lower altitude regions of central Greenland. Slow growth and expansion occurred as a result of a positive ice-elevation feedback and survival of ice during the summer months. The PFT surface coverages in the climate model, however, resulted only in inception of ice in the east with no expansion into the interior of the island for all selected Glimmer model parameter sets and boundary conditions.

When Glimmer was forced with the GCM output from the interactive vegetation simulations, ice-inception was more sensitive to the initial surface condition in the climate model rather than if TRIFFID coupling was in dynamic (seasonal variation) or equilibrium mode. The overall geometry of ice inception, however, was similar with isolated ice caps in the east and south but no significant regrowth over the whole island. This result agreed with the conclusion from Vizcaíno *et al.* (2008) of no significant build up of ice. Although the high altitude regions provided favourable conditions for ice inception due to the high albedo of the bare soil surface and the high altitude, the summer temperature response to the grass and shrub covered surface in the interior of Greenland prevented the establishment of any substantial ice-sheet.

In conclusion, with vegetation feedbacks included in HadCM3, the GrIS under preindustrial conditions exhibits some bistable behaviour with a maximum regrowth equivalent to only 16 % of the present day ice volume and no complete deglaciation. It has been shown, however, that future predictions of the GrIS are highly sensitive to a number of factors relating to the physical basis of the ice-sheet model. Current ice-sheet models, like Glimmer, do not have a firm representation of the fast flowing processes, neither are the parameters, which influence the ice physics, tightly constrained. As a result, future development of the ice-sheet model to improve the representation of these fast flowing processes and inclusion of basal sliding may lead to different behaviour of ice-sheet regrowth. Future regrowth predictions of the GrIS should be aired with some caution in the context of these sensitivities and deficiencies of the ice-sheet model.

### 7.1.5 The response of the GrIS to climate - vegetation - ice-sheet interactions during the LIG

The LIG, thought to be the last time the Arctic experienced warmer conditions than present and sea-level 4 to 8 m higher, provided a good test of the modelled interactions between land-surface, atmosphere, ocean and the cryosphere. The study presented in this thesis, is the first full GCM simulation where an ice-sheet was forced offline with a transient climate for the period 136ka to 120ka. At 130ka the average summer Greenland temperature anomaly relative to preindustrial was  $\sim 3^{\circ}\text{C}$  with and without vegetation feedbacks included. This was an underestimate compared with palaeodata which indicated a summer  $5^{\circ}\text{C}$  anomaly (Anderson *et al.*, 2006). This warming was fundamentally caused by the large insolation anomalies relative to present in the early to mid-LIG. The growth of ‘warmer’ vegetation types at high northern latitudes acted to amplify this warming. Indeed, the interactive vegetation simulations showed expansion of shrubs in northeast Siberia at the expense of grasses at the timing of peak interglacial warmth consistent with palaeo proxy vegetation data.

Transient experiments were performed with HadCM3 and Glimmer through the LIG. This used a methodology where Glimmer simulated (both with and without vegetation feedbacks included) the extent of the ice-sheet from 130ka to 120ka using linearly interpolated and weighted (no ice versus full ice) climate output between three snap-shot climate simulations (130, 125 and 120ka). This coupling methodology was based on the method of Pollard and DeConto (2009). Only the EISMINT-3 standard Glimmer model setup resulted in an acceptable minimum GrIS when compared with palaeodata from several Greenland ice cores. Evolution of the GrIS during the LIG for the tuned model parameter sets, however, was overly sensitive to this methodology resulting in almost complete collapse of the ice-sheet with and without vegetation feedbacks included. Only with vegetation feedbacks did the equivocal Dye-3 ice core become ice-free using the EISMINT-3 setup with a contribution to the sea-level highstand of 3 m.

Since the tuning was performed without this coupling methodology, simulations were also performed where the weighting function was excluded and Glimmer was forced with a transient climate with only the GrIS present climatologies. For all

Glimmer model parameter sets, this produced acceptable GrIS geometries with a range from 1.7 to 3.7 m with fixed vegetation and 1.9 to 3.0 m with dynamic vegetation, similar to the range of 1.5 to 5.5 m predicted by previous modelling studies. Dye-3 only became ice-free for the EISMINT-3 setup with interactive vegetation included. The ice coverage at Dye-3 in this case is clearly dependent on the Glimmer model parameter setup and boundary conditions rather than whether the coupling methodology developed here is implemented. Furthermore, vegetation feedbacks in the GCM appear to make a significant difference for EISMINT-3 whether the coupling is included or not.

Although no firm conclusion can be drawn from these results as to whether Dye-3 was indeed ice-free during the LIG and if vegetation feedbacks are necessary to predict the minimum GrIS, it is very likely the GrIS was smaller than present and therefore contributed to the sea-level highstand of this time period. In addition, the results confirm that there was most likely additional sources to explain this increase in sea-level from other Arctic icefields and perhaps also Antarctica. This could be a topic for future work.

## 7.2 Future work

There are several areas for improvement and development that have been discussed in previous sections of this thesis. However, this section describes in more detail how future experiments could be performed, and existing methods developed and improved both in terms of future and past GrIS modelling.

### 7.2.1 Extending the future GrIS regrowth modelling

All climate simulations have been performed under a preindustrial equilibrium climate assuming sufficient rebound of the Greenland bedrock from isostatic readjustment. Although Toniazzo *et al.* (2004) performed a simulation where the bedrock represented the present topography under the GrIS and found no major differences in climate response between this and a rebounded orography, they replaced the entire surface with fixed bare soil. Firstly, it would be interesting to run HadCM3 with interactive vegetation with the unrebounded present day bedrock to ascertain whether this would make a notable difference to vegetation dominance and distribu-

tion and hence the temperature and precipitation over Greenland. Secondly, since much of this bedrock lies below sea-level in the interior of the island, this region could also be replaced with a lake mask. This would certainly have an effect on the surface energy balance due to the low albedo of water (snow-free albedo of 0.06 in HadCM3 MOSES 2). Further, intermediary stages between unrebounded and fully rebounded could be simulated to determine a range in climate response and whether this had an effect on the offline Glimmer forcing results and the behaviour of GrIS regrowth.

Thirdly, although this thesis has examined in close detail the changes in climate due to altitude change and surface type change and in addition looked at the effect of surface roughness length, it would also be informative to isolate other feedback loops in the Earth system. For instance, equilibrium simulations with fixed SSTs and sea-ice could be performed with HadAM3 (Atmosphere only version of the Hadley Centre Model) to assess their importance on the climate over a melted Greenland.

Fourthly, sensitivity studies where the CO<sub>2</sub> concentration is varied in the atmosphere, similar to the work of Charbit *et al.* (2008), could be implemented to determine under what CO<sub>2</sub> regime the GrIS would remain completely ice-free or recover with significant regrowth. These simulations could be performed with and without vegetation feedbacks included. In addition, the feedback of vegetation on CO<sub>2</sub> concentration in the atmosphere could be assessed (see Figure 4.2). This was not included in any of the simulations in this thesis.

Fifthly, all GCM simulations assumed no changes in freshwater flux forcing as a result of either a ‘slow’ melt of the GrIS under an elevated CO<sub>2</sub> climate or a ‘fast’ melt where the THC collapsed but subsequently recovered to its initial state as modelled by Ridley *et al.* (2005). It is particularly computationally expensive to run a full GCM like HadCM3 for several thousand model years and coupled to an ice-sheet model. Therefore, simulations that model GrIS melt in response to a warmer than present climate and the resultant impact of increased freshwater flux on ocean circulation cannot be easily examined. However, one way to assess how a shutdown of the THC could affect the climate of a melted GrIS, is to impose cool SSTs in the North Atlantic to simulate this effect. It is also possible to run a coupled melting GrIS simulation with an EMIC such as CLIMBER (Ganopolski *et al.*, 1998b) for several thousand years to assess the impact of increased freshwater

fluxes on the MOC and the climate system as a whole.

Finally, future work should involve using a lower resolution AOGCM such as FAMOUS (Jones *et al.*, 2005), so several thousand years of transient climate can be asynchronously or fully coupled to the cryosphere component, with an ice-free Greenland imposed as an initial condition. This would include the missing ice-albedo temperature feedback process in this thesis. The inclusion of this feedback could significantly alter the results obtained here. For example, the presence of shrubs and grasses in southern Greenland from the interactive vegetation climate simulations would decrease the surface albedo resulting in a warmer Greenland and via the ice-albedo feedback, perhaps inhibit ice-sheet growth in Glimmer.

In terms of ice-sheet modelling, it would be interesting to perform simulations where basal sliding is included along with representation of basal sediment deformation and basal hydrology to assess the impact this might have on future regrowth. It could also be included in the LHS methodology and therefore might compensate for the higher PDD factors used in simulations presented here. A longer term goal would be to perform simulations with the higher order physics models currently being developed, which fully resolve the ablation zones and include the normal stress components neglected in the Shallow Ice Approximation.

### 7.2.2 Extending the LIG modelling

As previously noted in Chapter 6, the LHS methodology described in Section 2.5 should be applied to the transient LIG climate in conjunction with the coupling method that was developed. This would then determine a new set of parameters for the LIG time period that result in ice surface extent and volume which agrees with the ice core palaeodata and estimates of sea-level rise. In addition CO<sub>2</sub> and other greenhouse gases were constant in the suite of simulations performed in this thesis. It would be interesting to analyse the sensitivity of GrIS volume to this forcing as well as the large changes in insolation caused by changes in the Earth's orbital parameters.

A longer term goal would be to run transient coupled simulations of the LIG period with and without vegetation feedbacks included. This would be possible by running a full GCM, such as HadCM3, asynchronously coupled to Glimmer with accelerated forcing. The study of Calov *et al.* (2009) showed using an EMIC that

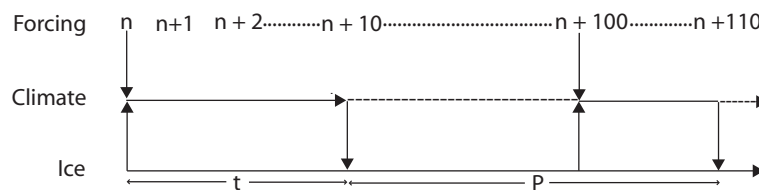


Figure 7.1: Diagram showing the asynchronous coupling between climate model and ice-sheet model where forcing corresponds to orbits and  $\text{CO}_2$  concentration. The horizontal axis shows the model years beginning at year  $n$  in the simulation. The vertical arrows show the direction of data flow.  $t_c$  and  $P$  denote the climate-module-computation time and the time interval of exchange respectively where  $t_c=10$  years and  $P=100$  years. The dashed lines indicate interruption in calling the climate module. This results in an acceleration  $A=P/t_c=10$  which implies that computation costs of the climate component is reduced by a factor of 10 compared with a synchronously coupled run (*modified from Calov et al. (2009)*).

simulations with time intervals of information exchange between 1 and 100 years and accelerations inside the interval 1 to 10 would result in a ratio of ice volume to reference ice volume (1:1 coupling) of 85 to 100 % and considered this satisfactory. Therefore, it would be potentially achievable to asynchronously couple HadCM3 to Glimmer with a climate-module computation time of 10 years and a time interval of information exchange of 100 years with an acceleration of a factor of 10 (see Figure 7.1 for more detail). The experiments which include vegetation feedbacks can use TRIFFID in equilibrium mode where the acceleration is also a factor of 10 (e.g. running HadCM3 with TRIFFID in equilibrium mode for 10 years corresponds to 100 years of vegetation time). It would, therefore, be computationally possible to simulate 10,000 years of LIG climate using this methodology. This methodology could also be applied to the GrIS regrowth experiments since equilibrium was reached within about 10,000 years for most surface types.

This LIG study also highlights the need for a complete, detailed and reliable ice core record spanning the entire LIG in order for a more robust comparison between model results and data. This is currently, being addressed by the NEEM project.

### 7.2.3 Other modelling studies

The methodology developed in this thesis could also be applied to other past changes in Earth's climate further back in time than the LIG. For example, simulations could be conducted under Pliocene conditions (e.g. Haywood and Valdes, 2004) to investigate the impact of vegetation and ice-sheet model parametric uncertainty on the



inception of the GrIS approximately 3Ma. This would complement the work by Lunt *et al.* (2008, 2009). It would provide a further opportunity to compare model output with geological and fossil evidence of past ice-sheet vegetation evolution at high latitudes.

This thesis has shown not only the importance of exploring vegetation feedbacks on the behaviour of GrIS evolution but also the complexity that exists between vegetation, atmosphere, ocean and cryosphere. The opportunity to develop more complex climate - ice-sheet - simulations which include model parametric uncertainty and interactions between all components of the Earth system over long and short timescales should be an essential part of future research of high latitude climates. In particular, the advent of new higher order physics in ice-sheet models should resolve many of the missing ice-sheet processes that occur at least on shorter timescales.



# Synergy between altitude and surface type change in terms of precipitation

| Experiment                        | Winter | Summer |
|-----------------------------------|--------|--------|
| lowGrIS                           | 0.33   | 0.26   |
| <hr/>                             |        |        |
| noGrIS <sub>mod</sub>             |        |        |
| Bare soil                         | 0.10   | 0.02   |
| C3 grass                          | 0.02   | 0.46   |
| C4 grass                          | 0.03   | 0.2    |
| Shrub                             | 0.04   | 0.49   |
| Broadleaf tree                    | 0.05   | 0.59   |
| Needleleaf tree                   | 0.04   | 0.54   |
| <hr/>                             |        |        |
| noGrIS <sub>reb</sub> (X)         |        |        |
| Bare soil                         | 0.27   | 0.28   |
| C3 grass                          | 0.26   | 0.62   |
| C4 grass                          | 0.29   | 0.58   |
| Shrub                             | 0.22   | 0.74   |
| Broadleaf tree                    | 0.27   | 1.05   |
| Needleleaf tree                   | 0.27   | 0.94   |
| <hr/>                             |        |        |
| lowGrIS+noGrIS <sub>mod</sub> (Y) |        |        |
| Bare soil                         | 0.42   | 0.28   |
| C3 grass                          | 0.31   | 0.72   |
| C4 grass                          | 0.30   | 0.46   |
| Shrub                             | 0.29   | 0.76   |
| Broadleaf tree                    | 0.28   | 0.85   |
| Needleleaf tree                   | 0.29   | 0.81   |
| <hr/>                             |        |        |
| X - Y                             |        |        |
| Bare soil                         | -0.15  | -0.01  |
| C3 grass                          | -0.05  | -0.10  |
| C4 grass                          | -0.01  | 0.12   |
| Shrub                             | -0.07  | -0.02  |
| Broadleaf tree                    | 0.00   | 0.20   |
| Needleleaf tree                   | -0.02  | 0.14   |

Table A.1: Synergy between altitude and surface type change in terms of precipitation for the winter and summer months. Averages are over the Greenland land surface in  $\text{mm day}^{-1}$ .



# APPENDIX B

## Temperature and precipitation anomalies for needleleaf: $z_0^{nl}$ and needleleaf: $z_0^{ice}$

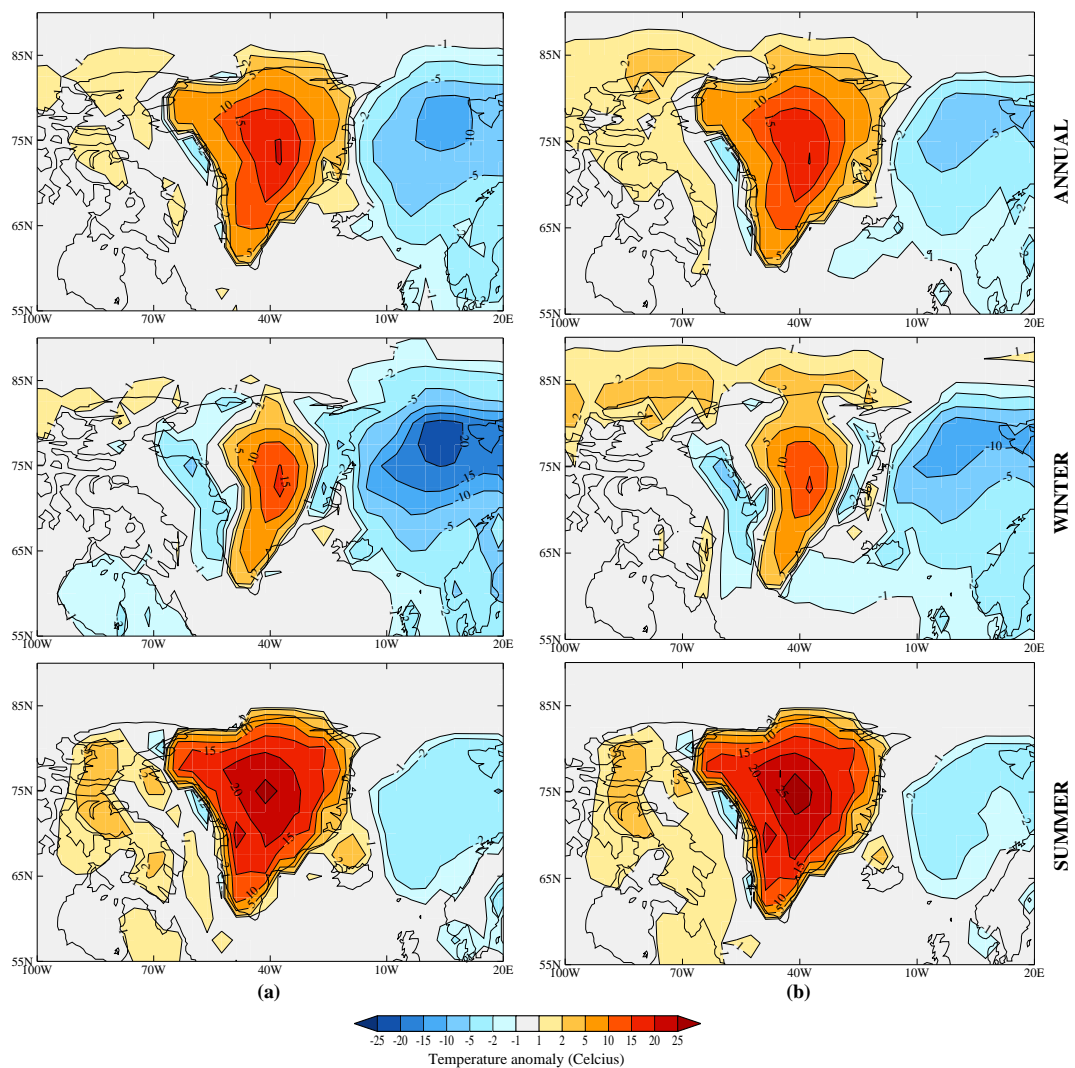


Figure B.1: Near-surface average annual, winter and summer temperature anomalies (in °C) for the noGrIS<sub>reb</sub> experiments (a) needleleaf: $z_0^{nl}$  minus control and (b) needleleaf: $z_0^{ice}$  minus control.

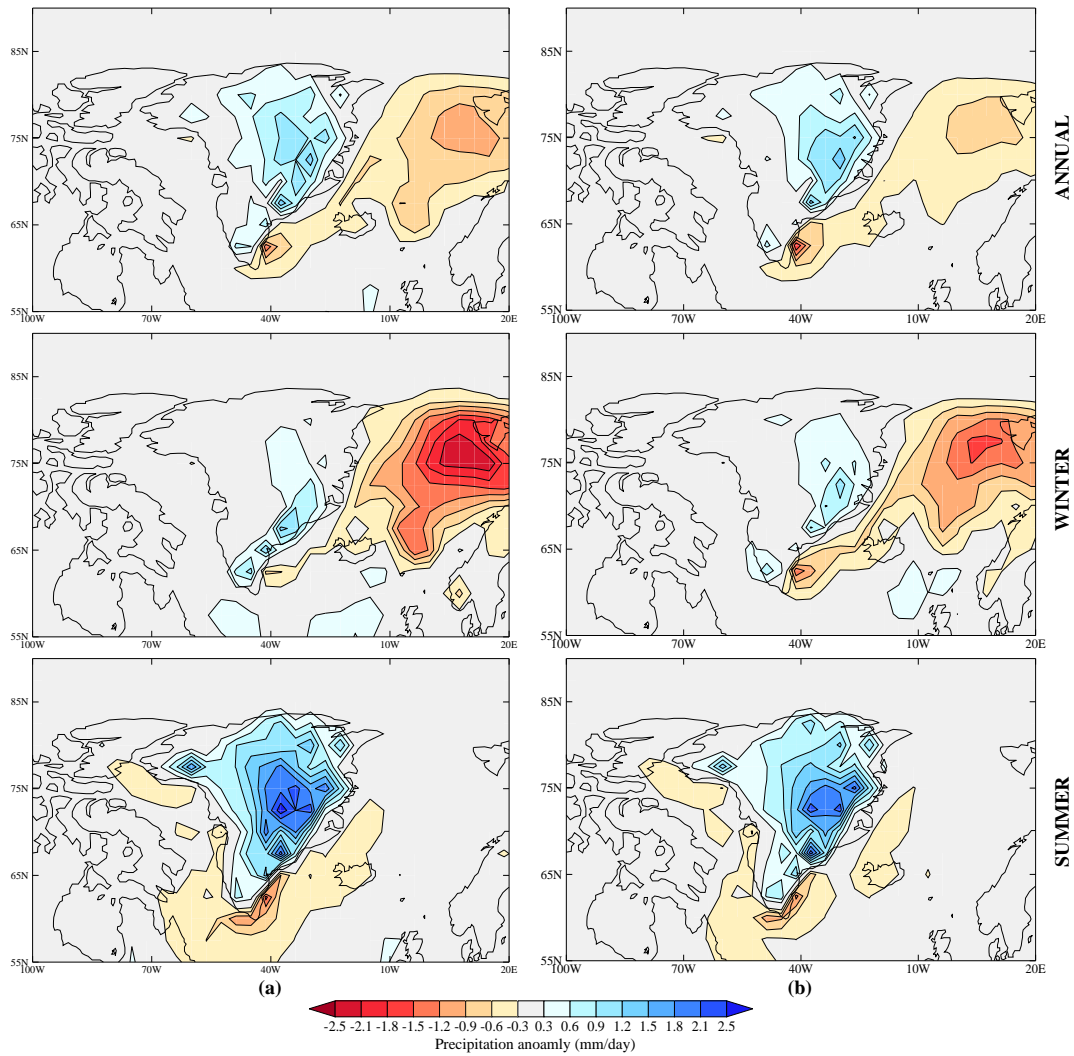


Figure B.2: Near-surface average annual, winter and summer precipitation anomalies (in  $\text{mm day}^{-1}$ ) for the noGrIS $_{reb}$  experiments (a) needleleaf: $nl_{z0}$  minus control and (b) needleleaf: $ice_{z0}$  minus control.

## Diagnostics for GrIS regrowth

| Glimmer setup   | EISMINT-3 | Recent tuning expts |      |      |      |      |
|---|-----------|---------------------|------|------|------|------|
|   |           | 63                  | 78   | 181  | 230  | 233  |
| <i>Volume (<math>\times 10^6 km^3</math>)</i>             |           |                     |      |      |      |      |
| Present day   | 3.30      | 3.06                | 3.25 | 3.37 | 3.44 | 3.03 |
| Bare soil   | 3.03      | 0.79                | 0.80 | 0.86 | 1.23 | 0.76 |
| C3 grass  | 0.26      | 0.23                | 0.24 | 0.25 | 0.30 | 0.22 |
| C4 grass  | 0.14      | 0.15                | 0.15 | 0.14 | 0.21 | 0.14 |
| Shrub   | 0.03      | 0.12                | 0.08 | 0.09 | 0.17 | 0.10 |
| Broadleaf trees   | 0.01      | 0.06                | 0.06 | 0.06 | 0.09 | 0.05 |
| Needleleaf trees  | 0.01      | 0.05                | 0.04 | 0.04 | 0.08 | 0.04 |
| <i>Sea-level equivalent height (m)</i>                    |           |                     |      |      |      |      |
| Present day   | 8.3       | 7.7                 | 8.2  | 8.5  | 8.7  | 7.6  |
| Bare soil   | 7.6       | 2.0                 | 2.0  | 2.2  | 3.1  | 1.9  |
| C3 grass  | 0.7       | 0.6                 | 0.6  | 0.6  | 0.8  | 0.6  |
| C4 grass  | 0.3       | 0.4                 | 0.4  | 0.3  | 0.5  | 0.4  |
| Shrub   | 0.1       | 0.3                 | 0.2  | 0.2  | 0.4  | 0.2  |
| Broadleaf tree  | 0.03      | 0.1                 | 0.1  | 0.2  | 0.2  | 0.1  |
| Needleleaf tree   | 0.03      | 0.1                 | 0.1  | 0.2  | 0.2  | 0.1  |
| <i>Ice surface extent (<math>\times 10^6 km^2</math>)</i> |           |                     |      |      |      |      |
| Present day   | 2.06      | 2.00                | 1.97 | 1.98 | 2.04 | 2.00 |
| Bare soil   | 1.90      | 0.89                | 0.87 | 0.87 | 1.07 | 0.89 |
| C3 grass  | 0.42      | 0.39                | 0.37 | 0.37 | 0.47 | 0.38 |
| C4 grass  | 0.30      | 0.31                | 0.30 | 0.28 | 0.38 | 0.30 |
| Shrub   | 0.12      | 0.28                | 0.21 | 0.22 | 0.34 | 0.24 |
| Broadleaf tree  | 0.06      | 0.17                | 0.15 | 0.15 | 0.25 | 0.15 |
| Needleleaf tree   | 0.06      | 0.15                | 0.13 | 0.14 | 0.23 | 0.14 |
| <i>Maximum ice thickness(km)</i>                          |           |                     |      |      |      |      |
| Present day   | 3.11      | 3.02                | 3.24 | 3.35 | 3.32 | 3.00 |
| Bare soil   | 3.27      | 2.18                | 2.28 | 2.36 | 2.75 | 2.14 |
| C3 grass  | 1.57      | 1.73                | 1.80 | 1.87 | 1.94 | 1.71 |
| C4 grass  | 1.41      | 1.52                | 1.58 | 1.61 | 1.92 | 1.49 |
| Shrub   | 0.91      | 1.44                | 1.34 | 1.38 | 1.90 | 1.31 |
| Broadleaf tree  | 0.88      | 1.26                | 1.32 | 1.37 | 1.40 | 1.22 |
| Needleleaf tree   | 0.87      | 1.25                | 1.23 | 1.29 | 1.39 | 1.14 |

Table C.1: GrIS diagnostics for the ice-sheet regrowth simulations where surface type is fixed as bare soil and each of the five PFTs in MOSES as discussed in Chapter 3. Each diagnostic represents the state of any ice sheet growth after 50,000 years, initialised from a rebounded bedrock with no ice. Present day modelled diagnostics are also shown for each of the Glimmer setups for comparison. Sea-level equivalent height corresponds to global sea-level and represents ice growth.

| Glimmer setup   | EISMINT-3 | Recent tuning expts |      |      |      |      |
|---|-----------|---------------------|------|------|------|------|
|   |           | 63                  | 78   | 181  | 230  | 233  |
| <i>Volume (<math>\times 10^6 km^3</math>)</i>             |           |                     |      |      |      |      |
| Present day   | 3.30      | 3.06                | 3.25 | 3.37 | 3.44 | 3.03 |
| Init. bare soil: equil. mode                              | 0.45      | 0.36                | 0.36 | 0.38 | 0.46 | 0.34 |
| Init. needleleaf tree: equil. mode                        | 0.39      | 0.27                | 0.26 | 0.28 | 0.35 | 0.25 |
| Init. bare soil: dynam. mode                              | 0.52      | 0.41                | 0.42 | 0.44 | 0.51 | 0.39 |
| Init. needleleaf tree: dynam. mode                        | 0.43      | 0.30                | 0.30 | 0.31 | 0.38 | 0.29 |
| <i>Sea-level equivalent height (m)</i>                    |           |                     |      |      |      |      |
| Present day   | 8.3       | 7.7                 | 8.2  | 8.5  | 8.7  | 7.6  |
| Init. bare soil: equil. mode                              | 1.1       | 0.9                 | 0.9  | 0.9  | 1.2  | 0.9  |
| Init. needleleaf tree: equil. mode                        | 1.0       | 0.7                 | 0.7  | 0.7  | 0.9  | 0.6  |
| Init. bare soil: dynam. mode                              | 1.3       | 1.0                 | 1.1  | 1.1  | 1.3  | 1.0  |
| Init. needleleaf tree: dynam. mode                        | 1.1       | 0.8                 | 0.8  | 0.8  | 1.0  | 0.7  |
| <i>Ice surface extent (<math>\times 10^6 km^2</math>)</i> |           |                     |      |      |      |      |
| Present day   | 2.06      | 2.00                | 1.97 | 1.98 | 2.04 | 2.00 |
| Init. bare soil: equil. mode                              | 0.64      | 0.56                | 0.53 | 0.53 | 0.61 | 0.54 |
| Init. needleleaf tree: equil. mode                        | 0.56      | 0.47                | 0.44 | 0.44 | 0.54 | 0.45 |
| Init. bare soil: dynam. mode                              | 0.69      | 0.60                | 0.57 | 0.57 | 0.65 | 0.58 |
| Init. needleleaf tree: dynam. mode                        | 0.61      | 0.49                | 0.47 | 0.47 | 0.56 | 0.48 |
| <i>Maximum ice thickness(km)</i>                          |           |                     |      |      |      |      |
| Present day   | 3.11      | 3.02                | 3.24 | 3.35 | 3.32 | 3.00 |
| Init. bare soil: equil. mode                              | 1.96      | 1.75                | 1.81 | 1.84 | 2.25 | 1.74 |
| Init. needleleaf tree: equil. mode                        | 1.96      | 1.73                | 1.77 | 1.81 | 2.08 | 1.69 |
| Init. bare soil: dynam. mode                              | 1.99      | 2.01                | 2.09 | 2.16 | 2.28 | 1.97 |
| Init. needleleaf tree: dynam. mode                        | 1.98      | 1.89                | 1.85 | 1.89 | 2.11 | 1.75 |

Table C.2: GrIS diagnostics for the ice-sheet regrowth simulations where surface type evolves initiated from bare soil and needleleaf tree when TRIFFID is equilibrium mode and dynamic mode as discussed in Chapter 4. Each diagnostic represents the state of any ice sheet growth after 50,000 years, initialised from a rebounded bedrock with no ice. Present day modelled diagnostics are also shown for each of the Glimmer setups for comparison. Sea-level equivalent height corresponds to global sea-level and represents ice growth.



# APPENDIX D

## The effect of the weighting function on LIG ice-sheet evolution

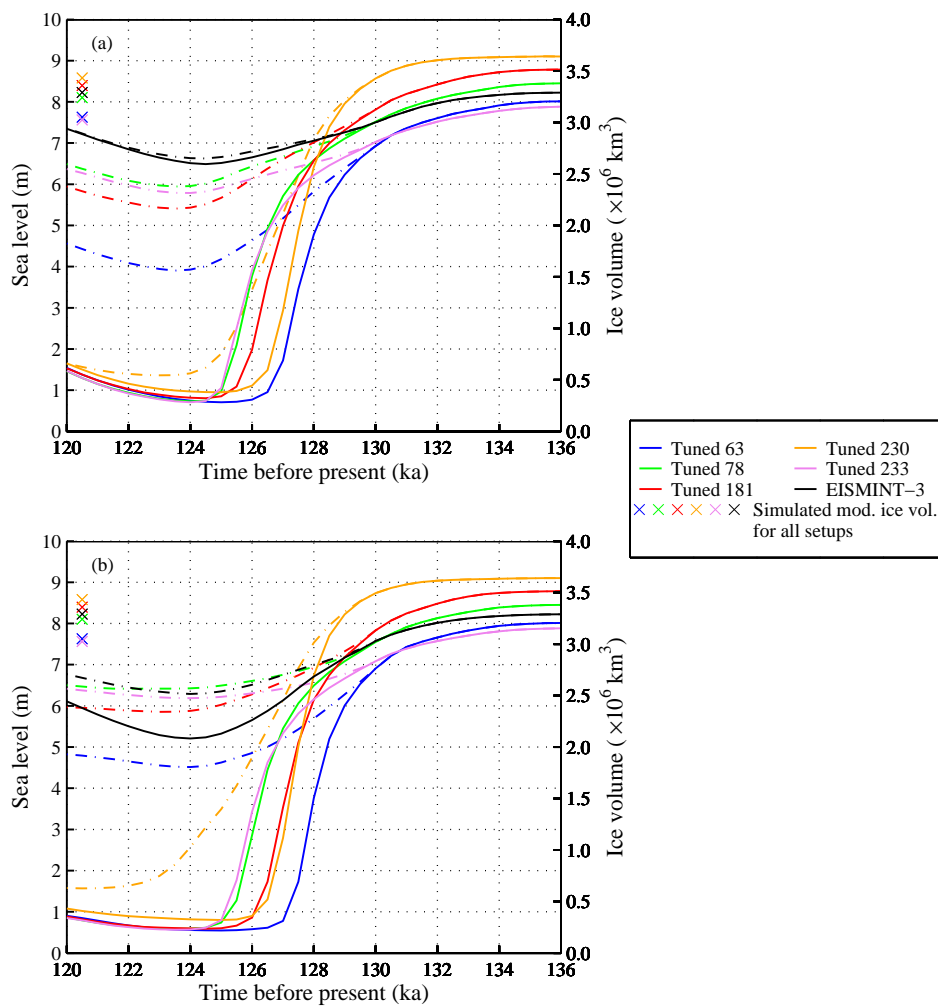


Figure D.1: Comparison between ice volume evolution when the model is initiated with a spun-up 136ka GrIS with and without the weighting function included (i.e. without weighting function Glimmer is forced only with the GrIS present climatologies) for EISMINT-3 and Glimmer tuned setups. (a) Fixed vegetation climate and (b) dynamic vegetation climates. The dot-dash lines correspond to when the weighting function is absent and the solid lines correspond to when it is included. Also shown near the left y-axis for each Glimmer setup is the present day simulated equilibrium ice volume/sea-level equivalent height.

# Bibliography

- Acton, D. (1989). Shield region (Soils of Canada). In R. J. Fulton, editor, *Quaternary Geology of Canada and Greenland*, volume no.1, Geology of Canada, page 675. Geological Survey of Canada, Ottawa.
- Alley, R. B., Meese, D. A., Shuman, C. A., Gow, A. J., Taylor, K. C., Grootes, P. M., White, J. W. C., Ram, M., Waddington, E. D., Mayewski, P. A., and Zielinski, G. A. (1993). Abrupt Increase in Greenland Snow Accumulation at the End of the Younger Dryas Event. *Nature*, **362**(6420), 527–529.
- Alley, R. B., Clark, P. U., Huybrechts, P., and Joughin, I. (2005). Ice-Sheet and Sea-Level Changes. *Science*, **310**, 456–460.
- Andersen, K. K., Azuma, N., Barnola, J. M., Bigler, M., Biscaye, P., Caillon, N., Chappellaz, J., Clausen, H. B., DahlJensen, D., Fischer, H., Fluckiger, J., Fritzsche, D., Fujii, Y., Goto-Azuma, K., Gronvold, K., Gundestrup, N. S., Hansson, M., Huber, C., Hvidberg, C. S., Johnsen, S. J., Jonsell, U., Jouzel, J., Kipfstuhl, S., Landais, A., Leuenberger, M., Lorrain, R., Masson-Delmotte, V., Miller, H., Motoyama, H., Narita, H., Popp, T., Rasmussen, S. O., Raynaud, D., Rothlisberger, R., Ruth, U., Samyn, D., Schwander, J., Shoji, H., Siggard-Andersen, M. L., Steffensen, J. P., Stocker, T., Sveinbjornsdottir, A. E., Svensson, A., Takata, M., Tison, J. L., Thorsteinsson, T., Watanabe, O., Wilhelms, F., White, J. W. C., and Project, N. G. I. C. a. (2004). High-resolution record of Northern Hemisphere climate extending into the last interglacial period. *Nature*, **431**(7005), 147–151.
- Anderson, P., Bermike, O., Bigelow, N., Brigham-Grette, J., Duvall, M., Edwards, M., Frechette, B., Funder, S., Johnsen, S., Knies, J., Koerner, R., Lozhkin, A., Marshall, S., Matthiessen, J., Macdonald, G., Miller, G., Montoya, M., Muhs, D., Otto-Bliesner, B., Overpeck, J., Reeh, N., Sejrup, H. P., Spielhagen, R., Turner, C., Velichko, A., and Members, C.-L. I. P. a. (2006). Last Interglacial Arctic

- warmth confirms polar amplification of climate change. *Quaternary Science Reviews*, **25**(13-14), 1383–1400.
- Aussenac, G. (2000). Interactions between forest stands and microclimate: Ecophysiological aspects and consequences for silviculture. *Annals of Forest Science*, **57**(3), 287–301.
- Bales, R. C., Guo, Q. H., Shen, D. Y., McConnell, J. R., Du, G. M., Burkhart, J. F., Spikes, V. B., Hanna, E., and Cappelen, J. (2009). Annual accumulation for Greenland updated using ice core data developed during 2000-2006 and analysis of daily coastal meteorological data. *Journal of Geophysical Research-Atmospheres*, **114**(D06116), doi:10.1029/2008JD011208.
- Bamber, J. L., Layberry, R., and Gogineni, P. (2001). A new ice thickness and bed data set for the Greenland ice sheet 1. Measurement, data reduction, and errors. *Journal of Geophysical Research*, **106**(D24), 33773–33780.
- Banks, D. (2008). *An Introduction to Thermogeology Ground Source Heating and Cooling*. Blackwell Publishing Ltd, Oxford, UK, 1st edition.
- Bennike, O. and Bocher, J. (1994). Land biotas of the last interglacial/glacial cycle on Jameson Land, East Greenland. *Boreas*, **23**(4), 479–487.
- Berger, A. and Loutre, M. F. (1991). Insolation Values for the Climate of the Last 10 Million Years. *Quaternary Science Reviews*, **10**(4), 297–317.
- Berger, A., Loutre, M. F., Kaspar, F., and Lorenz, S. (2007). Insolation During Interglacial. In F. Sirocko, M. Claussen, T. Litt, and M. Sánchez-Gōni, editors, *The Climate of Past Interglacials*, 7, Development in Quaternary Science, 7, pages 13–27. Elsevier, Oxford, 1st edition.
- Beringer, J., Chapin, F. S., Thompson, C. C., and McGuire, A. D. (2005). Surface energy exchanges along a tundra-forest transition and feedbacks to climate. *Agricultural and Forest Meteorology*, **131**(3-4), 143–161.
- Betts, A. K. and Ball, J. H. (1997). Albedo over the boreal forest. *Journal of Geophysical Research*, **102**(D24), 28901–28909.

- Betts, R. A., Cox, P. M., Collins, M., Harris, P. P., Huntingford, C., and Jones, C. D. (2004). The role of ecosystem-atmosphere interactions in simulated Amazonian precipitation decrease and forest dieback under global climate warming. *Theoretical and Applied Climatology*, **78**(1-3), 157–175.
- Bonan, G. B., Pollard, D., and Thompson, S. L. (1992). Effects of Boreal Forest Vegetation on Global Climate. *Nature*, **359**(6397), 716–718.
- Bonelli, S., Charbit, S., Kageyama, M., Woillez, M. N., Ramstein, G., Dumas, C., and Quiquet, A. (2009). Investigating the evolution of major Northern Hemisphere ice sheets during the last glacial-interglacial cycle. *Climate of the Past*, **5**(3), 329–345.
- Bougamont, M., Bamber, J. L., Ridley, J. K., Gladstone, R. M., Greuell, W., Hanna, E., Payne, A. J., and Rutt, I. (2007). Impact of model physics on estimating the surface mass balance of the Greenland ice sheet. *Geophysical Research Letters*, **34**(17), doi:10.1029/2007GL030700.
- Braconnot, P., Otto-Bliesner, B., Harrison, S., Joussaume, S., Peterchmitt, J. Y., Abe-Ouchi, A., Crucifix, M., Driesschaert, E., Fichefet, T., Hewitt, C. D., Kageyama, M., Kitoh, A., Laine, A., Loutre, M. F., Marti, O., Merkel, U., Ramstein, G., Valdes, P., Weber, S. L., Yu, Y., and Zhao, Y. (2007). Results of PMIP2 coupled simulations of the Mid-Holocene and Last Glacial Maximum - Part 1: experiments and large-scale features. *Climate of the Past*, **3**(2), 261–277.
- Braithwaite, R. J. (1995). Positive degree-day factors for ablation on the Greenland ice sheet studied by energy-balance modelling. *Journal of Glaciology*, **41**(137), 153–160.
- Bromwich, D. H., Cullather, R. I., Chen, Q., and Csatho, B. M. (1998). Evaluation of recent precipitation studies for Greenland ice sheet. *Journal of Geophysical Research-Atmospheres*, **103**(D20), 26007–26024.
- Brovkin, V., Bendtsen, J., Claussen, M., Ganopolski, A., Kubatzki, C., Petoukhov, V., and Andreev, A. (2002). Carbon cycle, vegetation, and climate dynamics in the Holocene: Experiments with the CLIMBER-2 model. *Global Biogeochemical Cycles*, **16**(4), doi:10.1029/2001GB001662.

- Bryan, K. (1969). A Numerical Method for the Study of the Circulation of the World Ocean. *Journal of Computational Physics*, **4**(3), 347–376.
- Bucharadt, S. L. and Dahl-Jensen, D. (2007). Estimating the basal melt rate at NorthGRIP using a Monte Carlo technique. *Annals of Glaciology*, **45**, 137–142.
- Burgess, E. W., Forster, R. R., Box, J. E., Mosley-Thompson, E., Bromwich, D. H., Bales, R. C., and Smith, L. C. (2010). A spatially calibrated model of annual accumulation rate on the Greenland Ice Sheet (1958-2007). *Journal of Geophysical Research-Earth Surface*, **115**(F02004), doi:10.1029/2009JF001293.
- Calov, R. and Hutter, K. (1996). The thermomechanical response of the Greenland ice sheet to various climate scenarios. *Climate Dynamics*, **12**(4), 243–260.
- Calov, R., Ganopolski, A., Claussen, M., Petoukhov, V., and Greve, R. (2005a). Transient simulation of the last glacial inception. Part I: glacial inception as a bifurcation in the climate system. *Climate Dynamics*, **24**(6), 545–561.
- Calov, R., Ganopolski, A., Petoukhov, V., Claussen, M., Brovkin, V., and Kubatzki, C. (2005b). Transient simulation of the last glacial inception. Part II: sensitivity and feedback analysis. *Climate Dynamics*, **24**(6), 563–576.
- Calov, R., Ganopolski, A., Kubatzki, C., and Clausen, M. (2009). Mechanisms and time scales of glacial inception simulated with an Earth system model of intermediate complexity. *Climate of the Past*, **5**, 245–258.
- Cattle, H. and Crossley, J. (1995). Modeling Arctic Climate-Change. *Philosophical Transactions of the Royal Society of London Series A-Mathematical Physical and Engineering Sciences*, **352**(1699), 201–213.
- Chalita, S. and Letreut, H. (1994). The Albedo of Temperate and Boreal Forest and the Northern-Hemisphere Climate - a Sensitivity Experiment Using the LMD-GCM. *Climate Dynamics*, **10**(4-5), 231–240.
- Chappellaz, J., Brook, E., Blunier, T., and Malaize, B. (1997). Ch4 and delta o-18 of o-2 records from antarctic and greenland ice: A clue for stratigraphic disturbance in the bottom part of the Greenland Ice Core Project and the Greenland Ice Sheet Project 2 ice cores. *Journal of Geophysical Research-Oceans*, **102**(C12), 26547–26557.

- Charbit, S., Paillard, D., and Ramstein, G. (2008). Amount of CO<sub>2</sub> emissions irreversibly leading to the total melting of Greenland. *Geophysical Research Letters*, **35**(L12503), doi:10.1029/2008GL033472.
- Cheddadi, R., Yu, G., Guiot, J., Harrison, S. P., and Prentice, I. C. (1997). The climate of Europe 6000 years ago. *Climate Dynamics*, **13**(1), 1–9.
- Claussen, M., Cox, P. M., Zeng, X., Viterbo, P., Beljaars, A. C. M., Betts, R. A., Bolle, H.-J., Chase, T., and Koster, R. (2004). The Global Climate. In P. Kabat, M. Claussen, P. Dirmeyer, J. Gash, L. Bravo de Guenni, M. Meybeck, R. Pielke, C. Vrsmarty, R. Hutjes, and S. Ltkemeier, editors, *Vegetation, Water, Humans and the Climate. A New Perspective on an Interactive System.*, Global Change - The IGBP Series, pages 33–53. Springer-Verlag, Berlin, Germany.
- Cosby, B. J., Hornberger, G. M., Clapp, R. B., and Ginn, T. R. (1984). A Statistical Exploration of the Relationships of Soil-Moisture Characteristics to the Physical-Properties of Soils. *Water Resources Research*, **20**(6), 682–690.
- Cox, M. D. (1984). A primitive equation, three dimensional model of the ocean. *GFDL ocean group Techn Rep 1*, pages 1–143.
- Cox, P. (2001). Description of the "TRIFFID" Dynamic Vegetation Model. *Hadley Centre technical note 24*, pages 1–16.
- Cox, P., Huntingford, C., and Harding, R. (1998). A canopy conductance and photosynthesis model for use in a GCM land surface scheme. *Journal of Hydrology*, **212-213**, 79–94.
- Cox, P. M., Betts, R. A., Bunton, C. B., Essery, R. L. H., Rowntree, P. R., and Smith, J. (1999). The impact of new land surface physics on the GCM simulation of climate and climate sensitivity. *Climate Dynamics*, **15**(3), 183–203.
- Cox, P. M., Betts, R. A., Jones, C. D., Spall, S. A., and Totterdell, I. J. (2000). Acceleration of global warming due to carbon-cycle feedbacks in a coupled climate model. *Nature*, **408**(6813), 184–187.
- Crowley, T. J. and Baum, S. K. (1995). Is the Greenland Ice-Sheet Bistable? *Paleo-oceanography*, **10**(3), 357–363.

- Crowley, T. J. and Kim, K. Y. (1994). Milankovitch Forcing of the Last Interglacial Sea-level. *Science*, **265**(5178), 1566–1568.
- Crucifix, M. and Loutre, M. F. (2002). Transient simulations over the last interglacial period (126-115 kyr BP): feedback and forcing analysis. *Climate Dynamics*, **19**(5-6), 417–433.
- Crucifix, M., Betts, R. A., and Cox, P. M. (2005). Vegetation and climate variability: a GCM modelling study. *Climate Dynamics*, **24**(5), 457–467.
- Cuffey, K. M. and Marshall, S. J. (2000). Substantial contribution to sea-level rise during the last interglacial from the Greenland ice sheet. *Nature*, **404**(6778), 591–594.
- Dahl-Jensen, D. (2005). The last interglacial and beyond: A northwest Greenland deep ice core drilling project. Available at:[http://www.pages-igbp.org/ipics/data/ipics\\_neem.pdf](http://www.pages-igbp.org/ipics/data/ipics_neem.pdf) [Accessed on 12 January 2010].
- Dahl-Jensen, D. and Gundestrup, N. (1987). Constitutive properties of ice at Dye 3, Greenland. In *The Physical Basis of Ice Sheet Modelling*, pages 31–43. International Association of Hydrological Sciences Publ.
- Dahl-Jensen, D. and Johnsen, S. J. (1986). Paleotemperatures Still Exist in the Greenland Ice-Sheet. *Nature*, **320**(6059), 250–252.
- Dansgaard, W. (2004). *Frozen Annals Greenland Ice Cap Research*. Narayana Press, Odder, Denmark.
- Dansgaard, W., Johnsen, S. J., Reeh, N., Gundestrup, N., Clausen, H. B., and Hammer, C. U. (1975). Climatic Changes, Norsemen and Modern Man. *Nature*, **255**(5503), 24–28.
- Dansgaard, W., Clausen, H. B., Gundestrup, N., Hammer, C. U., Johnsen, S. F., Kristinsdottir, P. M., and Reeh, N. (1982). A New Greenland Deep Ice Core. *Science*, **218**(4579), 1273–1277.
- Dansgaard, W., Clausen, H. B., Gundestrup, N., Johnsen, S., and Rygner, C. (1985). Dating and interpretation of two deep Greenland ice cores. In C. C. J. Lang-

- way, H. Oeschger, and W. Dansgaard, editors, *Greenland Ice Core: Geophysics, Geochemistry, and the Environment*, pages 71–76. American Geophysical Union, Washington, DC.
- Dansgaard, W., Johnsen, S. J., Clausen, H. B., Dahljensen, D., Gundestrup, N. S., Hammer, C. U., Hvidberg, C. S., Steffensen, J. P., Sveinbjornsdottir, A. E., Jouzel, J., and Bond, G. (1993). Evidence for General Instability of Past Climate from a 250-Kyr Ice-Core Record. *Nature*, **364**(6434), 218–220.
- Dasgupta, S., Laplante, B., Meisner, C., Wheeler, D., and Yan, J. (2009). The impact of sea level rise on developing countries: a comparative analysis. *Climatic Change*, **93**(3-4), 379–388.
- DeConto, R. M. and Pollard, D. (2003). Rapid Cenozoic glaciation of Antarctica induced by declining atmospheric CO<sub>2</sub>. *Nature*, **421**(6920), 245–249.
- deNoblet, N. I., Prentice, I. C., Joussaume, S., Texier, D., Botta, A., and Haxeltine, A. (1996). Possible role of atmosphere-biosphere interactions in triggering the last glaciation. *Geophysical Research Letters*, **23**(22), 3191–3194.
- Desprat, S., Goni, M. F. S., Turon, J. L., McManus, J. F., Loutre, M. F., Duprat, J., Malaize, B., Peyron, O., and Peypouquet, J. P. (2005). Is vegetation responsible for glacial insolation inception during periods of muted changes? *Quaternary Science Reviews*, **24**(12-13), 1361–1374.
- Dethloff, K., Dorn, W., Rinke, A., Fraedrich, K., Junge, M., Roeckner, E., Gayler, V., Cubasch, U., and Christensen, J. H. (2004). The impact of Greenland's deglaciation on the Arctic circulation. *Geophysical Research Letters*, **31**(L19201), doi:10.1029/2004GL020714.
- Drees, B. and Daniels, F. J. A. (2009). Mountain vegetation of south-facing slopes in continental West Greenland. *Phytocoenologia*, **39**(1), 1–25.
- Driesschaert, E., Fichefet, T., Goosse, H., Huybrechts, P., Janssens, I., Mouchet, A., Munhoven, G., Brovkin, V., and Weber, S. L. (2007). Modeling the influence of Greenland ice sheet melting on the Atlantic meridional overturning circulation during the next millennia. *Geophysical Research Letters*, **34**(10), doi:10.1029/2007GL029516.



- ECMWF (2006). ECMWF ERA-40 Re-Analysis data. Available from British Atmospheric Data Centre at: <http://badc.nerc.ac.uk/browse/badc/ecmwf-e40/data> [Accessed on 13 March 2009].
- Edwards, J. M. and Slingo, A. (1996). Studies with a flexible new radiation code .1. Choosing a configuration for a large-scale model. *Quarterly Journal of the Royal Meteorological Society*, **122**(531), 689–719.
- Edwards, N. and Marsh, R. (2005). Uncertainties due to transport-parameter sensitivity in an efficient 3-D ocean-climate model. *Climate Dynamics*, **24**(4), 415–433.
- Ekholm, S. (1996). A full coverage, high-resolution topographic model of Greenland computed from a variety of digital elevation data. *Journal of Geophysical Research*, **101**, 21961–21972.
- Essery, R. and Etchevers, P. (2004). Parameter sensitivity in simulations of snowmelt. *Journal of Geophysical Research-Atmospheres*, **109**(D20), doi:10.1029/2004JD005036.
- Essery, R., Best, M., and Cox, P. (2001). MOSES 2.2 Technical Documentation. *Hadley Centre technical note 30*, pages 1–30.
- Ettema, J., van den Broeke, M. R., van Meijgaard, E., van de Berg, W. J., Bamber, J. L., Box, J. E., and Bales, R. C. (2009). Higher surface mass balance of the Greenland ice sheet revealed by high-resolution climate modeling. *Geophysical Research Letters*, **36**, doi:10.1029/2009GL038110.
- Fabre, A., Letreguilly, A., Ritz, C., and Mangeney, A. (1995). Greenland under changing climates: sensitivity experiments with a new three-dimensional ice-sheet model. *Annals of Glaciology*, **21**, 1–7.
- Fausto, R. S., Ahlstrom, A. P., Van As, D., Boggild, C. E., and Johnsen, S. J. (2009). A new present-day temperature parameterisation for Greenland. *Journal of Glaciology*, **55**(189), 95–105.
- Fichefet, T., Poncin, C., Goosse, H., Huybrechts, P., Janssens, I., and Treut Le, H. (2003). Implications of changes in freshwater flux from the Greenland ice sheet for the climate of the 21st century. *Geophysical Research Letters*, **30**(17), 81–4.

- Flesche Kleiven, H., Jansen, E., Fronval, T., and Smith, T. (2002). Intensification of Northern Hemisphere glaciations in the circum Atlantic region (3.5-2.4 Ma) - ice-rafted detritus evidence. *Palaeogeography, Palaeoclimatology, Palaeoecology*, **184**, 213–223.
- Foley, J. A., Kutzbach, J. E., Coe, M. T., and Levis, S. (1994). Feedbacks between climate and boreal forests during the Holocene epoch. *Nature*, **371**, 52–54.
- Foley, J. A., Prentice, I. C., Ramankutty, N., Levis, S., Pollard, D., Sitch, S., and Haxeltine, A. (1996). An integrated biosphere model of land surface processes, terrestrial carbon balance, and vegetation dynamics. *Global Biogeochemical Cycles*, **10**(4), 603–628.
- Francis, J. E., Haywood, A. M., Ashworth, A. C., and Valdes, P. J. (2007). Tundra environments in the Neogene Sirius Group, Antarctica: evidence from the geological record and coupled atmosphere-vegetation models. *Journal of the Geological Society*, **164**, 317–322.
- Freedman, J. M., Fitzjarrald, D. R., Moore, K. E., and Sakai, R. K. (2001). Boundary layer clouds and vegetation-atmosphere feedbacks. *Journal of Climate*, **14**(2), 180–197.
- Friend, A. D., Stevens, A. K., Knox, R. G., and Cannell, M. G. R. (1997). A process-based, terrestrial biosphere model of ecosystem dynamics (Hybrid v3.0). *Ecological Modelling*, **95**(2-3), 249–287.
- Funder, S. (1989). Quaternary geology of the ice-free areas and adjacent shelves of Greenland. In R. J. Fulton, editor, *Quaternary Geology of Canada and Greenland*, volume no.1, Geology of Canada, pages 743–792. Geological Survey of Canada, Ottawa.
- Gallimore, R., Jacob, R., and Kutzbach, J. (2005). Coupled atmosphere-ocean-vegetation simulations for modern and mid-Holocene climates: role of extratropical vegetation cover feedbacks. *Climate Dynamics*, **25**(7-8), 755–776.
- Gallimore, R. G. and Kutzbach, J. E. (1996). Role of orbitally induced changes in tundra area in the onset of glaciation. *Nature*, **381**(6582), 503–505.

- Ganachaud, A. (2003). Large-scale mass transports, water mass formation, and diffusivities estimated from World Ocean Circulation Experiment (WOCE) hydrographic data. *Journal of Geophysical Research-Oceans*, **108**(C7), doi:10.1029/2002JC001565.
- Ganopolski, A., Kubatzki, C., Claussen, M., Brovkin, V., and Petoukhov, V. (1998a). The influence of vegetation-atmosphere-ocean interaction on climate during the mid-Holocene. *Science*, **280**(5371), 1916–1919.
- Ganopolski, A., Rahmstorf, S., Petoukhov, V., and Claussen, M. (1998b). Simulation of modern and glacial climates with a coupled global model of intermediate complexity. *Nature*, **391**(6665), 351–356.
- Gilmanov, T. G. and Oechel, W. C. (1995). New estimates of organic matter reserves and net primary productivity of the North American tundra ecosystems. *Journal of Biogeography*, **22**, 723–741.
- Glover, R. W. (1999). Influence of spatial resolution and treatment of orography on GCM estimates of the surface mass balance of the Greenland ice sheet. *Journal of Climate*, **12**(2), 551–563.
- Gordon, C., Cooper, C., Senior, C. A., Banks, H., Gregory, J. M., Johns, T. C., Mitchell, J. F. B., and Wood, R. A. (2000). The simulation of SST, sea ice extents and ocean heat transports in a version of the Hadley Centre coupled model without flux adjustments. *Climate Dynamics*, **16**(2-3), 147–168.
- Gotelli, N. J. (2001). *A Primer of Ecology*. Sinauer Associates, Sunderland, Massachusetts, 3rd edition.
- Gregory, D. and Rowntree, P. R. (1990). A Mass Flux Convection Scheme with Representation of Cloud Ensemble Characteristics and Stability-Dependent Closure. *Monthly Weather Review*, **118**(7), 1483–1506.
- Gregory, D., Kershaw, R., and Inness, P. M. (1997). Parametrization of momentum transport by convection .2. Tests in single-column and general circulation models. *Quarterly Journal of the Royal Meteorological Society*, **123**(541), 1153–1183.
- Gregory, D., Shutts, G. J., and Mitchell, J. R. (1998). A new gravity-wave-drag scheme incorporating anisotropic orography and low-level wave breaking: Impact

- upon the climate of the UK Meteorological Office Unified Model. *Quarterly Journal of the Royal Meteorological Society*, **124**(546), 463–493.
- Gregory, J. M. and Huybrechts, P. (2006). Ice-sheet contributions to future sea-level change. *Philosophical Transactions of the Royal Society a-Mathematical Physical and Engineering Sciences*, **364**(1844), 1709–1731.
- Gregory, J. M., Huybrechts, P., and Raper, S. C. B. (2004). Climatology - Threatened loss of the Greenland ice-sheet. *Nature*, **428**(6983), 616–616.
- Greve, R. (2000). On the response of the Greenland ice sheet to greenhouse climate change. *Climatic Change*, **46**(3), 289–303.
- Greve, R. (2005). Relation of measured basal temperatures and the spatial distribution of the geothermal heat flux for the Greenland ice sheet. *Annals of Glaciology*, **42**, 424–432.
- Greve, R. and Hutter, K. (1995). Polythermal three-dimensional modelling of the Greenland ice sheet with varied geothermal heat flux. *Annals of Glaciology*, **21**, 8–12.
- Gröger, M., Maier-Reimer, E., Mikolajewicz, U., Schurgers, C., Vizcaíno, M., and Winguth, A. (2007). Vegetation-Climate Feedbacks in Transient Simulations Over the Last Interglacial (128 000–113 000 yr BP). In F. Sirocko, M. Claussen, T. Litt, and M. Sánchez-Göni, editors, *The Climate of Past Interglacials*, 7, pages 563–572. Elsevier, Oxford, 1st edition.
- Grootes, P. M., Stuiver, M., White, J. W. C., Johnsen, S., and Jouzel, J. (1993). Comparison of Oxygen-Isotope Records from the GISP2 and GRIP Greenland Ice Cores. *Nature*, **366**(6455), 552–554.
- Hagdorn, M., Rutt, I., Payne, A. J., and Hebel, F. (2007). GLIMMER 1.0.4 Documentation. Technical report.
- Hanna, E. and Valdes, P. (2001). Validation of ECMWF (re)analysis surface climate data, 1979–1998, for Greenland and implications for mass balance modelling of the Ice Sheet. *International Journal of Climatology*, **21**(2), 171–195.

- Hanna, E., Huybrechts, P., Janssens, I., Cappelen, J., Steffen, K., and Stephens, A. (2005). Runoff and mass balance of the Greenland ice sheet: 1958-2003. *Journal of Geophysical Research-Atmospheres*, **110**(D13108), doi:10.1029/2004JD005641.
- Hanna, E., McConnell, J., Das, S., Cappelen, J., and Stephens, A. (2006). Observed and modeled Greenland ice sheet snow accumulation, 1958-2003, and links with regional climate forcing. *Journal of Climate*, **19**(3), 344–358.
- Hanna, E., Huybrechts, P., Steffen, K., Cappelen, J., Huff, R., Shuman, C., Irvine-Fynn, T., Wise, S., and Griffiths, M. (2008). Increased runoff from melt from the Greenland Ice Sheet: A response to global warming. *Journal of Climate*, **21**(2), 331–341.
- Hansson, M. and Holmen, K. (2001). High latitude biospheric activity during the last glacial cycle revealed by ammonium variations in Greenland ice cores. *Geophysical Research Letters*, **28**(22), 4239–4242.
- Haug, G. H. and Tiedemann, R. (1998). Effect of the formation of the isthmus of Panama on Atlantic Ocean thermohaline circulation. *Nature*, **393**(6686), 673–676.
- Haywood, A. M. and Valdes, P. J. (2004). Modelling Pliocene warmth: contribution of atmosphere, oceans and cryosphere. *Earth and Planetary Science Letters*, **218**(3-4), 363–377.
- Haywood, A. M. and Valdes, P. J. (2006). Vegetation cover in a warmer world simulated using a dynamic global vegetation model for the Mid-Pliocene. *Palaeogeography Palaeoclimatology Palaeoecology*, **237**(2-4), 412–427.
- Hebeler, F., Purves, R. S., and Jamieson, S. S. R. (2008). The impact of parametric uncertainty and topographic error in ice-sheet modelling. *Journal of Glaciology*, **54**(188), 899–919.
- Held, I. M. and Suarez, M. J. (1974). Simple albedo feedback models of the icecaps. *Tellus*, **26**(6), 613–629.
- Hillaire-Marcel, C., de Vernal, A., Bilodeau, G., and Weaver, A. J. (2001). Absence of deep-water formation in the Labrador Sea during the last interglacial period. *Nature*, **410**(6832), 1073–1077.

- Holland, M. M. and Bitz, C. M. (2003). Polar amplification of climate change in coupled models. *Climate Dynamics*, **21**(3-4), 221–232.
- Howat, I. M., Joughin, I., and Scambos, T. A. (2007). Rapid changes in ice discharge from Greenland outlet glaciers. *Science*, **315**(5818), 1559–1561.
- Hughes, J. K. (2003). *The Dynamic Response of the Global Atmosphere-Vegetation coupled system*. Ph.D. thesis, University of Reading.
- Hutter, K. (1983). *Theoretical Glaciology: Material Science of Ice and the Mechanics of Glaciers and Ice Sheets*. Mathematical Approaches to Geophysics. Springer, D. Reidel, Dordrecht: Netherlands.
- Huybrechts, P. (1997). Report of the Third EISMINT Workshop on Model Inter-comparison. Technical report, Grindelwald, Switzerland, 25-27 September 1997.
- Huybrechts, P. (2002). Sea-level changes at the LGM from ice-dynamic reconstructions of the Greenland and Antarctic ice sheets during the glacial cycles. *Quaternary Science Reviews*, **21**(1-3), 203–231.
- Huybrechts, P. and de Wolde, J. (1999). The dynamic response of the Greenland and Antarctic ice sheets to multiple-century climatic warming. *Journal of Climate*, **12**(8), 2169–2188.
- Huybrechts, P. and Payne, A. J. (1996). The EISMINT benchmarks for testing-ice sheet models. *Annals of Glaciology*, **23**, 1–12.
- Huybrechts, P. and T'Siobbel, S. (1995). Thermomechanical modelling of Northern Hemisphere ice sheets with a two-level mass balance parameterization. *Annals of Glaciology*, **21**, 111–116.
- Huybrechts, P. and T'Siobbel, S. (1997). A three-dimensional climate-ice-sheet model applied to the Last Glacial Maximum. *Annals of Glaciology*, **25**, 333–339.
- Huybrechts, P., Letreguilly, A., and Reeh, N. (1991). The Greenland Ice-Sheet and Greenhouse Warming. *Global and Planetary Change*, **89**(4), 399–412.
- Iman, R. L. and Helton, J. C. (1985). A comparison of uncertainty and sensitivity analysis techniques for computer models. Technical report, Sandia National Laboratories, Albuquerque NM.

- IPCC (2007). *Climate Change 2007: The Physical Sciences Basis. Contribution of Working Group I to the Fourth Assessment Report of the Intergovernmental Panel on Climate Change*. Cambridge University Press, Cambridge, United Kingdom and New York, NY, USA.
- Irvine, P. J., Lunt, D. J., Stone, E. J., and Ridgwell, A. (2009). The fate of the Greenland Ice Sheet in a geoengineered, high CO<sub>2</sub> world. *Environmental Research Letters*, **4**(045109), doi:10.1088/1748-9326/4/4/045109.
- Jansen, E., Overpeck, J., Briffa, K. R., Duplessy, J. C., Joos, F., Masson-Delmotte, V., Olago, D., Otto-Bliesner, B., Peltier, W. R., Rahmstorf, S., Ramesh, R., Raynaud, D., Rind, D., Solomina, O., Villalba, R., and Zhang, D. (2007). Palaeoclimate. In S. Solomon, D. Qin, M. Manning, Z. Chen, M. Marquis, K. B. Averyt, M. Tignor, and H. L. Miller, editors, *Climate Change 2007: The Physical Science Basis. Contribution of Working Group I to the Fourth Assessment Report of the Intergovernmental Panel on Climate Change*. Cambridge University Press, Cambridge, United Kingdom and New York, NY, USA.
- Janssens, I. and Huybrechts, P. (2000). The treatment of meltwater retention in mass-balance parameterizations of the Greenland ice sheet. *Annals of Glaciology*, **31**, 133–140.
- Johnsen, S. J., Clausen, H. B., Dansgaard, W., Gundestrup, N. S., Hansson, M., Jonsson, P., Steffensen, J. P., and Sveinbjornsdottir, A. E. (1992). A ‘deep’ ice core from East Greenland. *Meddeleser om Gronland, Geoscience*, **29**, 1–22.
- Johnsen, S. J., Clausen, H. B., Dansgaard, W., Gundestrup, N. S., Hammer, C. U., Andersen, U., Andersen, K. K., Hvidberg, C. S., DahlJensen, D., Steffensen, J. P., Shoji, H., Sveinbjornsdottir, A. E., White, J., Jouzel, J., and Fisher, D. (1997). The delta o-18 record along the Greenland Ice Core Project deep ice core and the problem of possible Eemian climatic instability. *Journal of Geophysical Research-Oceans*, **102**(C12), 26397–26410.
- Jones, C., Gregory, J., Thorpe, R., Cox, P., Murphy, J., Sexton, D., and Valdes, P. (2005). Systematic optimisation and climate simulation of FAMOUS, a fast version of HadCM3. *Climate Dynamics*, **25**(2-3), 189–204.

- Jones, C. P. (2004). Ancillary File Data Sources. *Unified Model Documentation Paper No. 70*, pages 1–42.
- Jones, P. D., New, M., Parker, D. E., Martin, S., and Rigor, I. G. (1999). Surface air temperature and its changes over the past 150 years. *Reviews of Geophysics*, **37**(2), 173–199.
- Joughin, I., Abdalati, W., and Fahnestock, M. (2004). Large fluctuations in speed on Greenland’s Jakobshavn Isbrae glacier. *Nature*, **432**(7017), 608–610.
- Joussaume, S., Taylor, K. E., Braconnot, P., Mitchell, J. F. B., Kutzbach, J. E., Harrison, S. P., Prentice, I. C., Broccoli, A. J., Abe-Ouchi, A., Bartlein, P. J., Bonfils, C., Dong, B., Guiot, J., Herterich, K., Hewitt, C. D., Jolly, D., Kim, J. W., Kislov, A., Kitoh, A., Loutre, M. F., Masson, V., McAvaney, B., McFarlane, N., de Noblet, N., Peltier, W. R., Peterschmitt, J. Y., Pollard, D., Rind, D., Royer, J. F., Schlesinger, M. E., Syktus, J., Thompson, S., Valdes, P., Vettoretti, G., Webb, R. S., and Wyputta, U. (1999). Monsoon changes for 6000 years ago: Results of 18 simulations from the Paleoclimate Modeling Intercomparison Project (PMIP). *Geophysical Research Letters*, **26**(7), 859–862.
- Jungclauss, J. H. (2006). Will Greenland melting halt the thermohaline circulation? *Geophysical research letters*, **33**(L17708), doi:10.1029/2006GL026815.
- Junge, M. M., Blender, R., Fraedrich, K., Gayler, V., Luksch, U., and Lunkeit, F. (2005). A world without Greenland: impacts on the Northern Hemisphere winter circulation in low- and high-resolution models. *Climate Dynamics*, **24**(2-3), 297–307.
- Kageyama, M., Charbit, S., Ritz, C., Khodri, M., and Ramstein, G. (2004). Quantifying ice-sheet feedbacks during the last glacial inception. *Geophysical Research Letters*, **31**(L24203), doi:10.1029/2004GL021339.
- Kaplan, J. O., Bigelow, N. H., Prentice, I. C., Harrison, S. P., Bartlein, P. J., Christensen, T. R., Cramer, W., Matveyeva, N. V., McGuire, A. D., Murray, D. F., Razzhivin, V. Y., Smith, B., Walker, D. A., Anderson, P. M., Andreev, A. A., Brubaker, L. B., Edwards, M. E., and Lozhkin, A. V. (2003). Climate change and Arctic ecosystems: 2. Modeling, paleodata-model comparisons,



- and future projections. *Journal of Geophysical Research-Atmospheres*, **108**(D19), doi:10.1029/2002JD002559.
- Kaspar, F., Kuhl, N., Cubasch, U., and Litt, T. (2005). A model-data comparison of European temperatures in the Eemian interglacial. *Geophysical Research Letters*, **32**(L11703), doi:10.1029/2005GL022456.
- Key, J. R., Collins, J. B., Fowler, C., and Stone, R. S. (1997). High-latitude surface temperature estimates from thermal satellite data. *Remote Sensing of Environment*, **61**(2), 302–309.
- Kienast, F., Tarasov, P., Schirmer, L., Grosse, G., and Andreev, A. A. (2008). Continental climate in the East Siberian Arctic during the last interglacial: Implications from palaeobotanical records. *Global and Planetary Change*, **60**(3-4), 535–562.
- Koerner, R. and Fischer, H. (2002). Ice-core evidence for widespread Arctic glacier retreat in the Last Interglacial and the early Holocene. *Annals of Glaciology*, **35**(1), 19–24.
- Koerner, R. M. (1989). Ice Core Evidence for Extensive Melting of the Greenland Ice-Sheet in the Last Interglacial. *Science*, **244**(4907), 964–968.
- Kopp, R. E., Simons, F. J., Mitrovica, J. X., Maloof, A. C., and Oppenheimer, M. (2009). Probabilistic assessment of sea level during the last interglacial stage. *Nature*, **462**(7275), 863–868.
- Krabill, W., Hanna, E., Huybrechts, P., Abdalati, W., Cappelen, J., Csatho, B. M., Frederick, E., Manizade, S., Martin, C., Sonntag, J., Swift, R., Thomas, R., and Yungel, J. (2004). Greenland Ice Sheet: Increased coastal thinning. *Geophysical Research Letters*, **31**(L24402), doi:10.1029/2004GL021533.
- Krinner, G., Viovy, N., de Noblet-Ducoudre, N., Ogee, J., Polcher, J., Friedlingstein, P., Ciais, P., Sitch, S., and Prentice, I. C. (2005). A dynamic global vegetation model for studies of the coupled atmosphere-biosphere system. *Global Biogeochemical Cycles*, **19**(GB1015), doi:10.1029/2003GB002199.

- Kristjánsson, J. E. and McInnes, H. (1999). The impact of Greenland on cyclone evolution in the North Atlantic. *Quarterly Journal of the Royal Meteorological Society*, **125**(560), 2819–2834.
- Kristjánsson, J. E., Thorsteinsson, S., and Rosting, B. (2009). Phase-locking of a rapidly developing extratropical cyclone by Greenland's orography. *Quarterly Journal of the Royal Meteorological Society*, **135**(645), 1986–1998.
- Kubatzki, C., Claussen, M., Calov, R., and Ganopolski, A. (2006). Sensitivity of the last glacial inception to initial and surface conditions. *Climate Dynamics*, **27**(4), 333–344.
- Kucharik, C. J., Foley, J. A., Delire, C., Fisher, V. A., Coe, M. T., Lenters, J. D., Young-Molling, C., Ramankutty, N., Norman, J. M., and Gower, S. T. (2000). Testing the performance of a Dynamic Global Ecosystem Model: Water balance, carbon balance, and vegetation structure. *Global Biogeochemical Cycles*, **14**(3), 795–825.
- Kutzbach, J. E., Gallimore, R. G., and Guetter, P. J. (1991). Sensitivity experiments on the effect of orbitally-caused insolation changes on the Interglacial climate of high northern latitudes. *Quaternary International*, **10-12**, 223–229.
- Lambeck, K. and Nakiboglu, S. M. (1980). Seamount Loading and Stress in the Ocean Lithosphere. *Journal of Geophysical Research*, **85**(Nb11), 6403–6418.
- Laskar, J., Robutel, P., Joutel, F., Gastineau, M., Correia, A. C. M., and Levrard, B. (2004). A long-term numerical solution for the insolation quantities of the Earth. *Astronomy & Astrophysics*, **428**(1), 261–285.
- Lawrence, K. T., Liu, Z. H., and Herbert, T. D. (2006). Evolution of the eastern tropical Pacific through Plio-Pleistocene glaciation. *Science*, **312**(5770), 79–83.
- Lee, W. (1970). On the global variations of terrestrial heat flow. *Phys. Earth Planet. Interiors*, **2**, 332–341.
- Lefebre, F., Gallee, H., Van Ypersele, J. P., and Huybrechts, P. (2002). Modelling of large-scale melt parameters with a regional climate model in south Greenland during the 1991 melt season. *Annals of Glaciology*, **35**, 391–397.

- Lemke, P., Ren, R., Alley, R. B., Allison, I., Carrasco, G., Flato, G., Fujii, Y., Kaser, G., Mote, P., Thomas, R. H., and Zhang, T. (2007). Observations: Changes in Snow, Ice and Frozen Ground. In S. Solomon, D. Qin, M. Manning, Z. Chen, M. Marquis, K. Averyt, M. Tignor, and H. Miller, editors, *The Physical Science Basis. Contribution of Working group 1 to the Fourth Assessment Report of the Intergovernmental Panel on Climate Change*, pages 337–383. Cambridge University Press, Cambridge.
- Letreguilly, A., Reeh, N., and Huybrechts, P. (1991a). The Greenland Ice-Sheet through the Last Glacial Interglacial Cycle. *Global and Planetary Change*, **90**(4), 385–394.
- Letreguilly, A., Huybrechts, P., and Reeh, N. (1991b). Steady-State Characteristics of the Greenland Ice-Sheet under Different Climates. *Journal of Glaciology*, **37**(125), 149–157.
- Leysinger Vieli, G. J.-M. C. and Gudmundsson, G. H. (2004). On estimating length fluctuations of glaciers caused by changes in climatic forcing. *Journal of Geophysical Research-Earth Surface*, **109**(F01007), doi:10.1029/2003JF000027.
- Lhomme, N., Clarke, G. K. C., and Marshall, S. J. (2005). Tracer transport in the Greenland Ice Sheet: constraints on ice cores and glacial history. *Quaternary Science Reviews*, **24**(1-2), 173–194.
- Loulergue, L., Parrenin, F., Blunier, T., Barnola, J. M., Spahni, R., Schilt, A., Raisbeck, G., and Chappellaz, J. (2007). New constraints on the gas age-ice age difference along the EPICA ice cores, 0-50 kyr. *Climate of the Past*, **3**(3), 527–540.
- Loutre, M. F. (1995). Greenland Ice-Sheet over the Next 5000 Years. *Geophysical Research Letters*, **22**(7), 783–786.
- Loutre, M. F., Berger, A., Crucifix, M., Desprat, S., and Sánchez-Göni, M. (2007). Interglacials as Simulated by the LLN 2-D NH and MoBidiC Climate Models. In F. Sirocko, M. Claussen, T. Litt, and M. Sanchez-Goni, editors, *The Climate of Past Interglacials, 7*, Development in Quaternary Science, 7, pages 547–561. Elsevier, Oxford, 1st edition.

- Loveland, T. R., Reed, B. C., Brown, J. F., Ohlen, D. O., Zhu, Z., Yang, L., and Merchant, J. W. (2000). Development of a global land cover characteristics database and IGBP DISCover from 1 km AVHRR data. *International Journal of Remote Sensing*, **21**(6-7), 1303–1330.
- Lozhkin, A. and Anderson, P. (1995). The Last Interglaciation in Northeast Siberia. *Quaternary Research*, **43**(2), 147–158.
- Luckman, A. and Murray, T. (2005). Seasonal variation in velocity before retreat of Jakobshavn Isbrae, Greenland. *Geophysical Research Letters*, **32**(L08501), 10.1029/2005GL022519.
- Luckman, A., Murray, T., de Lange, R., and Hanna, E. (2006). Rapid and synchronous ice-dynamic changes in East Greenland. *Geophysical Research Letters*, **33**(L03503), doi:10.1029/2005GL025428.
- Lumpkin, R. and Speer, K. (2007). Global ocean meridional overturning. *Journal of Physical Oceanography*, **37**(10), 2550–2562.
- Lunt, D. J., de Noblet-Ducoudre, N., and Charbit, S. (2004). Effects of a melted greenland ice sheet on climate, vegetation, and the cryosphere. *Climate Dynamics*, **23**(7-8), 679–694.
- Lunt, D. J., Foster, G. L., Haywood, A. M., and Stone, E. J. (2008). Late Pliocene Greenland glaciation controlled by a decline in atmospheric CO<sub>2</sub> levels. *Nature*, **454**(7208), 1102–1105.
- Lunt, D. J., Haywood, A. M., Foster, G. L., and Stone, E. J. (2009). The Arctic cryosphere in the Mid-Pliocene and the future. *Philosophical Transactions of the Royal Society a-Mathematical Physical and Engineering Sciences*, **367**(1886), 49–67.
- Luthi, D., Le Floch, M., Bereiter, B., Blunier, T., Barnola, J. M., Siegenthaler, U., Raynaud, D., Jouzel, J., Fischer, H., Kawamura, K., and Stocker, T. F. (2008). High-resolution carbon dioxide concentration record 650,000–800,000 years before present. *Nature*, **453**(7193), 379–382.

- Lynnerup, N., Arneborg, J., Heinemeier, J., and Nelson, E. (2009). The Greenland Norse: Large Scale Climate Changes to a Small Scale Society. *IOP Conference Series: Earth and Environmental Science*, **6**(072041), doi: 10.1088/1755-1307/6/7/072041.
- Lythe, M. B., Vaughan, D. G., and Consortium, B. a. (2001). BEDMAP: A new ice thickness and subglacial topographic model of Antarctica. *Journal of Geophysical Research-Solid Earth*, **106**(B6), 11335–11351.
- Macdonald, G. M., Edwards, T. W. D., Moser, K. A., Pienitz, R., and Smol, J. P. (1993). Rapid Response of Treeline Vegetation and Lakes to Past Climate Warming. *Nature*, **361**(6409), 243–246.
- Marshall, S. J. and Clarke, G. K. C. (1999). Ice sheet inception: subgrid hypsometric parameterization of mass balance in an ice sheet model. *Climate Dynamics*, **15**(7), 533–550.
- Mason, P. J. (1988). The Formation of Areally-Averaged Roughness Lengths. *Quarterly Journal of the Royal Meteorological Society*, **114**(480), 399–420.
- McKay, M. D., Beckman, R. J., and Conover, W. J. (1979). A Comparison of Three Methods for Selecting Values of Input Variables in the Analysis of Output from a Computer Code. *Technometrics*, **21**(2), 239–245.
- McPherson, R. A. (2007). A review of vegetation-atmosphere interactions and their influences on mesoscale phenomena. *Progress in Physical Geography*, **31**(3), 261–285.
- Meehl, G. A., Covey, C., Delworth, T., Latif, M., McAvaney, B., Mitchell, J. F. B., Stouffer, R. J., and Taylor, K. E. (2007). The WCRP CMIP3 multimodel dataset - A new era in climate change research. *Bulletin of the American Meteorological Society*, **88**(9), 1383–1394.
- Meissner, K. J., Weaver, A. J., Matthews, H. D., and Cox, P. M. (2003). The role of land surface dynamics in glacial inception: a study with the UVic Earth System Model. *Climate Dynamics*, **21**(7-8), 515–537.
- Mikolajewicz, U., Groger, M., Maier-Reimer, E., Schurgers, G., Vizcaino, M., and Winguth, A. M. E. (2007). Long-term effects of anthropogenic CO<sub>2</sub> emissions

- simulated with a complex earth system model. *Climate Dynamics*, **28**(6), 599–631.
- Milankovitch, M. (1941). *Kanon der Erdbestrahlungen und seine Anwendung auf das Eiszeitenproblem Belgrade. (English translation Canon of Insolation and the Ice-Age Problem)*. Israel Program for Scientific Translations, 1969, Jerusalem.
- Milton, S. F. and Wilson, C. A. (1996). The Impact of Parameterized Subgrid-scale Orographic Forcing on Systematic Errors in a Global NWP Model. *Monthly Weather Review*, **124**(9), 2023–2045.
- Montoya, M., von Storch, H., and Crowley, T. J. (2000). Climate simulation for 125 kyr BP with a coupled ocean-atmosphere general circulation model. *Journal of Climate*, **13**(6), 1057–1072.
- Mosby, H. (1962). Water, salt and heat balance of the North Polar Sea and the of the Norwegian Sea. *Geofysiske Publikasjoner (Geophysica Norvegica)*, **24**, 289313.
- Muhs, D. R., Ager, T. A., and Beget, J. E. (2001). Vegetation and paleoclimate of the last interglacial period, central Alaska. *Quaternary Science Reviews*, **20**(1-3), 41–61.
- Muhs, D. R., Simmons, K. R., and Steinke, B. (2002). Timing and warmth of the Last Interglacial period: new U-series evidence from Hawaii and Bermuda and a new fossil compilation for North America. *Quaternary Science Reviews*, **21**(12-13), 1355–1383.
- Murphy, B. F., Marsiat, I., and Valdes, P. J. (2002). Atmospheric contributions to the surface mass balance of Greenland in the HadAM3 atmospheric model. *Journal of Geophysical Research*, **107**(D21), 4556, doi:10.1029/2001JD000389.
- Murphy, C., Fealy, R., Charlton, R., and Sweeney, J. (2006). The reliability of an ‘off-the-shelf’ conceptual rainfall runoff model for use in climate impact assessment: uncertainty quantification using Latin hypercube sampling. *Area*, **38**(1), 65–78.
- Ohmura, A. (1987). New temperature distribution maps for Greenland. *Zeitschrift für Gletschertkunde und Glazialgeologie*, **23**(1), 1–45.

- Ohmura, A. and Reeh, N. (1991). New Precipitation and Accumulation Maps for Greenland. *Journal of Glaciology*, **37**(125), 140–148.
- Oppenheimer, M. and Alley, R. B. (2005). Ice sheets, global warming, and Article 2 of the UNFCCC. *Climatic Change*, **68**(3), 257–267.
- Otterman, J., Chou, M. D., and Arking, A. (1984). Effects of Nontropical Forest Cover on Climate. *Journal of Climate and Applied Meteorology*, **23**(5), 762–767.
- Otto-Bliesner, B. L., Marsha, S. J., Overpeck, J. T., Miller, G. H., Hu, A. X., and Mem, C. L. I. P. a. (2006a). Simulating Arctic Climate Warmth and Icefield Retreat in the Last Interglaciation. *Science*, **311**(5768), 1751–1753.
- Otto-Bliesner, B. L., Marshall, S. J., Overpeck, J. T., Miller, G. H., Hu, A. X., and members, C. L. I. P. (2006b). Supporting Online Material for: Simulating Arctic Climate Warmth and Icefield Retreat in the Last interglaciation. *Science Online*, **311**(1751), doi:0.1126/science.1120808.
- Overpeck, J. T., Otto-Bliesner, B. L., Miller, G. H., Muhs, D. R., Alley, R. B., and Kiehl, J. T. (2006). Paleoclimatic evidence for future ice-sheet instability and rapid sea-level rise. *Science*, **311**(5768), 1747–1750.
- Pacanowski, R. C. and Philander, S. G. H. (1981). Parameterization of Vertical Mixing in Numerical-Models of Tropical Oceans. *Journal of Physical Oceanography*, **11**(11), 1443–1451.
- Parizek, B. R. and Alley, R. B. (2004). Implications of increased Greenland surface melt under global-warming scenarios: ice-sheet simulations. *Quaternary Science Reviews*, **23**(9-10), 1013–1027.
- Pattyn, F. (2003). A new three-dimensional higher-order thermomechanical ice sheet model: Basic sensitivity, ice stream development, and ice flow across subglacial lakes. *Journal of Geophysical Research-Solid Earth*, **108**(B8), doi:10.1029/2002JB002329.
- Pattyn, F., Huyghe, A., De Brabander, S., and De Smedt, B. (2006). Role of transition zones in marine ice sheet dynamics. *Journal of Geophysical Research-Earth Surface*, **111**(F2), doi:10.1029/2005JF000394.

- Payne, A. and Sugden, D. (1990). Topography and Ice-Sheet Growth. *Earth Surface Processes and Landforms*, **15**(7), 625–639.
- Payne, A. J. (1999). A thermomechanical model of ice flow in West Antarctica. *Climate Dynamics*, **15**(2), 115–125.
- Peixoto, J. P. and Oort, A. H. (1992). *Physics of Climate*. Springer, New York, 1st edition.
- Pépin, L., Raynaud, D., Barnola, J. M., and Loutre, M. F. (2001). Hemispheric roles of climate forcings during glacial-interglacial transitions as deduced from the Vostok record and LLN-2D model experiments. *Journal of Geophysical Research-Atmospheres*, **106**(D23), 31885–31892.
- Petersen, G. N., Kristjansson, J. E., and Olafsson, H. (2004). Numerical simulations of Greenland's impact on the Northern Hemisphere winter circulation. *Tellus Series a-Dynamic Meteorology and Oceanography*, **56**(2), 102–111.
- Petit, J. R., Jouzel, J., Raynaud, D., Barkov, N. I., Barnola, J. M., Basile, I., Bender, M., Chappellaz, J., Davis, M., Delaygue, G., Delmotte, M., Kotlyakov, V. M., Legrand, M., Lipenkov, V. Y., Lorius, C., Pepin, L., Ritz, C., Saltzman, E., and Stievenard, M. (1999). Climate and atmospheric history of the past 420,000 years from the Vostok ice core, Antarctica. *Nature*, **399**(6735), 429–436.
- Pollard, D. and DeConto, R. M. (2009). Modelling West Antarctic ice sheet growth and collapse through the past five million years. *Nature*, **458**(7236), 329–U89.
- Pollard, D. and Thompson, S. L. (1997). Driving a high-resolution dynamic ice sheet model with GCM climate: ice-sheet initiation at 116,000BP. *Annals of Glaciology*, **25**, 296–304.
- Pope, V. D., Gallani, M. L., Rowntree, P. R., and Stratton, R. A. (2000). The impact of new physical parametrizations in the Hadley Centre climate model: HadAM3. *Climate Dynamics*, **16**(2-3), 123–146.
- Price, S. F., Conway, H., Waddington, E. D., and Bindschadler, R. A. (2008). Model investigations of inland migration of fast-flowing outlet glaciers and ice streams. *Journal of Glaciology*, **54**(184), 49–60.



- Randall, D. A., Wood, R. A., Bony, S., Colman, R., Fichefet, T., Fyfe, J., Kattsov, V., Pitman, A., Shukla, J., Srinivasan, J., Stouffer, R. J., Sumi, A., and Taylor, K. E. (2007). Climate Models and Their Evaluation. In S. D. Solomon, Q. M. Manning, Z. Chen, M. Marquis, K. B. Averyt, M. Tignor, and H. L. Miller, editors, *Climate Change 2007: The Physical Science Basis. Contribution of Working Group I to the Fourth Assessment Report of the Intergovernmental Panel on Climate Change*, pages 589–662. Cambridge University Press, Cambridge, United Kingdom and New York, NY, USA.
- Raynaud, D., Chappellaz, J., Ritz, C., and Martinerie, P. (1997). Air content along the Greenland Ice Core Project core: A record of surface climatic parameters and elevation in central Greenland. *Journal of Geophysical Research-Oceans*, **102**(C12), 26607–26613.
- Rayner, N. A., Parker, D. E., Horton, E. B., Folland, C. K., Alexander, L. V., Rowell, D. P., Kent, E. C., and Kaplan, A. (2003). Global analyses of sea surface temperature, sea ice, and night marine air temperature since the late nineteenth century. *Journal of Geophysical Research-Atmospheres*, **108**(D14), doi:10.1029/2002JD002670.
- Reeh, N. (1991). Parameterization of melt rate and surface temperature on the Greenland ice sheet. *Polarforschung*, **59**(3), 113–128.
- Ridley, J. K., Huybrechts, P., Gregory, J. M., and Lowe, J. A. (2005). Elimination of the Greenland ice sheet in a high CO<sub>2</sub> climate. *Journal of Climate*, **18**(17), 3409–3427.
- Rignot, E. and Kanagaratnam, P. (2006). Changes in the velocity structure of the Greenland ice sheet. *Science*, **311**(5763), 986–990.
- Rignot, E., Box, J. E., Burgess, E., and Hanna, E. (2008). Mass balance of the Greenland ice sheet from 1958 to 2007. *Geophysical Research Letters*, **35**(20), doi:10.1029/2008GL035417.
- Ritz, C. (1987). Time dependent boundary conditions for calculation of temperature fields in ice sheets. In ., editor, *The Physical Basis of Ice Sheet Modelling*, volume 170, pages 207–216. International Association of Hydrological Sciences Publ.

- Ritz, C., Fabre, A., and Letreguilly, A. (1997). Sensitivity of a Greenland ice sheet model to ice flow and ablation parameters: Consequences for the evolution through the last climatic cycle. *Climate Dynamics*, **13**(1), 11–24.
- Rostami, K., Peltier, W. R., and Mangini, A. (2000). Quaternary marine terraces, sea-level changes and uplift history of Patagonia, Argentina: comparisons with predictions of the ICE-4G (VM2) model of the global process of glacial isostatic adjustment. *Quaternary Science Reviews*, **19**(14-15), 1495–1525.
- Ruddiman, W. F. (1989). Forcing of Late Cenozoic Northern Hemisphere climate by plateau uplift in southern Asia and the American West. *Journal of Geophysical Research*, **94**, 18409–18427.
- Ruddiman, W. F. (2001). *Earth's Climate Past and Future*. W.H. Freeman and Company, New York, reprint edition.
- Rutt, I. C., Hagdorn, M., Hulton, N. R. J., and Payne, A. J. (2009). The Glimmer community ice sheet model. *Journal of Geophysical Research-Earth Surface*, **114**(F02004), doi:10.1029/2008JF001015.
- Salzmann, U., Haywood, A. M., Lunt, D. J., Valdes, P. J., and Hill, D. J. (2008). A new global biome reconstruction and data-model comparison for the Middle Pliocene. *Global Ecology and Biogeography*, **17**(3), 432–447.
- Scherer, R. P., Aldahan, A., Tulaczyk, S., Possnert, G., Engelhardt, H., and Kamb, B. (1998). Pleistocene collapse of the West Antarctic ice sheet. *Science*, **281**(5373), 82–85.
- Schneider von Deimling, T., Held, H., Ganopolski, A., and Rahmstorf, S. (2006). Climate sensitivity estimated from ensemble simulations of glacial climate. *Climate Dynamics*, **27**(2-3), 149–163.
- Schoof, C. (2006). A variational approach to ice stream flow. *Journal of Fluid Mechanics*, **556**, 227–251.
- Schoof, C. (2007). Ice sheet grounding line dynamics: Steady states, stability, and hysteresis. *Journal of Geophysical Research-Earth Surface*, **112**(F3), doi:10.1029/2006JF000664.

- Schurgers, G., Mikolajewicz, U., Groger, M., Maier-Reimer, E., Vizcaino, M., and Winguth, A. (2007). The effect of land surface changes on Eemian climate. *Climate Dynamics*, **29**(4), 357–373.
- Semtner, A. J. (1976). A Model for Thermodynamic Growth of Sea Ice in Numerical Investigations of Climate. *Journal of Physical Oceanography*, **6**(3), 379–389.
- Serreze, M. C. and Barry, R. G. (2005). *The Arctic Climate System*. Cambridge University Press, Cambridge, first edition.
- Serreze, M. C. and Hurst, C. M. (2000). Representation of mean Arctic precipitation from NCEP-NCAR and ERA reanalyses. *Journal of Climate*, **13**(1), 182–201.
- Serreze, M. C., Carse, F., Barry, R. G., and Rogers, J. C. (1997). Icelandic Low Cyclone Activity: Climatological Features, Linkages with the NAO, and Relationships with Recent Changes in the Northern Hemisphere Circulation. *Journal of Climate*, **10**(3), 453–464.
- Serreze, M. C., Barrett, Andrew, P., and Lo, F. (2005). Northern High-Latitude Precipitation as Depicted by Atmospheric Reanalyses and Satellite Retrievals. *Monthly Weather Review*, **133**(12), 3407–3430.
- Shapiro, N. M. and Ritzwoller, M. H. (2004). Inferring surface heat flux distributions guided by a global seismic model: particular application to Antarctica. *Earth and Planetary Science Letters*, **223**(1-2), 213–224.
- Shaver, G. R. and S., J. (1999). Response of Arctic ecosystems to climate change: results of long-term field experiments in Sweden and Alaska. *Polar Research*, **18**, 245–252.
- Shaver, G. R., Bret-Harte, S. M., Jones, M. H., Johnstone, J., Gough, L., Laundre, J., and Chapin, F. S. (2001). Species composition interacts with fertilizer to control long-term change in tundra productivity. *Ecology*, **82**(11), 3163–3181.
- Shuman, B., Bartlein, P., Logar, N., Newby, P., and Webb, T. (2002). Parallel climate and vegetation responses to the early Holocene collapse of the Laurentide Ice Sheet. *Quaternary Science Reviews*, **21**(16-17), 1793–1805.

- Siddall, M., Chappell, J., and Potter, E.-K. (2007). Eustatic Sea level During Past Interglacials. In F. Sirocko, M. Claussen, T. Litt, and M. Sánchez-Gōni, editors, *The Climate of Past Interglacials*, 7, Development in Quaternary Science, 7, pages 75–92. Elsevier, Oxford, 1st edition.
- Sitch, S., Smith, B., Prentice, I. C., Arneth, A., Bondeau, A., Cramer, W., Kaplan, J. O., Levis, S., Lucht, W., Sykes, M. T., Thonicke, K., and Venevsky, S. (2003). Evaluation of ecosystem dynamics, plant geography and terrestrial carbon cycling in the LPJ dynamic global vegetation model. *Global Change Biology*, **9**(2), 161–185.
- Slowey, N. C., Henderson, G. M., and Curry, W. B. (1996). Direct U-Th dating of marine sediments from the two most recent interglacial periods. *Nature*, **383**(6597), 242–244.
- Smethie, W. M. and Fine, R. (2001). Rates of North Atlantic Deep Water formation calculated from chlorofluorocarbon inventories. *Deep-Sea Research Part 1*, **48**, 189–215.
- Soucek, O. and Martinec, Z. (2008). Iterative improvement of the shallow-ice approximation. *Journal of Glaciology*, **54**(188), 812–822.
- Stearns, L. A. and Hamilton, G. S. (2007). Rapid volume loss from two East Greenland outlet glaciers quantified using repeat stereo satellite imagery. *Geophysical Research Letters*, **34**(L05503), doi:10.1029/2006GL028982.
- Steffen, K. and Box, J. (2001). Surface climatology of the Greenland ice sheet: Greenland Climate Network 1995-1999. *Journal of Geophysical Research*, **106**(D24), 33951–33964.
- Stirling, C. H., Esat, T. M., McCulloch, M. T., and Lambeck, K. (1995). High-Precision U-Series Dating of Corals from Western-Australia and Implications for the Timing and Duration of the Last Interglacial. *Earth and Planetary Science Letters*, **135**(1-4), 115–130.
- Stirling, C. H., Esat, T. M., Lambeck, K., and McCulloch, M. T. (1998). Timing and duration of the Last Interglacial: evidence for a restricted interval of widespread coral reef growth. *Earth and Planetary Science Letters*, **160**(3-4), 745–762.

- Stone, E. J., Lunt, D. J., Rutt, I. C., and Hanna, E. (2010). The effect of more realistic forcings and boundary conditions on the modelled geometry and sensitivity of the Greenland ice-sheet. *The Cryosphere Discussions*, **4**, 233–285.
- Szabo, B. J., Ludwig, K. R., Muhs, D. R., and Simmons, K. R. (1994). Th-230 Ages of Corals and Duration of the Last Interglacial Sea-Level High Stand on Oahu, Hawaii. *Science*, **266**(5182), 93–96.
- Talley, L. D., Reid, J. L., and Robbins, P. E. (2003). Data-Based Meridional Overturning Streamfunctions for the Global Ocean. *Journal of Climate*, **16**(19), 3213–3226.
- Tarasov, L. and Peltier, W. R. (2003). Greenland glacial history, borehole constraints, and Eemian extent. *Journal of Geophysical Research-Solid Earth*, **108**(B3), doi:10.1029/2001JB001731.
- Tarnocai, C. (1989). Arctic Canada (soils of Canada). In R. J. Fulton, editor, *Quaternary Geology of Canada and Greenland*, volume no.1, Geology of Canada, pages 675–676. Geological Survey of Canada, Ottawa.
- TEMPO (1996). Potential role of vegetation feedback in the climate sensitivity of high-latitude regions: A case study at 6000 years B.P. *Global Biogeochemical Cycles*, **10**(4), 727–736.
- Thompson, W. G. and Goldstein, S. L. (2005). Open-system coral ages reveal persistent suborbital sea-level cycles. *Science*, **308**(5720), 401–404.
- Toniazzo, T., Gregory, J. M., and Huybrechts, P. (2004). Climatic impact of a Greenland deglaciation and its possible irreversibility. *Journal of Climate*, **17**(1), 21–33.
- Uppala, S., Kallberg, P., Simmons, A., Andrae, U., Da Costa Bechtold, V., Fiorino, M., Gibson, K., Haseler, J., Hernandez, A., Kelly, G., Li, X., Onogi, K., Saarinen, S., Sokka, N., Allan, R., Andersson, E., Arpe, K., Balmaseda, M., Beljaars, A., Van de Berg, L., Bidlot, J., Bormann, N., Caires, S., Chevallier, F., Dethof, A., Dragosavac, M., Fisher, M., Fuentes, M., Hagemann, S., Holm, E., Hoskins, B. J., Isaksen, L., Janssen, P., Jenne, R., McNally, A., Mahfouf, J.-F., Morcrette, J., J., Rayner, N., Saunders, R., Simon, P., Sterl, A., Trenberth, K., Untch, A.,

- Vasiljevic, D., Viterbo, P., and Woollen, J. (2005). The ERA-40 re-analysis. *Quarterly Journal of the Royal Meteorological Society*, **131**(612), 2961–3013.
- Van de Wal, R. S. W. and Oerlemans, J. (1994). An Energy-Balance Model for the Greenland Ice-Sheet. *Global and Planetary Change*, **9**(1-2), 115–131.
- Van den Broeke, M. (2008). Partitioning of melt energy and meltwater fluxes in the ablation zone of the west Greenland ice sheet. *The Cryosphere*, **2**, 179–189.
- Van den Broeke, M., Bamber, J., Ettema, J., Rignot, E., Schrama, E., Jan van de Berg, W., Van Meijgaard, E., Velicogna, I., and Wouters, B. (2009). Partitioning Recent Greenland mass Loss. *Science*, **326**, 984–986.
- Van der Veen, C. J. and Payne, A. J. (2004). Modelling land-ice dynamics. In J. Bamber and A. Payne, editors, *Mass Balance of the Cryosphere Observations and Modelling of Contemporary and Future Changes*, pages 169–219. Cambridge University Press, Cambridge UK, first edition.
- Velicogna, I. (2009). Increasing rates of ice mass loss from the Greenland and Antarctic ice sheets revealed by GRACE. *Geophysical Research Letters*, **36**, doi:10.1029/2009GL040222.
- Velicogna, I. and Wahr, J. (2006). Acceleration of Greenland ice mass loss in spring 2004. *Nature*, **443**(7109), 329–331.
- Vizcaíno, M., Milkolajewicz, U., Groger, M., Maier-reimer, E., Schurgers, G., and Winguth, A. M. E. (2008). Long-term ice sheet-climate interactions under anthropogenic greenhouse forcing simulated with a complex Earth System Model. *Climate Dynamics*, **31**(6), 665690, doi:10.1007/s00382-008-0369-7.
- Wang, Z. M., Cochelin, A. S. B., Mysak, L. A., and Wang, Y. (2005). Simulation of the last glacial inception with the green McGill Paleoclimate Model. *Geophysical Research Letters*, **32**(12), 24203.
- Wara, M. W., Ravelo, A. C., and Delaney, M. L. (2005). Permanent El Nino-like conditions during the Pliocene warm period. *Science*, **309**(5735), 758–761.
- Webster, S. (2003). Orography ancillary file creation. *Unified Model Documentation Paper No. 74*, pages 1–6.

- Wetterich, S., Schirrmeister, L., Andreev, A. A., Pudenz, M., Plessen, B., Meyer, H., and Kunitsky, V. V. (2009). Eemian and Late Glacial/Holocene palaeoenvironmental records from permafrost sequences at the Dmitry Laptev Strait (NE Siberia, Russia). *Palaeogeography Palaeoclimatology Palaeoecology*, **279**(1-2), 73–95.
- Willerslev, E., Cappellini, E., Boomsma, W., Nielsen, R., Hebsgaard, M. B., Brand, T. B., Hofreiter, M., Bunce, M., Poinar, H. N., Dahl-Jensen, D., Johnsen, S., Steffensen, J. P., Bennike, O., Schwenninger, J. L., Nathan, R., Armitage, S., de Hoog, C. J., Alfimov, V., Christl, M., Beer, J., Muscheler, R., Barker, J., Sharp, M., Penkman, K. E. H., Haile, J., Taberlet, P., Gilbert, M. T. P., Casoli, A., Campani, E., and Collins, M. J. (2007a). Ancient biomolecules from deep ice cores reveal a forested Southern Greenland. *Science*, **317**(5834), 111–114.
- Willerslev, E., Cappellini, E., Boomsma, W., Nielsen, R., Hebsgaard, M. B., Brand, T. B., Hofreiter, M., Bunce, M., Poinar, H. N., Dahl-Jensen, D., Johnsen, S., Steffensen, J. P., Bennike, O., Schwenninger, J. L., Nathan, R., Armitage, S., de Hoog, C. J., Alfimov, V., Christl, M., Beer, J., Muscheler, R., Barker, J., Sharp, M., Penkman, K. E. H., Haile, J., Taberlet, P., Gilbert, M. T. P., Casoli, A., Campani, E., and Collins, M. J. (2007b). Supporting Online Material for Ancient Biomolecules from Deep Ice Cores Reveal a Forested Southern Greenland. *Science*, **317**(111), doi:10.1126/science.1141758.
- Wramneby, A., Smith, B., Zaehle, S., and Sykes, M. T. (2008). Parameter uncertainties in the modelling of vegetation dynamics - Effects on tree community structure and ecosystem functioning in European forest biomes. *Ecological Modelling*, **216**(3-4), 277–290.
- Yang, D. Q. (1999). An improved precipitation climatology for the Arctic Ocean. *Geophysical Research Letters*, **26**(11), 1625–1628.
- Zwally, H. J., Giovinetto, M. B., Li, J., Cornejo, H. G., Beckley, M. A., Brenner, A. C., Saba, J. L., and Yi, D. (2005). Mass changes of the Greenland and Antarctic ice sheets and shelves and contributions to sea-level rise: 1992-2002. *Journal of Glaciology*, **51**(175), 509–527.